ORTHOGONAL LINKER CHEMISTRIES APPLIED IN CORE-CROSSLINKED POLYMERIC MICELLES

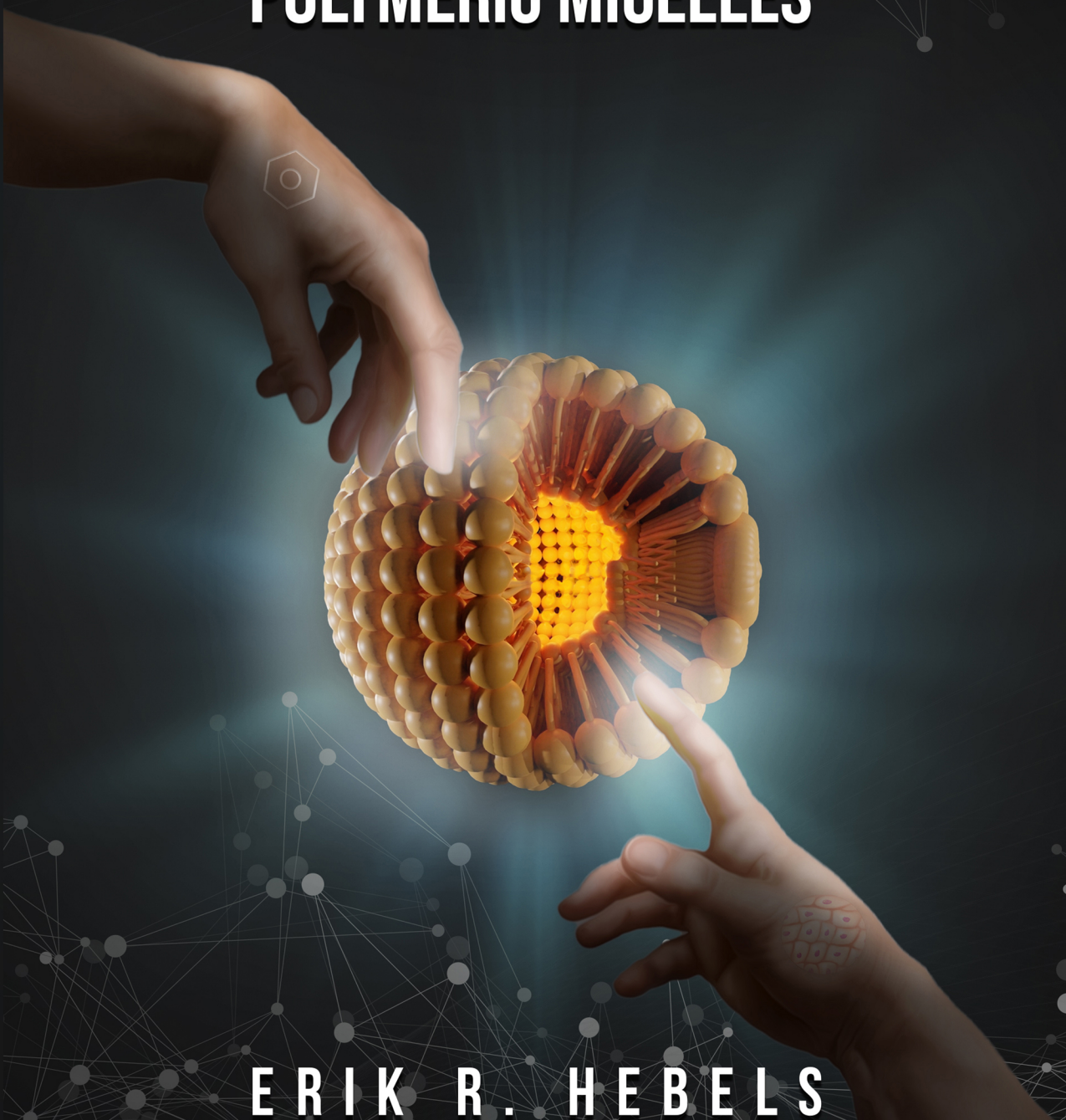

ERIK R. HEBELS

Orthogonal linker chemistries applied in core-crosslinked polymeric micelles

Erik R. Hebels

Author: Erik R. Hebels
Cover Design: Erik R. Hebels (conceptualization) and Xee Shan (graphic design work)
Printed by: Ridderprint

The printing of this thesis was financially supported by:
Utrecht Institute for Pharmaceutical Sciences (UIPS)
Cristal Therapeutics
Annemarie Hebels
ABN AMRO

ISBN: 978-94-6483-943-2

Orthogonal linker chemistries applied in core-crosslinked polymeric micelles

Orthogonale linkerchemie toegepast in polymere micellen

(met een samenvatting in het Nederlands)

Proefschrift

ter verkrijging van de graad van doctor aan de
Universiteit Utrecht
op gezag van de
rector magnificus, prof. dr. H.R.B.M. Kummeling,
ingevolge het besluit van het college voor promoties in het openbaar te verdedigen op
maandag 15 april 2024 des middags te 12.15 uur

door

Erik Reinhard Hebels

geboren op 26 mei 1995
te Seremban, Maleisië

Promotoren:
Prof. dr. ir. T. Vermonden
Prof. dr. ir. W.E. Hennink

Copromotor:
Dr. C.J.F. Rijcken

Beoordelingscommissie:
Prof. dr. M. Barz
Prof. dr. A. Meijerink
Dr. C.F. van Nostrum
Dr. ir. J.M.J. Paulusse
Prof. dr. M.J. Vicent

Dit proefschrift werd (mede) mogelijk gemaakt met financiële steun van de Nederlandse Organisatie voor Wetenschappelijk Onderzoek, NWO (NWA.ID.17.030) en Cristal Therapeutics.

“We are just going to do it.”

To my Family

Table of contents

CHAPTER 1

General Introduction

Nanocarriers

The field of nanomedicines concerns with the application of carriers with sizes ranging from 10-200 nm to develop drug products for the diagnosis and treatment of diseases. The main aims when formulating active pharmaceutical ingredients (APIs) into nanocarriers include enhancement of solubility, improvement of drug stability and facilitating targeted and controlled release, thereby enhancing therapeutics effects and reducing adverse events as compared to APIs administered in their free form. The type of nanocarriers employed to date can generally be classified into liposomes, lipid nanoparticles, antibody-drug conjugates, inorganic nanoparticles, polymer nanoparticles, dendrimers, micelles, polymer-drug conjugates, virus-derived vectors, nanocrystals, cell-derived carriers (such as exosomes) and protein-based nanoparticles (such as albumin systems) amongst others. [1] Being an emerging drug product class, there are currently around 100 nanomedicine classified drug products on the market with another 563 under clinical development, primarily focusing on applications in oncology among various other indications. [2] In context, there are over 20.000 prescription drug products currently approved for marketing by the food and drug administration (FDA). [3] The most well-known and recent examples of the application of nanocarriers are the mRNA COVID-19 vaccines developed by Moderna and Pfizer/BioNTech. [4] Both are examples of lipid based nanocarriers, the most prevalent category (33%) of nanomedicines accessible on the market or in various clinical stages. [2]

Among the above mentioned nanocarrier platforms, polymer based carriers and polymer-drug conjugates have attracted considerable attention (20% of nanomedicines accessible on the market or in various clinical stages). [2] An attractive feature in the polymer based nanomedicines class is that by modulating the chemical structure and/or physical structural assembly of the polymer building blocks, the properties of a nanocarrier can be broadly tuned. This unique feature of polymer based nanomedicines offers high chemical versatility as compared to lipid based nanomedicines which also facilitates manifold opportunities towards covalent conjugation of drug cargos as exemplified by polymer-drug conjugates. Additionally, exploiting suitable release linker chemistry, such as in polymer-drug conjugates, also offers control over release adding an additional dimension towards controlled and targeted therapy.

Core-crosslinked polymeric micelles

Polymeric micelles (PMs) represent a class of polymer based nanomedicines. [1,5,6] PMs are typically composed of diblock copolymers that are amphiphilic, meaning

a hydrophobic block that constitutes the PM core and a hydrophilic block forming a shell in aqueous environment. Polyethylene glycol (PEG) is widely employed as a hydrophilic block. As for the hydrophobic clock, thermosensitive polymers such as poly(*N*-isopropylacrylamide) [7,8] and poly(*N*-2-hydroxypropyl methacrylamide-lactate) (pHPMAmLac$_n$) [9] possess the ability to switch from a hydrated to a dehydrated state upon surpassing a certain temperature. This phenomenon is typically referred to as the lower critical solution temperature (LCST). [10] Hence, a diblock copolymer consisting of a PEG block and either a PNIPAM or PHPMAmLac$_n$ block in aqueous, organic solvent free, solution self-assembles into a PM state simply by surpassing a certain temperature (referred to as the critical micellization temperature (CMT, mostly equals the LCST)) at polymer concentrations above the so called critical micellization concentration (CMC). Furthermore, unlike PNIPAM, polymers based on PHPMAmLac$_n$ can hydrolyze under physiological conditions to form hydrophilic pHPMA chains and lactic acid. [11]

Although PMs show tremendous capability in the solubilization of hydrophobic APIs without further modification, the dynamic equilibrium between unimers and the PM state (i.e. micellization is reversible) limits their stability when administered *in vivo*. In order to trap PMs in their assembled state, covalent crosslinking of the micellar core can be employed as an effective method. In doing so, core-crosslinked polymeric micelles (CCPMs) are used which have significantly prolonged circulation time following administration compared to non-crosslinked PMs. [12] This increased circulation time is essential for increasing the accumulation of CCPMs in the tissues of interest, such as tumors, through a phenomenon referred to as the enhanced permeability and retention (EPR) effect. [13] Finally, to prevent premature leakage of physically loaded API from the CCPMs, covalent entrapment (or conjugation) also presents a useful tool to improve drug retention in the micelles, for which target relevant triggered release chemistry is increasingly pursued to achieve therapeutic successes (see figure 1). [14–18]

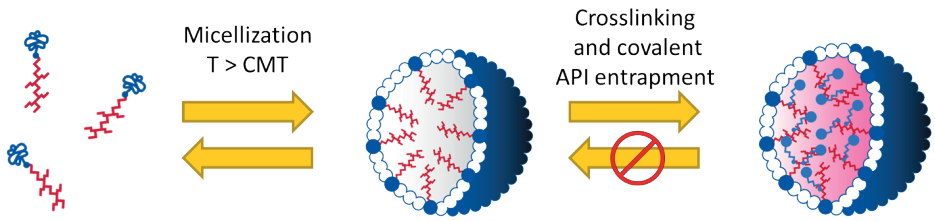

Figure 1: Micellization of thermosensitive block copolymers above their CMT (which is reversible) followed by crosslinking which prevents disassembly into the unimers state, also below the CMT. Additionally, covalent entrapment of the API prevents leakage from the CCPMs.

Core-crosslinking chemistry

Given the chemical versatility of polymers, a variable toolbox for the stabilization of PMs via core-crosslinking is possible. [19] Crosslinking of PMs has been carried out using diverse chemistries including radical polymerization [20,21], copper-catalyzed click chemistry [22,23], *N*-acryloxysuccinimide with amine coupling [24], bis-benzophenone mediated photo-cross-linking [25], diels-alder reaction [26], disulfide exchange [27,28] and thiol oxidation [29] amongst several others. In the case of methoxy poly(ethylene glycol)-b-poly[N-(2-hydroxypropyl) methacrylamide-lactate]) (mPEG-*b*-pHPMAmLac$_n$) polymers, functionalization of the thermosensitive block with methacrylic acid (mPEG-*b*-pHPMAmLac$_n$-MA) allows for core-crosslinking via a free radical polymerization approach following temperature induced PM formation in aqueous conditions. [30] Although an effective crosslinking tool, the nature of free radical chemistry limits the type of API cargo that can be present during the crosslinking reaction to relatively simple small molecules such as chemotherapeutics. Another interesting crosslinking approach has previously been applied in the case of PEG-PNIPAM based copolymers, where side chains with either cysteine residues or thioester residues were incorporated to achieve crosslinking via native chemical ligation (NCL). [31]

Native chemical ligation

Native chemical ligation (NCL), introduced by Kent and coworkers in 1994, is a mild bio-orthogonal reaction between a *N*-terminal cysteine residue and a thioester that readily proceeds under physiological conditions. [32,33] The initial nucleophilic attack onto the thioester is carried out by the thiol on cysteine and referred to as a trans-thioesterification, which is reversible (see figure 2). This intermediate then rapidly and spontaneously rearranges through an intramolecular *S*, *N*-acyl shift resulting in the formation of a physiologically irreversible amide or peptide bond. Given this 2-step mechanism, NCL reactions are both chemo- and regio-selective (which is typically referred to as “orthogonal”) and have therefore been primarily employed in peptide-peptide ligations to synthesize entire proteins. [34] In recent years, NCL has also been shown to be a powerful ligation tool in polymer conjugation applications including copolymer synthesis, micelle core-crosslinking and crosslinking of hydrophilic polymers to obtain hydrogels. [31,35,36] In addition, the reaction between cysteine and an oxo-ester (activated ester) resulting in an NCL type reaction has also been described, further expanding the ligation toolbox. [37]

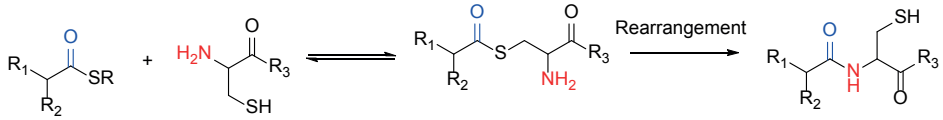

Figure 2: Mechanism of NCL starting from a thioester and an N-terminal cysteine residue, resulting in an amide bond.

Chemistry to enable triggered drug release

As mentioned above, the covalent attachment of API cargo to nanocarriers such as CCPMs is essential to ensure drug retention following *in vivo* administration. Importantly, an API also has to be released (ideally at the target site) to exert pharmacological effects which is where releasable linker chemistry plays a crucial role. One example is the aforementioned mPEG-*b*-pHPMAmLac$_n$-MA CCPM system, which has employed a methacrylated hydrolysable linker to covalently link the chemotherapeutic docetaxel that is sustainably released under physiological conditions due to hydrolysis. [38] The promising stability and releasability of this platform even allowed for its clinical evaluation. [39] There is, however, incentive to truly "trigger" the release of APIs more specifically at the target site of interest and not solely rely on the passive accumulation of CCPMs within the tumor and subsequent sustained release of APIs due to ester hydrolysis in time.

One way of achieving site selective API release is through light triggered release for laser guided therapy. A interesting type of materials to achieve such properties are gold nanoclusters (AuNCs). AuNCs are ligand stabilized gold structures in the sub 2 nm size range with photo-thermal and fluorescent properties and have previously been employed for the localized controlled delivery of doxorubicin. [40] Given their fluorescent properties, gold nanoclusters also offer opportunities for imaging and diagnostic purposes, extending the interest as tools within nanocarriers such as polymeric micelles. [41]

Another, more widely employed type of chemistry for triggered drug release is the use of the disulfide linkages which are sensitive to cleavage under reducing conditions found in the tumoral environment, due to the elevated concentration of glutathione. [42]

Trends in active pharmaceutical ingredients

In oncology, small molecule chemotherapeutics are most commonly used, especially for metastatic cases where surgery and radiotherapy are insufficient. [16] Nanocarriers, particularly targeted ones, are invaluable for improving tolerability and therapeutic outcomes in these cases. [43] However, over the last decades, increasingly chemically complex and fragile APIs

that are peptidic and biological in nature (beyond the classical small molecule drugs) have emerged for clinical use. Therapeutic peptides (2-50 amino acids), for example, represent an interesting class of APIs which structurally fall between small molecules and proteins with distinctive biochemical and therapeutic properties. [44] Since the introduction of solid phase peptide synthesis (SPPS) by Bruce Merrifield in 1963, [45] the chemical synthesis of peptides has been revolutionized and there are currently more than 100 therapeutic peptides approved for various indications [46] and more than 400 undergoing clinical trials. [47] Although promising, limitations often encountered by therapeutic peptides are pharmacokinetic issues such as low permeability to cell membranes, metabolic instability and short half-life due to rapid renal clearance. [47–50] Therefore, prodrug conjugates and other nanocarriers are increasingly being employed. [47,48]

Another important class of therapeutic agents are short/small interfering RNAs (siRNA). These are short, double stranded oligonucleotide sequences (about 20-25 nucleotides) that through binding to a complex called the RNA-induced silencing complex (RISC), recognizes complementary mRNA molecules resulting in cleavage and therefore in silencing the production of a relevant protein. With RNA interference having first been discovered in 1998, siRNA will become increasingly relevant in the future given the estimates that 75-85 % of the human genome is "undruggable". [51–53] Although much work has been done on improving siRNA serum stability, short circulation time and limited cellular uptake, the latter two are still lacking for which nanocarrier based solutions may play a pivotal role. [51,54–56]

Aims of this thesis

CCPMs have shown great potential in preclinical models and even clinical evaluation, with there being a continued need for the development of orthogonal linker chemistries for the crosslinking and triggered release of API cargos, also with increasing API complexity. The aim of this thesis is to expand the toolbox available to this regard:

- Implement NCL as a crosslinking tool to obtain CCPMs using two different, well described thermosensitive diblock copolymer systems, namely mPEG-PNIPAM and mPEG-pHPMAmLac$_n$.
- Study the crosslinking efficiency and stability of CCPMs formed by two different crosslinking approaches, either by using a small molecule crosslinker or with cross-reactive complementary polymers.
- Demonstrate improved compatibility of fragile compounds (therapeutic and diagnostic) with CCPMs using NCL as a crosslinking reaction.

- Assess the state of the art for the use of AuNCs in biomedical applications in diagnostic, therapeutic and theranostic capacity.
- Develop linking technologies, using light induced (AuNC based) and reduction sensitive (disulfide based) release triggers for the release of APIs.
- Apply reduction sensitive release linker technology to promising but challenging API classes, namely therapeutic peptides and siRNA, with entrapment in CCPMs.
- Keeping an eye on industrial appl icability

Thesis outline

In **chapter 2**, we address the use of the aforementioned gold nanoclusters across the biomedical field as tools for diagnostic, therapeutic and combination purposes to highlight their potential use in nanomedicines.

Following this, **chapter 3** implements gold nanoclusters into CCPMs crosslinked via oxo-ester mediated NCL using a mPEG-PNIPAM based copolymer system for the laser guided release of the chemotherapeutic doxorubicin, resulting in highly localized cancer cell killing activity *in vitro*.

Then, in **chapter 4** we transition to the formation of CCPMs via thioester mediated NCL using a biodegradable mPEG-pHPMAmLac$_n$ based copolymer system modified with thioesters and a small molecule dicysteine crosslinker. We investigate the CCPM stability as well as degradation under physiological conditions and the orthogonal click chemistry entrapment of model fragile dye compounds as well as cellular uptake of the nanoparticles *in vitro*.

Additionally, in **chapter 5** we study the effect of two crosslinking approaches using NCL on the crosslinking efficiency and degradation of mPEG-pHPMAmLac$_n$ based CCPMs. One approach resembles chapter 4, which uses a small molecule crosslinker whilst the other approach resembles chapter 3, where cross-reactive complementary polymers are employed (one polymer with cysteine and the other with thioester modifications).

Following this, in **chapter 6** we study two approaches towards loading a model peptide into CCPMs. The first follows the conventional example as employed in **chapter 4** as well, where the peptide is clicked on a crosslinker before CCPM formation. The alternative approach challenges this classical scheme and forms CCPMs first, that contain azides in the core followed by the clicking of the peptide.

With **chapter 7**, we describe a broadly applicable reduction sensitive release linker that can link an amine containing compound to an azide containing nanocarrier, which we apply to

an oncolytic therapeutic peptide via SPPS and click into pre-crosslinked CCPMs based on mPEG-pHPMAmLac$_n$ copolymers. It is aimed that the linked peptide can be released in unmodified (free amine) compound following exposure to reducing conditions.

Additionally, in **chapter 8** we further apply the technology described in **chapter 7** for the entrapment and release of amine containing and nuclease resistant siRNA to and from CCPMs, further highlighting the versatility of the platform.

Finally, **chapter 9** summarizes the results of this thesis and provides a discussion of the implications as well as future perspectives of the chemistry regarding CCPM formation, loading and release technologies described in this thesis.

References

(1) Gadekar, V.; Borade, Y.; Kannaujia, S.; Rajpoot, K.; Anup, N.; Tambe, V.; Kalia, K.; Tekade, R. K. Nanomedicines Accessible in the Market for Clinical Interventions. *J. Control. Release* **2021**, *330* (December 2020), 372–397.

(2) Shan, X.; Gong, X.; Li, J.; Wen, J.; Li, Y.; Zhang, Z. Current Approaches of Nanomedicines in the Market and Various Stage of Clinical Translation. *Acta Pharm. Sin. B* **2022**, *12* (7), 3028–3048.

(3) Fact Sheet: FDA at a Glance https://www.fda.gov/about-fda/fda-basics/fact-sheet-fda-glance#:~:text=There are over 20%2C000 prescription,different medical device product categories. (accessed 2022 -11 -04).

(4) Chung, J. Y.; Thone, M. N.; Kwon, Y. J. COVID-19 Vaccines: The Status and Perspectives in Delivery Points of View. *Adv. Drug Deliv. Rev.* **2021**, *170*, 1–25.

(5) Jones, M.-C.; Leroux, J.-C. Polymeric Micelles – a New Generation of Colloidal Drug Carriers. *Eur. J. Pharm. Biopharm.* **1999**, *48* (2), 101–111.

(6) Hwang, D.; Ramsey, J. D.; Kabanov, A. V. Polymeric Micelles for the Delivery of Poorly Soluble Drugs: From Nanoformulation to Clinical Approval. *Adv. Drug Deliv. Rev.* **2020**, *156*, 80–118.

(7) Najafi, M.; Hebels, E.; Hennink, W. E.; Vermonden, T. Poly(N -Isopropylacrylamide): Physicochemical Properties and Biomedical Applications. In *Temperature-Responsive Polymers*; John Wiley & Sons Ltd: Chichester, UK, 2018; pp 1–34.

(8) Topp, M. D. C.; Dijkstra, P. J.; Talsma, H.; Feijen, J. Thermosensitive Micelle-Forming Block Copolymers of Poly(Ethylene Glycol) and Poly(N -Isopropylacrylamide). *Macromolecules* **1997**, *30* (26), 8518–8520.

(9) Soga, O.; van Nostrum, C. F.; Ramzi, A.; Visser, T.; Soulimani, F.; Frederik, P. M.; Bomans, P. H. H.; Hennink, W. E. Physicochemical Characterization of Degradable Thermosensitive Polymeric Micelles. *Langmuir* **2004**, *20* (21), 9388–9395.

(10) Liu, R.; Fraylich, M.; Saunders, B. R. Thermoresponsive Copolymers: From Fundamental Studies to Applications. *Colloid Polym. Sci.* **2009**, *287* (6), 627–643.

(11) Soga, O.; van Nostrum, C. F.; Hennink, W. E. Poly(N -(2-Hydroxypropyl) Methacrylamide Mono/Di Lactate): A New Class of Biodegradable Polymers with Tuneable Thermosensitivity. *Biomacromolecules* **2004**, *5* (3), 818–821.

(12) Rijcken, C. J.; Snel, C. J.; Schiffelers, R. M.; van Nostrum, C. F.; Hennink, W. E. Hydrolysable Core-Crosslinked Thermosensitive Polymeric Micelles: Synthesis, Characterisation and in Vivo Studies. *Biomaterials* **2007**, *28* (36), 5581–5593.

(13) Maeda, H.; Wu, J.; Sawa, T.; Matsumura, Y.; Hori, K. Tumor Vascular Permeability and the EPR Effect in Macromolecular Therapeutics: A Review. *J. Control. Release* **2000**, *65* (1–2), 271–284.

(14) Shin, D. H.; Tam, Y. T.; Kwon, G. S. Polymeric Micelle Nanocarriers in Cancer Research. *Front. Chem. Sci. Eng.* **2016**, *10* (3), 348–359.

(15) Deng, Z.; Hu, J.; Liu, S. Disulfide-Based Self-Immolative Linkers and Functional Bioconjugates for Biological Applications. *Macromol. Rapid Commun.* **2020**, *41* (1), 1900531.

(16) Pérez-Herrero, E.; Fernández-Medarde, A. Advanced Targeted Therapies in Cancer: Drug Nanocarriers, the Future of Chemotherapy. *Eur. J. Pharm. Biopharm.* **2015**, *93*, 52–79.

(17) Varela-Moreira, A.; Shi, Y.; Fens, M. H. A. M.; Lammers, T.; Hennink, W. E.; Schiffelers, R. M. Clinical Application of Polymeric Micelles for the Treatment of Cancer. *Mater. Chem. Front.* **2017**, *1* (8), 1485–1501.

(18) Wu, Y.; Chen, W.; Meng, F.; Wang, Z.; Cheng, R.; Deng, C.; Liu, H.; Zhong, Z. Core-Crosslinked PH-Sensitive Degradable Micelles: A Promising Approach to Resolve the Extracellular Stability versus Intracellular Drug Release Dilemma. *J. Control. Release* **2012**, *164* (3), 338–345.

(19) Talelli, M.; Barz, M.; Rijcken, C. J. F.; Kiessling, F.; Hennink, W. E.; Lammers, T. Core-Crosslinked Polymeric Micelles: Principles, Preparation, Biomedical Applications and Clinical Translation. *Nano Today* **2015**, *10* (1), 93–117.

(20) Shuai, X.; Merdan, T.; Schaper, A. K.; Xi, F.; Kissel, T. Core-Cross-Linked Polymeric Micelles as Paclitaxel Carriers. *Bioconjug. Chem.* **2004**, *15* (3), 441–448.

(21) Liu, X.; Lee Miller II, A.; Waletzki, B. E.; Mamo, T. K.; Yaszemski, M. J.; Lu, L. Hydrolysable Core Crosslinked Particles for Receptor-Mediated PH-Sensitive Anticancer Drug Delivery. *New J. Chem.* **2015**, *39* (11), 8840–8847.

(22) Zhang, Z.; Yin, L.; Tu, C.; Song, Z.; Zhang, Y.; Xu, Y.; Tong, R.; Zhou, Q.; Ren, J.; Cheng, J. Redox-Responsive, Core Cross-Linked Polyester Micelles. *ACS Macro Lett.* **2013**, *2* (1), 40–44.

(23) Ma, X.; Liu, J.; Lei, L.; Yang, H.; Lei, Z. Synthesis of Light and Dual-redox Triple-stimuli-responsive Core-crosslinked Micelles as Nanocarriers for Controlled Release. *J. Appl. Polym. Sci.* **2019**, *136* (37), 47946.

(24) Zhang, J.; Jiang, X.; Zhang, Y.; Li, Y.; Liu, S. Facile Fabrication of Reversible Core Cross-Linked Micelles Possessing Thermosensitive Swellability. *Macromolecules* **2007**, *40* (25), 9125–9132.

(25) Kim, J. S.; Youk, J. H. Preparation of Core Cross-Linked Micelles Using a Photo-Cross-Linking Agent. *Polymer (Guildf).* **2009**, *50* (10), 2204–2208.

(26) Elter, J. K.; Quader, S.; Eichhorn, J.; Gottschaldt, M.; Kataoka, K.; Schacher, F. H. Core-Crosslinked Fluorescent Worm-Like Micelles for Glucose-Mediated Drug Delivery. *Biomacromolecules* **2021**, *22* (4), 1458–1471.

(27) Wei, R.; Cheng, L.; Zheng, M.; Cheng, R.; Meng, F.; Deng, C.; Zhong, Z. Reduction-Responsive Disassemblable Core-Cross-Linked Micelles Based on Poly(Ethylene Glycol)- b -Poly(N -2-Hydroxypropyl Methacrylamide)–Lipoic Acid Conjugates for Triggered Intracellular Anticancer Drug Release. *Biomacromolecules* **2012**, *13* (8), 2429–2438.

(28) Zhang, Y.; Wang, C.; Huang, Y.; Yan, H.; Liu, K. Core-Crosslinked Polymeric Micelles with High Doxorubicin Loading Capacity and Intracellular PH- and Redox-Triggered Payload Release. *Eur. Polym. J.* **2015**, *68*, 104–114.

(29) Matsumoto, S.; Christie, R. J.; Nishiyama, N.; Miyata, K.; Ishii, A.; Oba, M.; Koyama, H.; Yamasaki, Y.; Kataoka, K. Environment-Responsive Block Copolymer Micelles with a Disulfide Cross-Linked Core for Enhanced SiRNA Delivery. *Biomacromolecules* **2009**, *10* (1), 119–127.

(30) Hu, Q.; Rijcken, C. J. F.; van Gaal, E.; Brundel, P.; Kostkova, H.; Etrych, T.; Weber, B.; Barz, M.; Kiessling, F.; Prakash, J.; Storm, G.; Hennink, W. E.; Lammers, T. Tailoring the Physicochemical Properties of Core-Crosslinked Polymeric Micelles for Pharmaceutical Applications. *J. Control. Release* **2016**, *244*, 314–325.

(31) Najafi, M.; Kordalivand, N.; Moradi, M. A.; Van Den Dikkenberg, J.; Fokkink, R.; Friedrich, H.; Sommerdijk, N. A. J. M.; Hembury, M.; Vermonden, T. Native Chemical Ligation for Cross-Linking of Flower-Like Micelles. *Biomacromolecules* **2018**, *19* (9), 3766–3775.

(32) Agouridas, V.; El Mahdi, O.; Diemer, V.; Cargoët, M.; Monbaliu, J.-C. M.; Melnyk, O. Native Chemical Ligation and Extended Methods: Mechanisms, Catalysis, Scope, and Limitations. *Chem. Rev.* **2019**, *119* (12), 7328–7443.

(33) Dawson, P. E.; Muir, T. W.; Clark-Lewis, I.; Kent, S. B. Synthesis of Proteins by Native Chemical Ligation. *Science (80-.).* **1994**, *266* (5186), 776 LP – 779.

(34) Thapa, P.; Zhang, R. Y.; Menon, V.; Bingham, J. P. Native Chemical Ligation: A Boon to Peptide Chemistry. *Molecules* **2014**, *19* (9), 14461–14483.

(35) Pal, S.; Mandal, A.; Hong, L.; Ortuso, R. D.; Petri-Fink, A.; Salentinig, S.; Kilbinger, A. F. M. Native Chemical Ligation: Ultrafast Synthesis of Block Copolymers. *Macromolecules* **2022**, *55* (7), 2854–2860.

(36) Hu, B.-H.; Su, J.; Messersmith, P. B. Hydrogels Cross-Linked by Native Chemical Ligation. *Biomacromolecules* **2009**, *10* (8), 2194–2200.

(37) Wan, Q.; Chen, J.; Yuan, Y.; Danishefsky, S. J. Oxo-Ester Mediated Native Chemical Ligation: Concept and Applications. *J. Am. Chem. Soc.* **2008**, *130* (47), 15814–15816.

(38) Hu, Q.; Rijcken, C. J.; Bansal, R.; Hennink, W. E.; Storm, G.; Prakash, J. Complete Regression of Breast Tumour with a Single Dose of Docetaxel-Entrapped Core-Cross-Linked Polymeric Micelles. *Biomaterials* **2015**, *53*, 370–378.

(39) Rijcken, C. J. F.; De Lorenzi, F.; Biancacci, I.; Hanssen, R. G. J. M.; Thewissen, M.; Hu, Q.; Atrafi, F.; Liskamp, R. M. J.; Mathijssen, R. H. J.; Miedema, I. H. C.; Menke - van der Houven van Oordt, C. W.; van Dongen, G. A. M. S.; Vugts, D. J.; Timmers, M.; Hennink, W. E.; Lammers, T. Design, Development and Clinical Translation of CriPec®-Based Core-Crosslinked Polymeric Micelles. *Adv. Drug Deliv. Rev.* **2022**, *191*, 114613.

(40) Hembury, M.; Chiappini, C.; Bertazzo, S.; Kalber, T. L.; Drisko, G. L.; Ogunlade, O.; Walker-Samuel, S.; Krishna, K. S.; Jumeaux, C.; Beard, P.; Kumar, C. S. S. R.; Porter, A. E.; Lythgoe, M. F.; Boissière, C.; Sanchez, C.; Stevens, M. M. Gold–Silica Quantum Rattles for Multimodal Imaging and Therapy. *Proc. Natl. Acad. Sci.* **2015**, *112* (7), 1959–1964.

(41) Hembury, M.; Beztsinna, N.; Asadi, H.; Van Den Dikkenberg, J. B.; Meeldijk, J. D.; Hennink, W. E.; Vermonden, T. Luminescent Gold Nanocluster-Decorated Polymeric Hybrid Particles with Assembly-Induced Emission. *Biomacromolecules* **2018**, *19* (7), 2841–2848.

(42) Kennedy, L.; Sandhu, J. K.; Harper, M.-E.; Cuperlovic-Culf, M. Role of Glutathione in Cancer: From Mechanisms to Therapies. *Biomolecules* **2020**, *10* (10), 1429.

(43) Shi, J.; Kantoff, P. W.; Wooster, R.; Farokhzad, O. C. Cancer Nanomedicine: Progress, Challenges and Opportunities. *Nat. Rev. Cancer* **2017**, *17* (1), 20–37.

(44) Fosgerau, K.; Hoffmann, T. Peptide Therapeutics: Current Status and Future Directions. *Drug Discov. Today* **2015**, *20* (1), 122–128.

(45) Merrifield, R. B. Solid Phase Peptide Synthesis. I. The Synthesis of a Tetrapeptide. *J. Am. Chem. Soc.* **1963**, *85* (14), 2149–2154.

(46) D'Aloisio, V.; Dognini, P.; Hutcheon, G. A.; Coxon, C. R. PepTherDia: Database and Structural Composition Analysis of Approved Peptide Therapeutics and Diagnostics. *Drug Discov. Today* **2021**, *26* (6), 1409–1419.

(47) Ilangala, A. B.; Lechanteur, A.; Fillet, M.; Piel, G. Therapeutic Peptides for Chemotherapy: Trends and Challenges for Advanced Delivery Systems. *Eur. J. Pharm. Biopharm.* **2021**, *167*, 140–158.

(48) Lau, J. L.; Dunn, M. K. Therapeutic Peptides: Historical Perspectives, Current Development Trends, and Future Directions. *Bioorg. Med. Chem.* **2018**, *26* (10), 2700–2707.

(49) Boohaker, R. J.; Lee, M. W.; Vishnubhotla, P.; Perez, J. M.; Khaled, A. R. The Use of Therapeutic Peptides to Target and to Kill Cancer Cells. *Curr. Med. Chem.* **2015**, *19* (22), 3794–3804.

(50) Marqus, S.; Pirogova, E.; Piva, T. J. Evaluation of the Use of Therapeutic Peptides for Cancer Treatment. *J. Biomed. Sci.* **2017**, *24* (1), 21.

(51) Narasipura, E. A.; VanKeulen-Miller, R.; Ma, Y.; Fenton, O. S. Ongoing Clinical Trials of Nonviral SiRNA Therapeutics. *Bioconjug. Chem.* **2023**, *34* (7), 1177–1197.

(52) Neklesa, T. K.; Winkler, J. D.; Crews, C. M. Targeted Protein Degradation by PROTACs. *Pharmacol. Ther.* **2017**, *174*, 138–144.

(53) Pathmanathan, S.; Grozavu, I.; Lyakisheva, A.; Stagljar, I. Drugging the Undruggable Proteins in Cancer: A Systems Biology Approach. *Curr. Opin. Chem. Biol.* **2022**, *66*, 102079.

(54) Selvam, C.; Mutisya, D.; Prakash, S.; Ranganna, K.; Thilagavathi, R. Therapeutic Potential of Chemically Modified SiRNA: Recent Trends. *Chem. Biol. Drug Des.* **2017**, *90* (5), 665–678.

(55) Kenski, D. M.; Butora, G.; Willingham, A. T.; Cooper, A. J.; Fu, W.; Qi, N.; Soriano, F.; Davies, I. W.; Flanagan, W. M. SiRNA-Optimized Modifications for Enhanced In Vivo Activity. *Mol. Ther. - Nucleic Acids* **2012**, *1* (1), e5.

(56) Choung, S.; Kim, Y. J.; Kim, S.; Park, H.-O.; Choi, Y.-C. Chemical Modification of SiRNAs to Improve Serum Stability without Loss of Efficacy. *Biochem. Biophys. Res. Commun.* **2006**, *342* (3), 919–927.

CHAPTER 2

Gold nanoclusters: imaging, therapy and theranostic roles in biomedical applications

Sanne M. van de Looij[1], Erik R. Hebels[1], Martina Viola[1], Mathew Hembury[1], Sabrina Oliveira[1,2], and Tina Vermonden[1]

[1]Department of Pharmaceutics, Utrecht Institute for Pharmaceutical Sciences (UIPS), Science for Life, Utrecht University, P.O. Box 80082, 3508 TB Utrecht, the Netherlands.
[2]Department of Biology, Cell Biology, Neurobiology and Biophysics, Faculty of Science, Utrecht University, Utrecht, The Netherlands

Bioconjugate Chem. 2022, 33, 1, 4–23

Abstract

For the past two decades, atomic gold nanoclusters (AuNCs, ultrasmall clusters of several to one hundred gold atoms, having a total diameter of <2 nm) have emerged as promising agents in the diagnosis and treatment of cancer. Owing to their small size, significant quantisation occurs to their conduction band, which leads to emergent photonic properties and the disappearance of the plasmonic responses observed in larger gold nanoparticles. For example, AuNCs exhibit native luminescent properties, which have been well-explored in literature. Using proteins, peptides or other biomolecules as structural scaffolds or capping ligands, required for the stabilization of AuNCs, improves their biocompatibility, while retaining their distinct optical properties. This paved the way for the use of AuNCs in fluorescent bioimaging, which later developed into multimodal imaging combined with computer tomography and magnetic resonance imaging as examples. The development of AuNC-based systems for diagnostic applications in cancer treatment was then made possible by employing active or passive tumour targeting strategies. Finally, the potential therapeutic applications of AuNCs are extensive, having been used as light activated- and radiotherapy agents, as well as nanocarriers for chemotherapeutic drugs, which can be bound to the capping ligand or directly to the AuNCs *via* different mechanisms. In this review, we present an overview of the diverse biomedical applications of AuNCs in terms of cancer imaging, therapy and combinations thereof, as well as highlighting some additional applications relevant to biomedical research.

Introduction

For the past few decades, cancer has been a major public health concern, being the second leading cause of mortality worldwide.[1] It has become clear that upon earlier detection of the tumour, the 5-year survival rates of patients are improved.[2,3] Detection and identification of the disease before metastasis is thus critical when treating cancer.[4] Therefore, while priority must be given to providing treatment options for these patients, designing new, or improving already existing cancer detection methods is crucial to improve treatment success.

Recently, gold nanoclusters (AuNCs) have emerged as a promising detection approach in biomedical imaging, due to their unique molecule-like properties and good biocompatibility.1 Gold, as an element in particular, is an attractive inert noble metal with good biocompatibility and substantial history in biomedical applications.5 AuNCs are ultrasmall clusters of several to one hundred gold atoms, having a total diameter of less than 2 nm.6 As opposed to gold nanoparticles with a diameter larger than 2 nm and having a continuous band of electronic energy, distinct electron excitation levels start to appear when the size of the gold core becomes comparable to the Fermi wavelength of an electron (~0.5 nm).1,6–9 Because of the quantum confinement effects,10 significant quantisation of the conduction band occurs6 and the AuNC can be energetically considered as a molecule.1 This leads to unique optical properties such as fluorescence, which is caused by electron transitions between these electron energy levels upon light activation.4 Considering AuNCs absorb light in the near-infrared (NIR) range between 650 and 900 nm,6 they are especially useful in a biological window of cancer diagnostics. NIR light has a tissue penetration between that of optical light and X-rays, and is relatively harmless to healthy cells, in contrast to wavelengths that are currently used for medicinal purposes.11 Besides that, fluorescent probes that emit light in the NIR range have the advantage of having minimum interference from background fluorescence and light scattering in biological systems.1,12 In addition to their photoluminescence, AuNC based systems generally also are biocompatible, more photostable than commonly used organic dyes, possess a large Stokes shift, and a long luminescence lifetime.1,8 By utilising surface protecting ligands, also known as capping ligands, the AuNCs can be stabilised to prevent coalescence.9 Also, with the help of these ligands, the specific photoluminescent wavelengths can be tuned by adapting either the size or the surface-chemistry of the metal core.10 By performing reduction of gold in solution in the presence of thiols or macromolecular templating agents, nanocluster and ligands can be covalently bound.13 AuNCs are not only applicable as a tool for *in vivo* bioimaging. By conjugating drugs to either the capping ligands or the AuNCs directly,

the system can aid in therapy too. Additionally, because of the inherent properties of AuNCs, such as a good photothermal conversion, other types of triggered therapy are also within reach.

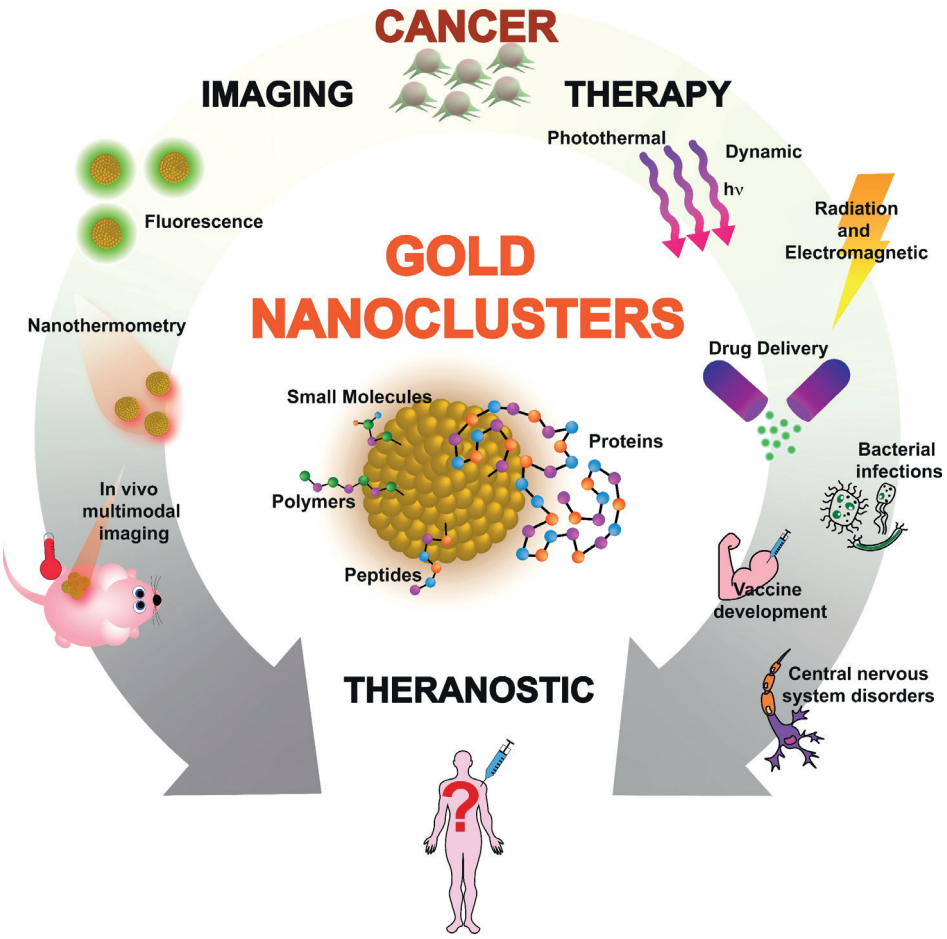

Scheme 1: Schematic illustration of AuNCs with various classes of capping ligands, investigated for potential use in imaging, therapy, and theranostic platforms.

Herein, a review regarding cancer nanomedicines with AuNCs is given, a platform where medical imaging and cancer cell-targeted therapy can be integrated. The development of AuNCs over the past few years will be discussed in terms of imaging, therapy and theranostic applications to provide an overview of research that has been executed thus far. A theranostic system is defined as a material that combines therapy and diagnostic imaging in one platform.[14] They deliver therapeutic drugs or aid in another form of

therapy, while also acting as or delivering a diagnostic imaging agent at the same time. Moreover, the potential applications of AuNCs in neurological disorders, antibiotics and vaccine development will be discussed briefly (scheme 1), followed by a discussion to determine the knowledge gap and future perspectives.

AuNCs in fluorescent bioimaging

Most of the research conducted has focussed on using thiols, bovine serum albumin or glutathione as capping ligands to obtain stabilized fluorescent AuNCs.[13] However, many different capping ligands have been used in the synthesis to improve the quantum yield of the luminescent emission (QY) or pharmacokinetic factors. The QY of the ligand-protected AuNCs is an essential parameter for the characterisation of their light emission properties,[15] where a higher QY is an indication for increased photoluminescent signal. It is the ratio of the amount of photons that is emitted, to the amount of photons that is absorbed.[16]

One of the current challenges in the development of AuNCs for bioimaging techniques is that the ligand-protected AuNCs often have a very low QY of less than 1%, limiting their *in vivo* applications.[13] Alongside that, the colloidal stability of the protected AuNCs is usually not optimal either, nor are the biodistribution or clearance and accumulation in target organs.[17] Nevertheless, multiple research groups have aimed to figure out how to adapt the surface-chemistry of the AuNCs to solve all these problems. Wu *et al.* (2010) have found that the most effective strategy to enhance fluorescence from AuNCs is to employ ligands with electron-rich atoms (e.g. N, O, S, P) and groups (e.g. carboxylic acid, amines).[9,10] AuNCs are often developed with polymers as capping ligands, or endogenous biomolecules, such as peptides, proteins and DNA in order to increase their biocompatibility. Table 1 and table 2 give an overview of some relevant articles for fluorescent bioimaging systems employing AuNCs, and additional fluorescent properties of AuNCs, respectively.

Fluorescence of AuNCs with different capping ligands

Well-explored are the bovine serum albumin (BSA)-AuNCs, which were first reported by Xie *et al.* in 2009.[18] They synthesised red emitting BSA-AuNCs ($\lambda_{em\ max}$ = 640 nm) with QY of approximately 6%. However, later research found an unsatisfying colloidal stability and biodistribution,[17,19] providing challenges for *in vivo* applications. Yet, BSA-templated AuNCs have been extensively studied in the context of targeting and drug delivery,[13] considering their ability to be functionalised with targeting molecules such as the monoclonal antibody herceptin or the synthetic vitamin folic acid. BSA is not the only protein that has been investigated as a template for AuNC synthesis. Also transferrin ($\lambda_{em\ max}$ = 710 nm, QY= 7.7%),[20] lysozyme type VI ($\lambda_{em\ max}$ = 455 nm, QY= 56%),[21] lysozyme (λ_{em}

$_{max}$ = 657 nm),[22] keratin-Ag ($\lambda_{em\ max}$ = 710 nm, QY= 10.5%),[23] pepsin ($\lambda_{em\ max}$ = 670 nm, QY= 3.5%),[24] insulin ($\lambda_{em\ max}$ = 670 nm, QY= 7%),[25] RNase-A ($\lambda_{em\ max}$ = 682 nm, QY= 12.1%),[26] DNase 1 ($\lambda_{em\ max}$ = 640 nm),[27] horseradish peroxidase ($\lambda_{em\ max}$ = 650 nm),[28] ovalbumin, urease and immunoglobulin G have been investigated as a template for AuNC synthesis, amongst others. In these studies, different sizes of AuNCs were employed, so part of the differences in fluorescent properties can be attributed to that variable. On several occasions, it was shown that the proteins kept their endogenous functions even after the AuNC synthesis.[26,27]

Xu *et al.* performed a systematic review in which they determined the influence of the protein templates on the AuNC fluorescence, based on the protein characteristics.[29] It was found that protein templates with many cysteine residues cause a shift in the fluorescent emission to higher wavelengths (red shift). They also appear to cause shorter fluorescent lifetimes.[29]

By making use of zwitterionic and bidentate thiol molecules as capping ligands, Chen *et al.* (2017) have reported short wavelength infrared (SWIR, λ= 1–2 μm) emitting AuNCs with a QY of 0.6% to 3.8% for emission wavelengths between 1000 and 900 nm, respectively.[30]

DNA-templated AuNC synthesis has also been performed.[31] The emission colour of the AuNCs is mainly dependent on the degree of metal reduction, while the DNA sequence and chain length only plays a minor role in the specific fluorescent emission. An optimised process yielded AuNCs with a QY of about 3%.[31]

The tripeptide glutathione (GSH) has been commonly used as a AuNC surface ligand because of its limited interaction and affinity to cellular proteins.[1] It has been found that glutathione reduces the accumulation of AuNCs in the liver and the spleen, while improving renal clearance, leading to at least 50% of GSH-coated AuNCs to be effectively removed from the body via the urinary systems within 24 hours after IV-injection.[32] Zhou *et al.* reported a QY of 3.5% and a photoluminescence in the NIR range of approximately 560 nm.[32] In addition to this, the findings of Luo *et al.* in 2012[33] showed that in the context of GSH-Au complexes, a lower ratio of thiol-to-gold (1.5 : 1 instead of 2 : 1) and controlled aggregation by solvent mixing in the synthesis of AuNCs can lead to a higher QY of around 15%.[13,33] Metal nanocluster aggregation induced emission is a now a promising and well-recognized phenomenon, providing efficient syntheses of highly luminescent nanoclusters. For a detailed review of aggregation induced emission of metal nanoclusters, the reader is referred to Bera *et al.* 2021.[34]

In 2004, Zheng *et al.* discovered a synthesis for highly fluorescent, water-soluble and size-tuneable AuNCs using poly(amidoamine) (PAMAM) dendrimers.[35] They found a way

to encapsulate the AuNCs with different sizes with PAMAM dendrimers to obtain a new platform for *in vivo* applications. The nanoclusters were reported with well-defined excitation and emission spectra ranging from UV to NIR, with QYs between 70 and 10%, respectively, depending on the size of the gold clusters.[35] Since then, more research has been done with polymers or dendrimers as templates for AuNCs, using poly(*N*-vinylpyrrolidone) (PVP),[36] polyethylenimine (PEI),[37] or thiol-terminated PMMA (poly(methyl methacrylate)) polymers.[38] More recently, an approach was described using copolymers comprised of oligo(ethylene glycol) methyl ether methacrylate (OEGMA) and 2-(acetylthio)ethyl methacrylate (AcSEMA) monomers.[39] Hembury *et al.* combined AuNCs and thermosensitive diblock copolymers consisting of poly(ethylene glycol) (PEG) and poly(N-isopropylacrylamide) (PNIPAM),[6] and obtained a QY of 3.6% at a maximum emission wavelength of 720 nm.

Not only polymers, but also polymeric micelles have been explored as possible encapsulation scaffolds for AuNCs. Because of their ability to encapsulate other compounds besides the AuNCs, polymeric micelles are usually investigated as theranostic systems. In terms of imaging, Al Zaki *et al.* investigated gold-loaded polymeric micelles for computed tomography (CT) imaging.[40] They synthesised polymeric micelles consisting of the amphiphilic diblock polymer poly(ethylene glycol)-*b*-poly(Ɛ-caprolactone). The AuNCs were encapsulated within the hydrophobic core of these micelles. Whereas the CT imaging capabilities of the micelles were investigated, the fluorescent properties were not looked into at all.[40] This is in contrast to the research of Chen *et al*. in 2013, where the fluorescence of the amphiphilic gold-loaded polymeric micelles was investigated (λ_{em} = 610 nm).[41]

Imaging in the near infrared II (NIR-II) region of between 1100-1700 nm is attracting wide interests owing to reduced tissue scattering as compared to the NIR-I region (750-900 nm).[42] In line with this, Liu *et al.* in 2019[43] synthesized atomically precise GSH capped Au_{25} clusters that emit fluorescence between 1100-1350 nm by charge transfer between GSH and the gold core. Metal doping of these AuNCs, with copper for example, increases the QY up to 5-fold. *In vivo* imaging of primary and even metastatic tumours following IV injection of these AuNCs could be performed in mice with excitation at 808 nm and emission of 1300-1700 nm. Cerebral blood vessel imaging was possible as well due to the long wavelength emission in this NIR-II region which allows penetration of the skull.[43]

AuNCs in in vivo multi-modal bioimaging

The applicability of AuNCs and hybrid materials including AuNCs as tumour imaging agents has been investigated *in vivo* involving techniques such as X-ray computed tomography, NIR fluorescent imaging, positron emission tomography (PET) and magnetic resonance imaging (MRI).[1,44] Each imaging technique has its own advantages

and disadvantages. Multimodal imaging is a combination of multiple imaging techniques, combining the best features of each. Having a single imaging agent that could be used for multiple imaging techniques therefore gives advantages over imaging with one technique alone. When imaging for cancer diagnostics, the amount of imaging agent that accumulates in the tumour should be high compared to other organs. The platform should, therefore, target the tumour, either via passive- or active targeting.

Passive targeting is done by exploiting the enhanced permeability and retention (EPR) effect, a process that occurs in regions of the body with a high degree of hypoxia and/or inflammation. Both are typical for the tumour microenvironment.[45,46] The tumour vasculature has several abnormalities due to their rapid and disordered growth, resulting in gaps in the endothelium, which provide opportunity for AuNC containing nanoparticle platforms ranging from 10 to 500 nm in the blood serum to extravasate into the tumour tissue.

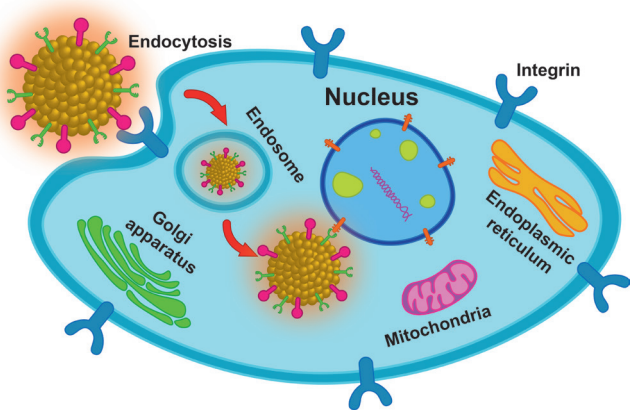

Scheme 2: Schematic illustration of receptor mediated endocytosis of active targeted AuNCs.

Active targeting can be achieved by conjugating targeting ligands to the nanoclusters, to obtain cellular uptake via receptor mediated endocytosis as illustrated in scheme 2. Examples of targeting ligands are folic acid (FA), hyaluronic acid (HA), methionine or cyclic RGD.[1] By employing active targeting, there is an altered biodistribution with a possible higher tumour uptake, causing a strong fluorescent signal for tumour sites *in vivo*. This was demonstrated by several studies, such as Liu *et al.* who showed that folic acid functionalised, trypsin-protected AuNCs (FA-try-AuNCs) could be used for *in vivo* imaging in mice.[47] The FA-try-AuNCs were injected intratumorally in nude mice bearing HeLa tumours of 8 mm. The NIR fluorescent signal in the tumours was detectable immediately from injection and up to twelve hours after injection. In subcutaneously injected healthy control mice, the fluorescent signal could be seen spread over the

entire body five minutes post-injection, which disappeared slowly after twelve hours, indicating metabolism and degradation of the AuNCs. A final experiment showed that upon subcutaneous injection, the tumour site was visible after 30 minutes, although less clear than when injection happens intratumorally (Figure 1).[47]

BSA-stabilised AuNCs coated with FA or HA showed similar fluorescent properties *in vivo*, and accumulate in either HeLa or Hep-2 tumours, respectively.[48] Gadolinium-functionalised AuNCs can generally be used for MRI. Gold-silica quantum rattles (mesoporous silica nanoparticles filled with both AuNCs and gold nanoparticles) have also been reported for multimodal imaging involving MRI.[49] Dependent on the other modifications or conjugations to the AuNC, NIR fluorescent imaging and CT imaging can also be performed.[1] The shortwave infrared emitting AuNCs that Chen *et al*. synthesised showed great potential for *in vivo* imaging with a higher contrast than conventional NIR imaging, while also allowing for PET-scans.[30] Additionally, by coupling iodine-124 to a peptide protected AuNC, as was done by Han *et al.* in 2019, the obtained system could be used for PET and fluorescent dual-imaging in lung cancer.[50] They reported the production of these AuNCs by conjugating tumour-targeting peptide luteinizing hormone releasing hormone to human serum albumin (HSA), and using this as a template for AuNC synthesis.[50]

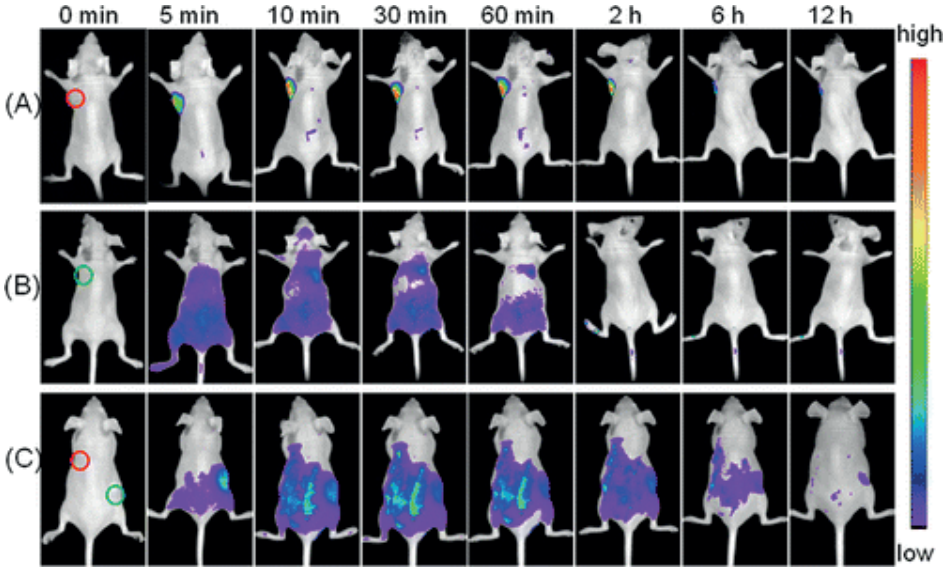

Figure 1: In vivo time-dependent tumour imaging by NIR fluorescence imaging. The FA-try-AuNCs were injected (A) intratumorally in HeLa tumour-bearing mice, (B) subcutaneously into the left forelimb region of normal nude (control) mice, and (C) tumour-bearing mice. The red circle and green circle indicate the tumour site and injection site respectively. Reproduced from Ref.[47], Copyright (2013), with permission of American Chemical Society.

The lysozyme-capped AuNCs that were designed by Liu *et al.* in 2016 show great promise for diagnostic purposes.[51] By making use of bi-modal bioimaging consisting of NIR fluorescence and CT imaging *in vivo*, cancer tissue and healthy tissues can be distinguished more easily. They found that by adding folic acid as a targeting agent to the lysozyme-capped AuNCs, they accumulated in the tumour site of HeLa tumour-bearing mice following IV administration.[51] When not using the folic acid modification, the fluorescence of the AuNCs did not appear at the tumour site. When injecting the AuNCs for the purpose of CT imaging, positive signal enhancements could be seen in the liver and kidney one hour after injection, meaning that the AuNCs mainly accumulate in these organs in the absence of tumour tissue.[51]

In 2013, Hu *et al*. even managed to develop gold-gadolinium nanoclusters for high-performance triple-modal imaging with NIR fluorescence, CT and MR imaging in a single agent *in vivo*.[52] While doing *in vitro* research, they found that at a concentration as low as 2.1 μM, the hybrid nanoclusters exhibited remarkable signals for NIR fluorescence, CT and MRI. This triple-modal contrast agent capability was further tested in MCF-7 tumour-bearing mice, where the *in vitro* results were confirmed. The gold-gadolinium nanoclusters also showed a high tumour accumulation and quick renal clearance *in vivo*.[52] Another triple-modal imaging platform was described in 2015 by Hembury *et al.* utilizing the aforementioned gold-silica quantum rattles. In this case, NIR, MR and photoacoustic imaging (PAI) could be performed using this single agent in *in vitro* and *in vivo* settings.[49]

Table 1: Overview of key properties of the AuNC-based systems from the studies mentioned in the section: 'AuNCs in fluorescent bioimaging'.

Reference	Capping ligand	Additional functionality	Excitation/ Emission	Quantum Yield	CT/MRI/ PET/PAI
Hembury, 2018[6]	PEG-PNIPAM	-	550/720 nm	3.6%	-
Xie, 2009[18]	BSA	-	480/640 nm	6%	-
Wang, 2013[20]	Transferrin	-	380/710 nm	7.7%	-
Chen, 2012[21]	Lysozyme type VI	-	380/455 nm	56%	-
Wei, 2010[22]	Lysozyme	-	360/657 nm	7%	-
West, 2014[27]	Dnase-1	-	460/640 nm	Not reported	-
Wen, 2011[28]	Horseradish peroxidase	-	365/650 nm	Not reported	-
Li, 2020[23]	Keratin	Ag ions	470/710 nm	10.5%	-
Kawasaki, 2011[24]	Pepsin	-	360/670 nm	3,50%	-
Liu, 2011[25]	Insulin	-	400/670 nm	7%	-
Kong, 2013[26]	RNase-A	-	470/682 nm	12.1%	-
Chen, 2017[30]	Zwitterionic/bidentate thiol molecules	-	532/1000-900 nm	0.6 - 3.8%	-
Lopez, 2015[31]	DNA	-	560/764 nm	3%	-
Zhou, 2011[32]	GSH	-	420/560 nm	3.5%	-
Han, 2019[50]	HSA	Tumour-targeting peptide luteinizing hormone release hormone, iodine 124	Not reported	Not reported	PET
Zheng, 2004[35]	PAMAM dendrimer	-	340/380 nm to 760/880 nm	70% - 10%	-
Santiago González, 2010[36]	PVP	-	240/350 nm	12.5%	-
Duan, 2007[37]	PEI	-	353/445 nm	10-20%	-
Hussain, 2005[38]	Thiol-terminated PMMA	-	Not reported	Not reported	-
Adnan, 2017[39]	OEGMA-AcSEMA	-	440/640-660 nm	0.24 and 0.17%	-
Al Zaki, 2014[40]	Polymeric micelle	-	Not reported	Not reported	CT
Chen, 2013[41]	Polymeric micelle	-	405/610 nm	Not reported	-
Liu, 2013[47]	Trypsin	Folic acid	520/690 nm	6.5%	-
Zhang, 2014[48]	BSA	Folic acid or Hyaluronic acid	370 or 470/600 nm	~15%	-
Liu, 2016[51]	Lysozyme	Folic acid	550/690 nm	19.61%	CT
Hu, 2013[52]	None	Gadolinium ions	435-480/600-800 nm	Not reported	CT, MRI
Hembury, 2015[49]	Mesoporous silica shells	Gold nanoparticles	680/800-860 nm	0.02%	MRI, PAI
Liu, 2019[43]	GSH	Doped nanocluster	808/1300-1700 nm	0.67% (Cu-doped)	-

Additional fluorescence-based applications of AuNCs

The photoluminescent properties of AuNCs have been researched not only in the context of NIR, CT and MR imaging, but also in diagnostics via nanothermometry or biosensing of heavy metals, small biomolecules, proteins and cancer biomarkers.

The intracellular temperature is an important parameter in most cellular activities, including gene expression, cell division and metabolism.[53,54] When abnormal processes occur within the cell, such as cancer cell growth or inflammation, this may result in intracellular temperature changes.[53] AuNCs can be used as intracellular nanothermometers because of the high temperature-sensitivity of their fluorescence lifetime and emission intensity.[55] It was found that both of these factors change drastically within a physiologically relevant temperature range of 15 to 45 °C.[53,55] By making use of fluorescence lifetime imaging microscopy (FLIM), the thermometric properties of AuNCs were tested on several occasions.[53–55] In 2013, Shang *et al.* used lipoic-acid protected AuNCs to show that the fluorescent emission intensity and fluorescence lifetime both have a negative linear relationship with temperature between 15 and 45°C.[55] They showed a temperature resolution between 0.1 and 0.3°C in phosphate buffered saline (PBS), and between 0.3 and 0.5°C in HeLa cells (Figure 2). Even temperature differences between subcellular locations could be identified.[55] Similar results were reported for glutathione-capped AuNCs by Zhang *et al.* in 2019, who showed a temperature resolution of 0.73°C in hepatic stellate cells within a temperature range from 35 to 43°C.[53] Also PAMAM-protected AuNCs demonstrated possible use as nanothermometers.[54] The described AuNC-based temperature probes compare well to already existing fluorescence-based nanothermometers, which present temperature resolutions between 0.1 and 2°C and with a few exceptions between 0.001 and 0.01°C.[56] Of these, only a few temperature probes that employ NIR fluorescence to limit interference from autofluorescence of biological samples have been investigated. Green fluorescent protein (GFP) can also serve as a temperature probe and was used to accurately determine the temperature in GFP-transfected HeLa cells with a resolution of 0.4°C.[57]

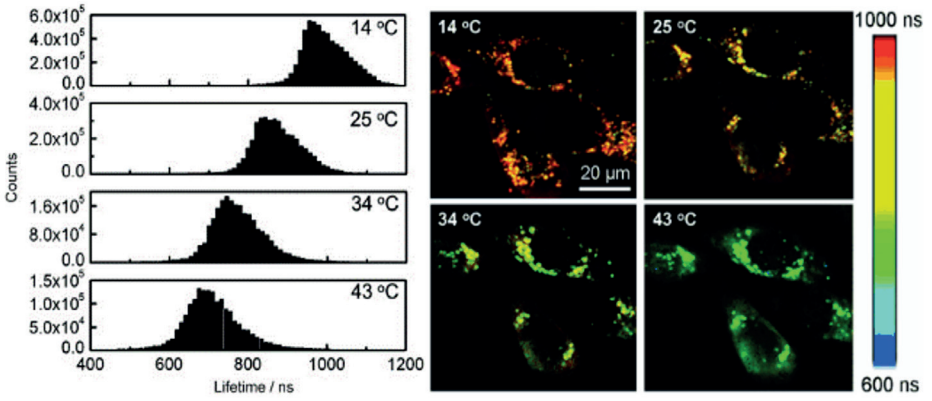

Figure 2: In vitro fluorescent imaging of AuNCs by making use of fluorescence lifetime imaging. Left: Average lifetime histograms of intracellular gold nanoclusters at varying temperatures. Right: FLIM images of HeLa cells with internalised AuNCs at varying temperatures. Adapted from Ref.[55], Copyright (2013), with permission of John Wiley and Sons.

The PAMAM-protected AuNCs could also be used for the intracellular sensing of $Cr_2O_7^{2-}$ (dichromate), owing to the fluorescence quenching effects at room temperature in the presence of trace amounts of this ion, with a limit of detection (LOD) of 1.9 µM.[54] AuNCs have been studied quite often for the application of sensitive probes for biosensing. Keratin-Ag-AuNCs[19] have a sensing ability for the heavy metal mercury(II). The LOD was found to be 2.31 nM, showing that these keratin protected, silver-modified AuNCs are sensitive enough for the detection of mercury in tap water.[19] The sensing of mercury(II) in cellular compartments was also investigated. However, in complex samples the fluorescence quenching effects with increasing mercury concentration were difficult to measure. Yet, it was eventually manageable in fish samples.[13] GSH-capped AuNCs turned out to be sensitive, but not selective to mercury, lead, and copper ions. Besides heavy metals and inorganic ions, also the concentrations of small biomolecules and proteins can also be determined by making use of the fluorescence properties of AuNCs.[13] Chicken egg ovalbumin-based AuNCs were employed for biosensing phosphate-containing biomolecules, such as ATP and pyrophosphate.[58] Glucose-oxidase-functionalised AuNCs were able to sense glucose with a lower detection limit of 0.7 µM.[59] Trypsin-stabilised AuNCs, as described by Liu *et al.* in 2013[47], were able to sense heparin in human serum samples with a linear range between 0.1 and 4.0 µg/mL and a LOD of 0.05 µg/mL. AuNCs can also be used for the detection and quantification of cancer biomarkers such as neuron-specific enolase,[60] dopamine in the cerebrospinal fluid,[61] interleukin-6,[62] and protein kinase A,[63] amongst others.[13]

In an additional application, Colombé *et al.* investigated whether AuNCs could be used for image-guided surgery in mice.[64] In cancers such as Head and Neck Squamous Cell Carcinoma (HNSCC), tumour resection is difficult due to many complex structures in this area that should not be damaged, such as nerves, tendons and small muscles. By making use of real-time image-guided surgery, these structures may be preserved while allowing for complete tumour excision with good margins.[64] NIR fluorescence image-guided surgery is a method that has been validated in mice.[65] Because NIR fluorescence provides good optical contrast between healthy and cancer tissue in case of tumour-targeting fluorescent probes,[65] the probability of efficient tumour resection is improved. Currently, NIR image-guided surgery with the help of fluorophores is under investigation in clinical trials.[66,67] However, the use of AuNCs as an imaging agent is still in the pre-clinical phase.[64] It was found that NIR image-guided surgery using zwitterionic or pegylated moieties as capping ligands on AuNCs increases the survival time compared to control animals without image-guidance, as well as the number of mice without any local recurrent tumours due to better detection of tumour residues.[64]

Table 2: Overview of key properties of the AuNC-based systems from the studies mentioned in the section: 'Additional fluorescence-based applications of AuNCs'.

Reference	Capping-ligand	Other functionality	Excitation/ Emission	QY	Application	Result
Wang, 2018[19]	Keratin	Ag ions	400/725 nm	10.7%	Sensing Mercury(II)	Lower limit of detection of 2.31 nM
Liu, 2013[47]	Trypsin	Folic acid	520/690 nm	6.5%	Sensing heparin	Lower limit of detection 0.05 μg/mL, sense heparin in human serum with a linear range between 0.1 and 4.0 μg/mL
Zhang, 2019[53]	GSH	-	430/610 nm	Not reported	Temperature sensing	Temperature resolution of 0.73°C in hepatic stellate cells between 35 and 43°C
Yang, 2019[54]	PAMAM dendrimer	-	390/453 nm	18%	Temperature sensing, sensing dichromate	Distinguish temperature in the range of 15 to 80°C. Lower limit of detection of 1.9 μM
Shang, 2013[55]	Lipoic-acid	-	580/710 nm	Not reported	Temperature sensing	Temperature resolution between 0.3 and 0.5°C in HeLa cells between 15 and 45°C.
Selvaprakash, 2014[58]	Chicken egg ovalbumin	-	370/640 nm	6.6%	Sensing ATP and pyrophosphate	Lower limit of detection ATP 19 μM, lower limit of detection pyrophosphate 5 μM
Xia, 2013[59]	Glucose-oxidase	-	507/650 nm	~7%	Sensing of Glucose	Lower limit of detection of 0.7 μM within a linear range between 2.0 and 140 nM
Peng, 2012[60]	Calcium carbonate	Horseradish peroxidase/ antibody conjugates	Not reported /605 nm	Not reported	Sensing neuron-specific enolase	Lower limit of detection 2.0 pg/mL via fluorescent detection.
Govindaraju, 2017[61]	BSA	-	450/650 nm	~8%	Sensing dopamine in the cerebrospinal fluid	Lower limit of detection 0.830 nM in cerebrospinal fluid. Linear range between 0 and 10 nM.
Yang, 2013[62]	Poly-diallyldimethyl ammonium chloride/ Boron nitride	-	405/565 nm	Not reported	Sensing interleukin-6	Lower limit of detection 0.03 ng/mL, with a logarithmic range between 0.1 and 500 ng/mL
Liu, 2017[63]	Peptide (NH2-CCYLRRASLG-COOH)	-	330/405 nm	Not reported	Sensing activity protein kinase A	Lower limit of detection 0.02 U/mL. Activity of protein kinase A can be detected in the range between 0.05 and 1.6 U/mL activity.

AuNCs as a tool in therapy

The unique properties of AuNCs are not only useful for bioimaging and diagnostics, but they can also be employed in advanced therapeutic strategies against cancer. AuNCs can assist in radiotherapy, thermal therapy or facilitate drug delivery.[68–70] Drugs may be encapsulated together with the AuNCs in protein or polymeric scaffolds, or can be covalently bound to the capping ligand itself. The therapeutic uses of AuNCs will be discussed in the following section including photothermal and photodynamic therapies, electromagnetic and radiotherapy and drug delivery. The relevant published studies that employ AuNCs for the purpose of therapy are summarised in table 3.

Photothermal and photodynamic therapy

Photothermal therapy (PTT) is a form of phototherapy that is often applied in the treatment of cancer when tumours cannot be removed by surgery.[71,72] In PTT, the destruction of cancer cells is achieved via the induction of hyperthermia, by raising the tumour temperature to 41-47°C for tens of minutes.[71] By denaturing intracellular proteins and destroying cellular membranes, the tumour cells are killed via apoptosis or necrosis.[73] PTT involves a photothermal agent that is injected in the body either locally or by IV administration. Upon excitation of the photothermal agent, typically by NIR light,[74] photo-energy is converted into thermal energy within the cells that have taken up the photothermal agent.[72] Tumour cells, particularly in the centre of the tumour, are more susceptible to heat than healthy cells[75], improving the selectivity of photo-thermal therapy. As opposed to bioimaging agents, the ideal photothermal agent has a low fluorescence QY, to obtain an optimal conversion of radiation into heat instead of fluorescence emission.[76]

Photodynamic therapy (PDT) is a process that uses a photosensitiser, typically with visible light activation, instead of a photothermal agent. Upon activation, the photosensitisers start generating reactive oxygen species (ROS), thereby eliciting phototoxicity.[77] Advantages that both PTT and PDT have, is that they are relatively selective for cancer tissue because of the locally applied light. However, when using either strategy on their own, there are some disadvantages. In PDT there is limited tissue penetration of visible light. Furthermore, singlet oxygen ($^1O_2$), a reactive oxygen species amongst others that is released upon activation of the photosensitisers, is not always lethal for whole tumour, owing in part to limited diffusion.[72,78] It is therefore important that the PDT platform is sufficiently small to ensure complete coverage of the tumour. Since the tumour microenvironment is often hypoxic and oxygen is crucial for the effectiveness of PDT, this also creates challenges.[79] In PTT, there is the problem of limited photothermal conversion efficiency[72] and the development of thermotolerance.[71] Because of this, the therapies often need to be combined in order to reduce the risk of relapse or recurring cancer.

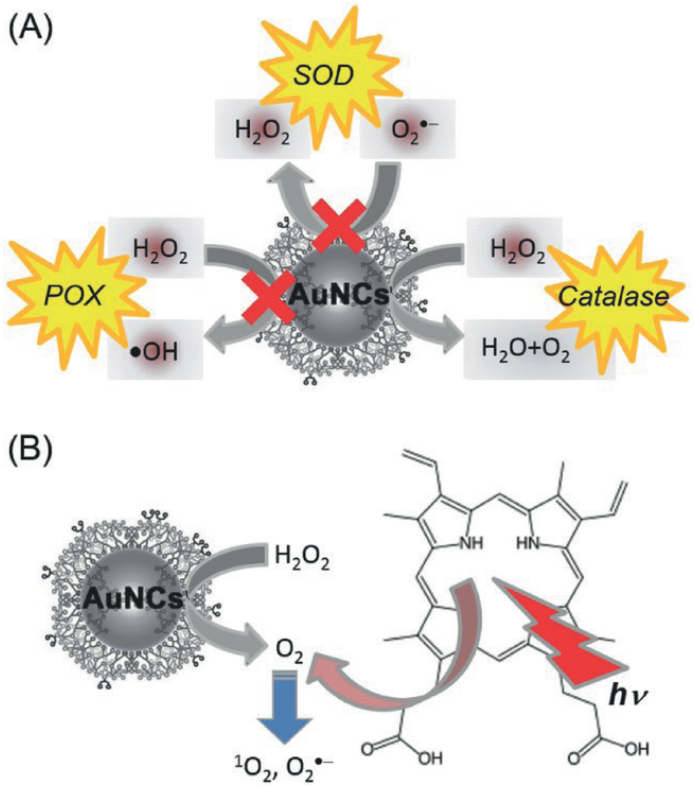

Scheme 3: Schematic illustration of A) the enzyme-like activities of NH_2-PAMAM-AuNCs, which can catalyse H_2O_2 to produce O_2 via their catalase-like activity and B) a simple strategy of conventional PDT combined with self-supplied O_2 via the catalase-like activity of NH_2-PAMAM-AuNCs, resulting in an increase of $^1O_2$ and $O_2\bullet^-$ generation. Reproduced from Ref.[80], Copyright (2017), with permission of John Wiley and Sons.

Since PTT and PDT work via a different mechanism, combined therapy needs both visible and NIR light activation and different drugs to obtain the desired results.[72] This combination adds complexity and reduces its usability in the clinic. However, AuNCs may provide an opportunity to combine PTT and PDT in one platform, only requiring a single wavelength for light activation. This was shown by Liu and colleagues in 2019, who reported captopril-stabilised AuNCs that could be used for combined PDT and PTT with near-infrared light activation at a wavelength of 808 nm.[72] They showed a photothermal conversion of 41.1%, laying a strong foundation for promoting the use of AuNCs for PTT. Furthermore, these AuNCs were able to generate enough singlet oxygen for efficient PDT. These results were confirmed *in vivo* by treating cutaneous squamous cell carcinoma tumour-bearing mice with either intra tumoral injection of captopril-capped AuNCs combined with light treatment, or light treatment alone. It was found that

the temperature within the tumour increased by 28.1°C ± 6.8°C in the mice treated with AuNCs compared to 8.4°C ± 2.1°C in mice receiving laser treatment only.[72] Whereas the tumour volumes for all control mice increased, the tumour volumes for the mice that received AuNC treatment decreased significantly. The contributions of PDT and PTT in killing tumour cells *in vivo* was estimated (by use of an ROS scavenger to quench the effect of PDT) to be around 71% and 29%, respectively.[72]

In literature, there have also been reports on AuNCs designed to reduce hypoxia. An example of this is the reported amine terminated PAMAM dendrimer-encapsulated AuNCs (NH_2-PAMAM-AuNCs), which have the intrinsic ability to produce O_2 for PDT via catalase-like activity over a broad pH range (see scheme 3).[80] Because of the extra oxygen present in tumour tissue, the enhanced PDT efficacy was statistically significant. However, the AuNCs themselves were not used for PDT. Instead, an established photosensitiser (protoporphyrin IX) was used. Still, the notion that NH_2-PAMAM-AuNCs have the ability to alleviate hypoxic conditions could be interesting for future research.[80]

Radiation and electromagnetic therapy

Nowadays, one of the leading therapeutic options for treating cancer is radiotherapy.[81,82] Radiotherapy kills tumour cells via treatment with high energy radiation, typically mega volt X-ray or gamma ray radiation with a dose between 3 and 6 Gy.[81,83] While it is generally very effective, one of the main setbacks of this treatment option is that it can also cause serious damage to the healthy tissues surrounding the tumour site.[81] When using a radiosensitiser, the efficacy of a radiation dose is increased.[81] This way, a lower radiation dose can be used for the therapy, one that is relatively safe to healthy cells that have not taken up the radiosensitiser. Radiosensitisers also enhance the outcome of radiation therapy, even when tumour cells are radioresistant (e.g. hypoxic).[84] When a radiosensitizer is irradiated with X-rays, secondary effects are generated, for example scattered photons, electrons, electron-positron pairs, or fluorescence. These secondary effects can then aid in destroying cells.[84] Gold is an especially good radiosensitizer, considering its large atomic number and its therefore high absorbance of radiation, which leads to an enhancement of radiotherapy of up to a 100 times compared to tissue without radiosensitizer.[84] While larger gold nanoparticles have already been studied for their potential in radiation therapy, the disadvantage of limited *in vivo* applicability because of unsatisfying biodistribution and clearance,[85] has provided incentive for the smaller AuNCs to be investigated for this application as well.

GSH-capped and BSA-capped AuNCs were tested for enhancement of radiotherapy, by Zhang *et al.* in 2014.[83] *In vitro* studies demonstrated that the GSH- and BSA-AuNCs

enhanced the radiosensitivity by 30% and 21%, respectively, relative to radiation alone. This difference may be due to improved cell uptake of GSH-AuNCs because of their smaller size or zwitterionic surface chemistry. *In vivo*, the GSH-AuNCs with radiation showed a statistically significant decrease in tumour growth, where after 20 days, the tumour volume was 35% smaller compared to the tumour after radiation alone. The BSA-AuNCs however, had no significant reduction in tumour growth after treatment compared to their control, showing a difference with radiation alone of around 10%.[83]

Ghahremani *et al.* investigated BSA-AuNCs for the purpose of megavoltage radiation therapy of breast cancer cells.[86] Using an AS1411 aptamer moiety conjugated to the BSA-AuNCs as a targeting agent for nucleolin, they were able to efficiently target these cancer cells. *In vitro* it was found that the combination of the Aptamer-BSA-AuNCs with megavoltage radiation therapy (between 6 and 25 MV)[84] leads to efficient cancer cell death, enhanced by the AuNCs with a factor of 2.7 compared to scontrols.[86] Besides that, Cifuentes-Rius *et al.* found that BSA-AuNCs can also be applied in electromagnetic radiation therapy.[87] Upon 8 minute light activation with 15W microwaves (1 GHz electromagnetic fields), cell viability decreased in six types of mammalian cell lines. At a gold concentration of 50 μg/mL, approximately 50% of the B-lymphocytes, 68% of prostate cancer cells, and 28% of neuroblastoma cells died via induction of apoptosis and necrosis.[87]

AuNCs as a platform for drug delivery

AuNCs have been reported to act as a tool for drug delivery itself, primarily without light activation. For example, the natural flavonoid kaempferol was conjugated to BSA-protected AuNCs via physical interactions and tested for its anticancer properties in lung cancer cells.[88] Flavonoids are well known for their antioxidant activity and can possibly be used for the treatment of cancer,[88–91] microbial infection and angiogenesis, amongst others.[89] While showing little to no cytotoxicity in healthy human kidney cells, kaempferol-BSA-AuNCs were able to kill over 50% of the cancer cells at a concentration of 25 μg/mL *in vitro*. Additionally, the kaempferol-BSA-AuNCs were shown to slow down the migration rate of HeLa cells. Although the purpose of the AuNCs within the drug delivery system was to provide imaging possibilities ($\lambda_{ex}/\lambda_{em}$= 550/650 nm), no cell imaging experiments have been reported.[88]

In a similar manner, Lakshmi *et al.* synthesised a flavonoid based drug delivery system, using quercetin as drug-conjugate.[91] The quercetin was bound to BSA-AuNCs via Au-OH interactions and showed good cellular uptake. The intention of the AuNCs was to use them for their fluorescent bioimaging properties ($\lambda_{ex}/\lambda_{em}$= 360/568 nm), but since these results were not reported on cellular experiments, the quercetin-BSA-AuNCs are

not considered theranostic here. They did show high cytotoxicity in lung cancer cells, whereas minimal cell death occurred in healthy fibroblasts .[91]

There has also been research for a drug carrier using AuNCs that focuses on controlled drug release. Latorre *et al.* published an article in 2019 where BSA-AuNCs were investigated as nanocarriers for combined chemotherapy against cancer, targeting mainly cancer stem cells.[92] To this end, they functionalised the BSA-AuNCs with both doxorubicin (DOX) and a camptothecin analogue SN38 to inhibit topoisomerase II and I in target cells. Herein, the AuNCs serve only as a structural scaffold. Although the results in clinical trials for the combination of free DOX and SN38 have not been satisfactory, it has previously shown to be one of the most synergistic combinations of chemotherapy when injected as a polymer-drug conjugate.[93] Thiols were introduced to the BSA by reacting the BSA-AuNCs with 2-iminothiolane. SN38 was then coupled to BSA with a redox-sensitive linker that is cleaved in a reducing environment, which contains, for example, a relatively high concentration of glutathione. DOX was modified with a pH-sensitive linker that breaks in a slightly acidic environment, as is the case in endosomes and lysosomes. The disulphide bond and maleimide in the linkers enabled conjugation to the thiols of BSA. A schematic overview of the synthesis and the modified chemotherapeutics are depicted in scheme 4.[92] *In vitro* toxicity studies in MCF7, MDA-MB-231 and Panc-1 cells showed that the BSA-AuNCs with both chemotherapeutics exhibited enhanced cytotoxicity compared to BSA-AuNCs with only one of the drugs. These bi-functionalised AuNCs were shown to induce highly efficient DNA damage, allowing their effective use against cancer stem cells by significantly reducing the size and number of mammospheres at concentrations as low as 0.08 µM.[92]

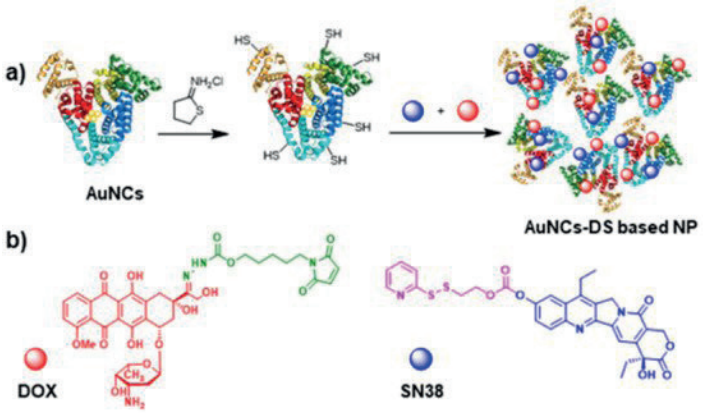

Scheme 4: (A) Schematic overview of synthesis of DOX and camptothecin SN38 functionalised BSA-AuNCs (depicted as coils with small yellow circles in the centre). (B) DOX (red) modified with pH-sensitive linker (green) and SN38 (blue) modified with a redox-sensitive linker (pink). Reproduced from Ref.[92], Copyright (2019), with permission of Multidisciplinary Digital Publishing Institute.

AuNCs have not only been investigated as a drug carrier *in vitro* and *in vivo*. El-Mageed *et al.* found *in silico* that AuNCs have the ability to act as a drug delivery system for D-penicillamine in cancer treatment.[94] This research focussed mostly on modelling the potential interactions and binding energies between D-penicillamine and gold. It was found that the drug would be coupled to the gold core mainly via physical interactions. Examples of these are the Au-O/S/N bonds, hydrogen bonds and electrostatic bonds.[94]

Recently, Hebels *et al*. reported a first in class platform employing AuNCs for light induced tumour cell killing.[11] The AuNCs were formed into a stabilized core-crosslinked micelle system based on PEG and thermosensitive poly(N-isopropylacrylamide) (PNIPAM). These micelles contained free thiols from cysteine moieties incorporated into the system. A QY of 3% was reported ($\lambda_{ex}/\lambda_{em}$=550/720 nm). Thiol-containing DOX (DOX-SH) was obtained by thiol modification of DOX with 2-iminothiolane and then covalently linked into the AuNCs during their formation. This DOX-SH-AuNC micelle formulation was shown to be toxic to MDA-MB-231 breast cancer cells upon light activation with a 650 nm laser in a highly localized fashion, highlighting the potential use of AuNCs as a tool in laser guided drug release therapies.[11]

AuNCs employed in theranostic platforms

According to Kelkar *et al.* the ultimate goal of the theranostic field is to design a single agent that provides the ability to image and monitor diseased tissue, while also showing sufficient drug delivery and treatment efficacy.[14] In this section, a review is given on the current advances in theranostic approaches employing AuNCs. Herein, a division is made between three types of theranostic platforms, depending on the function of the AuNCs within the whole complex. The AuNCs can be used solely for imaging, namely in cellular imaging experiments, be only employed for their ability to aid in therapeutic approaches, or have a function in both imaging and therapy. Table 3 summarises the articles that are mentioned in the following section, to provide a comprehensive overview.

Theranostic systems employing AuNCs as a tool for imaging

In 2012, an article was published by Chen *et al.,* who synthesised a drug delivery system by combining BSA-capped AuNCs, poly(L-lactide) (PLA) and a folic acid-conjugated sulphated polysaccharide (GPPS-FA).[95] The BSA-AuNCs formed the core of the particles, PLA the inner shell, and GPPS-FA the outer shell with FA as targeting moieties. Camptothecin was used as a hydrophobic anticancer drug that was encapsulated in the PLA inner shell of the nanocarrier. The drug-release profile showed a rapid release in the first hour due to adsorption or weak interactions in the hydrophilic shell, followed by sustained

release up to 15 hours from the hydrophobic fraction. Interestingly, the empty nanocarriers already exhibited a mild cytotoxicity in HeLa cells, which was significantly enhanced when the nanocarriers were loaded with camptothecin by encapsulation. Imaging was performed *in vitro* by confocal scanning microscopy on HeLa cells (λ_{ex} = 496 nm). [95]

A good example of a theranostic approach in drug delivery and cancer bioimaging, where AuNCs are solely used for their fluorescent properties, was developed by Muthu *et al.* in 2015.[96] They designed a vitamin E tocopheryl polyethylene glycol 1000 succinate (TPGS) micelle conjugated with transferrin for transferrin-targeted co-delivery of the drug docetaxel and fluorescent AuNCs. Docetaxel and the AuNCs were encapsulated in the lipophilic core of the micelle. The system exhibited cytotoxic properties in transferrin receptor overexpressing breast cancer cells, and the micelles emitted fluorescence (λ_{ex}/ λ_{em}= 365/620 nm) *in vitro*. The biodistribution proved to be satisfactory with a good clearance, where the transferrin-targeted micelles reached an IC_{50} value 72 fold lower than that of the FDA-approved docetaxel formulation.[96]

Croissant *et al.* managed to develop a nanocarrier system that encapsulated both gemcitabine and DOX in a mesoporous silica nanoparticle containing BSA-AuNCs for the treatment of ovarian and breast cancers.[97] In this theranostic system, the AuNCs were not involved in the encapsulation of the drugs. Gemcitabine and DOX were both immobilised with an acid-sensitive linker and released with a pH trigger that resulted in almost complete killing of cancer cells. The biodistribution of the entire system was investigated by imaging (λ_{em}= 600 nm) *in vivo*, showing good tumour targeting efficiency.[97]

Theranostic systems employing AuNCs as a tool for therapy

An approach to a dual-targeting theranostic platform was looked into by Chen *et al.* in 2016.[98] L-histidine-capped AuNCs were coupled to cyclic RGD for extracellular targeting, and to the aptamer AS1411 for nuclear targeting. DOX was then immobilised onto the nanocarrier by forming a covalent bond between the primary amine on DOX and the activated carbonyl group of histidine. This formed a drug-delivery system with a high tumour cell affinity. However, a distinct drug release profile has not been reported. Still, cancer cell inhibition occurred *in vitro* as well as *in vivo*. Using the quadrupolar anthracene-based near-infrared dye MPA, the complex showed potential towards bioimaging applications.[98]

AuNCs can also be applied in formulations for the delivery of biological drugs. Lei *et al.* reported the synthesis of GSH-oligoarginine-capped AuNCs as a nanocarrier for delivery of nerve growth factor (NGF) small interfering RNA (siRNA) in pancreatic cancer.[99] The use of AuNCs to assist in the delivery of siRNA was shown to be beneficial, considering

the gold increased the stability of siRNA in serum, as well as the circulation time, cellular uptake and tumour accumulation *in vivo*. With the help of the Cy5 NIR dye, the uptake in cells was visualised by fluorescence. In an *in vivo* subcutaneous model, the average tumour growth was reduced by 52% compared to saline control. In the orthotopic pancreatic cancer model in Balb/c nude mice, it was shown that the designed formulation decreased tumour sizes compared to saline controls, while also showing a low expression level for NGF mRNA and NGF protein. The aim to target tumour-neuron interaction by silencing the NGF gene in pancreatic cancer to inhibit progression was therefore fulfilled.[99]

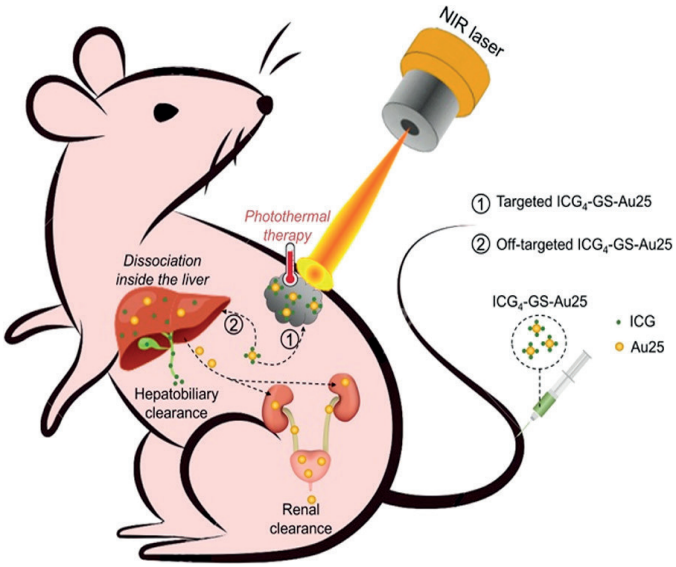

Scheme 5: Schematic representation of ICG-GSH-AuNC mediated photothermal cancer therapy and their in vivo clearance pathways after dissociation in the liver. Reproduced from Ref.[100], Copyright (2020), with permission of American Chemical Society.

Jiang *et al.* demonstrated that GSH-AuNCs coupled to the fluorescent dye indocyanine green (ICG) via amide coupling could enable a switchable fluorescence and enhance the photothermal efficacy of free ICG (see scheme 5).[100] When coupled to the GSH-AuNCs, the fluorescence of the ICG was almost completely quenched. However, it was instantaneously recovered once ICG was released ($\lambda_{ex}/\lambda_{em}$ ICG= 760/825 nm). The gold itself does not show any fluorescence at this excitation wavelength. It was found that the photochemical stability of ICG increased due to conjugation with the GSH-AuNCs. During a 15-minute light activation *in vitro*, a rapid increase in temperature of approximately 20°C was seen, with minimal decay. Contrastingly, free ICG and free GSH-AuNCs only exhibited a slight temperature increase, of approximately 10 and 5°C,

respectively. ICG-GSH-AuNCs also showed reduced inherent cytotoxicity compared to free ICG, suggesting that the efficient tumour killing is primarily achieved through PTT. *In vivo*, mice were irradiated with the laser for 8 minutes at a power density of 0.8 W/cm^2, showing similar results to *in vitro* studies. After PTT with ICG-GSH-AuNCs, the breast cancer tumours disappeared within two weeks, whereas PTT with free ICG or PBS displayed no therapeutic efficacy. This might partially be because the AuNCs prolong the blood circulation and enhance tumour targeting, as well as increase the photothermal performance compared to free ICG.[100]

Theranostic systems employing AuNCs for imaging and therapy

AuNCs have often been described for the simultaneous imaging and delivery of chemotherapeutic drugs. An example is described in the study of Zhou *et al*.[101] In this work, cisplatin is delivered as a prodrug conjugated to folic acid functionalised BSA-AuNCs to metastasised breast cancer. The drug release for this chemotherapy was based on a redox sensitive linker that coupled the cisplatin to the AuNCs. The AuNCs were then tested for their fluorescence ($\lambda_{ex}/\lambda_{em}$ = 415/670 nm) and biodistribution *in vivo*. Here, the AuNCs showed good tumour targeting efficiency with inhibition of growth and lung metastasis of 4T1 tumours, whilst avoiding accumulation in healthy organs.[101]

Khandelia *et al.* also investigated BSA-capped AuNCs, but for the delivery of DOX with concurrent single-photon or two-photon imaging of cancer cells.[102] They determined that the emission by two-photon fluorescence falls within the NIR range ($\lambda_{ex}/\lambda_{em}$ = 505/655 nm), thereby showing promise for *in vivo* imaging. They also tested the cytotoxicity of the empty BSA-AuNCs and the release of DOX to human cervical cancer cells *in vitro*. It was found that the BSA-AuNCs had no inherent cytotoxicity. When DOX was implemented, an IC_{50} of 6.3 µg/mL of DOX was determined, which is less toxic than free DOX (IC_{50} = 0.82 µg/mL). This could possibly be explained by incomplete release of DOX over the 36 hour incubation time.[102]

By inhibiting the EGFR, VEGFR and AKT signalling pathways using the dual drugs vandetanib and epigallocatechin gallate (EGCG), Kumar *et al.* showed a way to circumvent tamoxifen-resistance in breast cancer cells.[103] They designed a mesoporous silica drug delivery system that encapsulates EGCG. The silica particles are then modified to present thiols at their surface, followed by covalent bonding of AuNCs via gold-thiol interactions. Vandetanib was then coupled to the AuNCs to form the complete nanocarrier. Using the fluorescence of the AuNCs ($\lambda_{ex}/\lambda_{em}$ = 530/670 nm), the nanocarrier could be localised intracellularly. Tumour growth was delayed *in vivo* by the inhibition

of EGFR, VEGFR and AKT. Considering that these proteins are overexpressed in tamoxifen resistant cancer cells, inhibiting them may sensitise the tumour cells to tamoxifen chemotherapy.[103]

The flavonoid curcumin[89,90] has been investigated as a drug-conjugate in theranostic systems as well. Curcumin capped AuNCs were brightly fluorescent ($\lambda_{ex}/\lambda_{em}$= 550/650 nm). Furthermore, curcumin-AuNCs showed almost no toxicity in mortal cell lines (~100% cell survival) compared to a high lethality in human cervical cancer cells (~15% cell survival) at a concentration of 100 µg/mL. The drug delivery system also caused a reduction of the HeLa cell migration rate.[89] In another study on curcumin-BSA-AuNCs,[90] the nanocarriers exhibited a higher inhibition efficiency in neuroblastoma tumour cell growth than free curcumin or BSA-AuNCs alone, with an IC_{50} value of 14.3 nM. In fact, there appeared to be a synergistic induction of cellular apoptosis for this particular nanocarrier system.[90]

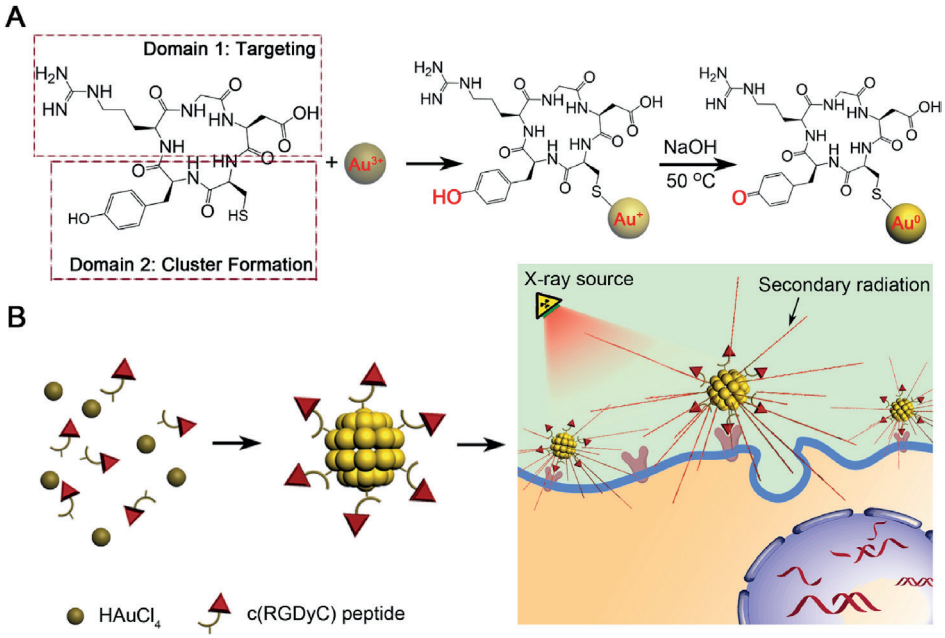

Scheme 6: Schematic illustration of RGD peptide-modified AuNC formation and application for enhanced radiotherapy. (A) The cysteine and tyrosine residues capture Au^{3+} ions and reduce them to Au^0 under alkaline conditions, respectively. (B) RGD peptide-modified AuNCs accumulate in αvβ3 integrin-positive cancer cells and interact with incident radiation intensively, generating secondary radiation, and leading to radiation enhancement effect. Reproduced from Ref.[81], Copyright (2017), with permission of Elsevier.

Wang *et al*. found that when the phosphatase and tensin homologue (PTEN) tumour suppressor gene is conjugated to AuNCs, the complex can be used to inhibit liver tumour growth as well as fluorescent imaging.[104] Using the low pH and high concentration of reductive substances (e.g. GSH and NADP+) in the tumour microenvironment, PTEN-AuNCs were synthesized *in situ* by injecting the AuNC precursor and PTEN DNA. It was subsequently found that the PTEN-AuNC complexes can inhibit or even prevent liver tumour proliferation, invasion and metastasis *in vitro*. Additionally, cancer growth was inhibited significantly in mice, and the imaging possibilities of the complex were also shown.[104]

Chen *et al.* investigated HSA and catalase co-modified alkyl thiolated AuNCs (AuNC-HSA/CAT) in photodynamic therapy combined with fluorescent imaging (λ_{ex}/λ_{em}=365/600-650 nm).[79] Using the NIR-II region for light activation with a wavelength of 1064 nm for 20 minutes, they showed that PDT utilising AuNCs is indeed possible at this long wavelength. Because the CAT moiety is also attached to the AuNCs, the problem of hypoxia in the tumours was alleviated. This was illustrated by a significant tumour volume reduction when performing PDT with the AuNC-HSA/CAT, compared to a moderate inhibition of tumour growth for the AuNC-HSA. Treatment with the laser or AuNC-HSA/CAT alone had no effect on tumour volume.[79]

Radiation therapy was also explored as a modality in theranostic AuNCs by Liang *et al*. They proposed to use RGD peptide-modified AuNCs as tumour-targeting radiotherapy enhancers (see scheme 6).[81] With this particular targeting moiety, the $\alpha_v\beta_3$ integrin-positive cancer cells can be stained, and then killed by radiotherapy with a higher efficacy compared to radiation alone. For the mice treated with the RGD peptide-modified AuNCs and radiotherapy, the tumour volume only increased by 30% over a period of 14 days, compared to an increase of over 130% for radiation alone. The RGD peptide-modified AuNCs were shown to have inherent fluorescent properties (λ_{ex}/λ_{em}=488/660 nm), as well as CT imaging capabilities.[81]

In 2019, Luo *et al*. described Cysteine-Tyrosine-Prostate Specific Membrane Antigen-targeted AuNCs (CY-PSMA-AuNCs) as radiosensitizers for therapy of prostate cancer.[84] Besides radiosensitisation, the CY-PSMA-AuNCs also had *in vitro* fluorescent (λ_{ex}/λ_{em}= 490/700 nm) and *in vivo* CT properties. Fast elimination of the CY-PSMA-AuNCs from the mice via renal clearance was observed during the biodistribution studies. *In vivo* testing showed that the tumour growth was inhibited much better in mice bearing PSMA overexpressing tumours as compared to negative tumours after IV injection. In both cases, 18 days after being given a radiation dose of 6 Gy, the tumour size increased by only 94% and 311%, respectively. Compared to the control mice with PBS injections

plus radiation, who exhibited a tumour growth of up to 430%, these results show that the AuNCs indeed act as radiosensitizers and by functionalisation with PSMA show potential for active targeting applications.[84]

Al Zaki *et al*. synthesised polymeric micelles loaded with AuNCs for the application of CT-guided radiation therapy, where the AuNCs act as radiosensitisers.[40] The micelles, consisting of an amphiphilic diblock polymer poly(ethylene glycol)-*b*-poly(Ɛ-caprolactone) contained tightly packed 1.9 nm sized AuNCs (GPMs). It was determined *in vivo* that following IV injection, the GPMs served as imaging contrast agents for CT imaging, which were used for better visualisation of the tumour boundaries. The GPMs exhibited a radiosensitisation enhancement ratio of approximately 1.2 *in vitro*, while a statistically significant improved survival rate was observed in tumour-bearing mice treated with GPMs compared to radiotherapy without GPMs.[40]

Some theranostic platforms have been developed to incorporate imaging and multiple types of therapy together. An example of this is the AuNC containing vehicle designed by Yang *et al.* in 2019.[105] GSH-capped AuNCs conjugated to graphene oxide functionalised with hyaluronic acid as targeting agent were synthesised for fluorescent image-guided synergetic delivery of 5-fluorouracil and phototherapy. Because of the inhibition of the fluorescence of the AuNCs in the presence of graphene oxide, controlled fluorescence turn-on imaging can be realised. Upon cleavage of the glycosidic linkages by hyaluronidase, the HA-GSH-AuNCs were released from the graphene oxide, leading to restoration of the fluorescence ($\lambda_{ex}/\lambda_{em}$= 580/675 nm). Subsequently, under light activation at 638 nm, photodynamic therapy could occur. Besides that, the light activation caused the loaded 5-fluorouracil to be released quickly and the graphene oxide to exhibit its photothermal properties. This leads to an enzyme and laser-controlled fluorescence, along with chemotherapeutic, photothermal and photodynamic functionalities. *In vitro* cytotoxicity studies showed the efficacy of the triple therapy where 84.3% of the lung cancer cells died, which was significantly enhanced compared to the chemotherapy or phototherapy alone.[105]

Li *et al.* designed the above mentioned (table 1) keratin-templated AuNCs functionalised with silver and gadolinium ions.[23] They showed an enhanced fluorescence intensity, biocompatibility and colloid stability, and were able to provide *in vivo* MRI as well as NIR fluorescence imaging ($\lambda_{ex}/\lambda_{em}$= 525/710 nm). Subsequently, under light activation at 638 nm, photodynamic therapy could occur. Besides that, by employing a redox sensitive linker, DOX could be selectively released in cancer cells where the concentration of glutathione is high, at both neutral and low pH. In breast cancer bearing mice, the formulation achieved a significant reduction of tumour growth.[23]

Besides acting as sensitizers in radiotherapy, as agents in phototherapy, and drug delivery applications, AuNCs themselves can also show therapeutic efficacy. Wang *et al.* developed a therapy involving *in situ* biosynthesised AuNCs that could effectively slow down tumour progress by inhibiting the activity of the PI3K-AKT pathway.[106] It was found that 24 hours after a tail vein injection with $HAuCl_4$, 2.5 nm large AuNCs had formed in the liver tumour, while also showing that the AuNCs were preferentially formed at that site by measuring their intrinsic fluorescence. After 38 days, the tumours of the mice treated with the AuNCs exhibited reduced growth compared to mice treated with PBS injections. By performing RNA-sequence analysis it was determined that the expression of proteins targeted by the PI3K-AKT signalling pathway had decreased. This was further confirmed by real-time PCR and western blots *in vitro*. Based on these results, the authors speculated that the inhibition of the PI3K-AKT pathway was the main cause of the observed reduction in tumour growth upon treatment with *in situ* biosynthesised AuNCs.[106]

AuNCs for other therapeutic applications

AuNCs have not only been investigated for their unique properties in cancer bioimaging, therapy and theranostic systems, but have also shown promise in other areas of biomedical research such as vaccine development and treatment or prevention of bacterial infection. Recent interest regarding the applicability of AuNCs in central nervous system (CNS) disorders has emerged as well. To provide an overview, the articles mentioned in the following section have also been summarised in table 3.

AuNCs in vaccine development

Several research groups have investigated AuNCs for their immunological properties as well as their potential towards simultaneous fluorescence imaging.[107–109] Fernández *et al.* studied the immunological properties of AuNCs in human dendritic cells (DCs), as well as their cellular uptake.[107] Using the fluorescence intensity of the AuNCs, they found that the zwitterionic AuNCs were readily taken up by DCs, which subsequently triggered DC maturation. This was achieved to a lesser extent with PEGylated AuNCs and larger gold nanoparticles. Immunological analysis revealed that the zwitterionic AuNCs cause T helper 1 and T regulatory cell responses, while not leading to proliferation of natural killer cells and cytotoxic T cells. These results encourage the further investigation of AuNCs in vaccines.[107]

In 2014, Tao *et al*. had already looked into AuNCs as vaccines using dual-delivery of an antigen and an adjuvant while the AuNCs simultaneously acted as an imaging

agent.[108] To this end, they conjugated the adjuvant cytosine-phosphate-guanine (CpG) oligodeoxynucleotides (ODNs) to the antigen ovalbumin, and used this as a template for the synthesis of the AuNCs. Based on the secretion of immunostimulatory cytokines TNF-α and IL-6, it was determined that the AuNC containing system induced the maturation of APCs. It was also found that the concurrent delivery of the CpG ODNs and of ovalbumin enhanced cellular immunity. Besides that, the conjugation of CpG ODN and ovalbumin to the gold caused an increased stability and enhanced cellular uptake, further increasing immunostimulatory activities. The notion that the AuNCs could therefore be used as vaccine vehicle was then further confirmed in mice, which developed an enhanced anti-ovalbumin IgG response.

Wang *et al.* aimed to develop a vaccine against hepatitis E, by preparing AuNCs *in situ* within the monomers of the hepatitis E vaccine (HEVA).[110] The presence of AuNCs caused a facile synthesis of HEVA aggregates (HEVA/Au), which possess high potency in provoking antibody responses compared to the single monomers. The inherent blue fluorescence of the HEVA/Au solution allowed for tracking of the vaccine aggregates in cells and *in vivo* (λ_{ex}/λ_{em} = 365/410 nm, QY = 6%). Cell uptake experiments showed that the HEVA/Au was easily taken up by liver and immune cells, where it was mainly present in the cytosol and lysosomal compartments. *In vivo* biodistribution studies showed accumulation of HEVA/Au in the liver, heart, kidney, lymph nodes and spleen. Whereas HEVA was toxic at concentrations above 0.1 mg/mL, HEVA/Au showed no cytotoxicity at a concentration of 1 mg/mL, displaying its improved safety profile. Furthermore, the antibody immune response was enhanced by the HEVA/Au, by influencing the Th1/Th2 immune response *in vivo*.[110]

AuNCs in the prevention and treatment of bacterial infection

Phototherapy is not only useful in treating cancer but can also be applied for dispersing biofilms. In 2020, Xie *et al.* published a study that investigated the potential of DNase-functionalised AuNCs in eradicating bacteria that are shielded by biofilms.[111] They reported that DNase can assist in enzymolysis, thereby breaking down the extracellular polymeric substance matrix, which subsequently exposes the bacteria to the AuNCs. PDT and PTT were then induced by 808 nm light activation. With a photothermal conversion of 6.6% and abundant ROS generation, the combination led to killing of approximately 90% of the biofilm-shielded bacteria. No additional photosensitizer was employed and the $^1O_2$ species detected originate from the DNase-functionalized AuNCs themselves.[111]

AuNCs have also been investigated as a bactericidal agent itself. Zheng *et al.* developed 6-mercaptohexanoic acid-protected AuNCs that could kill both Gram-positive (*S.*

aureus, S. epidermidis, Bacillus subtilis) and Gram-negative (*E. coli, Pseudomonas aeruginosa)* bacteria owing to their small size when compared to gold nanoparticles.[112] At a concentration of 0.1 mM on the basis of Au atoms, the AuNCs killed more than 90% bacteria within 2 hours of incubation. It was found that the AuNCs exhibit an IC_{50} against S. aureus comparable with widely used antibiotics such as ampicillin and penicillin.[112]

The group of Jiang *et al*. also prepared quaternary ammonium-glutathione-capped AuNCs (QA-GSH-AuNCs) for the treatment of multidrug-resistant (MDR) Gram-positive bacteria, such as methicillin-resistant *S. aureus* (MRSA) and vancomycin-resistant *Enterococci* (VRE).[113] The QA-GSH-AuNCs exhibited bright fluorescence that could be used for bacterial cell counting ($\lambda_{ex}/\lambda_{em}$= 362/592 nm). Because of the positive charge of the capping ligand, the QA-GSH-AuNCs were able to penetrate the bacterial cell wall and damage it. This was followed by ROS formation and disruption of intracellular metabolic pathways, thereby killing the bacteria. By comparing the QA-GSH-AuNCs to commonly used antibiotics, it was found that the time-kill kinetics are similar, and that the dose-dependent inhibition of *S. aureus* growth was alike to that of vancomycin. Interestingly, it was shown that the QA-GSH-AuNCs had a broader antibacterial spectrum than any of the tested established antibiotics (ampicillin, oxacillin, linezolid and vancomycin), including for VRE and MRSA, without inducing drug resistance at subinhibitory levels. *In vivo*, the toxicity to healthy cells and elimination half-life (7.5 ± 2.1 h) was satisfactory. The QA-GSH-AuNCs were able to prevent death of mice infected with MRSA for 16 days at a concentration of 40 mg/kg, which was similar to the effective dose of vancomycin.[113]

As a follow-up study, Xie *et al*. aimed to use the QA-GSH-AuNCs for the prevention of oral biofilm formation, also called plaque, to reduce bacterial infection of teeth caused by Invisalign aligners.[114] This was done by allowing the QA-GSH-AuNCs to adsorb onto the aligners to make an antibacterial coating against *S. mutans*. The QA-GSH-AuNCs have a minimal inhibitory concentration of 4 μg/mL *in vitro*, killing the bacteria via destruction of the membrane integrity. The QA-GSH-AuNCs showed negligible toxicity and inflammation in mice but were highly efficient in preventing the attachment and biofilm development of *S. mutans, S. aureus, S epidermidis* and their MDR counterparts. It was found that the *S. mutans* biofilms had 85% less biomass and 95% less cell viability on QA-GSH-AuNCs-coated aligners. The antibacterial activity of the coated aligners was shown to remain present for several cycles of use and after storage for three months. This approach could be extended to many other medical devices to reduce bacterial-induced oral diseases.[114]

Very recently, a modification of Auranofin, an FDA approved gold(I)-complex with tetraacetylated thioglucose (Ac_4GlcSH) and triethylphosphine (PEt_3) ligands employed as anti-inflammatory aid in rheumatoid arthritis, was reported for use as a nano-antibiotic.[115] Here, AuNCs (instead of gold(I)) were functionalized with mixed phosphine and glycolyl thiol ligands by ligand exchange of PPh_3-capped AuNCs. This resulted in improved activity against MDR *P. aeruginosa* (up to 4 fold) whilst reducing cytotoxicity to human A549 cells (up to 24 fold) when compared to Auranofin, further highlighting the potential of AuNCs in antimicrobial applications.[115]

AuNCs in central nervous system disorders

Another application of AuNCs that has gained recent interest, is their ability to cross the blood-brain-barrier (BBB) owing to their small size.[116] Because of this, Xiao *et al.* explored the potential of dihydrolipoic acid-capped AuNCs as probes for therapy in central nervous system (CNS) disorders, such as traumatic brain injury, stroke, Parkinson's Disease (PD) and Alzheimer's disease,[116] by detecting neuroinflammation. They found that these AuNCs could effectively reduce proinflammatory processes in microglial BV2 cells *in vitro*, indicating that these dihydrolipoic acid-capped AuNCs have potential in becoming a therapeutic agent in CNS disorders.[116]

Another example of AuNCs acting as a therapeutic agent in CNS disorders, was reported by Gao *et al.* in 2019.[117] Based on their results, they suspect that *N*-isobutyryl-*L*-cysteine (L-NIBC) protected AuNCs can serve as a novel form of therapeutics for the treatment of PD. They found that *in vitro* the L-NIBC-AuNCs prevent the aggregation and fibril formation of α-Synuclein, while having a neuroprotective effect and improving behavioural disorders in a PD mouse model *in vivo* at a dose of 20 mg/kg.[117]

Table 3: Overview of key properties of the AuNC-based systems from the studies mentioned in the section: 'AuNCs as a tool in therapy', 'AuNCs employed in theranostic platforms' and 'AuNCs for other biomedical applications'.

Reference	Capping ligand	Targeting ligand	Disease type	Function AuNCs	Excitation/ emission wavelength	Drug-delivery	Linker/ Interaction	Specifics	Results
Liu, 2019[72]	Captopril		Cutaneous squamous cell carcinoma	Photodynamic therapy and Photothermal therapy				NIR laser 808 nm	Photothermal conversion of 41%,
Liu, 2017[80]	PAMAM-NH_2		Lung cancer	Alleviate hypoxia for photodynamic therapy				532 nm laser, power density 200 mW/cm^2 PDT with photosensitiser	Reduced hypoxic conditions in tumour tissue improved photodynamic therapy efficacy with statistical significance.
Cifuentes-Rius, 2017[87]	BSA		Six mammalian cell-lines	Electromagnetic radiation therapy				8 minutes, 15W, 1 GHz electro-magnetic fields	Death in six types of mammalian cells via apoptosis and necrosis at 50 ug/mL AuNCs
Ghahremani, 2018[86]	BSA	AS1411 aptamer	Breast cancer	Megavoltage radiation therapy				0, 2, 4, 6 Gy gamma rays tested	Factor 2.7 enhanced radiation therapy
Zhang, 2014[83]	GSH		Cervical cancer	Radiotherapy				5 Gy gamma-rays from 137Cs (photon energy 662 keV) with an activity of 3600 Ci	Enhanced radiosensitivity of 30%, possibly due to higher cell-uptake, after 20 days 35% smaller tumour volume compared to radiation alone
Zhang, 2014[83]	BSA		Cervical cancer	Radiotherapy				5 Gy gamma-rays from 137Cs (photon energy 662 keV) with an activity of 3600 Ci	Enhanced radiosensitivity of 21%, no significant tumour volume reduction compared to radiation alone
El-Mageed, 2020[94]	D-penicillamine		Cancer	Drug delivery		D-penicillamine	Interactions: Au-O/S/N bond, hydrogen and electrostatic bond	Calculated *in silico*	Calculated the interactions and binding energies between D-penicillamine and gold nanoclusters.
Latorre, 2019[92]	BSA		Breast and pancreatic cancer	Drug delivery		DOX and SN38	pH- or redox-sensitive	Conjugation to BSA by disulphide and maleimide linkers	Enhanced cytotoxicity, leads to apoptosis. Also effective against cancer stem cells
Govindaraju, 2019[88]	BSA		Lung cancer	Drug delivery	550/650 nm	Kaempferol	Physical interactions		No cytotoxicity in healthy human kidney cells, cytotoxic in lung cancer cells
Lakshmi, 2019[91]	BSA		Lung cancer	Drug delivery (fluorescence not tested in cells)	360/568 nm	Quercetin	Au-OH interaction		Good cellular uptake and bioimaging properties. High cytotoxicity in lung cancer cells, minimal death in normal fibroblast cells.

Reference	Capping ligand	Targeting ligand	Disease type	Function AuNCs	Excitation/ emission wavelength	Drug-delivery	Linker/ Interaction	Specifics	Results
Lei, 2017[99]	GSH-oligoarginine		Pancreatic cancer	Improving stability and circulation time	430/596 nm	NGF siRNA	Adsorbing via electrostatic interaction	Loading capacity of 226 µmol siRNA per g GNC	Target tumour-neuron interaction by silencing NGF gene successful
Hebels, 2021[11]	PEG-PNIPAM core-crosslinked polymeric micelles		Breast Cancer	Triggered drug delivery by NIR light activation	550/720 nm	DOX-SH	Au-S bonds		Highly localized cytotoxicity on MDA-MB-231 cells upon 650 nm light activation
Chen, 2012[95]	BSA-GPPS	Folic acid	Cervical cancer	Fluorescent imaging	480/620 nm	Camptothecin	Encapsulated		Empty nanocarriers had mild cytotoxicity in HeLa cells
Croissant, 2016[97]	BSA		Ovarian and breast cancer	Fluorescent imaging	??/645 nm	Gemcitabine and doxorubicin	pH sensitive	Mesoporous silica nanoparticle	Accumulated in kidney and liver
Muthu, 2015[96]	TPGS micelle	Transferrin	Breast cancer	Fluorescent imaging	365/620 nm	Docetaxel	Encapsulated in lipophilic core		IC50 value up to 72-fold lower than FDA-approved docetaxel formulation.
Jiang, 2020[100]	GSH		Breast cancer	Photothermal therapy				Indocyanine green as NIR fluorescent dye	The AuNCs managed to completely eradicate tumours
Chen, 2016[98]	L-histidine	Cyclic RGD and AS1411 aptamer	Malignant glioma	Drug delivery		Doxorubicin	Covalent bond between amine DOX and activated carboxyl group of histidine	Near-infrared dye for fluorescent imaging	Drug release profile not reported
Jiang, 2020[100]	GSH		Breast cancer	Drug delivery, enhance photothermal therapy, improve stability and circulation time	760/825 (ICG)	Indocyanine green (ICG)	Covalent bond via NHS/ amine coupling between GSH and ICG	*In vivo*: 808 nm NIR laser, 0.8 W/ cm^2 power density for 8 minutes	14 days after PTT, breast cancer tumours disappeared for mice treated with ICG-GSH-AuNCs. Free ICG and PBS in combination with PTT showed to therapeutic efficacy.
Luo, 2019[84]	CY	PSMA	Prostate cancer	Fluorescent imaging, CT imaging and Radiotherapy	490/700 nm				Functional in PSMA positive and PSMA negative tumours
Al Zaki, 2014[40]	Polymeric micelles		Fibrosarcoma	CT imaging and radiotherapy				6 Gy X-ray radiation	Radiosensitisation of about 1.2, Kaplan-Meier survival curve shows improved survival
Wang, 2020[104]	PTEN		Liver cancer	Fluorescent imaging and Act as a drug	490 nm			*In situ* biosynthesis after injection of HAuCl4 and PTEN DNA	PTEN-AuNC complexes can inhibit or even prevent liver tumour proliferation, invasion and metastasis
Govindaraju, 2018[89]	BSA and curcumin		Cervical cancer	Fluorescent imaging and drug delivery	550/650 nm	Curcumin	Capping ligand		No cytotoxicity in mortal cell lines, high lethality in human cervical cancer cells

Reference	Capping ligand	Targeting ligand	Disease type	Function AuNCs	Excitation/ emission wavelength	Drug-delivery	Linker/ Interaction	Specifics	Results
Fu, 2018[90]	BSA		Neuroblastoma	Fluorescent imaging and drug delivery	510/634 nm	Curcumin	Encapsulated		Higher inhibition efficiency compared to free curcumin or BSA-AuNCs alone
Zhou, 2016[101]	BSA	Folic acid	Metastasised breast cancer	Fluorescent imaging and drug delivery	415/670 nm	Cisplatin	Redox-sensitive		Did not accumulate in healthy organs
Khandelia, 2015[102]	BSA		Cervical cancer	Fluorescent imaging and drug delivery	505/655 nm	Doxorubicin	Electrostatic interactions and hydrogen bonding	Encapsulation efficiency 83.05%	Lower cytotoxicity than free DOX, possibly due to incomplete release
Kumar, 2018[103]	Thiol - mesoporous silica		Tamoxifen resistant breast cancer	Fluorescent imaging and drug delivery	530/670 nm	EGCG and Vandetanib	Vandetanib bound to Au, EGCG encapsulated in silica	Inhibition of EGFR, VEGFR and AKT pathway	Tumour growth was slowed down
Wang, 2019[106]	None		Liver cancer	Fluorescent imaging, act as a drug	Confirmed *in vivo*			*In situ* biosynthesis after injection of HAuCl4	After 38 days reduced tumour growth, reduces signalling in PI3K-AKT pathway
Chen, 2018[79]	HSA-CAT		Breast cancer	Fluorescent imaging and Photodynamic therapy	365/600-650 nm			NIR-II light excitation 1064 nm for 20 minutes	Due to the CAT functionality, hypoxia was alleviated, PDT is possible
Yang, 2019[105]	GSH	Hyaluronic acid	Lung cancer	Fluorescent imaging and Photodynamic therapy	580/675 nm	5-fluorouracil	Light/enzyme triggered	Conjugation to graphene, also PTT at 638 nm	Controlled fluorescence and PDT. Light- and enzyme triggered drug release, PTT due to graphene
Liang, 2017[81]	RGD peptide	RGD peptide	Breast and cervical cancer	Fluorescent imaging, CT imaging and radiotherapy	488/660 nm			6 Gy X-ray radiation at 160 kVp	Tumours only increased 30% in volume compared to 130% for radiation alone
Li, 2020[23]	Keratin		Breast cancer	Fluorescent imaging, MRI, drug delivery	525/710 nm	Doxorubicin	Redox-sensitive	Gadolinium and silver ions for MRI and enhanced fluorescence	Significant reduction of tumour growth, enhanced fluorescent intensity, biocompatibility and colloid stability, NIR fluorescence
Fernández, 2015[107]	zwitterionic ligand		Vaccines	DC maturation					Zwitterionic AuNCs cause T helper 1 regulatory cell responses in the form of cytokines, while not leading to proliferation of NK cells and cytotoxic T cells
Tao, 2014[108]	CpG-ODN-Ovalbumin		Vaccines	Fluorescent imaging, delivery of antigen and adjuvant	490/595 nm				Secretion of TNF-alpha and IL-6 release, gold nanoclusters cause maturation of APCs. Mice developed enhanced anti-ovalbumin IgG response

Reference	Capping ligand	Targeting ligand	Disease type	Function AuNCs	Excitation/ emission wavelength	Drug-delivery	Linker/ Interaction	Specifics	Results
Tao, 2015[109]	Thiolated CpG-ODN-Ovalbumin peptide		Vaccines	Fluorescent imaging, delivery of antigen and adjuvant	500/600 nm				CpG-ODN-AuNCs can promote cross-presentation by simultaneous delivery of antigen and adjuvant
Wang, 2016[110]	HEVA		Hepatitis E Vaccines	Fluorescent imaging, improve immune response and safety profile	365/410 nm		Bonds between Au and cysteine or histidine		Improved safety profile and immunotherapy efficacy *in vivo* by influencing a Th1/Th2 response.
Zheng, 2017[112]	6-mercapto-hexanoic acid		Bacterial infection	Act as a drug					Can kill both gram-positive and gram-negative bacteria. IC50 against S. aureus comparable with ampicillin and penicillin
Xie, 2020[111]	DNase		Bacterial infection	Photodynamic therapy and Photothermal therapy				NIR laser 808 nm	Photothermal conversion of 6.59% - Kills 90% of biofilm-shielded bacteria
Xie, 2018[113]	GSH	QA	Bacterial infection	Act as a drug	362/592 nm		Au-S bonds	*In vivo* concentration of 40 mg/kg	Comparable with vancomycin in terms of time-kill kinetics and dose-dependent inhibition of *S. aureus*. Has a broader antibacterial spectrum, including VRE and MRSA
Xie, 2020[114]	GSH	QA	Prevention of bacterial infection	Act as a drug	360/610 nm		Au-S bonds, electrostatic interaction between AuNC and aligners		Able to prevent biofilm formation in the oral cavity by absorbing on the Invisalign aligners. Active against *S. aureus, S. mutans* and other gram-positive bacteria.
Ndugire, 2021[115]	Phosphine and glycosyl ligands	Glycans	Bacterial infection	Act as a drug	Not reported		Au-S and Au-P bonds		Increased bactericidal activity against *P. aeruginosa* and reduced cytotoxicity to A549 cells as compared to Auranofin (gold (I) analogue)
Xiao, 2020[116]	Dihydrolipoic acid		CNS disorders	Fluorescent imaging and neuroprotection	405/685 nm				Gold nanoclusters can penetrate the blood-brain barrier
Gao, 2019[117]	L-NIBC		Parkinson's Disease	Act as a drug					Neuroprotective effect in PD mouse model, prevent aggregation and fibril formation of alpha-synuclein

Discussion

In the past two decades, the NIR fluorescence of AuNCs, its origin and how to tune it have been thoroughly studied. Design strategies using proteins, peptides or other biological molecules as structural scaffolds for the synthesis of AuNCs were developed to preserve the AuNCs' attractive photoluminescent properties while increasing the biocompatibility. This paved the way for the use of AuNCs in NIR fluorescent bioimaging. AuNCs were also investigated for therapeutic applications, involving drug delivery, phototherapy and radiotherapy, amongst others. In particular, a lot of research focused on combining imaging and therapy in a single platform. Although many different definitions exist of what a theranostic platform is, in this review AuNC containing platforms are considered as theranostic when the imaging and therapeutic properties have been tested in cellular experiments or *in vivo*.

Looking at the extensive research done on the topic of AuNCs as theranostic tools, particularly in cancer, numerous approaches have been investigated so far and yet there has been no report of AuNCs being investigated in clinical trials. There is a chance that this is simply because AuNCs are a relatively new field of research, and that not enough preclinical studies have been conducted yet. The earlier developed, larger gold nanoparticles have been under investigation in clinical trials for several years already.[118] Considering the current drawbacks of gold nanoparticles, mainly caused by controversial and inconsistent outcomes *in vitro* and *in vivo*, one could argue for the superiority of AuNCs. Whereas some gold nanoparticles can exhibit disadvantages including toxicity, species-specific differences in biodistribution and physiological response, relatively large size, and RES organ accumulation,[118] AuNCs presented so far show little to no inherent toxicity, good biocompatibility, satisfactory biodistribution and renal clearance. Depending on the capping-ligand, the cellular uptake efficiency and clearance is either improved or decreased. In general, AuNCs accumulate well in cells via endocytic pathways.[107] A set of experiments comparing the clearance of AuNCs and gold nanoparticles concluded that the size of the AuNCs is an advantage here.[84] Using the same capping ligand, targeting agent and amount of gold, the gold nanoparticles accumulated twice as much in the liver compared to the AuNCs.[84] In addition to that, earlier obtained results from Tsvirkun *et al*. in 2018, stated that they found a reverse correlation between gold nanoparticle size and tumour uptake via CT imaging.[119] From these studies, a careful conclusion could be drawn that the AuNCs can be superior to the larger gold nanoparticles for cancer therapy applications *in vivo* with regard to tumour uptake, toxicity, biodistribution and clearance, which could contribute to improved treatment outcome.

In other fields, AuNCs and gold nanoparticles compare well. With the appropriate surface modifications, gold nanoparticles too can cross the BBB.[118] AuNCs have been found to do this because of their small size.[116] They can also both be used for applications in drug delivery, active targeting, photothermal and photodynamic therapy (usually with conjugated photosensitiser), and CT imaging.[118]

Another feature of AuNCs is that they can be used for various applications such as the sensing of heavy metals, biological molecules and intracellular temperature. Even in surgery, the AuNCs may be of use, for example in robot-assisted fluorescence-guided surgery. Furthermore, the use of AuNCs (amongst other metal nanoclusters) as bactericidal agents has also gained increasing interest.[120]

However, it is imperative to look at both sides of the coin as there are limits to the use of AuNCs as diagnostic and therapeutic agents as well. One example is the limitations that arise from the AuNCs' native fluorescence peaks being most commonly in the NIR range. Deep tissue imaging (imaging with a depth from millimetres to centimetres) requires imaging wavelengths between 650 and 900 nm, because then only little amounts of absorption from water and blood occur.[121] Nevertheless, the window is not optimal either because of autofluorescence of tissues that cause some background noise. So, even though the tissue penetration of NIR-I and NIR-II light is better than that of visible light and UV-light, the imaging capability is not deeper than one or two centimetres.[122] This is in contrast with other imaging techniques that are currently in use for the purpose of diagnostics. CT, MRI and PET imaging have unlimited tissue penetration, but they each have their own shortcomings.[123] Major limitations of CT are that it uses ionizing radiation and that is has a low soft tissue sensitivity. MRI has a high spatial resolution but has the disadvantage that the overall sensitivity is low. PET imaging, on the other hand, has excellent sensitivity, but is very costly and has a low spatial resolution.[123] When applying NIR-fluorescent imaging alone, not enough functional information can be obtained. However, multimodal fluorescent imaging, where fluorescence imaging is combined with other imaging possibilities, has emerged as a promising tool for imaging with improved sensitivity and accuracy.[123] Considering that AuNCs have already been researched for multimodal fluorescent imaging, the limitations of NIR light may be overcome.

Currently, indocyanine green is the only fluorescent dye approved by the FDA for clinical use. The IRDye 800CW has entered clinical trials conjugated to antibodies, thus as targeted tracers.[123,124] These dyes have a slight advantage over NIR-fluorescent AuNCs in the way that they also emit light with a high intensity in the NIR-II window, providing a higher

imaging contrast and even deeper tissue penetration.[125] However, without coupling them to another functionality, they do not have the possibility for multimodal imaging.

Another, perhaps more important aspect of AuNCs that may hinder their progress to human studies, is that GSH-capped AuNCs may cause epigenetic modifications in healthy cells at non-cytotoxic levels.[126] The notion that they have a direct effect on epigenetic processes could cause unwanted side-effects during diagnosis or treatment. Still, as far as our knowledge goes, it has only been reported once, and should thus be investigated more in-depth before drawing conclusions.

As illustrated in this review, various biomolecules (including peptides and proteins) but also various other materials such as polymers may be employed as capping ligands for AuNCs. This provides opportunities for reducing toxicity, improving biocompatibility and targeting, which ultimately make AuNCs an attractive and versatile tool for biomedical applications.[127,128] Furthermore, the increase in AuNC related publications over the last 15 years for imaging, sensing and therapy speaks volumes towards the increased interest for AuNCs in biomedical applications, increasing confidence that clinical translation may not be too far off anymore.[129–132]

Future perspectives

All in all, while promising research focused on enabling the use of the emergent properties of AuNCs has been developed, translation of this laboratory knowledge to functional clinical technology will take time. To efficiently image cancer tissue, employing targeting ligands such as folic acid, hyaluronic acid or the aptamer AS1411 on the surface, has shown to improve uptake in tumour cells by active targeting. By means of fluorescence imaging and CT imaging, tumours can then be diagnosed accurately. With only minor modifications to the surface chemistry, PET and MRI are also within reach. Ideally, the AuNC-containing system would be used for diagnosis first, before locally activating treatment. This would reduce side-effects while providing a highly efficient solution to inhibit tumour growth. In this regard, acid-, enzyme- or redox-sensitive linkers can help pave the way towards achieving localized release. Drug-release or therapy triggered by external factors, such as local light activation with a (NIR-)laser, could also be a solution for this. Additionally, photothermal, photodynamic and radiation therapy may also serve as alternative therapies in different combinations. For the application of photothermal therapy, a balance should be found between photoluminescence and photothermal conversion for optimal results. In the end, the most powerful theranostic approach would consist of both multimodal imaging and combination therapy. Perhaps one day, AuNCs

will be the new golden standard in the diagnosis and treatment of cancer or other newly emerging fields of application in infectious diseases and neurological disorders.

Acknowledgments

The Netherlands Organization for Scientific Research (NWO/Aspasia 015.009.038 and NWO/Industrial Doctorates NWA.ID.17.030) is acknowledged for funding. All authors declare that they have no financial/commercial Conflict of Interest.

List of abbreviations

AcSEMA	2-(acetylthio)ethyl methacrylate
APC	Antigen Presenting Cells
ATP	Adenosine triphosphate
AuNC	Gold nanocluster
BBB	Blood Brain Barrier
BSA	Bovine Serum Albumin
CAT	Catalase
CNS	Central Nervous System
CpG	Cytosine-phosphate-guanine
CT	Computed Tomography
CY	Cysteine
DC	Dendritic Cells
DNA	Deoxyribose nucleic acid
DOX	Doxorubicin
DOX-SH	Doxorubicin-iminothiolane
EGCG	Epigallocatechin gallate
EGFR	Epidermal Growth Factor Receptor
EPR	Enhanced Permeability and Retention
FA	Folic Acid
FDA	Food and Drug Administration
FLIM	Fluorescence lifetime imaging microscopy
GFP	Green Fluorescent Protein
GPM	Poly(ethylene glycol)-b-poly(E-caprolactone) micelles containing AuNCs
GPPS	Sulphated polysaccharide
GSH	Glutathione
HA	Hyaluronic acid

HEVA	Hepatitis E vaccine
HNSCC	Head and Neck Squamous Cell Carcinoma
HSA	Human Serum Albumin
IC50	Inhibiting Concentration 50%
ICG	Indocyanine Green
IgG	Immunoglobulin G
IL	Interleukin
IV	Intravenous
L-NIBC	N-isobutyryl-L-cysteine
LOD	Limit of Detection
Lys	Lysozyme
MDR	Multidrug resistant
MMP2	Matrix metalloproteinase-2
MPA	Quadrupolar anthracene-based dye
MRI	Magnetic Resonance Imaging
MRSA	Methicillin-resistant S. Aureus
NADP+	Nicotinamide adenine dinucleotide phosphate
NGF	Nerve Growth Factor
NIR	Near Infrared
NIR-II	NIR light in the second biological window between 1000-1400 nm
ODN	Oligodeoxynucleotides
OEGMA	Oligo(ethylene glycol) methyl ether methacrylate
PAI	Photoacoustic imaging
PAMAM	Poly(amidoamine) dendrimer
PBS	Phosphate Buffered Saline
PCR	Polymerase Chain Reaction
PD	Parkinson’s Disease
PDT	Photodynamic Therapy
PEG	Poly(ethylene glycol)
PEI	Polyethyleneimine
PET	Positron Emission Tomography
PLA	Poly(L-Lactide)
PMMA	Poly(methyl methacrylate)
PNIPAM	Poly(N-isopropylacrylamide)
PSMA	Prostate Specific Membrane Antigen

PTEN	Phosphatase and tensin homologue tumour suppressor gene
PTT	Photothermal Therapy
PVP	Poly(N-vinylpyrrolidone)
QA	Quaternary ammonium
QY	Luminescence Quantum Yield
RES	Reticuloendothelial system
RGD	Arginine-Glycine-Aspartic acid
RNA	Ribonucleic acid
ROS	Reactive Oxygen Species
siRNA	Small interfering RNA
SWIR	Short wavelength infrared
TNF-a	Tumour Necrosis Factor
TPGS	Vitamin E tocopheryl polyethylene glycol 1000 succinate
Try	Trypsin
UV	Ultraviolet
VEGFR	Vascular Epidermal Growth Factor Receptor
VRE	Vancomycin-resistant Enterococci

References

(1) Li, H.; Li, H.; Wan, A. Luminescent Gold Nanoclusters for in Vivo Tumor Imaging. *Analyst* **2020**, *145* (2), 348–363.

(2) Siegel, R. L.; Miller, K. D.; Jemal, A. Cancer Statistics, 2019. *CA. Cancer J. Clin.* **2019**, *69* (1), 7–34.

(3) Soper, S. A.; Rasooly, A. Cancer: A Global Concern That Demands New Detection Technologies. *Analyst* **2016**, *141* (2), 367–370.

(4) Zhang, Q.; Yang, M.; Zhu, Y.; Mao, C. Metallic Nanoclusters for Cancer Imaging and Therapy. *Curr. Med. Chem.* **2017**, *24* (999), 1–1.

(5) Zheng, Y.; Wu, J.; Jiang, H.; Wang, X. Gold Nanoclusters for Theranostic Applications. *Coord. Chem. Rev.* **2021**, *431*, 213689.

(6) Hembury, M.; Beztsinna, N.; Asadi, H.; Van Den Dikkenberg, J. B.; Meeldijk, J. D.; Hennink, W. E.; Vermonden, T. Luminescent Gold Nanocluster-Decorated Polymeric Hybrid Particles with Assembly-Induced Emission. *Biomacromolecules* **2018**, *19* (7), 2841–2848.

(7) Jin, R. Quantum Sized, Thiolate-Protected Gold Nanoclusters. *Nanoscale* **2010**, *2* (3), 343–362.

(8) Cantelli, A.; Battistelli, G.; Guidetti, G.; Manzi, J.; Di Giosia, M.; Montalti, M. Luminescent Gold Nanoclusters as Biocompatible Probes for Optical Imaging and Theranostics. *Dye. Pigment.* **2016**, *135*, 64–79.

(9) Yang, T.-Q.; Peng, B.; Shan, B.-Q.; Zong, Y.-X.; Jiang, J.-G.; Wu, P.; Zhang, K. Origin of the Photoluminescence of Metal Nanoclusters: From Metal-Centered Emission to Ligand-Centered Emission. *Nanomaterials* **2020**, *10* (2), 261.

(10) Wu, Z.; Jin, R. On the Ligand's Role in the Fluorescence of Gold Nanoclusters. *Nano Lett.* **2010**, *10* (7), 2568–2573.

(11) Hebels, E. R.; Najafi, M.; van den Dikkenberg, J.; Beztsinna, N.; van de Looij, S.; Wilbie, D.; Meeldijk, J.; Hembury, M.; Vermonden, T. Luminescent Gold Nanocluster-Decorated Polymeric Hybrid Particles for Laser Guided Therapy. *Eur. Polym. J.* **2021**, *152* (October 2020), 110467.

(12) Yu, N.; Huang, L.; Zhou, Y.; Xue, T.; Chen, Z.; Han, G. Near-Infrared-Light Activatable Nanoparticles for Deep-Tissue-Penetrating Wireless Optogenetics. *Adv. Healthc. Mater.* **2019**, *8* (6), 1801132.

(13) Chen, L.-Y.; Wang, C.-W.; Yuan, Z.; Chang, H.-T. Fluorescent Gold Nanoclusters: Recent Advances in Sensing and Imaging. *Anal. Chem.* **2015**, *87* (1), 216–229.

(14) Kelkar, S. S.; Reineke, T. M. Theranostics: Combining Imaging and Therapy. *Bioconjug. Chem.* **2011**, *22* (10), 1879–1903.

(15) Cheng, Y.; Lu, G.; He, Y.; Shen, H.; Zhao, J.; Xia, K.; Gong, Q. Luminescence Quantum Yields of Gold Nanoparticles Varying with Excitation Wavelengths. *Nanoscale* **2016**, *8* (4), 2188–2194.

(16) Chistopoulos, T. K.; Diamandis, E. P. Fluorescence Immunoassays. In *Immunoassay*; Elsevier, 1996; pp 309–335.

(17) Zhang, X. D.; Wu, D.; Shen, X.; Liu, P. X.; Fan, F. Y.; Fan, S. J. In Vivo Renal Clearance, Biodistribution, Toxicity of Gold Nanoclusters. *Biomaterials* **2012**, *33* (18), 4628–4638.

(18) Xie, J.; Zheng, Y.; Ying, J. Y. Protein-Directed Synthesis of Highly Fluorescent Gold Nanoclusters. *J. Am. Chem. Soc.* **2009**, *131* (3), 888–889.

(19) Wang, J.; Ma, S.; Ren, J.; Yang, J.; Qu, Y.; Ding, D.; Zhang, M.; Yang, G. Fluorescence Enhancement of Cysteine-Rich Protein-Templated Gold Nanoclusters Using Silver(I) Ions and Its Sensing Application for Mercury(II). *Sensors Actuators, B Chem.* **2018**, *267*, 342–350.

(20) Wang, Y.; Chen, J. T.; Yan, X. P. Fabrication of Transferrin Functionalized Gold Nanoclusters/Graphene Oxide Nanocomposite for Turn-on near-Infrared Fluorescent Bioimaging of Cancer Cells and Small Animals. *Anal. Chem.* **2013**, *85* (4), 2529–2535.

(21) Chen, T.-H.; Tseng, W.-L. (Lysozyme Type VI)-Stabilized Au8 Clusters: Synthesis Mechanism and Application for Sensing of Glutathione in a Single Drop of Blood. *Small* **2012**, *8* (12), 1912–1919.

(22) Wei, H.; Wang, Z.; Yang, L.; Tian, S.; Hou, C.; Lu, Y. Lysozyme-Stabilized Gold Fluorescent Cluster: Synthesis and Application as Hg^{2+} Sensor. *Analyst* **2010**, *135* (6), 1406.

(23) Li, Y.; Cao, Y.; Wei, L.; Wang, J.; Zhang, M.; Yang, X.; Wang, W.; Yang, G. The Assembly of Protein-Templated Gold Nanoclusters for Enhanced Fluorescence Emission and Multifunctional Applications. *Acta Biomater.* **2020**, *101*, 436–443.

(24) Kawasaki, H.; Hamaguchi, K.; Osaka, I.; Arakawa, R. Ph-Dependent Synthesis of Pepsin-Mediated Gold Nanoclusters with Blue Green and Red Fluorescent Emission. *Adv. Funct. Mater.* **2011**, *21* (18), 3508–3515.

(25) Liu, C.-L.; Wu, H.-T.; Hsiao, Y.-H.; Lai, C.-W.; Shih, C.-W.; Peng, Y.-K.; Tang, K.-C.; Chang, H.-W.; Chien, Y.-C.; Hsiao, J.-K.; Cheng, J.-T.; Chou, P.-T. Insulin-Directed Synthesis of Fluorescent Gold Nanoclusters: Preservation of Insulin Bioactivity and Versatility in Cell Imaging. *Angew. Chemie Int. Ed.* **2011**, *50* (31), 7056–7060.

(26) Kong, Y.; Chen, J.; Gao, F.; Brydson, R.; Johnson, B.; Heath, G.; Zhang, Y.; Wu, L.; Zhou, D. Near-Infrared Fluorescent Ribonuclease-A-Encapsulated Gold Nanoclusters: Preparation, Characterization, Cancer Targeting and Imaging. *Nanoscale* **2013**, *5* (3), 1009–1017.

(27) West, A. L.; Griep, M. H.; Cole, D. P.; Karna, S. P. DNase 1 Retains Endodeoxyribonuclease Activity Following Gold Nanocluster Synthesis. *Anal. Chem.* **2014**, *86* (15), 7377–7382.

(28) Wen, F.; Dong, Y.; Feng, L.; Wang, S.; Zhang, S.; Zhang, X. Horseradish Peroxidase Functionalized Fluorescent Gold Nanoclusters for Hydrogen Peroxide Sensing. *Anal. Chem.* **2011**, *83* (4), 1193–1196.

(29) Xu, Y.; Sherwood, J.; Qin, Y.; Crowley, D.; Bonizzoni, M.; Bao, Y. The Role of Protein Characteristics in the Formation and Fluorescence of Au Nanoclusters. *Nanoscale* **2014**, *6* (3), 1515–1524.

(30) Chen, Y.; Montana, D. M.; Wei, H.; Cordero, J. M.; Schneider, M.; Le Guével, X.; Chen, O.; Bruns, O. T.; Bawendi, M. G. Shortwave Infrared in Vivo Imaging with Gold Nanoclusters. *Nano Lett.* **2017**, *17* (10), 6330–6334.

(31) Lopez, A.; Liu, J. DNA-Templated Fluorescent Gold Nanoclusters Reduced by Good's Buffer: From Blue-Emitting Seeds to Red and near Infrared Emitters. *Can. J. Chem.* **2015**, *93* (6), 615–620.

(32) Zhou, C.; Long, M.; Qin, Y.; Sun, X.; Zheng, J. Luminescent Gold Nanoparticles with Efficient Renal Clearance. *Angew. Chemie Int. Ed.* **2011**, *50* (14), 3168–3172.

(33) Luo, Z.; Yuan, X.; Yu, Y.; Zhang, Q.; Leong, D. T.; Lee, J. Y.; Xie, J. From Aggregation-Induced Emission of Au(I)–Thiolate Complexes to Ultrabright Au(0)@Au(I)–Thiolate Core–Shell Nanoclusters. *J. Am. Chem. Soc.* **2012**, *134* (40), 16662–16670.

(34) Bera, D.; Goswami, N. Driving Forces and Routes for Aggregation-Induced Emission-Based Highly Luminescent Metal Nanocluster Assembly. *J. Phys. Chem. Lett.* **2021**, *12* (37), 9033–9046.

(35) Zheng, J.; Zhang, C.; Dickson, R. M. Highly Fluorescent, Water-Soluble, Size-Tunable Gold Quantum Dots. *Phys. Rev. Lett.* **2004**, *93* (7).

(36) Santiago González, B.; Rodríguez, M. J.; Blanco, C.; Rivas, J.; López-Quintela, M. A.; Martinho, J. M. G. One Step Synthesis of the Smallest Photoluminescent and Paramagnetic PVP-Protected Gold Atomic Clusters. *Nano Lett.* **2010**, *10* (10), 4217–4221.

(37) Duan, H.; Nie, S. Etching Colloidal Gold Nanocrystals with Hyperbranched and Multivalent Polymers: A New Route to Fluorescent and Water-Soluble Atomic Clusters. *J. Am. Chem. Soc.* **2007**, *129* (9), 2412–2413.

(38) Hussain, I.; Graham, S.; Wang, Z.; Tan, B.; Sherrington, D. C.; Rannard, S. P.; Cooper, A. I.; Brust, M. Size-Controlled Synthesis of Near-Monodisperse Gold Nanoparticles in the 1−4 Nm Range Using Polymeric Stabilizers. *J. Am. Chem. Soc.* **2005**, *127* (47), 16398–16399.

(39) Adnan, N. N. M.; Ahmad, S.; Kuchel, R. P.; Boyer, C. Exploring the Potential of Linear Polymer Structures for the Synthesis of Fluorescent Gold Nanoclusters. *Mater. Chem. Front.* **2017**, *1* (1), 80–90.

(40) Al Zaki, A.; Joh, D.; Cheng, Z.; De Barros, A. L. B.; Kao, G.; Dorsey, J.; Tsourkas, A. Gold-Loaded Polymeric Micelles for Computed Tomography-Guided Radiation Therapy Treatment and Radiosensitization. *ACS Nano* **2014**, *8* (1), 104–112.

(41) Chen, D.; Luo, Z.; Li, N.; Lee, J. Y.; Xie, J.; Lu, J. Amphiphilic Polymeric Nanocarriers with Luminescent Gold Nanoclusters for Concurrent Bioimaging and Controlled Drug Release. *Adv. Funct. Mater.* **2013**, *23* (35), 4324–4331.

(42) Ma, H.; Wang, J.; Zhang, X. D. Near-Infrared II Emissive Metal Clusters: From Atom Physics to Biomedicine. *Coord. Chem. Rev.* **2021**, *448*, 214184.

(43) Liu, H.; Hong, G.; Luo, Z.; Chen, J.; Chang, J.; Gong, M.; He, H.; Yang, J.; Yuan, X.; Li, L.; Mu, X.; Wang, J.; Mi, W.; Luo, J.; Xie, J.; Zhang, X. Atomic-Precision Gold Clusters for NIR-II Imaging. *Adv. Mater.* **2019**, *31* (46), 1901015.

(44) Porret, E.; Le Guével, X.; Coll, J.-L. Gold Nanoclusters for Biomedical Applications: Toward in Vivo Studies. *J. Mater. Chem. B* **2020**, *8* (11), 2216–2232.

(45) Talelli, M.; Barz, M.; Rijcken, C. J. F.; Kiessling, F.; Hennink, W. E.; Lammers, T. Core-Crosslinked Polymeric Micelles: Principles, Preparation, Biomedical Applications and Clinical Translation. *Nano Today* **2015**, *10* (1), 93–117.

(46) Torchilin, V. Tumor Delivery of Macromolecular Drugs Based on the EPR Effect. *Adv. Drug Deliv. Rev.* **2011**, *63* (3), 131–135.

(47) Liu, J. M.; Chen, J. T.; Yan, X. P. Near Infrared Fluorescent Trypsin Stabilized Gold Nanoclusters as Surface Plasmon Enhanced Energy Transfer Biosensor and in Vivo Cancer Imaging Bioprobe. *Anal. Chem.* **2013**, *85* (6), 3238–3245.

(48) Zhang, P.; Yang, X. X.; Wang, Y.; Zhao, N. W.; Xiong, Z. H.; Huang, C. Z. Rapid Synthesis of Highly Luminescent and Stable Au20 Nanoclusters for Active Tumor-Targeted Imaging in Vitro and in Vivo. *Nanoscale* **2014**, *6* (4), 2261–2269.

(49) Hembury, M.; Chiappini, C.; Bertazzo, S.; Kalber, T. L.; Drisko, G. L.; Ogunlade, O.; Walker-Samuel, S.; Krishna, K. S.; Jumeaux, C.; Beard, P.; Kumar, C. S. S. R.; Porter, A. E.; Lythgoe, M. F.; Boissière, C.; Sanchez, C.; Stevens, M. M. Gold–Silica Quantum Rattles for Multimodal Imaging and Therapy. *Proc. Natl. Acad. Sci.* **2015**, *112* (7), 1959–1964.

(50) Han, W.; Yang, W.; Gao, F.; Cai, P.; Wang, J.; Wang, S.; Xue, J.; Gao, X.; Liu, Y. Iodine-124 Labeled Gold Nanoclusters for Positron Emission Tomography Imaging in Lung Cancer Model. *J. Nanosci. Nanotechnol.* **2019**, *20* (3), 1375–1382.

(51) Liu, Y.; Tian, G. F.; He, X. W.; Li, W. Y.; Zhang, Y. K. Microwave-Assisted One-Step Rapid Synthesis of near-Infrared Gold Nanoclusters for NIRF/CT Dual-Modal Bioimaging. *J. Mater. Chem. B* **2016**, *4* (7), 1276–1283.

(52) Hu, D. H.; Sheng, Z. H.; Zhang, P. F.; Yang, D. Z.; Liu, S. H.; Gong, P.; Gao, D. Y.; Fang, S. T.; Ma, Y. F.; Cai, L. T. Hybrid Gold-Gadolinium Nanoclusters for Tumor-Targeted NIRF/CT/MRI Triple-Modal Imaging in Vivo. *Nanoscale* **2013**, *5* (4), 1624–1628.

(53) Zhang, H.; Han, W.; Cao, X.; Gao, T.; Jia, R.; Liu, M.; Zeng, W. Gold Nanoclusters as a Near-Infrared Fluorometric Nanothermometer for Living Cells. *Microchim. Acta* **2019**, *186* (6), 1–6.

(54) Yang, L.; Lou, X.; Yu, F.; Liu, H. Cross-Linking Structure-Induced Strong Blue Emissive Gold Nanoclusters for Intracellular Sensing. *Analyst* **2019**, *144* (8), 2765–2772.

(55) Shang, L.; Stockmar, F.; Azadfar, N.; Nienhaus, G. U. Intracellular Thermometry by Using Fluorescent Gold Nanoclusters. *Angew. Chemie Int. Ed.* **2013**, *52* (42), 11154–11157.

(56) Wang, X. D.; Wolfbeis, O. S.; Meier, R. J. Luminescent Probes and Sensors for Temperature. *Chem. Soc. Rev.* **2013**, *42* (19), 7834–7869.

(57) Donner, J. S.; Thompson, S. A.; Kreuzer, M. P.; Baffou, G.; Quidant, R. Mapping Intracellular Temperature Using Green Fluorescent Protein. *Nano Lett.* **2012**, *12* (4), 2107–2111.

(58) Selvaprakash, K.; Chen, Y. C. Using Protein-Encapsulated Gold Nanoclusters as Photoluminescent Sensing Probes for Biomolecules. *Biosens. Bioelectron.* **2014**, *61*, 88–94.

(59) Xia, X.; Long, Y.; Wang, J. Glucose Oxidase-Functionalized Fluorescent Gold Nanoclusters as Probes for Glucose. *Anal. Chim. Acta* **2013**, *772*, 81–86.

(60) Peng, J.; Feng, L.-N.; Zhang, K.; Li, X.-H.; Jiang, L.-P.; Zhu, J.-J. Calcium Carbonate-Gold Nanocluster Hybrid Spheres: Synthesis and Versatile Application in Immunoassays. *Chem. - A Eur. J.* **2012**, *18* (17), 5261–5268.

(61) Govindaraju, S.; Ankireddy, S. R.; Viswanath, B.; Kim, J.; Yun, K. Fluorescent Gold Nanoclusters for Selective Detection of Dopamine in Cerebrospinal Fluid. *Sci. Rep.* **2017**, *7* (1), 1–12.

(62) Yang, G. H.; Shi, J. J.; Wang, S.; Xiong, W. W.; Jiang, L. P.; Burda, C.; Zhu, J. J. Fabrication of a Boron Nitride-Gold Nanocluster Composite and Its Versatile Application for Immunoassays. *Chem. Commun.* **2013**, *49* (91), 10757–10759.

(63) Liu, Q.; Na, W.; Wang, L.; Su, X. Gold Nanocluster-Based Fluorescent Assay for Label-Free Detection of Protein Kinase and Its Inhibitors. *Microchim. Acta* **2017**, *184* (9), 3381–3387.

(64) Colombé, C.; Le Guével, X.; Martin-Serrano, A.; Henry, M.; Porret, E.; Comby-Zerbino, C.; Antoine, R.; Atallah, I.; Busser, B.; Coll, J.-L.; Righini, C. A.; Sancey, L. Gold Nanoclusters as a Contrast Agent for Image-Guided Surgery of Head and Neck Tumors. *Nanomedicine Nanotechnology, Biol. Med.* **2019**, *20*, 102011.

(65) Atallah, I.; Milet, C.; Henry, M.; Josserand, V.; Reyt, E.; Coll, J.-L.; Hurbin, A.; Righini, C. A. Near-Infrared Fluorescence Imaging-Guided Surgery Improves Recurrence-Free Survival Rate in Novel Orthotopic Animal Model of Head and Neck Squamous Cell Carcinoma. *Head Neck* **2016**, *38* (S1), E246–E255.

(66) De Boer, E.; Warram, J. M.; Tucker, M. D.; Hartman, Y. E.; Moore, L. S.; De Jong, J. S.; Chung, T. K.; Korb, M. L.; Zinn, K. R.; Van Dam, G. M.; Rosenthal, E. L.; Brandwein-Gensler, M. S. In Vivo Fluorescence Immunohistochemistry: Localization of Fluorescently Labeled Cetuximab in Squamous Cell Carcinomas. *Sci. Rep.* **2015**, *5* (1), 1–11.

(67) Hernot, S.; van Manen, L.; Debie, P.; Mieog, J. S. D.; Vahrmeijer, A. L. Latest Developments in Molecular Tracers for Fluorescence Image-Guided Cancer Surgery. *Lancet Oncol.* **2019**, *20* (7), e354–e367.

(68) Cui, H.; Shao, Z.-S.; Song, Z.; Wang, Y.-B.; Wang, H.-S. Development of Gold Nanoclusters: From Preparation to Applications in the Field of Biomedicine. *J. Mater. Chem. C* **2020**, *8* (41), 14312–14333.

(69) Sood, K.; Shanavas, A. The Role of Gold Nanoclusters as Emerging Theranostic Agents for Cancer Management. *Curr. Pathobiol. Rep.* **2021**, *9* (2), 33–42.

(70) Sonia; Komal; Kukreti, S.; Kaushik, M. Gold Nanoclusters: An Ultrasmall Platform for Multifaceted Applications. *Talanta* **2021**, *234* (March), 122623.

(71) Karaki, N.; Ali, H. H.; El Kak, A. Gold Nanoparticles as Promising Agents for Cancer Therapy. In *Nanoparticle Drug Delivery Systems for Cancer Treatment*; Gali-Muhtasib, H., Chouaib, R., Eds.; Jenny Stanford Publishing: Singapore, 2020; pp 235–270.

(72) Liu, P.; Yang, W.; Shi, L.; Zhang, H.; Xu, Y.; Wang, P.; Zhang, G.; Chen, W. R.; Zhang, B.; Wang, X. Concurrent Photothermal Therapy and Photodynamic Therapy for Cutaneous Squamous Cell Carcinoma by Gold Nanoclusters under a Single NIR Laser Irradiation. *J. Mater. Chem. B* **2019**, *7* (44), 6924–6933.

(73) Melamed, J. R.; Edelstein, R. S.; Day, E. S. Elucidating the Fundamental Mechanisms of Cell Death Triggered by Photothermal Therapy. *ACS Nano* **2015**, *9* (1), 6–11.

(74) Kim, J.; Piao, Y.; Hyeon, T. Multifunctional Nanostructured Materials for Multimodal Imaging, and Simultaneous Imaging and Therapy. *Chem. Soc. Rev.* **2009**, *38* (2), 372–390.

(75) Bettaieb, A.; K., P.; A., D. Hyperthermia: Cancer Treatment and Beyond. In *Cancer Treatment - Conventional and Innovative Approaches*; IntechOpen: London, UK, 2013; pp 257–283.

(76) Chen, Q.; Wang, C.; Zhan, Z.; He, W.; Cheng, Z.; Li, Y.; Liu, Z. Near-Infrared Dye Bound Albumin with Separated Imaging and Therapy Wavelength Channels for Imaging-Guided Photothermal Therapy. *Biomaterials* **2014**, *35* (28), 8206–8214.

(77) Morton, C.; Szeimies, R. M.; Sidoroff, A.; Wennberg, A. M.; Basset-Seguin, N.; Calzavara-Pinton, P.; Gilaberte, Y.; Hofbauer, G.; Hunger, R.; Karrer, S.; Lehmann, P.; Piaserico, S.; Ulrich, C.; Braathen, L. European Dermatology Forum Guidelines on Topical Photodynamic Therapy. *Eur. J. Dermatology* **2015**, *25* (4), 296–311.

(78) Bhandari, C.; Guirguis, M.; Savan, N. A.; Shrivastava, N.; Oliveira, S.; Hasan, T.; Obaid, G. What NIR Photodynamic Activation Offers Molecular Targeted Nanomedicines: Perspectives into the Conundrum of Tumor Specificity and Selectivity. *Nano Today* **2021**, *36*, 101052.

(79) Chen, Q.; Chen, J.; Yang, Z.; Zhang, L.; Dong, Z.; Liu, Z. NIR-II Light Activated Photodynamic Therapy with Protein-Capped Gold Nanoclusters. *Nano Res.* **2018**, *11* (10), 5657–5669.

(80) Liu, C.-P.; Wu, T.-H.; Liu, C.-Y.; Chen, K.-C.; Chen, Y.-X.; Chen, G.-S.; Lin, S.-Y. Self-Supplying O_2 through the Catalase-Like Activity of Gold Nanoclusters for Photodynamic Therapy against Hypoxic Cancer Cells. *Small* **2017**, *13* (26), 1700278.

(81) Liang, G.; Jin, X.; Zhang, S.; Xing, D. RGD Peptide-Modified Fluorescent Gold Nanoclusters as Highly Efficient Tumor-Targeted Radiotherapy Sensitizers. *Biomaterials* **2017**, *144*, 95–104.

(82) Su, Y.; Xue, T.; Liu, Y.; Qi, J.; Jin, R.; Lin, Z. Luminescent Metal Nanoclusters for Biomedical Applications. *Nano Res.* **2019**, *12* (6), 1251–1265.

(83) Zhang, X.-D.; Chen, J.; Luo, Z.; Wu, D.; Shen, X.; Song, S.-S.; Sun, Y.-M.; Liu, P.-X.; Zhao, J.; Huo, S.; Fan, S.; Fan, F.; Liang, X.-J.; Xie, J. Enhanced Tumor Accumulation of Sub-2 Nm Gold Nanoclusters for Cancer Radiation Therapy. *Adv. Healthc. Mater.* **2014**, *3* (1), 133–141.

(84) Luo, D.; Wang, X.; Zeng, S.; Ramamurthy, G.; Burda, C.; Basilion, J. P. Targeted Gold Nanocluster-Enhanced Radiotherapy of Prostate Cancer. *Small* **2019**, *15* (34), 1900968.

(85) De Jong, W. H.; Hagens, W. I.; Krystek, P.; Burger, M. C.; Sips, A. J. A. M.; Geertsma, R. E. Particle Size-Dependent Organ Distribution of Gold Nanoparticles after Intravenous Administration. *Biomaterials* **2008**, *29* (12), 1912–1919.

(86) Ghahremani, F.; Shahbazi-Gahrouei, D.; Kefayat, A.; Motaghi, H.; Mehrgardi, M. A.; Javanmard, S. H. AS1411 Aptamer Conjugated Gold Nanoclusters as a Targeted Radiosensitizer for Megavoltage Radiation Therapy of 4T1 Breast Cancer Cells. *RSC Adv.* **2018**, *8* (8), 4249–4258.

(87) Cifuentes-Rius, A.; Ivask, A.; Das, S.; Penya-Auladell, N.; Fabregas, L.; Fletcher, N. L.; Houston, Z. H.; Thurecht, K. J.; Voelcker, N. H. Gold Nanocluster-Mediated Cellular Death under Electromagnetic Radiation. *ACS Appl. Mater. Interfaces* **2017**, *9* (47), 41159–41167.

(88) Govindaraju, S.; Roshini, A.; Lee, M.-H.; Yun, K. Kaempferol Conjugated Gold Nanoclusters Enabled Efficient for Anticancer Therapeutics to A549 Lung Cancer Cells. *Int. J. Nanomedicine* **2019**, *14*, 5147–5157.

(89) Govindaraju, S.; Rengaraj, A.; Arivazhagan, R.; Huh, Y. S.; Yun, K. Curcumin-Conjugated Gold Clusters for Bioimaging and Anticancer Applications. *Bioconjug. Chem.* **2018**, *29* (2), 363–370.

(90) Fu, C.; Ding, C.; Sun, X.; Fu, A. Curcumin Nanocapsules Stabilized by Bovine Serum Albumin-Capped Gold Nanoclusters (BSA-AuNCs) for Drug Delivery and Theranosis. *Mater. Sci. Eng. C* **2018**, *87*, 149–154.

(91) Lakshmi, B. A.; Kim, S. Quercetin Mediated Gold Nanoclusters Explored as a Dual Functional Nanomaterial in Anticancer and Bio-Imaging Disciplines. *Colloids Surfaces B Biointerfaces* **2019**, *178*, 230–237.

(92) Latorre; Latorre; Castellanos; Diaz; Lazaro-Carrillo; Aguado; Lecea; Romero-Pérez; Calero; Sanchez-Puelles; Villanueva; Somoza. Multifunctional Albumin-Stabilized Gold Nanoclusters for the Reduction of Cancer Stem Cells. *Cancers (Basel)*. **2019**, *11* (7), 969.

(93) Camacho, K. M.; Kumar, S.; Menegatti, S.; Vogus, D. R.; Anselmo, A. C.; Mitragotri, S. Synergistic Antitumor Activity of Camptothecin-Doxorubicin Combinations and Their Conjugates with Hyaluronic Acid. *J. Control. Release* **2015**, *210*, 198–207.

(94) El-Mageed, H. R. A.; Mustafa, F. M.; Abdel-Latif, M. K. The Ability of Gold Nanoclusters as a New Nanocarrier for D-Penicillamine Anticancer Drug: A Computational Chemistry Study. *Struct. Chem.* **2020**, *31* (2), 781–793.

(95) Chen, T.; Xu, S.; Zhao, T.; Zhu, L.; Wei, D.; Li, Y.; Zhang, H.; Zhao, C. Gold Nanocluster-Conjugated Amphiphilic Block Copolymer for Tumor-Targeted Drug Delivery. *ACS Appl. Mater. Interfaces* **2012**, *4* (11), 5766–5774.

(96) Muthu, M. S.; Kutty, R. V.; Luo, Z.; Xie, J.; Feng, S. S. Theranostic Vitamin E TPGS Micelles of Transferrin Conjugation for Targeted Co-Delivery of Docetaxel and Ultra Bright Gold Nanoclusters. *Biomaterials* **2015**, *39*, 234–248.

(97) Croissant, J. G.; Zhang, D.; Alsaiari, S.; Lu, J.; Deng, L.; Tamanoi, F.; Almalik, A. M.; Zink, J. I.; Khashab, N. M. Protein-Gold Clusters-Capped Mesoporous Silica Nanoparticles for High Drug Loading, Autonomous Gemcitabine/Doxorubicin Co-Delivery, and in-Vivo Tumor Imaging. *J. Control. Release* **2016**, *229*, 183–191.

(98) Chen, D.; Li, B.; Cai, S.; Wang, P.; Peng, S.; Sheng, Y.; He, Y.; Gu, Y.; Chen, H. Dual Targeting Luminescent Gold Nanoclusters for Tumor Imaging and Deep Tissue Therapy. *Biomaterials* **2016**, *100*, 1–16.

(99) Lei, Y.; Tang, L.; Xie, Y.; Xianyu, Y.; Zhang, L.; Wang, P.; Hamada, Y.; Jiang, K.; Zheng, W.; Jiang, X. Gold Nanoclusters-Assisted Delivery of NGF SiRNA for Effective Treatment of Pancreatic Cancer. *Nat. Commun.* **2017**, *8* (1), 1–15.

(100) Jiang, X.; Du, B.; Huang, Y.; Yu, M.; Zheng, J. Cancer Photothermal Therapy with ICG-Conjugated Gold Nanoclusters. *Bioconjug. Chem.* **2020**, *31* (5), 1522–1528.

(101) Zhou, F.; Feng, B.; Yu, H.; Wang, D.; Wang, T.; Liu, J.; Meng, Q.; Wang, S.; Zhang, P.; Zhang, Z.; Li, Y. Cisplatin Prodrug-Conjugated Gold Nanocluster for Fluorescence Imaging and Targeted Therapy of the Breast Cancer. *Theranostics* **2016**, *6* (5), 679–687.

(102) Khandelia, R.; Bhandari, S.; Pan, U. N.; Ghosh, S. S.; Chattopadhyay, A. Gold Nanocluster Embedded Albumin Nanoparticles for Two-Photon Imaging of Cancer Cells Accompanying Drug Delivery. *Small* **2015**, *11* (33), 4075–4081.

(103) Kumar, B. N. P.; Puvvada, N.; Rajput, S.; Sarkar, S.; Mahto, M. K.; Yallapu, M. M.; Pathak, A.; Emdad, L.; Das, S. K.; Reis, R. L.; Kundu, S. C.; Fisher, P. B.; Mandal, M. Targeting of EGFR, VEGFR2, and Akt by Engineered Dual Drug Encapsulated Mesoporous Silica-Gold Nanoclusters Sensitizes Tamoxifen-Resistant Breast Cancer. *Mol. Pharm.* **2018**, *15* (7), 2698–2713.

(104) Wang, M.; Wang, L.; Feng, H.; Jiang, H.; Zhou, J.; Wang, X. Precise Therapeutic Effect of Self-Assembling Gold Nanocluster–PTEN Complexes on an Orthotropic Model of Liver Cancer. *J. Cancer Res. Clin. Oncol.* **2020**, *146* (4), 875–882.

(105) Yang, Y.; Wang, S.; Wang, C.; Tian, C.; Shen, Y.; Zhu, M. Engineered Targeted Hyaluronic Acid–Glutathione-Stabilized Gold Nanoclusters/Graphene Oxide–5-Fluorouracil as a Smart Theranostic Platform for Stimulus-Controlled Fluorescence Imaging-Assisted Synergetic Chemo/Phototherapy. *Chem. – An Asian J.* **2019**, *14* (9), 1418–1423.

(106) Wang, M.; Yu, Z.; Feng, H.; Wang, J.; Wang, L.; Zhang, Y.; Yin, L.; Du, Y.; Jiang, H.; Wang, X.; Zhou, J. In Situ Biosynthesized Gold Nanoclusters Inhibiting Cancer Development via the PI3K-AKT Signaling Pathway. *J. Mater. Chem. B* **2019**, *7* (35), 5336–5344.

(107) Fernández, T. D.; Pearson, J. R.; Leal, M. P.; Torres, M. J.; Blanca, M.; Mayorga, C.; Le Guével, X. Intracellular Accumulation and Immunological Properties of Fluorescent Gold Nanoclusters in Human Dendritic Cells. *Biomaterials* **2015**, *43* (1), 1–12.

(108) Tao, Y.; Ju, E.; Li, Z.; Ren, J.; Qu, X. Engineered CpG-Antigen Conjugates Protected Gold Nanoclusters as Smart Self-Vaccines for Enhanced Immune Response and Cell Imaging. *Adv. Funct. Mater.* **2014**, *24* (7), 1004–1010.

(109) Tao, Y.; Zhang, Y.; Ju, E.; Ren, H.; Ren, J. Gold Nanocluster-Based Vaccines for Dual-Delivery of Antigens and Immunostimulatory Oligonucleotides. *Nanoscale* **2015**, *7* (29), 12419–12426.

(110) Wang, H.; Ding, Y.; Su, S.; Meng, D.; Mujeeb, A.; Wu, Y.; Nie, G. Assembly of Hepatitis e Vaccine by ': In Situ ' Growth of Gold Clusters as Nano-Adjuvants: An Efficient Way to Enhance the Immune Responses of Vaccination. *Nanoscale Horizons* **2016**, *1* (5), 394–398.

(111) Xie, Y.; Zheng, W.; Jiang, X. Near-Infrared Light-Activated Phototherapy by Gold Nanoclusters for Dispersing Biofilms. *ACS Appl. Mater. Interfaces* **2020**, *12* (8), 9041–9049.

(112) Zheng, K.; Setyawati, M. I.; Leong, D. T.; Xie, J. Antimicrobial Gold Nanoclusters. *ACS Nano* **2017**, *11* (7), 6904–6910.

(113) Xie, Y.; Liu, Y.; Yang, J.; Liu, Y.; Hu, F.; Zhu, K.; Jiang, X. Gold Nanoclusters for Targeting Methicillin-Resistant *Staphylococcus Aureus* In Vivo. *Angew. Chemie Int. Ed.* **2018**, *57* (15), 3958–3962.

(114) Xie, Y.; Zhang, M.; Zhang, W.; Liu, X.; Zheng, W.; Jiang, X. Gold Nanoclusters-Coated Orthodontic Devices Can Inhibit the Formation of Streptococcus Mutans Biofilm. *ACS Biomater. Sci. Eng.* **2020**, *6* (2), 1239–1246.

(115) Ndugire, W.; Raviranga, N. G. H.; Lao, J.; Ramström, O.; Yan, M. Gold Nanoclusters as Nanoantibiotic Auranofin Analogues. *Adv. Healthc. Mater.* **2021**, *2101032*, 2101032.

(116) Xiao, L.; Wei, F.; Zhou, Y.; Anderson, G. J.; Frazer, D. M.; Lim, Y. C.; Liu, T.; Xiao, Y. Dihydrolipoic Acid-Gold Nanoclusters Regulate Microglial Polarization and Have the Potential To Alter Neurogenesis. *Nano Lett.* **2020**, *20* (1), 478–495.

(117) Gao, G.; Chen, R.; He, M.; Li, J.; Wang, L.; Sun, T. Gold Nanoclusters for Parkinson's Disease Treatment. *Biomaterials* **2019**, *194*, 36–46.

(118) Singh, P.; Pandit, S.; Mokkapati, V. R. S. S.; Garg, A.; Ravikumar, V.; Mijakovic, I. Gold Nanoparticles in Diagnostics and Therapeutics for Human Cancer. *Int. J. Mol. Sci.* **2018**, *19* (7), 1979.

(119) Tsvirkun, D.; Ben-Nun, Y.; Merquiol, E.; Zlotver, I.; Meir, K.; Weiss-Sadan, T.; Matok, I.; Popovtzer, R.; Blum, G. CT Imaging of Enzymatic Activity in Cancer Using Covalent Probes Reveal a Size-Dependent Pattern. *J. Am. Chem. Soc.* **2018**, *140* (38), 12010–12020.

(120) Zheng, K.; Xie, J. Cluster Materials as Traceable Antibacterial Agents. *Accounts Mater. Res.* **2021**, accountsmr.1c00186.

(121) Gao, X.; Cui, Y.; Levenson, R. M.; Chung, L. W. K.; Nie, S. In Vivo Cancer Targeting and Imaging with Semiconductor Quantum Dots. *Nat. Biotechnol.* **2004**, *22* (8), 969–976.

(122) Smith, A. M.; Mancini, M. C.; Nie, S. Bioimaging: Second Window for in Vivo Imaging. *Nat. Nanotechnol.* **2009**, *4* (11), 710–711.

(123) Zhao, J.; Chen, J.; Ma, S.; Liu, Q.; Huang, L.; Chen, X.; Lou, K.; Wang, W. Recent Developments in Multimodality Fluorescence Imaging Probes. *Acta Pharmaceutica Sinica B*. Chinese Academy of Medical Sciences May 2018, pp 320–338.

(124) Liu, R.; Xu, Y.; Xu, K.; Dai, Z. Current Trends and Key Considerations in the Clinical Translation of Targeted Fluorescent Probes for Intraoperative Navigation. *Aggregate* **2021**, *2* (3), 1–23.

(125) Hemmer, E.; Benayas, A.; Légaré, F.; Vetrone, F. Exploiting the Biological Windows: Current Perspectives on Fluorescent Bioprobes Emitting above 1000 Nm. *Nanoscale Horizons* **2016**, *1* (3), 168–184.

(126) Ma, Y.; Fu, H.; Zhang, C.; Cheng, S.; Gao, J.; Wang, Z.; Jin, W.; Conde, J.; Cui, D. Chiral Antioxidant-Based Gold Nanoclusters Reprogram DNA Epigenetic Patterns. *Sci. Rep.* **2016**, *6* (1), 1–12.

(127) Genji Srinivasulu, Y.; Yao, Q.; Goswami, N.; Xie, J. Interfacial Engineering of Gold Nanoclusters for Biomedical Applications. *Mater. Horizons* **2020**, *7* (10), 2596–2618.

(128) Su, D.; Gao, L.; Gao, F.; Zhang, X.; Gao, X. Peptide and Protein Modified Metal Clusters for Cancer Diagnostics. *Chem. Sci.* **2020**, *11* (22), 5614–5629.

(129) Cifuentes-Rius, A.; Deepagan, V. G.; Xie, J.; Voelcker, N. H. Bright Future of Gold Nanoclusters in Theranostics. *ACS Appl. Mater. Interfaces* **2021**, *13* (42), 49581–49588.

(130) Zheng, K.; Xie, J. Engineering Ultrasmall Metal Nanoclusters as Promising Theranostic Agents. *Trends Chem.* **2020**, *2* (7), 665–679.

(131) Xiao, Y.; Wu, Z.; Yao, Q.; Xie, J. Luminescent Metal Nanoclusters: Biosensing Strategies and Bioimaging Applications. *Aggregate* **2021**, *2* (1), 114–132.

(132) Zare, I.; Chevrier, D. M.; Cifuentes-Rius, A.; Moradi, N.; Xianyu, Y.; Ghosh, S.; Trapiella-Alfonso, L.; Tian, Y.; Shourangiz-Haghighi, A.; Mukherjee, S.; Fan, K.; Hamblin, M. R. Protein-Protected Metal Nanoclusters as Diagnostic and Therapeutic Platforms for Biomedical Applications. *Mater. Today* **2021**.

CHAPTER 3

Luminescent gold nanocluster-decorated polymeric hybrid particles for targeted therapy

Erik R. Hebels[1], Marzieh Najafi[1], Joep van den Dikkenberg[1], Nataliia Beztsinna[1], Sanne van de Looij[1], Danny Wilbie[1], Johannes Meeldijk[2], Mathew Hembury[1,] and Tina Vermonden[1,*]*

[1]Department of Pharmaceutics, Utrecht Institute for Pharmaceutical Sciences (UIPS), Science for Life, Utrecht University, P.O. Box 80082, 3508 TB Utrecht, the Netherlands.
[2]Electron Microscopy Group, Utrecht University, Padualaan 8, 3584 CH Utrecht, The Netherlands

European Polymer Journal, 2021, 152, 110467

Abstract

Gold nanoclusters or ultrasmall gold atom clusters (AuNCs, <2 nm in diameter) exhibit emergent photonic properties in the near-infrared (NIR) spectrum due to the quantization of their conduction band. This gives rise to attractive NIR luminescent properties that offer great promises for imaging and diagnostic purposes in biomedical applications. AuNCs also absorb NIR light in the biological window inducing photothermal events that can facilitate localized drug release and synergistic thermal therapy. Here, we designed a micellar system based on poly(ethylene glycol) (PEG) and thermosensitive poly(*N*-isopropylacrylamide) (PNIPAM) copolymerized with functional monomers to allow for micellar core-crosslinking via oxo-ester mediated native chemical ligation (OMNCL). These micelles are decorated with AuNCs (<2 nm) and covalently bound thiolated doxorubicin, which allow for both precise intracellular imaging as well as light-induced cell killing. The polymer bound AuNCs exhibit a NIR luminescent emission maximum at ~720 nm with a quantum yield of ~3%. Internalization studies of the micellar system on MDA-MB-231 cancer cells showed that doxorubicin remains bound within the micelles in the cytosolic region after 24 hour incubation. Upon NIR light irradiation at 650 nm, highly localized cell death is observed, which is limited only to the irradiated area. This innovative hybrid material design of the the AuNC-decorated micelles enables an efficient combination of live imaging and precisely controlled therapy.

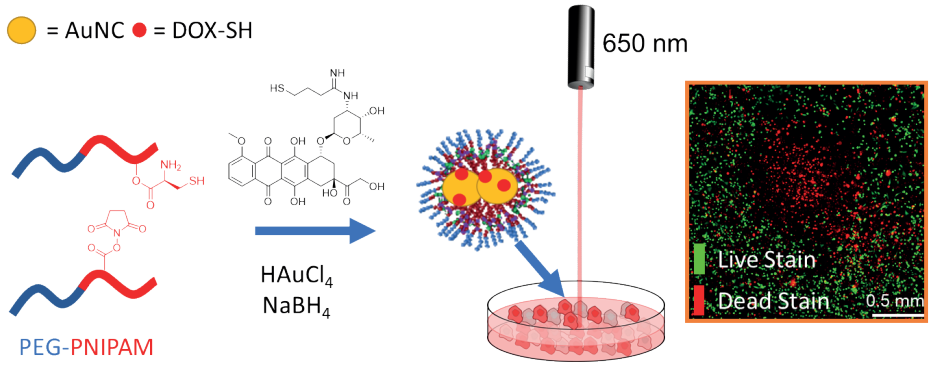

Introduction

Gold particles in the nanometer size range have received increasing attention in the past decade for biomedical applications due to their interesting physical properties and physiological compatibility.[1,2] In the sub-100 nm size range, gold nanoparticles exhibit plasmonic properties that allow transduction of optical and near infra-red (NIR) light into heat and thereby present opportunities for laser targeted drug delivery.[3] Gold nanoparticles have been extensively investigated as drug delivery tools themselves, but they have also been incorporated into various other drug delivery systems such as liposomes to aid cargo protection.[4,5] By employing temperature-labile interactions to encapsulate drug molecules into such a gold nanoparticle containing system, the production of heat can serve as the trigger to release drug molecules in a localized fashion upon light irradiation. Additionally, the localized heating effects produced can contribute to synergistic treatment actions, particularly for the cytotoxic action of chemotherapeutics (*e.g.* Doxorubicin and Cisplatin).[6–8] Furthermore, gold nanoparticles approaching the low nanometer size range (<2 nm, ~200-300 atoms) start exhibiting molecule like properties. In contrast to larger plasmonic gold nanoparticles (>2 nm), these ultrasmall gold nanoparticles or gold nanoclusters (AuNCs) possess discrete electronic energy levels allowing for one-electron HOMO-LUMO transitions as opposed to collective-electron plasmon excitation.[9] This additional property allows for luminescent features that can be employed for diagnostic applications.[2]

Light in the NIR region (650-900 nm) is particularly interesting as a trigger for therapeutic and diagnostic purposes as it is well tolerated by healthy cells as compared to other forms of light currently applied in oncology, such as X-rays. By being within the so-called biological absorption window, NIR light still retains high levels of tissue penetration when compared to wavelengths in the optical spectrum.[10,11] For this reason, recent interest in developing systems utilizing NIR light to induce photothermal effects, two-photon excitations and upconversions for the triggered release of drug compounds from nanocarrier systems for cancer therapy has increased.[12]

With regards to photothermal based cancer therapy, the ideal nanocarrier should possess strong light absorption, small particle size for deep tumor penetration, controlled surface chemistry allowing systemic administration and long circulation times, low inherent toxicity as well as biodegradability. For this purpose, the use of polymeric micelles as nanocarriers is of particular interest and such systems have previously been described combined with gold nanorods for triggered release of doxorubicin (DOX)[13] and photothermal cell killing by delivery of IR-780.[14] However, gold nanoparticle (>2 nm) and nanocluster (<2 nm) containing micellar systems described to date typically feature non-

core-crosslinked polymeric micelles, which could negatively affect formulation stability *in vivo*. Furthermore, drug loading in these hybrid systems is typically based on hydrophobic interactions instead of covalent bonding which could lead to premature drug release *in vivo*.[15–17] Finally, AuNCs (<2 nm) have primarily only been explored for use as diagnostic tools [18] and for the tracking of drug loaded nanocarriers.[19–21] The few examples existing for AuNC incorporated NIR triggered cytotoxicity systems are aimed at photodynamic therapy or release of non-covalently entrapped chemotherapeutic agents.[22–24]

Previously, we showed that AuNCs with imaging capabilities could be formed onto thermosensitive amphiphilic polymers formed by reversible addition−fragmentation chain transfer (RAFT) polymerization by use of free thiol endcaps obtained after aminolysis of the chain transfer agent.[25] Here, we re-designed this approach to a core-crosslinked micellar system based on thermosensitive poly(ethylene glycol)$_{5000}$-poly(*N*-isopropylacrylamide-co-*N*-hydroxypropyl methacrylamide-cysteine) (**PNC**) and a complementary polymer, poly(ethylene glycol)$_{5000}$-poly(*N*-isopropylacrylamide-*co*-acrylic acid *N*-hydroxysuccinimide) (**PNA**). The thermosensitive blocks of *N*-isopropyl acrylamide (NIPAM) allow these polymers to self-assemble into micelles upon increasing temperature.[26] Upon micelle formation, physiologically irreversible amide bonds are formed *via* oxo-ester mediated native chemical ligation (OMNCL), resulting in covalently core crosslinked micelles with free thiols to allow formation of AuNCs. [27] The aim of this study was to investigate whether AuNCs together with thiol-derivatized doxorubicin (DOX) could be incorporated stably in these micelles via the excess free thiols in the core of the micelles and to investigate the potential of this hybrid drug delivery system for use against resilient tumor cells. To this purpose, the system was evaluated for laser triggered drug release and cancer cell killing showing its potential as highly localized photothermal anti-cancer treatment.

Materials and methods

All materials were obtained from Sigma Aldrich (Zwijndrecht, The Netherlands) unless indicated otherwise. Boc-Cysteine(Acm)-*N*-hydroxypropylacrylamide (Boc-Cys(Acm)-HPMA) was synthesized according to a previously described procedure.[28] Dimethylformamide (DMF), dichloromethane (DCM), trifluoroacetic acid (TFA) and diethyl ether were obtained from Biosolve (Valkenswaard, The Netherlands). Phosphate buffered saline (PBS buffer) pH 7.4 (8.2 g/L NaCl, 3.1 g/L $Na_2HPO_4 \cdot 12H_2O$, 0.3 g/L $NaH_2PO_4 \cdot 2H_2O$) was purchased from B. Braun (Melsungen, Germany). Dulbecco's Modified Eagle Medium (DMEM) high glucose content and fetal bovine serum (FBS) were purchased from Sigma-Aldrich (Zwijndrecht, The Netherlands). Phenol red free OptiMEM medium was purchased from Thermo Fisher Scientific (Bleiswijk, The Netherlands).

Synthesis

Reversible Addition−Fragmentation Chain Transfer (RAFT) Polymerization of Poly(ethylene glycol)$_{5000}$-Poly(N-isopropylacrylamide-co-N-Hydroxypropyl methacrylamide-Cysteine) (**PNC**)

Poly(ethylene glycol) methyl ether 2-(dodecylthiocarbonothioylthio)-2-methylpropionate (PEG_{5000}-CTA, 1 g, 0.19 mmol), *N*-isopropylacrylamide (NIPAM, 2 g, 18 mmol), 2,2′-azobis(2-methylpropionitrile) (AIBN, 6 mg, 0.04 mmol) as initiator ([CTA]:[AIBN] = 5:1), Boc-Cys(Acm)-HPMA (0.54 g, 1.3 mmol) and dry DMF (to acquire a monomer concentration of 300 mg/mL) were added into a Schlenk flask and the mixture was degassed by 4 freeze-vacuum-thaw cycles, backfilled with N_2 gas and placed in an oil bath at 70°C. After 45 hours, the polymer was precipitated in cold diethyl ether, centrifuged, washed with cold diethyl ether and dried under N_2 flow. ^{1}H NMR and GPC were used to characterize the protected polymer.

The Boc protecting groups were removed by dissolving the obtained diblock polymer in DCM/TFA (1:1 v/v, 100 mL) and stirring for 2 hours at room temperature. The polymer was then precipitated in diethyl ether and a solid was obtained by vacuum filtration. The Acm protecting groups were removed by dissolving the polymer in MeOH/H2O (1:1 v/v, 100 mL) under a N_2 atmosphere followed by addition of HCl (1 M, 1 mL) and iodine in MeOH (0.2 M, 16 mL). This brown mixture was stirred for 1 hour at RT after which the excess iodine was quenched using some drops of 1 M ascorbic acid solution and the solution was neutralized by addition of Na2CO3. TCEP (500 mg, 2 mmol) was added to the solution to reduce the formed disulfide bridges and this mixture was stirred for 16 hours. Dialysis was performed using 12-14 kDa cutoff membranes at room temperature for 3 days. The final deprotected polymer was obtained after lyophilization and characterized by ^{1}H NMR and GPC. Free primary amines (from HPMA-cysteine monomers) were detected by TNBSA assay.[29]

RAFT Polymerization of Poly(ethylene glycol)$_{5000}$-Poly(N-isopropylacrylamide-co-Acrylic acid N-Hydroxysuccinimide) (**PNA**)

Poly(ethylene glycol) methyl ether 2-(dodecylthiocarbonothioylthio)-2-methylpropionate (PEG_{5000}-CTA, 0.5 g, 0.09 mmol), *N*-isopropylacrylamide (NIPAM, 1 g, 9 mmol), 2,2′-azobis(2-methylpropionitrile) (AIBN, 3 mg, 0.02 mmol) as initiator ([CTA]:[AIBN] = 5:1), Acrylic acid *N*-hydroxysuccinimide (NAS, 0.1 g, 0.6 mmol) and dry DMF (to acquire a monomer concentration of 300 mg/mL) were added into a Schlenk flask and the mixture was degassed by 4 freeze-vacuum-thaw cycles, backfilled with N_2 gas and placed in an oil bath at 70°C. After 45 hours, the polymer was precipitated in cold diethyl ether, centrifuged, washed with cold diethyl ether and dried under N_2 flow. Characterization was done by ^{1}H NMR and GPC.

Core-crosslinked micelle synthesis

PNC and PNA polymers were dissolved seperately in PBS in an ice bath with a polymer concentration of 30 mg/mL. After 2 hours of dissolution, the polymer solutions were mixed at a 2:1 PNC to PNA ratio and pipetted into PBS at 55 °C in an oil bath reaching a final polymer concentration of 5 mg/mL and the reaction was left to proceed for 2 hours. For cell experiments, particle formulations were purified with two runs through PD10 columns employing milliQ water as eluent and filtered through a 0.45 µm syringe filter.

Gold nanocluster formation

Typically, AuNCs were formed by addition of $HAuCl_4.2H_2O$ to the core-crosslinked micelle solution in PBS at a molar ratio of 3:1 of thiol (based on monomer determination by ^{1}H-NMR) to Au unless mentioned otherwise. After 1 hour of stirring, 3 eq. relative to Au of aqueous $NaBH_4$ was added to reduce nucleated gold clusters to Au(0) and the solution was left to stir for 16 hours.

DOX thiol modification (DOX-SH)

Thiol moieties were introduced onto doxorubicin using 2-iminothiolane (Traut's reagent).[30] DOX.HCl (56 mg, 97 µmol) was weighed into a small reaction flask and dissolved in 1 mL DMF. The 2-iminothiolane (19 mg, 140 µmol) was dissolved in 2 mL DMF and triethylamine (TEA) (40 µL, 292 µmol) was added before transferring this solution to the DOX.HCl solution. The reaction mixture was stirred for 16 hours at RT after which the product was precipitated in cold diethyl ether, centrifuged, washed with diethyl ether and a solid red crystalline powder was obtained. Characterization was done using ^{1}H NMR, ESI-MS and LC-MS.

DOX-SH was incorporated into the core-crosslinked micelles during the gold nanocluster formation, employing 2 mol eq. relative to the PNC polymer.

Polymer and particle characterization

Magnetic resonance (NMR) spectroscopy

^{1}H NMR (400 MHz) spectra were measured on an Agilent 400-MR NMR spectrometer (Agilent Technologies, Santa Clara, USA). The residual solvent peak of $CDCl_3$ (δ = 7.26 ppm) was used to calibrate chemical shifts.

Gel permeation chromatography (GPC)

GPC was performed using a PLgel 5 μm mixed-D column (Polymer Laboratories) and employing a refractive index detector (RID). DMF containing 10 mM LiCl was used as eluent. The elution rate was set to 1 mL min^{-1} and the column temperature was set to 65 °C. The typical sample concentration employed was 10 mg/mL. As calibration standards, PEG polymers of narrow and defined molecular weights were used.

Cloud point measurement

The cloud points of the P(NIPAM) containing polymers in PBS were determined by measurement of light scattering at a 90° angle upon the onset of opalescence. Scattered light intensity was measured using a Jasco FP-8300 spectrophotometer employing an excitation and emission wavelength of 550 nm with 1 nm slit width and a response time of 1 second. Temperature was ramped from 10 °C to 60 °C at 1 °C per minute.

Dynamic light scattering (DLS)

Particle size was investigated using DLS on a Malvern CGS-3 goniometer coupled to an ALV/LSE-5003 autocorrelator, with a temperature controlled sample holder and a He-Ne laser (25 mW, 633 nm). Measurements were done at 90° scattering angle at varying temperatures. Solvent viscosity was adjusted by the software and both z-average radius and polydispersity were calculated by the ALV and DTS software.

Photoluminescent profiling

A Jasco FP-8300 spectrophotometer was used to measure photoluminescence arising from the PNC bound AuNCs in 10 mm quartz cuvettes. A response time of 1 second, 5 nm slit width and resolution of 0.5 nm was employed. Emission spectra were recorded from 560 to 900 nm using an excitation wavelength of 550 nm and for temperature profiling, the temperature was ramped from 10 °C to 60 °C at 1 °C per minute.

Electron microscopy

Transmission Electron Microscopy (TEM) was employed to characterize the morphology of the AuNC containing micelles. Brightfield TEM and High Angle Annular Dark Field Scanning TEM (HAADF-STEM) images were obtained with a Tecnai20F (Thermo Fisher Scientific) microscope equipped with a model 694 Gatan CCD camera and an Energy-Dispersive X-ray Spectroscopy (EDS) detector (EDAX), employing an accelerating voltage of 200 kV. Samples were diluted in Milli-Q water (1 mg/mL) and left at the desired

temperature (10 or 45 °C) for 30 min before being drop-deposited on 200 mesh carbon coated copper TEM grids (Agar Scientific) prior to analysis. Due to rapidly occurring sample damage, bright field TEM and HAADF-STEM images were not acquired on the same specimen locations. Images were scaled and processed using ImageJ.

UV-Vis spectroscopy

DOX-SH contained within the micelle formulations was quantified using 10 mm path-length disposable polystyrene cuvettes in a Shimadzu UV 2450 spectrophotometer at 500 nm. DOX.HCl was used as a reference standard (see SI figure 1) with calibrations ranging from ~170 to ~70 μM in milliQ and DOX-SH concentration within the micelle formulation determined after subtracting the absorbance of non-DOX-SH containing gold nanocluster micelles at the same particle concentration (2.5 mg/mL total polymer content).

Absorbance spectra measurements were recorded with a 0.5 nm resolution. For quantum yield determination, spectra were measured from 300 to 900 nm in 10 mm quartz cuvettes at 25 °C.

Quantum yield

Quantum Yields (QYs) of PNC bound AuNCs were measured using Qdot 800 Carbonyl Quantum Dots (Invitrogen; QY = 0.62) as a reference in milliQ water. Appropriate sample dilutions were made to minimize luminescence quenching due to internal reabsorption, keeping the extinction coefficient E below 0.2 absorbance at the excitation wavelength (550 nm). QYs were calculated according to the following equation;

$$QY = QY_{ref} \frac{I\, n^2\, (1 - 10^{-E})^{ref}}{I_{ref}\, n_{ref}^2\, 1 - 10^{-E}}$$

where *I* is the integrated luminescence intensity (600-900 nm), *n* is the refractive index and *ref* denotes the Qdot 800 reference sample. [31]

Size exclusion chromatography

In order to analyze free drug and bound drug fractions, a desalting column from GE Healthcare was used (HiTrap 5 mL Sephadex G-25). The column was equilibrated using milliQ water or buffer (PBS pH 7.2 or ammonium acetate 10mM, pH = 5) at a flow rate of 1 mL/min for 30 minutes and the samples were injected with a typical volume of 50 μL. Chromatograms were recorded with UV/Vis detection at wavelengths of 254 nm and 500 nm.

Cytotoxicity and internalization studies

Cell culture

MDA-MB-231 cells were obtained from American Type Culture Collection (ATCC HTB-26), cultured and maintained at 37 °C in an incubator regulated with 5% CO_2, 95% air and saturated humidity. Roswell Park Memorial Institute (RPMI) 1640 medium supplemented with 10% Fetal Bovine Serum (FBS) was employed as the cell culture medium, no antibiotics were added. Cells were passaged upon reaching 80% confluency every 2-4 days using trypsin ethylenediaminetetraacetic acid (trypsin-EDTA).

DOX and DOX-SH IC_{50} measurements

MDA-MB-231 cells were plated onto black polystyrene (with micro-clear bottom) 96 well plates (Greiner #655090) at a density of 1 x 10^4 cells per well and incubated for 24 hours. Free and micelle bound drugs were diluted to the appropriate concentrations with RPMI 10% FBS medium and 100 μL of each dilution added to the well plate after aspiration followed by another 100 μL of medium in triplicate. After incubation for either 24 hours or 48 hours, the medium was aspirated and 100 μL of alamarBlue stain diluted in medium was added (50 μM resazurin). After 2-3 hours of incubation, fluorescence was recorded using a Mithras plate reader at 600 nm (λ_{ex} = 530 nm). Data were background subtracted and normalized by the fluorescence intensity recorded of untreated cells of the same well plate. The IC_{50} is defined as the drug concentration at 50% cell viability.

Laser confocal scanning microscopy

MDA-MB-231 cells were plated onto 6-chamber Ibidi slides (Ibidi, Germany) with a cell density of 4 x 10^4 cells per chamber and incubated for 24 hours. Free and micelle bound drugs were diluted to the appropriate concentrations with RPMI 10% FBS medium and 120 μL of each dilution added to the well plate after aspiration followed by another 30 μL of medium in triplicate. After 24 hours of incubation time, medium was removed, the cells were washed 3 times with PBS and fixed with 4% (v/v) paraformaldehyde (PFA) in PBS. Before fixation, Hoechst 33342 stain (10 nM, 10 min at 37 °C) was used to stain the cell nuclei and Oregon Green labeled Wheat Germ Agglutinin (WGA) (5 ug/mL, 15 min at 37°C) to stain cell membranes (Thermo Fisher Scientific, Naarden, The Netherlands). The slides were visualized using a confocal microscope (Leica TCS SP8 X MP), and the images were processed with LAS X (Leica Microsystems) and ImageJ.

Laser cytotoxicity and life/dead staining epifluorescence microscopy

MDA-MB-231 cells were plated onto 24 well plates (Greiner Cellstar) with a cell density of 4 x 10^4 cells per chamber and incubated for 24 hours using Dulbecco's Modified Eagle Medium (DMEM). Drug formulations were added to a particle concentration of 1 mg/mL. After 24 hours of incubation time, the medium was replaced with 150 µL phenol red free OptiMEM medium and the cells irradiated 60 minutes with a 650 nm laser at 300 mW. Cells were stained 24 hours after laser irradiation with Calcein-AM/Propidium Iodide Life/Dead stain and imaged using a Keyence BZ-9000E epifluorescence microscope. BZ-II analyzer software was employed for imaging with GFP, DAPI and TexasRED filters and stitching.

Results and discussion

Reversible Addition−Fragmentation Chain Transfer (RAFT) polymerization was employed using a commercially available poly(ethylene glycol) (PEG) chain transfer agent targeting a conversion of approximatively 80% in order to obtain low polydispersity. The PNC polymer was synthesized to obtain a diblock polymer with a hydrophilic part of PEG_{5000} and a thermosensitive hydrophobic part of poly(*N*-isopropylacrylamide) (PNIPAM) that also contains cysteine residues from the copolymerized *N*-hydroxypropyl methacrylamide-cysteine) (HPMA-Cys) (figure 1A). A complementary polymer containing copolymerized acrylic acid *N*-hydroxysuccinimide (NAS) instead of HPMA-Cys was also synthesized to enable core-crosslinking of micelles formed with both PNC and PNA via oxo-ester mediated native chemical ligation (OMNCL).[27] Successful polymerization was confirmed by ^{1}H NMR (SI figures 2-4) and gel permeation chromatography (GPC) of the PNA polymers and protected PNC polymers. The polymers were found to have a number-average molecular weight of 15.3 and 15.9 kDa, respectively (~ 85% conversion). Dispersity was found to be 1.5 and 1.4 for protected PNC and PNA, respectively. Furthermore, the cloud points for PNC and PNA polymers were 33 °C and 29 °C respectively, which is in line with previous results of polymers obtained by atom transfer radical polymerization (figure 1B).[32] RAFT polymerization was chosen here to fall in line with our previous study on AuNC incorporation into PEG_{5000}-*b*-PNIPAM-SH polymers. [2]

A)

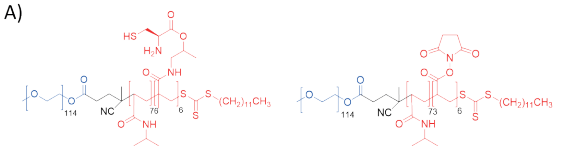

PNC: PEG-P(NIPAM-*co*-HPMA-Cys)-CTA **PNA**: PEG-P(NIPAM-*co*-NAS)-CTA

B)

	eq. NIPAM		eq. (HPMA-Cys or NAS)		M_n (kDa)[a]	M_n (kDa)[b]	PDI[b]	Cloud Point (°C)
	Feed	Obtained[a]	Feed	Obtained[a]				
PNC	97	76	7	6	15.9	16.0	1.5	33
PNA	97	73	7	6	15.3	15.0	1.4	29

C)

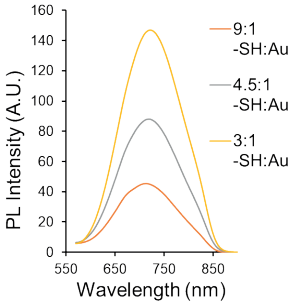

Figure 1: A) Structures of PNC and PNA polymers. B) Table summarizing the physical and chemical properties of protected PNC and PNA polymers and C) photoluminescence (PL) spectra of PNC capped AuNCs (λex = 550 nm) formed with 9:1 (orange), 4.5:1 (grey) and 3:1 (yellow) (mol:mol) of thiol to gold ratio. a Determined by 1H NMR b Determined by GPC.

The presence of free thiol moieties in the deprotected PNC polymer was confirmed by Ellmann's assay,[33] though colorimetric quantification resulted in much lower values (2.0 equivalents per chain) than expected based on the amount of functional monomers detected by ^{1}H NMR of the protected polymer (6.0 equivalents per chain). Likely, disulfide formation and potentially steric hindrance within the micellar core prevented reaction with the Ellman's reagent. Instead, the amine groups of the cysteine residues were quantified using a trinitrobenzenesulfonic acid (TNBSA) assay following a previously published procedure,[33] which resulted in 5.7 amines per polymer chain corresponding to the ^{1}H NMR results.

AuNCs (<2 nm) were formed onto the PNC polymer using different weight ratios of gold(III) chloride trihydrate ($HAuCl_4.3H_2O$). Different concentrations of gold salt solution were added to an excess of thiolated PNC polymers to form gold(I)-thiol complexes before the final reduction to gold(0) using sodium borohydride ($NaBH_4$) to investigate whether sufficient thiols are present for successful AuNC (<2 nm) formation. Their photoluminescent profiles (Figure 1C) show a proportional increase in photoluminescent intensity with increasing gold content (having a peak emission wavelength of ~720 nm).[9,34] Furthermore, the measured quantum yields were 3.0%, 3.0% and 2.5% for the 9:1, 4.5:1 and 3:1 (mol:mol, -SH:Au) ratios respectively. These quantum yields are comparable to polymer-gold nanocluster hybrids previously developed within our group (3.6%) [2] and significantly higher when compared to other gold nanocluster based systems described in the literature (<1%), indicating sufficient thiols are present for the gold quantities employed. [35,36]

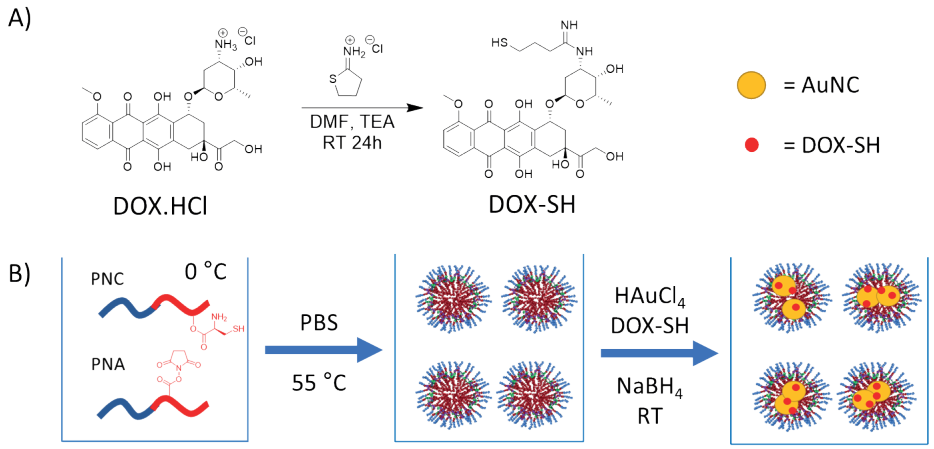

Scheme 1: Schematic representation of the modification of doxorubicin (A) and formation of core-crosslinked micelles (B) with simultaneous incorporation of DOX-SH and gold nanocluster formation into the pre-crosslinked PNC-PNA micelles.

The formation of core-crosslinked gold nanocluster micelles formed from PNC and PNA polymers using a heat shock procedure was investigated using two approaches: OMNCL-crosslinking before or after nanocluster formation (SI scheme 1). Both approaches resulted in AuNC containing micelles with sizes of around 60 nm diameter at room temperature. However, DLS measurements after addition of excess TCEP showed that stable micelles could only be achieved by first forming core-crosslinked micelles and subsequent formation of AuNCs. The inefficient core-crosslinking in the second method could be due to unavailable thiol moieties after nanocluster formation, which are required for the native chemical ligation reaction between PNC and PNA and potentially steric hindrance caused by the presence of AuNCs. It is therefore necessary to crosslink the polymers before the introduction of AuNCs. Hence, only results regarding this pre-crosslinking approach will further be discussed (Scheme 1B).

The temperature dependent photoluminescent profile of the gold nanocluster containing micelles was investigated. The photoluminescence profile of gold nanocluster containing micelles formed by the pre-crosslinking approach showed a spiked increase in intensity with increasing temperature (Figure 2). This behavior is explained by the shrinkage of the micelles and consequent change in environment (SI table 1) bringing the AuNCs into closer proximity, which is consistent with the gold-polymer hybrids developed previously.[2] The highest intensity is found at a temperature of 37 °C, followed by a decrease in photoluminescent intensity due to thermal quenching effects, common to fluorophore behaviour.[37] Summarizing, the fluorescent properties

of the AuNCs are retained with the pre-crosslinking approach and signal intensity is enhanced at a physiological temperature of 37 ºC.

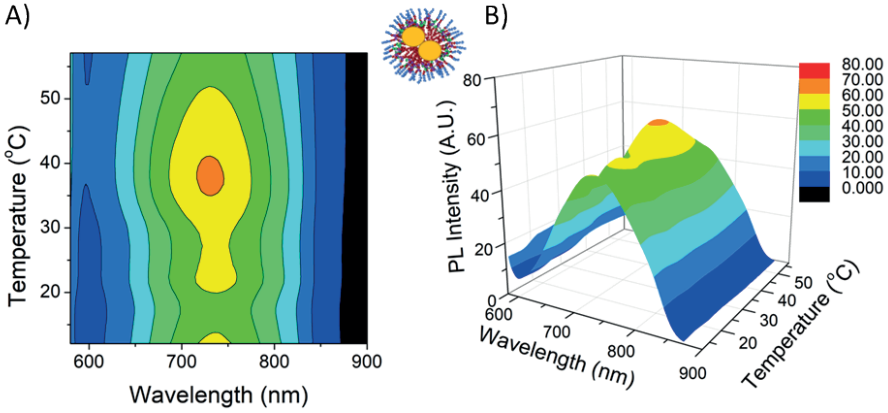

Figure 2: Photoluminescent properties of gold nanocluster containing micelles. (A) Temperature-dependent heat map and (B) corresponding 3D photoluminescent profile showing enhanced NIR emission at physiological temperature of 37 °C. (λex = 550 nm).

For the covalent incorporation of doxorubicin into the micelle formulation, doxorubicin was modified with 2-iminothiolane (Traut's reagent) to contain thiol functionalities (SI figures 6&7). This allows for covalent attachment to the AuNCs or the polymer (scheme 1) to have the closest possible proximity towards the heat source and, therefore, the highest probability of subsequent release upon irradiation.[38] Furthermore, modification with 2-iminothiolane preserves the positive charge in the amino sugar moiety with a secondary amine. Although, recently it has been shown that free NH_2 groups are not essential for the cytostatic activity of anthracyclines.[39] Indeed, the IC_{50} of free DOX-SH and DOX.HCl on MDA-MB-231 cells after 48 hours of drug incubation was found to be 12 µM and 1 µM respectively, showing a slight decrease in cytostatic activity of DOX after modification with 2-iminothiolane (SI figure 8A). Successful DOX-SH encapsulation within the gold micelle system was shown by use of size exclusion (SI figure 9). Upon addition of TCEP, DOX-SH is released confirming a thiol-based nature of encapsulation, which can be attributed to gold-thiol, thiol-thiol bonds or a mixture of both types of bonds. Micelles and free doxorubicin were separated with a HiTrap desalting column and a significant difference in retention time of both fractions was found (micelle bound fractions (Mr > 5000 Da) with an R_t of 2 minutes and free DOX-SH starting at an R_t of 10 minutes). This separation enabled the quantification of the DOX-SH content within the micelles by UV-Vis spectroscopy, which was found to be 105 µM for a 2.5 mg/mL (2.8% w/w loading) total polymer concentration micelle solution.

The presence of the AuNCs within the micelles was investigated by transmission electron microscopy (TEM). Figure 3 shows the images obtained for AuNC micelles loaded with DOX-SH. In the bright field TEM, the observed dark clusters are closer together with increasing temperature, confirming the expected change in nanocluster proximity (figure 3A). The order of magnitude of the AuNC containing micelle area also corresponds to sizes measured by DLS (SI table 1 and SI table 2B). High angle annular dark field scanning TEM (HAADF-STEM) was used to complement the bright field TEM images, highlighting all gold structures present within the micellar system, seen as bright white spots (figure 3B). Finally EDS measurements confirmed the identity of gold within the micelles (SI figure 5). In conclusion, the data obtained show the presence of AuNCs located within the core of the core-crosslinked micelles, the density of which increases at elevated temperature.

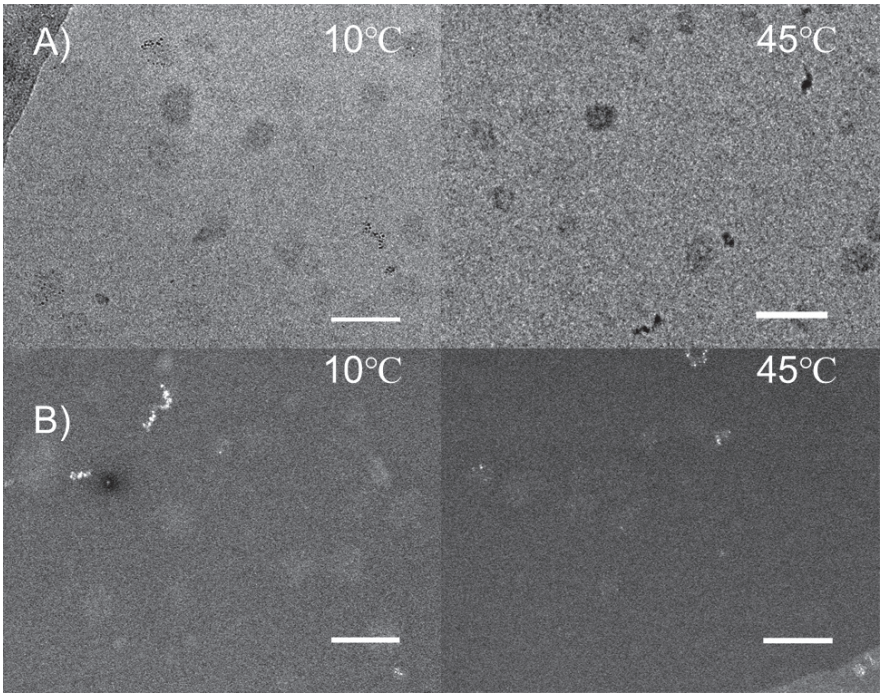

Figure 3: Morphology of DOX-SH gold nanocluster loaded PNA-PNC micelles. A) Brightfield transmission electron microscopy (TEM) images and B) high-angle annular dark field scanning transmission electron microscopy (HAADF-STEM) images at 10 °C and 45 °C. Scale bars: 100 nm.

Internalization studies were performed on MDA-MB-231 cells to investigate the accumulation of DOX-SH containing AuNC-micelles (figure 4). In the cells treated

with the DOX-containing AuNC micelle formulation, the native fluorescent signal of DOX-SH accumulates inside the treated cells' cytosolic region after 24 hours. Free DOX typically accumulates inside the nucleus, which is essential for cytotoxic activity from DNA intercalation to be exerted. [7] This absence of DOX signal inside the nucleus (SI figure 10) supports the hypothesis that DOX-SH remains bound within the micelles after being internalized for 24 hours.

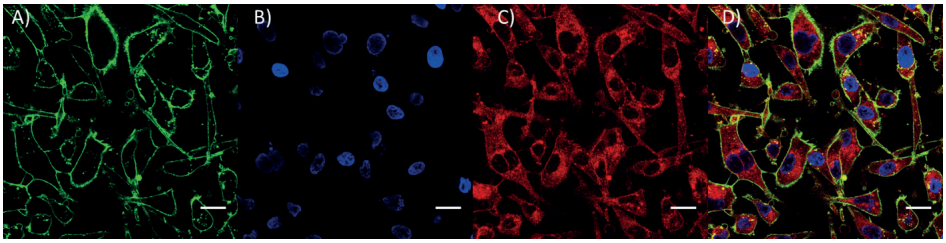

Figure 4: Laser confocal scanning microscopy images of MDA-MB-231 cells incubated for 24 hours with DOX-SH loaded gold nanocluster micelles. Cells are stained for A) cell membranes (oregon green labelled wheat germ agglutinin (WGA), green), B) nucleus (Hoechst 33342, blue. C) DOX-SH is localized by its native fluorescence emission at 595 nm (red). D) Overlay of the three channels. Scale bars: 20 µm.

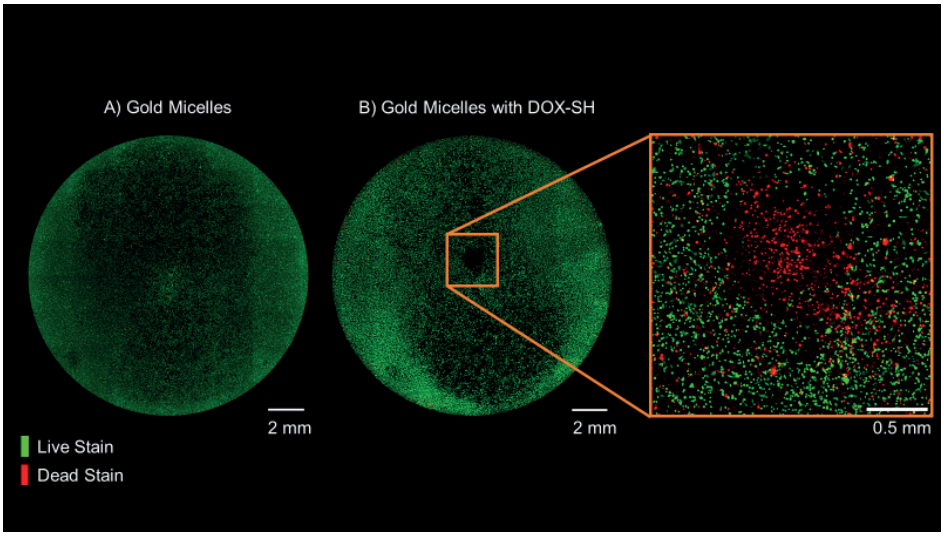

Figure 5: Representative LIVE/DEAD microscopy images of MDA-MB-231 cells treated for 24 hours with gold nanocluster micelles A) containing or B) without DOX-SH and irradiated for 60 minutes (650 nm, 17 W.cm^{-2}). Cells were stained 24 hours after laser irradiation.

The light triggered cytotoxic capacity of the DOX-SH loaded gold nanocluster micelles was investigated on MDA-MB-231 after 24 hour incubation with the micelles. Upon NIR light treatment (650 nm, 17 W.cm-^{2}), cell death was observed in cells treated with the DOX-SH gold nanocluster micelle formulation localized within the laser spot (figure 5). In contrast, cells incubated with AuNC micelles without DOX-SH did not elicit any cell death, demonstrating the need for both AuNCs and DOX-SH. Synergistic action between DOX-SH and local photothermal events caused by the AuNCs may be significantly contributing to enhanced cumulant cytotoxic effects as has also been described in other systems.[6,7] The herein observed cytotoxicity results also indicate the anticipated release of bound DOX-SH from the cytosolic region to result in its action within the nucleus. Furthermore, the DOX-SH containing AuNC micelle formulation showed no cytotoxicity without irradiation during additional 24 hour cell viability assays (SI figure 8B).

Conclusions

The herein described results highlight the potential of exploiting thiol-based loading of cytotoxic compounds with AuNCs for laser triggered cell killing. Furthermore, by encapsulating these entities within a core-crosslinked micellar formulation, the physiological stability of such systems can be greatly enhanced allowing cellular internalization without premature drug release.

Supporting information paragraph

Illustration of AuNC micelle formulation approaches (SI scheme 1); DLS data of AuNC micelles with different gold ratios and effects of temperature change (SI table1); DLS data of AuNC micelles and effect of TCEP (SI table 2); AuNC UV-Vis spectra of DOX. HCl and DOX-SH with TCEP (SI figure 1); ^{1}H NMR of PNC and PNA polymers (SI figures 2-4); EDS spectrum of DOX-SH loaded AuNC micelles (SI figure 5); ^{1}H NMR spectrum of DOX-SH (SI figure 6); high resolution mass spectrum of DOX-SH (SI figure 7); cell viability assays of free drugs and formulations (SI figure S8); and release of DOX-SH upon TCEP addition by size exclusion (SI figure 9).

Acknowledgments

The Netherlands Organization for Scientific Research (NWO/Aspasia 015.009.038, NWO/VIDI 13457 and NWO/Industrial Doctorates NWA.ID.17.030 is acknowledged for funding. We thank Prof. W.E. Hennink for scientific discussions. We thank J.A.W. Jong for comments on the manuscript.

References

(1) Daniel, M.-C.; Astruc, D. Gold Nanoparticles: Assembly, Supramolecular Chemistry, Quantum-Size-Related Properties, and Applications toward Biology, Catalysis, and Nanotechnology. *Chem. Rev.* **2004**, *104* (1), 293–346.

(2) Hembury, M.; Beztsinna, N.; Asadi, H.; Van Den Dikkenberg, J. B.; Meeldijk, J. D.; Hennink, W. E.; Vermonden, T. Luminescent Gold Nanocluster-Decorated Polymeric Hybrid Particles with Assembly-Induced Emission. *Biomacromolecules* **2018**, *19* (7), 2841–2848.

(3) Boisselier, E.; Astruc, D. Gold Nanoparticles in Nanomedicine: Preparations, Imaging, Diagnostics, Therapies and Toxicity. *Chem. Soc. Rev.* **2009**, *38* (6), 1759–1782.

(4) Mathiyazhakan, M.; Wiraja, C.; Xu, C. A Concise Review of Gold Nanoparticles-Based Photo-Responsive Liposomes for Controlled Drug Delivery. *Nano-Micro Lett.* **2018**, *10* (1), 10.

(5) Dreaden, E. C.; Austin, L. A.; Mackey, M. A.; El-Sayed, M. A. Size Matters: Gold Nanoparticles in Targeted Cancer Drug Delivery. *Ther. Deliv.* **2012**, *3* (4), 457–478.

(6) Hauck, T. S.; Jennings, T. L.; Yatsenko, T.; Kumaradas, J. C.; Chan, W. C. W. Enhancing the Toxicity of Cancer Chemotherapeutics with Gold Nanorod Hyperthermia. *Adv. Mater.* **2008**, *20* (20), 3832–3838.

(7) Yan, F.; Duan, W.; Li, Y.; Wu, H.; Zhou, Y.; Pan, M.; Liu, H.; Liu, X.; Zheng, H. NIR-Laser-Controlled Drug Release from DOX/IR-780-Loaded Temperature-Sensitive-Liposomes for Chemo-Photothermal Synergistic Tumor Therapy. *Theranostics* **2016**, *6* (13), 2337–2351.

(8) Mendes, R.; Pedrosa, P.; Lima, J. C.; Fernandes, A. R.; Baptista, P. V. Photothermal Enhancement of Chemotherapy in Breast Cancer by Visible Irradiation of Gold Nanoparticles. *Sci. Rep.* **2017**, *7* (1), 10872.

(9) Qian, H.; Zhu, M.; Wu, Z.; Jin, R. Quantum Sized Gold Nanoclusters with Atomic Precision. *Acc. Chem. Res.* **2012**, *45* (9), 1470–1479.

(10) Weissleder, R. A Clearer Vision for in Vivo Imaging. *Nat. Biotechnol.* **2001**, *19* (4), 316–317.

(11) Jain, P. K.; Huang, X.; El-Sayed, I. H.; El-Sayed, M. A. Noble Metals on the Nanoscale: Optical and Photothermal Properties and Some Applications in Imaging, Sensing, Biology, and Medicine. *Acc. Chem. Res.* **2008**, *41* (12), 1578–1586.

(12) Yang, G.; Liu, J.; Wu, Y.; Feng, L.; Liu, Z. Near-Infrared-Light Responsive Nanoscale Drug Delivery Systems for Cancer Treatment. *Coord. Chem. Rev.* **2016**, *320–321*, 100–117.

(13) Zhong, Y.; Wang, C.; Cheng, L.; Meng, F.; Zhong, Z.; Liu, Z. Gold Nanorod-Cored Biodegradable Micelles as a Robust and Remotely Controllable Doxorubicin Release System for Potent Inhibition of Drug-Sensitive and -Resistant Cancer Cells. *Biomacromolecules* **2013**, *14* (7), 2411–2419.

(14) He, B.; Hu, H.; Tan, T.; Wang, H.; Sun, K.; Li, Y.; Zhang, Z. IR-780-Loaded Polymeric Micelles Enhance the Efficacy of Photothermal Therapy in Treating Breast Cancer Lymphatic Metastasis in Mice. *Acta Pharmacol. Sin.* **2018**, *39* (1), 132–139.

(15) Talelli, M.; Iman, M.; Varkouhi, A. K.; Rijcken, C. J. F.; Schiffelers, R. M.; Etrych, T.; Ulbrich, K.; van Nostrum, C. F.; Lammers, T.; Storm, G.; Hennink, W. E. Core-Crosslinked Polymeric Micelles with Controlled Release of Covalently Entrapped Doxorubicin. *Biomaterials* **2010**, *31* (30), 7797–7804.

(16) Talelli, M.; Barz, M.; Rijcken, C. J. F.; Kiessling, F.; Hennink, W. E.; Lammers, T. Core-Crosslinked Polymeric Micelles: Principles, Preparation, Biomedical Applications and Clinical Translation. *Nano Today* **2015**, *10* (1), 93–117.

(17) Rijcken, C. J.; Snel, C. J.; Schiffelers, R. M.; van Nostrum, C. F.; Hennink, W. E. Hydrolysable Core-Crosslinked Thermosensitive Polymeric Micelles: Synthesis, Characterisation and in Vivo Studies. *Biomaterials* **2007**, *28* (36), 5581–5593.

(18) Zhang, Q.; Yang, M.; Zhu, Y.; Mao, C. Metallic Nanoclusters for Cancer Imaging and Therapy. *Curr. Med. Chem.* **2018**, *25* (12), 1379–1396.

(19) Chen, T.; Xu, S.; Zhao, T.; Zhu, L.; Wei, D.; Li, Y.; Zhang, H.; Zhao, C. Gold Nanocluster-Conjugated Amphiphilic Block Copolymer for Tumor-Targeted Drug Delivery. *ACS Appl. Mater. Interfaces* **2012**, *4* (11), 5766–5774.

(20) Zhou, F.; Feng, B.; Yu, H.; Wang, D.; Wang, T.; Liu, J.; Meng, Q.; Wang, S.; Zhang, P.; Zhang, Z.; Li, Y. Cisplatin Prodrug-Conjugated Gold Nanocluster for Fluorescence Imaging and Targeted Therapy of the Breast Cancer. *Theranostics* **2016**, *6* (5), 679–687.

(21) Chen, H.; Li, B.; Ren, X.; Li, S.; Ma, Y.; Cui, S.; Gu, Y. Multifunctional Near-Infrared-Emitting Nano-Conjugates Based on Gold Clusters for Tumor Imaging and Therapy. *Biomaterials* **2012**, *33* (33), 8461–8476.

(22) Vankayala, R.; Kuo, C.-L.; Nuthalapati, K.; Chiang, C.-S.; Hwang, K. C. Nucleus-Targeting Gold Nanoclusters for Simultaneous In Vivo Fluorescence Imaging, Gene Delivery, and NIR-Light Activated Photodynamic Therapy. *Adv. Funct. Mater.* **2015**, *25* (37), 5934–5945.

(23) Song, X.-R.; Goswami, N.; Yang, H.-H.; Xie, J. Functionalization of Metal Nanoclusters for Biomedical Applications. *Analyst* **2016**, *141* (11), 3126–3140.

(24) Hembury, M.; Chiappini, C.; Bertazzo, S.; Kalber, T. L.; Drisko, G. L.; Ogunlade, O.; Walker-Samuel, S.; Krishna, K. S.; Jumeaux, C.; Beard, P.; Kumar, C. S. S. R.; Porter, A. E.; Lythgoe, M. F.; Boissière, C.; Sanchez, C.; Stevens, M. M. Gold–Silica Quantum Rattles for Multimodal Imaging and Therapy. *Proc. Natl. Acad. Sci.* **2015**, *112* (7), 1959–1964.

(25) Hembury, M.; Beztsinna, N.; Asadi, H.; Van Den Dikkenberg, J. B.; Meeldijk, J. D.; Hennink, W. E.; Vermonden, T. Luminescent Gold Nanocluster-Decorated Polymeric Hybrid Particles with Assembly-Induced Emission. *Biomacromolecules* **2018**, *19* (7), 2841–2848.

(26) Najafi, M.; Hebels, E.; Hennink, W. E.; Vermonden, T. Poly(N -Isopropylacrylamide): Physicochemical Properties and Biomedical Applications. In *Temperature-Responsive Polymers*; John Wiley & Sons Ltd: Chichester, UK, 2018; pp 1–34.

(27) Boere, K. W. M.; Van Den Dikkenberg, J.; Gao, Y.; Visser, J.; Hennink, W. E.; Vermonden, T. Thermogelling and Chemoselectively Cross-Linked Hydrogels with Controlled Mechanical Properties and Degradation Behavior. *Biomacromolecules* **2015**, *16* (9), 2840–2851.

(28) Boere, K. W. M.; Soliman, B. G.; Rijkers, D. T. S.; Hennink, W. E.; Vermonden, T. Thermoresponsive Injectable Hydrogels Cross-Linked by Native Chemical Ligation. *Macromolecules* **2014**, *47* (7), 2430–2438.

(29) Habeeb, A. F. S. A. Determination of Free Amino Groups in Proteins by Trinitrobenzenesulfonic Acid. *Anal. Biochem.* **1966**, *14* (3), 328–336.

(30) Cabral, H.; Kataoka, K. Progress of Drug-Loaded Polymeric Micelles into Clinical Studies. *J. Control. Release* **2014**, *190*, 465–476.

(31) Grabolle, M.; Spieles, M.; Lesnyak, V.; Gaponik, N.; Eychmüller, A.; Resch-Genger, U. Determination of the Fluorescence Quantum Yield of Quantum Dots: Suitable Procedures and Achievable Uncertainties. *Anal. Chem.* **2009**, *81* (15), 6285–6294.

(32) Najafi, M.; Kordalivand, N.; Moradi, M. A.; Van Den Dikkenberg, J.; Fokkink, R.; Friedrich, H.; Sommerdijk, N. A. J. M.; Hembury, M.; Vermonden, T. Native Chemical Ligation for Cross-Linking of Flower-Like Micelles. *Biomacromolecules* **2018**, *19* (9), 3766–3775.

(33) Kuhlmann, M.; Reimann, O.; Hackenberger, C. P. R.; Groll, J. Cysteine-Functional Polymers via Thiol-Ene Conjugation. *Macromol. Rapid Commun.* **2015**, *36* (5), 472–476.

(34) Aldeek, F.; Muhammed, M. A. H.; Palui, G.; Zhan, N.; Mattoussi, H. Growth of Highly Fluorescent Polyethylene Glycol- and Zwitterion-Functionalized Gold Nanoclusters. *ACS Nano* **2013**, *7* (3), 2509–2521.

(35) Jin, R. Atomically Precise Metal Nanoclusters: Stable Sizes and Optical Properties. *Nanoscale* **2015**, *7* (5), 1549–1565.

(36) Goswami, N.; Yao, Q.; Luo, Z.; Li, J.; Chen, T.; Xie, J. Luminescent Metal Nanoclusters with Aggregation-Induced Emission. *J. Phys. Chem. Lett.* **2016**, *7* (6), 962–975.

(37) Liu, Z.; Huang, Y.; Yi, X.; Fu, B.; Yuan, G.; Wang, J.; Li, J.; Zhang, Y. Analysis of Photoluminescence Thermal Quenching: Guidance for the Design of Highly Effective p-Type Doping of Nitrides. *Sci. Rep.* **2016**, *6* (1), 32033.

(38) Borzenkov, M.; Chirico, G.; D'Alfonso, L.; Sironi, L.; Collini, M.; Cabrini, E.; Dacarro, G.; Milanese, C.; Pallavicini, P.; Taglietti, A.; Bernhard, C.; Denat, F. Thermal and Chemical Stability of Thiol Bonding on Gold Nanostars. *Langmuir* **2015**, *31* (29), 8081–8091.

(39) Denel-Bobrowska, M.; Marczak, A. Structural Modifications in the Sugar Moiety as a Key to Improving the Anticancer Effectiveness of Doxorubicin. *Life Sci.* **2017**, *178*, 1–8.

Supplementary information

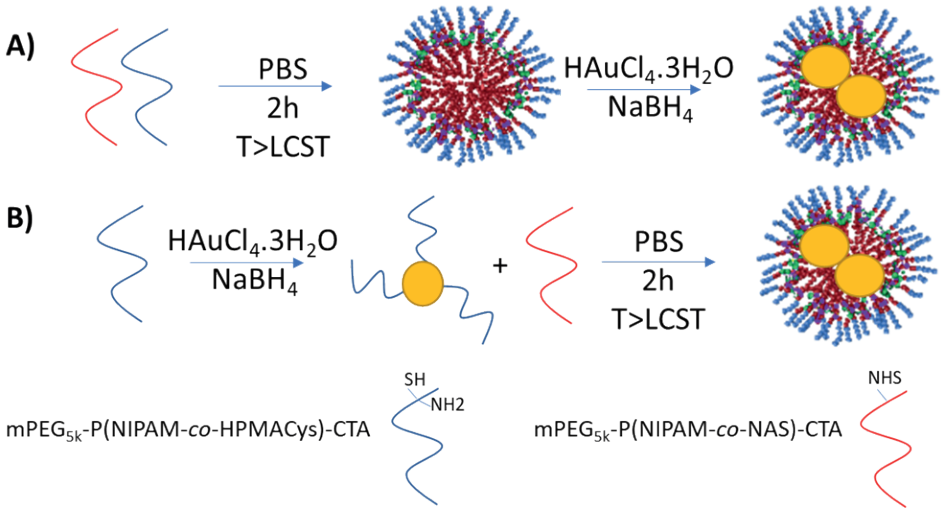

Scheme S1: Illustration of the formation of gold nanocluster core crosslinked micelles using A) the pre-crosslink approach where core crosslinked micelles are formed first and AuNCs are reduced into the micelles or B) the post-crosslink approach where the AuNCs are formed first using the HPMACys polymer and the crosslinking procedure with NAS polymer is applied afterwards. A PNC to PNA ratio of 2:1 was employed in both cases.

Table S1: DLS data showing the sizes of the AuNC micelles prepared with different ratios of gold and the effect of temperature on micelle size. Samples were measured at 25°C, cooled to 12°C and then heated to ~53 °C.

	T (°C)	Count (kcps)	Z-Ave (nm)	PDI
AuNC Micelle 9:1 (-SH_{NMR}: Au)	25	884	73	0.19
	12	667	75	0.23
	53	292	48	0.12
AuNC Micelle 4.5:1 (-SH_{NMR}: Au)	25	636	63	0.21
	11	493	64	0.21
	53	1047	41	0.13
AuNC Micelle 3:1 (-SH_{NMR}: Au)	25	490	59	0.26
	11	409	61	0.26
	54	976	40	0.15

Table S2: DLS data showing the effect of adding an excess of TCEP on A) gold NC containing micelles obtained by the post-crosslinking approach described above and B) empty micelles which represent the first step of the pre-crosslink approach. Measurements were made in PBS with an approximate polymer concentration of 5 mg mL^{-1}.

	T (°C)	Count (kcps)	Z-Ave (nm)	PDI
A) Post-CCL gold NC micelles	25	747	61	0.17
+ TCEP	25	1002	97	0.41
B) Pre-CCL micelles	25	838	64	0.18
+ TCEP	25	641	63	0.17

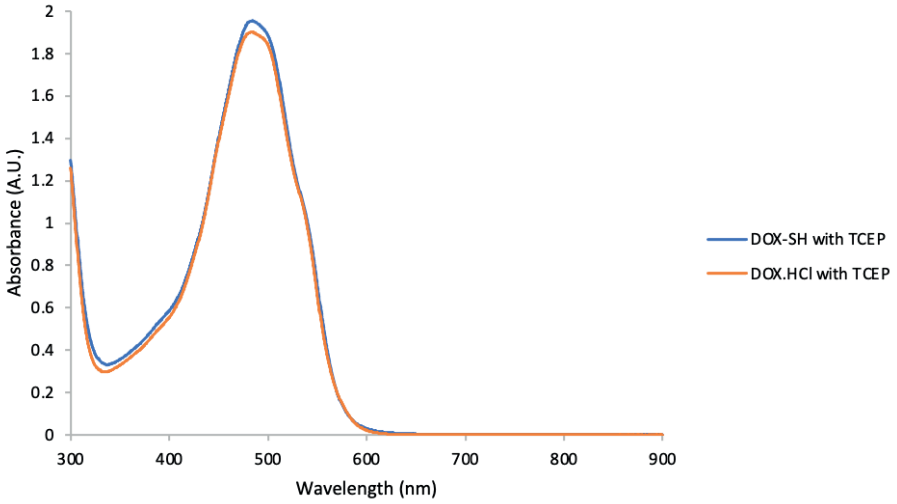

Figure S1:UV-Vis absorbance spectra obtained for equal concentrations of DOX-SH (Blue) and DOX.HCl (Orange) diluted in PBS in the presence of excess TCEP. The UV-Vis spectra of the two compounds are almost identical, which supports the use of DOX.HCl as a reference standard for the quantification of DOX-SH.

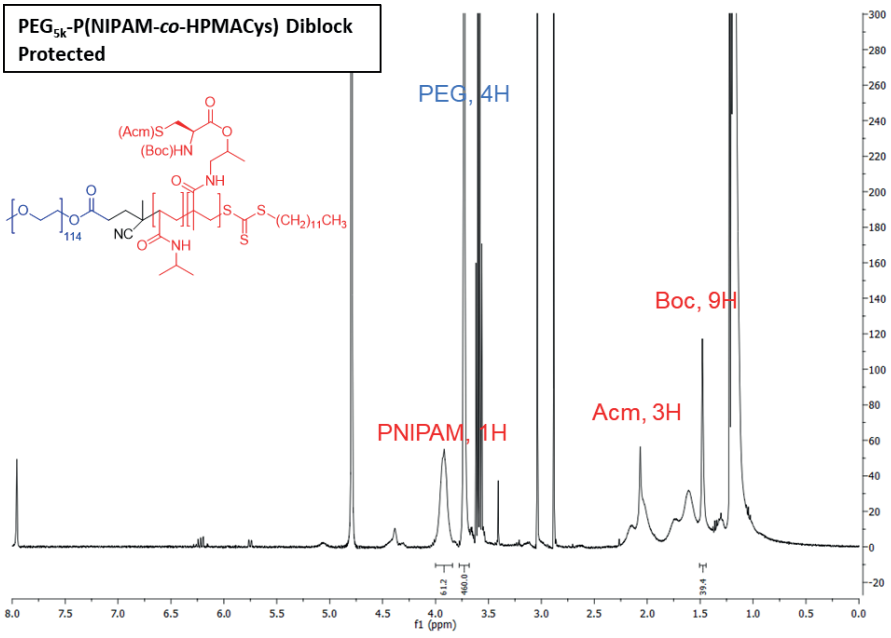

Figure S2: [1]H NMR spectrum of the protected PEG5k-P(NIPAM-co-HPMACys)-CTA diblock polymer. Taken in deuterated DMSO. Residual solvents can be seen at δ = 3.6, 1.2 (diethyl ether) and δ = 8, 2.86, 2.94 (DMF).

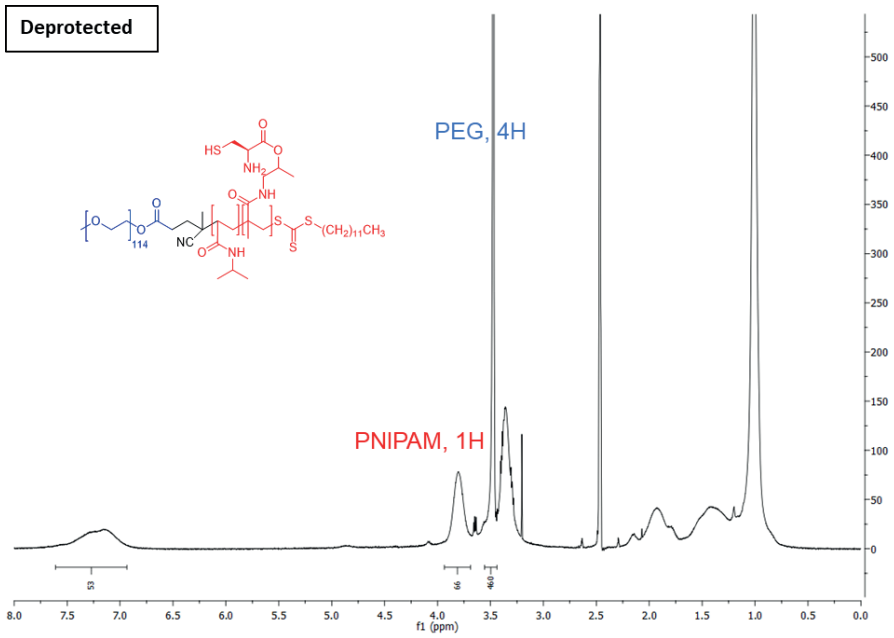

Figure S3: [1]H NMR spectra of both the deprotected PEG5k-P(NIPAM-co-HPMACys)-CTA Diblock polymer. Taken in deuterated DMSO.

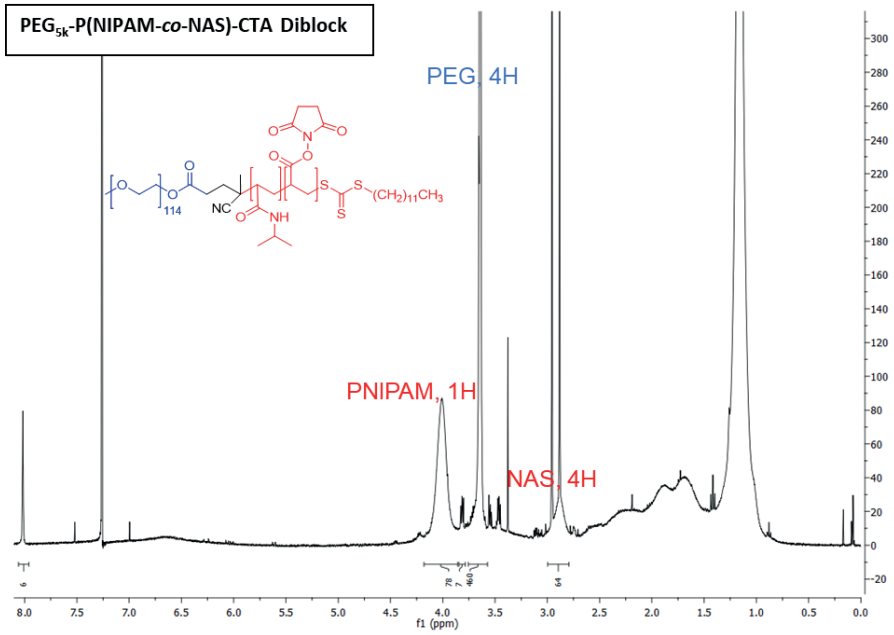

Figure S4: [1]H NMR spectrum of the PEG5k-P(NIPAM-co-NAS)-CTA Diblock polymer. Taken in CDCl3. Residual solvents can be seen at δ = 8, 2.86, 2.94 (DMF).

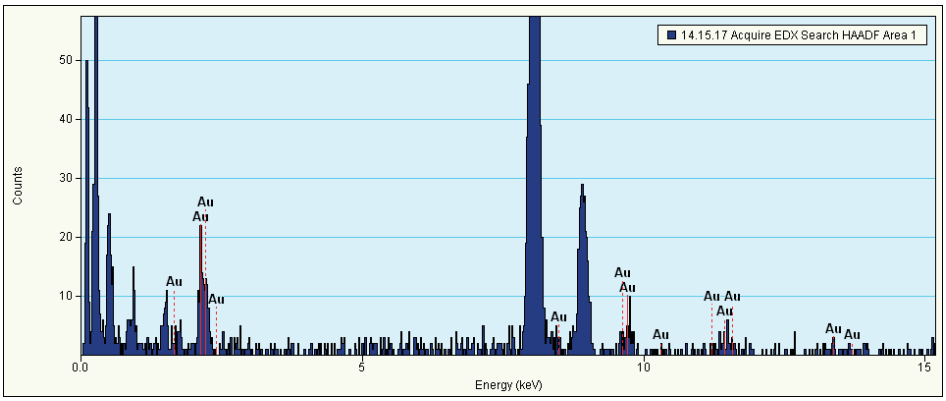

Figure S5: Energy-dispersive x-ray spectrum showing the presence of gold with peaks at 2.4, 9.7 and 11.6 keV.

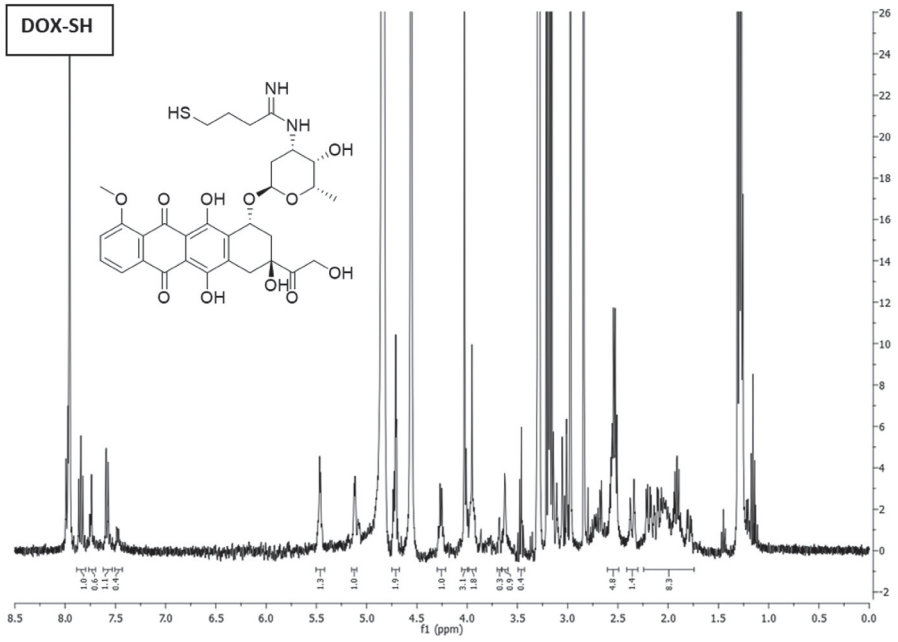

Figure S6: 1H NMR spectrum of thiolated doxorubicin (DOX-SH). Taken in CD3OD. Residual solvents can be seen at δ = 8, 2.86, 2.94 (DMF). After incorporation in micelles, non-reacted impurities have been removed via size exclusion and/or dialysis.

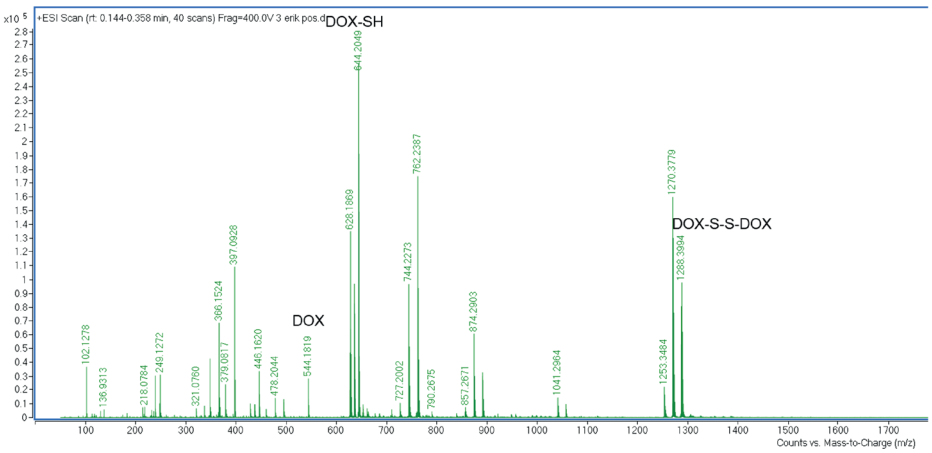

Figure S7: High resolution mass spectrum of DOX-SH sample. Expected mass of DOX-SH is 644.20 m/z. Dimers of DOX-SH are seen at 1288.4, likely due to disulfide bonding.

Cytotoxicity assays were performed on MDA-MB-231 cancer cells to assess the inherent cytostatic activity of both the free drugs and the micellar formulations. Figure S8 highlights that although DOX-SH is less cytotoxic as compared to unmodified DOX. HCl, the IC_{50} remains in the low µM range (12 µM and 1 µM after 48 hour incubation for DOX-SH and DOX.HCl respectively). The results also show that a 24 hour drug incubation is not sufficient for the free drugs to kill the cells even at high concentrations which is likely an attribute of the slow doubling time of MDA-MB-231 cells (previously reported to be around 1.3 days). [39] Since DNA intercalation and subsequent DNA damage are believed to play a role in the cytotoxic action of DOX, sufficient time for apoptotic mechanisms to take action is required to observe cell death. [40] Figure S8 also shows that the gold nanocluster micelles with and without DOX-SH are non-toxic even at the highest particle concentration employed (42 µM DOX concentration).

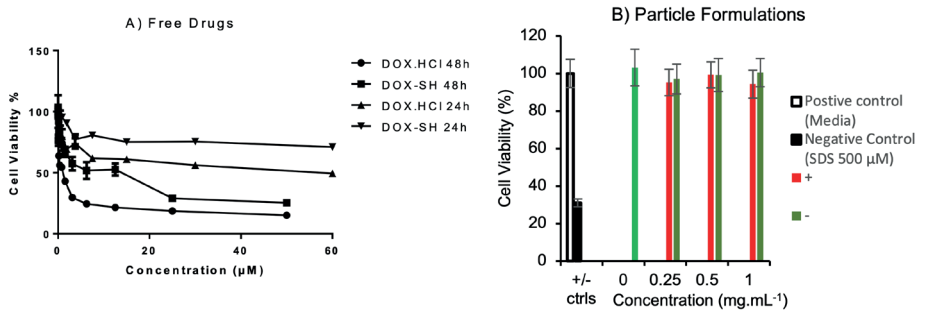

Figure S8: MDA-MB-231 cell viability assays. A) Free drug formulations of DOX-SH and DOX. HCl incubated for 24 and 48 hours and B) Gold nanocluster micelle formulations with DOX-SH (red) and without (green) at varying particle concentrations after 24 hour incubation.

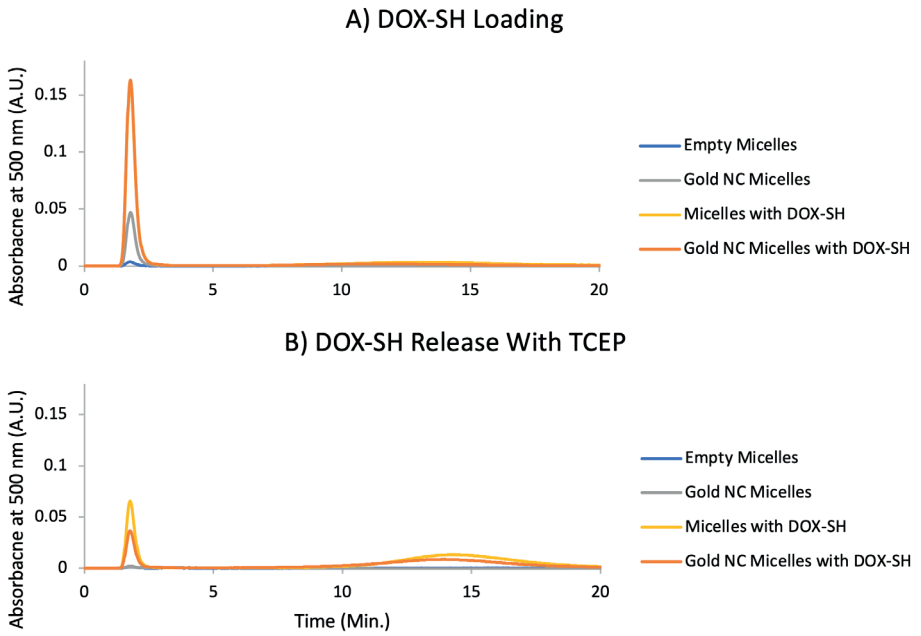

Figure S9: HiTrap column size exclusion (Mr > 5000) chromatograms showing A) loading of DOX-SH in the micelle samples and B) release of DOX-iminothiolane due to treatment with excess TCEP. Data is shown for empty micelles (blue), gold NC micelles (grey), micelles with DOX-SH (yellow) and gold NC micelles with DOX-iminothiolane (orange). These samples had been dialysed overnight at 4 °C against demi water employing 10 kDa cutoff membranes. Micellar formulations are seen to elute after 2 minutes whilst free DOX-SH elutes after 10 minutes. Ammonium acetate at pH 5 was used as elution buffer and the column was run at R.T.

Figure S10 shows the rapid accumulation of free DOX in the nucleus of MDA-MB-231 cells, imaged two hours after drug addition.

MDA-MB-231 cells were plated onto a 96 well plate (Greiner CellStar® 655090) with a cell density of 1 x 10^4 cells per well and incubated for 24 hours in RPMI + 10% FBS. The cells were washed 3x using PBS, and supplemented with fresh RPMI containing 10 µM Hoechst 33342, as well as DOX.HCl resulting in a concentration of 26 µM. The plate was visualized after 2 hours of incubation using a Yokogawa CV7000 spinning disc confocal microscope. Hoechst 33342 was imaged using 405nm excitation. Doxorubicin was imaged using the 488 laser. The images were processed using ImageJ.

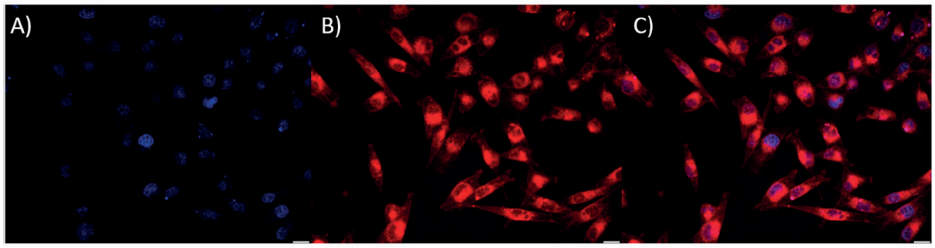

Figure S10: Spinning disc confocal images of MDA-MB-231 cells incubated for 2 hours with doxorubicin hydrochloride. Cells are stained for A:nucleus (Hoecsht 33342, Blue); B: Doxorubicin is localized by its native fluorescence emission at 595 nm (red). C: Overlay of the two channels, showing colocalization of the signals. Scale bars: 20µm.

CHAPTER 4

Orthogonal covalent entrapment of cargo into biodegradable polymeric micelles via native chemical ligation

Erik R. Hebels[1], Felix Bindt[1], Johanna Walther[1], Michiel van Geijn[2], Jimmy Weterings[2], Qizhi Hu[2], Claudio Colombo[2], Rob Liskamp[2], Cristianne J. F. Rijcken[2], Wim E. Hennink[1] and Tina Vermonden[1]

[1] Division of Pharmaceutics, Utrecht Institute for Pharmaceutical Sciences (UIPS), Utrecht University, 3508 TB Utrecht, the Netherlands.
[2] Cristal Therapeutics, 6229 EV Maastricht, the Netherlands

Biomacromolecules 2023, 24, 10, 4385–4396

Abstract

Polymeric micelles (PMs) are promising platforms for enhanced tissue targeting of entrapped therapeutic agents. Strategies to circumvent premature release of entrapped drugs include crosslinking of the micellar core as well as covalent attachment of the drug cargo. The chemistry employed to obtain crosslinked micelles needs to be mild to also allow entrapment of fragile molecules, such as certain peptides, proteins, oligonucleotides, and fluorescent dyes. Native chemical ligation (NCL) is a mild bio-orthogonal reaction between a *N*-terminal cysteine residue and a thioester that proceeds under physiological conditions. Here, we designed a trifunctional crosslinker containing two cysteine residues for the micelle core-crosslinking reaction and an azide residue for ring-strained alkyne conjugation of fluorescent dyes. We applied this approach to thermosensitive methoxypolyethylene glycol-*b*-*N*-(2-hydroxypropyl)methacrylamide-lactate (mPEG-*b*-HPMAmLac$_n$) based block copolymers of a core-crosslinked polymeric micelle (CCPM) system by attaching thioester residues (using ethyl thioglycolate-succinic anhydride, ETSA) for NCL crosslinking with the trifunctional crosslinker under physiological conditions. By use of mild copper-free click chemistry, we coupled fluorescent dyes, Sulfo.Cy5 and BODIPY, to the core *via* the azide residue present on the crosslinker by triazole ring formation. In addition, we employed a recently developed cycloheptyne strain promoted click reagent (TMTHSI, CliCr®) in comparison to the frequently employed cyclooctyne derivative (DBCO), both achieving successful dye entrapment. The size of the resulting CCPMs could be tuned between 50-100 nm by varying the molecular weight of the thermosensitive block and ETSA content. *In vitro* cell experiments showed successful internalization of the dye entrapped CCPMs which did not affect cell viability up to a polymer concentration of 2 mg/mL in PC3 cells. These fluorescent dye entrapped CCPMs can be applied in diagnostic imaging and the chemistry developed in this study serves as a steppingstone towards covalently entrapped fragile drug compounds with tunable release in CCPMs.

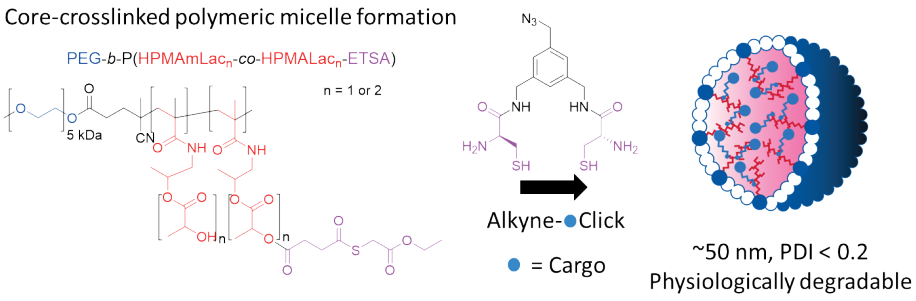

Introduction

Polymeric micelle (PM) based nanoparticles have emerged in the last decades as a promising platform for tissue targeting of drugs, particularly for applications in cancer therapy. PMs are hallmarked by their colloidal core-shell structure emerging from the constituent amphiphilic block copolymers that spontaneously self-assemble above the critical micellization concentration (CMC). Owing to their synthetic nature, block copolymers used to produce PMs allow for specific versatile tuning of chemical and physical properties, which can be used to tune particle characteristics. [1,2] Although to present date only a few PM based products have reached the market, several clinical trials making use of new generation PM systems are underway. [3–5]

Tumor directed targeting of nanoparticulate therapeutics, such as PMs, is mostly based on passive accumulation at the tumor site due to leaky vasculature within the tissue and extended circulation time of the nanoparticles compared to the free drug. Such passive accumulation is commonly referred to as the enhanced permeability and retention (EPR) effect [6,7] and is dependent on a number of factors including the size of the nanoparticle, circulation kinetics as well as tumor and patient type, asserting the need for rational design and patient stratification. [8,9] Particles need to fall within a size range between ~5-200 nm to avoid clearance by renal excretion and uptake by the mononuclear phagocyte system (MPS). [10,11] Furthermore, to facilitate deep tumor penetration, particularly for poorly vascularized tumors, a size of around 50 nm or less is preferable. [12–14] The size of PMs can typically be tuned by varying the molecular weight of the constituent amphiphilic block copolymers. [15,16] Finally, polyethylene glycol (PEG) surface modification has been employed as a frequently applied stealth polymer block to evade MPS uptake and extend circulation time of nanoparticle systems. [17–19]

The stability of PM systems in circulation as well as stable entrapment of the drug cargo is crucial for effective drug retention until the target tissue is reached. Due to the inherent equilibrium of amphiphilic block copolymers in the monomeric (or unimers) and assembled PM state, adsorption of these unimers to plasma proteins and excessive dilution drive the disassembly of PMs when administered into circulation. [20] Disassembly can be circumvented by introducing crosslinks between the block copolymers in the assembled polymeric micelle by chemical approaches [21–24] but also by introduction of additional physical interactions such as stereo-complex formation [25] or π-π stacking [26–29]. The same stability consideration applies to the interaction of PMs with the cargo to prevent premature release from the PM system by interaction with competing plasma proteins. [22,30]

Crosslinking of the hydrophobic blocks within the PM to yield core-crosslinked polymeric micelles (CCPMs) is one of the approaches employed to achieve PM stabilization. To this end, a promising CCPM platform (CriPec®) was developed and is currently undergoing clinical investigation for the treatment of solid tumors using docetaxel as chemotherapeutic drug cargo. [31–34] These CCPMs consist of thermosensitive block copolymers that are crosslinked upon micellization by free radical polymerization of methacrylate functionalized side chains present on the core forming part of the block copolymer. Furthermore, the docetaxel cargo, conjugated with a hydrolysable linker also comprising a methacrylate moiety, is covalently attached to the hydrophobic core using the same free radical chemistry. [35]

Using free radical chemistry, only a select group of molecules including chemotherapeutic agents such as docetaxel as methacrylate derivative can be conjugated. Many compounds, including new generation pharmaceuticals, are of biological and peptide nature [36] or have fragile moieties that would be damaged by this approach (particularly lysine, tryptophan and methionine residue containing entities). [37,38] Furthermore, several fluorescent dyes that are interesting for imaging purposes are also incompatible with free radical chemistry due to their conjugated unsaturated nature. [39] These challenges highlight the need for compatible crosslinking approaches in PM systems to expand the PM encapsulated drug and dye repertoire.

Native chemical ligation (NCL), introduced by Kent and coworkers in 1994, is a mild bio-orthogonal reaction between a *N*-terminal cysteine residue and a thioester that readily proceeds under physiological conditions. [40,41] Previously, we have shown the use of NCL for the crosslinking of PMs by complementary reaction of two *N*-isopropyl acrylamide based copolymers modified with either cysteine or thioglycolate residues. [42] Recently, the ultrafast synthesis of block copolymers via NCL was also demonstrated. [43]

Here, we designed a trifunctional crosslinker containing two cysteine residues and an azide functionality to employ NCL as a crosslinking strategy for the formation of CCPMs and simultaneous drug entrapment. The cysteine residues can react with thioglycolate modified copolymers *via* NCL while the azide functionality can be employed for (copper-free) click chemistry coupling of drugs or fluorescent dye conjugates. Thermosensitive $mPEG_{5000}$-*b*-P($HPMAmLac_1$-*co*-$HPMAmLac_2$) block copolymers were functionalized with thioester side chains to allow NCL reaction with the crosslinker under physiological conditions. We investigated the tunability of the size and chemical degradability of the CCPMs as well as the conjugation of dyes Sulfo.Cy5 and BODIPY. Further, we employed the frequently used strain promoted cyclooctyne derivative (BCN) and a

recently developed cycloheptyne click reagent (TMTHSI, CliCr®) [44] respectively to demonstrate versatility of the system, and cell experiments were performed *in vitro* to evaluate cell uptake and cytocompatibility.

Materials and methods

Materials

All materials were obtained from Sigma Aldrich (Zwijndrecht, the Netherlands) unless indicated otherwise. Ethylthioglycolate-succinic acid (ETSA) was synthesized according to a previously published procedure (Figure S1.10 for NMR).[45] The 2-(methoxy polyethylene glycol)-4,4-azobis(4-cyanopentanoic acid) ($mPEG_{5000})_2$-ABCPA) free radical macroinitiator was synthesized according to a previously published procedure.[15] *N*-2-hydroxypropyl methacrylamide monolactate ($HPMAmLac_1$) and dilactate ($HPMAmLac_2$) as well as 3,3,6,6-tetramethylthiacycloheptyne sulfoximine functionalized 4,4-difluoro-4-bora-3a,4a-diaza-s-indacene 650 (BODIPY-TMTHSI) were obtained by custom synthesis from Symeres (Nijmegen, the Netherlands). Dibenzocyclooctyne functionalized sulfonated cyanine 5 (Sulfo.Cy5-DBCO) was obtained from Lumiprobe (Hannover, Germany). All solvents were obtained from Biosolve (Valkenswaard, the Netherlands).

Synthesis

Trifunctional crosslinker synthesis

*Synthesis compound **1***: In a typical reaction, 1,3,5-tris(bromomethyl)benzene (10.0 g, 28.0 mmol) was dissolved in 20 mL DMF and the obtained solution was, after addition of sodium azide (2.7 g, 42.0 mmol), stirred for 16 hours at RT. The reaction mixture was then diluted with 100 mL ethyl acetate and filtered to remove precipitated salts. The filtrate was then washed (60 mL) twice with 0.1 M HCl, once with brine, dried over anhydrous sodium sulfate, concentrated using a rotavapor and residual solvent was removed under vacuum overnight at RT. The obtained oil was then dissolved in diethyl ether to which a few drops of methanol were added and adsorbed onto silica gel on a rotavapor. 1-(Azidomethyl)-3,5-bis(bromomethyl)benzene (compound **1**, Scheme 1) was obtained by two successive silica column purifications using 24:1 hexanes : diethyl ether as eluent (R_f = ~0.4 in 9:1 hexane : diethyl ether), yielding 2.6 gram (29%) of a faint yellow viscous liquid. ^{1}H NMR (400 MHz, chloroform-d): δ 7.39 (s, 1H), 7.28 (s, 2H), 4.47 (s, 4H), 4.37 (s, 2H). [46]

*Synthesis compound **2***: Intermediate compound **2** (azidomethyl-3,5-di(phthalamidomethyl) benzene) was obtained by dissolving compound **1** (2.1 g, 6.6 mmol) in 20 mL dry DMF

and stirring with potassium phthalimide (2.8 g, 15.1 mmol) for 16 hours at 50 °C under an argon atmosphere. The mixture was diluted in 150 mL DCM and filtered to remove precipitated KBr. The filtrate was washed (100 mL) twice with milliQ water, once with brine, dried over anhydrous sodium sulfate, concentrated on a rotavapor and residual solvent was removed under vacuum at RT, yielding 2.8 g (94%) of white solid. ^{1}H NMR (400 MHz, chloroform-d): δ 7.86 – 7.80 (m, 4H), 7.73 – 7.67 (m, 4H), 7.46 (s, 1H), 7.24 (s, 2H), 4.81 (s, 4H), 4.27 (s, 2H).

*Phthalimide deprotection of compound **2** to **3**:* Compound **2** (2.8 g, 6.2 mmol) was subsequently deprotected to yield compound **3** (azidomethyl-3,5-di(aminomethyl) benzene) using hydrazine hydrate (0.9 mL, 13.6 mmol) in 100 mL methanol and boiling under reflux for 3 hours. After cooling to RT, 150 mL milliQ water was added followed by 25 mL concentrated HCl and the mixture was boiled under reflux for 2 hours. The white suspension was then filtered to remove salts, concentrated using a rotavapor, and dried overnight under vacuum yielding a white solid HCl salt containing inorganic salt impurities, 2.3 g. ^{1}H NMR (400 MHz, DMSO-d6): δ 8.66 (s, 6H), 7.61 (s, 1H), 7.51 (s, 2H), 4.48 (s, 2H), 3.99 (q, J = 5.8 Hz, 4H).

*Synthesis compound **4**:* Boc-Cys(Acm)-OH residues were coupled to the crude compound **3** (0.60 g) to obtain the protected form of the dicysteine crosslinker, compound **4**. Boc-Cys(Acm)-OH (1.5 g, 5.0 mmol) was dissolved in 5 mL dry DMSO, after which hexafluorophosphate azabenzotriazole tetramethyl uronium (HATU) (1.9 g, 5.0 mmol) and *N*,*N*-diisopropylethylamine (DIPEA) (7.9 mL, 45.4 mmol) were added and the mixture was stirred for 15 minutes. Compound **3** was added and the reaction mixture was stirred for 16 hours at RT. The mixture was diluted with 100 mL chloroform, washed (100 mL) twice with 0.1 M HCl, twice with saturated $NaHCO_3$, once with brine, dried over anhydrous sodium sulfate, concentrated using a rotavapor and dried under vacuum overnight. The obtained solid was dissolved in methanol, dispersed and subsequently concentrated in silica gel and purified by silica column chromatography employing 19:1 DCM : MeOH as eluent (R_f = ~0.3), yielding 0.79 g (70% yield relative to compound **2**). ^{1}H NMR (400 MHz, DMSO-d6): δ 8.46 (t, J = 6.2 Hz, 2H), 8.36 (t, J = 6.0 Hz, 2H), 7.16 – 7.09 (m, 3H), 6.96 (d, J = 8.4 Hz, 2H), 4.38 (s, 2H), 4.31 – 4.11 (m, 10H), 2.94 – 2.61 (m, 4H), 1.80 (s, 6H), 1.37 (s, 18H).

*Acetamidomethyl (Acm) deprotection of compound **4**:* Compound **4** was deprotected to obtain the disulfide crosslinker compound **5**. For this, compound **4** (0.38 g, 0.51 mmol) was dissolved in 9 mL methanol. To this solution, 18 mL 0.1 M HCl and subsequently 9 mL 0.4 M I_2 in methanol were added to deprotect the thiol Acm protecting groups. The

reaction mixture was stirred for 1 hour at RT, after which excess iodine was removed by addition of 1M aqueous ascorbic acid solution until the solution turned to a white suspension. Chloroform was added to the mixture and concentrated on a rotavapor at 40°C. The formed white product precipitate was vacuum filtered. Additional chloroform and water were added to wash the precipitate and this filter process was repeated 5 times. ^{1}H NMR (400 MHz, DMSO-d6): δ 8.46 (s, 2H), 7.15 – 7.00 (m, 5H), 4.34 (s, 2H), 4.30 – 4.16 (m, 6H), 3.13 – 2.79 (m, 4H), 1.36 (s, 18H).

*Tert-butoxycarbonyl (Boc) deprotection of compound **4**:* To remove the Boc protecting group, the precipitate was dissolved in 20 mL DCM/TFA/water 49:49:2 and stirred at RT for 1 hour. The mixture was concentrated using a rotavapor, followed by coevaporation first with DCM and then hexane after which residual solvents were removed under vacuum overnight, yielding 0.29 g (91% relative to compound **4**) of a yellowish crystalline solid. ^{1}H NMR (400 MHz, DMSO-d6) δ 9.22 (s, 2H), 8.48 (s, 6H), 7.20 (s, 1H), 7.17 (s, 2H), 4.41 (s, 2H), 4.30 – 3.92 (m, 6H), 3.40 – 2.98 (m, 4H). HR-MS: Expected mass for $C_{15}H_{22}N_7O_2S_2^+$ is 396.1271, found 396.1271.

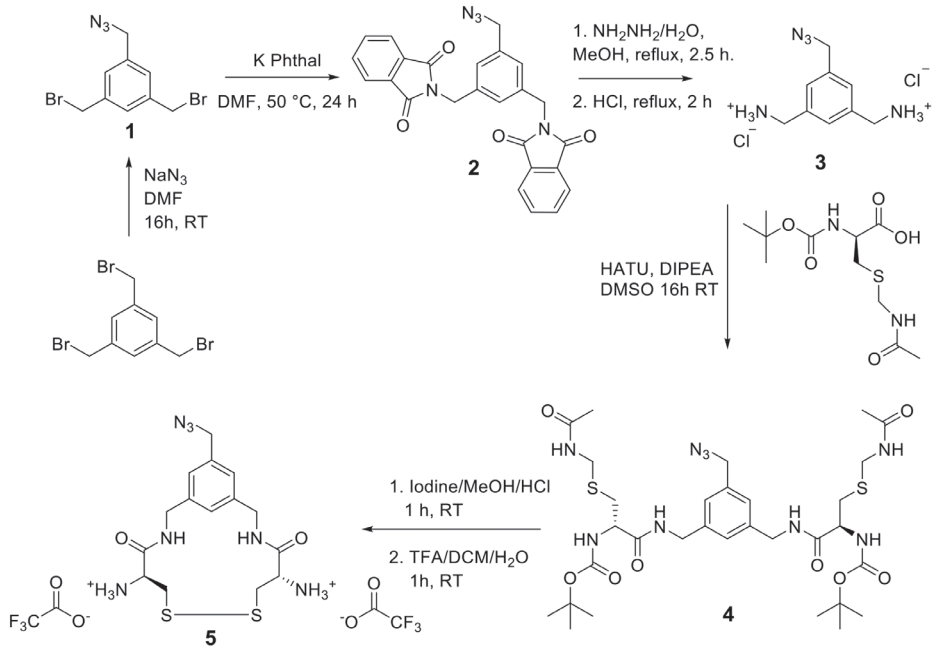

*Scheme 1: Synthesis of the azide containing di-cysteine crosslinker (Compound **5**).*

Thermosensitive block copolymer library synthesis and thioester modification

A five membered library of $mPEG_{5000}$-*b*-P($HPMAmLac_1$-*co*-$HPMAmLac_2$) block copolymers (polymer **P**(monomer to initiator ratio)**,** Scheme 2) was synthesized by free radical polymerization following a previously published procedure.[16] Briefly, varying amounts (160-480 mg) of $(mPEG_{5000})_2$-ABCPA macroinitiator were weighed into a Schlenk tube followed by HPMAm-monolactate ($HPMAmLac_1$, 274 mg) and HPMAm-dilactate ($HPMAmLac_2$, 326 mg). ACN was added to result in a 300 mg/mL monomer concentration. These amounts resulted in a fixed ratio of 53:47 $HPMAmLac_1$: $HPMAmLac_2$ and feed molar ratios of monomer/initiator of 150, 125, 100, 75 and 50 were used. The tubes were sealed by a rubber septum and 5 freeze-vacuum-thaw cycles were applied, backflushed with nitrogen and placed into a pre-heated oil bath at 70 °C for 24 hours. The reaction mixtures were cooled to RT, and the obtained products were precipitated 3 times in diethyl ether and placed under vacuum overnight, yielding white solids. The synthesized polymers were characterized by GPC and NMR (Figure S1.9).

The different block copolymers were functionalized in a subsequent reaction to obtain $mPEG_{5000}$-*b*-P($HPMAmLac_n$-*co*-$HPMAmLac_n$-ETSA) block copolymers (polymer **Pn-E(**ETSA functionalization percentage**)**). Stock solutions of thioester ETSA (50 mg/mL), DPTS (20 mg/mL) and DCC (50 mg/mL) in dry DCM were prepared. Polymer **Pn** was weighed and dissolved in dry DCM (final concentration of 100 mg/mL), followed by addition of ETSA with a feed ratio of 10 and 15 mol% relative to $HPMAmLac_n$ functionalization, 0.1 equivalents (to ETSA) of DPTS and finally 1.1 equivalents (to ETSA) of DCC. The reaction mixtures were stirred at RT for 24 hours. The mixtures were then filtered using a 0.2 μm PTFE syringe filter to remove precipitated DCU. Subsequently, the polymers were precipitated twice in diethyl ether and dried under vacuum overnight. The synthesized polymers were characterized using GPC and NMR analysis (Figure S1.11).

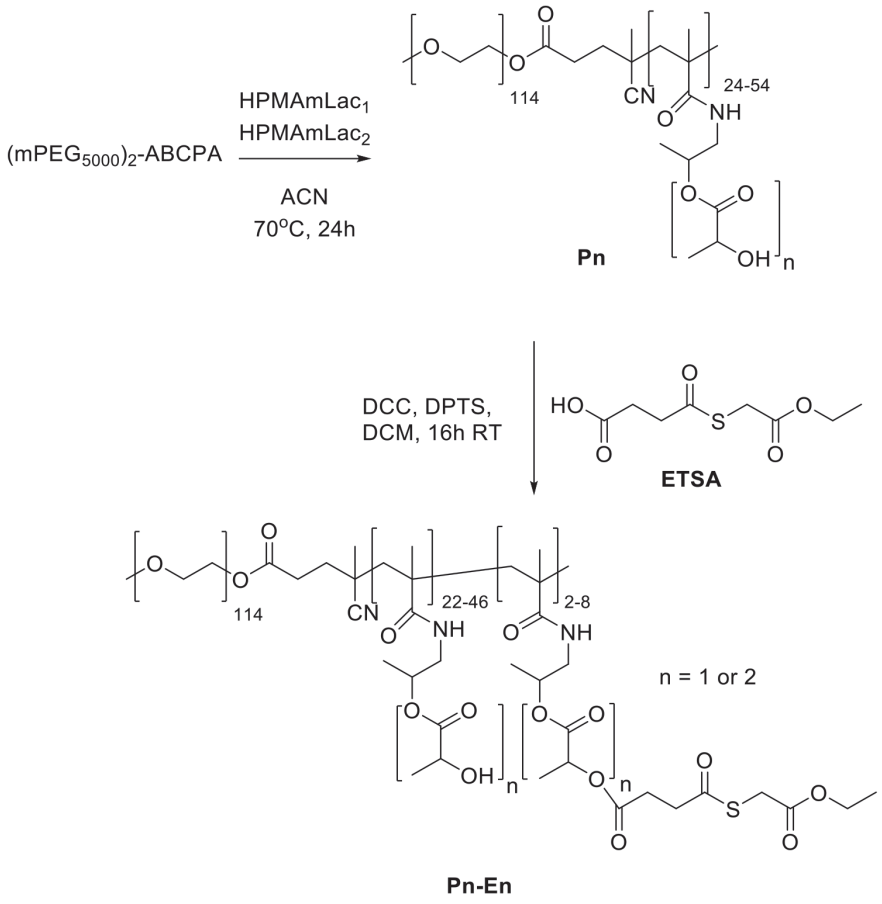

*Scheme 2: Synthesis of $mPEG_{5000}$-b-P(HPMAmLac$_1$-co-HPMAmLac$_2$) polymers (polymer **Pn**) by free radical polymerization using a (methoxy polyethylene glycol)$_2$-4,4-azobis(4-cyanopentanoic acid) ($(mPEG_{5000})_2$-ABCPA) macroinitiator and subsequent ETSA coupling to attain polymer **Pn-En**.*

Core-crosslinked polymeric micelle (CCPM) formation and purification

The $mPEG_{5000}$-*b*-P(HPMAmLac$_n$-*co*-HPMAmLac$_n$-ETSA) polymers (polymer **Pn-En**) were dissolved in phosphate buffer (100 mM Na_2HPO_4, adjusted to pH 7.4 using HCl) to 20 mg/mL whilst stirring in an ice bath. The crosslinker (compound **5**) was dissolved in DMSO (75 mg/mL) and 3 equivalents (to crosslinker) of tris(2-carboxyethyl)phosphine (TCEP) in DMSO (112.5 mg/mL) was added to reduce the disulfide bonds. After 20 minutes, the crosslinker/TCEP mixture (having 1.5 equivalents of cysteine residues relative to the ETSA residues on the polymer chains) was placed in a water bath pre-heated to 37 °C whilst stirring and the polymer solution (typically 1 mL) was then added. After 1 hour of crosslinking, the obtained core-crosslinked micelles were filtered using

0.2 μm RC syringe filters (rinsed with additional phosphate buffer resulting in a 2-fold dilution) and subsequently purified using a G-25 sephadex packed 5 mL HiTrap desalting column with an M_w cutoff of 5000 Da (GE healthcare, Uppsala, Sweden).

Bicyclo[6.1.0]non-4-yn-9-ylmethanol (BCN-OH) copper-free click conjugation with crosslinker (compound 6)

Crosslinker compound **5** (11 mg, 17 μmol) was weighed into a glass vial followed by BCN-OH (3.5 mg, 23 μmol) and 100 μL DMSO (see Scheme 3). The reaction mixture was left stirring for 2 hours RT after which the product in the vial was lyophilized overnight. The dried solid was analyzed by ^{1}H-NMR, IR spectroscopy and ESI-MS (Figures S6.1 and S2.2).

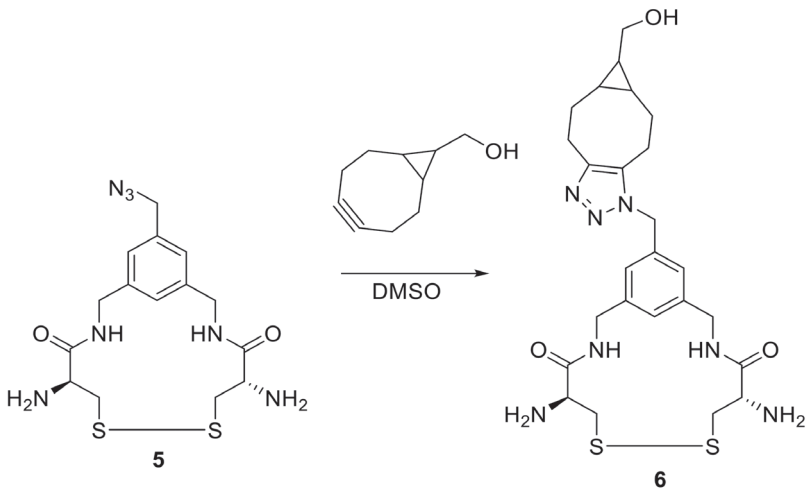

Scheme 3: One pot reaction of the trifunctional crosslinker with BCN-OH. BCN-OH is clicked to the trifunctional crosslinker (compound 5) in DMSO and dried for analysis to confirm azide based coupling.

Sulfo.Cy5-DBCO loaded CCPM formation (compound 7 construct)

Prior to CCPM formation, a Sulfo.Cy5-crosslinker conjugate was obtained in a one pot reaction as shown in Scheme 4. The crosslinker (compound **5**) was dissolved in DMSO (75 mg/mL). Sulfo.Cy5-DBCO was dissolved in DMSO to 10 mg/mL, 2% mass relative to the polymer added to the crosslinker (6.5 mol. % relative to crosslinker) and the mixture was stirred for 1 hour at RT. TCEP (dissolved to 112.5 mg/mL in DMSO) was then added in 3-fold molar excess to the mixture to reduce the disulfide bonds.

After 20 minutes, the mixture was placed in a water bath pre-heated to 37 °C. $mPEG_{5000}$-*b*-P(HPMAmLac$_n$-*co*-HPMAmLac$_n$-ETSA) (polymer **Pn-En**), dissolved in phosphate buffer (100 mM Na_2HPO_4, adjusted to pH 7.4 using HCl) to 20 mg/mL on an ice bath, was added to the crosslinker/Sulfo.Cy5/TCEP mixture and the reaction mixture was stirred for 1 hour. The obtained CCPMs were purified as described above.

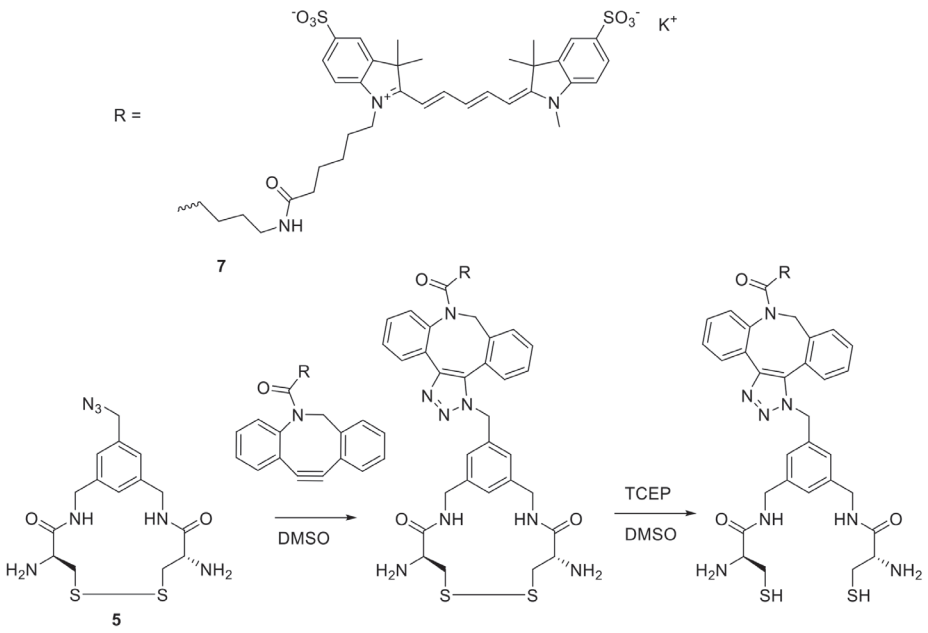

*Scheme 4: One pot reaction of the trifunctional crosslinker with the DBCO functionalized Sulfo. Cy5. Sulfo.Cy5-DBCO is clicked to the trifunctional crosslinker (compound 5) after which the disulfide bonds are reduced using TCEP for NCL crosslinking of the crosslinker-Cy5 conjugate with **Pn-En** to obtain CCPMs.*

BODIPY-TMTHSI loaded CCPM formation (compound 8 construct)

Prior to CCPM formation, a BODIPY-crosslinker conjugate was obtained in a one pot reaction as shown in Scheme 5. The same procedure as described above for the Sulfo. Cy5-crosslinker conjugate was employed.

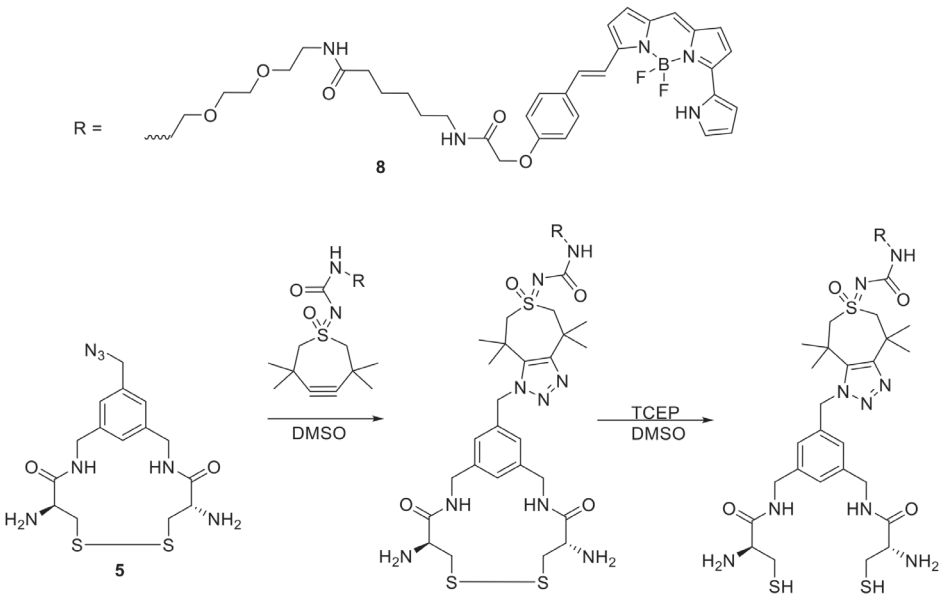

*Scheme 5: One pot reaction of the trifunctional crosslinker with the TMTHSI functionalized BODIPY dye. BODIPY-TMTHSI is clicked to the trifunctional crosslinker (compound 5) after which the disulfide bonds are reduced using TCEP for NCL crosslinking of the crosslinker-BODIPY conjugate with **Pn-En** to obtain CCPMs.*

Crosslinker, polymer and particle characterization

Nuclear magnetic resonance (NMR) spectroscopy

^{1}H, ^{13}C and ^{1}H-^{13}C heteronuclear single quantum correlation (HSQC) NMR spectra were recorded on an Agilent 400-MR NMR spectrometer (Agilent Technologies, Santa Clara, USA). Residual solvent peaks of $CDCl_3$ (δ = 7.26 ppm) or D_6 DMSO (δ = 2.50 ppm) were used to calibrate chemical shifts.

Infrared spectroscopy (IR)

IR spectra were recorded with solid samples using a ATRU equipped Spectrum 2 (Perkin Elmer, Llantrisant, UK) and reported in cm^{-1}.

Mass spectrometry (MS)

Three methods of MS were employed in this work. High resolution (HR)-MS was performed on a 6560 Ion Mobility Q-TOF LC/MS (Agilent technologies, Santa Clara, USA). Normal resolution electrospray ionization (ESI)-MS measurements were

performed on a microTOF-Q II (Bruker,). Matrix assisted laser desorption ionization (MALDI)-MS were performed on a Ultraflextreme (Bruker,), employing α-cyano-4-hydroxycinnamic acid as matrix.

Thin layer chromatography (TLC)

TLC was carried out using aluminum bound silica plates obtained from Merck Darmstadt (SiO_2, Kieselgel 60 F254). Compounds were visualized by UV detection at 254 nm and, where applicable, stained with ninhydrin in DCM to visualize amines/amides or 10% triphenylphosphine in DCM followed by ninhydrin to visualize azides.

Gel permeation chromatography (GPC)

GPC for polymer analysis was performed using an Alliance 2695 (Waters) chromatography system with two PLgel 5 µm mixed-D columns (Polymer Laboratories) in series at a column temperature of 65 °C and employing a refractive index detector. DMF supplemented with 10 mM LiCl was employed as eluent with an elution rate of 1 mL/min. Sample concentration was typically 5 mg/mL and PEGs of narrow and defined molecular weights obtained from PSS (Germany) were used as calibration standards. Recording of data and calculations of molecular weights were done with Waters Empower 32 software.

For the GPC analysis of empty CCPMs, serially connected TSKGel G5000PWXL 10 µm (first column) and G6000PXWL 13 µm (second column) 7.8 x 300 mm columns (Tosoh Bioscience, Griesheim, Germany) were employed at a column temperature of 25 ^{o}C and isocratic flow of 0.3 mL/min of 100 mM $NaNO_3$ supplemented with 10 mM Na_2HPO_4/ NaH_2PO_4 (pH 7.2). A Waters 2487 UV detector was employed measuring absorbance at 235 nm.

High performance liquid chromatography (HPLC)

HPLC analysis was performed using an Alliance 2695 chromatography system with an XBridge C18 column (5 µm, 4.6 x 150 mm, Waters) at a column temperature of 30 °C and employing an Alliance 2487 ultra-violet (UV) detector at 210 and 650 or 700 nm. Acetonitrile/water supplemented with either 0.1% perchloric acid or 0.1% formic acid was used as eluent at a flow of 1 mL/min and a gradient of 5 to 95% ACN over 20 minutes.

Ultra-high performance liquid chromatography (UHPLC)

UHPLC analysis for lactic and succinic acid quantification was performed using an Acquity (Waters) chromatography system with an HSS T3 column (1.8 µm, 2.1 x 150 mm, Waters) at a column temperature of 30 °C and employing a Waters TUV detector at 210 nm. KH_2PO_4 buffer (10 mM, pH = 2.5) was used as isocratic eluent at a flow of 0.85 mL/min for 2.5 minutes followed by an increasing gradient of acetonitrile supplemented with 0.1% phosphoric acid from 0% to 90% over 1 minute.

Total polymer content analysis

Total polymer content of empty micelles before and after purification was determined through lactic acid concentration by UHPLC after hydrolysis as reported previously. [35] Briefly, 100 µL of the diluted micellar dispersion was incubated with 100 µL NaOH (6 M) for 2 hours at 60 °C followed by the addition of 200 µL HCl (6 M). After addition of 200 µL of eluent (10 mM KH_2PO_4, pH = 2.5) for further dilution, samples were run on UHPLC as described above. Sodium lactate was employed as reference standard to determine lactic acid concentration.

The total polymer content was calculated as follows: Amount of polymer = measured amount of lactic acid × (M+5000)/ [90.08 × (m + 2n)], where M is the M_n of the thermosensitive block P(HPMAmLac$_n$); m and n are the number of repeat units of HPMAmLac$_1$ and HPMAmLac$_2$ in the block copolymer respectively (determined by ^{1}H NMR). The molecular weight of lactic acid is 90.08 g/mol.

Cloud point (CP) measurement

The CPs of the different thermosensitive polymers in phosphate buffer (100 mM Na_2HPO_4, adjusted to pH 7.4 using HCl, 5 mg/mL polymer) were determined by measurement of light scattering at a 90° angle upon the onset of opalescence. Scattered light intensity was measured using a Jasco FP-8300 spectrophotometer employing an excitation and emission wavelength of 550 nm with 1 nm slit width and a response time of 1 second. Temperature was ramped from 2 °C to 50 °C at 1 °C per minute.

Dynamic light scattering (DLS).

The size of the CCPMs was determined by DLS using a Malvern Zetasizer nano series ZS90 with a measurement angle of 90°. Measurements were typically carried out at 2, 25 and 37 °C. Unless stated otherwise, the concentration of the micellar dispersions was approximately 7.5 mg/mL in phosphate buffer (100 mM Na_2HPO_4, adjusted to pH

7.4 using HCl). For the S.Cy5 and BODIPY loaded CCPMs, a narrow band filter was employed with a 100x sample dilution in milliQ to mitigate interference from the dyes.

CCPM physical stability

The physical stability of the CCPMs was investigated in the presence of increasing surfactant sodium dodecyl sulfate (SDS) concentration. CCPMs were prepared as described above using the P100-E15 polymer and filtered with a 0.2 μm syringe filter. Non-crosslinked control micelles were prepared using the same procedure but without addition of crosslinker. The samples (400 μL) were spiked stepwise with either 10 or 20 μL of SDS (20% solution), gently mixed and measured using DLS at 25 ^{o}C.

CCPM hydrolytic stability

Size exclusion purified empty CCPMs were 5x diluted in phosphate buffer (100 mM Na_2HPO_4, adjusted to pH 7.4 using HCl) to a concentration of 1.5 mg/mL, incubated at 37 ^{o}C and degradation was monitored by derived count rate (DCR), Z-Ave and PDI measured by DLS on a Zetasizer Nano S (Malvern Panalytical). Measurements were terminated when the DCR dropped below 5% initial kcps or PDI exceeded 0.5. Lactic acid release was quantified using the UHPLC method described above, injecting 20 μL 7.5 mg/mL micellar suspension diluted with 10 μL 1 M HCl and 20 μL milliQ. Total lactic acid content was determined by hydrolyzing 20 μL micellar suspension overnight with 10 μL 1 M NaOH, followed by addition of 20 μL 1 M HCl.

Cytotoxicity and internalization studies

Cell culture

Prostate cancer cells obtained from American Type Culture Collection (PC3 ATCC CRL-1435) were cultured and maintained at 37 ^{o}C with McCoy's medium supplemented with 10% fetal bovine serum (FBS) in an incubator regulated with 5% CO_2, 95% air and saturated humidity. Cells were passaged every 2-4 days upon reaching 80% confluency using trypsin ethylenediaminetetraacetic acid (trypsin-EDTA).

Cell viability

PC3 cells were plated into black polystyrene 96 well plates (with micro-clear bottom, Greiner #655090) at a density of 1.5 x 10^4 cells per well and incubated for 24 hours at 37 ^{o}C. The medium was aspirated and 100 μL dilutions of purified BODIPY loaded CCPMs

in McCoy's medium supplemented with 10% FBS were added in triplicate. After 24 hours, 20 µL of MTS staining solution (CellTiter 96® AQ_{ueous}, Promega) was added. Following a 1 hour incubation, absorbance intensity (490 nm) was recorded using a Mithras plate reader. Data were background subtracted and normalized using medium only wells and untreated cells respectively of the same plate.

Cellular uptake

Microscopy

PC3 cells were plated into black polystyrene 96 well plate (Greiner #655090) at 60% confluency per well in McCoy's medium with 10% FBS and supplemented with 1% penicillin/streptomycin. The following day, non-labelled and BODIPY loaded CCPMs were added to the cells in triplicate at a final concentration of 0.1 mg/ml and incubated for 24 hours. Prior to confocal microscopy, the cells were treated with 2 µg/ml Hoechst 33342 for 10 minutes in an incubator at 37 °C, 5% CO_2. The cells were imaged in OptiMEM on Yokogawa CV 7000 Microscope (60x water immersion objective lens).

Fluorescence-activated cell sorting (FACS)

PC3 cells were plated into 12-well plates with a cell confluency of 60% per well and incubated for 24 hours at 37 °C, 5% CO_2 in an incubator. Non-labelled and BODIPY loaded CCPMs were diluted to 0.1 mg/mL with McCoy's medium supplemented with 10% FBS and 1% penicillin/streptomycin and after aspiration of culture medium 1000 µL of CCPM dispersion was added to the cells in triplicate. After 24 hour incubation, the treatment medium was removed and the cells washed with PBS. The cells were then harvested using trypsin, transferred into 5 mL polystyrene tubes, and resuspended in PBS supplemented with 5% FBS. Cell associated fluorescence was detected using a FACSCanto II flow cytometer (BD canto II) with 1 x 10^4 cells per sample.

Results and discussion

Di-cysteine, azide functionalized crosslinker synthesis

We designed a trifunctional crosslinker to employ NCL as a crosslinking strategy for the formation of core-crosslinked polymeric micelles (CCPMs) and simultaneous encapsulation of model compounds (fluorescent dyes) under mild conditions. The crosslinker contains two cysteine residues needed for NCL, connected *via* a benzylic core that also contains an azide moiety for use as a click chemistry handle (compound **5**, Scheme 1). First, a nucleophilic substitution with sodium azide was employed to introduce

an azide moiety onto 1,3,5-tris(bromomethyl)benzene. A statistical mixture of mono, di and tri azide-substituted compounds was obtained and compound **1** was isolated after column purification. The close retention times of the statistically substituted products required strenuous fractionation, where particularly unreacted 1,3,5-tris(bromomethyl) benzene was the most difficult impurity to separate from compound **1**. Therefore, instead of 1.0 equivalent to target a single substitution, 1.5 equivalents of sodium azide were employed to reduce the amount of starting reagent remaining. The identity of compound **1** was confirmed by ^{1}H NMR analysis (Figure S1.1).

In the next step, Gabriel synthesis [47] was employed to substitute the two remaining benzyl bromines with amine functionalities (compound **3**), which involved an intermediate compound **2**: (azidomethyl-3,5-di(phthalamidomethyl)benzene). The phthalimides were introduced by a nucleophilic substitution of the bromides with potassium phthalimide in DMF and after purification, the identity of compound **2** was confirmed by NMR (Figure S1.2). The phthalimide moieties were subsequently converted to amines by reflux boiling with hydrazine hydrate followed by HCl treatment to attain compound **3**. Since multiple attempts to extract compound **3** from the aqueous solution failed, this compound was isolated as a crude HCl salt. The identity of compound **3** was confirmed by ^{1}H NMR (Figure S1.3 and S1.4)

We coupled protected cysteine residues to the amines of compound **3** (azidomethyl-3,5-di(aminomethyl)benzene) using the coupling reagent HATU. A great excess of base (20 equivalents DIPEA) had to be added to neutralize remaining HCl salts in compound **3**. Compound **4** was obtained *via* silica column purification and its structure was confirmed by ^{1}H NMR analysis (Figure S1.5). A good yield of 70% of compound **4** for two steps starting from compound **2** was obtained.

The final crosslinker (compound **5**) was obtained by deprotecting compound **4**. We removed the Acm protecting group first by use of iodine oxidation. Successful Acm deprotection of compound **4** was confirmed by ^{1}H NMR analysis (Figure S1.6). Subsequently, Boc deprotection was carried out using a DCM/TFA/water mixture. After this deprotection step, the reaction mixture was concentrated and finally placed under vacuum yielding compound **5** as TFA salt in a quantitative yield. The identity of compound **5** was confirmed by ^{1}H NMR, HR-MS, IR, and HSQC NMR analysis (Figures S1.7, S1.8, S2.1 and S6.1).

Polymer synthesis

We synthesized thermosensitive mPEG$_{5000}$-*b*-P(HPMAmLac$_1$-*co*-HPMAmLac$_2$) block copolymers (polymer **Pn**) with varying molecular weights of the thermosensitive

P(HPMAmLac$_n$) block *via* free radical polymerization as described in detail previously. [16] By varying the molar ratio of monomer/macroinitiator (150, 125, 100, 75 and 50 for **P150, P125, P100, P75** and **P50,** respectively), polymers with varying P(HPMAmLac$_n$) block lengths and constant mPEG$_{5000}$ length were obtained (table 1). Generally, a conversion of around 80% was achieved after 24 hour polymerization. Owing to the nature of free radical polymerization, dispersity values between 1.4 and 1.7 were found, as also reported previously. [16]

The different polymers were functionalized with both 10 and 15 mol% ETSA (relative to the amount of HPMAmLac$_n$ groups) to provide thioester handles for the native chemical ligation reaction, yielding polymers **Pn-E10 and Pn-E15**, respectively (table 1). By using 1.1 equivalents of the DCC coupling reagent, efficient coupling of ETSA to the hydroxyl groups of the P(HPMAmLac$_n$) block could be achieved as was identified by NMR (Figure S1.11). Additional confirmation of ETSA content was determined by UHPLC quantification of succinic acid after basic hydrolysis of **P100-E15**, finding back 12 mol% ETSA content (Figure S4.1 for chromatogram). Furthermore, free ETSA (that could interfere with the polymer chain crosslinking) was not detected in the purified mPEG$_{5000}$-*b*-P(HPMAmLac$_n$-*co*-HPMAmLac$_n$-ETSA) using HPLC analysis (Figure S3.1).

Table 1: Characteristics of mPEG$_{5000}$-b-P(HPMAmLac$_1$-co-HPMAmLac$_2$) block copolymers before and after functionalization with ETSA.

	eq. HPMAmLac$_1$ per PEG chain		eq. HPMAmLac$_2$ per PEG chain						ETSA 10 mol% feed		ETSA 15 mol% feed	
	Feed	Obtained[a]	Feed	Obtained[a]	Lac$_1$/ Lac$_2$ Ratio	M_n (kDa)[a]	PDI[b]	Cloud Point (°C)	Obtained (mol%)[a]	Cloud Point (°C)	Obtained (mol%)[a]	Cloud Point (°C)
P150	40	31	35	23	1.37	18.2	1.48	35	7.5	10	13.9	3
P125	33	28	29	22	1.27	17.4	1.69	35	8.1	10	14.0	3
P100	27	22	24	19	1.15	15.2	1.70	31	6.5	13	14.1	5
P75	20	16	18	13	1.21	12.6	1.66	31	7.1	13	15.4	5
P50	13	13	12	11	1.18	11.1	1.43	34	7.4	14	16.0	8

[a] *determined by NMR* [b] *determined by GPC.*

The cloud point (CP) of the unmodified polymers is in agreement with previous findings [16] and modification with ETSA resulted in a decrease in CP (from around 31-35 °C to 3-14 °C) due to increased hydrophobicity of the thermosensitive polymer block.

Core-crosslinked micelle formation

Core-crosslinked polymeric micelles (CCPMs) were prepared using the 6.5-8.1 and 13.9-16.0 mol% (relative to $HPMAmLac_n$) ETSA modified polymers (**Pn-En,** table 1) in combination with crosslinker **5**. The crosslinker was treated with an excess of TCEP to break the disulfide bonds and introduce free thiols for the NCL reaction. During micellization at 37 °C for 1 hour, reaction of the cysteine groups of the crosslinker with the thioester functional groups present on the $mPEG_{5000}$-*b*-P($HPMAmLac_n$-*co*-$HPMAmLac_n$-ETSA) polymers resulted in the formation of amide bonds. Thioglycolate was released as side product and subsequently removed by size exclusion chromatography, as confirmed by HPLC analysis (Figure S3.2).

Decreasing the molecular weight of the polymer chains decreased the size of the obtained CCPMs (table 2), following a similar trend observed previously for the methacrylated derivative of this PEG-P($HPMAmLac_n$) polymer system. [16] Furthermore, increasing the ETSA content from 6.5-8.1 to 13.9-16.0 mol% resulted in substantially reduced micelle size, likely due to an increased hydrophobicity and consequently lower CP of the P($HPMAmLac_n$) block causing a denser hydrophobic core.

Table 2: Characteristics of CCPMs formed from the $mPEG_{5000}$-b-P($HPMAmLac_n$-co-$HPMAmLac_n$-ETSA) polymers libraries. DLS measurements were done at 25 °C.

	Z-Ave (nm)	PDI	Derived Count Rate (kcps)
P150-E10	119	0.11	103692
P150-E15	79	0.12	56642
P125-E10	115	0.15	93010
P125-E15	73	0.09	62030
P100-E10	68	0.07	38570
P100-E15	50	0.05	20466
P75-E10	61	0.08	16351
P75-E15	45	0.04	12168
P50-E10	57	0.18	6571
P50-E15	42	0.06	7110

Particle size plays a crucial role in nanocarrier systems intended for tumoral targeting and exploiting prolonged circulation kinetics and tumor disposition *via* the EPR effect. [6–14] Nanoparticles with a size of around 50 nm showed effective tumor accumulation and penetration. [12–14] Since the decrease in hydrodynamic diameter (Z-Ave) of the CCPMs levels off (40-50 nm) for polymers smaller than P100-E15 (15.2 kDa), the P100-E15 particle formulation was selected as lead formulation for further experiments. This choice was made to maximize the number of ETSA moieties available for crosslinking

whilst still obtaining small CCPM sizes. The subsequent re-syntheses of the P100-E15 based CCPMs (including re-synthesized polymers) resulted in consistent Z-Ave values of between 47-53 nm, with a nearly neutral zeta potential of -4 mV as expected for PEGylated particles.

The total polymer content of the P100-E15 CCPM dispersion before and after purification by filtration and size exclusion procedure was determined. The purified CCPM sample had a polymer concentration of 7.5 mg/mL which is very close to the expected value of 7.0 mg/mL based on dilution factors, indicating no significant losses of polymer during purification (Figure S4.2). Furthermore, the single peak found from SEC of CCPMs demonstrates that no free polymer chains remained in the micellar dispersion and thus confirming complete polymer incorporation into the micelles (Figure S5.1). The depletion of the crosslinker peak in the crude sample shown by HPLC (Figure S3.2) also demonstrates complete incorporation into the system.

The stability of the CCPMs was investigated using DLS experiments by incubating the micellar dispersions with increasing concentrations of SDS, employing particles formed using the P100-E15 polymer (Figure 1). PMs that were not covalently crosslinked dissociated at an SDS concentration of 5 mg/mL as seen by the rapid drop in size and huge increase in PDI. At concentrations above its CMC(1.7-2.3 mg/mL), SDS is known to solubilize amphiphilic block copolymers into a mixed micelle system resulting in destabilization of the PMs. [48] In contrast, the crosslinked micelles maintained an almost constant PDI (<0.1) and gradual increase in size with increasing surfactant concentration. Notably, there is a proportional increase in Z-Ave from 47 to 87 nm of the crosslinked micelles with increasing SDS concentration, which is consistent with results observed previously for similar CCPMs and can likely be ascribed to the absorption of SDS by the micelles. [23] This observation indicates that stable CCPMs were formed exploiting crosslinker **5**.

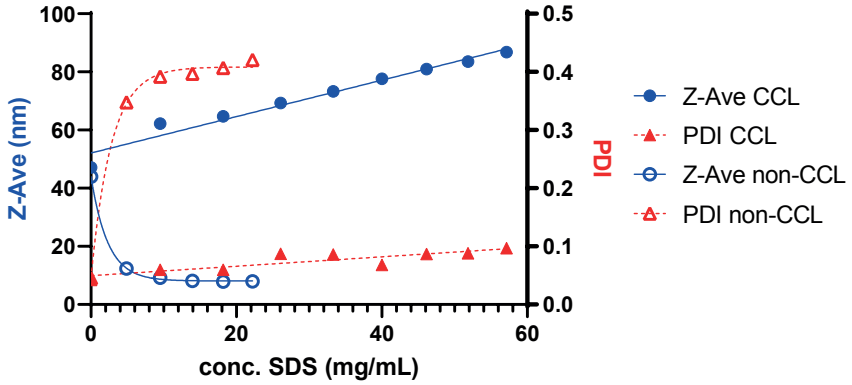

Figure 1: Effect of increasing concentrations of SDS on crosslinked micelles (filled shapes) and non-crosslinked micelles (hollow shapes) as measured by DLS at 25 °C.

Degradation characteristics of CCPMs based on P100-E15 were investigated by DLS measurements, in accordance with a previously published procedure. [16] Figure 2 shows an 90% decrease in light scattering intensity (SI) over a period of 480 hours upon their incubation under physiological conditions (37 °C, pH 7.4). The diameter of the CCPMs increased from 47 to 56 nm, indicating swelling of the particles accompanied by a substantial increase in PDI. The degradation of the CCPMs is caused by the ester hydrolysis of lactate moieties in the free and crosslinked HPMAmLac$_n$ side chains as has been previously reported. [49,50] This also results in the release of lactic acid as shown in figure 2, with a 60% of total lactic acid content release after 480 hours(90% decrease in SI). Importantly, these results show that the CCPMs degrade under physiological conditions through the expected ester hydrolysis of lactate side chains and lactate esters in the crosslinks, which is a crucial feature for *in vivo* applications.

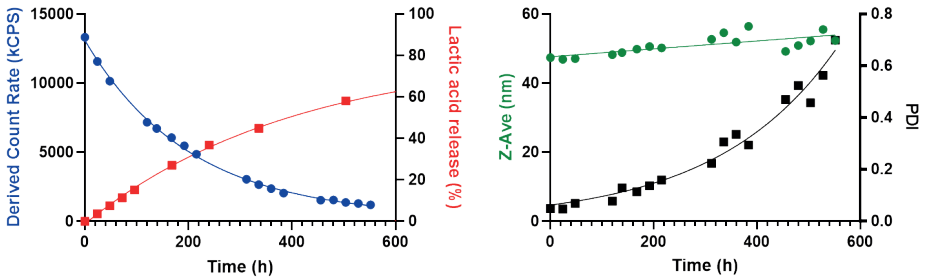

Figure 2: Degradation characteristics of P100-E15 based CCPMs under physiological conditions (pH 7.4, 37 °C) at a polymer concentration of 7.5 mg/mL. Derived count rate (blue circles), Z-Ave (green circles) and PDI (black squares) were determined by DLS measurements at 37°C. Lactic acid formed % (black triangles) was determined by UPLC.

Dye loading

To demonstrate the versatile options to covalently entrap model compounds using the trifunctional crosslinker, we loaded the CCPMs with two different dyes, Sulfo.Cy5 and BODIPY, employing two different copper-free click chemistry handles (dibenzocyclooctyne (DBCO) and 3,3,6,6-tetramethylthiacycloheptyne (TMTHSI), respectively). A third ring strained alkyne, bicyclo[6.1.0]non-4-yn-9-ylmethanol (BCN) was employed to model the click reaction and gain sufficient quantities for NMR and IR analysis.

Since ring strained alkyne functionalities such as BCN and DBCO are known to react with free thiols present on cysteines, [51,52] the dyes need to be clicked to the crosslinker in the oxidized disulfide form. We therefore coupled BCN-OH in slight excess with the azide and performed NMR and IR to confirm that azide-alkyne coupling rather than thiol-alkyne formation occurred (Figure S6.1). Indeed, an upshift of the crosslinker protons neighboring the azide was observed in the NMR spectra and a depletion of the azide signal at 2100 cm^{-1} in the IR spectra confirmed the formation of a triazole ring following the azide-alkyne click reaction. Furthermore, the identity of the coupled product was confirmed by mass spectrometry (Figure S2.2).

Both Sulfo.Cy5-DBCO as well as BODIPY-TMTHSI can react with azides by strain-promoted azide alkyne cyclo-addition reaction. After the click reaction, the disulfides were reduced using TCEP to render the dye-crosslinker conjugates ready for the NCL crosslinking reaction, as confirmed by MALDI-MS (Figures S2.3 and S2.4). Both the clicking of the dyes as well as opening of the disulfide bridges was performed in a simple one-pot fashion.

The successful entrapment of either Sulfo.Cy5-DBCO or BODIPY-TMTHSI into the CCPMs was shown by HPLC of samples before purification (Figures S3.3 and S3.4). Entrapment was analyzed on the CCPMs as such since this approach of dye entrapment is non-reversible. A significant increase in absorbance at 650 nm was found for Sulfo. Cy5 and BODIPY entrapped CCPMs compared to empty CCPMs accompanied by the depletion of free dye signal, indicating successful entrapment with >95% efficiency. DLS measurements of the purified CCPMs using a fluorescence filter setup found a Z-Ave of 47 and 52 nm with a PDI of 0.04 and 0.14 for the S.Cy5 and BODIPY loaded CCPMs respectively, showing that dye cargo incorporation did not significantly alter CCPM size.

Cell viability and internalization

To demonstrate the cytocompatibility of our dye loaded CCPMs and their possible cellular internalization, [53] we performed *in vitro* cell studies using the BODIPY-TMTHSI formulation. Prostate cancer cells (PC3), that previously have shown high uptake of similar CCPMs, [44] were cultured to visualize uptake of the BODIPY loaded CCPMs. These CCPMs had a 2% dye weight ratio relative to the polymers and were incubated for 24 hours at a polymer concentration of 0.1 mg/mL with the cells.

Significant uptake of the CCPMs was observed for BODIPY entrapped CCPMs as shown by the laser confocal scanning microscopy imaging (Figure 3 A and B). Uptake was further confirmed by cell associated fluorescence flow cytometry measurements (Figure S7.1), which is in line with previously published results employing a similar PEGylated CCPM system. [44]

Importantly, no cytotoxicity on the PC3 cells up to at least a CCPM concentration of 2 mg/mL (20-fold higher than the uptake study) was observed, indicating a good cytocompatibility (Figure 3 C).

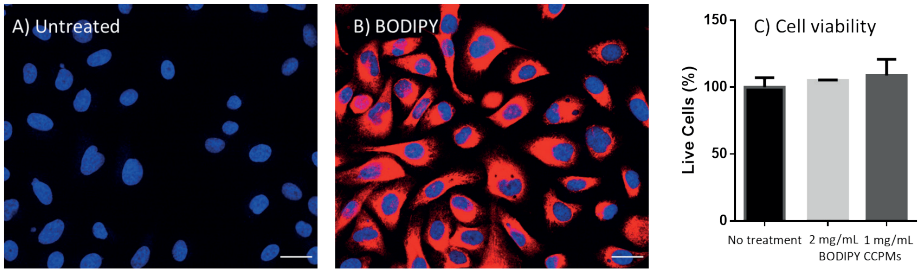

Figure 3: Confocal laser scanning microscopy images of PC3 cells incubated for 24 hours with empty CCPMs (A) or BODIPY loaded CCPMs (B). Cells were treated with 2 µg/ml Hoechst nuclei stain (blue signal) prior to microscopy. Scale bar – 30 µm. Cell viability was determined in triplicate by MTS staining for BODIPY loaded CCPMs (C).

Conclusion

New generations of pharmaceuticals are increasingly becoming biological and peptide based in nature, increasing their fragility towards chemistries such as free radical reactions. The entrapment of these fragile compounds in nanoparticles for extended circulation and tumor accumulation is of interest not just for therapeutic efficiency and safety, but also cost reduction for which orthogonal chemistries need to be developed. We developed a physiologically degradable CCPM platform stabilized by mild, biorthogonal

NCL crosslinking with a clickable azide handles for potential (pro)drug conjugation. By using the fluorescent dyes Sulfo.Cy5 and BODIPY as model compounds, we demonstrated successful entrapment and cytocompatibility of these CCPMs. Clearly, for the entrapment of active pharmaceutical compounds and subsequent (triggered) release of active pharmaceutical compounds, successful linker (prodrug) design is paramount and future work will be focused towards this avenue. The platform described here serves as a steppingstone for the orthogonal entrapment of therapeutics into CCPMs and to provide manifold opportunities towards imaging and therapy.

Supporting information paragraph

^{1}H NMR spectra of compounds **1-5**, polymer P100, ETSA and polymer P100E15 (Figures S1.1-1.11); Mass spectra of crosslinker, crosslinker coupled to BCN-OH, crosslinker coupled to Suflo.Cy5-DBCO, crosslinker coupled to BODIPY-TMTHSI (Figures S2.1-2.4); HPLC chromatograms of P100E15 and ETSA, CCPMs before and after purification, CCPMs loaded with Sulfo.Cy5, CCPMs loaded with BODIPY (Figures S3.1-3.4); UHPLC chromatograms of NaOH hydrolyzed P100E15 for ETSA and total polymer content determination (Figures S4.1 and S4.2); Size exclusion chromatogram of purified empty CCPMs (Figure S5.1); Schematic representation of azide selective crosslinker reaction with BCN-OH showing ^{1}H NMR and IR data (Figure S6.1); Cell associated fluorescence of PC3 cells incubated with BODIPY loaded CCPMs (Figure S7.1).

Conflicts of interest

The authors declare that there is no conflict of interest.

Acknowledgements

We would like to acknowledge G.P. Bosman and J. Sastre Torano for the measurement of high resolution mass spectra, C.Y Lau for his advice on synthesis, M. Otten for the IR measurements and B.W.M. Kuipers for the assistance with DLS measurements of dye loaded CCPMs. The Dutch Research Council (NWO) and Cristal Therapeutics are acknowledged for funding (NWA.ID.17.030).

List of abbreviations

ABCPA:	4,4-azobis(4-cyanopentanoic acid)
ACN:	Acetonitrile
BCN:	Bicyclo[6.1.0]nonyne
BODIPY:	4,4-difluoro-4-bora-3a,4a-diaza-s-indacene
CCPM:	core-crosslinked polymeric micelle
CMC:	critical micellization concentration
CP:	cloud point
CMT:	critical micellization temperature
DCC:	*N,N'*-dicyclohexylcarbodiimide
DCM:	Dichloromethane
DCR:	derived count rate
DCU:	dicyclohexylurea
DLS:	dynamic light scattering
DMF:	Dimethyl formamide
DMSO:	Dimethyl sulfoxide
DPTS:	*N,N*-dimethylaminopyridinium *p*-toluenesulfonate
ETSA:	ethylthioglycolate-succinic acid
ESI:	Electrospray ionization
FBS:	fetal bovine serum
GPC:	gel permeation chromatography
HATU:	hexafluorophosphate azabenzotriazole tetramethyl uronium
$HPMAmLac_n$:	*N*-2-hydroxypropyl methacrylamide mono/di lactate
HPLC:	High pressure liquid chromatography
IR:	Infra-red
MALDI:	Matrix assisted laser desorption ionization
mPEG:	methoxy polyethylene glycol
MPS:	mononuclear phagocyte system
MS:	Mass spectrometry
MTS:	3-(4,5-dimethylthiazol-2-yl)-5-(3-carboxymethoxyphenyl)-2-(4-sulfophenyl)-2H-tetrazolium
NCL:	native chemical ligation
PDI:	polydispersity index
PEG:	polyethylene glycol
PM:	polymeric micelle
Pn:	$mPEG_{5000}$-*b*-P($HPMAmLac_1$-*co*-$HPMAmLac_2$) copolymer

Pn-En:	$mPEG_{5000}$-*b*-P(HPMAmLac$_n$-*co*-HPMAmLac$_n$-ETSA) copolymer
PTFE:	polytetrafluoroethylene
SDS:	sodium dodecyl sulfate
Sulfo.Cy5:	Sulfonated cyanine 5
TCEP:	tris(2-carboxyethyl)phosphine
TFA:	Trifluoroacetic acid
TMTHSI:	3,3,6,6-tetramethylthiacycloheptyne sulfoximine
UHPLC:	Ultra high pressure liquid chromatography

References

(1) Cabral, H.; Miyata, K.; Osada, K.; Kataoka, K. Block Copolymer Micelles in Nanomedicine Applications. *Chem. Rev.* **2018**, *118* (14), 6844–6892.

(2) Wan, Z.; Zheng, R.; Moharil, P.; Liu, Y.; Chen, J.; Sun, R.; Song, X.; Ao, Q. Polymeric Micelles in Cancer Immunotherapy. *Molecules* **2021**, *26* (5), 1220.

(3) Varela-Moreira, A.; Shi, Y.; Fens, M. H. A. M.; Lammers, T.; Hennink, W. E.; Schiffelers, R. M. Clinical Application of Polymeric Micelles for the Treatment of Cancer. *Mater. Chem. Front.* **2017**, *1* (8), 1485–1501.

(4) Hwang, D.; Ramsey, J. D.; Kabanov, A. V. Polymeric Micelles for the Delivery of Poorly Soluble Drugs: From Nanoformulation to Clinical Approval. *Adv. Drug Deliv. Rev.* **2020**, *156*, 80–118.

(5) Houdaihed, L.; Evans, J. C.; Allen, C. Overcoming the Road Blocks: Advancement of Block Copolymer Micelles for Cancer Therapy in the Clinic. *Mol. Pharm.* **2017**, *14* (8), 2503–2517.

(6) Maeda, H.; Wu, J.; Sawa, T.; Matsumura, Y.; Hori, K. Tumor Vascular Permeability and the EPR Effect in Macromolecular Therapeutics: A Review. *J. Control. Release* **2000**, *65* (1–2), 271–284.

(7) Fang, J.; Nakamura, H.; Maeda, H. The EPR Effect: Unique Features of Tumor Blood Vessels for Drug Delivery, Factors Involved, and Limitations and Augmentation of the Effect. *Adv. Drug Deliv. Rev.* **2011**, *63* (3), 136–151.

(8) Lammers, T.; Kiessling, F.; Hennink, W. E.; Storm, G. Drug Targeting to Tumors: Principles, Pitfalls and (Pre-) Clinical Progress. *J. Control. Release* **2012**, *161* (2), 175–187.

(9) Wang, J.; Byrne, J. D.; Napier, M. E.; Desimone, J. M. More Effective Nanomedicines through Particle Design. *Small* **2011**, *7* (14), 1919–1931.

(10) Soo Choi, H.; Liu, W.; Misra, P.; Tanaka, E.; Zimmer, J. P.; Itty Ipe, B.; Bawendi, M. G.; Frangioni, J. V. Renal Clearance of Quantum Dots. *Nat. Biotechnol.* **2007**, *25* (10), 1165–1170.

(11) Sun, C.; Lee, J. S. H.; Zhang, M. Magnetic Nanoparticles in MR Imaging and Drug Delivery. *Adv. Drug Deliv. Rev.* **2008**, *60* (11), 1252–1265.

(12) Wang, J.; Mao, W.; Lock, L. L.; Tang, J.; Sui, M.; Sun, W.; Cui, H.; Xu, D.; Shen, Y. The Role of Micelle Size in Tumor Accumulation, Penetration, and Treatment. *ACS Nano* **2015**, *9* (7), 7195–7206.

(13) Tang, L.; Yang, X.; Yin, Q.; Cai, K.; Wang, H.; Chaudhury, I.; Yao, C.; Zhou, Q.; Kwon, M.; Hartman, J. A.; Dobrucki, I. T.; Dobrucki, L. W.; Borst, L. B.; Lezmi, S.; Helferich, W. G.; Ferguson, A. L.; Fan, T. M.; Cheng, J. Investigating the Optimal Size of Anticancer Nanomedicine. *Proc. Natl. Acad. Sci.* **2014**, *111* (43), 15344–15349.

(14) Cabral, H.; Matsumoto, Y.; Mizuno, K.; Chen, Q.; Murakami, M.; Kimura, M.; Terada, Y.; Kano, M. R.; Miyazono, K.; Uesaka, M.; Nishiyama, N.; Kataoka, K. Accumulation of Sub-100 Nm Polymeric Micelles in Poorly Permeable Tumours Depends on Size. *Nat. Nanotechnol.* **2011**, *6* (12), 815–823.

(15) Bagheri, M.; Bresseleers, J.; Varela-Moreira, A.; Sandre, O.; Meeuwissen, S. A.; Schiffelers, R. M.; Metselaar, J. M.; Van Nostrum, C. F.; Van Hest, J. C. M.; Hennink, W. E. Effect of Formulation and Processing Parameters on the Size of MPEG- b-p(HPMA-Bz) Polymeric Micelles. *Langmuir* **2018**, *34* (50), 15495–15506.

(16) Hu, Q.; Rijcken, C. J. F.; van Gaal, E.; Brundel, P.; Kostkova, H.; Etrych, T.; Weber, B.; Barz, M.; Kiessling, F.; Prakash, J.; Storm, G.; Hennink, W. E.; Lammers, T. Tailoring the Physicochemical Properties of Core-Crosslinked Polymeric Micelles for Pharmaceutical Applications. *J. Control. Release* **2016**, *244*, 314–325.

(17) Alberg, I.; Kramer, S.; Schinnerer, M.; Hu, Q.; Seidl, C.; Leps, C.; Drude, N.; Möckel, D.; Rijcken, C.; Lammers, T.; Diken, M.; Maskos, M.; Morsbach, S.; Landfester, K.; Tenzer, S.; Barz, M.; Zentel, R. Polymeric Nanoparticles with Neglectable Protein Corona. *Small* **2020**, *16* (18), 1907574.

(18) Owens III, D.; Peppas, N. Opsonization, Biodistribution, and Pharmacokinetics of Polymeric Nanoparticles. *Int. J. Pharm.* **2006**, *307* (1), 93–102.

(19) Gref, R.; Minamitake, Y.; Peracchia, M. T.; Trubetskoy, V.; Torchilin, V.; Langer, R. Biodegradable Long-Circulating Polymeric Nanospheres. *Science (80-.).* **1994**, *263* (5153), 1600–1603.

(20) Mahmud, A.; Xiong, X.-B.; Aliabadi, H. M.; Lavasanifar, A. Polymeric Micelles for Drug Targeting. *J. Drug Target.* **2007**, *15* (9), 553–584.

(21) Read, E. S.; Armes, S. P. Recent Advances in Shell Cross-Linked Micelles. *Chem. Commun. (Camb).* **2007**, No. 29, 3021–3035.

(22) Talelli, M.; Barz, M.; Rijcken, C. J. F.; Kiessling, F.; Hennink, W. E.; Lammers, T. Core-Crosslinked Polymeric Micelles: Principles, Preparation, Biomedical Applications and Clinical Translation. *Nano Today* **2015**, *10* (1), 93–117.

(23) Rijcken, C. J.; Snel, C. J.; Schiffelers, R. M.; van Nostrum, C. F.; Hennink, W. E. Hydrolysable Core-Crosslinked Thermosensitive Polymeric Micelles: Synthesis, Characterisation and in Vivo Studies. *Biomaterials* **2007**, *28* (36), 5581–5593.

(24) Deng, C.; Jiang, Y.; Cheng, R.; Meng, F.; Zhong, Z. Biodegradable Polymeric Micelles for Targeted and Controlled Anticancer Drug Delivery: Promises, Progress and Prospects. *Nano Today* **2012**, *7* (5), 467–480.

(25) Kang, N.; Perron, M.-È.; Prud'homme, R. E.; Zhang, Y.; Gaucher, G.; Leroux, J.-C. Stereocomplex Block Copolymer Micelles: Core−Shell Nanostructures with Enhanced Stability. *Nano Lett.* **2005**, *5* (2), 315–319.

(26) Carstens, M. G.; Bevernage, J. J. L.; van Nostrum, C. F.; van Steenbergen, M. J.; Flesch, F. M.; Verrijk, R.; de Leede, L. G. J.; Crommelin, D. J. A.; Hennink, W. E. Small Oligomeric Micelles Based on End Group Modified MPEG−Oligocaprolactone with Monodisperse Hydrophobic Blocks. *Macromolecules* **2007**, *40* (1), 116–122.

(27) Shi, Y.; van Steenbergen, M. J.; Teunissen, E. A.; Novo, L.; Gradmann, S.; Baldus, M.; van Nostrum, C. F.; Hennink, W. E. Π–Π Stacking Increases the Stability and Loading Capacity of Thermosensitive Polymeric Micelles for Chemotherapeutic Drugs. *Biomacromolecules* **2013**, *14* (6), 1826–1837.

(28) Shi, Y.; Lammers, T.; Storm, G.; Hennink, W. E. Physico-Chemical Strategies to Enhance Stability and Drug Retention of Polymeric Micelles for Tumor-Targeted Drug Delivery. *Macromol. Biosci.* **2017**, *17* (1), 1600160.

(29) Fang, H.; Zhao, X.; Gu, X.; Sun, H.; Cheng, R.; Zhong, Z.; Deng, C. CD44-Targeted Multifunctional Nanomedicines Based on a Single-Component Hyaluronic Acid Conjugate with All-Natural Precursors: Construction and Treatment of Metastatic Breast Tumors in Vivo. *Biomacromolecules* **2020**, *21* (1), 104–113.

(30) Bae, Y.; Kataoka, K. Intelligent Polymeric Micelles from Functional Poly(Ethylene Glycol)-Poly(Amino Acid) Block Copolymers. *Adv. Drug Deliv. Rev.* **2009**, *61* (10), 768–784.

(31) Pipeline – Cristal Therapeutics https://cristaltherapeutics.com/programs/pipeline/ (accessed 2021 -02 -15).

(32) Miedema, I. H. C.; Zwezerijnen, G. J. C.; Oprea-Lager, D. E.; Verheul, H. M. W.; Vugts, D. J.; Huisman, M. C.; Mathijssen, R. H. J.; Rijcken, C. J. F.; Hu, Q.; Dongen, G. a. M. S. van; Menke, C. W. First-in-Human Imaging of Nanoparticle Entrapped Docetaxel (CPC634) in Patients with Advanced Solid Tumors Using 89 Zr-Df-CPC634 PET/CT. *J. Clin. Oncol.* **2019**, *37* (15_suppl), 3093–3093.

(33) Atrafi, F.; van Eerden, R. A. G.; van Hylckama Vlieg, M. A. .; Oomen-de Hoop, E.; de Bruijn, P.; Lolkema, M. P.; Moelker, A.; Rijcken, C. J.; Hanssen, R.; Sparreboom, A.; Eskens, F. A. L. M.; Mathijssen, R. H. J.; Koolen, S. L. W. Intratumoral Comparison of Nanoparticle Entrapped Docetaxel (CPC634) with Conventional Docetaxel in Patients with Solid Tumors. *Clin. Cancer Res.* **2020**, *26* (14), 3537–3545.

(34) Atrafi, F.; Dumez, H.; Mathijssen, R. H. J.; Menke van der Houven van Oordt, C. W.; Rijcken, C. J. F.; Hanssen, R.; Eskens, F. A. L. M.; Schöffski, P. A Phase I Dose-Escalation and Pharmacokinetic Study of a Micellar Nanoparticle with Entrapped Docetaxel (CPC634) in Patients with Advanced Solid Tumours. *J. Control. Release* **2020**, *325* (June), 191–197.

(35) Hu, Q.; Rijcken, C. J.; Bansal, R.; Hennink, W. E.; Storm, G.; Prakash, J. Complete Regression of Breast Tumour with a Single Dose of Docetaxel-Entrapped Core-Cross-Linked Polymeric Micelles. *Biomaterials* **2015**, *53*, 370–378.

(36) Stolnik, S.; Shakesheff, K. Formulations for Delivery of Therapeutic Proteins. *Biotechnol. Lett.* **2009**, *31* (1), 1–11.

(37) Shirangi, M.; Sastre Toraño, J.; Sellergren, B.; Hennink, W. E.; Somsen, G. W.; Van Nostrum, C. F. Methyleneation of Peptides by N, N, N, N -Tetramethylethylenediamine (TEMED) under Conditions Used for Free Radical Polymerization: A Mechanistic Study. *Bioconjug. Chem.* **2015**, *26* (1), 90–100.

(38) Cadée, J. A.; Van Steenbergen, M. J.; Versluis, C.; Heck, A. J. R.; Underberg, W. J. M.; Den Otter, W.; Jiskoot, W.; Hennink, W. E. Oxidation of Recombinant Human Interleukin-2 by Potassium Peroxodisulfate. *Pharm. Res.* **2001**, *18* (10), 1461–1467.

(39) Nakagawa, Y.; Hori, H.; Yamamoto, I.; Terada, H. Characteristic Bleaching Profiles of Cyanine Dyes Depending on Active Oxygen Species in the Controlled Fenton Reaction. *Biol. Pharm. Bull.* **1993**, *16* (11), 1061–1064.

(40) Agouridas, V.; El Mahdi, O.; Diemer, V.; Cargoët, M.; Monbaliu, J.-C. M.; Melnyk, O. Native Chemical Ligation and Extended Methods: Mechanisms, Catalysis, Scope, and Limitations. *Chem. Rev.* **2019**, *119* (12), 7328–7443.

(41) Dawson, P. E.; Muir, T. W.; Clark-Lewis, I.; Kent, S. B. Synthesis of Proteins by Native Chemical Ligation. *Science (80-.).* **1994**, *266* (5186), 776 LP – 779.

(42) Najafi, M.; Kordalivand, N.; Moradi, M. A.; Van Den Dikkenberg, J.; Fokkink, R.; Friedrich, H.; Sommerdijk, N. A. J. M.; Hembury, M.; Vermonden, T. Native Chemical Ligation for Cross-Linking of Flower-Like Micelles. *Biomacromolecules* **2018**, *19* (9), 3766–3775.

(43) Pal, S.; Mandal, A.; Hong, L.; Ortuso, R. D.; Petri-Fink, A.; Salentinig, S.; Kilbinger, A. F. M. Native Chemical Ligation: Ultrafast Synthesis of Block Copolymers. *Macromolecules* **2022**, *55* (7), 2854–2860.

(44) Weterings, J.; Rijcken, C. J. F.; Veldhuis, H.; Meulemans, T.; Hadavi, D.; Timmers, M.; Honing, M.; Ippel, H.; Liskamp, R. M. J. TMTHSI, a Superior 7-Membered Ring Alkyne Containing Reagent for Strain-Promoted Azide-Alkyne Cycloaddition Reactions. *Chem. Sci.* **2020**, *11* (33), 9011–9016.

(45) Hu, B.-H.; Su, J.; Messersmith, P. B. Hydrogels Cross-Linked by Native Chemical Ligation. *Biomacromolecules* **2009**, *10* (8), 2194–2200.

(46) Werkhoven, P. R.; van de Langemheen, H.; van der Wal, S.; Kruijtzer, J. A. W.; Liskamp, R. M. J. Versatile Convergent Synthesis of a Three Peptide Loop Containing Protein Mimic of Whooping Cough Pertactin by Successive Cu(I)-Catalyzed Azide Alkyne Cycloaddition on an Orthogonal Alkyne Functionalized TAC-Scaffold. *J. Pept. Sci.* **2014**, *20* (4), 235–239.

(47) Gabriel, S. Ueber Eine Darstellungsweise Primärer Amine Aus Den Entsprechenden Halogenverbindungen. *Berichte der Dtsch. Chem. Gesellschaft* **1887**, *20* (2), 2224–2236.

(48) Van Stam, J.; Creutz, S.; De Schryver, F. C.; Jérôme, R. Tuning of the Exchange Dynamics of Unimers between Block Copolymer Micelles with Temperature, Cosolvents, and Cosurfactants. *Macromolecules* **2000**, *33* (17), 6388–6395.

(49) Neradovic, D.; van Steenbergen, M. J.; Vansteelant, L.; Meijer, Y. J.; van Nostrum, C. F.; Hennink, W. E. Degradation Mechanism and Kinetics of Thermosensitive Polyacrylamides Containing Lactic Acid Side Chains. *Macromolecules* **2003**, *36* (20), 7491–7498.

(50) de Jong, S. .; Arias, E. .; Rijkers, D. T. .; van Nostrum, C. .; Kettenes-van den Bosch, J. .; Hennink, W. . New Insights into the Hydrolytic Degradation of Poly(Lactic Acid): Participation of the Alcohol Terminus. *Polymer (Guildf).* **2001**, *42* (7), 2795–2802.

(51) Tian, H.; Sakmar, T. P.; Huber, T. A Simple Method for Enhancing the Bioorthogonality of Cyclooctyne Reagent. *Chem. Commun.* **2016**, *52* (31), 5451–5454.

(52) van Geel, R.; Pruijn, G. J. M.; van Delft, F. L.; Boelens, W. C. Preventing Thiol-Yne Addition Improves the Specificity of Strain-Promoted Azide–Alkyne Cycloaddition. *Bioconjug. Chem.* **2012**, *23* (3), 392–398.

(53) Behzadi, S.; Serpooshan, V.; Tao, W.; Hamaly, M. A.; Alkawareek, M. Y.; Dreaden, E. C.; Brown, D.; Alkilany, A. M.; Farokhzad, O. C.; Mahmoudi, M. Cellular Uptake of Nanoparticles: Journey inside the Cell. *Chem. Soc. Rev.* **2017**, *46* (14), 4218–4244.

Supporting information (SI)

NMR spectra

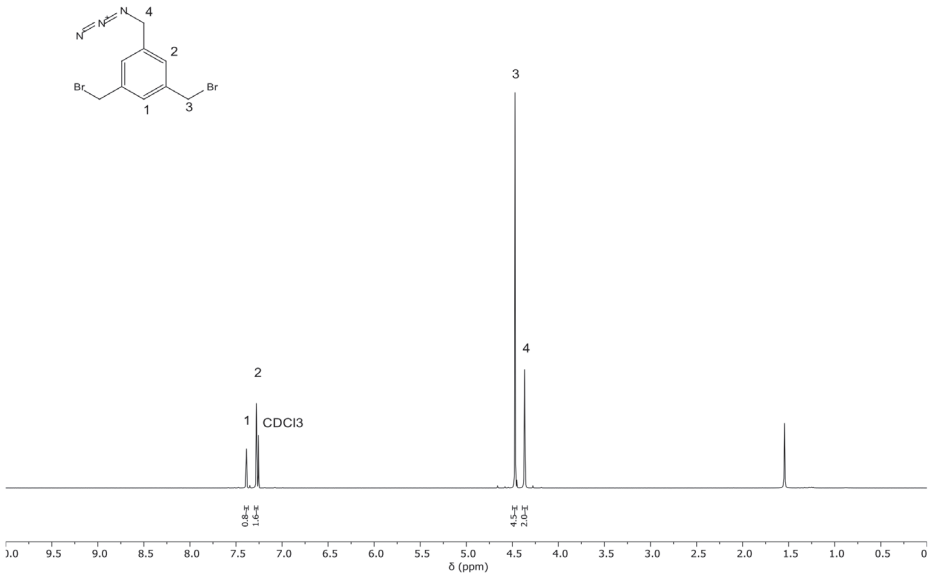

*Figure S1.1: [1]H NMR spectrum of compound **1** (1-(azidomethyl)-3,5-bis(bromomethyl)benzene). The solvent was $CDCl_3$.*

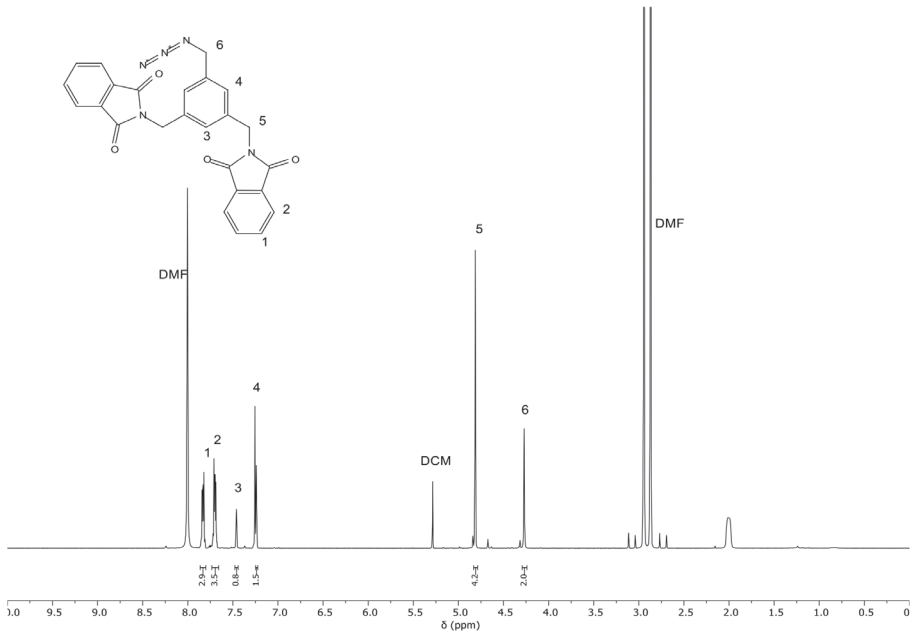

*Figure S1.2: [1]H NMR spectrum of compound **2** (1-(azidomethyl)-3,5-bis(phthalamidomethyl) benzene). The solvent was $CDCl_3$.*

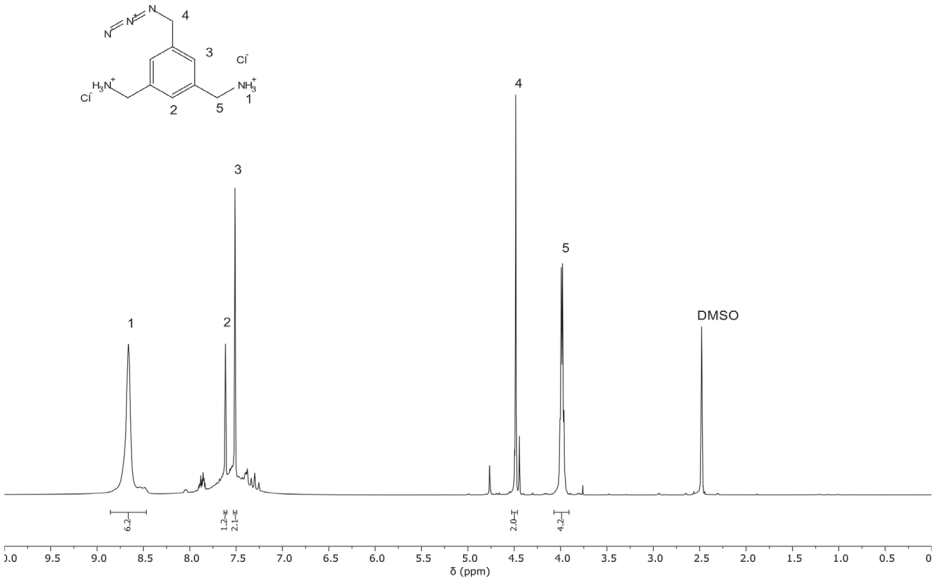

*Figure S1.3: [1]H NMR spectrum of compound **3** (1-(azidomethyl)-3,5-bis(aminomethyl)benzene). The solvent was deuterated DMSO.*

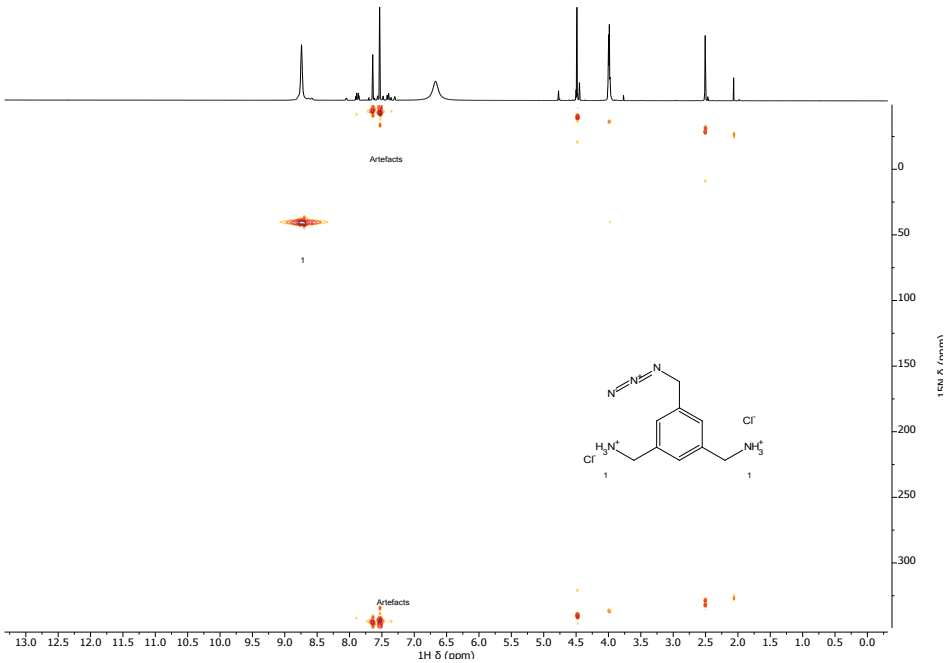

*Figure S1.4: [15]N HSQC NMR spectrum of compound **3**. The solvent was deuterated DMSO.*

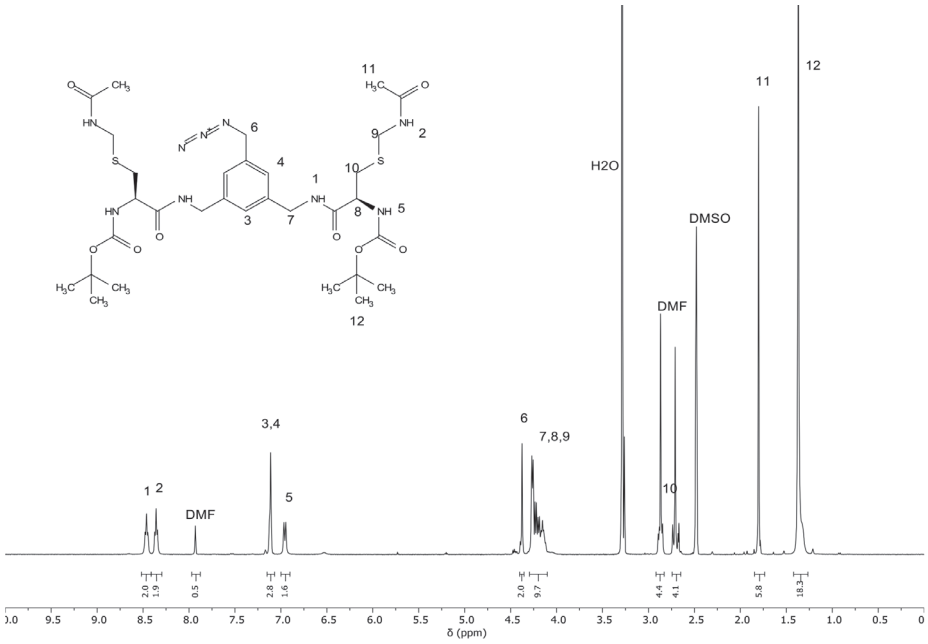

*Figure S1.5: [1]H NMR spectrum of compound **4**. The solvent was deuterated DMSO.*

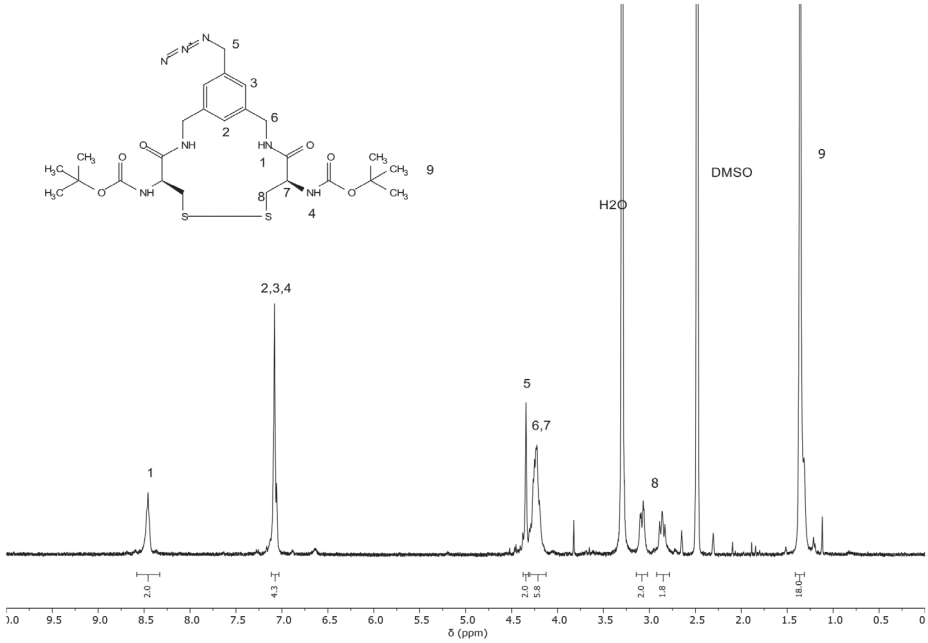

*Figure S1.6: [1]H NMR spectrum of Acm deprotected compound **4**. The solvent was deuterated DMSO.*

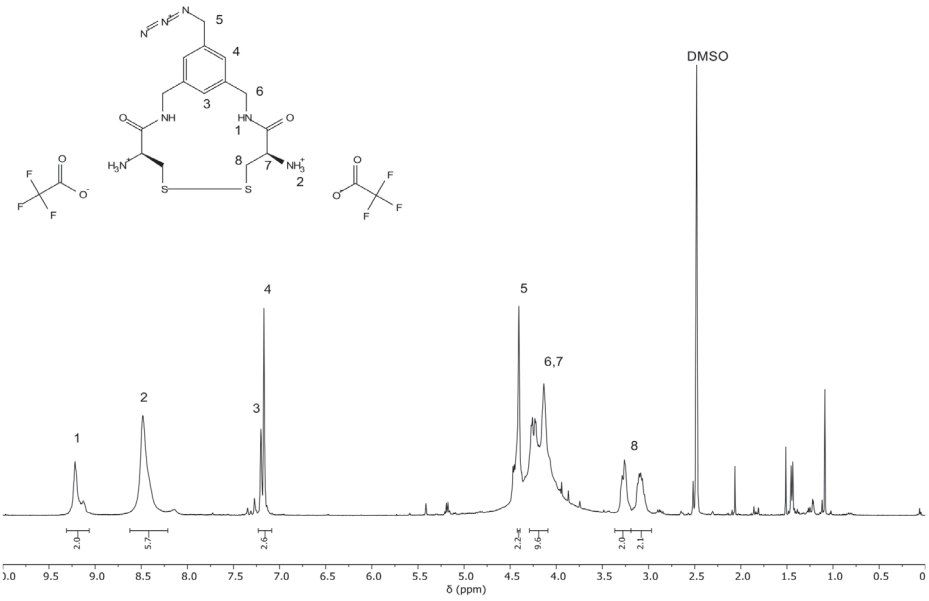

*Figure S1.7: [1]H NMR spectrum of compound **5**. The solvent was deuterated DMSO.*

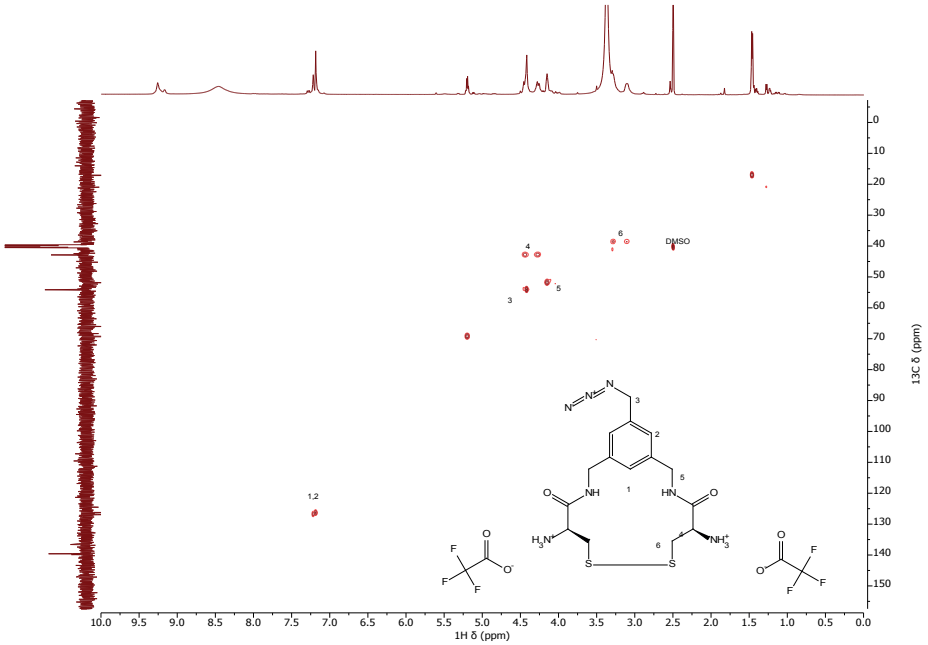

*Figure S1.8: HSQC NMR spectrum of compound **5**. The solvent was deuterated DMSO with a molecular sieve after rotary evaporation with toluene.*

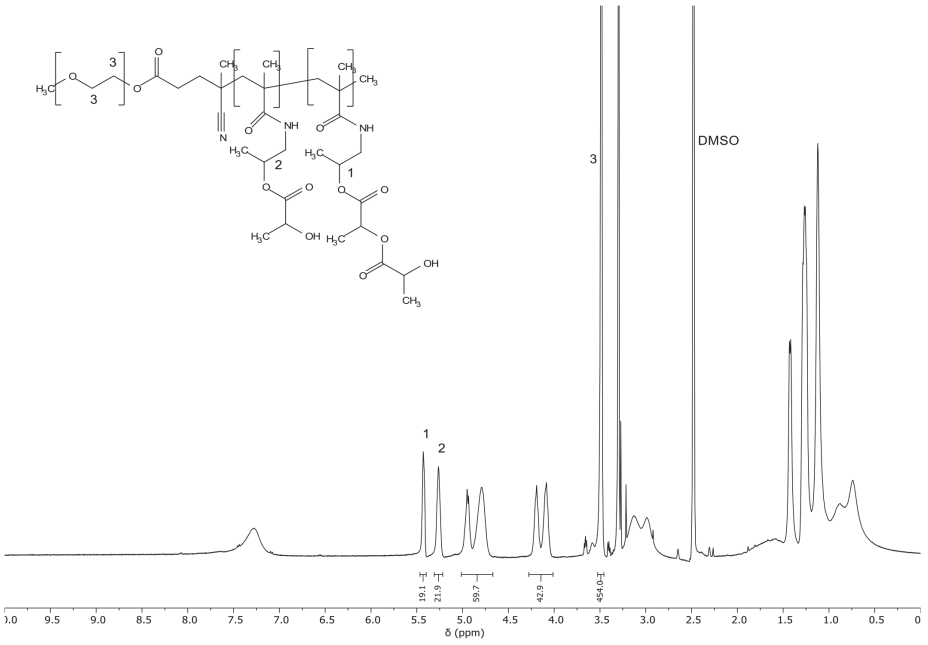

*Figure S1.9: [1]H NMR spectrum of polymer **P100** (PEG_{5000}-b-P(HPMAmLac$_1$-co-HPMAmLac$_2$)). The solvent was deuterated DMSO.*

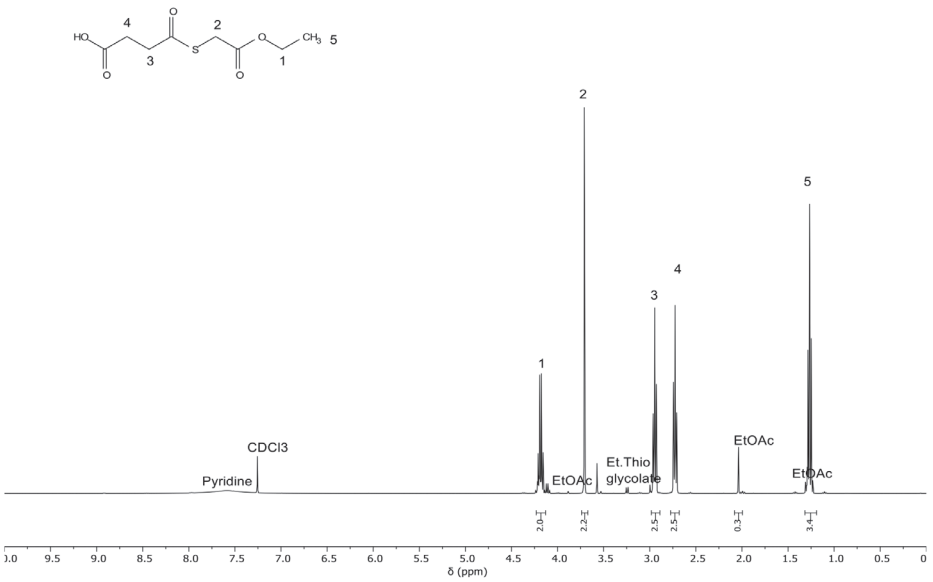

Figure S1.10: [1]H NMR spectrum of Ethyl Thioglycolate-Succinic Acid (ETSA). The solvent was $CDCl_3$.

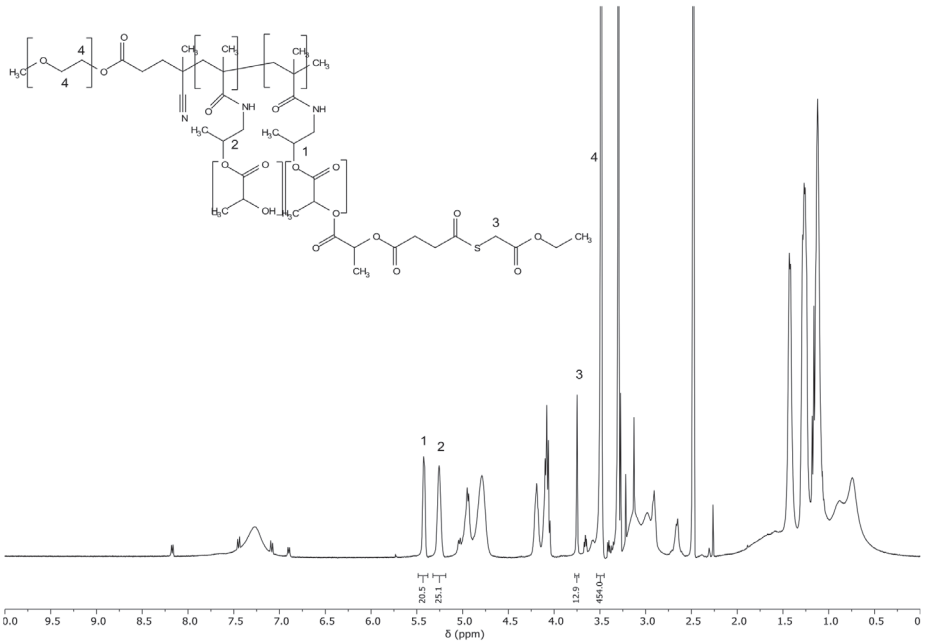

*Figure S1.11: [1]H NMR spectrum of polymer **P100-E15** (PEG_{5000}-b-P(HPMAmLac$_n$-co-HPMAmLac$_n$-ETSA)). The solvent was deuterated DMSO. Expected integral for coupled ETSA based on feed of **P100-E15** was 12.0, measured 12.9*

Mass spectra

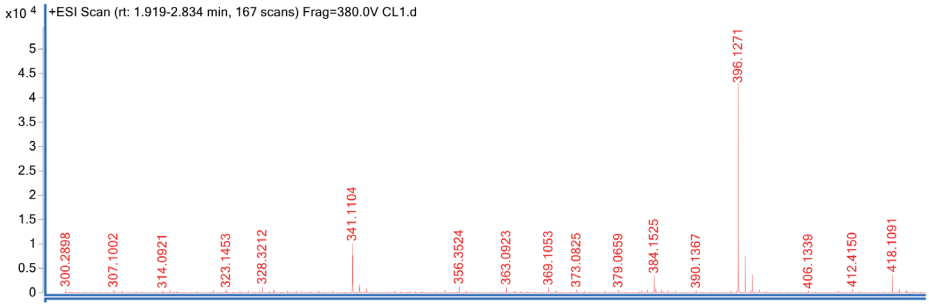

Figure S2.1: HR-MS spectrum of the trifunctional crosslinker, compound 5. Expected mass for $C_{15}H_{22}N_7O_2S_2^+$ is 396.1271, measured 396.1271.

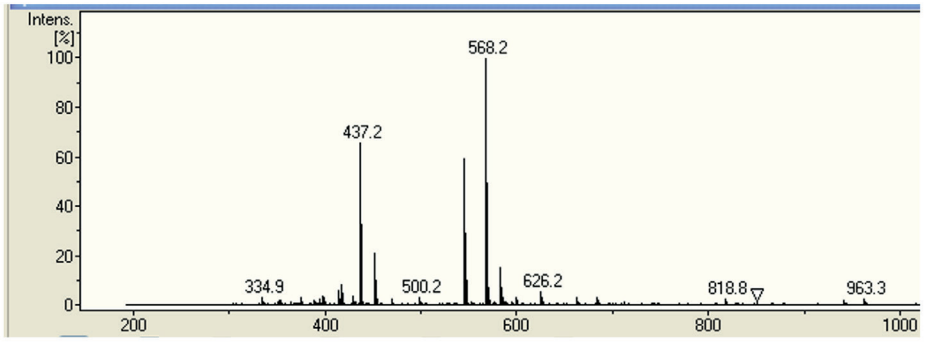

Figure S2.2: ESI-MS spectrum of the trifunctional crosslinker, compound 5 coupled with BCN-OH. Expected mass for $C_{25}H_{35}N_7O_3S_2^+$ is 546.2 and $C_{25}H_{35}N_7O_3S_2Na^+$ is 568.2, measured 568.2.

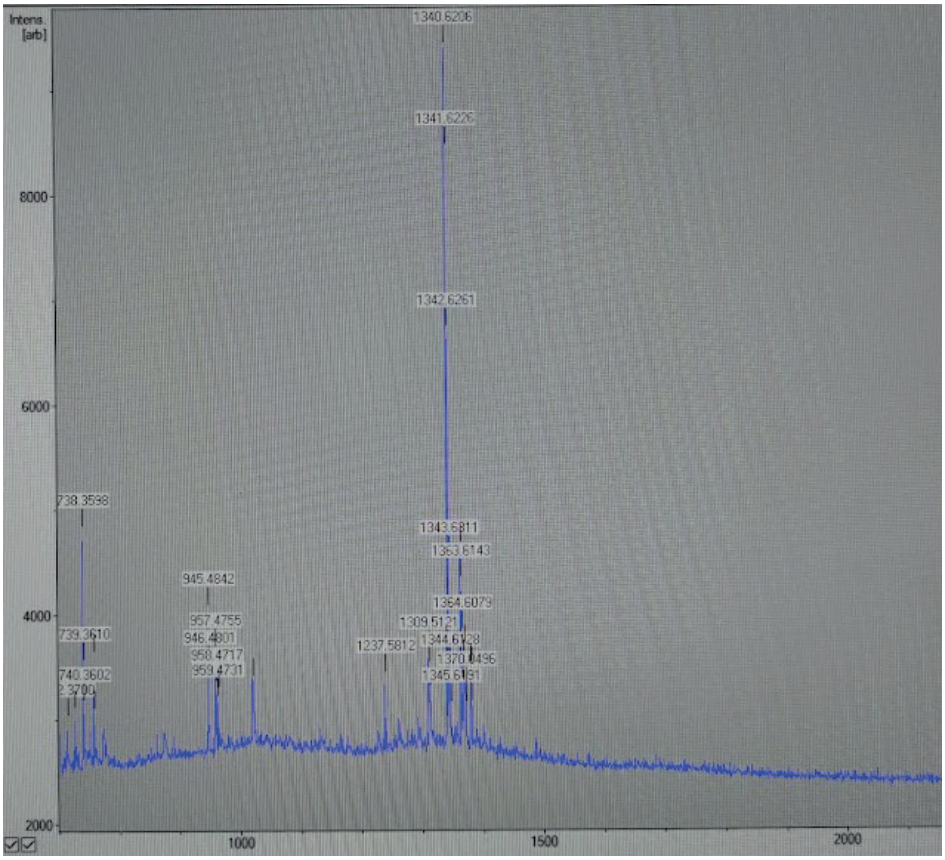

Figure S2.3: MALDI-MS spectrum of the trifunctional crosslinker, compound 5 coupled with Sulfo. Cy5-DBCO after TCEP reduction. Expected mass for $C_{68}H_{82}N_{11}O_{10}S_4^+$ is 1340.5, measured 1340.6.

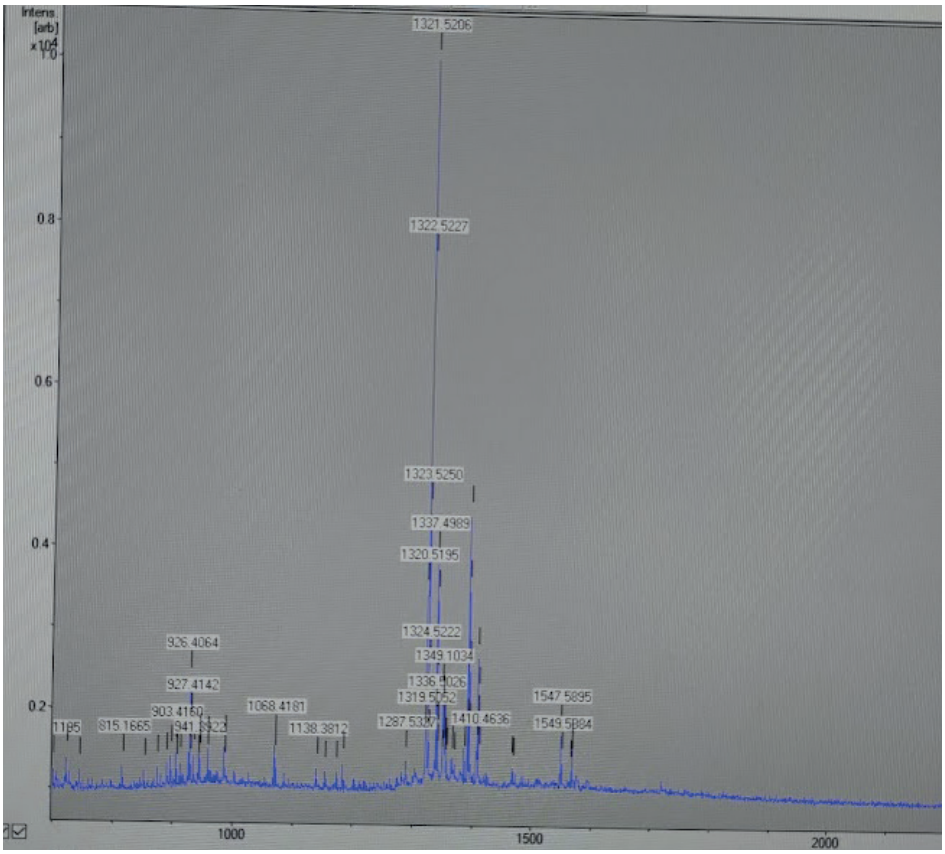

Figure S2.4: MALDI-MS spectrum of the trifunctional crosslinker, compound 5 coupled with BODIPY-TMTHSI after TCEP reduction. Expected mass for $C_{61}H_{82}N_{14}O_9S_3BF_2^+$ is 1299.6 and $C_{61}H_{81}N_{14}O_9S_3BF_2Na^+$ is 1321.5, measured 1321.5.

HPLC chromatograms

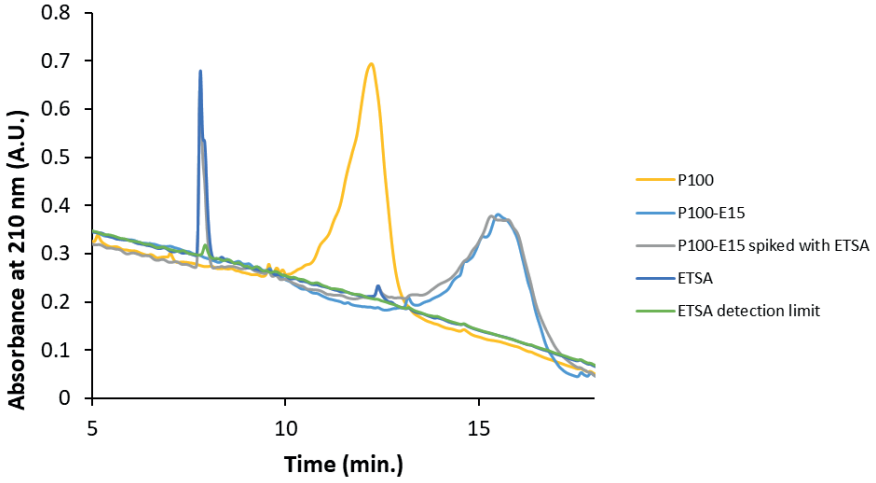

Figure S3.1: HPLC chromatograms of lead $mPEG_{5000}$-b-P(HPMAmLac$_1$-co-HPMAmLac$_2$) polymer before (yellow) and after (light blue) ETSA (blue) functionalization, including a spiked sample (grey) and 60 µg/mL ETSA (green) injection marking the detection limit. Injected at 10 mg/mL polymer concentration and 1 mg/mL ETSA concentration.

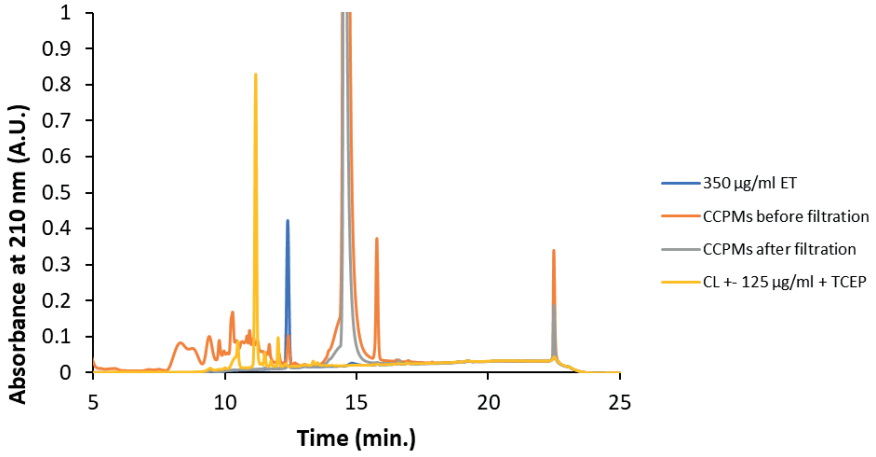

Figure S3.2: HPLC chromatograms of CCPMs before (orange) and after (grey) purification as well as ethyl thioglycolate (blue) and crosslinker treated with TCEP (yellow) references.

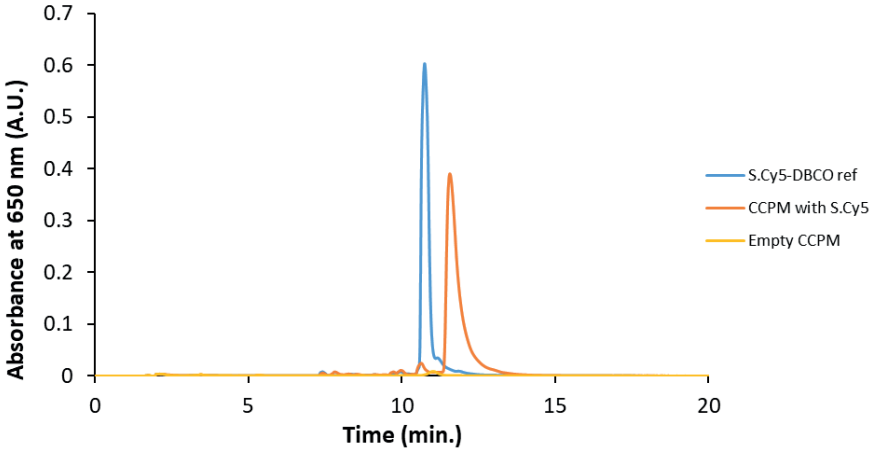

Figure S3.3: HPLC chromatograms of empty CCPMs (yellow), Sulfo-Cy5 loaded CCPMs (orange) and free Sulfo-Cy5-DBCO (blue). Samples taken before size exclusion purification of micelles.

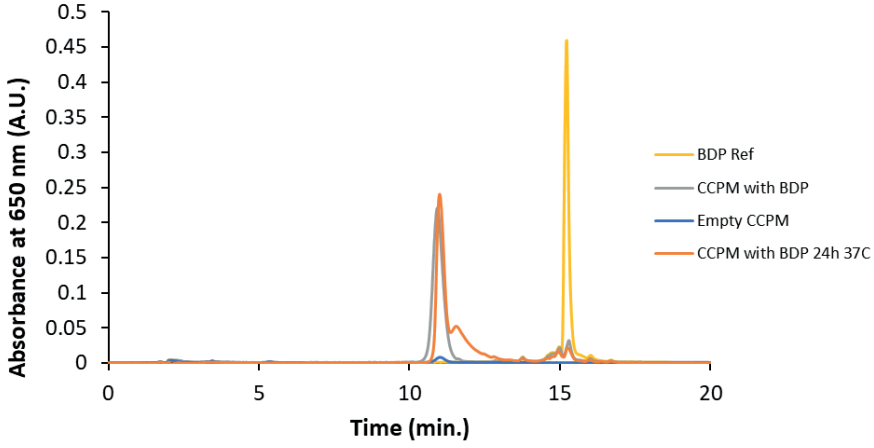

Figure S3.4: HPLC chromatograms of empty CCPMs (blue), BODIPY loaded CCPMs (grey) and free BODIPY-TMTHSI (yellow). Samples taken before size exclusion purification of micelles. After purification, the BODIPY loaded CCPMs were incubated at 37°C (orange) to confirm no undesired dye release occurred.

UHPLC chromatograms

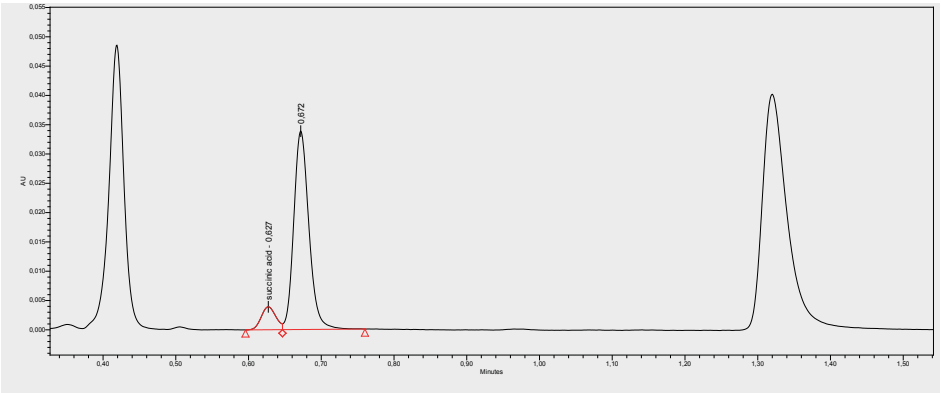

Figure S4.1: UHPLC traces of mPEG$_{5000}$-b-P(HPMAmLac$_n$-co-HPMAmLac$_n$-ETSA) polymer P100-E15 after NaOH hydrolysis for the quantification of succinic acid to determine ETSA content.

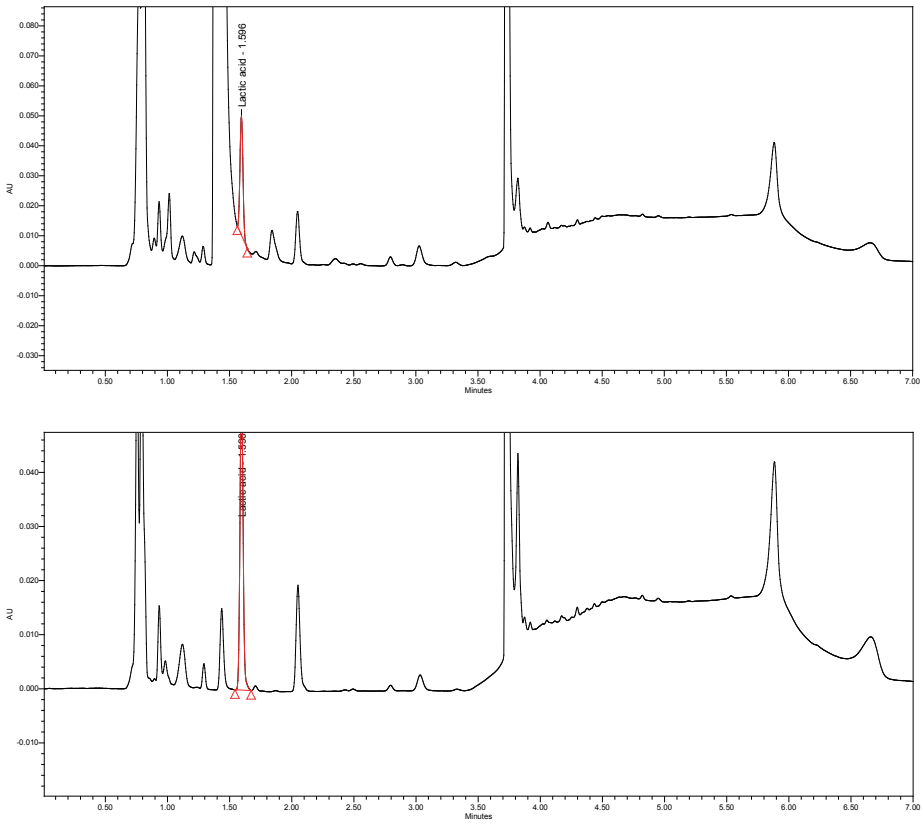

Figure S4.2: UHPLC traces before (top) and after (bottom) purification of CCPMs formed from mPEG$_{5000}$-b-P(HPMAmLac$_n$-co-HPMAmLac$_n$-ETSA) polymer P100-E15. The CCPMs were hydrolyzed in NaOH for the quantification of lactic acid to determine the total polymer content. The purified CCPM sample was found to have a polymer concentration of 7.5 mg/mL which is very close to the expected value of 7.0 mg/mL, based on dilution. (indicating no significant losses during purification). The crude sample resulted in an underestimate of 15.4 mg/mL out of the expected 18.5 mg/mL which is attributed to the interference of a neighboring peak (DMSO) with the lactic acid peak in the chromatogram.

Size exclusion chromatograms

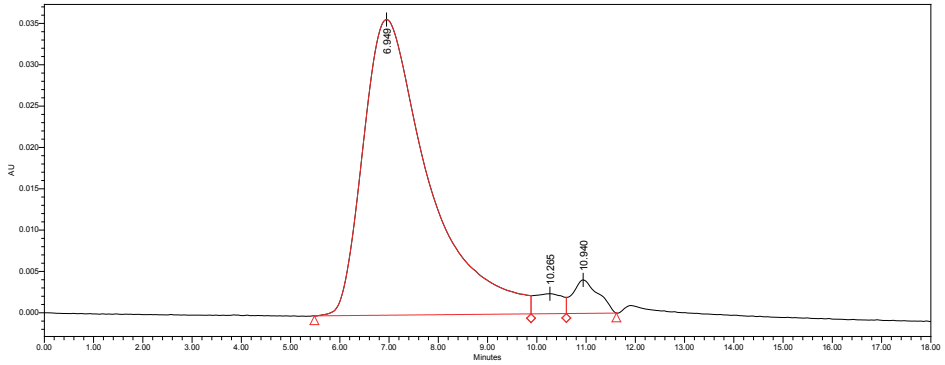

Figure S5.1: Size exclusion chromatogram of empty CCPMs. Detection at 235 nm.

Illustrative figures

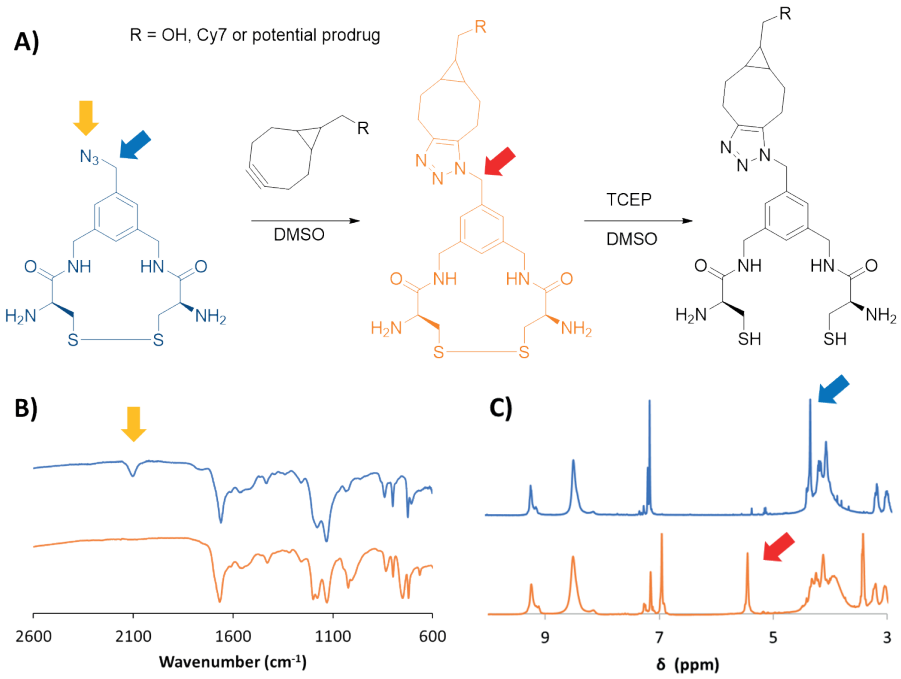

Figure S6.1: A) Schematic representation of the reaction between the crosslinker azide and a BCN functionality. Azide and a BCN functionality followed by TCEP induced disulfide reduction. B) IR spectra of the crosslinker before (blue) and after (orange) the click reaction with BCN-OH. C) NMR spectra of the crosslinker before (blue) and after (orange) the click reaction with BCN-OH. The results shown indicate that the crosslinker-BCN reaction results in the anticipated triazole ring formation.

Flow cytometry

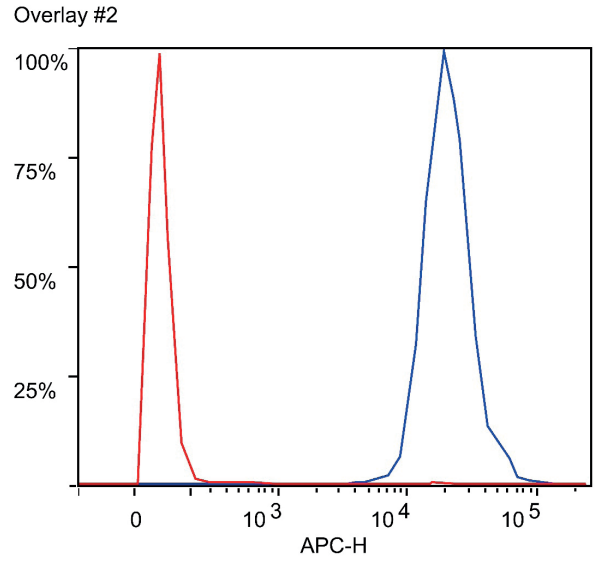

Color	Population	Event	% Total
	PC3 [BDPlabelled_CriPec_24h_BDP1_001.fcs]	5017	50,17
	PC3 [Untreated_24h_Tube_001_012.fcs]	6874	68,74

Figure S7.1: Cell associated fluorescence of PC3 cells incubated for 24 hours with BODIPY loaded CCPMs.

CHAPTER 5

Mechanistic study on the degradation of hydrolysable core-crosslinked polymeric micelles

Erik R. Hebels[1], Mies J. van Steenbergen[1], Ragna Haegebaert[3], Cornelis W. Seinen[4], Barbara S. Mesquita[1], Antoinette van den Dikkenberg[1], Katrien Remaut[3], Cristianne J. F. Rijcken[2], Bas G.P. van Ravensteijn[1], Wim E. Hennink[1] and Tina Vermonden[1*]*

[1] Department of Pharmaceutics, Utrecht Institute for Pharmaceutical Sciences (UIPS), Utrecht University, 3508 TB Utrecht, the Netherlands.
[2] Cristal Therapeutics, 6229 EV Maastricht, the Netherlands
[3] Laboratory for General Biochemistry and Physical Pharmacy, Ghent University, Ottergemsesteenweg 460, 9000 Gent, Belgium
[4] Division Laboratories, Pharmacy and Biomedical Genetics, Central Diagnostic Lab, University Medical Center Utrecht, Heidelberglaan 100, 3584 CX Utrecht, the Netherlands

Langmuir 2023, 39, 34, 12132–12143

Abstract

Core-crosslinked polymeric micelles (CCPMs) are an attractive class of nanocarriers for drug delivery. Two crosslinking approaches to form CCPMs exist: either via a low molecular weight crosslinking agent to connect homogeneous polymer chains with reactive handles, or via cross-reactive handles on polymers to link them to each other (complementary polymers). Previously, CCPMs based on methoxy poly(ethylene glycol)-*b*-poly[*N*-(2-hydroxypropyl) methacrylamide-lactate] (mPEG-*b*-PHPMAmLac$_n$) modified with thioesters were crosslinked via native chemical ligation (NCL, a reaction between a cysteine residue and thioester resulting in an amide bond) using a bifunctional cysteine containing crosslinker. These CCPMs are degradable under physiological conditions due to hydrolysis of the ester groups present in the crosslinks. The rapid onset of degradation observed previously, as measured by light scattering intensity, questions the effectiveness of crosslinking via a bifunctional agent. Particularly due to the possibility of intrachain crosslinks that can occur using such a small crosslinker, we investigated the degradation mechanism of CCPMs generated via both approaches using various analytical techniques. CCPMs based on complementary polymers degraded slower at pH 7.4 and 37 °C than CCPMs with a crosslinker (half-life of light scattering intensity was approximately 170 versus 80 h, respectively). Through comparative analysis of the degradation profiles of the two different CCPMs, we conclude that partially ineffective intrachain crosslinks are likely formed using the small crosslinker, which contributed to more rapid CCPM degradation. Overall, this study shows that the type of crosslinking approach can significantly affect degradation kinetics and this should be taken into consideration when developing new degradable CCPM platforms.

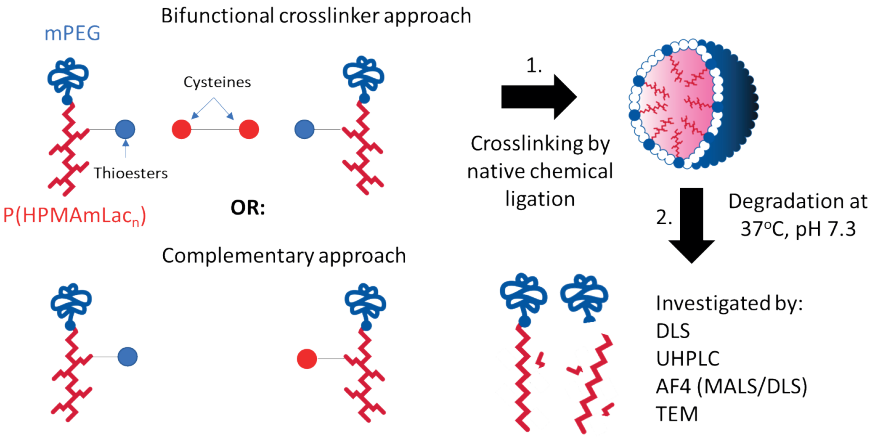

Introduction

Polymeric micelles (PMs) are sub-100 nm sized colloidal particles composed of amphiphilic block copolymers, with a hydrophobic block that constitutes the PM core and a hydrophilic block forming the shell in aqueous environments at polymer concentrations above the critical micellization concentration (CMC). PMs are a promising class of nanocarriers for the formulation and delivery of therapeutics in the body. [1–3] Crosslinking of the PM core by covalent bonds to form core-crosslinked polymeric micelles (CCPMs) greatly enhances the stability of PMs in circulation by halting the equilibrium between unimers and the PM state that can lead to rapid and unwanted destabilization upon administration.[4–6]

Crosslinking of PMs has been carried out using diverse chemistries including, among others, radical polymerization [7–10], copper-catalyzed click chemistry [11,12], *N*-acryloxysuccinimide with amine coupling [13], bis-benzophenone mediated photo-crosslinking [14], Diels-Alder reaction [15], disulfide exchange [16,17] and thiol oxidation [18], and native chemical ligation (NCL).[19] Generally speaking, these crosslinking strategies can be divided into two principle approaches: 1) by using a bifunctional crosslinking agent to connect polymer chains with reactive handles and 2) using cross-reactive handles (referred to in this paper as complementary) present on the different polymer chains to link with one another. [20] Additionally, polymers and/or crosslinks constituting the CCPMs have most commonly been designed to degrade under physiological conditions by pH dependent hydrolysis [8,9,21,22], reduction sensitive cleavage [23–26] as well as combinations of these [12,17,27–29] and to a lesser extent photo sensitive cleavage.[30] Although these degradation strategies are mostly designed to facilitate triggered cargo release at the target site, the ability of CCPMs to degrade under physiologically relevant conditions is important for the clearance of the nanocarrier following administration *in vivo*.

To facilitate degradation, polymers based on degradable *N*-2-hydroxypropyl methacrylamide lactate (HPMAmLac$_n$) monomers have been developed previously. Ester bonds present in the side chains of PHPMAmLac$_n$ can be hydrolyzed under physiological conditions (pH 7.4 and 37 ^{o}C) which results in hydrophilic HPMA-rich polymer chains and lactic acid that are expected to be cleared from circulation (if PHPMA sizes are less than 100 kDa [31]) and metabolized, respectively. [32–34] Additionally, polymers based on HPMAmLac$_n$ are thermosensitive,[32] allowing for convenient temperature induced micellization for PEG containing block copolymers.[33] By functionalization of the polymer side chains with reactive handles, crosslinking of the micellar core after temperature induced micellization can be achieved as was done via free radical

reactions of methacrylated methoxy poly(ethylene glycol)-*b*-poly[*N*-(2-hydroxypropyl) methacrylamide-lactate] (mPEG-*b*-PHPMAmLac$_n$) block copolymers, also known as CriPec® (which has been evaluated as drug carrier in (pre) clinical studies). [10,35]

Recently, we reported the use of NCL (a reaction between a cysteine and a thioester forming an amide bond) as an orthogonal crosslinking reaction in mPEG-*b*-PHPMAmLac$_n$ block copolymers for the formation of CCPM using a bifunctional crosslinking agent. [36] The advantage of this NCL crosslinking strategy is that no free radical reactions are needed that can potentially damage sensitive cargo. Briefly, by increasing the temperature of an aqueous solution of thermosensitive mPEG-*b*-PHPMAmLac$_n$ block copolymers modified with thioesters, micelles were formed, which were subsequently stabilized by a crosslinker with two cysteine handles allowing amide bond formation via NCL. Degradation of these CCPMs under physiological conditions occurs through ester hydrolysis of the HPMAmLac$_n$ side chains present in the crosslinks, analogous to the CriPec® system. Although stable CCPMs (resistant to destabilization by surfactants) with tunable sizes were achieved by this approach, a rapid onset of degradation under physiological conditions, as measured by decreasing light scattering intensity, was observed. This rapid onset of degradation was unexpected as it suggests that the CCPMs start to disintegrate immediately upon exposure to these conditions, without a lag time which would be expected from hydrolysis of the excessive number of crosslinks (~6 connection points per polymer chain were present [36]) before destabilization of the CCPMs. A possible explanation is that the use of a bifunctional crosslinking agent to prepare CCPMs can lead to intramolecular and thus ineffective crosslinks (see scheme 1A).

In the present study, the degradation of CCPMs formed via NCL with a bifunctional crosslinker was investigated in depth. The degradation of these CCPMs was compared with CCPMs formed from complementary polymers by interchain crosslinking, where intrachain crosslinking cannot occur (scheme 1B). Several analytical techniques were employed to gain insights into the degradation mechanism of both types of micelles, including dynamic light scattering (DLS), ultra-high performance liquid chromatography (UHPLC), asymmetric flow field flow fractionation (AF4), multi-angle light scattering (MALS) and transmission electron microscopy (TEM) imaging.

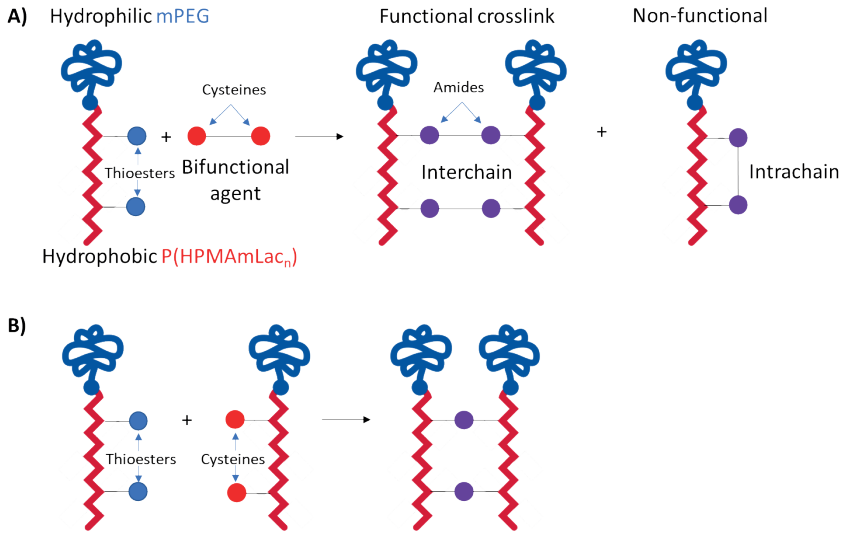

Scheme 1: Representation of possible linkage outcomes using A) a bifunctional crosslinking agent approach or B) a complementary polymer approach.

Experimental section

Materials

All materials were obtained from Sigma Aldrich (Zwijndrecht, the Netherlands) unless indicated otherwise. Ethylthioglycolate-succinic acid (ETSA) was synthesized according to a previously published procedure. [37] The 2-(methoxy polyethylene glycol)-4,4-azobis(4-cyanopentanoic acid) (mPEG$_{5000}$)$_2$-ABCPA) free radical macroinitiator was synthesized according to a previously published procedure.[38] *N*-2-hydroxypropyl methacrylamide monolactate (HPMAmLac$_1$) and dilactate (HPMAmLac$_2$) were provided by Cristal Therapeutics (the syntheses have been described previously). [39] All solvents were obtained from Biosolve (Valkenswaard, the Netherlands).

Synthesis

Bifunctional crosslinker synthesis (compound 2)

A crosslinker with two cysteine residues was synthesized, similar to a previously published procedure. [40] Boc-Cys(Trt)-OH (1.46 g, 3.15 mmol) and 1-[bis(dimethylamino) methylene]-1H-1,2,3-triazolo[4,5-b]pyridinium 3-oxid hexafluorophosphate (HATU) (1.14 g, 3.00 mmol) were dissolved in 10 mL dry dichloromethane (DCM), followed by addition of *N*,*N*-diisopropylethylamine (DIPEA) (1.57 mL, 8.99 mmol) and finally

ethylene diamine (0.10 mL, 1.50 mmol). After overnight stirring at RT, the reaction mixture was diluted with 30 mL DCM, washed 3 times with 30 mL saturated aqueous $NaHCO_3$ solution, dried over sodium sulfate and concentrated. Purification was done via silica chromatography using ethyl acetate : hexane 7:3 as eluent (R_f = 0.5), which after concentrating yielded 0.99 g (70%) of N-N' bis[N-tert-butyloxycarbonyl-S-triphenylmethyl-cysteinyl] ethylendiamine (scheme 2, compound **1**), an off-white gooey semi solid (See figure S1.1 for NMR). ^{1}H NMR (400 MHz, DMSO): δ 7.85 (s, 2H), 7.37 – 7.20 (m, 30H), 6.84 (d, J = 8.5 Hz, 2H), 3.89 (q, J = 7.5 Hz, 2H), 3.06 – 2.95 (m, 4H), 2.33 (qd, J = 11.9, 6.9 Hz, 4H), 1.37 (s, 18H).

Deprotection: To remove the tert-butyloxycarbonyl (Boc) and trityl (Trt) protecting groups, compound **1** (0.30 g, 0.32 mmol)) was added to 10 mL of DCM : trifluoroacetic acid (TFA) : triisopropyl silane (TIS) solution (50:47:3 %volume) and the mixture was subsequently stirred for 15 min after which the formed N-N' bis-cysteinyl- ethylendiamine (scheme 2, compound **2**) was precipitated in diethyl ether. After rinsing and centrifuging with additional diethyl ether, the precipitate was dried under N_2 flow. The obtained white solid was then dissolved in 5 mL milliQ water and purified by preparative reverse phase high performance liquid chromatography (Prep-RP-HPLC) on a Waters 2535 quaternary gradient module with Waters 2489 UV/Visible detector (detection at 210 and 280 nm) and ReproSil-Pur 120 C18-AQ (10 µm, 25 mm x 250 mm, Dr. Maisch) column. Acetonitrile (ACN)/water supplemented with 0.1% formic acid was used as eluent at a flow of 25 mL/min and a gradient of 5 to 100% ACN over 60 min. After freeze drying, the pure fractions yielded 73 mg (64%) of fluffy white solid (See figure S1.2 for NMR). ^{1}H NMR (400 MHz, DMSO): δ 8.60 – 8.51 (m, 2H), 3.90 (t, J = 5.6 Hz, 2H), 3.22 – 3.14 (m, 2H), 2.92 (dd, J = 5.6, 1.8 Hz, 4H). As no formate counterion protons were detected, ^{19}F NMR was conducted to quantify the amount of trifluoroacetate counterions remaining using trifluoroethanol as internal standard, described in the NMR section below.

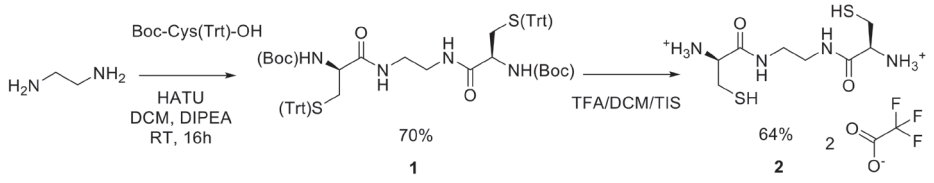

*Scheme 2: Synthesis of the N-N' bis-cysteinyl-ethylendiamine crosslinker (compound **2**).*

Thermosensitive block copolymer synthesis and its derivatization with thioester or cysteine groups

A block copolymer poly(ethylene glycol)-*b*-poly(N-(2-hydroxypropyl) methacrylamide-lactate) ($mPEG_{5000}$-*b*-P($HPMAmLac_n$-*co*-$HPMAmLac_n$, further abbreviated as **P100**) was synthesized by free radical polymerization following a previously published procedure (scheme 3). [10,36] In short, $(mPEG_{5000})_2$-ABCPA macroinitiator (400 mg) was weighed into a Schlenk tube followed by HPMAm-monolactate ($HPMAmLac_1$, 457 mg) and HPMAm-dilactate ($HPMAmLac_2$, 544 mg, 1.97 mL from a 276 mg/mL stock solution in ACN), resulting in a monomer/initiator molar ratio of 100/1 and a $HPMAmLac_1$: $HPMAmLac_2$ molar feed ratio of 53:47. Additional ACN (2.7 mL) was added to dilute the mixture to a final monomer with initiator concentration of 300 mg/mL. The tube was sealed by a rubber septum and 5 freeze-pump-thaw cycles were applied, backflushed with nitrogen and placed into an oil bath of 70 °C for 24 h. Next, the reaction mixture was cooled down to RT, and the obtained polymer was precipitated 3 times in diethyl ether and dried under nitrogen. The polymer was then dissolved in 1:1 ACN/water and freeze dried. The obtained block copolymer **P100**, yielding 1.06 g (76%), was analyzed by NMR and GPC (figures S1.3 and S2.1).

Thioester derivatization: **P100** was functionalized with ETSA to obtain $mPEG_{5000}$-*b*-P($HPMAmLac_n$-*co*-$HPMAmLac_n$-ETSA) block copolymer (scheme 3, abbreviated as **P100E15**). Stock solutions of ETSA (50 mg/mL), *N,N*-dimethylaminopyridinium *p*-toluenesulfonate (DPTS, 20 mg/mL) and *N,N'*-dicyclohexylcarbodiimide (DCC, 50 mg/mL) in dry DCM were prepared. **P100** (16 kDa, determined by NMR) was weighed (1050 mg, 66 μmol) and dissolved in dry DCM (final concentration of 100 mg/mL), followed by addition of ETSA (97 mg, 440 μmol), with a feed ratio of 15 mol% relative to $HPMAmLac_n$ functionalities, DPTS (12 mg, 44 μmol) and DCC (100 mg, 482 μmol). The reaction mixture was stirred at RT for 24 h. The mixture was then filtered using a 0.2 μm PTFE syringe filter to remove precipitated *N,N*'-dicyclohexylurea (DCU). Subsequently, the polymer was precipitated twice in diethyl ether and dried under vacuum overnight. The obtained block copolymer **P100E15**, yielding 0.90 g (86%), was analyzed by NMR and GPC (figures S1.4 and S2.1).

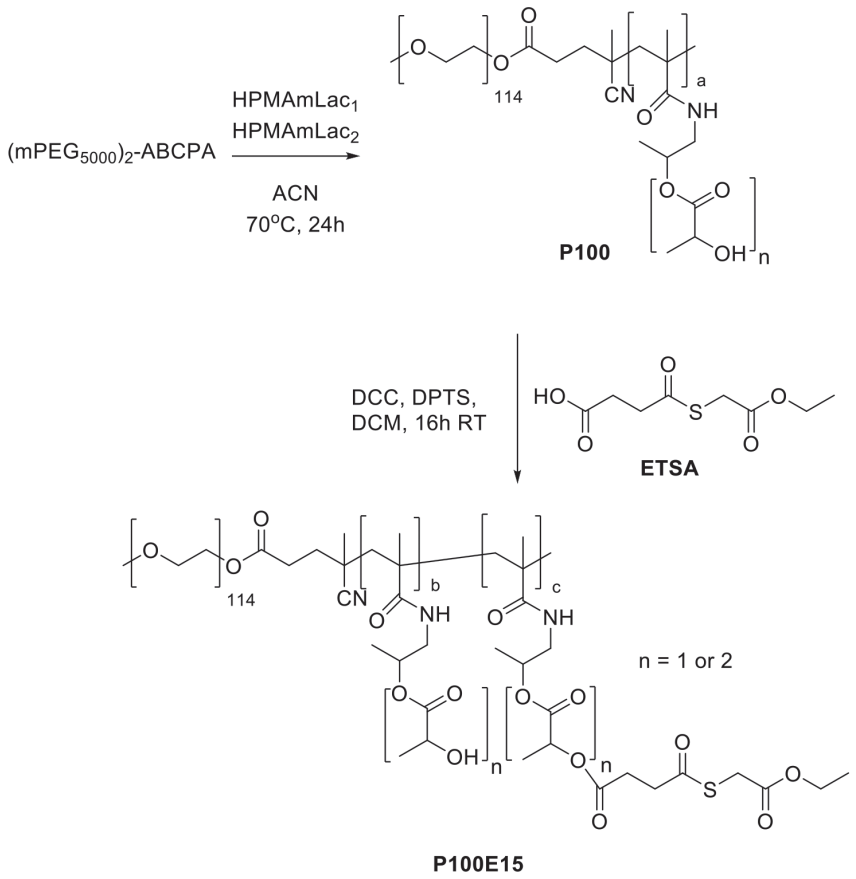

*Scheme 3: Synthesis of $mPEG_{5000}$-b-P(HPMAmLac$_1$-co-HPMAmLac$_2$) (polymer **P100**) by free radical polymerization using a (methoxy polyethylene glycol)$_2$-4,4-azobis(4-cyanopentanoic acid) ($(mPEG_{5000})_2$-ABCPA) macroinitiator and subsequent ETSA coupling to obtain polymer **P100E15**.*

Cysteine derivatization: The same procedure was applied as described above, with Boc-Cys(Trt)-OH (50 mg/mL in dry DCM) instead of ETSA, resulting in $mPEG_{5000}$-*b*-P(HPMAmLac$_n$-*co*-HPMAmLac$_n$-Cys(Trt)Boc) (scheme 4, further abbreviated as **P100C15 prot**). **P100C15 prot** was analyzed by NMR spectroscopy using the integral of the Boc protons for the quantification of cysteine moieties (figure S1.5). Next, Boc and trityl deprotection was carried out by dissolving 300 mg **P100C15 prot** in 5 mL DCM followed by addition of 5 mL TFA : water : TIS solution (90:5:5 %volume) and stirring at RT. After 2 h, the deprotected polymer $mPEG_{5000}$-*b*-P(HPMAmLac$_n$-*co*-HPMAmLac$_n$-Cys) (further abbreviated as **P100C15**) was precipitated in diethyl ether and dried under vacuum. **P100C15**, yielding 0.23 g (76%), was analyzed by GPC (figure S2.1).

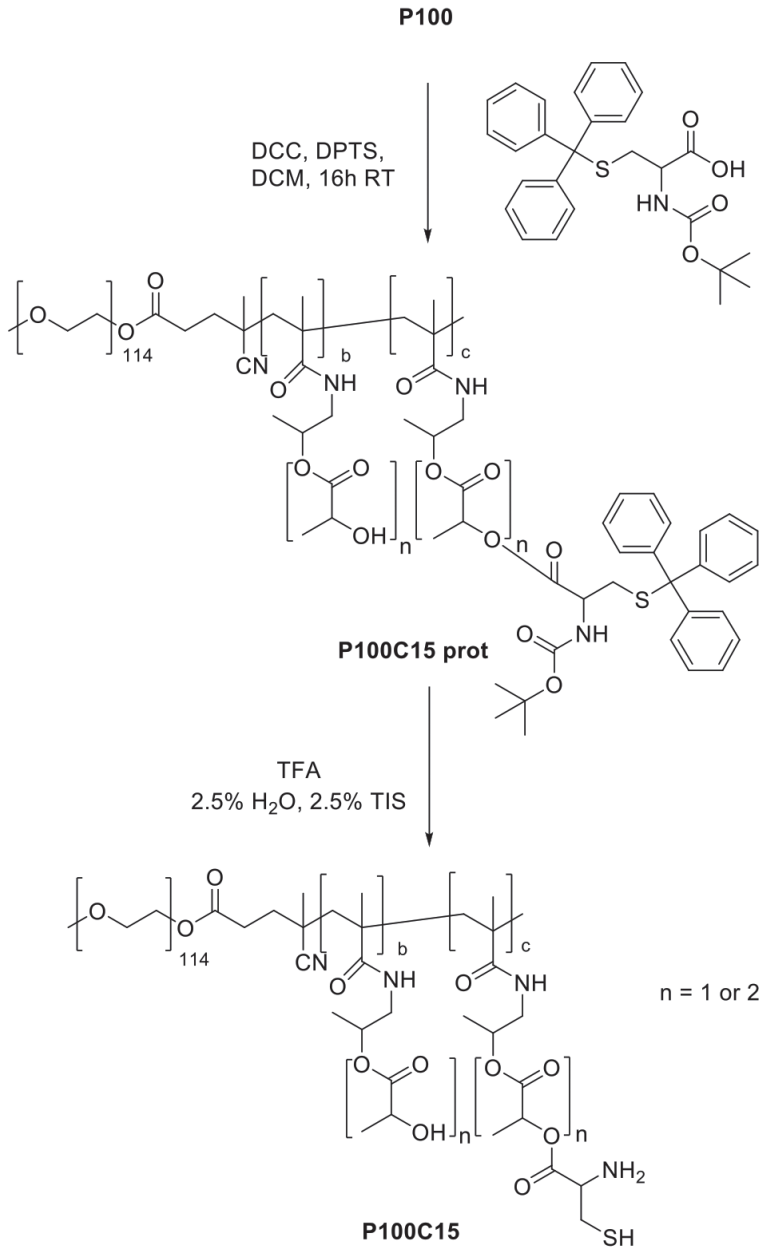

*Scheme 4: Synthesis of cysteine modified polymer **P100C15**.*

Core-crosslinked polymeric micelle (CCPM) formation and purification

Crosslinker approach: **P100E15** (23 kDa, determined by NMR, 120 mg, 5.2 µmol of polymer chains, 46.0 µmol of ETSA handles) was dissolved in 6 mL phosphate buffer (100 mM Na_2HPO_4, adjusted to pH 7.4 using HCl) whilst stirring in an ice bath. The *N*-*N*' bis-cysteinyl-ethylendiamine crosslinker (compound **2,** 9.3 mg of the TFA salt (see figure S1.2), 18.8 µmol, 37.6 µmol of cysteine handles; (0.80 ± 0.05 equivalents of cysteine to ETSA handles) was dissolved (75 mg/mL) in milliQ and tris(2-carboxyethyl) phosphine (TCEP, 19.5 mg, 78.0 µmol) in milliQ (112.5 mg/mL) was added to reduce possible present disulfide bonds. After 20 min, the crosslinker/TCEP mixture was placed in a water bath of 37 °C whilst stirring and the polymer solution was then added. After 1.5 h, the dispersion of formed CCPMs was filtered through a 0.2 µm RC syringe filter and purified by tangential flow filtration (TFF) against phosphate buffer (100 mM Na_2HPO_4, adjusted to pH 7.4 using HCl) employing an mPES membrane (50 kDa, 20 cm^2) for 40-50 washing volumes. The CCPM dispersion was then filtered again using a 0.2 µm RC syringe filter. Polymer concentration was determined similarly to a previously described total hydrolysis method, [36] described in the characterization section.

Complementary approach: **P100E15** (60 mg, 2.7 µmol of polymer chains, 23.5 µmol of ETSA handles) and **P100C15** (60 mg, 3.6 µmol of polymer chains, 22.4 µmol of cysteine handles) were separately dissolved in phosphate buffer (100 mM Na_2HPO_4, adjusted to pH 7.4 using HCl) to 20 mg/mL whilst stirring in an ice bath. Then, TCEP (9.5 mg, 38 µmol) was added to **P100C15**, to reduce any potential disulfide formation, followed by **P100E15** and the mixture was heated to 37 °C whilst stirring (0.95 ± 0.05 equivalents of cysteine to ETSA handles). After 1.5 h, the same purification procedure as described for CCPM formation via the small-molecule crosslinker approach was employed.

Crosslinker, polymer and particle characterization

Nuclear magnetic resonance (NMR) spectroscopy

^1H and ^{19}F NMR spectra were recorded on an Agilent 400-MR NMR spectrometer (Agilent Technologies, Santa Clara, USA). The residual solvent peak of D_6 DMSO (δ = 2.50 ppm) was used to calibrate ^1H chemical shifts.

Trifluoroacetate (TF-acetate) quantification in crosslinker (compound 2)

The crosslinker (compound **2**) was weighed (6.0 mg) together with an internal standard, trifluoroethanol (7.1 mg), dissolved in 0.5 mL D_6 DMSO and a ^{19}F NMR spectrum (figure S1.6) was recorded with a relaxation delay of 40 s (5-fold exceeding the highest

T_1 measured of 6.5 s). Relative integral area was used to calculate the mass of TF-acetate present in the crosslinker sample and was found to be 3.0 mg. The expected mass content of two TF-acetate counterions to the two amines in the 6 mg crosslinker sample is 2.8 mg, which is in good agreement with the measured content. The molecular weight of the crosslinker employed in this work is therefore 494.4 g/mol (compound **2** with 2 TF-acetate ions).

Gel permeation chromatography (GPC)

GPC analysis was performed using an Alliance 2695 (Waters) chromatography system with two PLgel 5 μm mixed-D columns (Polymer Laboratories) in series at a column temperature of 65 °C and employing a differential refractive index detector. DMF supplemented with 10 mM LiCl was employed as eluent with an elution rate of 1 mL/min. Sample concentrations were 10 mg/mL with 50 μL injections and PEGs of narrow and defined molecular weights obtained from PSS (Germany) were used as calibration standards. Recording of data was done with Waters Empower 32 software.

Cloud point (CP) measurement

The CPs of **P100E15** and **P100C15** in phosphate buffer (100 mM Na_2HPO_4, adjusted to pH 7.4 using HCl, 5 mg/mL polymer) were determined by measurement of light scattering at a 90° angle upon the onset of opalescence. Scattered light intensity was measured using a Jasco FP-8300 spectrophotometer at a wavelength of 550 nm. The temperature was ramped from 2 to 50 °C at a rate of 1 °C/min.

CCPM hydrolytic degradation

Purified CCPMs obtained via the crosslinker and complementary polymer approach were incubated at 37 °C and degradation was monitored using the following described techniques over a period of 192 h.

Dynamic light scattering (DLS)

The hydrodynamic size, scattering intensity and dispersity of the CCPMs (approximately 15 mg/mL polymer concentration) was determined by DLS using a Malvern Zetasizer nano series S (Malvern Panalytical Ltd, UK) with a measurement angle of 173° at a temperature of 37 °C.

For the bulk DLS degradation data, the derived count rate relative to the timepoint 0 measurement was normalized for the sake of comparison between the two systems. (originally 11 and 13 Mcps for the crosslinker and complementary based CCPMs respectively at timepoint 0 h).

Ultra-high performance liquid chromatography (UHPLC)

UHPLC analysis was performed using an Acquity (Waters, US) chromatography system with an HSS T3 column (1.8 µm, 2.1 x 100 mm, Waters) at a column temperature of 50 °C and employing a Waters TUV detector at 210 nm. KH_2PO_4 buffer (10 mM, pH = 2.5) was used as isocratic eluent at a flow rate of 0.5 mL/min for 2.5 min followed by an increasing gradient of acetonitrile supplemented with 0.1% phosphoric acid from 0% to 90% over 1 min. The injection volume was 5 µL.

Ethyl thioglycolate (ET) formation kinetics of both CCPM systems were determined by repeated injections during crosslinking within the sample holder at 37 °C, employing the same molar ratios described in the synthesis section above for a 1 mL (instead of 6 mL) sample. ET dilutions (200-1000 µg/mL) in phosphate buffer (100 mM Na_2HPO_4, adjusted to pH 7.4 using HCl) were used as reference standard. The ET formation % was calculated from the amount of ET expected based on the cysteine residues added (the cysteine residues being the limiting reagent).

Total polymer content of CCPMs after purification was determined through lactic acid concentration determination by UHPLC after hydrolysis, similarly as reported previously.[41] Briefly, the micellar dispersion was diluted 5-fold (to theoretical maximum of ~4 mg/mL based on polymer feed) in phosphate buffer (100 mM Na_2HPO_4, adjusted to pH 7.4 using HCl), 20 µL of the dilution was mixed with 10 µL NaOH (1 M) and subsequently incubated for 24 h at RT followed by the addition of 20 µL HCl (1 M). Sodium lactate was employed as reference standard to determine lactic acid concentration. The total polymer concentration was calculated as follows: Amount of polymer = measured amount of lactic acid × (M+5000)/ [90.08 × (m + 2n)], where M is the M_n of the thermosensitive block P(HPMAmLac$_n$); m and n are the number of repeat units of HPMAmLac$_1$ and HPMAmLac$_2$ in the block copolymer respectively (determined by ^{1}H NMR).

Lactic acid formation of the degrading CCPMs was quantified by injecting 20 µL of micellar dispersion (~20 mg/mL theoretical maximum polymer concentration based on feed) diluted with 10 µL 1 M HCl and 20 µL milliQ. The intact CCPM peak signals were simultaneously recorded.

Asymmetric flow field flow fractionation (AF4)

AF4 was performed using a AF2000 system (Postnova Analytics GmbH, Germany), equipped with an absorbance 2487 and fluorescence 2475 detector (Waters, USA), a PN3150 RI detector (Postnova Analytics GmbH, Germany), a PN3621b multi-angle light scattering (MALS) detector with 21 detection angles with a 488 nm laser (Postnova Analytics GmbH, Germany) and a Zetasizer Nano SZ (Malvern Panalytical Ltd, UK). The separation channel included a 500 µm spacer and a regenerated cellulose membrane with a 10 kDa cutoff (Postnova Analytics GmbH, Germany). Phosphate buffered saline (PBS, 137 mM NaCl, 2.7 mM KCl, 8 mM Na_2HPO_4, and 2 mM KH_2PO_4, pH 7.4) filtered with an Omipore™ 0.1 µm PTFE membrane (Merck Millipore Ltd, Ireland) was used as mobile phase. Samples of CCPMs (60 µL of ~15 mg/mL) were injected into the channel with an autosampler, focused for 7 min at a focus flow rate of 4.3 mL/min and crossflow of 4.0 mL/min, and separated using the elution profile given in table 1. Data were analyzed and processed using NovaFFF AF2000 software (Postnova Analytics GmbH, Germany). A sphere model was employed for fitting MALS data and to calculate the radius of gyration (R_g).

Table 1: Elution profile employed for the fractionation of CCPMs

Elution Step	Time (min)	Crossflow (mL/min)	Type	Exponent
1	5	4.0	constant	-
2	30	4.0 to 0.10	power	0.2
3	30	0.10 to 0.05	power	0.8
4	20	0.05 to 0.00	constant	-
5	10	0.00	constant	-

Transmission electron microscopy (TEM) visualization

For the TEM visualization, 15 µL of CCPM dispersion (1250 x diluted in milliQ water) was dropped onto a layer of activated carbon film supported on a 100 mesh hexagonal copper grid and incubated for 15 min. CCPMs/polymers not bound to the activated carbon film were washed away with several drops of PBS pH 7.4. Subsequently the sample was fixated using 1% glutaraldehyde in PBS for 10 min and the grid was extensively washed with several drops of milliQ water. Next, 150 µL of a negative staining solution (a mixture of 2% uranyl oxalate and 0.15 % methylcellulose in an ammonium acetate buffer pH 7.0) was applied for a 15 min incubation after which the excess was blotted away using filter paper and the sample was air dried for at least 1 h at RT. Images were obtained on a FEI Tecnai G2 20 TWIN electron microscope which was operated at an acceleration voltage of 120 kV and a spot size of 3. Images were recorded using RADIUS software.

Results and discussion

Native chemical ligation (NCL) is a strategy to prepare CCPMs, [36] and two crosslinking approaches were evaluated in view of the degradation characteristics of the resulting CCPMs in this study. CCPMs were prepared by crosslinking **P100E15** with a bifunctional agent (compound **2**) or by reacting **P100E15** with **P100C15** (see scheme 5). The 'crosslinker approach' could result in CCPMs with both intra- and intermolecular crosslinks whereas the 'complementary polymer approach' yields CCPMs with only intermolecular crosslinks.

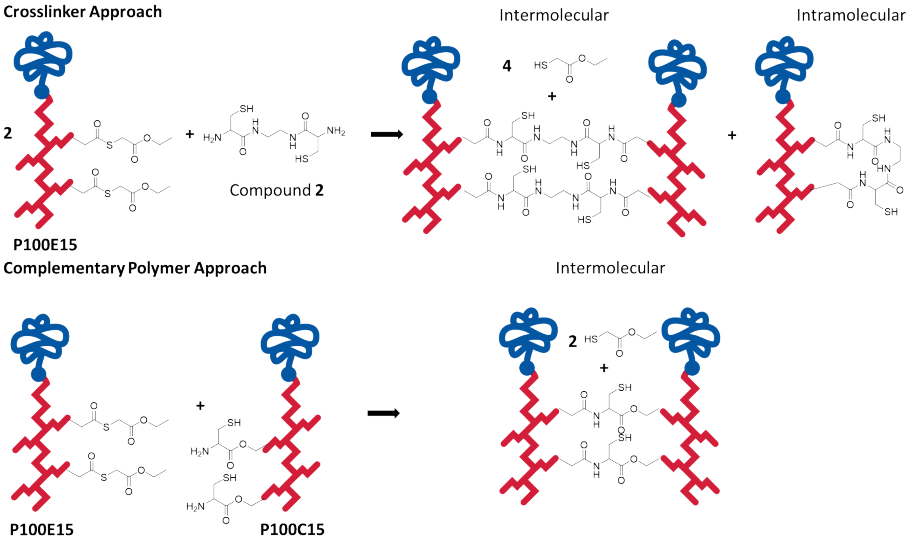

*Scheme 5: Representation of two copolymer chains crosslinking via NCL through either a crosslinker or a complementary polymer approach. Note: **P100E15** has 8.8 thioester units and **P100C15** has 6.3 cysteine units per polymer chain. The crosslinker approach requires 2 amide bond formations per crosslink whilst the complementary approach requires only one.*

Crosslinker synthesis

The bifunctional cysteine crosslinker (compound **2**) was synthesized using an adapted procedure [40] and its identity was confirmed by NMR analysis (see figure S1.2).

Polymer synthesis

The synthesized $mPEG_{5000}$-*b*-P($HPMAmLac_1$-*co*-$HPMAmLac_2$) (**P100**) polymers had an M_n of 15.8 and 17.8 kDa (from two different batches) as determined by NMR analysis, in agreement with previous results. [36] Both functionalized polymers were obtained by derivatization of part of the lactic acid side groups of **P100** with either ETSA (**P100E15**)

or Boc-Cys(Trt)-OH, which was followed by TFA deprotection of the latter to yield **P100C15**. The extent of ETSA and Boc-Cys(Trt)-OH derivatization of available lactate side chains was 14.0 and 12.1 mol % units per polymer chain (feed was 15 mol% in both cases, indicating high derivatization yields) with an M_n of 23 and 17 kDa, respectively, as determined by NMR analysis. The higher M_n of **P100E15** is likely caused by the purification procedure using diethyl ether, with lower molecular weight polymer chains failing to precipitate. The ETSA modification results in a more hydrophobic polymer (and thereby better solubilized in the ether layer) than cysteine, which explains why an increased M_n was not observed for **P100C15**. GPC analysis showed that the molecular weight and molecular weight distribution of both modified polymers were well conserved (see figure S2.1). The CPs (above this temperature, micelles are formed) were 33, 5 and 18 °C for **P100**, **P100E15** and **P100C15**, respectively. Derivatization with more hydrophobic handles explains the observed decrease in CP, with ETSA being a more hydrophobic functionalization than cysteine as also observed previously.[19]

CCPM synthesis

CCPMs were formed either by using **P100E15** with crosslinker (compound **2**) or **P100E15** with **P100C15**, with ETSA in slight excess compared to cysteine residues. The formation of ethyl thioglycolate (a byproduct of the NCL reaction) was determined by UHPLC (figure 1) and reflects the extent of amide bond and thus crosslink formation.

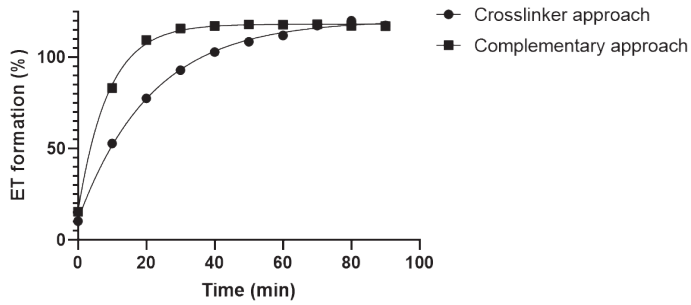

Figure 1: Kinetics of ethyl thioglycolate (ET) formation from the NCL crosslinking reaction via the crosslinker (circles) and complementary polymer (squares) approach, determined by UHPLC and expressed as a percentage of maximal ET that can be formed theoretically.

Figure 1 shows that ET was formed as expected with approximately 115% ET formation in both the crosslinking systems after 90 min (expressed as a percentage of ET release expected based on the cysteine feed). The 115% ET formation falls in the range of experimental errors expected from NMR measurements of the polymer(s) (± 10%), ET concentration

determination (± 2-5%) and weighing (± 1-2 %). Importantly, the cysteine groups had quantitatively reacted within 90 min. The concentration of **P100E15** in the crosslinker approach is twice as high as in the complementary polymer approach and approximately the same holds for the cysteine content (exemplified in scheme 5), therefore there is a similar crosslink density (defined as total of both inter- and intramolecular links) in both systems. The initial slower rate of ET formation in the crosslinker approach may be explained by the hydrophilic crosslinker having to diffuse into the hydrophobic micellar core, in contrast to the complementary approach where reactive groups are in close proximity upon micellization.

TFF purification was done to remove the formed ET and remaining impurities (such as TCEP). Polymer losses due to purification were investigated by total hydrolysis and subsequent lactic acid quantification by UHPLC, similarly to a previously published procedure. [36] Losses typically ranged between 20-30%, resulting in a total polymer concentration of approximately 15 mg/mL, out of the initial 20 mg/mL feed during crosslinking.

TEM imaging confirmed that crosslinking by either approach resulted in stabile spherical particles in the 50 nm diameter size range, in contrast to non-crosslinked free polymer samples that destabilize during preparation with the negative staining technique (see figure 2).

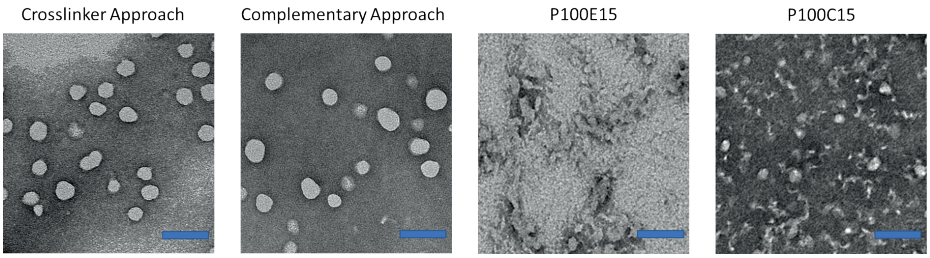

*Figure 2: Negative staining TEM images of crosslinker and complementary polymer based CCPMs after purification as well as non-crosslinked polymeric micelles based on **P100E15** and **P100C15**. Scale bars set to 100 nm.*

CCPM degradation

The degradation of the two different CCPMs was studied under physiological conditions (pH 7.4, 37 °C). Batch mode DLS measurements

Figure 3 shows the degradation of the two different CCPMs as determined by batch mode DLS (direct bulk measurement of a sample in a cuvette). The scattering intensity (SI, a metric

previously employed to follow CCPM degradation [10,36]) depends on particle concentration, particle radius and refractive index increment of the CCPMs. [42] However, for a dispersion with a fixed particle concentration and particle mass, SI increase in particle size due to swelling is exactly compensated by the resulting change in specific refractive index increment (see supporting information section 5). [43–45] Interestingly, figure 3 shows an immediate decrease in SI in time for the crosslinker based CCPMs as we also observed previously [36] whereas the SI of complementary polymer CCPMs showed a decrease after a certain lag time of 25-50 hours. The time to decrease SI to 50% was also substantially different, approximately 80 versus 170 h for the crosslinker and complementary polymer approach, respectively. The percentage amount of lactic acid formation was equal for both systems, ruling out different hydrolysis rates (possibly resulting from different core environments) being responsible for the observed difference in decrease of SI. The mass loss due to lactic acid formation from both CCPMs after 192 h was approximately 9 %, which cannot solely explain the observed decrease in SI. Furthermore, the lactic acid formation kinetics are in good agreement with previous kinetic data for a similar polymer. [39]

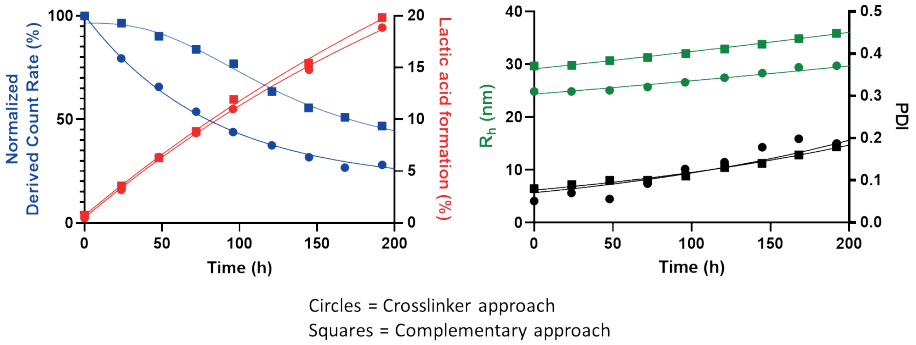

Figure 3: Degradation characteristics of crosslinker (circles) and complementary polymer (squares) based CCPMs under physiological conditions (pH 7.4, 37 °C) at a polymer concentration of ~15 mg/mL. Normalized derived count rate (blue), R_h (green) and PDI (black) were determined by DLS measurements at 37 °C. Lactic acid formed % (red) was determined by UHPLC.

Table 2: Initial micelle and CCPM sizes as determined by batch DLS at 25 °C.

	P100E15 not crosslinked	P100C15 not crosslinked	Crosslinker approach	Complementary Approach
Rh (nm)	25	32	25	30

Shortly after preparation, the crosslinker CCPMs based on **P100E15** and compound **2** had a smaller radius of hydration (R_h) than the complementary CCPMs based on **P100E15** and **P100C15** (table 2), which can be explained the higher hydrophobicity of **P100E15**

(as compared to **P100C15**) that results in micelles with a lower extent of hydration of the hydrophobic core of the micelles. During the 192 h incubation at pH 7.4 and 37°C, the R_h of the CCPMs increased to 28 and 35 nm, for the crosslinker and complementary approach, respectively, which is discussed in the degradation mechanism section. PDI increased during degradation which is also in line with previously published findings, being associated to the degradation of particles in batch DLS measurements. [10,36] Similar results were obtained by accelerated degradation of the CCPMs at pH 9.5, 25°C (figure S4.1). The accelerated degradation is due to the increased rate of lactate ester hydrolysis which is driven by first order kinetics with respect to OH^- concentration above a pH of 5. [8,46] Taken together, it is demonstrated that CCPMs prepared by reacting **P100E15** with **P100C15** (complementary approach) degrade slower than CCPMs obtained by reaction of **P100E15** with compound **2** (crosslinking approach).

AF4/DLS/MALS measurements

The degradation of CCPMs was also studied using AF4 to analyze the CCPM distribution and soluble polymer species formed during hydrolysis. A decrease in both RI and 90° light scattering signal resulting from eluting CCPMs (R_t = 50 min) over the degradation timepoints was observed (figure 4 A and B), with a faster decrease for the CCPMs prepared using the crosslinker approach. The RI fractograms (figure 4 A) also show an increase of soluble polymer species (figure 4 D), smaller in size as hallmarked by their short retention time (R_t = 22 min) and lack of light scattering (figure 4 B). Given that a 10 kDa membrane was employed for the fractionation, these emerging peaks are likely soluble mPEG-*b*-P(HPMAmLac$_n$) chains, that are partially hydrolyzed with a CP above 25 °C (AF4 measurement temperature) and no longer chemically linked to the CCPMs. Additionally, partially hydrolyzed P(HPMAmLac$_n$) as well as fully hydrolyzed P(HPMA) and mPEG polymers can be expected following the ester bond cleavage connecting the two blocks. [39] The values of the integrated CCPM RI peaks in time are shown in figure 4 C and support the trend also found by batch DLS in figure 3, namely a faster degradation of the crosslinker based CCPMs as compared to the complementary polymer CCPMs. Importantly, the SI intensity decrease shown in figure 4 C is comparable with the SI measured by batch DLS in figure 3. In figure 4 E, values of R_g and R_h at the peak SI are reported (in contrast to batch DLS where the entire sample was measured). Surprisingly, figure 4 E shows that the radius of hydration (R_h) at peak SI remained rather constant and equal for both CCPM types (25 nm). This contrast to figure 3 is explained by the difference between batch DLS measurements (affected by the whole distribution) to the AF4 separation method, where the R_h at the highest SI (most abundant species in the distribution) is reported, highlighting the importance of size separation techniques for CCPM analysis. [47] Furthermore, the radius of gyration (R_g) at peak SI increased during degradation of both CCPM types (from 10 to 18 nm, meaning an increase in R_g/R_h ratio from 0.4 to 0.7), which suggests a loss in mass density due to hydrophilization of the core [48] as can be expected from the hydrolysis of the lactic acid side chains.

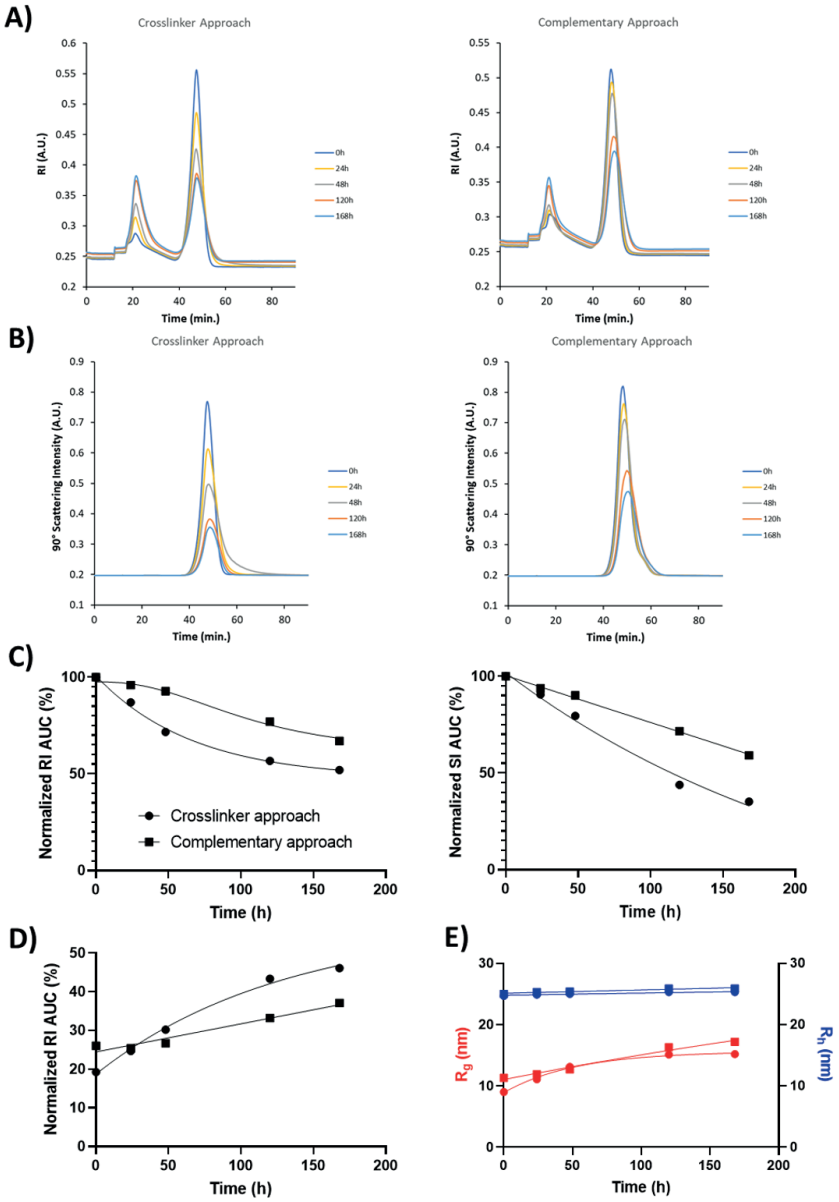

Figure 4: Degradation characteristics of crosslinker and complementary polymer based CCPMs under physiological conditions (pH 7.4, 37 °C) at a polymer concentration of ~20 mg/mL fractionated by AF4. A) Fractograms recorded by refractive index, B) Fractograms recorded by SLS at 90°C angle, C) normalized refractive index and scattering intensity AUC of the CCPM signals (R_t = 50 min) in fractograms of A and B, respectively, D) normalized refractive index AUC of the R_t = 22 min peaks in the fractograms of A and E) peak SI R_g and R_h values recorded by MALS and DLS (circles = crosslinker approach, squares = complementary polymer approach). Peaks at R_t = 50 min represent CCPMs and peaks at R_t = 22 min represent soluble (partially) hydrolyzed mPEG-b-P(HPMAmLac$_n$), P(HPMAmLac$_n$), P(HPMA) and mPEG polymers, which are chemically not connected to the CCPMs.

Degradation mechanism

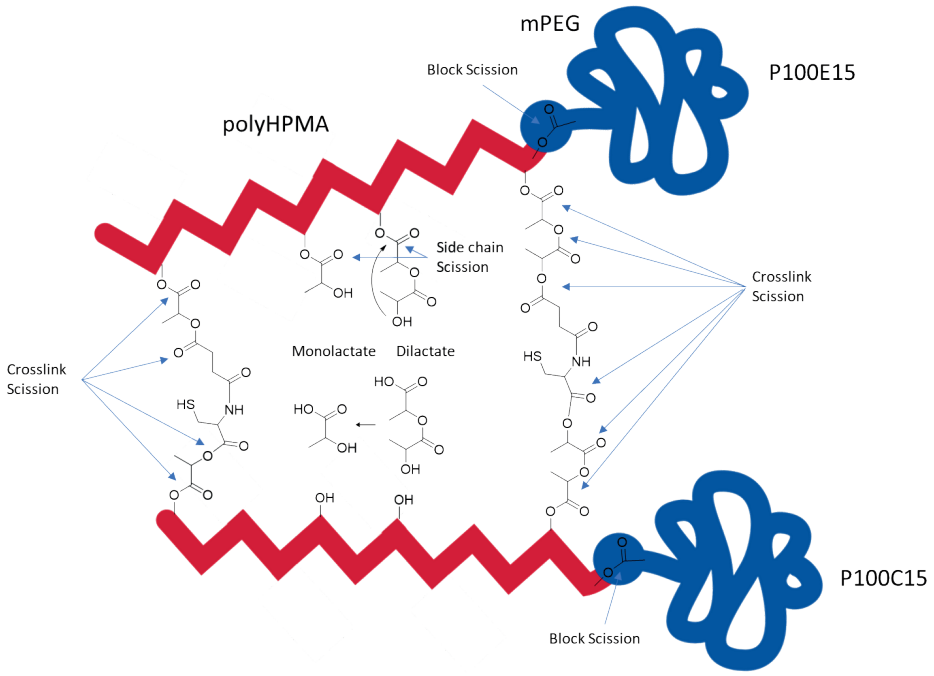

*Scheme 6: Hydrolysis mechanism of NCL based CCPMs, using the complementary **P100E15** with **P100C15** CCPMs. The dilactate side chains hydrolyze 6 times faster than both monolactate side chains and the esters involved in the crosslinks (4-6 esters per crosslink), due to an internal attack of the terminal alcohol.* [8,39] *It is thus expected that dilactate side chains and crosslinks are cleaved at a similar rate (a crosslink requires only one scission to become ineffective).*

Taken together, degradation of the CCPMs is due to hydrolysis of ester bonds present in $HPMAmLac_1$ and $HPMAmLac_2$ side chains and of the ester bonds present in crosslinks (scheme 6). Further, an ester bond connects the mPEG block to the poly(HPMA) block, whose hydrolysis results in block scission. [39] The hydrolysis rate of $HPMAmLac_2$ is 6 times faster than $HPMAmLac_1$ and is ascribed to the intramolecular attack of the terminal alcohol onto the carbonyl group connecting HPMA with the dilactate. [39] $HPMAmLac_2$ is a more hydrophobic monomer than $HPMAmLac_1$ and is responsible for lowering the CP of HPMA-lactate based polymers below 37 °C as has been shown previously. [32] In fact, the CPs of $PHPMAmLac_1$ and $PHPMAmLac_2$ homopolymers have been reported to be 13 and 65°C, respectively, indicating that hydrolysis of $HPMAmLac_2$ units to hydrophilic HPMA units increases the CP above 37 °C. Thus, upon incubation of CCPMs at pH 7.4 and 37 °C, $HPMAmLac_2$ side chains are hydrolyzed in time resulting in a loss of mass as well as an increase in hydrophilicity of the core. The increase in hydrophilicity was also

observed by UHPLC, where a decrease in retention time during degradation of the CCPM peaks was observed (see figure S3.1 for chromatograms and figure S4.3 for normalized AUCs). This increased hydrophilicity and resulting swelling of the core explains the observed slight increase in hydrodynamic radius (R_h) of the CCPMs measured by batch mode DLS (figure 3). Interestingly, this increase in size was not observed with the AF4 measurements of the CCPM species where peak SI R_h remained constant, but peak SI R_g increased (figure 4 E). This finding highlights the more detailed distribution insights that separation techniques such as AF4 can provide in extension to batch mode DLS, as has previously also been described. [47,49] Nonetheless, batch mode DLS provides the global average and in this work remains leading for the trends observed. Besides hydrolysis of lactic acid side chains, ester bonds in the crosslinks (4-6 esters are present per crosslink, see scheme 6) are hydrolyzed which finally results in formation of soluble HPMA-rich polymer chains that are extracted from the CCPMs. This loss of mass due to formation of lactic acid and soluble polymer chains is likely responsible for the observed decrease in scattering intensity in figure 3 as well as figure 4 C. The increase in hydrophilicity as well as loss of core mass due to $HPMAmLac_2$ hydrolysis may explain the increase in R_g as shown in figure 4 C. Simultaneously, when the ester bonds in the crosslinks between the polymer chains are hydrolyzed, destabilization of the CCPMs occurs.

Assuming that a particle is degraded when the number of hydrolyzed crosslinks surpasses a critical value and that the hydrolytic rate constant for all crosslinks is equal, we simulated the degradation curves with regard to crosslink density in figure S4.2, which shows that CCPMs with a low crosslink density undergo rapid decay, whereas higher crosslink densities result in an S-curve with a lag-time before decaying.

Moving back to our hypothesis on how the crosslinker or complementary CCPM formation approach affects the degradation characteristics, the complementary approach clearly showed slower degradation in terms of SI and RI signal, while still showing similar swelling behavior (R_h and R_g) and lactic acid formation as the crosslinker approach (hydrolysis proceeds equally fast). Since a comparable amount of crosslinks (intermolecular and potential intramolecular) were formed as discussed in the CCPM synthesis section, this strongly suggests that the complementary approach resulted in CCPMs with a significantly higher effective (intermolecular) crosslink density than the crosslinker approach. This is best explained by intrachain reactions of the crosslinker with the same polymer, lowering effective crosslink density.

Conclusion

CCPMs were formed by two different crosslinking strategies; with a bifunctional crosslinking agent or by using a complementary polymer approach, employing native chemical ligation as a crosslinking reaction. We aimed to study and compare the degradation of these 2 types of CCPMs under physiological conditions. It was found that the crosslinker based CCPMs had a considerably faster degradation rate as compared to the complementary polymer approach. This is likely due to the occurrence of intramolecular reactions resulting in ineffective crosslinks by using a bifunctional crosslinker which are avoided by employing complementary polymers. These intramolecular crosslinking inefficiencies of a crosslinker approach certainly also apply in a broader scope to other CCPM systems and should be taken into consideration in their design.

Supporting information paragraph

^{1}H NMR spectra of the (de)protected crosslinker, **P100**, **P100E15** and protected **P100C15** (figures S1.1-1.5), GPC chromatograms of **P100**, **P100E15** and deprotected **P100C15** (figure S2.1) and UHPLC chromatograms of different degradation timepoints of the CCPMs formed via the crosslinker or complementary polymer approach (figure S3.1), CCPM degradation characteristics measured by DLS under accelerated conditions (pH 9.5, 25 ^{o}C) (figure S4.1), simulation of expected particle degradation with varying crosslinking densities (figure S4.2) and a mathematical explanation of expected changes in SI of swelling particles in section 5 (including figure S5.1).

Conflicts of interest

The authors declare that there is no conflict of interest.

Acknowledgements

We acknowledge the Cell Microscopy Core of the Center for Molecular Medicine, UMC Utrecht for providing microscopy training and service. The Dutch Research Council (NWO), Research Foundation Flanders (FWO) and Cristal Therapeutics are acknowledged for funding (NWA.ID.17.030).

List of abbreviations

ABCPA:	4,4-azobis(4-cyanopentanoic acid)
ACN:	acetonitrile
AF4:	asymmetric flow field-flow fractionation
CCPM:	core-crosslinked polymeric micelle
CMC:	critical micellization concentration
CP:	cloud point
CMT:	critical micellization temperature
DCC:	*N,N'*-dicyclohexylcarbodiimide
DCM:	dichloromethane
DCR:	derived count rate
DCU:	dicyclohexylurea
DLS:	dynamic light scattering
DMF:	dimethyl formamide
DMSO:	dimethyl sulfoxide
DPTS:	*N,N*-dimethylaminopyridinium *p*-toluenesulfonate
ETSA:	ethylthioglycolate-succinic acid
GPC:	gel permeation chromatography
HATU:	hexafluorophosphate azabenzotriazole tetramethyl uronium
$HPMAmLac_n$:	*N*-2-hydroxypropyl methacrylamide mono/di lactate
HPLC:	high pressure liquid chromatography
MALS:	multi-angle light scattering
mPEG:	methoxy polyethylene glycol
NCL:	native chemical ligation
PDI:	polydispersity index
PEG:	polyethylene glycol
PM:	polymeric micelle
P100:	$mPEG_{5000}$-*b*-P($HPMAmLac_1$-*co*-$HPMAmLac_2$) copolymer
P100C15:	$mPEG_{5000}$-*b*-P($HPMAmLac_n$-*co*-$HPMAmLac_n$-Cysteine) copolymer
P100E15:	$mPEG_{5000}$-*b*-P($HPMAmLac_n$-*co*-$HPMAmLac_n$-ETSA) copolymer
PTFE:	polytetrafluoroethylene
RI:	refractive index
SLS:	static light scattering
TCEP:	tris(2-carboxyethyl)phosphine
TEM:	transmission electron microscopy
TFA:	trifluoroacetic acid
UHPLC:	ultra-high performance liquid chromatography

References

(1) Varela-Moreira, A.; Shi, Y.; Fens, M. H. A. M.; Lammers, T.; Hennink, W. E.; Schiffelers, R. M. Clinical Application of Polymeric Micelles for the Treatment of Cancer. *Mater. Chem. Front.* **2017**, *1* (8), 1485–1501.

(2) Cabral, H.; Miyata, K.; Osada, K.; Kataoka, K. Block Copolymer Micelles in Nanomedicine Applications. *Chem. Rev.* **2018**, *118* (14), 6844–6892.

(3) Ghezzi, M.; Pescina, S.; Padula, C.; Santi, P.; Del Favero, E.; Cantù, L.; Nicoli, S. Polymeric Micelles in Drug Delivery: An Insight of the Techniques for Their Characterization and Assessment in Biorelevant Conditions. *J. Control. Release* **2021**, *332* (February), 312–336.

(4) Talelli, M.; Barz, M.; Rijcken, C. J. F.; Kiessling, F.; Hennink, W. E.; Lammers, T. Core-Crosslinked Polymeric Micelles: Principles, Preparation, Biomedical Applications and Clinical Translation. *Nano Today* **2015**, *10* (1), 93–117.

(5) Fan, W.; Zhang, L.; Li, Y.; Wu, H. Recent Progress of Crosslinking Strategies for Polymeric Micelles with Enhanced Drug Delivery in Cancer Therapy. *Curr. Med. Chem.* **2019**, *26* (13), 2356–2376.

(6) van Nostrum, C. F. Covalently Cross-Linked Amphiphilic Block Copolymer Micelles. *Soft Matter* **2011**, *7* (7), 3246.

(7) Shuai, X.; Merdan, T.; Schaper, A. K.; Xi, F.; Kissel, T. Core-Cross-Linked Polymeric Micelles as Paclitaxel Carriers. *Bioconjug. Chem.* **2004**, *15* (3), 441–448.

(8) Rijcken, C. J.; Snel, C. J.; Schiffelers, R. M.; van Nostrum, C. F.; Hennink, W. E. Hydrolysable Core-Crosslinked Thermosensitive Polymeric Micelles: Synthesis, Characterisation and in Vivo Studies. *Biomaterials* **2007**, *28* (36), 5581–5593.

(9) Liu, X.; Lee Miller II, A.; Waletzki, B. E.; Mamo, T. K.; Yaszemski, M. J.; Lu, L. Hydrolysable Core Crosslinked Particles for Receptor-Mediated PH-Sensitive Anticancer Drug Delivery. *New J. Chem.* **2015**, *39* (11), 8840–8847.

(10) Hu, Q.; Rijcken, C. J. F.; van Gaal, E.; Brundel, P.; Kostkova, H.; Etrych, T.; Weber, B.; Barz, M.; Kiessling, F.; Prakash, J.; Storm, G.; Hennink, W. E.; Lammers, T. Tailoring the Physicochemical Properties of Core-Crosslinked Polymeric Micelles for Pharmaceutical Applications. *J. Control. Release* **2016**, *244*, 314–325.

(11) Zhang, Z.; Yin, L.; Tu, C.; Song, Z.; Zhang, Y.; Xu, Y.; Tong, R.; Zhou, Q.; Ren, J.; Cheng, J. Redox-Responsive, Core Cross-Linked Polyester Micelles. *ACS Macro Lett.* **2013**, *2* (1), 40–44.

(12) Ma, X.; Liu, J.; Lei, L.; Yang, H.; Lei, Z. Synthesis of Light and Dual-redox Triple-stimuli-responsive Core-crosslinked Micelles as Nanocarriers for Controlled Release. *J. Appl. Polym. Sci.* **2019**, *136* (37), 47946.

(13) Zhang, J.; Jiang, X.; Zhang, Y.; Li, Y.; Liu, S. Facile Fabrication of Reversible Core Cross-Linked Micelles Possessing Thermosensitive Swellability. *Macromolecules* **2007**, *40* (25), 9125–9132.

(14) Kim, J. S.; Youk, J. H. Preparation of Core Cross-Linked Micelles Using a Photo-Cross-Linking Agent. *Polymer (Guildf).* **2009**, *50* (10), 2204–2208.

(15) Elter, J. K.; Quader, S.; Eichhorn, J.; Gottschaldt, M.; Kataoka, K.; Schacher, F. H. Core-Crosslinked Fluorescent Worm-Like Micelles for Glucose-Mediated Drug Delivery. *Biomacromolecules* **2021**, *22* (4), 1458–1471.

(16) Wei, R.; Cheng, L.; Zheng, M.; Cheng, R.; Meng, F.; Deng, C.; Zhong, Z. Reduction-Responsive Disassemblable Core-Cross-Linked Micelles Based on Poly(Ethylene Glycol)-b -Poly(N -2-Hydroxypropyl Methacrylamide)–Lipoic Acid Conjugates for Triggered Intracellular Anticancer Drug Release. *Biomacromolecules* **2012**, *13* (8), 2429–2438.

(17) Zhang, Y.; Wang, C.; Huang, Y.; Yan, H.; Liu, K. Core-Crosslinked Polymeric Micelles with High Doxorubicin Loading Capacity and Intracellular PH- and Redox-Triggered Payload Release. *Eur. Polym. J.* **2015**, *68*, 104–114.

(18) Matsumoto, S.; Christie, R. J.; Nishiyama, N.; Miyata, K.; Ishii, A.; Oba, M.; Koyama, H.; Yamasaki, Y.; Kataoka, K. Environment-Responsive Block Copolymer Micelles with a Disulfide Cross-Linked Core for Enhanced SiRNA Delivery. *Biomacromolecules* **2009**, *10* (1), 119–127.

(19) Najafi, M.; Kordalivand, N.; Moradi, M. A.; Van Den Dikkenberg, J.; Fokkink, R.; Friedrich, H.; Sommerdijk, N. A. J. M.; Hembury, M.; Vermonden, T. Native Chemical Ligation for Cross-Linking of Flower-Like Micelles. *Biomacromolecules* **2018**, *19* (9), 3766–3775.

(20) Talelli, M.; Barz, M.; Rijcken, C. J. F.; Kiessling, F.; Hennink, W. E.; Lammers, T. Core-Crosslinked Polymeric Micelles: Principles, Preparation, Biomedical Applications and Clinical Translation. *Nano Today* **2015**, *10* (1), 93–117.

(21) Zhang, L.; Bernard, J.; Davis, T. P.; Barner-Kowollik, C.; Stenzel, M. H. Acid-Degradable Core-Crosslinked Micelles Prepared from Thermosensitive Glycopolymers Synthesized via RAFT Polymerization. *Macromol. Rapid Commun.* **2008**, *29* (2), 123–129.

(22) Wu, Y.; Chen, W.; Meng, F.; Wang, Z.; Cheng, R.; Deng, C.; Liu, H.; Zhong, Z. Core-Crosslinked PH-Sensitive Degradable Micelles: A Promising Approach to Resolve the Extracellular Stability versus Intracellular Drug Release Dilemma. *J. Control. Release* **2012**, *164* (3), 338–345.

(23) Kuang, G.; Zhang, Q.; He, S.; Wu, Y.; Huang, Y. Reduction-Responsive Disulfide Linkage Core-Cross-Linked Polymeric Micelles for Site-Specific Drug Delivery. *Polym. Chem.* **2020**, *11* (44), 7078–7086.

(24) Birhan, Y. S.; Darge, H. F.; Hanurry, E. Y.; Andrgie, A. T.; Mekonnen, T. W.; Chou, H. Y.; Lai, J. Y.; Tsai, H. C. Fabrication of Core Crosslinked Polymeric Micelles as Nanocarriers for Doxorubicin Delivery: Self-Assembly, in Situ Diselenide Metathesis and Redox-Responsive Drug Release. *Pharmaceutics* **2020**, *12* (6), 1–22.

(25) Wei, R.; Cheng, L.; Zheng, M.; Cheng, R.; Meng, F.; Deng, C.; Zhong, Z. Reduction-Responsive Disassemblable Core-Cross-Linked Micelles Based on Poly(Ethylene Glycol)- b -Poly(N -2-Hydroxypropyl Methacrylamide)–Lipoic Acid Conjugates for Triggered Intracellular Anticancer Drug Release. *Biomacromolecules* **2012**, *13* (8), 2429–2438.

(26) Li, A.; Zhang, D. Synthesis and Characterization of Cleavable Core-Cross-Linked Micelles Based on Amphiphilic Block Copolypeptoids as Smart Drug Carriers. *Biomacromolecules* **2016**, *17* (3), 852–861.

(27) Jin, R.; Sun, J.; Zhou, L.; Guo, X.; Cao, A. Dual-Responsive Click-Crosslinked Micelles Designed for Enhanced Chemotherapy for Solid Tumors. *Biomater. Sci.* **2020**, *8* (9), 2507–2513.

(28) Su, Z.; Xu, Y.; Wang, Y.; Shi, W.; Han, S.; Shuai, X. A PH and Reduction Dual-Sensitive Polymeric Nanomicelle for Tumor Microenvironment Triggered Cellular Uptake and Controlled Intracellular Drug Release. *Biomater. Sci.* **2019**, *7* (9), 3821–3831.

(29) Sang, X.; Yang, Q.; Shi, G.; Zhang, L.; Wang, D.; Ni, C. Preparation of PH/Redox Dual Responsive Polymeric Micelles with Enhanced Stability and Drug Controlled Release. *Mater. Sci. Eng. C* **2018**, *91* (May), 727–733.

(30) Bauer, T. A.; Eckrich, J.; Wiesmann, N.; Kuczelinis, F.; Sun, W.; Zeng, X.; Weber, B.; Wu, S.; Bings, N. H.; Strieth, S.; Barz, M. Photocleavable Core Cross-Linked Polymeric Micelles of Polypept(o)Ides and Ruthenium(<scp>ii</Scp>) Complexes. *J. Mater. Chem. B* **2021**, *9* (39), 8211–8223.

(31) Cartlidge, S. A.; Duncan, R.; Lloyd, J. B.; Kopečkova—Rejmanová, P.; Kopeček, J. Soluble, Crosslinked N-(2-Hydroxypropyl)Methacrylamide Copolymers as Potential Drug Carriers. *J. Control. Release* **1987**, *4* (4), 253–264.

(32) Soga, O.; van Nostrum, C. F.; Hennink, W. E. Poly(N -(2-Hydroxypropyl) Methacrylamide Mono/Di Lactate): A New Class of Biodegradable Polymers with Tuneable Thermosensitivity. *Biomacromolecules* **2004**, *5* (3), 818–821.

(33) Soga, O.; van Nostrum, C. F.; Ramzi, A.; Visser, T.; Soulimani, F.; Frederik, P. M.; Bomans, P. H. H.; Hennink, W. E. Physicochemical Characterization of Degradable Thermosensitive Polymeric Micelles. *Langmuir* **2004**, *20* (21), 9388–9395.

(34) Soga, O.; van Nostrum, C. F.; Fens, M.; Rijcken, C. J. F.; Schiffelers, R. M.; Storm, G.; Hennink, W. E. Thermosensitive and Biodegradable Polymeric Micelles for Paclitaxel Delivery. *J. Control. Release* **2005**, *103* (2), 341–353.

(35) Rijcken, C. J. F.; De Lorenzi, F.; Biancacci, I.; Hanssen, R. G. J. M.; Thewissen, M.; Hu, Q.; Atrafi, F.; Liskamp, R. M. J.; Mathijssen, R. H. J.; Miedema, I. H. C.; Menke - van der Houven van Oordt, C. W.; van Dongen, G. A. M. S.; Vugts, D. J.; Timmers, M.; Hennink, W. E.; Lammers, T. Design, Development and Clinical Translation of CriPec®-Based Core-Crosslinked Polymeric Micelles. *Adv. Drug Deliv. Rev.* **2022**, *191*, 114613.

(36) Hebels, E. R.; Bindt, F.; Walther, J.; van Geijn, M.; Weterings, J.; Hu, Q.; Colombo, C.; Liskamp, R.; Rijcken, C.; Hennink, W. E.; Vermonden, T. Orthogonal Covalent Entrapment of Cargo into Biodegradable Polymeric Micelles via Native Chemical Ligation. *Biomacromolecules* **2022**.

(37) Hu, B.-H.; Su, J.; Messersmith, P. B. Hydrogels Cross-Linked by Native Chemical Ligation. *Biomacromolecules* **2009**, *10* (8), 2194–2200.

(38) Bagheri, M.; Bresseleers, J.; Varela-Moreira, A.; Sandre, O.; Meeuwissen, S. A.; Schiffelers, R. M.; Metselaar, J. M.; Van Nostrum, C. F.; Van Hest, J. C. M.; Hennink, W. E. Effect of Formulation and Processing Parameters on the Size of MPEG- b-p(HPMA-Bz) Polymeric Micelles. *Langmuir* **2018**, *34* (50), 15495–15506.

(39) Neradovic, D.; van Steenbergen, M. J.; Vansteelant, L.; Meijer, Y. J.; van Nostrum, C. F.; Hennink, W. E. Degradation Mechanism and Kinetics of Thermosensitive Polyacrylamides Containing Lactic Acid Side Chains. *Macromolecules* **2003**, *36* (20), 7491–7498.

(40) Ziaco, B.; Pensato, S.; D'Andrea, L. D.; Benedetti, E.; Romanelli, A. Semisynthesis of Dimeric Proteins by Expressed Protein Ligation. *Org. Lett.* **2008**, *10* (10), 1955–1958.

(41) Hu, Q.; Rijcken, C. J.; Bansal, R.; Hennink, W. E.; Storm, G.; Prakash, J. Complete Regression of Breast Tumour with a Single Dose of Docetaxel-Entrapped Core-Cross-Linked Polymeric Micelles. *Biomaterials* **2015**, *53*, 370–378.

(42) Falke, S.; Betzel, C. Dynamic Light Scattering (DLS); Springer International Publishing, 2019; pp 173–193.

(43) Ponomareva, E.; Tadgell, B.; Hildebrandt, M.; Krüsmann, M.; Prévost, S.; Mulvaney, P.; Karg, M. The Fuzzy Sphere Morphology Is Responsible for the Increase in Light Scattering during the Shrinkage of Thermoresponsive Microgels. *Soft Matter* **2022**, *18* (4), 807–825.

(44) van der Kooij, H. M.; Spruijt, E.; Voets, I. K.; Fokkink, R.; Cohen Stuart, M. A.; van der Gucht, J. On the Stability and Morphology of Complex Coacervate Core Micelles: From Spherical to Wormlike Micelles. *Langmuir* **2012**, *28* (40), 14180–14191.

(45) Hsieh, A.; Corti, D. S.; Franses, E. I. Rayleigh and Rayleigh-Debye-Gans Light Scattering Intensities and Spetroturbidimetry of Dispersions of Unilamellar Vesicles and Multilamellar Liposomes. *J. Colloid Interface Sci.* **2020**, *578*, 471–483.

(46) de Jong, S. .; Arias, E. .; Rijkers, D. T. .; van Nostrum, C. .; Kettenes-van den Bosch, J. .; Hennink, W. . New Insights into the Hydrolytic Degradation of Poly(Lactic Acid): Participation of the Alcohol Terminus. *Polymer (Guildf).* **2001**, *42* (7), 2795–2802.

(47) Hu, Y.; Crist, R. M.; Clogston, J. D. The Utility of Asymmetric Flow Field-Flow Fractionation for Preclinical Characterization of Nanomedicines. *Anal. Bioanal. Chem.* **2020**, *412* (2), 425–438.

(48) Lobanov, M. Y.; Bogatyreva, N. S.; Galzitskaya, O. V. Radius of Gyration as an Indicator of Protein Structure Compactness. *Mol. Biol.* **2008**, *42* (4), 623–628.

(49) Quattrini, F.; Berrecoso, G.; Crecente-Campo, J.; Alonso, M. J. Asymmetric Flow Field-Flow Fractionation as a Multifunctional Technique for the Characterization of Polymeric Nanocarriers. *Drug Deliv. Transl. Res.* **2021**, *11* (2), 373–395.

(50) Roux, S.; Zékri, E.; Rousseau, B.; Paternostre, M.; Cintrat, J.-C.; Fay, N. Elimination and Exchange of Trifluoroacetate Counter-Ion from Cationic Peptides: A Critical Evaluation of Different Approaches. *J. Pept. Sci.* **2008**, *14* (3), 354–359.

Supporting information (SI)

NMR spectra

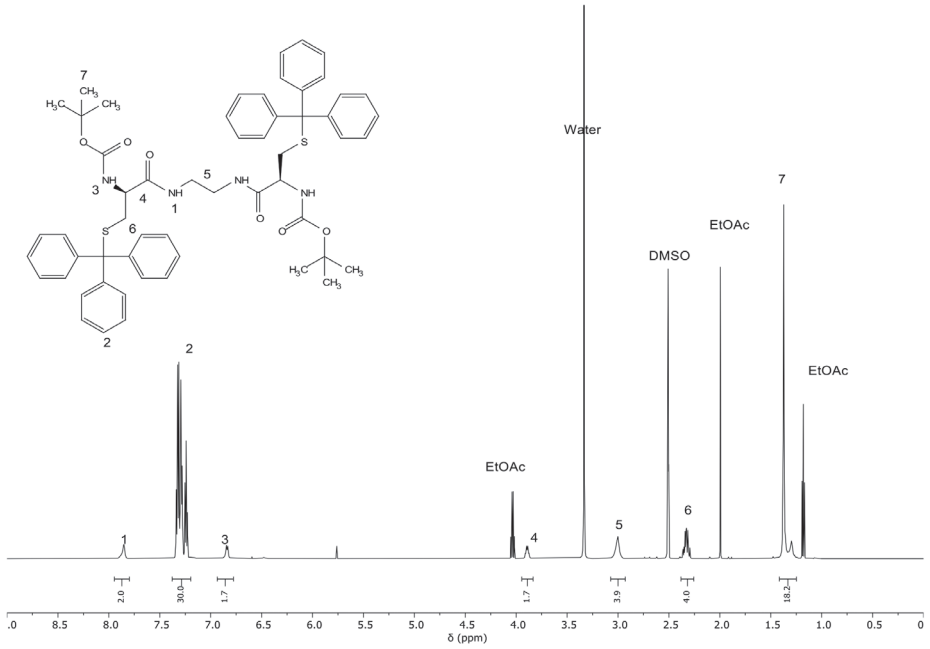

*Figure S1.1: [1]H NMR spectrum of the protected dicysteine crosslinker (compound **1**). The solvent was deuterated DMSO.*

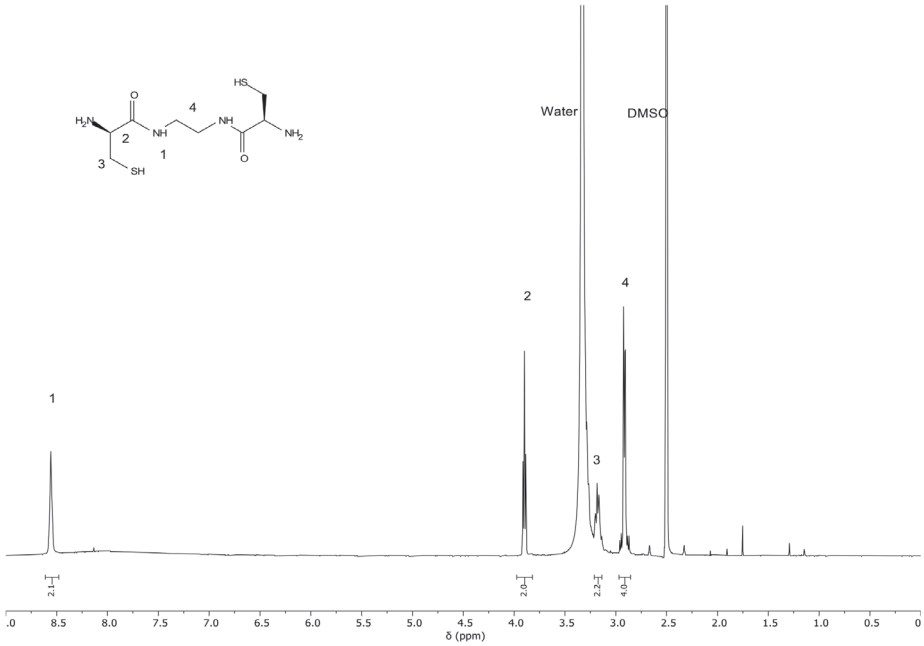

*Figure S1.2: [1]H NMR spectrum of the dicysteine crosslinker (compound **2**). The solvent was deuterated DMSO. Spectrum matches a previously reported one. [40] Although formic acid was employed as modifier during the Prep-RP-HPLC purification procedure, the formate counterion signal was not detected in the [1]H NMR spectrum. Through [19]F NMR (figure S1.6), it was shown that TF-acetate resulting from the deprotection employing TFA remained the exclusive counterion of the amine salt, which was hence incorporated into the molecular weight calculations of the crosslinker in this work. The challenges to exchange or remove TF-acetate salts in peptides have been described elsewhere. [50]*

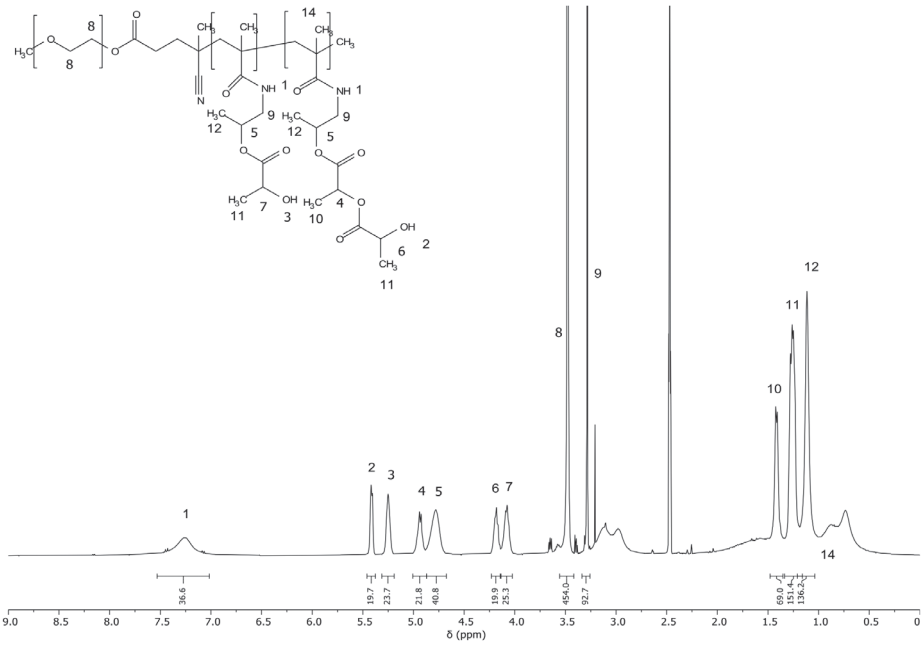

Figure S1.3: [1]H NMR spectrum of ***P100*** *(PEG_{5000}-b-P(HPMAmLac$_1$-co-HPMAmLac$_2$)). The solvent was deuterated DMSO.*

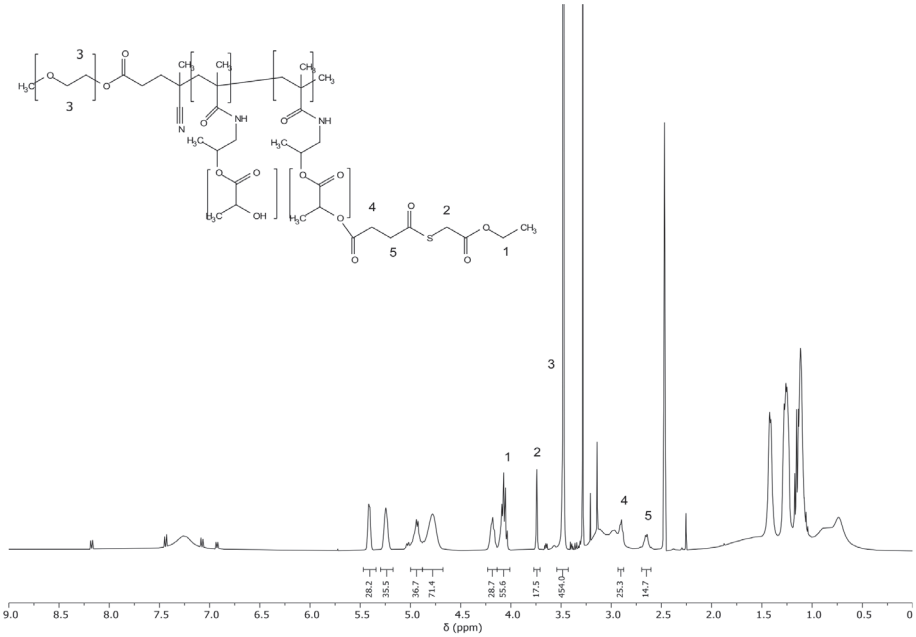

*Figure S1.4: ^{1}H NMR spectrum of **P100E15** (PEG_{5000}-b-P(HPMAmLac$_n$-co-HPMAmLac$_n$-ETSA)). The solvent was deuterated DMSO.*

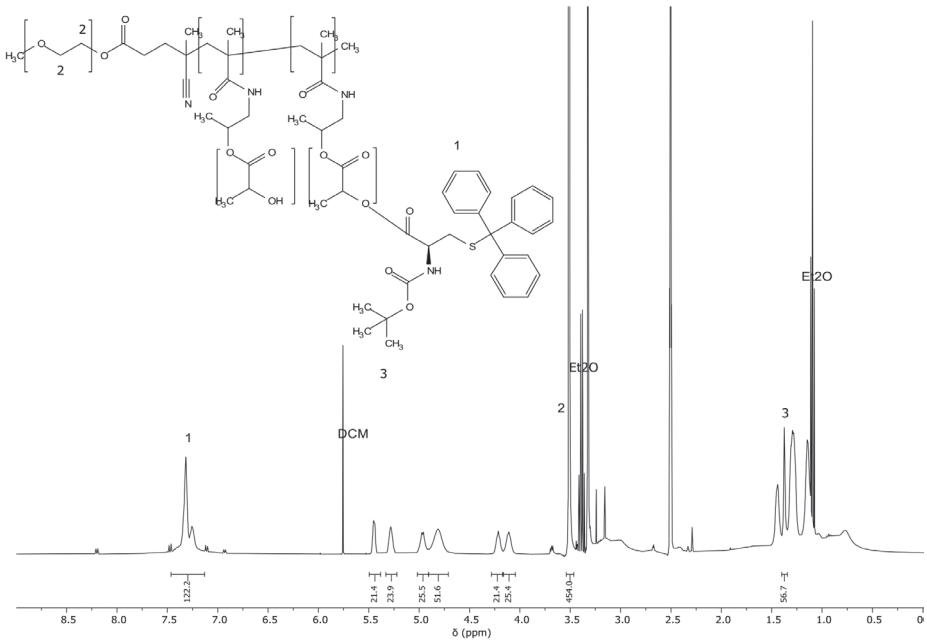

Figure S1.5: [1]H NMR spectrum of ***P100C15 prot*** *(PEG_{5000}-b-P(HPMAmLac$_n$-co-HPMAmLac$_n$-Cys(Trt)-Boc)). The solvent was deuterated DMSO.*

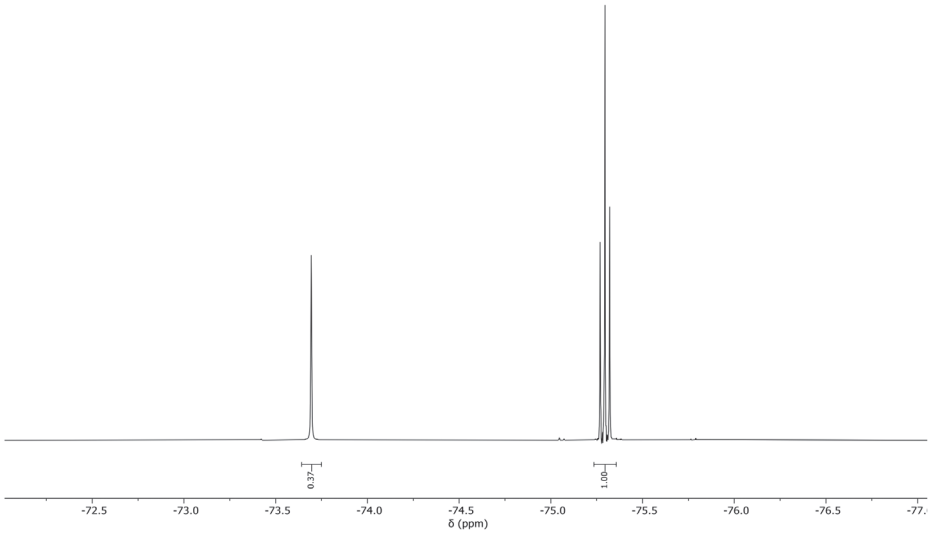

Figure S1.6: [19]F NMR spectrum of the crosslinker (compound ***2****, singlet signal) including an internal reference (trifluoroethanol, triplet signal). The amounts of crosslinker and trifluoroethanol were 6.0 mg (12 µmol) and 7.1 mg (71 µmol), respectively. The solvent was deuterated DMSO.*

GPC chromatograms

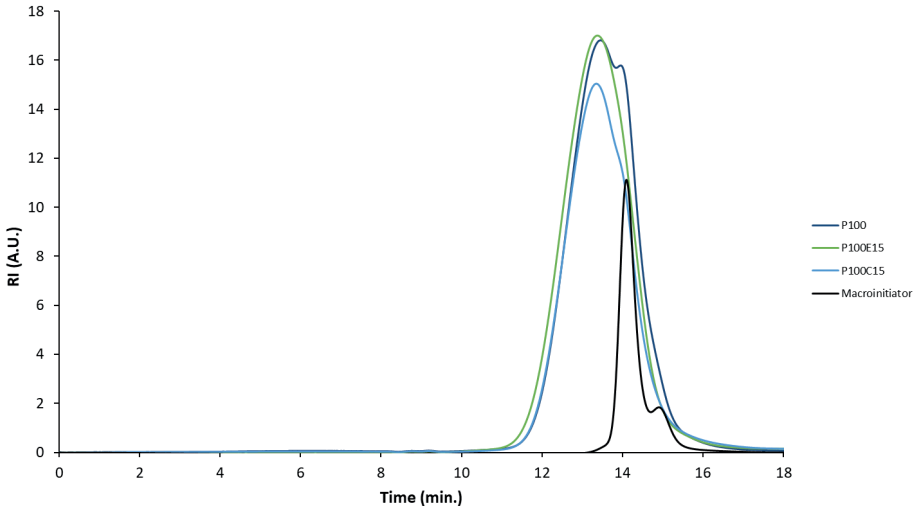

	GPC M_n (kDa)	Đ	NMR M_n (kDa)
P100	14.9	1.72	15.8 and 17.8
P100E15	17.0	1.80	22.5
P100C15	15.6	1.79	16.9
Macroinitiator	10.8	1.04	-

*Figure S2.1: GPC chromatograms and analysis of **P100** (blue) which was modified with either ETSA to **P100E15** (green) or Boc-Cys(Trt)-OH followed by deprotection to **P100C15** (light blue). Detection by RI. ETSA and Boc-Cys(Trt)-OH derivatization of available lactate side chains was 14.0 and 12.1 mol % units per polymer chain, respectively, as determined by NMR. The observed deviations in absolute values for Mn extracted from NMR and GPC are common, as both techniques rely on a different approach to extract these molecular weights. A small amount (<5%) of remaining macroinitiator (black) may be responsible for the slight shoulder observed in **P100**.*

UHPLC chromatograms

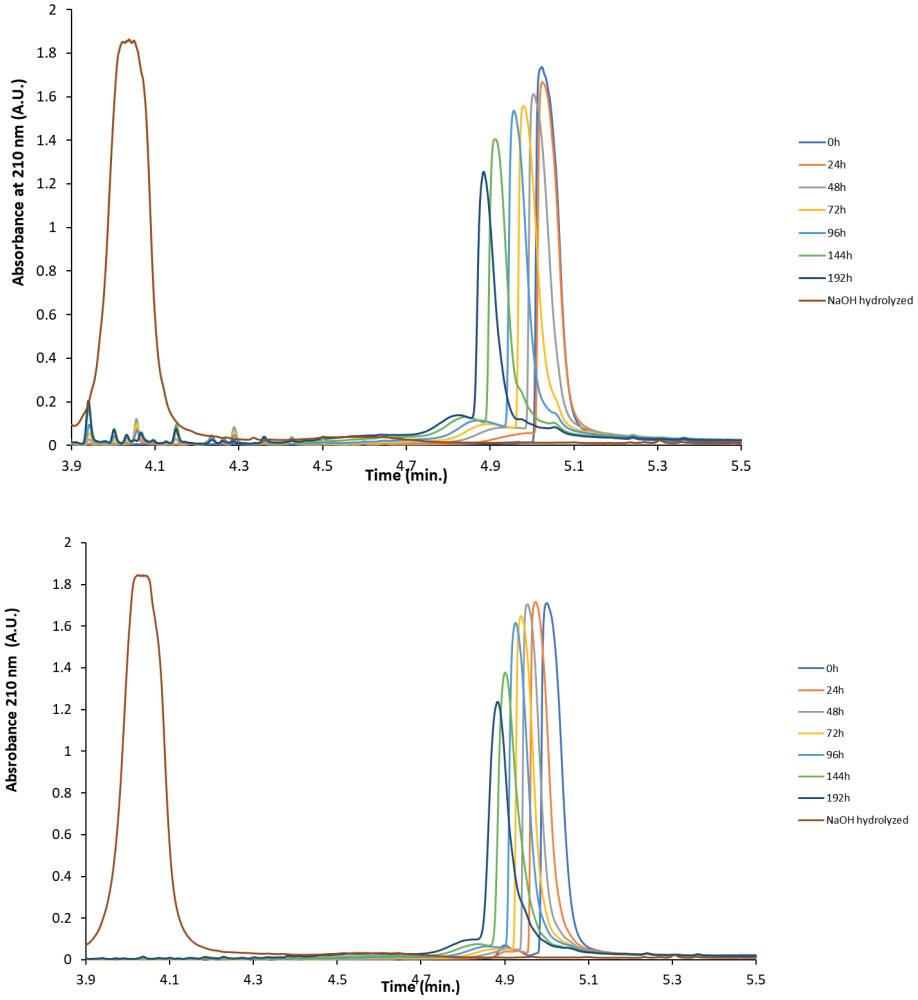

Figure S3.1: UHPLC chromatograms of degrading CCPMs (R_t between 4.8 and 5.1) formed by either the crosslinker (top) or complementary polymer (bottom) approach. Complete hydrolysis of the CCPMs resulted in the disappearance of the ascribed CCPM peaks and appearance of a more hydrophilic species at R_t = 4.0,

4. Additional figures

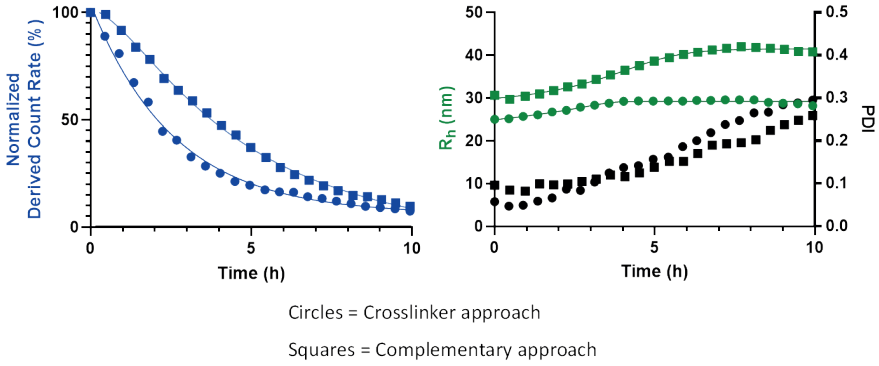

Figure S4.1: Degradation characteristics of crosslinker (circles) and complementary polymer (squares) based CCPMs under accelerated hydrolysis conditions (pH 9.5, 25 °C) at a polymer concentration of ~15 mg/mL. Normalized derived count rate (blue), Z-Ave (green) and PDI (black) were determined by DLS measurements at 25°C.

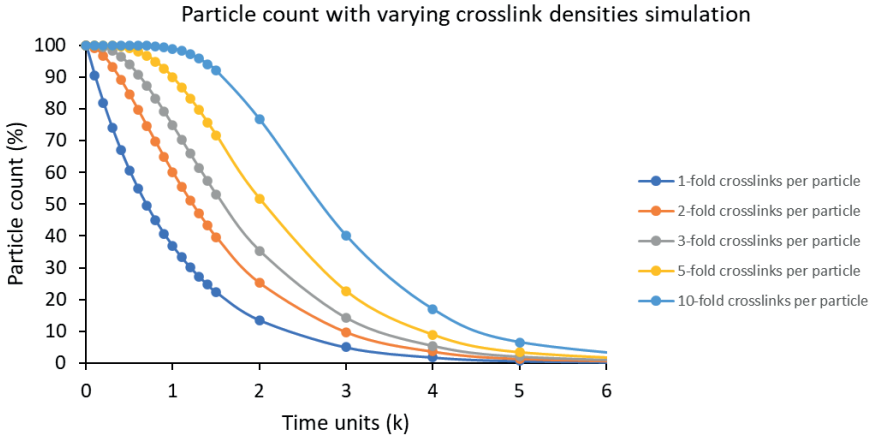

Figure S4.2: Simulated degradation characteristics of crosslinked particles undergoing hydrolysis with different crosslinking densities. The assumptions made are that a particle is degraded when all crosslinks are hydrolyzed (1-fold crosslinks being the critical number of crosslinks required for stability) and that the hydrolytic rate constant (following first order decay kinetics) for all crosslinks has the same value (taken as k = 1). With increasing percentage of crosslinks, a lag time for particle disintegration becomes apparent for the S-shaped degradation curves.

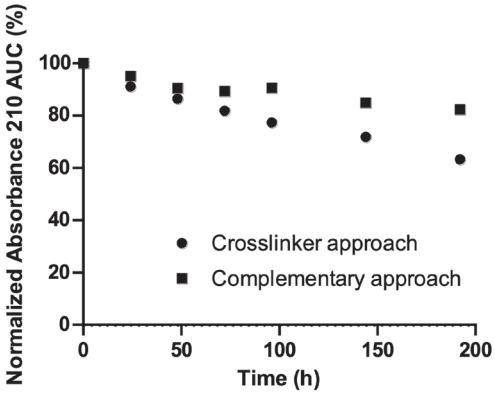

Figure S4.3: Degradation characteristics of crosslinker (circles) and complementary (squares) polymer based CCPMs under physiological conditions (pH 7.4, 37 °C), determined by UHPLC (R_t between 4.8 and 5.1) and recorded at 210 nm absorbance.

5. Swelling of colloidal particles and scattering intensity

Assuming that the particles are small compared to the wavelenght of light (λ), the scattered intensity (I_θ) at a certain angle (θ) can be described using the Rayleigh-Debye-Gans (RDG) formalism:

$$\frac{I_\theta}{I_0} \propto \lambda^{-4} \cdot V_p^2 \cdot \frac{m^2 - 1}{m^2 + 2} \cdot P(\theta) \quad \textbf{(1)}$$

where V_p is the volume of the RDG scatterer and $P(\theta)$ the particle's form factor. m is defined as the ratio of the refractive index of the particle (n_p) and the dispersing medium (n_s):

$$m = \frac{n_p}{n_s} \quad \textbf{(2)}$$

Since the V_p is proportional to the radius of the particle (R_p) to the power 6, Eq. **(1)** can also be written as, giving the well-known dependence of the scattered intensity to the particle size:

$$\frac{I_\theta}{I_0} \propto \lambda^{-4} \cdot R_p^6 \cdot \frac{m^2 - 1}{m^2 + 2} \cdot P(\theta) \quad \textbf{(3)}$$

Considering that $m \approx 1$ for most polymer/solvent combination, Eq. **(3)** can be simplified (via a Taylor expansion) to:

$$\frac{I_\theta}{I_0} \propto \lambda^{-4} \cdot R_p^6 \cdot (m-1)^2 \cdot P(\theta) \tag{4}$$

In the case of particles that swell by infusion of solvent, not only the dependence of the scattered intensity on the particle size, but also the change in n_p has to be considered when determining the scattered intensity. The refractive index of a composite particle (in this case polymer and solvent) can be written as:

$$n_p = \phi \cdot n_{polym} + (1-\phi) \cdot n_s \tag{5}$$

with φ the volume fraction of polymer inside a single scatterer. This volume fraction is related to R_p:

$$\phi = \frac{V_{polym}}{V_{particle}} \propto R_p^{-3} \tag{6}$$

Rewriting $(m-1)$ in terms of n_p, n_s and φ gives:

$$(m-1) = \left(\frac{n_p}{n_s} - 1\right) = \left(\frac{n_p - n_s}{n_s}\right) \tag{7a}$$

$$(m-1) = \frac{(\phi \cdot n_{polym} + (1-\phi) \cdot n_s) - n_s}{n_s} = \frac{\phi \cdot (n_{polym} - n_s)}{n_s} \tag{7b}$$

Plugging this result into Eq. (4) yields:

$$\frac{I_\theta}{I_0} \propto \lambda^{-4} \cdot R_p^6 \cdot \phi^2 \left(\frac{n_{polym} - n_s}{n_s}\right)^2 \cdot P(\theta) \tag{8}$$

Considering the relation between φ and Rp (as given by Eq. **(6)**, the final relation for the scattered intensity of solven-swelling particles is obtained:

$$\frac{I_\theta}{I_0} \propto \lambda^{-4} \cdot R_p^6 \cdot R_p^{-6} \left(\frac{n_{polym} - n_s}{n_s}\right)^2 \cdot P(\theta) = \lambda^{-4} \left(\frac{n_{polym} - n_s}{n_s}\right)^2 \cdot P(\theta) \tag{9}$$

From Eq. **(9)** we learn that the scattered intensity becomes independent of the particle size, as increases in scattered intensity upon swelling are compensated by a loss of contrast between the dispersing medium and the particle core.

CHAPTER 6

Improved trifunctional crosslinker synthesis and click entrapment of a peptide into core-crosslinked polymeric micelles

Erik R. Hebels[1], Matt Timmers[1,2], Rob Liskamp[2,3,4], Cristianne J.F. Rijcken[2], Wim E. Hennink[1] and Tina Vermonden[1]

[1] Division of Pharmaceutics, Utrecht Institute for Pharmaceutical Sciences (UIPS), Utrecht University, 3508 TB Utrecht, the Netherlands.
[2] Cristal Therapeutics, 6229 EV Maastricht, the Netherlands
[3] Department of Biochemistry, Cardiovascular Research Institute Maastricht (CARIM), Maastricht University, Maastricht 6229 ER, the Netherlands
[4] School of Chemistry, University of Glasgow, Glasgow G12 8QQ, U.K.

Abstract

Polymeric micelles (PMs) are promising delivery vehicles for enhanced tissue targeting of entrapped therapeutic agents. Strategies to circumvent premature micelle destabilization and release of entrapped drugs, as well as e.g. imaging agents, include crosslinking of the micellar core (to obtain core-crosslinked PMs or CCPMs) as well as covalent attachment of the drug cargo. Typically, to allow entrapment of fragile cargos (such as peptides, proteins, oligonucleotides, and fluorescent dyes), the chemistry employed to obtain crosslinked micelles needs to be mild and compatible with functional groups present in the cargo. In chapter 4, we reported on the use of native chemical ligation (NCL, a mild bio-orthogonal reaction between a *N*-terminal cysteine residue and a thioester that proceeds under physiological conditions) as a crosslinking reaction to obtain CCPMs. This system employed a trifunctional crosslinker containing two cysteine residues for the micelle core-crosslinking reaction and an azide residue for ring-strained alkyne conjugation of cargos, obtainable with reasonable yields (typically 60 % over the final 4 steps). The polymer was based on methoxypolyethylene glycol-*b*-*N*-(2-hydroxypropyl)methacrylamide-lactate (mPEG-*b*-HPMAmLac$_n$) block copolymers derivatized with thioester residues (using ethyl thioglycolate-succinic anhydride, ETSA) for NCL crosslinking with the trifunctional crosslinker under physiological conditions. Model fluorescent dyes containing a ring strained alkyne were clicked onto the trifunctional crosslinker and then used for crosslinking, using a conventional approach where the cargo is present during CCPM formation. Here, we firstly optimized the reaction path to obtain the trifunctional crosslinker, improving the yield from 60 to 80 % over the final 4 steps, primarily by improving upon the Gabriel conversion. Second, we investigate the click entrapment of a peptide cargo with an irreversible linkage. To this end, we employed a recently developed 7 membered ring strained alkyne, 3,3,6,6-tetramethylthiacycloheptyne sulfoximine (TMTHSI), which was N-terminally conjugated to a model peptide (SAAEWFEKL) via standard solid phase peptide synthesis (SPPS). This is a first-in-class example showing peptide conjugation of a ring strained alkyne via standard SPPS. The click entrapment of the TMTHSI-SAAEWFEKL construct was investigated before and after NCL crosslinking, utilizing the intrinsic fluorescence of the tryptophan residue present in the peptide. It was found that clicking both before and after crosslinking resulted in >95 % entrapment. This work highlights CCPM formation before click entrapment as a viable and efficient route, suggesting that crosslinking chemistry orthogonal with the cargo such as NCL is not required for successful entrapment.

Introduction

Polymeric micelles (PMs) have emerged as a promising platform for targeted drug delivery due to their ability to entrap therapeutic agents and accumulate in tumor tissues up on intravenous administration exploiting the so-called enhanced permeability and retention (EPR) effect. [1–5] The ability to control the release of entrapped drugs is a key feature in the development of PMs as drug delivery vehicles. One approach to improve stability and thereby drug retention in PMs is through the crosslinking of the micelle core, resulting in the formation of core-crosslinked polymeric micelles (CCPMs). [6–8] Importantly, covalent attachment of the drug cargo via preferably a reversible linker is used to prevent premature drug release, increase drug retention and (triggered) release at the site of action. [9–11] Clearly, the crosslinking chemistry employed to form CCPMs and covalently entrap the cargo must be mild and compatible with the entrapment of fragile cargoes such as peptides, proteins, oligonucleotides, and fluorescent dyes.

Recently, native chemical ligation (NCL) has been utilized as a crosslinking reaction to form CCPMs to facilitate entrapment of fragile cargos. NCL is a bio-orthogonal reaction that occurs between a N-terminal cysteine residue and a thioester under physiological conditions. In chapter 4, a trifunctional crosslinker containing two cysteine residues for micelle core-crosslinking and an azide residue for ring-strained alkyne conjugation of a cargo was used to form CCPMs. This trifunctional crosslinker was obtained in reasonable yields (60% relative to the first intermediate). [12] The block copolymer utilized in this system was based on methoxypolyethylene glycol-*b*-*N*-(2-hydroxypropyl)methacrylamide-lactate (mPEG-*b*-HPMAmLac$_n$), which was derivatized with thioester residues for NCL crosslinking with the trifunctional crosslinker. Model dye entrapment was achieved by mixing the cargo with the disulfide stabilized crosslinker (click reaction), opening of the disulfide bond (reduction) and mixing this construct with the polymers before elevating the temperature resulting in micellization and subsequent crosslinking by native chemical ligation.

Here, we aimed to improve the synthesis route of the trifunctional crosslinker employed for NCL based CCPM formation to obtain higher yields. Following this, we explored a new method for cargo entrapment after CCPM formation, this time with a model peptide cargo (SAAEWFEKL amide, which is structurally related to SIINFEKL, an antigenic peptide used for stimulation of mouse ovalbumin specific CD8+ cells [13]). To obtain a clickable construct, a recently developed 7-membered ring strained alkyne, 3,3,6,6-tetramethylthiacycloheptyne sulfoximine (TMTHSI) was employed via standard solid-phase peptide synthesis (SPPS) to generate TMTHSI-SAAEWFEKL. The click entrapment of the TMTHSI-SAAEWFEKL construct is evaluated before and after NCL crosslinking using tryptophan fluorescence.

Materials and methods

Materials

All materials were obtained from Sigma Aldrich (Zwijndrecht, the Netherlands) unless indicated otherwise. The 2-(methoxy polyethylene glycol)-4,4-azobis(4-cyanopentanoic acid) ($mPEG_{5000})_2$-ABCPA) free radical macroinitiator was synthesized according to a previously published procedure. [14] *N*-2-hydroxypropyl methacrylamide monolactate ($HPMAmLac_1$) and dilactate ($HPMAmLac_2$) as well as 3,3,6,6-tetramethylthiacycloheptyne sulfoximine functionalized 4,4-difluoro-4-bora-3a,4a-diaza-s-indacene 650 (BODIPY-TMTHSI) were obtained by custom synthesis from Symeres (Nijmegen, the Netherlands). Dibenzocyclooctyne functionalized sulfonated cyanine 5 (Sulfo.Cy5-DBCO) was obtained from Lumiprobe (Hannover, Germany). All solvents were obtained from Biosolve (Valkenswaard, the Netherlands).

Synthesis

Trifunctional crosslinker synthesis

*Synthesis compound **1***: 1,3,5-tris(bromomethyl)benzene (15.0 g, 42.0 mmol) was dissolved in 30 mL DMF and the obtained solution was, after addition of sodium azide (4.1 g, 63.0 mmol), stirred for 16 hours at RT. The reaction mixture was then diluted with 150 mL ethyl acetate and filtered to remove precipitated sodium bromide. The filtrate was then washed (100 mL) twice with 0.1 M HCl, once with brine, dried over anhydrous sodium sulfate, concentrated using a rotavapor and residual solvent was removed under vacuum overnight at RT. The obtained oil was then dissolved in diethyl ether to which a few drops of methanol were added and after addition of silicagel adsorbed by evaporation in vacuo of the solvent. 1-(Azidomethyl)-3,5-bis(bromomethyl)benzene (compound **1**, Scheme 1) was obtained by two successive silica column purifications using 24:1 hexanes : diethyl ether as eluent (R_f = ~0.4 in 9:1 hexane : diethyl ether), yielding 3.6 gram (27%) of a faint yellow viscous liquid. ^{1}H NMR (400 MHz, chloroform-d): δ 7.39 (s, 1H), 7.28 (s, 2H), 4.47 (s, 4H), 4.37 (s, 2H). [12,15]

*Synthesis compound **2***: Intermediate compound **2** (di-tert-butyl (3-(azidomethyl)-5-((bis(tert-butoxycarbonyl)amino)methyl)benzyl)iminodicarbonate) was obtained by dissolving di-tert-butyl iminodicarboxylate (1.4 g, 6.6 mmol) and NaH (160 mg, 6.6 mmol) in 10 mL dry DMF in an ice bath, followed by the addition of compound **1** (1.0 g, 3.1 mmol) in 5 mL dry DMF and stirring for 16 hours at RT. The mixture was quenched with 70 mL saturated NH_4Cl solution whilst on an ice bath and extracted 3 times with 60 mL EtOAc. The organic layers were combined, washed (70 mL) twice with brine, dried

over anhydrous sodium sulfate and concentrated. Silica column purification was done using 1:1 hexanes : EtOAc as eluent (R_f = ~0.7), yielding 1.9 gram (100 %) of a white powder. ^{1}H NMR (400 MHz, chloroform-d): δ 7.18 (s, 1H), 7.10 (s, 2H), 4.74 (s, 4H), 4.27 (s, 2H), 1.43 (s, 36H).

*Preparation of **3** by removal of Boc-groups in compound **2**:* Compound **2** (1.7 g, 2.9 mmol) was subsequently deprotected to yield compound **3** (azidomethyl-3,5-di(aminomethyl) benzene) using 5 mL concentrated HCl in 25 mL methanol and stirring at RT for 1 hour. The mixture was concentrated, dissolved in 20 mL milliQ water and lyophilized overnight, yielding 0.7 g (95 % yield) of white solid. ^{1}H NMR (400 MHz, DMSO-d6): δ 8.66 (s, 6H), 7.61 (s, 1H), 7.51 (s, 2H), 4.48 (s, 2H), 3.99 (q, J = 5.8 Hz, 4H).

*Synthesis compound **4**:* Boc-Cys(Acm)-OH residues were coupled to the crude compound **3** (320 mg, 1.2 mmol) to obtain the protected form of the dicysteine crosslinker, compound **4**. Boc-Cys(Acm)-OH (780 mg, 2.7 mmol) was dissolved in 10 mL dry DMSO together with hexafluorophosphate azabenzotriazole tetramethyl uronium (HATU) (1.0 g, 2.7 mmol) and the mixture was stirred for 15 minutes. Compound **3** was dissolved in 5 mL dry DMSO followed by *N*,*N*-diisopropylethylamine (DIPEA) (4.2 mL, 24.2 mmol) and added and the HATU reaction mixture, which was then stirred for 2 hours at RT. The mixture was diluted with 35 mL chloroform, washed (30 mL) thrice with 0.1 M HCl, twice with saturated $NaHCO_3$, once with brine, dried over anhydrous sodium sulfate, concentrated using a rotavapor and dried under vacuum overnight. The obtained solid was dissolved in methanol, dispersed and subsequently concentrated in silica gel and purified by silica column chromatography employing 9:1 DCM : MeOH as eluent (R_f = ~0.5), yielding 0.89 g (99 % yield). ^{1}H NMR (400 MHz, DMSO-d6): δ 8.46 (t, J = 6.2 Hz, 2H), 8.36 (t, J = 6.0 Hz, 2H), 7.16 – 7.09 (m, 3H), 6.96 (d, J = 8.4 Hz, 2H), 4.38 (s, 2H), 4.31 – 4.11 (m, 10H), 2.94 – 2.61 (m, 4H), 1.80 (s, 6H), 1.37 (s, 18H). ESI-MS: Expected mass for $C_{31}H_{49}N_9O_8S_2Na^+$ was 762.3, found 761.4.

*Acetamidomethyl (Acm) deprotection of compound **4**:* Compound **4** was deprotected to obtain the disulfide crosslinker compound **5**. For this, compound **4** (300 mg, 0.41 mmol) was dissolved in 9 mL methanol. To this solution, 18 mL 0.1 M HCl and subsequently 9 mL 0.4 M I_2 in methanol were added to remove the thiol Acm protecting groups. The reaction mixture was stirred for 30 minutes at RT, after which excess iodine was removed by addition of 1 M aqueous ascorbic acid solution until the solution turned to a white suspension. Chloroform was added to the mixture and concentrated on a rotavapor at 40°C. The formed white product precipitate was vacuum filtered. Additional chloroform and water were added to wash the precipitate and this filter process was repeated 5 times

and finally the precipitate was dried under vacuum. ^{1}H NMR (400 MHz, DMSO-d6): δ 8.46 (s, 2H), 7.15 – 7.00 (m, 5H), 4.34 (s, 2H), 4.30 – 4.16 (m, 6H), 3.13 – 2.79 (m, 4H), 1.36 (s, 18H).

*Deprotection of compound **4**:* To remove the Boc protecting group, the precipitate was dissolved in 3 mL hexafluoro isopropanol (HFIP), followed by 3 mL isopropyl alcohol and 4 mL concentrated HCl. After 10 minutes of stirring, 100 mL diethyl ether was added and the precipitate filtered and washed with additional diethyl ether and finally dried under vacuum, yielding 160 mg (85% relative to compound **4**) of a fine white crystalline powder (compound **5**). ^{1}H NMR (400 MHz, DMSO-d6) δ 9.22 (s, 2H), 8.48 (s, 6H), 7.20 (s, 1H), 7.17 (s, 2H), 4.41 (s, 2H), 4.30 – 3.92 (m, 6H), 3.40 – 2.98 (m, 4H). HR-MS: Expected mass for $C_{15}H_{22}N_7O_2S_2^+$ is 396.1271, found 396.1271.

Solid phase peptide synthesis of SAAEWFEKL-NH_2

Synthesis of the model peptide amide SAAEWFEKL was performed by microwave solid phase peptide synthesis (SPPS) in a Liberty Blue™ peptide synthesizer (CEM Corp., Matthews, NC, USA) following a standard Fmoc/tBu protocol on a 0.1 mmol scale. A high swelling Tentagel® XV rink amide resin (loading 0.2-0.4 mmol/g) (Rapp Polymere, Tuebingen, Germany) was employed as solid support. Standard couplings of amino acids were performed at 0.2 M in dimethyl formamide (DMF) using DIC/OxymaPure® activation, with the first lysine loaded in a double coupling procedure (the coupling method used was optimized to the corresponding amino acid according to the recommended operation of Liberty Blue™). Fmoc removal was carried out using 20 % piperidine in DMF. Modification of SAAEWFEKL with the click handle TMTHSI was carried out before cleavage/final deprotection from the solid support.

TMTHSI-SAAEWFEKL conjugate synthesis

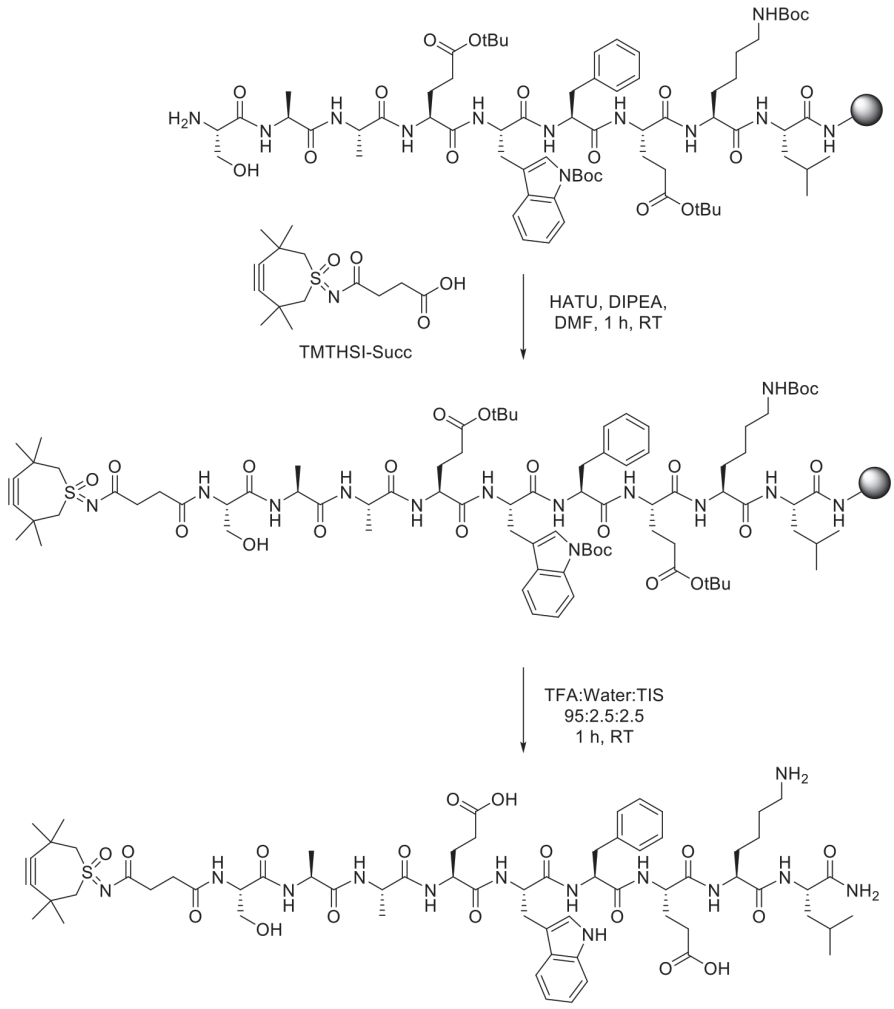

Scheme 1: On-the-resin synthesis of TMTHSI-SAAEWFEKL with N-terminal selective modification.

The coupling of TMTHSI to resin bound SAAEWFEKL was performed to obtain selective N-terminal conjugation. About 40 µmol of resin content was suspended in 3 mL DMF followed by DIPEA (42 µL, 240 µmol). TMTHSI-succinic acid derivative (12 mg, 40 µmol) and HATU (17 mg, 44 µmol) was dissolved in 2 mL DMF and added to the resin. After stirring for 1 hour at RT, the resin was washed 3 times with 10 mL DMF, 3 times 10 mL DCM and shortly dried under nitrogen flow. The peptide conjugate was then cleaved/deprotected by stirring for 1 hour using 5 mL trifluoroacetic acid (TFA)

: triisopropylsilane (TIS) : water, 95:2.5:2.5 (v/v/v). Following filtration, the crude peptide was precipitated in 45 mL cold diethyl ether, centrifuged, washed with diethyl ether, dried under nitrogen flow, dissolved in milliQ water : acetonitrile (ACN) 1:1 and lyophilized. MALDI-MS: Expected mass for $C_{65}H_{94}N_{13}O_{17}S^+$ is 1360.66, found 1360.40, 1382.39 (Na^+ adduct) and 1399.36 (K^+ adduct).

Core-crosslinked polymeric micelle (CCPM) formation

The thermosensitive diblock co-polymer and subsequently CCPMs were synthesized as described previously [12] (**Chapter 4**), utilizing the 15% ETSA feed polymer $mPEG_{5000}$-*b*-P(HPMAmLac$_n$-*co*-HPMAmLac$_n$-ETSA) (**P100-E15**). However, here the crosslinker as an HCl salt (compound **5**) with the improved synthesis was employed for CCPM formation, employing identical equivalencies as described in **Chapter 4**.

SAAEWFEKL entrapped CCPMs

Two approaches were investigated to click-entrap TMTHSI-SAAEWFEKL into the azide containing CCPMs, both aiming at a 10% weight loading of peptide to polymer.

The first approach involves the clicking of TMTHSI-SAAEWFEKL to the crosslinker (compound **5**) before the NCL crosslinking reaction. Crosslinker **5** (1.6 mg, 3.4 µmol, to match equimolar cysteine to ETSA groups in the polymer) was dissolved in DMSO to 75 mg/mL and TMTHSI-SAAEWFEKL (2.0 mg, 1.5 µmol, to attain 10 % weight feed to polymer) in phosphate buffer (100 mM Na_2HPO_4, adjusted to pH 7.4 using HCl) to 20 mg/mL and the two were mixed for 10 minutes at RT. A 10% weight feed of peptide to polymer was selected as an ambitious loading target whilst also ensuring an excess of azides (2-fold). Then, TCEP (2.5 mg, 10 µmol) dissolved in phosphate buffer to 112.5 mg/mL was added, the mixture transferred into an ice cold solution of P100-E15 (20 mg, 15.8 kDa, 1.3 µmol polymer chains, 6.5 µmol ETSA handles) in phosphate buffer at 20 mg/mL and heated to 37 ^oC. After 1 hour of crosslinking, the obtained CCPMs were filtered using 0.2 µm RC syringe filters (rinsed with additional phosphate buffer resulting in a 2-fold dilution) and subsequently purified using a G-25 sephadex packed 5 mL HiTrap desalting column with an M_w cutoff of 5000 Da (GE healthcare, Uppsala, Sweden).

In the second approach, CCPMs were formed and purified first, and TMTHSI-SAAEWFEKL was added afterwards. The same CCPM formation procedure as described above was followed and TMTHSI-SAAEWFEKL (0.75 mg, 0.60 µmol, to also attain 10 % weight feed to polymer), dissolved in phosphate buffer (100 mM Na_2HPO_4, adjusted to pH 7.4 using HCl) to 20 mg/mL, was added to the purified CCPMs

(having a concentration of 7.5 mg/mL). This results in the same molar ratio of peptide to crosslinker as employed in the approach above. No further purification was conducted.

Crosslinker, polymer and particle characterization

Nuclear magnetic resonance (NMR) spectroscopy

^{1}H, ^{13}C and ^{1}H-^{13}C heteronuclear single quantum correlation (HSQC) NMR spectra were recorded on an Agilent 400-MR NMR spectrometer (Agilent Technologies, Santa Clara, USA). Residual solvent peaks of $CDCl_3$ (δ = 7.26 ppm) or D_6 DMSO (δ = 2.50 ppm) were used to calibrate chemical shifts.

Mass spectrometry (MS)

Matrix assisted laser desorption ionization (MALDI)-MS were performed on a Ultraflextreme (Bruker), employing α-cyano-4-hydroxycinnamic acid (HCCA) as matrix. Spotting was done by 1 µL of sample followed by 1 µL of matrix solution (saturated solution of HCCA in 30:70 v/v acetonitrile : water, supplemented with 0.1% TFA) and drying under N_2 flow. Azide reactivity of TMTHSI-SAAEWFEKL was confirmed by addition of 1 µL benzyl azide solution (0.5M in DCM, Sigma) to the sample before spotting onto the MALDI plate.

Thin layer chromatography (TLC)

TLC was carried out using aluminum bound silica plates obtained from Merck Darmstadt (SiO_2, Kieselgel 60 F254). Compounds were visualized by UV detection at 254 nm and, where applicable, stained with ninhydrin in DCM to visualize amines/amides or 10% triphenylphosphine in DCM followed by ninhydrin to visualize azides.

High performance liquid chromatography (HPLC)

HPLC analysis was performed using an Alliance 2695 chromatography system with an Xbridge C18 column (5 µm, 4.6 x 150 mm, Waters) at a column temperature of 30 °C and employing an Alliance 2487 ultra-violet (UV) detector at 210 and 650 or 700 nm. Acetonitrile/water supplemented with either 0.1% perchloric acid or 0.1% formic acid was used as eluent at a flow of 1 mL/min and a gradient of 5 to 95% ACN over 20 minutes.

Dynamic light scattering (DLS).

The size of the CCPMs was determined by DLS using a Malvern Zetasizer nano series ZS90 with a measurement angle of 90°. Measurements were typically carried out at 2,

25 and 37 °C. Unless stated otherwise, the concentration of the micellar dispersions was approximately 7.5 mg/mL in phosphate buffer (100 mM Na_2HPO_4, adjusted to pH 7.4 using HCl).

Results and discussion

The click entrapment of a model peptide into CCPMs was investigated, comparing a conventional approach where the click reaction to an azide containing crosslinker is carried out before CCPM formation to an alternative approach where CCPMs are formed first and the peptide is entrapped via click conjugation afterwards.

Optimized trifunctional crosslinker synthesis

We improved on a previously reported [12] (**Chapter 4**) synthesis of a trifunctional crosslinker containing two cysteine residues and one azide residue (see scheme 1 for the route described in this work). The initial step to obtain compound **1** through statistical nucleophilic substitution of tribromomethyl benzene by sodium azide and extensive flash chromatography purification was kept the same as described previously, with a comparable yield being obtained (27% currently vs 29% obtained previously). Higher yields than this are unlikely to be achievable given that the target molecule requires substitution of only one out of three electrophilic sites. Fortunately, this lowest yielding step is the first to be carried out with relatively cheap reagents and therefore large quantities can be employed. It was therefore of interest to optimize the yields of the subsequent steps to obtain the trifunctional crosslinker (previously 60% from compound **1** till crosslinker).

Previously, the amine introduction of 1-(azidomethyl)-3,5-bis(bromomethyl)benzene (compound **1**) to azidomethyl-3,5-di(aminomethyl)benzene (compound **3**) was conducted via a Gabriel synthesis [16] using potassium phthalimide. High yields (94%) of the intermediate compound (azidomethyl-3,5-di(phthalamidomethyl)benzene) were obtained previously. However, the subsequent phthalimide deprotection by use of hydrazine resulted in excessive mass loss due to the presence of inorganic salt impurities that could not be removed given the hydrophilicity of compound **3**. The yield could therefore only be reported over 2 steps resulting in compound **4**, which was 70% relative to the phthalimide intermediate.

Here, we opted for an alternative Gabriel reagent by use of di-tert-butyl iminodicarboxylate [17] which allows for much milder (such as lower temperature) deprotection conditions and avoiding the use of hydrazine (which is likely responsible for the impurities observed

previously). The initial nucleophilic substitution of the bromo-alkane (compound **1**) is achieved through sodium hydride activation of di-tert-butyl iminodicarboxylate (resulting in deprotonation of the amine) followed by addition of compound **1** and resulted in a quantitative yield (100%, figure S1.1). The subsequent deprotection of the diboc groups in compound **2** could then be carried out in MeOH/HCl at room temperature, after which compound **3** was isolated by lyophilization, resulting in an almost quantitative yield (95%, figure S1.2). The HATU coupling of protected cysteine to obtain compound **4** (figure S1.3) resulted in a quantitative yield (99%) with reaction time having been significantly reduced (2 hours currently vs 16 hours previously). The yield for the conversion of compound **2** to compound **4** here was 94% (as compared to the 70% obtained previously using the phthalimide approach).

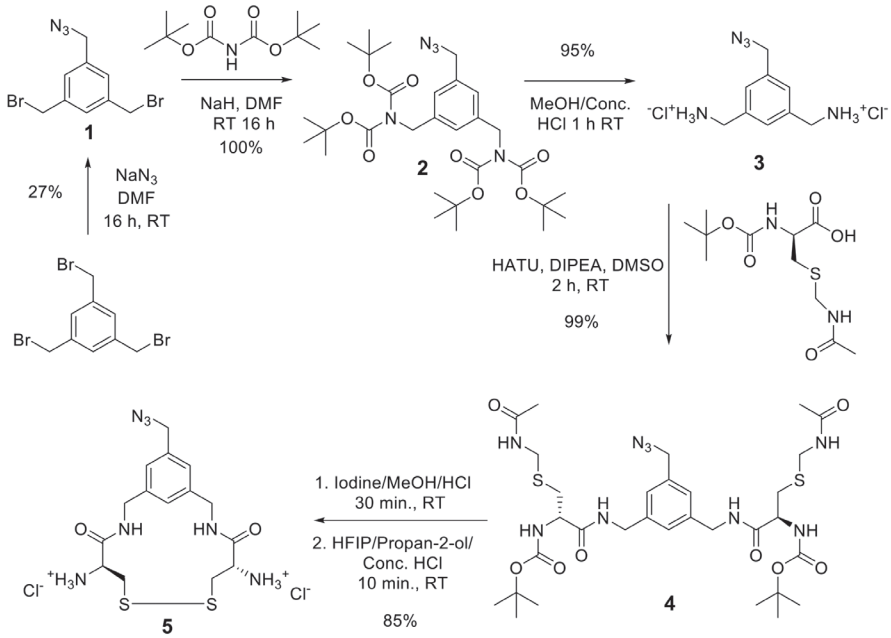

*Scheme 2: Synthesis of the azide containing di-cysteine trifucntional crosslinker (Compound **5**).*

We proceeded with the initial deprotection of the acetamidomethyl (Acm) groups of compound **4** using the same conditions described previously, but with 30 minutes instead of 1 hour reaction time (figure S1.4). Finally, the tert-butoxycarbonyl (Boc) deprotection was done by addition of HFIP and propan-2-ol for solubilization of the disulfide intermediate followed by concentrated HCl resulting in cleavage of the Boc group (see figure S1.5) over 10 minutes (instead of DCM/trifluoroacetic acid/water employed

previously for 1 hour). Following solvent removal under vacuum, a fine crystalline white powder was obtained as an HCl salt that is easier to handle when weighing in place of the yellowish crystalline solid trifluoroacetate salt obtained previously, with a comparable yield (85% currently vs 91% previously).

The overall yield for the conversion of the difficult to obtain 1-(azidomethyl)-3,5-bis(bromomethyl)benzene (compound **1**) to the trifunctional crosslinker (compound **5**) using the new synthesis route is therefore 80% as compared to 60% obtained previously, which is a significant improvement.

TMTHSI-SAAEWFEKL synthesis

The described stability of the TMTHSI click handle towards TFA deprotection conditions [18] allows for on the resin conjugation of this click handle and subsequent selective N-terminal modification of peptides (Fmoc deprotected N-terminus, protected side chains whilst on the resin). To confirm this, we synthesized a model peptide structurally related to the well-studied antigen SIINFEKL[19] whose sequence we altered to minimize the risk of peptide nanofiber formation that has recently been described (this would potentially hamper entrapment in nanoparticles). [20] The sequence SAAEWFEKL was selected, eliminating the possibility of β-sheet stacking and also incorporating a tryptophan residue that allows detection of this model peptide by fluorescence. [21] We employed a 1:1 equivalency ratio of TMTHSI-succinimide to expected peptide content on the resin following SPPS and used straightforward HATU coupling for the amide bond formation. Following peptide cleavage/deprotection, precipitation and lyophilization, no further purification steps were undertaken and the identity confirmed by MALDI-MS (figure S2.1) with no significant detection of unreacted SAAEWFEKL, demonstrating complete conjugation. Additionally, >80% purity was confirmed by HPLC which is acceptable given no further purification was carried out (see figure 1). To confirm that reactivity of the TMTHSI handle towards azides was preserved, benzyl azide (in large excess) was added to TMTHSI-SAAEWFEKL and complete conversion (>95%) of the click reaction was observed by MALDI-MS (figure S2.2). These results confirm that TMTHSI survives SPPS cleavage conditions and can be employed for N-terminal peptide modification. [22]

CCPM formation and TMTHSI-SAAEWFEKL entrapment

The two approaches followed to form CCPMs and entrap TMTHSI-SAAEWFEKL are depicted in scheme 3. Approach A) will hereon be referred to as before crosslink and approach B) as after crosslink. The before crosslink approach follows a conventional

procedure previously described for the entrapment of fluorescent dyes (chapter **4**), [12] generating an intermediate of crosslinker-TMTHSI-SAAEWFEKL in addition to the excess crosslinker, which was confirmed by mass spectrometry (see figure S2.3). Following mixing with the dissolved polymer and micellization upon increase in temperature, CCPMs loaded with SAAEWFEKL were generated as can be seen by the HPLC chromatogram recording tryptophan fluorescence [21] in figure 1 (red). Additionally, no free TMTHSI-SAAEWFEKL was detected, which is both due to complete entrapment (>95%) at a 10% weight of peptide to polymer feed, and due to effective purification by size exclusion (see figure 1).

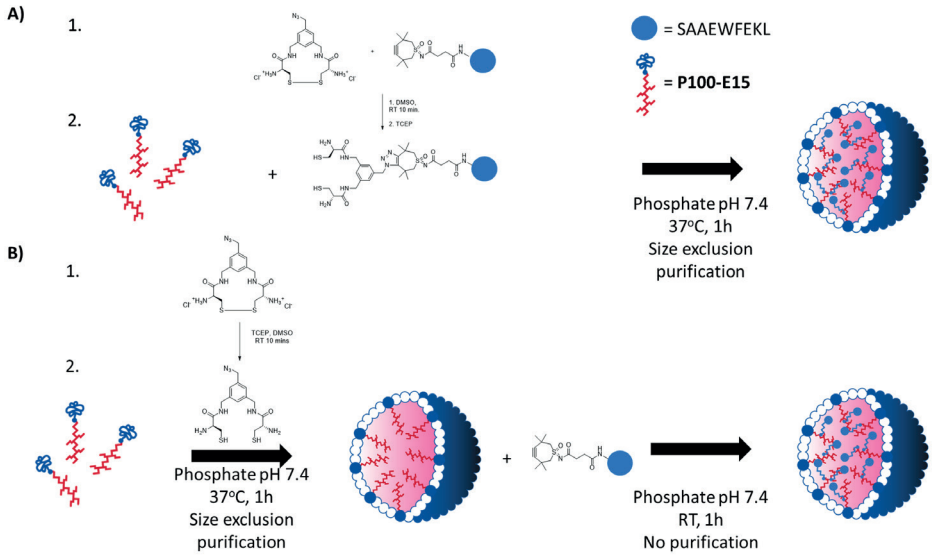

*Scheme 3: CCPM formation and click entrapment of TMTHSI-SAAEWFEKL either by A) clicking of the crosslinker (**5**) to TMTHSI-SAAEWFEKL followed by disulfide reduction, mixing with polymer **P100-E15**, micellization and crosslinking or B) disulfide reduction of crosslinker, CCPM formation with crosslinker (**5**) and polymer **P100-E15** followed by purification and finally addition of TMTHSI-SAAEWFEKL. No final purification step was carried out in approach B).*

Using the after crosslink approach, CCPMs were formed by mixing of the dissolved polymer with reduced crosslinker and micellization upon increase in temperature. The CCPMs were then purified by size exclusion to remove any remaining ethyl thioglycolate (a side product of the NCL reaction with a free thiol that could react with a ring strained alkyne) [23]. The core-azide containing CCPMs were then stirred with TMTHSI-SAAEWFEKL (adjusted to match the equivalents relative to polymer/ crosslinker of the before crosslink approach) at room temperature and analyzed by

HPLC without further purification (figure 1, orange). Remarkably, CCPMs with a similar retention time to the before crosslink approach were obtained with a potentially even higher fluorescent signal, with >95% entrapment of TMTHSI-SAAEWFEKL (<5% free TMTHSI-SAAEWFEKL remaining in the chromatogram). This suggests not only that clicking of a peptide structure after CCPM formation is as efficient as the click before crosslink approach, even at the feed of peptide employed which was 10% weight relative to polymer. Since a non-cleavable linkage was employed, no release of peptide could be studied to directly assess loading.

DLS measurements were carried out and the results are shown in table 1. No significant differences in hydrodynamic diameter as well as polydispersity (PDI) between empty and both types of loaded CCPMs were observed. The light scattering intensity of loaded CCPMs was slightly higher than that of the empty, the highest being the after crosslink loaded CCPMs (synthesis was done once, DLS carried out with 3 repeat measurements). This is likely due to an increase in specific refractive index increment as a result of increased density of the core.

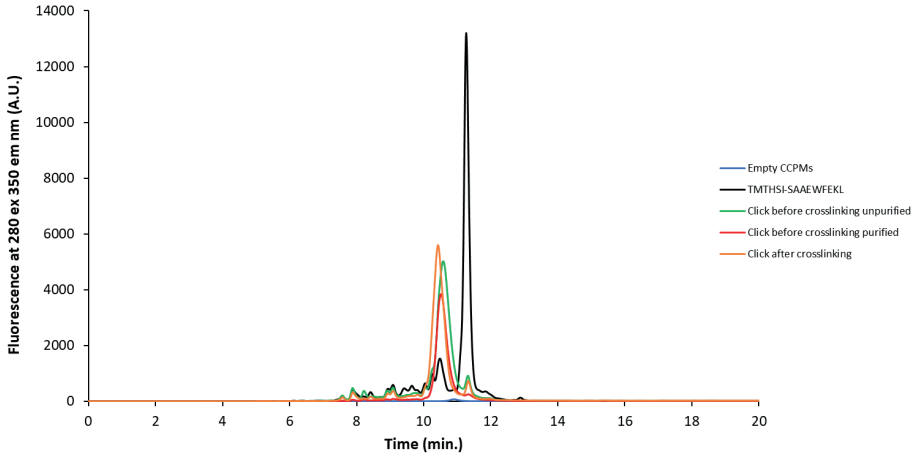

Figure 1: HPLC chromatograms of empty CCPMs (blue), free TMTHSI-SAAEWFEKL (black), CCPMs loaded with SAAEWFEKL with the before crosslink click approach (red), including a sample before purification by size exclusion (green) and after crosslinking (orange). Recorded with $\lambda_{ex}/\lambda_{em}$ 280/350 nm fluorescence. The higher fluorescence of CCPMs clicked after crosslinking may also be resulting from co-elution with an overlapping peak at R_t = 10.5 in the TMTHSI-SAAEWFEKL sample.

Table 1: DLS measurements of SAAEWFEKL loaded CCPMs formed via the two approaches. The average of 3 repeat measurements is reported.

Sample Name	Temperature °C	Z-Average d.nm	PDI	Derived Count Rate kcps
Empty CCPMs	25	50	0.06	7161
Before crosslink SAAEWFEKL CCPMs	25	51	0.04	7778
After crosslink SAAEWFEKL CCPMs	25	53	0.04	8433

Conclusion

In an effort to expand the range of chemistries available for the entrapment of therapeutic cargos into CCPMs, we explored whether a model peptide could be click entrapped into a previously described CCPMs based on NCL with a before and after crosslink approach. We improved the synthesis of the crosslinker employed in the generation of NCL based CCPMs which was employed to answer this research question. Both approaches (before and after crosslinking) were found to be effective for the entrapment of TMTHSI-SAAEFEKL with loaded CCPMs retaining a similar size as compared to empty CCPMs. A >95% entrapment efficiency was obtained for both the click before and after crosslink approach, which is surprisingly effective considering a feed of 10 weight% of peptide to polymer was employed. The advantage of clicking into already formed CCPMs is that other crosslinking chemistries (such as free radical chemistry [24]) that would otherwise be damaging to the cargo could be employed for CCPM formation and entrapment would still be possible, which is a significant shift in synthetic procedures. It will therefore be of interest to develop cleavable linkers that can be incorporated using this click approach to entrap therapeutic peptides.

Conflicts of interest

The authors declare that there is no conflict of interest.

Acknowledgements

The Dutch Research Council (NWO) and Cristal Therapeutics are acknowledged for funding (NWA.ID.17.030).

References

(1) Varela-Moreira, A.; Shi, Y.; Fens, M. H. A. M.; Lammers, T.; Hennink, W. E.; Schiffelers, R. M. Clinical application of polymeric micelles for the treatment of cancer. *Mater. Chem. Front.* **2017**, *1* (8), 1485–1501, DOI: 10.1039/c6qm00289g.

(2) Cabral, H.; Miyata, K.; Osada, K.; Kataoka, K. Block Copolymer Micelles in Nanomedicine Applications. *Chem. Rev.* **2018**, *118* (14), 6844–6892, DOI: 10.1021/acs.chemrev.8b00199.

(3) Ghezzi, M.; Pescina, S.; Padula, C.; Santi, P.; Del Favero, E.; Cantù, L.; Nicoli, S. Polymeric micelles in drug delivery: An insight of the techniques for their characterization and assessment in biorelevant conditions. *J. Control. Release* **2021**, *332* (February), 312–336, DOI: 10.1016/j.jconrel.2021.02.031.

(4) Fang, J.; Nakamura, H.; Maeda, H. The EPR effect: Unique features of tumor blood vessels for drug delivery, factors involved, and limitations and augmentation of the effect. *Adv. Drug Deliv. Rev.* **2011**, *63* (3), 136–151, DOI: 10.1016/j.addr.2010.04.009.

(5) Nishiyama, N.; Kataoka, K. Current state, achievements, and future prospects of polymeric micelles as nanocarriers for drug and gene delivery. *Pharmacol. Ther.* **2006**, *112* (3), 630–648, DOI: 10.1016/j.pharmthera.2006.05.006.

(6) Talelli, M.; Barz, M.; Rijcken, C. J. F.; Kiessling, F.; Hennink, W. E.; Lammers, T. Core-crosslinked polymeric micelles: Principles, preparation, biomedical applications and clinical translation. *Nano Today* **2015**, *10* (1), 93–117, DOI: 10.1016/j.nantod.2015.01.005.

(7) Fan, W.; Zhang, L.; Li, Y.; Wu, H. Recent Progress of Crosslinking Strategies for Polymeric Micelles with Enhanced Drug Delivery in Cancer Therapy. *Curr. Med. Chem.* **2019**, *26* (13), 2356–2376, DOI: 10.2174/0929867324666171121102255.

(8) van Nostrum, C. F. Covalently cross-linked amphiphilic block copolymer micelles. *Soft Matter* **2011**, *7* (7), 3246, DOI: 10.1039/c0sm00999g.

(9) Talelli, M.; Iman, M.; Varkouhi, A. K.; Rijcken, C. J. F.; Schiffelers, R. M.; Etrych, T.; Ulbrich, K.; van Nostrum, C. F.; Lammers, T.; Storm, G.; Hennink, W. E. Core-crosslinked polymeric micelles with controlled release of covalently entrapped doxorubicin. *Biomaterials* **2010**, *31* (30), 7797–7804, DOI: 10.1016/j.biomaterials.2010.07.005.

(10) Hu, Q.; Rijcken, C. J.; Bansal, R.; Hennink, W. E.; Storm, G.; Prakash, J. Complete regression of breast tumour with a single dose of docetaxel-entrapped core-cross-linked polymeric micelles. *Biomaterials* **2015**, *53*, 370–378, DOI: 10.1016/j.biomaterials.2015.02.085.

(11) Meng, X.; Gao, M.; Deng, J.; Lu, D.; Fan, A.; Ding, D.; Kong, D.; Wang, Z.; Zhao, Y. Self-immolative micellar drug delivery: The linker matters. *Nano Res.* **2018**, *11* (12), 6177–6189, DOI: 10.1007/s12274-018-2134-5.

(12) Hebels, E. R.; Bindt, F.; Walther, J.; van Geijn, M.; Weterings, J.; Hu, Q.; Colombo, C.; Liskamp, R.; Rijcken, C.; Hennink, W. E.; Vermonden, T. Orthogonal Covalent Entrapment of Cargo into Biodegradable Polymeric Micelles via Native Chemical Ligation. *Biomacromolecules* **2023**, *24* (10), 4385–4396, DOI: 10.1021/acs.biomac.2c00865.

(13) Dersh, D.; Yewdell, J. W.; Wei, J. A SIINFEKL-Based System to Measure MHC Class I Antigen Presentation Efficiency and Kinetics. In *Methods in Molecular Biology*; 2019; Vol. 1988, pp 109–122, DOI: 10.1007/978-1-4939-9450-2_9.

(14) Bagheri, M.; Bresseleers, J.; Varela-Moreira, A.; Sandre, O.; Meeuwissen, S. A.; Schiffelers, R. M.; Metselaar, J. M.; Van Nostrum, C. F.; Van Hest, J. C. M.; Hennink, W. E. Effect of Formulation and Processing Parameters on the Size of mPEG- b-p(HPMA-Bz) Polymeric Micelles. *Langmuir* **2018**, *34* (50), 15495–15506, DOI: 10.1021/acs.langmuir.8b03576.

(15) Werkhoven, P. R.; van de Langemheen, H.; van der Wal, S.; Kruijtzer, J. A. W.; Liskamp, R. M. J. Versatile convergent synthesis of a three peptide loop containing protein mimic of whooping cough pertactin by successive Cu(I)-catalyzed azide alkyne cycloaddition on an orthogonal alkyne functionalized TAC-scaffold. *J. Pept. Sci.* **2014**, *20* (4), 235–239, DOI: 10.1002/psc.2624.

(16) Gibson, M. S.; Bradshaw, R. W. The Gabriel Synthesis of Primary Amines. *Angew. Chemie Int. Ed. English* **1968**, *7* (12), 919–930, DOI: 10.1002/anie.196809191.

(17) Ragnarsson, U.; Grehn, L. Novel Gabriel reagents. *Acc. Chem. Res.* **1991**, *24* (10), 285–289, DOI: 10.1021/ar00010a001.

(18) Weterings, J.; Rijcken, C. J. F.; Veldhuis, H.; Meulemans, T.; Hadavi, D.; Timmers, M.; Honing, M.; Ippel, H.; Liskamp, R. M. J. TMTHSI, a superior 7-membered ring alkyne containing reagent for strain-promoted azide–alkyne cycloaddition reactions. *Chem. Sci.* **2020**, *11* (33), 9011–9016, DOI: 10.1039/D0SC03477K.

(19) Li, D.; Kordalivand, N.; Fransen, M. F.; Ossendorp, F.; Raemdonck, K.; Vermonden, T.; Hennink, W. E.; van Nostrum, C. F. Reduction-Sensitive Dextran Nanogels Aimed for Intracellular Delivery of Antigens. *Adv. Funct. Mater.* **2015**, *25* (20), 2993–3003, DOI: 10.1002/adfm.201500894.

(20) Kamalov, M.; Kählig, H.; Rentenberger, C.; Müllner, A. R. M.; Peterlik, H.; Becker, C. F. W. Ovalbumin Epitope SIINFEKL Self-Assembles into a Supramolecular Hydrogel. *Sci. Rep.* **2019**, *9* (1), 2696, DOI: 10.1038/s41598-019-39148-8.

(21) Ghisaidoobe, A.; Chung, S. Intrinsic Tryptophan Fluorescence in the Detection and Analysis of Proteins: A Focus on Förster Resonance Energy Transfer Techniques. *Int. J. Mol. Sci.* **2014**, *15* (12), 22518–22538, DOI: 10.3390/ijms151222518.

(22) Timmers, M.; Kipper, A.; Frey, R.; Notermans, S.; Voievudskyi, M.; Wilson, C.; Hentzen, N.; Ringle, M.; Bovino, C.; Stump, B.; Rijcken, C. J. F.; Vermonden, T.; Dijkgraaf, I.; Liskamp, R. Exploring the Chemical Properties and Medicinal Applications of Tetramethylthiocycloheptyne Sulfoximine Used in Strain-Promoted Azide–Alkyne Cycloaddition Reactions. *Pharmaceuticals* **2023**, *16* (8), 1155, DOI: 10.3390/ph16081155.

(23) van Geel, R.; Pruijn, G. J. M.; van Delft, F. L.; Boelens, W. C. Preventing Thiol-Yne Addition Improves the Specificity of Strain-Promoted Azide–Alkyne Cycloaddition. *Bioconjug. Chem.* **2012**, *23* (3), 392–398, DOI: 10.1021/bc200365k.

(24) Hu, Q.; Rijcken, C. J. F.; van Gaal, E.; Brundel, P.; Kostkova, H.; Etrych, T.; Weber, B.; Barz, M.; Kiessling, F.; Prakash, J.; Storm, G.; Hennink, W. E.; Lammers, T. Tailoring the physicochemical properties of core-crosslinked polymeric micelles for pharmaceutical applications. *J. Control. Release* **2016**, *244*, 314–325, DOI: 10.1016/j.jconrel.2016.07.012.

Supporting information

NMR spectra

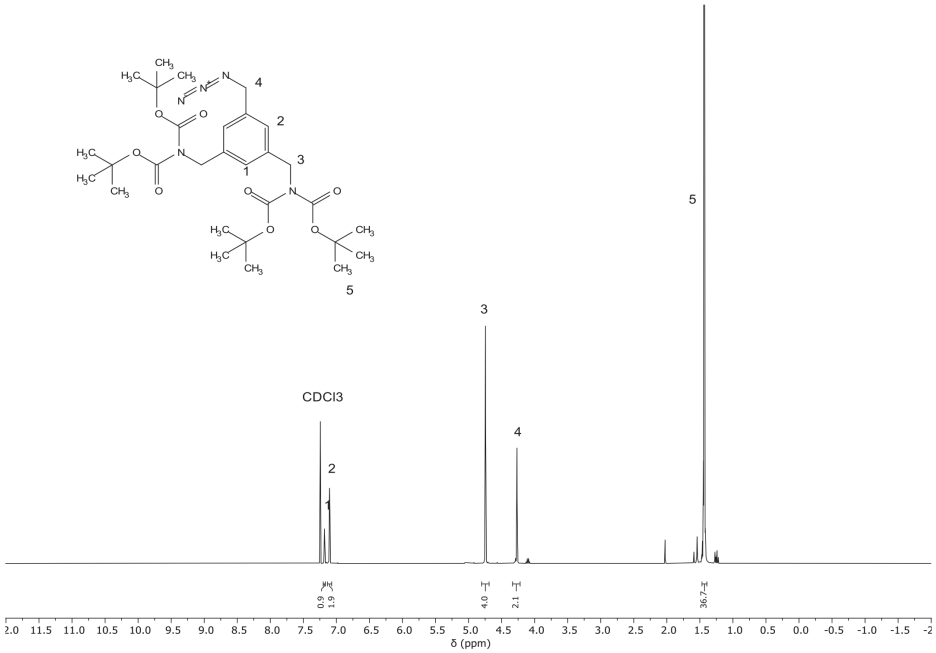

Figure S1.1: [1]H NMR spectrum of compound ***2*** *(di-tert-butyl (3-(azidomethyl)-5-((bis(tert-butoxycarbonyl)amino)methyl)benzyl)iminodicarbonate). The solvent was* $CDCl_3$.

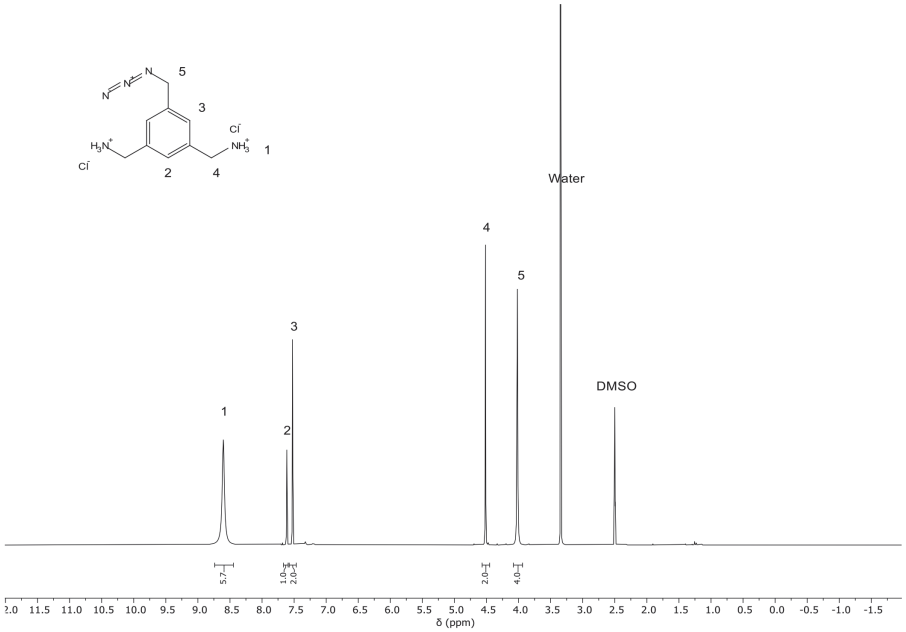

*Figure S1.2: [1]H NMR spectrum of compound **3** (azidomethyl-3,5-di(aminomethyl)benzene). The solvent was DMSO-d6.*

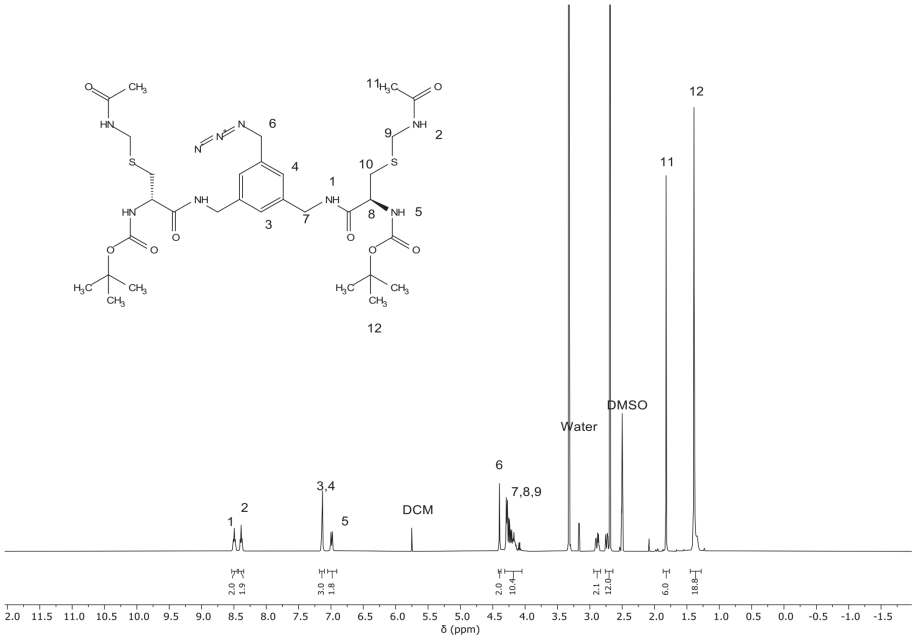

*Figure S1.3: [1]H NMR spectrum of compound **4**. The solvent was DMSO-d6.*

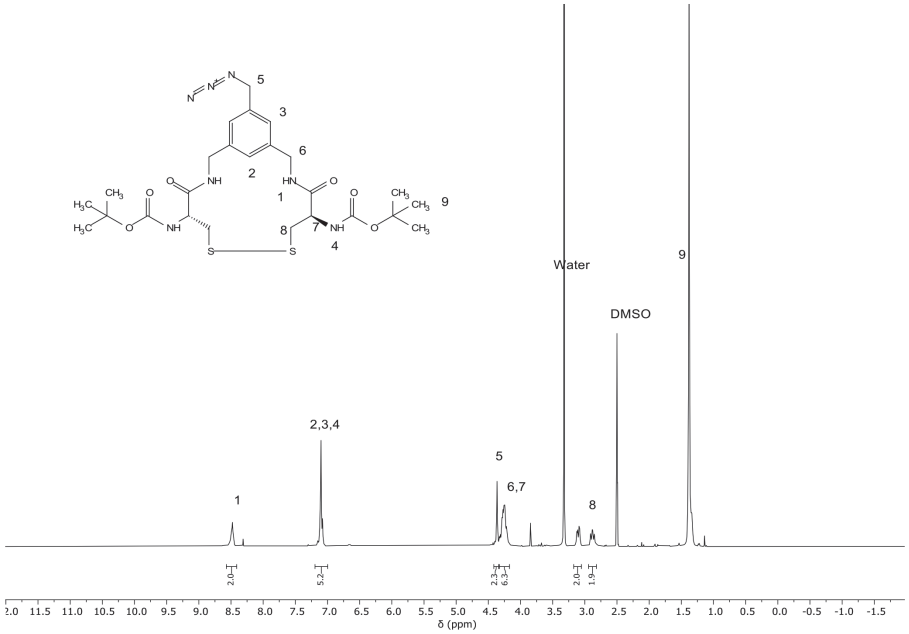

*Figure S1.4: [1]H NMR spectrum of Acm deprotected compound **4**. The solvent was DMSO-d6.*

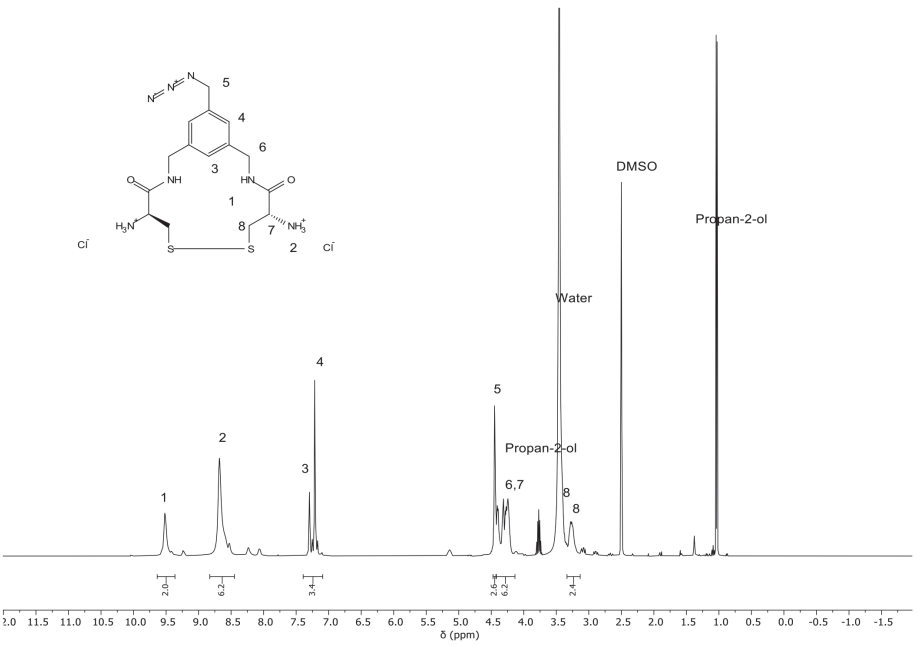

*Figure S1.5: [1]H NMR spectrum of compound **5**. The solvent was DMSO-d6.*

2. Mass spectrometry spectra

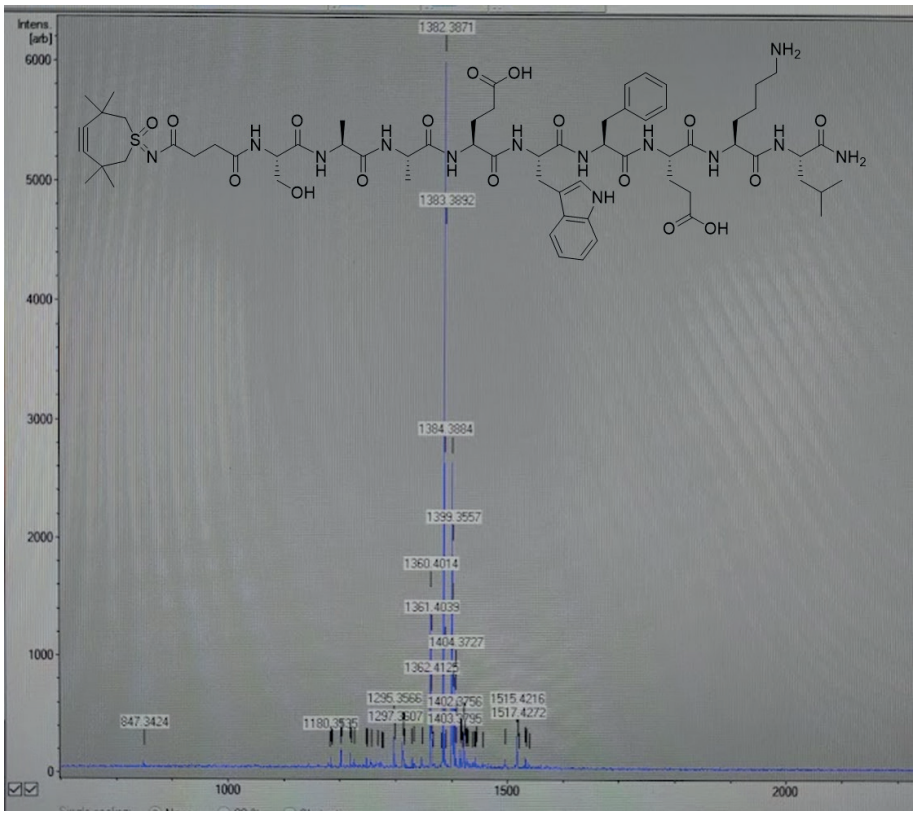

Figure S2.1: MALDI-MS spectrum of TMTHSI-SAAEWFEKL (structure shown). Expected mass for $C_{65}H_{94}N_{13}O_{17}S^+$ is 1360.66, found 1360.40, 1382.39 (Na^+ adduct) and 1399.36 (K^+ adduct).

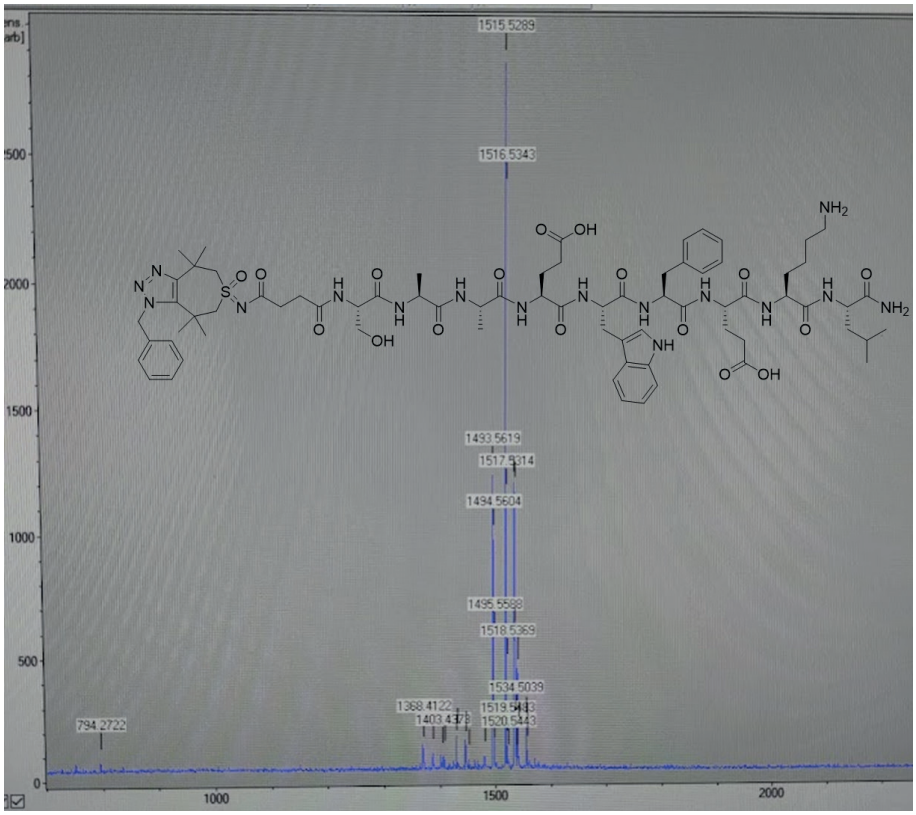

Figure S2.2: MALDI-MS spectrum of TMTHSI-SAAEWFEKL reacted with added benzyl azide to confirm functionality of the click handle (structure shown). Expected mass for $C_{72}H_{101}N_{16}O_{17}S^{+}$ is 1493.72 found 1493.56 and 1515.53 (Na^{+} adduct).

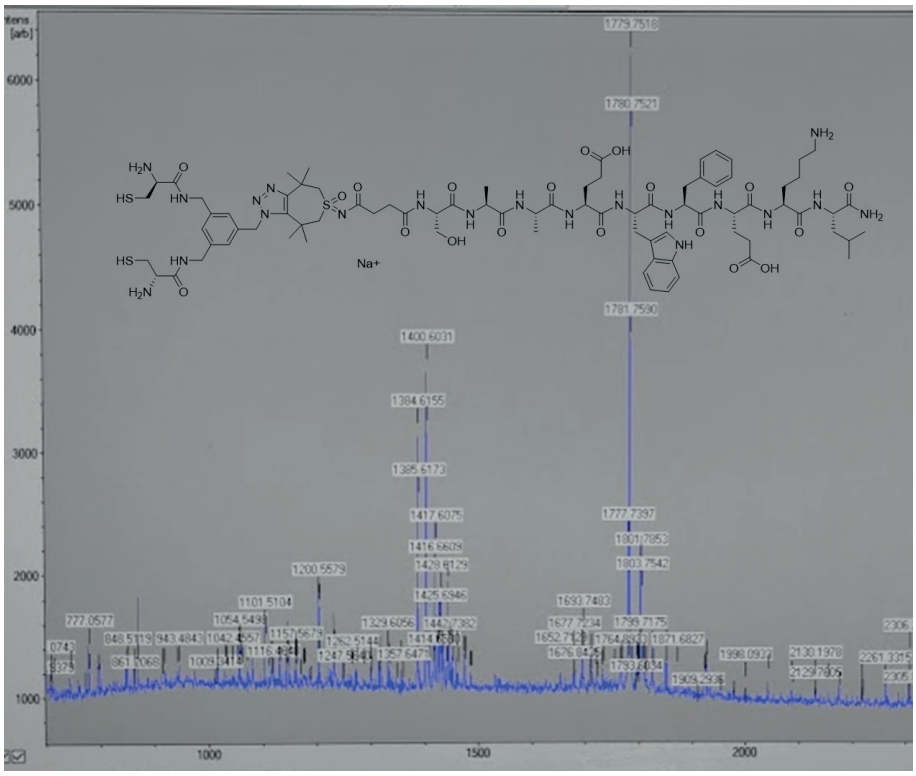

Figure S2.3: MALDI-MS spectrum of Crosslinker-TMTHSI-SAAEWFEKL after reduction with TCEP (structure shown). Expected mass for $C_{80}H_{116}N_{20}O_{19}S_3Na^+$ is 1779.78, found 1779.75 (Na^+ adduct).

CHAPTER 7

Versatile click linker enabling native peptide release from nanocarriers upon redox trigger

Erik R. Hebels[1], Stefanie Dietl[1], Matt Timmers[1,2], Jaimie Hak[1], Antionette van den Dikkenberg[1], Cristianne J. F. Rijcken[2], Wim E. Hennink[1], Rob M. J. Liskamp[2,3,4], and Tina Vermonden[1]

[1] Division of Pharmaceutics, Utrecht Institute for Pharmaceutical Sciences (UIPS), Utrecht University, 3508 TB Utrecht, the Netherlands.
[2] Cristal Therapeutics, 6229 EV Maastricht, the Netherlands
[3] Department of Biochemistry, Cardiovascular Research Institute Maastricht (CARIM), Maastricht University, Maastricht 6229 ER, the Netherlands
[4] School of Chemistry, University of Glasgow, Glasgow G12 8QQ, U.K.

Bioconjugate Chem. 2023, 34, 12, 2375–2386

Abstract

Nanocarriers have shown their ability to extend the circulation time of drugs, enhance tumor uptake and tune drug release. Therapeutic peptides are a class of drug compounds where nanocarrier mediated delivery can potentially improve their therapeutic index. To this end, there is an urgent need for orthogonal covalent linker chemistry facilitating the straightforward on-the-resin peptide generation, nanocarrier conjugation as well as the triggered release of the peptide in its native state. Here, we present a copper-free clickable ring strained alkyne linker being conjugated to the N-terminus of the oncolytic peptide LTX-315 via standard solid phase peptide synthesis (SPPS). The linker contains 1) a recently developed 7 membered ring strained alkyne; 3,3,6,6-tetramethylthiacycloheptyne sulfoximine (TMTHSI), 2) a disulfide bond which is sensitive to the reducing cytosolic and tumor environment and 3) a thiobenzyl carbamate spacer enabling release of the native peptide upon cleavage of the disulfide via 1,6 elimination. We demonstrate convenient 'clicking' of the hydrophilic linker-peptide conjugate to preformed pegylated core-crosslinked polymeric micelles (CCPMs) of 50 nm containing azides in the hydrophobic core under aqueous conditions at room temperature resulting in a loading capacity of 8 mass % of peptide to polymer (56 % loading efficiency). This entrapment of hydrophilic cargo into/to a crosslinked hydrophobic core is a new and counter-intuitive approach for this class of nanocarriers. The release of LTX-315 from the CCPMs was investigated *in vitro* and rapid release upon exposure to glutathione (within minutes) followed by slower 1,6 elimination (within an hour) resulting in the formation of the native peptide. Finally, cytotoxicity of LTX CCPMs as well as uptake of sulfo-cyanine 5 loaded CCPMs was investigated by cell culture, demonstrating successful tumor cell killing at concentrations similar to that the free peptide treatment.

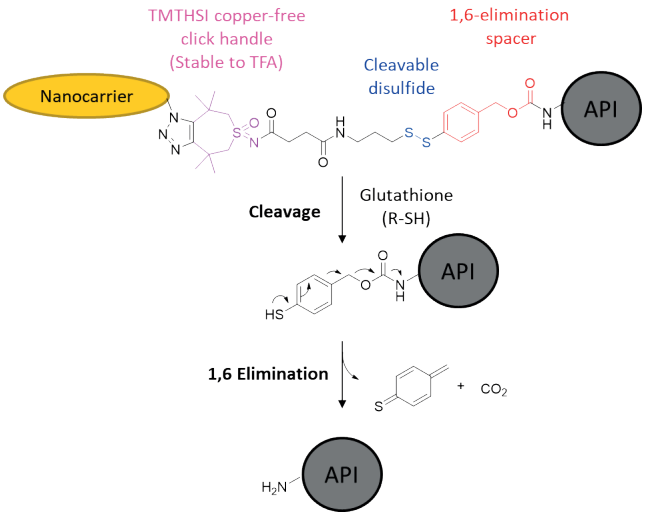

Introduction

Nanocarriers loaded with drugs offer several advantages, including the protection of drugs from premature degradation, prolonged circulation time, selective tissue targeting, cellular internalization, and controlled drug release. [1–3] To this end, covalent (temporary) entrapment of drugs improves stability of the platform during circulation. [4] For novel active pharmaceutical ingredients (APIs) such as therapeutic peptides, [5,6] there is a need for mild orthogonal chemistry to facilitate conjugation of such (prodrug) entities to nanocarrier vehicles. [7] Whilst employing a biologically relevant trigger, target-selective release should result in the native peptide, hence without any remaining conjugation fragment. [8]

Since the introduction of self-immolative connectors by Katzenellenbogen and co-workers in 1981, [9] a plethora of examples for the triggered traceless release of APIs has been described. These include antibody-drug conjugates, [10] polymer-drug conjugates, [11] supramolecular hydrogel-drug conjugates, [12] DNA-drug conjugates, [13] liposome loaded prodrugs, [14] as well as carriers that themselves self-immolate. [15] Reduction sensitive linkages (RSLs) such as the disulfide bond are particularly interesting release triggers owing to the increased levels of glutathione (GSH) in the cytosol as well as the tumor environment (in the case of oncology applications) as compared to plasma and extracellular fluids. [16–18] By utilizing the previously described 1,6 elimination chemistry of thiobenzyl carbamates, [19] conveniently short RSL handles that rapidly dissociate upon disulfide cleavage can be synthesized (see scheme 1). Examples for the native release of peptides and proteins from carriers and polymers upon exposure to mild reducing conditions have been described, further highlighting the potential of RSL release strategies. [20–22]

Although much work on self-immolative linker chemistry has been conducted on the releasability of cargos, less focus has been given to the convenient and efficient prodrug to carrier conjugation. Copper-free click chemistry presents an attractive approach owing to the mild, non-cytotoxic and generally orthogonal nature of this chemistry that even allows for coupling reactions *in vivo*. [23–25] However, in the case of site specifically modified peptide-linker conjugates, the click handle has to withstand relatively harsh deprotection conditions such as trifluoroacetic acid (TFA) treatment commonly employed during standard solid phase peptide synthesis (SPPS).

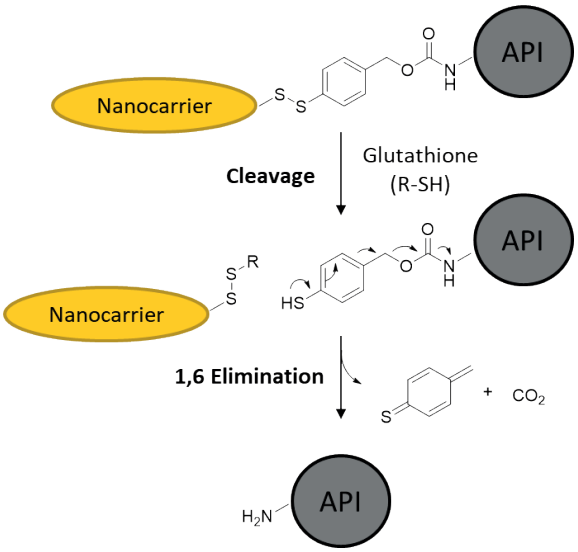

Scheme 1: Glutathione mediated cleavage and subsequent 1,6 elimination of the thiobenzyl carbamate intermediate resulting in the release of the native amine containing API. [19]

Current readily available ring strained alkynes such as dibenzocyclooctyne (DBCO, which is rather bulky and hydrophobic) and the later improved bicyclo[6.1.0]non-4-yn-9-ylmethanol (BCN, which is less bulky but still hydrophobic) have limited applications in SPPS since they do not endure the typical TFA deprotection conditions, requiring multi-step procedures. [26] A recently developed 7-membered ring strained alkyne, 3,3,6,6-tetramethylthiacycloheptyne sulfoximine (TMTHSI), was demonstrated as compared to DBCO and BCN a more reactive and more hydrophilic click handle and, importantly, stable during TFA deprotection reactions. [27,28] Furthermore, the higher hydrophilicity of the TMTHSI click handle allows for linker/conjugate applications in aqueous solutions which is particularly beneficial for conjugation of peptides to nanoparticles dispersed in water.

In this work, we aimed to design and synthesize an amine reactive RSL linker based on thiobenzyl carbamate chemistry with TMTHSI as a reactive click handle for conjugation to an azide containing carrier. By making use of the TFA resistance of TMTHSI, we site-specifically conjugate this linker to the N-terminus of LTX-315 (a multi-amine containing oncolytic peptide under clinical investigation by intra-tumoral injection) [29–31] via an on-the-resin approach using standard SPPS. To demonstrate straightforward conjugation of the linker-peptide conjugate to a nanocarrier, we selected clinically evaluated [4,32–36] core-crosslinked polymeric micelles (CCPMs) based on partially methacrylated methoxy poly(ethylene

glycol)-b-poly[*N*-(2-hydroxypropyl) methacrylamide-lactate]) (mPEG-*b*-pHPMAmLac$_n$-MA) polymers that we partially modified with azidoacetic acid to introduce azide handles into the hydrophobic CCPM core. Finally, we investigated the release kinetics of LTX-315 under reducing conditions as well as the cellular uptake and cytotoxicity of the platform *in vitro* to demonstrate the functionality, efficiency, and versatility of the designed linker.

Materials and methods

Materials

The copper-free click handle 3,3,6,6-tetramethylthiacycloheptyne sulfoximine (TMTHSI) conjugated with succinic acid (TMTHSI-succ) as well as methacrylated methoxy poly(ethylene glycol)-b-poly[*N*-(2-hydroxypropyl) methacrylamide-lactate]) (mPEG-b-pHPMAmLac$_n$-MA) with an M_n of 20 kDa was provided by Cristal Therapeutics (Maastricht, the Netherlands) and synthesized as described previously.[27,32] Dibenzocyclooctyne functionalized sulfonated cyanine 5 (Sulfo.Cy5-DBCO) was obtained from Lumiprobe (Hannover, Germany). All other materials were obtained from Sigma Aldrich (Zwijndrecht, the Netherlands) unless indicated otherwise. All solvents were obtained from Biosolve (Valkenswaard, the Netherlands).

Synthesis

Linker synthesis

*Synthesis compound **1***: In a typical reaction, aldrithiol™-2 (3.9 g, 17.6 mmol) was dissolved in 10 mL dichloromethane (DCM)/MeOH (1/1 v/v), to which cysteamine hydrochloride (1.0 g, 8.8 mmol) dissolved in 20 mL MeOH was added dropwise whilst bubbling with nitrogen. After 16 hours of stirring at RT, the mixture was dropped in 1 L of cold diethyl ether whilst stirring to precipitate the formed compound **1** and left to stir for 30 minutes followed by filtration through a sintered glass filter. The obtained yellow solid was redissolved in 20 mL MeOH, and 1 L diethyl ether was subsequently added to the same flask to precipitate again. Then, the isolated solid was re-dissolved in 20 mL methanol, precipitated in 200 mL diethyl ether, centrifuged and dried under nitrogen, yielding 1.5 g (74 %) of pyridine dithioethylamine hydrochloride, a flaky white solid. ^{1}H NMR (400 MHz, D_2O): δ 8.31 (ddt, J = 5.0, 1.7, 0.8 Hz, 1H), 7.69 (tdd, J = 7.4, 1.8, 0.7 Hz, 1H), 7.61 (dq, J = 8.1, 0.9 Hz, 1H), 7.19 (ddt, J = 7.5, 5.0, 0.9 Hz, 1H), 3.20 (t, 2H), 2.97 (t, J = 6.3 Hz, 2H). See Figure S1.1 for ^{1}H NMR spectrum.

*Synthesis compound **2***: $LiAlH_4$ (1.5 g, 39.0 mmol) was suspended in 30 mL of dry THF whilst stirring in an ice bath and 4-mercaptobenzoic acid (2 g, 13.0 mmol) dissolved in

30 mL dry THF was added dropwise. After addition, the ice bath was removed and the reaction mixture was left to stir overnight at RT. The reaction was quenched with 3 mL milliQ water in an ice bath and 100 mL of 2 N HCl was added to acidify the reaction mixture. Compound **2** was then extracted 3 times with 100 mL EtOAc, washed with 100 mL milliQ, 100 mL brine, dried over anhydrous sodium sulfate and concentrated. The obtained off-white semi-solid was purified by silica chromatography employing 2:1 hexane : EtOAc as eluent (R_f = 0.3), yielding 1.5 g (82%) of 4-mercaptobenzyl alcohol as a white solid. ^{1}H NMR (400 MHz, $CDCl_3$) δ 7.28 – 7.20 (m, 4H), 4.62 (s, 2H). See Figure S1.2 for ^{1}H NMR spectrum.

*Synthesis compound **3***: Compound **2** (0.71 g, 3.2 mmol) was dissolved in 10 mL MeOH and compound **1** (0.60 g, 3.4 mmol), dissolved in 20 mL DCM, was added dropwise with bubbling nitrogen whilst stirring. After 30 minutes, the reaction mixture was diluted with DCM, and applied onto a silica column employing 9:1 DCM : MeOH until elution of the yellow mercaptopyridine side product, followed by 9:1 DCM : MeOH with 1-3% triethylamine to elute compound **3** (R_f = 0.3). No concentrating was done to prevent disproportionation reactions, the next reaction being conducted in the elution solvent.

*Synthesis compound **4***: A successive reaction step was conducted directly using compound **3** in the elution solvent (approximately 250 mL 9:1 DCM : MeOH, 1-3 % triethylamine). TMTHSI-succinic acid (0.21 g, 0.68 mmol) was weighed together with hexafluorophosphate azabenzotriazole tetramethyl uronium (HATU) (0.29 g, 0.75 mmol), dissolved in 10 mL DMF and added to the excess compound **3** (4-fold based on the starting reagents used for compound **3**). After stirring for 30 minutes, the reaction mixture was washed 3 times with 100 mL 0.1 N HCl, once with saturated $NaHCO_3$, once with brine, dried over sodium sulfate and filtered. The product was not concentrated or further isolated. The identity of compound **4** was confirmed by TLC-MS: expected mass for $C_{23}H_{32}N_2O_4S_3Na^+$ is 519.1, found 518.8.

*Synthesis compound **5***: In the final step, bis(pentafluorophenyl) carbonate (0.54 g, 1.37 mmol) was added to the washed compound **4** mixture, followed by *N*,*N*-diisopropylethylamine (DIPEA) (1.2 mL, 6.8 mmol) and a catalytic amount of 4-dimethylaminopyridine (DMAP). The reaction was monitored by TLC. After 1-2 hours, the reaction mixture was washed 3 times with 100 mL 0.1 N HCl, 2 times with saturated $NaHCO_3$, once with brine, dried over sodium sulfate and concentrated to obtain a brown oil. The oil was redissolved in EtOAc and run on a silica column employing 1:1 hexane : EtOAc until elution of unreacted bis(pentafluorophenyl) carbonate, followed by only EtOAc (R_f = 0.5). After concentrating, 0.41 g of gooey off-white solid was obtained

with a yield of 85 % with respect to TMTHSI-succ. ^{1}H NMR (400 MHz, DMSO-d6): δ 8.01 (t, *J* = 5.7 Hz, 1H), 7.61 (d, *J* = 8.3 Hz, 2H), 7.50 (d, *J* = 8.6 Hz, 2H), 5.40 (s, 2H), 3.90 (d, *J* = 13.9 Hz, 2H), 3.69 (d, *J* = 13.9 Hz, 2H), 3.37 – 3.24 (m, 2H), 2.84 (t, *J* = 6.3 Hz, 2H), 2.42 (t, *J* = 7.2 Hz, 2H), 2.27 (t, *J* = 7.2 Hz, 2H), 1.35 (s, 6H), 1.18 (s, 6H). ^{19}F NMR (565 MHz, DMSO-d6): δ -154.11 (d, *J* = 19.5 Hz, 2F), -157.26 (t, *J* = 23.1 Hz, 1F), -162.11 – -162.22 (m, 2F). TLC-MS: Expected mass for $C_{30}H_{31}N_2O_6S_3F_5Na^+$ is 729.1, found 729.8. See Figure S3.1 for HPLC chromatogram of the purified compound **5**.

Peptide synthesis

Synthesis of LTX-315 (KKWWKKW-Dip-K-NH_2) was performed by microwave solid phase peptide synthesis (SPPS) in a Liberty Blue™ peptide synthesizer (CEM Corp., Matthews, NC, USA) following a standard Fmoc/tBu protocol on a 0.1 mmol scale. A high swelling Tentagel® XV rink amide resin (loading 0.2-0.4 mmol/g) (Rapp Polymere, Tuebingen, Germany) was employed as solid support. Standard couplings of amino acids were performed at 0.2 M in dimethyl formamide (DMF) using DIC/OxymaPure® activation, with the first lysine loaded in a double coupling procedure (the coupling method used was optimized to the corresponding amino acid according to the recommended operation of Liberty Blue™). Fmoc removal was carried out using 20 % piperidine in DMF. Modification of LTX-315 with click linker (compound **5**) was carried out before cleavage/final deprotection from the solid support as described in detail in the next paragraph.

Linker-LTX conjugate synthesis

The coupling of the click linker (compound **5**) with LTX-315 was performed on the resin to attain selective N-terminal conjugation. About 0.05 mmol resin content (half batch from the SPPS) was suspended in 5 mL dimethylacetamide (DMAC)/DCM (1:1 v/v) followed by addition of DIPEA (170 µL, 1.0 mmol). Compound **5** was dissolved in DCM to a 50 mg/mL stock solution and added to the resin (700 µL, 35 mg, 0.05 mmol) followed by a catalytic amount of DMAP (1 mg, 8.2 µmol). After stirring for 1.5 hours at RT, the resin was washed 3 times with 10 mL DMF/DCM (1:1 v/v), 3 times 10 mL DCM and subsequently dried under nitrogen flow. The peptide conjugate was then cleaved/deprotected by stirring for 1 hour using 5 mL trifluoroacetic acid (TFA) : triisopropylsilane (TIS) : water, 95:2.5:2.5 (v/v/v). Following filtration, the crude peptide was precipitated in 45 mL cold diethyl ether, centrifuged, washed with diethyl ether, dried under nitrogen flow, dissolved in milliQ water : acetonitrile (ACN) 1:1 and lyophilized.

The lyophilized crude peptide-linker conjugate (35 mg) was dissolved in 4 mL of 5% ACN in milliQ water supplemented with 0.1% formic acid and filtered using a 0.45 µm recombined cellulose syringe filter. Fractionation was carried out using preparative reverse phase high performance liquid chromatography (Prep-RP-HPLC) on a Waters 2535 quaternary gradient module with Waters 2489 UV/Visible detector (detection at 210 and 280 nm) and ReproSil-Pur 120 C18-AQ (10 µm, 25 mm x 250 mm, Dr. Maisch) column. ACN/water supplemented with 0.1% formic acid was used as eluent at a flow of 25 mL/min and a gradient of 5 to 95% ACN over 60 minutes. Fractions were manually collected, analyzed by HPLC (Figure S3.2) and MALDI-MS (Figure S2.1) and pure fractions were combined and lyophilized (see Figure S3.3 for HPLC of the pooled linker-LTX conjugate).

Polymer derivatization with azides

Azide functionalities were introduced onto the thermosensitive block of (mPEG-*b*-pHPMAmLac$_n$-MA, polymer **P,** characteristics are reported in Figure S1.5) as shown in scheme 2, a detailed description of the synthesis of this polymer is described by Hu et al. [32] Stock solutions of azidoacetic acid (AAA) (50 mg/mL), DPTS (20 mg/mL) and DCC (50 mg/mL) in dry DCM were prepared. The mPEG-b-pHPMAmLac$_n$-MA polymer (1.0 g, 50 µmol, based on M_n of 20 kDa determined by NMR, containing 2.6 mmol of free -OH groups) was dissolved in dry DCM (final concentration 100 mg/mL), followed by addition of AAA with a feed ratio of 5.5 mol% (14.5 mg, 143 µmol), 11.0 mol% (29.0 mg, 287 µmol) and 16.5 mol% (43.5 mg, 430 µmol) relative to HPMAmLac$_n$-OH groups, 0.1 equivalents to AAA) of DPTS and finally 1.1 equivalents (to AAA) of DCC. The reaction mixtures were stirred at RT for 16 hours. The mixture were then filtered using a 0.2 µm PTFE syringe filter, the polymers were precipitated thrice in diethyl ether and dried under vacuum overnight. The azide modification was confirmed by IR spectroscopy (Figure S5.1). The obtained polymers were further characterized for composition, molecular weight, CP as described in the characterization section. The synthesized polymers with 5.5, 11.0 and 16.5% AAA feed are referred to as **PA5**, **10** and **15** respectively.

Core-crosslinked polymeric micelle (CCPM) formation

CCPM formation was carried out following a previously published procedure. [32] In detail, an ice cold solution of polymer **PA15** (4.15 mL, 24.1 mg/mL) was stirred and purged with N_2 for 15 minutes and mixed with tetramethylethylenediamine (TEMED, 125 µL, 120 mg/mL), both dissolved in phosphate buffer (100 mM Na_2HPO_4, adjusted

to pH 7.3 using HCl). The mixture was warmed to 40 °C and after 10 minutes, 0.5 mL of ethanol was added (following the previously described procedure [32]) dropwise to the now opalescent mixture. After 15 minutes, potassium persulfate (KPS, 338 µL, 30 mg/mL, dissolved in phosphate buffer (100 mM Na_2HPO_4, adjusted to pH 7.3 using HCl) was added to the micellar dispersion whilst under N_2 flow. After 1 h, the CCPM dispersion was filtered through a 0.2 µm RC syringe filter and purified by tangential flow filtration (TFF) against HEPES buffer (10 mM HEPES, adjusted to pH 7.3 using NaOH) at a polymer concentration of 10 mg/mL, employing an mPES membrane (50 kDa cut off, 20 cm^2, MicroKros® filter modules, Repligen) for 40-50 washing volumes. Following TFF, 1 mL of 1 M HEPES buffer was added resulting in ~100 mM HEPES salt content with pH 7.3 and the dispersion was filtered again with a 0.2 µm RC syringe filter. The polymer concentration of the obtained dispersion was determination as described in the characterization section.

CCPM loading

The lyophilized linker-LTX conjugate was dissolved in milliQ (6.0 mg, 2.7 µmol) to 20 mg/mL, added to 6 mL of TFF purified CCPMs (~7 mg/mL, 7.2 µmol total azide content, determined by hydrolysis followed by UHPLC as described in the characterization section) and stirred for 3 hours at room temperature. An excess of azides (2.6 fold) was employed to promote quantitative coupling of the linker-LTX conjugate. Purification was carried out by TFF as described above, however using 100 mM HEPES and only 10 washing volumes to reduce polymer losses at this stage (see Scheme 4 for complete overview).

CCPMs loaded with fluorescent sulfonated cyanine 5 (S.Cy5) for cell uptake studies were prepared by mixing 100 µL of S.Cy5-DBCO (dissolved to 10 mg/mL in DMSO, 1.0 µmol) with 5 mL of TFF purified CCPMs (~7 mg/mL, 6.0 µmol total azide content) and stirring for 3 hours at room temperature. Purification was carried out by TFF as described above.

Characterization

Nuclear magnetic resonance (NMR) spectroscopy

^1H NMR spectra were recorded on an Agilent 400-MR NMR spectrometer (400 MHz) (Agilent Technologies, Santa Clara, USA). Residual solvent peaks of $CDCl_3$ (δ = 7.26 ppm), D_2O (δ = 4.79) or D_6 DMSO (δ = 2.50 ppm) were used to calibrate chemical shifts. ^{19}F NMR spectra were recorded on a Bruker Avance Neo spectrometer (565 MHz).

Infrared spectroscopy (IR)

IR spectra were recorded with solid polymer samples using a ATRU equipped Spectrum 2 (Perkin Elmer, Llantrisant, UK) and reported as normalized transmission in cm^{-1}.

Thin layer chromatography (TLC)

TLC was performed using aluminum bound silica plates obtained from Merck Darmstadt (SiO_2, Kieselgel 60 F254). Compounds were visualized by UV detection at 254 nm and, where applicable, stained with ninhydrin in DCM to visualize amines or potassium permanganate in 10% NaOH to visualize alkynes.

Mass spectrometry (MS)

TLC-MS spectra were recorded on an expres**ion**® high performance compact mass spectrometer equipped with a Plate Express™ TLC plate reader (Advion, Ithaca, USA).

Matrix assisted laser desorption ionization (MALDI)-MS spectra were recorded on a Ultraflextreme (Bruker Daltonics, Bremen, Germany), loading 1 µL of sample solution with 1 µL of matrix (10 mg/mL α-cyano-4-hydroxycinnamic acid in 30% ACN with 0.1% TFA).

High performance liquid chromatography (HPLC)

HPLC analysis was performed using an Alliance 2695 chromatography system with an XBridge C18 column (5 µm, 4.6 x 150 mm, Waters) at a column temperature of 25 °C and employing an Alliance 2487 ultra-violet (UV) detector at 210 nm and Alliance 2475 fluorescence (FL) detector at $\lambda_{ex}/\lambda_{em}$ 280/350 nm. Acetonitrile/water supplemented with 0.1% formic acid was used as eluent at a flow of 1 mL/min and a gradient of 5 to 95% ACN over 20 minutes.

Gel permeation chromatography (GPC)

GPC for polymer analysis was performed using an Alliance 2695 (Waters) chromatography system with two PLgel 5 µm mixed-D columns (Polymer Laboratories) in series at a column temperature of 65 °C and employing a refractive index detector. DMF supplemented with 10 mM LiCl was employed as eluent with an elution rate of 1 mL/min. Sample concentration was typically 10 mg/mL and PEGs of narrow and defined molecular weights obtained from PSS (Germany) were used as calibration standards. Recording of data and calculations of molecular weights were done with Waters Empower 32 software.

Cloud point (CP) measurements

Using an adapted procedure, [37] the CPs of the different thermosensitive polymers in phosphate buffer (100 mM Na_2HPO_4, adjusted to pH 7.3 using HCl, 5 mg/mL polymer) were determined by measurement of light scattering at a 90° angle upon the onset of opalescence. Scattered light intensity was measured using a Jasco FP-8300 spectrophotometer employing a wavelength of 550 nm with 1 nm slit width and a response time of 1 second. Temperature was ramped from 2 to 50 °C at 1 °C per minute.

Dynamic light scattering (DLS).

The size of the CCPMs was determined by DLS using a Malvern Zetasizer nano series ZS90 at a measurement angle of 90°. Measurements were carried out at 25 °C. Unless stated otherwise, the concentration of the micellar dispersions was approximately 10 mg/mL in either phosphate buffer (100 mM Na_2HPO_4, adjusted to pH 7.3 using HCl) or HEPES buffer (100 mM HEPES, adjusted to pH 7.3 using NaOH). The ζ-potential was determined with a Zetasizer Nano Z (Malvern ALV CGS-3, Malvern, UK) after 1000 x dilution in 10 mM HEPES buffer at pH 7.4 (settings: temperature 25 °C, viscosity 0.8872 cP, RI 1.330, dielectric constant 78.5).

Ultra-high performance liquid chromatography (UHPLC)

UHPLC analysis for the quantification of azidoacetic acid and lactic acid was performed using an Acquity (Waters) chromatography system with an HSS T3 column (1.7 µm, 2.1 x 100 mm, Waters) at a column temperature of 50 °C, sample temperature of 20 °C and employing a Acquity PDA detector at 210 nm. KH_2PO_4 buffer (10 mM, pH = 2.5) was used as isocratic eluent at a flow of 0.5 mL/min for 2.5 minutes followed by an increasing gradient of acetonitrile supplemented with 0.1% phosphoric acid from 0% to 90% over 3 minutes.

UHPLC analysis for LTX-315 release quantification was performed using an Acquity (Waters) chromatography system with an CSH™ C18 column (1.7 µm, 2.1 x 50 mm, Waters) at a column temperature of 50 °C, sample temperature of 20 °C and employing a Acquity FL detector at $\lambda_{ex}/\lambda_{em}$ 280/350 nm. Acetonitrile/water supplemented with 0.1% formic acid was used as eluent at a flow of 0.5 mL/min and a gradient of 5 to 95% ACN over 10 minutes.

Polymer concentration determination

The polymer concentration of the CCPM dispersions was determined through lactic acid concentration by UHPLC after hydrolysis as reported previously. [38] Briefly, 20 µL of the CCPM dispersion was incubated with 10 µL NaOH (1 M) for at least 2 hours at 37 °C followed

by the addition of 20 µL HCl (1 M). Samples were run on UHPLC as described above. Sodium lactate was employed as reference standard to determine lactic acid concentration.

The polymer amount was calculated as follows: Amount of polymer = measured amount of lactic acid × (M+5000)/ [90.08 × (m + 2n)], where M is the M_n of the thermosensitive block P(HPMAmLac$_n$); m and n are the number of repeat units of HPMAmLac$_1$ and HPMAmLac$_2$ in the block copolymer (**P**) respectively (determined by ^{1}H NMR, 24.8 and 26.8 units, respectively).

Azide content quantification by NaOH hydrolysis

The extent of AAA functionalization of the **PA5**, **10** and **15** polymers as well as **PA15** CCPMs was determined following a forced hydrolysis protocol and subsequent UHPLC analysis. The polymers were dissolved at 20 mg/mL in phosphate buffer (100 mM Na_2HPO_4, adjusted to pH 7.3 using HCl), of which 20 µL was mixed with 10 µL 1 M NaOH and incubated for 3 hours at 37 °C. Then, 20 µL of 1 M HCl was added and the samples were measured by UHPLC as described above. Calibrations of AAA were run with a range of 100-1000 µg/mL and the amount of azides per polymer chain calculated (moles of AAA divided by moles of polymer).

Release of LTX-315 from CCPMs

To 180 µL of purified LTX loaded CCPMs was added either 20 µL of 50 mM or 100 µM GSH (obtained from Sigma Aldrich, reduced form) dissolved in HEPES (100 mM, adjusted to pH 7.3 using NaOH) resulting in a GSH concentration of 5 mM and 10 µM, respectively, and the samples were analyzed by UHPLC with 5 µL injections at a 10 minute interval for 80 minutes. Area under the curve (AUC) of the cleaved intermediate and native peptide was determined by integration using the empower software (Waters), and the AUC ratios were calculated relative to the highest AUC. For the release quantification, calibrations of free LTX-315 with a range of 100-500 µg/mL were generated and a sample treated with 5 mM GSH for 90 minutes was quantified.

Cytotoxicity and internalization studies

Cell culture

HeLa cells were cultured and maintained at 37 °C with dulbecco's modified eagle medium (DMEM) supplemented with 10% fetal bovine serum (FBS) in an incubator regulated with 5% CO_2, 95% air and saturated humidity. Cells were passaged every 2-4 days upon reaching 80% confluency using trypsin ethylenediaminetetraacetic acid (trypsin-EDTA).

Cell viability

HeLa cells were plated into black polystyrene 96 well plates (Agilent #204626-100) at a density of 1.0 x 10^4 cells per well and incubated for 24 hours at 37 °C. The medium was aspirated and 100 µL dilutions (dilutions made in 100 mM HEPES buffer, 5x dilution of sample into medium)) of LTX loaded CCPMs, empty CCPMs and free LTX-315 in DMEM medium supplemented with 10% FBS and with 1% penicillin/streptomycin were added in triplicate. After 24 hours, 20 µL of MTS staining solution (CellTiter 96® AQ_{ueous}, Promega) was added. Following a 2 hour incubation, absorbance (490 nm) was recorded using a Mithras plate reader. Data were background subtracted and normalized using medium only wells and untreated cells of the same plate.

Cellular uptake

Confocal microscopy

HeLa cells with a cell density of 5000 cells/well were plated into a black polystyrene 96 well plate (Agilent #204626-100) in DMEM medium with 10% FBS and supplemented with 1% penicillin/streptomycin. The following day, HEPES dilutions of S.Cy5 loaded CCPMs (5x diluted in medium) were added to the cells in triplicate and incubated for 24 hours at 37 °C. Prior to confocal microscopy, the cells were treated with 2 µg/ml Hoechst 33342 for 10 minutes in an incubator at 37 °C, 5% CO_2. The cells were imaged in OptiMEM on Yokogawa CV 7000 Microscope (40x water immersion objective lens). The Cy5 fluorescence was measured by excitation at 638nm and emission at 676/29nm and the fluorescence of the Hoechst 33342 by excitation 405nm and emission at 445/45nm.

Flow cytometry

HeLa cells were plated into 96-well plates with a cell density of 5.000 cells per well and incubated for 1, 3, 6, 24 and 48 hours at 37 °C, 5% CO_2. Dilutions of S.Cy5 loaded CCPMs purified by TFF (dilutions made in 100 mM HEPES buffer, 5x dilution of sample into medium) in DMEM medium supplemented with 10% FBS and 1% penicillin/streptomycin were prepared and after aspiration of culture medium, 100 µL of CCPM dispersion was added to the cells in triplicate. After incubation, the treatment medium was removed and the cells washed with PBS. The cells were then harvested using 50 µL of trypsin followed by an incubation of 3 minutes at 37 °C, 5% CO_2 to detach the cells. The cells were resuspended into culture medium and washed with PBS. The cells were fixated with 1% paraformaldehyde for 15 minutes and washed three times with 1% BSA solution. Finally the cell associated fluorescence was detected using a FACSCanto II

flow cytometer (BD canto II) with 5 x 10^4 cells per sample. The Cy5 fluorescence was measured by excitation at 633nm and emission at 660/20nm.

Results and discussion

Linker synthesis

We designed a linker to couple an amine-containing peptide to a nanoparticle and subsequently release the native peptide under reducing conditions as found in the cytosol of cells and in tumor environments. This linker contains on one end an amine reactive pentafluorophenyl carbonate and on the other end TMTHSI as clickable handle for conjugation to azide-containing nanoparticles, bridged by a spacer that self-immolates upon cleavage of the connecting disulfide (see schemes 1 and 2). In doing so, this advances upon previously reported similar strategies employing RSL chemistries through incorporation of a robust click handle. [20,22]

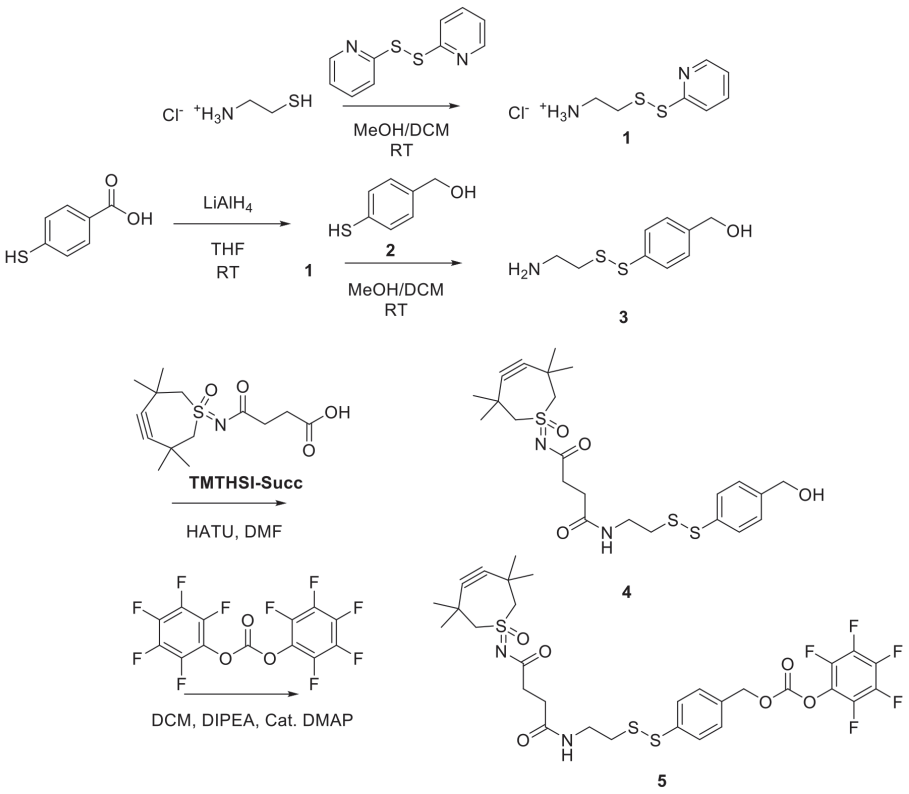

*Scheme 2: Synthesis scheme of the amine reactive, TMTHSI incorporated RSL linker (Compound **5**).*

Starting with cysteamine.HCl, the thiopyridine activated disulfide **1** was prepared via a known reaction with aldrithiol (2,2′-dithiodipyridine). Purification by repeated precipitation in diethyl ether (removing unreacted aldrithiol and the 2-thiopyridine byproduct) was efficient for obtaining the flaky white solid. The $LiAlH_4$ reduction of 4-mercaptobenzoic acid yielded 4-mercaptobenzyl alcohol (**2**), following a previously described method. [20,39] Reaction of compound **1** with **2** under nitrogen yielded the disulfide containing building block **3**. Purification of compound **3** was done by silica column chromatography. We proceeded with the coupling of TMTHSI-succinic acid to compound **3** present in the fraction (9:1 CH_2Cl_2 : MeOH with 1-3% triethylamine), whilst ensuring a large excess (5-fold) of compound **3**. The identity of compound **4** was confirmed by TLC-MS (see Figure S2.4). The pentafluorophenyl activation of compound **4** to yield compound **5** (aimed linker) was carried out after a few washing steps, for which DMAP was used as catalyst. The identity of compound **5** was confirmed by NMR (Figure S1.3) and TLC-MS (Figure S2.5) attaining a final yield of 86 % relative to TMTHSI-succ. ^{19}F NMR analysis further confirmed the intended pentafluorophenyl carbonate activation occurred, ruling out a potential dimerized carbonate ester (Figure S1.4). The purity (>95 %) of compound **5** was established by HPLC (see Figure S3.1).

Linker-LTX on resin conjugation

The stability of the TMTHSI click handle towards TFA deprotection conditions [27,28] allows for on the resin conjugation of the linker and subsequent selective N-terminal modification of peptides (Fmoc deprotected N-terminus, protected side chains whilst on the resin). Particularly a peptide such as LTX-315 (containing 5 lysine residues) benefits from this site-specific approach to obtain a well-defined and characterizable conjugate (scheme 3). We employed a 1:1 equivalency ratio of linker to theoretical peptide content on resin to limit use of the click linker (compound **5**) reagent (up to 6-fold excess of reagents are employed in standard SPPS modifications [40]). Using DMAP as catalyst, successful conjugation was indeed shown from disappearance of the linker from the reaction mixture as seen by TLC. The linker-LTX conjugate was obtained through preparative HPLC, and identity/high purity (1962 Da, > 90 %) was confirmed by MALDI-MS/HPLC (Figure S2.1 and S3.2). Unconjugated LTX-315 peptide (45 mol%) was also obtained after preparative HPLC, demonstrating that the linker was indeed the limiting reagent as intended and 9.4 mg (or 4.8 nmol) of linker-LTX conjugate and 5.6 mg (3.9 nmol) of unconjugated LTX-315 were isolated, corresponding with a conjugation yield of 55 %.

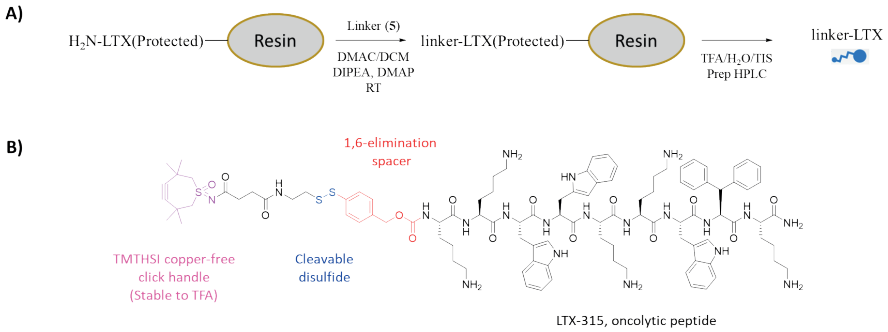

Scheme 3: Overview of A) the on-resin synthesis of the linker-LTX conjugate and B) the structure of the N-terminal modified linker-LTX-315 conjugate.

Polymer derivatization

We selected a previously described polymeric micellar system based on thermosensitive methacrylated methoxy poly(ethylene glycol)-b-poly[*N*-(2-hydroxypropyl) methacrylamide-lactate]) (mPEG-b-pHPMAmLac$_n$-MA) (abbreviated as polymer **P,** see Figure S1.5) [32] for coupling of the linker-LTX conjugate. Polymer **P** is used as building block for CCPMs through free radical polymerization above its cloud point (CP, which depends on copolymer composition of the thermosensitive block) in aqueous buffer. Eight % of the available hydroxyl moieties on the side chains were modified with methacrylate moieties (enabling crosslinking, resulting in a polymer with a CP of 11 °C). The remaining 92 % of the hydroxyl side groups of polymer P are available for additional modification and azides were introduced *via* a Steglich esterification [41] with azidoacetic acid (AAA) to obtain polymer **PA** (see scheme 4). AAA was selected as it is the smallest existing azide containing carboxylic acid (to minimize possible impact on the polymer characteristics such as CP, see table 1).

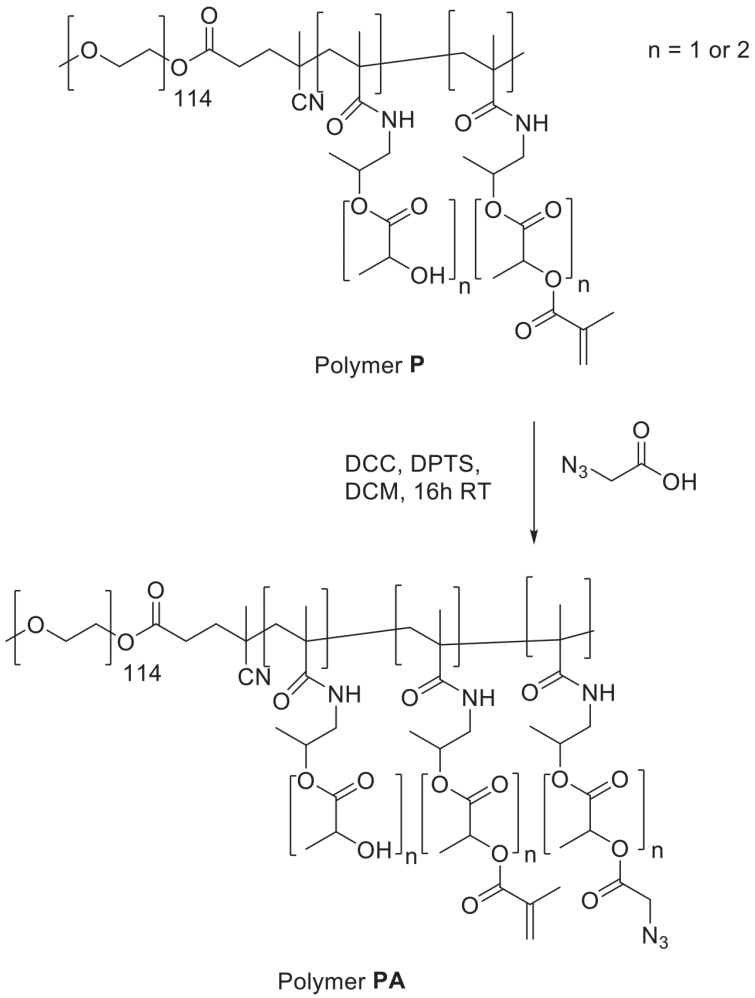

*Scheme 4: Modification of the mPEG-b-pHPMAmLac$_n$-MA polymer (**P**) with azidoacetic acid to yield (**PA**). Polymer **P** has an mPEG block of 5 kDa and based on NMR analysis, there are an average of approximately 23 and 28 units of HPMAmLac$_1$ and HPMAmLac$_2$ per polymer chain, respectively. Additionally, there are approximately 7 methacrylate functionalities per polymer chain. The total M_n is thus approximately 20 kDa. The extent of azide derivatization in polymer **PA** is reported in table 1.*

Table 1: Characteristics of azide functionalized mPEG-b-pHPMAmLac$_n$-MA polymers, feed is expressed in units per polymer chain (mol/mol).

	Azides per polymer chain		M_n (kDa)[b]	M_n (kDa)[c]	$Đ$[c]	Cloud Point (°C)[d]	Micelle diameter (nm)[e]	Micelle PDI[e]
	Feed	Obtained[a]						
P	-	-	19.6	22.3	1.68	11	58	0.04
PA5	2.6	1.3	19.0	23.3	1.76	8	55	0.05
PA10	5.2	3.3	18.8	24.0	1.95	5	53	0.02
PA15	7.7	5.3	19.7	24.6	2.03	1	48	0.03

[a] Determined by NaOH hydrolysis followed by ultra-high performance liquid chromatography (UHPLC) analysis
[b] Determined by ^{1}H NMR analysis
[c] Determined by gel permeation chromatography (GPC) analysis using PEG calibration standards for the average number molecular weight (M_n) and polydispersity ($Đ$) of the polymer.
[d] Determined by onset of light scattering at a 90° angle of the polymer dissolved in phosphate buffer (100 mM Na_2HPO_4, adjusted to pH 7.3 using HCl).
[e] Determined by dynamic light scattering (DLS) analysis of non-crosslinked polymers at 25 °C in phosphate buffer (100 mM Na_2HPO_4, adjusted to pH 7.3 using HCl).

Successful azide modification in a feed ratio dependent manner was confirmed by IR spectroscopy (Figure S5.1) and quantification achieved through NaOH hydrolysis of the polymer followed by UHPLC analysis of reformed AAA. The coupling efficiency ranged from 50-70%. Increased azidoacetic acid derivatization in **PA** resulted in a linear decrease in CP as well as hydrodynamic diameter of non-crosslinked micelles measured at 25 °C, due to the increased hydrophobicity resulting in stronger dehydration of the core. [42]

CCPM entrapment and release

CCPMs of PA15 were obtained by free radical polymerization of the methacrylated side chains after micellization at 40°C (well above the CP of 1 °C) in phosphate buffer (pH 7.3) with 10% ethanol, following a previously described procedure (Figure 1A). [32] This core-crosslinking reaction has to be conducted before introduction of the linker-LTX conjugate (in contrast to mixing before crosslinking [38,42]), as larger peptides (particularly those containing lysine, methionine and tryptophan residues) are prone to side-reactions under the conditions employed here. [43,44] Following tangential flow filtration (TFF) purification of the CCPMs, a diameter of 57 nm with a PDI of <0.1 was measured by DLS, slightly larger than the non-crosslinked micelles based on the same polymers (48 nm). This increase in diameter has been observed previously in analogous systems, [32] and is attributed to the presence of 10% ethanol which swells the core at the moment of crosslinking, the latter being initiated by addition of potassium persulfate (KPS). TFF purification was carried out using HEPES buffer as salt exchange as phosphate salts

caused precipitation of the linker-LTX conjugate, as previously reported for other lysine containing peptides. [45] The polymer content after TFF purification, as determined by lactic acid content with UHPLC after NaOH hydrolysis, was 43 mg, indicating losses of around 30% using this purification method (polymer feed during crosslinking was 60 mg). Additionally, AAA content was found to be lowered to 3.2 azides per polymer chain (compared to 5.3 azides per polymer chain of the non-crosslinked polymer), likely caused by aggregation of higher hydrophobic azide containing CCPMs.

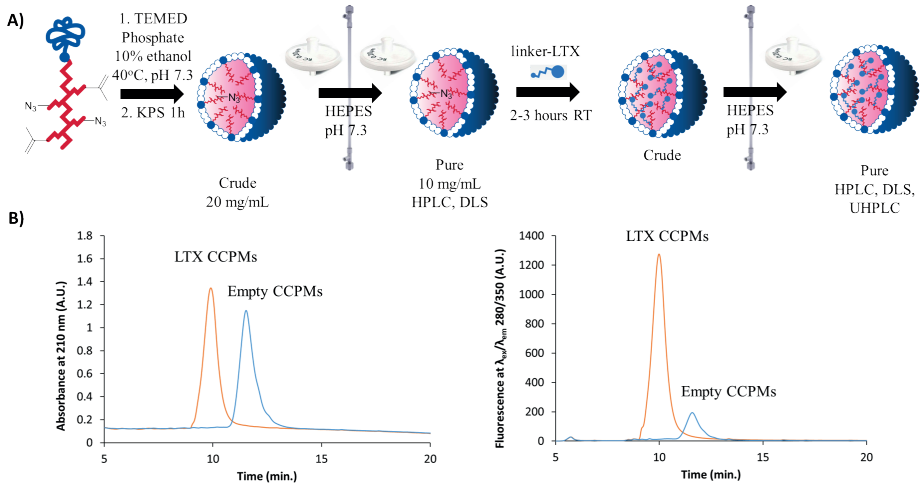

Figure 1: A) Overview of the synthesis of CCPMs and subsequent covalent coupling of the linker-LTX conjugate, including filtration, TFF purification and analytical steps and B) HPLC chromatograms of the LTX loaded CCPMs after TFF purification (orange), compared to reference empty CCPMs (blue), recorded with 210 nm absorbance (left) and $\lambda_{ex}/\lambda_{em}$ 280/350 nm fluorescence (right). The small signal of empty CCPMs in the right chromatogram is attributed to light scattering.

We clicked the linker-LTX conjugate, dissolved in water, into the CCPM obtained after TFF (in 100 mM HEPES buffer, pH 7.3) by simple mixing the peptide solution and micellar dispersion at room temperature for 3 hours (Figure 1 A). An excess amount of azides relative to linker-LTX conjugate (2.6 fold) was employed with the CCPMs to promote efficient entrapment. The degree of the peptide coupling was determined by analyzing the micelles using HPLC and hallmarked by a shift in retention time and the presence of a LTX associated tryptophan fluorescence signal at $\lambda_{ex}/\lambda_{em}$ 280/350 nm [46] of the CCPMs as compared to empty CCPMs (Figure 1 B). A substantial decrease (>95%, based on absorbance) in the linker-LTX peak was recorded prior to TFF purification (Figure S3.3), demonstrating that the LTX conjugate had almost quantitatively reacted, as anticipated.

The LTX CCPMs had a Z-Ave of 59 nm with a PDI of 0.07 as determined by DLS, indicating the CCPMs retained their size after loading (57 nm for empty CCPMs) as would be expected from a crosslinking-before-loading approach. The polymer content of LTX loaded CCPMs was 38.4 mg, which corresponds to a slight loss of 10% loss that occurred during the final TFF purification. It is noted that the volume after TFF purification was adjusted to the starting volume.

Given the hydrophilicity of LTX-315 and the linker-LTX conjugate (exemplified by the short retention time on HPLC, Figure S3.2 and S3.3 as well as the excellent solubility in water), it is counter-intuitive that this linker-LTX conjugate can penetrate into the hydrophobic CCPM core and subsequently undergo the click reaction. [47,48] The robust click reaction is anticipated to be the driving force and trap the conjugate upon entering or encountering the core. Additionally, azides located on the outermost parts of the hydrophobic core are likely responsible for the click conjugation since an excess amount of azides was employed, embedding LTX within the hydrophilic PEG layer. The 5 kDa PEG shell thickness of micelles has previously been reported to be in the range of 5-10 nm, [49,50] which could fully shield even the unlikely extended conformation of LTX-315, having a contour length of 3.2 nm (assuming 0.35 nm per amino acid). [51] In buffer of pH 7.3, both empty CCPMs and LTX CCPMs had a neutral zeta potential (-2.1 ± 8.9 and -0.2 ± 9.6 mV, respectively) demonstrating PEG shielding of the loaded LTX-315 with protonated lysine residues indeed occurred. Finally, we also entrapped the fluorescent dye S.Cy5-DBCO (non-reducible conjugation for imaging purposes) in CCPMs. A >95% entrapment was achieved based on absorbance (see Figure S3.4), further highlighting the high efficiency of a click-entrapment of a hydrophilic compound in the hydrophobic core.

We investigated the release of LTX from the purified CCPMs at glutathione (GSH) concentrations resembling those found in the cytosol of living cells (5 mM) and blood (10 μM) [16–18,20] by UHPLC (Figure 2). Release of LTX from the micelles in HEPES with 10 μM GSH and at 37 °C was slow (less than 10 % during incubation for 1.5 hours). However, upon incubation of the CCPMs in HEPES with 5 mM GSH and the same temperature, rapid cleavage of the disulfide bond was observed, releasing the thiobenzyl intermediate that then subsequently underwent 1,6 elimination yielding the native peptide, LTX-315, reaching a plateau within 60 minutes (see Figure S4.1 for illustration of chromatograms). Initial rapid disulfide cleavage was also previously reported for aliphatic disulfides in hydrophilic nanogels (for the release of ovalbumin in the presence of GSH). The observed rapid disulfide cleavage in our study suggests that the linker-LTX conjugate likely resides within the hydrophilic PEG corona rather than in the less accessible hydrophobic core. [52] The identity of released/native LTX-315 was further

confirmed by MALDI-MS (Figure S2.3).

The releasable LTX content from the CCPMs upon exposure to 5 mM GSH was quantified with a calibration free LTX-315. Figure 2 and Figure S4.1 show that the released amount of LTX reached a plateau after around 60 minutes incubation. The maximum released amount corresponds with 8 % mass loading of LTX-315 with respect to polymer content. This in turn points to 56 % entrapment efficiency of the total LTX-315 feed, which was determined by GSH treatment of the reaction sample before purification. Entrapment losses can be attributed (other than conjugation efficiency) to losses during TFF purification, reaction of linker-LTX conjugate with traces of uncoupled azido acetic acid (Figure S2.6 showing the presence of uncoupled AAA-linker-LTX), disproportionation of the linker-LTX conjugate (Figure S2.2 showing the presence of a dimer LTX-SS-LTX), and finally side product formation resulting in incomplete 1,6 elimination as previously described for dithiobenzyl carbamates. [22] Importantly, the potential side products and impurities are efficiently removed by TFF purification as shown in figure S3.5.

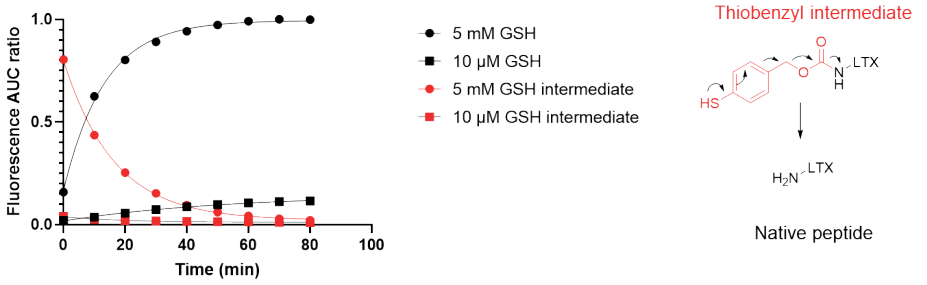

Figure 2: Release kinetics of LTX-315 from LTX CCPMs under reducing conditions in the cytosol (5 mM GSH, circles) versus typical plasma concentration (10 µM GSH, squares). The thiobenzyl carbamate intermediate that undergoes 1,6 elimination to yield native LTX-315 was detected as well (squares). See Figure S4.1 for illustration of obtained chromatograms. Recorded with $\lambda_{ex}/\lambda_{em}$ 280/350 nm fluorescence, expressed as AUC ratio to maximal recorded fluorescence.

Cellular internalization and toxicity

We investigated the cytotoxicity of LTX CCPMs on HeLa cancer cells using an MTS assay (Figure 3). The HeLa cells incubated with LTX CCPMs showed significantly reduced cell viability. On the other hand, incubation of the cells with empty CCPMs diluted to match the concentration of the LTX loaded CCPMs (1.4 mg/mL CCPM content as the highest) showed a slight decrease in cell viability, demonstrating minimal toxicity of the nanocarrier itself, in line with previous reports. [53,54]. LTX-315 is a cationic membrane penetrating lytic peptide, that in its free form is taken up by cells to exerts its

effects (also highlighted by the cytotoxicity of free LTX in figure 3). [29] Therefore, the CCPMs could either be internalized by the cells and release their cargo intracellularly or release cargo extracellularly in the culture environment.

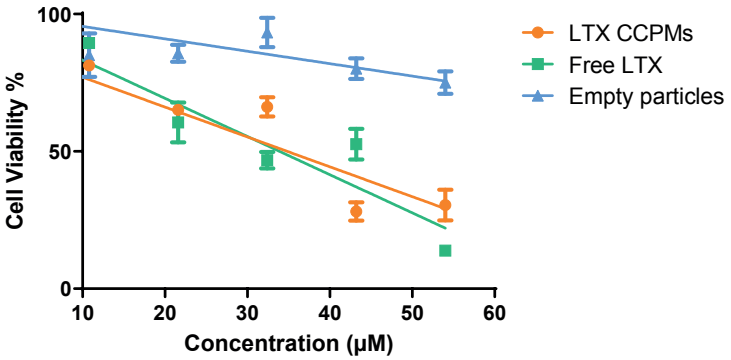

Figure 3: Cell viability of HeLa cells after incubation with LTX CCPMs (orange), free LTX-315 peptide (green) or empty CCPMs (blue) for 24 hours at 37 °C, as determined by MTS assays. Error bars represent the standard error of mean of 3 wells.

The cellular internalization of CCPMs was studied by using S.Cy5 labeled CCPMs (Figure 4). A time dependent increase in intracellular fluorescence was observed, with accumulation in regions outside the nucleus (likely within endosomal compartments) in a similar fashion as reported previously for pro-apoptotic peptide nanoparticles. [20] These results indicate that CCPM uptake and subsequent intracellular release play a role but do not fully explain the observed cytotoxicity (after 24 hours not all CCPMs are taken up, yet similar toxicity to free LTX-315 is found). It is also unlikely that the CCPMs release the peptide in sufficient amounts in the non-reducing cell culture medium at the start of the incubation with the intact cells. However, the equally potent cytotoxic effect of free and CCPM entrapped LTX is likely due to complete release of LTX from all CCPMs in the culture medium following initial cell lysis, exposing reducing agents such as GSH. Additional studies on stability in plasma as well as sterically hindered disulfide iterations of the linker would be of interest to explore in future studies. [55]

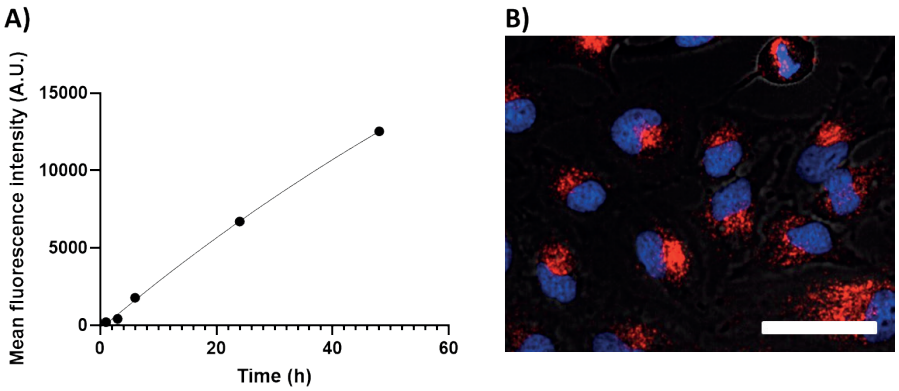

Figure 4: HeLa cell uptake of S.Cy5 labelled CCPMs (not loaded with LTX) at a concentration of 1.4 mg/mL represented by A) transition of mean cell fluorescence intensity as determined by flow cytometry and B) overlayed laser confocal scanning microscopy image after 24 h incubation at 37 °C with S.Cy5 loaded CCPMs showing brightfield, nuclear stain (blue) and S.Cy5 loaded CCPMs (red). Scale bar set to 25 µm.

Conclusion

A versatile click-based linker chemistry for the covalent entrapment and reduction triggered release of native therapeutic peptides from nanocarriers was developed. The linker described here is an example of a straightforward N-terminal site-specific peptide derivatization via solid phase chemistry to generate a clickable peptide-construct. This work also showcases a peptide-linker entrapment into already generated CCPMs. This way, crosslinking chemistry such as free-radical polymerization can be employed for particle formation without the risk of damaging the therapeutic cargo. Furthermore, a high loading capacity and entrapment efficiency is attained with this click approach and rapid native peptide release results upon exposure to cytosolic/tumor relevant reducing conditions. Finally, any other compound with an amine could be considered for conjugation with this linker, multi-lysine peptides being particularly challenging owing to the presence of multiple amines. This opens application towards other amine containing APIs and other azide containing nanocarriers or drug delivery systems.

Conflicts of interest

The authors declare that there is no conflict of interest.

Acknowledgements

We would like to acknowledge Tim Hogervorst and John Kruijtzer for the advice and assistance with peptide synthesis. The Dutch Research Council (NWO) and Cristal Therapeutics are acknowledged for funding (NWA.ID.17.030).

List of abbreviations

AAA:	azidoacetic acid
ACN:	acetonitrile
AUC:	area under curve
CCPM:	core-crosslinked polymeric micelle
CP:	cloud point
DCC:	*N,N'*-dicyclohexylcarbodiimide
DCM:	dichloromethane
DIPEA:	*N,N*-diisopropylethylamine
DLS:	dynamic light scattering
DMAP:	4-dimethylaminopyridine
DMEM:	dulbecco's modified eagle medium
DMF:	dimethyl formamide
DMSO:	dimethyl sulfoxide
DPTS:	*N,N*-dimethylaminopyridinium *p*-toluenesulfonate
FBS:	fetal bovine serum
GPC:	gel permeation chromatography
HATU:	hexafluorophosphate azabenzotriazole tetramethyl uranium
HeLa:	Cervical cancer cells isolated from Henrietta Lacks
$HPMAmLac_n$:	*N*-2-hydroxypropyl methacrylamide mono/di lactate
HPLC:	high performance liquid chromatography
IR:	infra-red
KPS:	potassium persulfate
MA:	methacrylic acid
MALDI:	matrix assisted laser desorption ionization
mPEG:	methoxy polyethylene glycol
MS:	mass spectrometry
MTS:	3-(4,5-dimethylthiazol-2-yl)-5-(3-carboxymethoxyphenyl)-2-(4-sulfophenyl)-2H-tetrazolium
NMR:	nuclear magnetic resonance spectroscopy
P:	mPEG-*b*-$pHPMAmLac_n$-MA

PA:	mPEG-*b*-pHPMAmLac$_n$-MA-AAA
PM:	polymeric micelle
RT:	room temperature
TEMED:	tetramethylethylenediamine
TFF:	tangential flow filtration
THF:	tetrahydrofuran
TLC:	thin layer chromatography
TMTHSI:	1-imino-3,3,6,6-tetramethyl-4,5-didehydro-2,3,6,7-tetrahydro-1H-1λ6-thiepine 1-oxide
TMTHSI-Succ:	TMTHSI conjugated with Succinic acid
UHPLC:	ultra-high performance liquid chromatography

References

(1) M. Rabanel, J.; Aoun, V.; Elkin, I.; Mokhtar, M.; Hildgen, P. Drug-Loaded Nanocarriers: Passive Targeting and Crossing of Biological Barriers. *Curr. Med. Chem.* **2012**, *19* (19), 3070–3102.

(2) Wang, N.; Cheng, X.; Li, N.; Wang, H.; Chen, H. Nanocarriers and Their Loading Strategies. *Adv. Healthc. Mater.* **2019**, *8* (6), 1801002.

(3) Mazumdar, S.; Chitkara, D.; Mittal, A. Exploration and Insights into the Cellular Internalization and Intracellular Fate of Amphiphilic Polymeric Nanocarriers. *Acta Pharm. Sin. B* **2021**, *11* (4), 903–924.

(4) Rijcken, C. J. F.; De Lorenzi, F.; Biancacci, I.; Hanssen, R. G. J. M.; Thewissen, M.; Hu, Q.; Atrafi, F.; Liskamp, R. M. J.; Mathijssen, R. H. J.; Miedema, I. H. C.; Menke - van der Houven van Oordt, C. W.; van Dongen, G. A. M. S.; Vugts, D. J.; Timmers, M.; Hennink, W. E.; Lammers, T. Design, Development and Clinical Translation of CriPec®-Based Core-Crosslinked Polymeric Micelles. *Adv. Drug Deliv. Rev.* **2022**, *191*, 114613.

(5) Uhlig, T.; Kyprianou, T.; Martinelli, F. G.; Oppici, C. A.; Heiligers, D.; Hills, D.; Calvo, X. R.; Verhaert, P. The Emergence of Peptides in the Pharmaceutical Business: From Exploration to Exploitation. *EuPA Open Proteomics* **2014**, *4*, 58–69.

(6) Henninot, A.; Collins, J. C.; Nuss, J. M. The Current State of Peptide Drug Discovery: Back to the Future? *J. Med. Chem.* **2018**, *61* (4), 1382–1414.

(7) Chen, K.-J.; Plaunt, A. J.; Leifer, F. G.; Kang, J. Y.; Cipolla, D. Recent Advances in Prodrug-Based Nanoparticle Therapeutics. *Eur. J. Pharm. Biopharm.* **2021**, *165*, 219–243.

(8) Gavriel, A. G.; Sambrook, M. R.; Russell, A. T.; Hayes, W. Recent Advances in Self-Immolative Linkers and Their Applications in Polymeric Reporting Systems. *Polym. Chem.* **2022**, *13* (22), 3188–3269.

(9) Carl, P. L.; Chakravarty, P. K.; Katzenellenbogen, J. A. A Novel Connector Linkage Applicable in Prodrug Design. *J. Med. Chem.* **1981**, *24* (5), 479–480.

(10) Elgersma, R. C.; Coumans, R. G. E.; Huijbregts, T.; Menge, W. M. P. B.; Joosten, J. A. F.; Spijker, H. J.; de Groot, F. M. H.; van der Lee, M. M. C.; Ubink, R.; van den Dobbelsteen, D. J.; Egging, D. F.; Dokter, W. H. A.; Verheijden, G. F. M.; Lemmens, J. M.; Timmers, C. M.; Beusker, P. H. Design, Synthesis, and Evaluation of Linker-Duocarmycin Payloads: Toward Selection of HER2-Targeting Antibody–Drug Conjugate SYD985. *Mol. Pharm.* **2015**, *12* (6), 1813–1835.

(11) Kopeček, J.; Yang, J. Polymer Nanomedicines. *Adv. Drug Deliv. Rev.* **2020**, *156*, 40–64.

(12) Sáez, J. A.; Escuder, B.; Miravet, J. F. Supramolecular Hydrogels for Enzymatically Triggered Self-Immolative Drug Delivery. *Tetrahedron* **2010**, *66* (14), 2614–2618.

(13) Tan, X.; Li, B. B.; Lu, X.; Jia, F.; Santori, C.; Menon, P.; Li, H.; Zhang, B.; Zhao, J. J.; Zhang, K. Light-Triggered, Self-Immolative Nucleic Acid-Drug Nanostructures. *J. Am. Chem. Soc.* **2015**, *137* (19), 6112–6115.

(14) Wang, Z.; Wu, H.; Liu, P.; Zeng, F.; Wu, S. A Self-Immolative Prodrug Nanosystem Capable of Releasing a Drug and a NIR Reporter for in Vivo Imaging and Therapy. *Biomaterials* **2017**, *139*, 139–150.

(15) Gisbert-Garzarán, M.; Manzano, M.; Vallet-Regí, M. Self-Immolative Chemistry in Nanomedicine. *Chem. Eng. J.* **2018**, *340* (December 2017), 24–31.

(16) Kennedy, L.; Sandhu, J. K.; Harper, M.-E.; Cuperlovic-Culf, M. Role of Glutathione in Cancer: From Mechanisms to Therapies. *Biomolecules* **2020**, *10* (10), 1429.

(17) Deng, Z.; Hu, J.; Liu, S. Disulfide-Based Self-Immolative Linkers and Functional Bioconjugates for Biological Applications. *Macromol. Rapid Commun.* **2020**, *41* (1), 1900531.

(18) Brülisauer, L.; Gauthier, M. A.; Leroux, J. C. Disulfide-Containing Parenteral Delivery Systems and Their Redox-Biological Fate. *J. Control. Release* **2014**, *195*, 147–154.

(19) Senter, P. D.; Pearce, W. E.; Greenfield, R. S. Development of a Drug-Release Strategy Based on the Reductive Fragmentation of Benzyl Carbamate Disulfides. *J. Org. Chem.* **1990**, *55* (9), 2975–2978.

(20) Suma, T.; Cui, J.; Müllner, M.; Fu, S.; Tran, J.; Noi, K. F.; Ju, Y.; Caruso, F. Modulated Fragmentation of Proapoptotic Peptide Nanoparticles Regulates Cytotoxicity. *J. Am. Chem. Soc.* **2017**, *139* (11), 4009–4018.

(21) Zalipsky, S.; Mullah, N.; Engbers, C.; Hutchins, M. U.; Kiwan, R. Thiolytically Cleavable Dithiobenzyl Urethane-Linked Polymer–Protein Conjugates as Macromolecular Prodrugs: Reversible PEGylation of Proteins. *Bioconjug. Chem.* **2007**, *18* (6), 1869–1878.

(22) He, M.; Li, J.; Han, H.; Borges, C. A.; Neiman, G.; Røise, J. J.; Hadaczek, P.; Mendonsa, R.; Holm, V. R.; Wilson, R. C.; Bankiewicz, K.; Zhang, Y.; Sadlowski, C. M.; Healy, K.; Riley, L. W.; Murthy, N. A Traceless Linker for Aliphatic Amines That Rapidly and Quantitatively Fragments after Reduction. *Chem. Sci.* **2020**, *11* (33), 8973–8980.

(23) Agard, N. J.; Prescher, J. A.; Bertozzi, C. R. A Strain-Promoted [3 + 2] Azide-Alkyne Cycloaddition for Covalent Modification of Biomolecules in Living Systems. *J. Am. Chem. Soc.* **2004**, *126* (46), 15046–15047.

(24) Kim, E.; Koo, H. Biomedical Applications of Copper-Free Click Chemistry: In Vitro , in Vivo , and Ex Vivo. *Chem. Sci.* **2019**, *10* (34), 7835–7851.

(25) Yoon, H. Y.; Lee, D.; Lim, D.; Koo, H.; Kim, K. Copper-Free Click Chemistry: Applications in Drug Delivery, Cell Tracking, and Tissue Engineering. *Adv. Mater.* **2022**, *34* (10), 2107192.

(26) La–Venia, A.; Dzijak, R.; Rampmaier, R.; Vrabel, M. An Optimized Protocol for the Synthesis of Peptides Containing Trans -Cyclooctene and Bicyclononyne Dienophiles as Useful Multifunctional Bioorthogonal Probes. *Chem. – A Eur. J.* **2021**, *27* (54), 13632–13641.

(27) Weterings, J.; Rijcken, C. J. F.; Veldhuis, H.; Meulemans, T.; Hadavi, D.; Timmers, M.; Honing, M.; Ippel, H.; Liskamp, R. M. J. TMTHSI, a Superior 7-Membered Ring Alkyne Containing Reagent for Strain-Promoted Azide–Alkyne Cycloaddition Reactions. *Chem. Sci.* **2020**, *11* (33), 9011–9016.

(28) Timmers, M.; Kipper, A.; Frey, R.; Notermans, S.; Voievudskyi, M.; Wilson, C.; Hentzen, N.; Ringle, M.; Bovino, C.; Stump, B.; Rijcken, C. J. F.; Vermonden, T.; Dijkgraaf, I.; Liskamp, R. Exploring the Chemical Properties and Medicinal Applications of Tetramethylthiocycloheptyne Sulfoximine Used in Strain-Promoted Azide–Alkyne Cycloaddition Reactions. *Pharmaceuticals* **2023**, *16* (8), 1155.

(29) Mirjolet, J.-F.; Haug, B. E.; Mortensen, B.; Berg, K.; Camilio, K. A.; Stensen, W.; Bichat, F.; Serin, G.; Eliassen, L. T.; Svendsen, J. S.; Rekdal, Ø. Discovery of a 9-Mer Cationic Peptide (LTX-315) as a Potential First in Class Oncolytic Peptide. *J. Med. Chem.* **2016**, *59* (7), 2918–2927.

(30) Spicer, J.; Marabelle, A.; Baurain, J.-F.; Jebsen, N. L.; Jøssang, D. E.; Awada, A.; Kristeleit, R.; Loirat, D.; Lazaridis, G.; Jungels, C.; Brunsvig, P.; Nicolaisen, B.; Saunders, A.; Patel, H.; Galon, J.; Hermitte, F.; Camilio, K. A.; Mauseth, B.; Sundvold, V.; Sveinbjørnsson, B.; Rekdal, Ø. Safety, Antitumor Activity, and T-Cell Responses in a Dose-Ranging Phase I Trial of the Oncolytic Peptide LTX-315 in Patients with Solid Tumors. *Clin. Cancer Res.* **2021**, *27* (10), 2755–2763.

(31) LTX-315 and Adoptive T-cell Therapy in Advanced Soft Tissue Sarcoma (ATLAS-IT-04) - Full Text View - ClinicalTrials.gov https://www.clinicaltrials.gov/ct2/show/NCT03725605 (accessed 2022 -08 -29).

(32) Hu, Q.; Rijcken, C. J. F.; van Gaal, E.; Brundel, P.; Kostkova, H.; Etrych, T.; Weber, B.; Barz, M.; Kiessling, F.; Prakash, J.; Storm, G.; Hennink, W. E.; Lammers, T. Tailoring the Physicochemical Properties of Core-Crosslinked Polymeric Micelles for Pharmaceutical Applications. *J. Control. Release* **2016**, *244*, 314–325.

(33) Talelli, M.; Morita, K.; Rijcken, C. J. F.; Aben, R. W. M.; Lammers, T.; Scheeren, H. W.; van Nostrum, C. F.; Storm, G.; Hennink, W. E. Synthesis and Characterization of Biodegradable and Thermosensitive Polymeric Micelles with Covalently Bound Doxorubicin-Glucuronide Prodrug via Click Chemistry. *Bioconjug. Chem.* **2011**, *22* (12), 2519–2530.

(34) Atrafi, F.; Dumez, H.; Mathijssen, R. H. J.; Menke van der Houven van Oordt, C. W.; Rijcken, C. J. F.; Hanssen, R.; Eskens, F. A. L. M.; Schöffski, P. A Phase I Dose-Escalation and Pharmacokinetic Study of a Micellar Nanoparticle with Entrapped Docetaxel (CPC634) in Patients with Advanced Solid Tumours. *J. Control. Release* **2020**, *325* (March), 191–197.

(35) Miedema, I. H. C.; Zwezerijnen, G. J. C.; Huisman, M. C.; Doeleman, E.; Mathijssen, R. H. J.; Lammers, T.; Hu, Q.; van Dongen, G. A. M. S.; Rijcken, C. J. F.; Vugts, D. J.; Menke-van der Houven van Oordt, C. W. PET-CT Imaging of Polymeric Nanoparticle Tumor Accumulation in Patients. *Adv. Mater.* **2022**, *34* (21), 2201043.

(36) Atrafi, F.; van Eerden, R. A. G.; van Hylckama Vlieg, M. A. M.; Oomen-de Hoop, E.; de Bruijn, P.; Lolkema, M. P.; Moelker, A.; Rijcken, C. J.; Hanssen, R.; Sparreboom, A.; Eskens, F. A. L. M.; Mathijssen, R. H. J.; Koolen, S. L. W. Intratumoral Comparison of Nanoparticle Entrapped Docetaxel (CPC634) with Conventional Docetaxel in Patients with Solid Tumors. *Clin. Cancer Res.* **2020**, *26* (14), 3537–3545.

(37) Soga, O.; van Nostrum, C. F.; Ramzi, A.; Visser, T.; Soulimani, F.; Frederik, P. M.; Bomans, P. H. H.; Hennink, W. E. Physicochemical Characterization of Degradable Thermosensitive Polymeric Micelles. *Langmuir* **2004**, *20* (21), 9388–9395.

(38) Hu, Q.; Rijcken, C. J.; Bansal, R.; Hennink, W. E.; Storm, G.; Prakash, J. Complete Regression of Breast Tumour with a Single Dose of Docetaxel-Entrapped Core-Cross-Linked Polymeric Micelles. *Biomaterials* **2015**, *53*, 370–378.

(39) Sun, T.; Morger, A.; Castagner, B.; Leroux, J. C. An Oral Redox-Sensitive Self-Immolating Prodrug Strategy. *Chem. Commun.* **2015**, *51* (26), 5721–5724.

(40) Stahl, P. J.; Cruz, J. C.; Li, Y.; Michael Yu, S.; Hristova, K. On-the-Resin N-Terminal Modification of Long Synthetic Peptides. *Anal. Biochem.* **2012**, *424* (2), 137–139.

(41) Neises, B.; Steglich, W. Simple Method for the Esterification of Carboxylic Acids. *Angew. Chemie Int. Ed. English* **1978**, *17* (7), 522–524.

(42) Soga, O.; van Nostrum, C. F.; Hennink, W. E. Poly(N -(2-Hydroxypropyl) Methacrylamide Mono/Di Lactate): A New Class of Biodegradable Polymers with Tuneable Thermosensitivity. *Biomacromolecules* **2004**, *5* (3), 818–821.

(43) Shirangi, M.; Sastre Toraño, J.; Sellergren, B.; Hennink, W. E.; Somsen, G. W.; Van Nostrum, C. F. Methyleneation of Peptides by N, N, N, N -Tetramethylethylenediamine (TEMED) under Conditions Used for Free Radical Polymerization: A Mechanistic Study. *Bioconjug. Chem.* **2015**, *26* (1), 90–100.

(44) Cadée, J. A.; Van Steenbergen, M. J.; Versluis, C.; Heck, A. J. R.; Underberg, W. J. M.; Den Otter, W.; Jiskoot, W.; Hennink, W. E. Oxidation of Recombinant Human Interleukin-2 by Potassium Peroxodisulfate. *Pharm. Res.* **2001**, *18* (10), 1461–1467.

(45) Strandberg, E.; Schweigardt, F.; Wadhwani, P.; Bürck, J.; Reichert, J.; Cravo, H. L. P.; Burger, L.; Ulrich, A. S. Phosphate-Dependent Aggregation of [KL]n Peptides Affects Their Membranolytic Activity. *Sci. Rep.* **2020**, *10* (1), 12300.

(46) Ghisaidoobe, A.; Chung, S. Intrinsic Tryptophan Fluorescence in the Detection and Analysis of Proteins: A Focus on Förster Resonance Energy Transfer Techniques. *Int. J. Mol. Sci.* **2014**, *15* (12), 22518–22538.

(47) Talelli, M.; Barz, M.; Rijcken, C. J. F.; Kiessling, F.; Hennink, W. E.; Lammers, T. Core-Crosslinked Polymeric Micelles: Principles, Preparation, Biomedical Applications and Clinical Translation. *Nano Today* **2015**, *10* (1), 93–117.

(48) Li, Q.; Li, X.; Zhao, C. Strategies to Obtain Encapsulation and Controlled Release of Small Hydrophilic Molecules. *Front. Bioeng. Biotechnol.* **2020**, *8* (May), 1–6.

(49) Szymusiak, M.; Kalkowski, J.; Luo, H.; Donovan, A. J.; Zhang, P.; Liu, C.; Shang, W.; Irving, T.; Herrera-Alonso, M.; Liu, Y. Core–Shell Structure and Aggregation Number of Micelles Composed of Amphiphilic Block Copolymers and Amphiphilic Heterografted Polymer Brushes Determined by Small-Angle X-Ray Scattering. *ACS Macro Lett.* **2017**, *6* (9), 1005–1012.

(50) Li, M.; Jiang, S.; Simon, J.; Paßlick, D.; Frey, M.-L.; Wagner, M.; Mailänder, V.; Crespy, D.; Landfester, K. Brush Conformation of Polyethylene Glycol Determines the Stealth Effect of Nanocarriers in the Low Protein Adsorption Regime. *Nano Lett.* **2021**, *21* (4), 1591–1598.

(51) Ainavarapu, S. R. K.; Brujić, J.; Huang, H. H.; Wiita, A. P.; Lu, H.; Li, L.; Walther, K. A.; Carrion-Vazquez, M.; Li, H.; Fernandez, J. M. Contour Length and Refolding Rate of a Small Protein Controlled by Engineered Disulfide Bonds. *Biophys. J.* **2007**, *92* (1), 225–233.

(52) Li, D.; Kordalivand, N.; Fransen, M. F.; Ossendorp, F.; Raemdonck, K.; Vermonden, T.; Hennink, W. E.; van Nostrum, C. F. Reduction-Sensitive Dextran Nanogels Aimed for Intracellular Delivery of Antigens. *Adv. Funct. Mater.* **2015**, *25* (20), 2993–3003.

(53) Soga, O.; van Nostrum, C. F.; Fens, M.; Rijcken, C. J. F.; Schiffelers, R. M.; Storm, G.; Hennink, W. E. Thermosensitive and Biodegradable Polymeric Micelles for Paclitaxel Delivery. *J. Control. Release* **2005**, *103* (2), 341–353.

(54) Talelli, M.; Iman, M.; Varkouhi, A. K.; Rijcken, C. J. F.; Schiffelers, R. M.; Etrych, T.; Ulbrich, K.; van Nostrum, C. F.; Lammers, T.; Storm, G.; Hennink, W. E. Core-Crosslinked Polymeric Micelles with Controlled Release of Covalently Entrapped Doxorubicin. *Biomaterials* **2010**, *31* (30), 7797–7804.

(55) Gao, W.-C.; Tian, J.; Shang, Y.-Z.; Jiang, X. Steric and Stereoscopic Disulfide Construction for Cross-Linkage via N -Dithiophthalimides. *Chem. Sci.* **2020**, *11* (15), 3903–3908.

Supporting information (SI)

NMR spectra

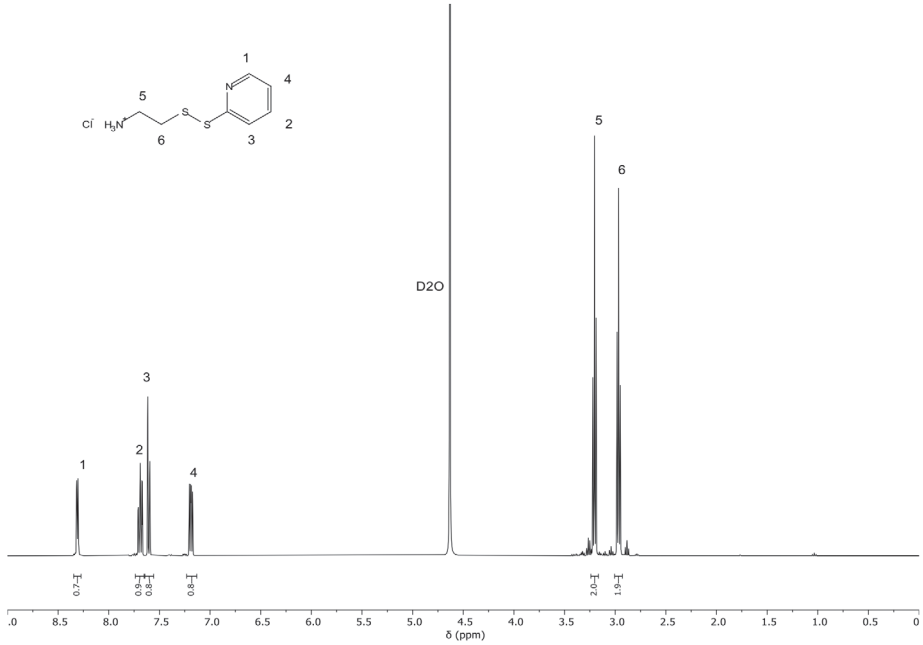

*Figure S1.1: [1]H NMR spectrum of compound **1** (pyridine dithioethylamine hydrochloride). The solvent was D_2O.*

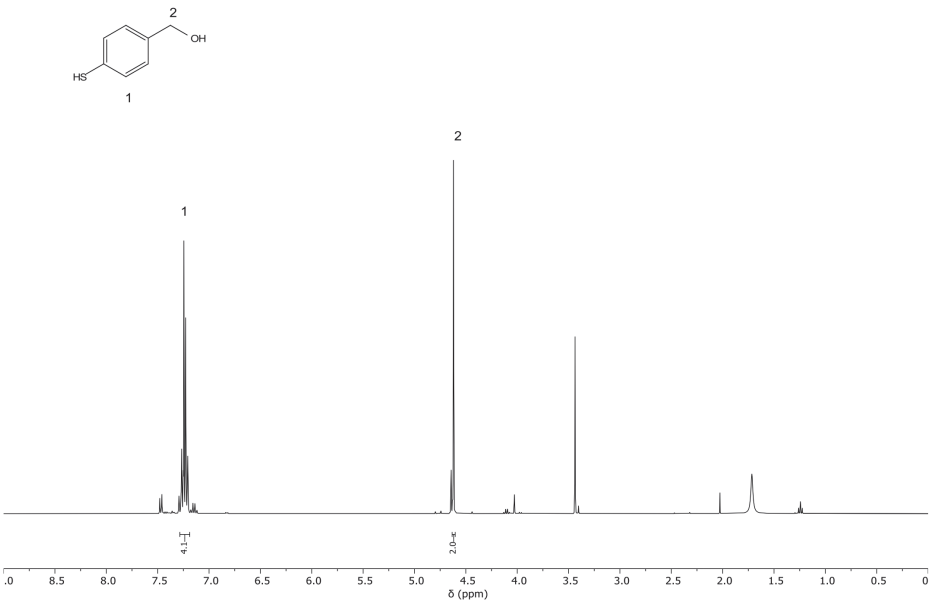

*Figure S1.2: [1]H NMR spectrum of compound **2** (4-mercaptobenzyl alcohol). The solvent was $CDCl_3$.*

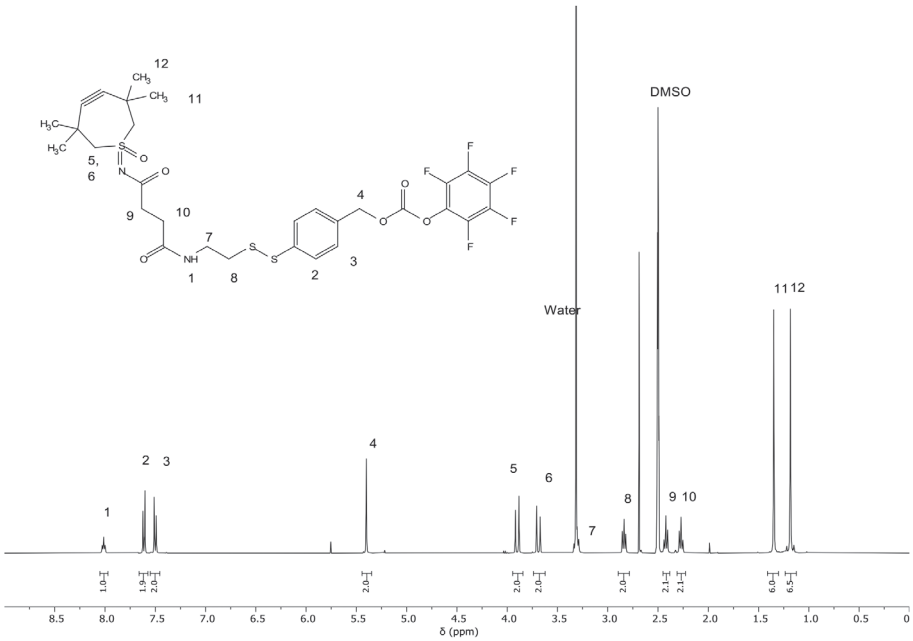

*Figure S1.3: [1]H NMR spectrum of the linker, compound **5**. The solvent was DMSO-d6.*

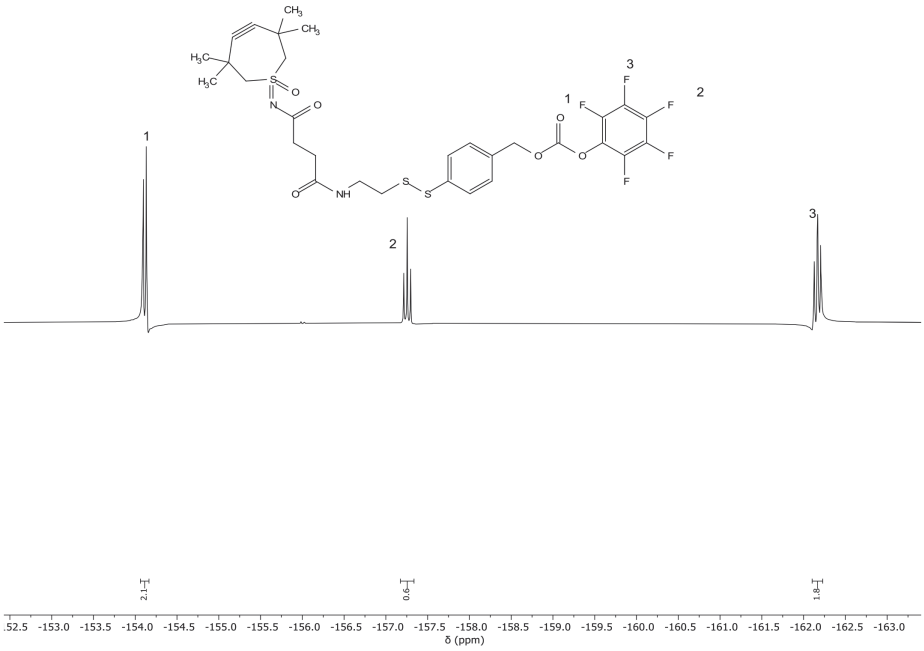

*Figure S1.4: ^{19}F NMR spectrum of compound **5**. The solvent was DMSO-d6.*

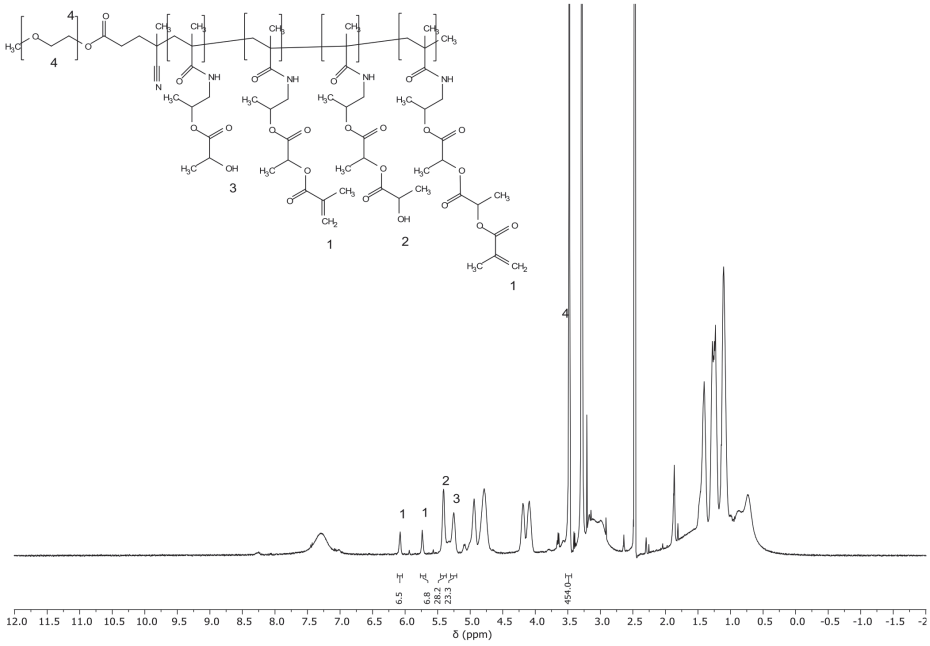

*Figure S1.5: [1]H NMR spectrum of mPEG-b-pHPMAmLac$_n$-MA, polymer **P** has an mPEG molecular weight of 5 kDa and based on NMR analysis, there are approximately 23 and 28 units of HPMAmLac$_1$ and HPMAmLac$_2$ per polymer chain, respectively. Additionally, there are approximately 7 methacrylate functionalities per polymer chain. The total M_n is thus approximately 20 kDa. The solvent was DMSO-d6.*

Mass spectra

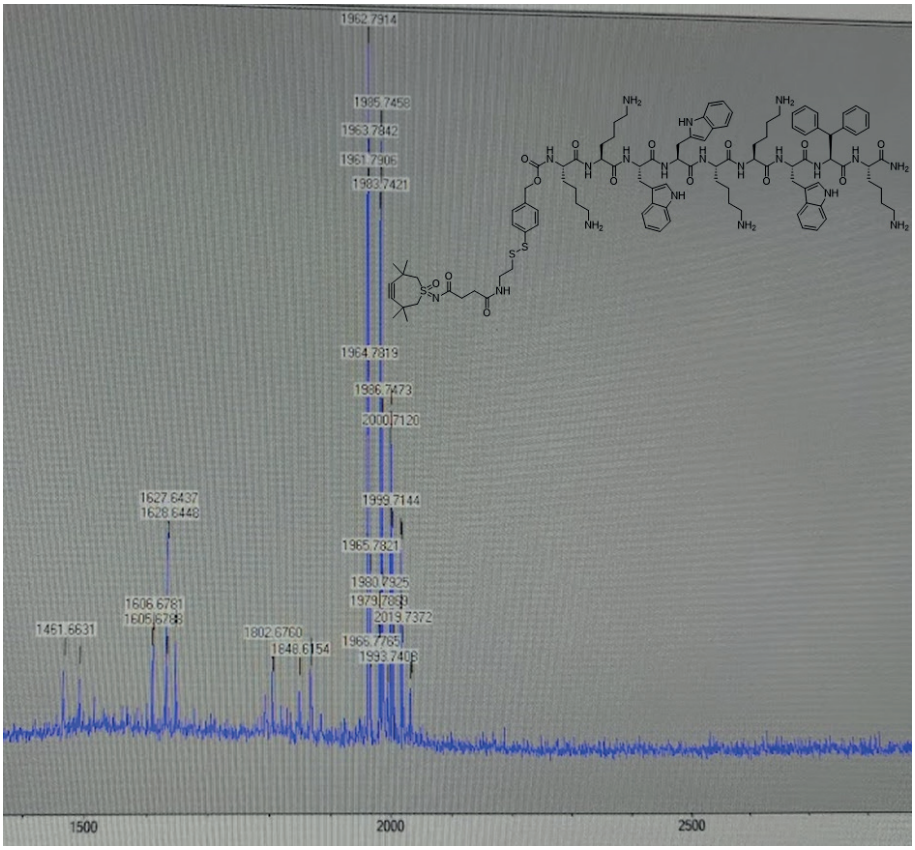

Figure S2.1: MALDI-MS spectrum of the preparative HPLC purified Linker-LTX conjugate (structure shown). Expected mass for $C_{102}H_{137}N_{20}O_{14}S_3^+$ is 1962.0, measured 1961.8, 1983.7 (Na^+ adduct) and 1999.7 (K^+ adduct).

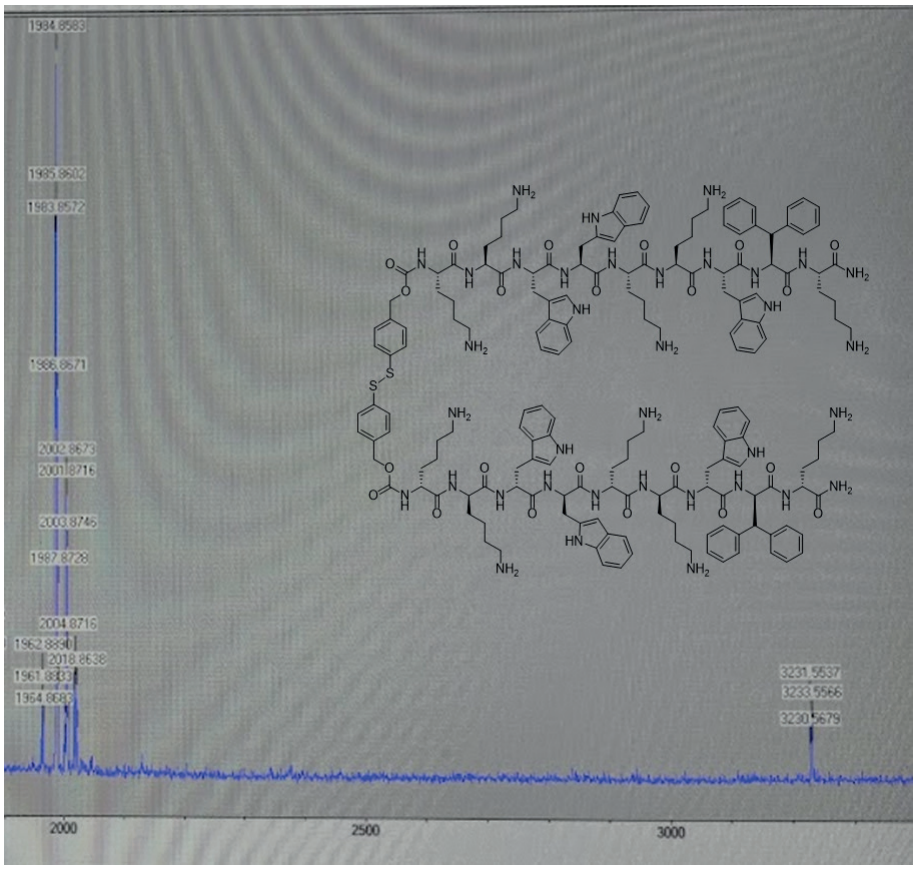

Figure S2.2: MALDI-MS spectrum of the preparative HPLC purified Linker-LTX conjugate after freeze drying and dissolution in milliQ. Expected mass for $C_{102}H_{137}N_{20}O_{14}S_3^+$ and $C_{102}H_{136}N_{20}O_{14}S_3Na^+$ is 1962.0 and 1984.0, measured 1961.8 and 1983.9 respectively. Signal of the dimer (structure shown) resulting from disulfide disproportionation was also detected, expected mass for $C_{172}H_{222}N_{36}O_{22}S_2Na^+$ is 3230.7, measured 3230.6.

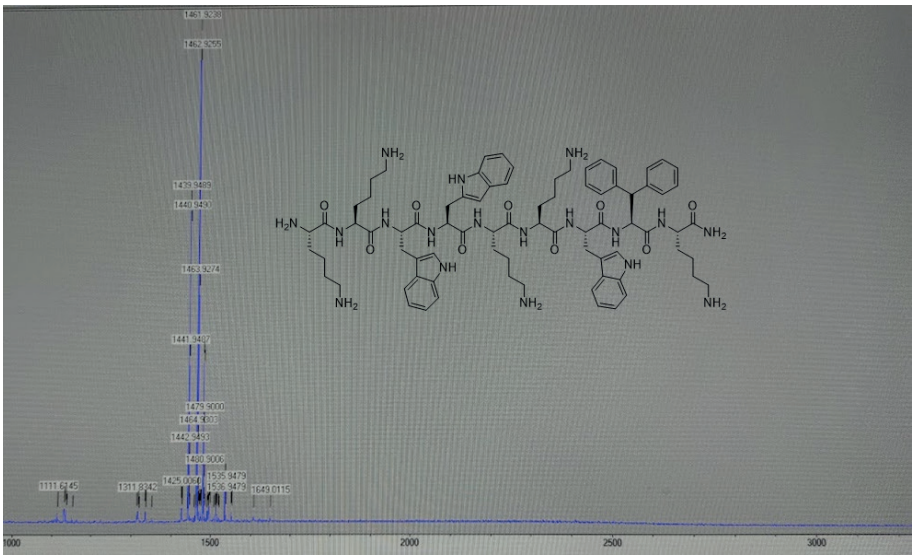

Figure S2.3: MALDI-MS spectrum of the LTX loaded CCPMs after treatment with 5 mM GSH. Expected mass for $C_{78}H_{107}N_{18}O_9^+$ is 1439.8, measured 1439.9 and 1461.9 (Na^+ adduct) respectively.

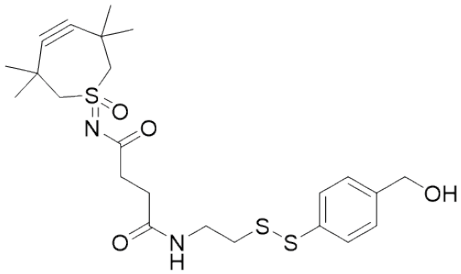

4

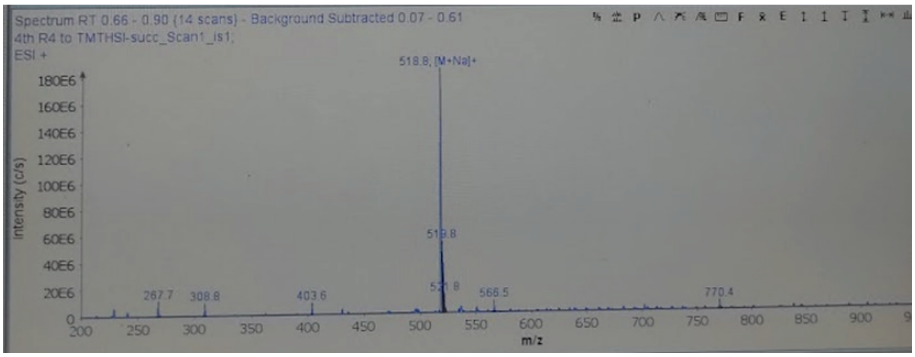

*Figure S2.4: TLC-MS spectrum of compound **4**. Expected mass for $C_{23}H_{32}N_2O_4S_3Na^+$ is 519.1, found 518.8.*

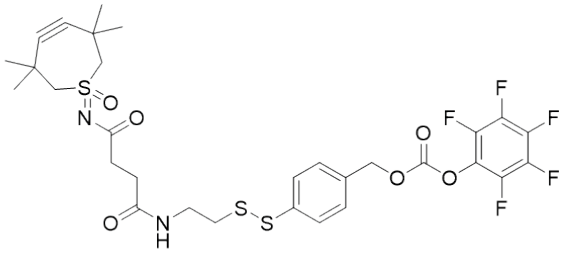

5

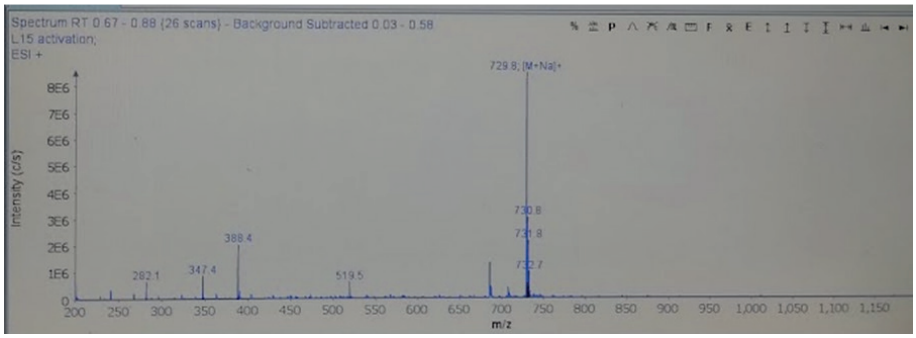

*Figure S2.5: TLC-MS spectrum of compound **5**. Expected mass for $C_{30}H_{31}N_2O_6S_3F_5Na^+$ is 729.1, found 729.8*

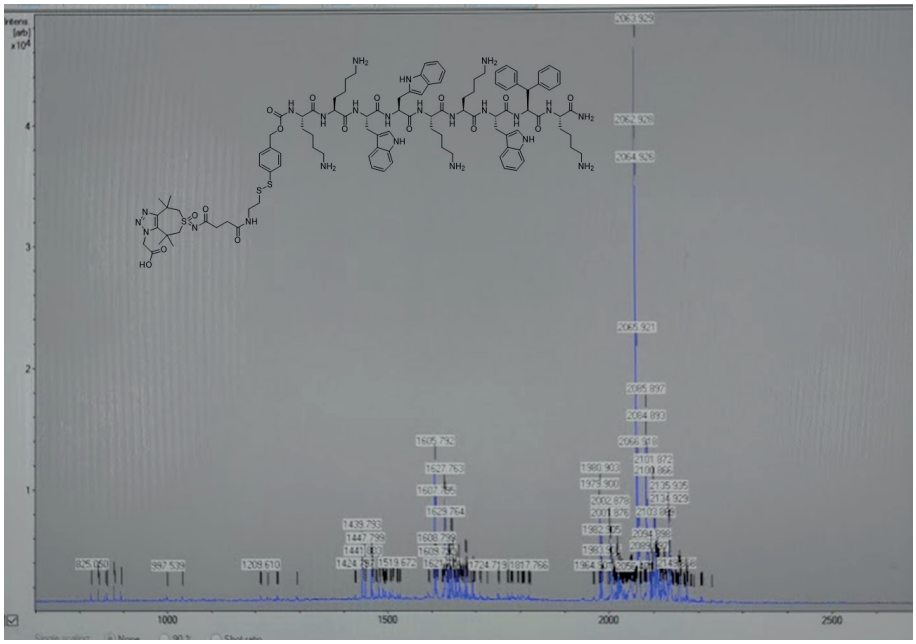

Figure S2.6: MALDI-MS spectrum of a fraction (see figure S3.3, orange chromatogram, R_t = 9.0 mins) that emerged during the click entrapment of linker-LTX into the CCPMs, indicating the presence of uncoupled AAA-linker-LTX. $C_{104}H_{140}N_{23}O_{16}S_3^+$ is 2063.0, measured 2062.9.

HPLC chromatograms

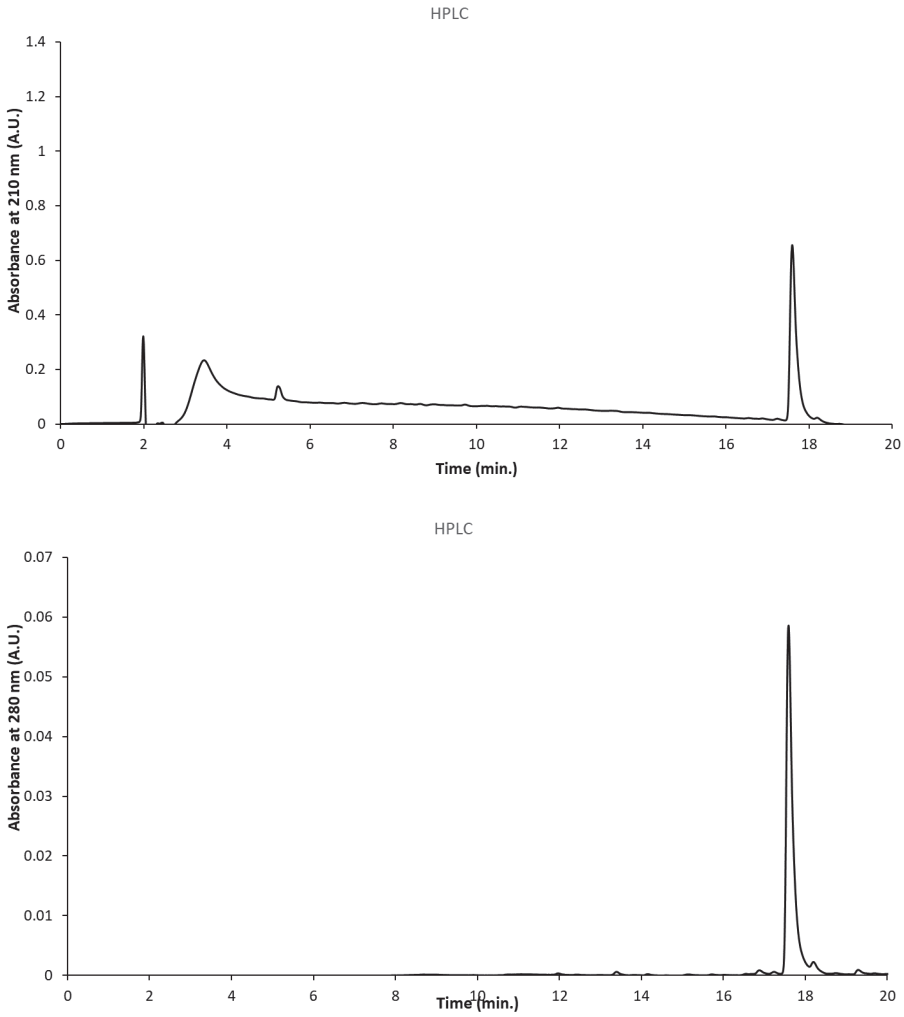

*Figure S3.1: HPLC chromatograms of the linker (compound **5**), recorded with 210 nm (top) and 280 nm absorbance (bottom). The linker was dissolved in 50% ACN modified with 0.1% formic acid.*

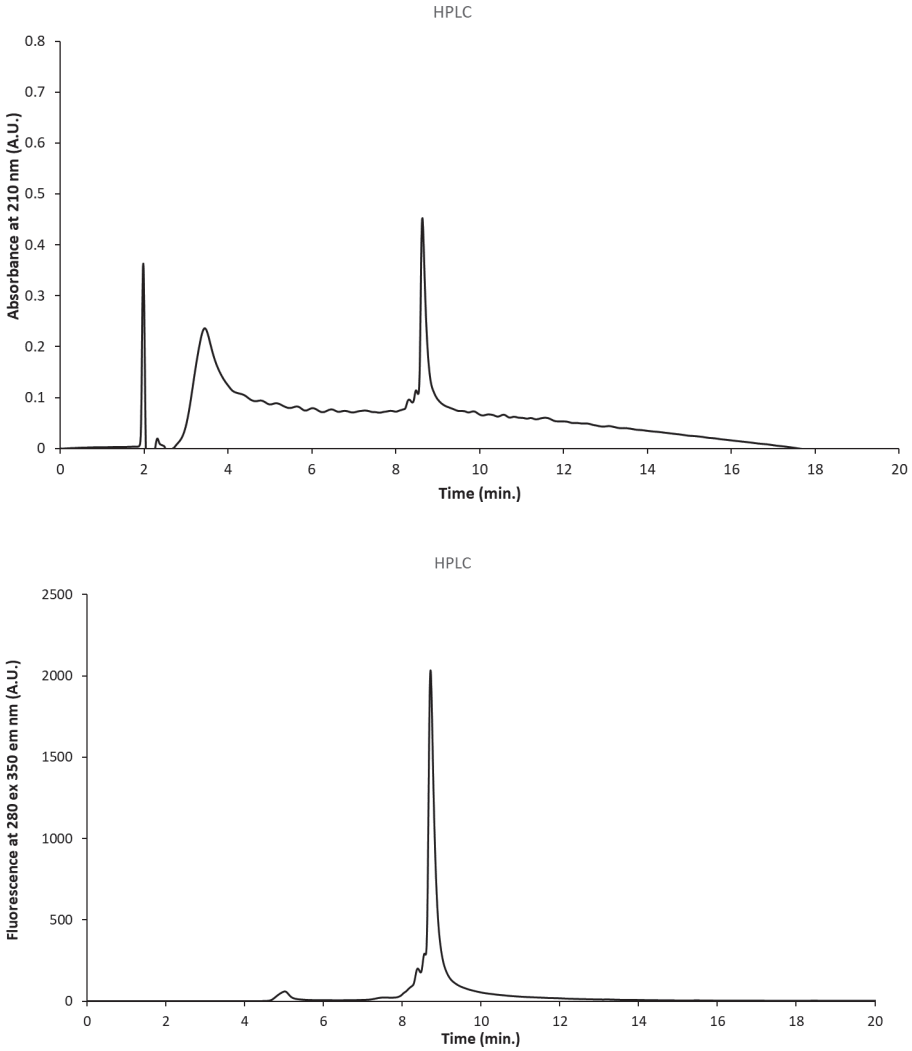

Figure S3.2: HPLC chromatograms of the pure fraction of Linker-LTX, recorded with 210 nm absorbance (top) and $\lambda_{ex}/\lambda_{em}$ 280/350 nm fluorescence (bottom).

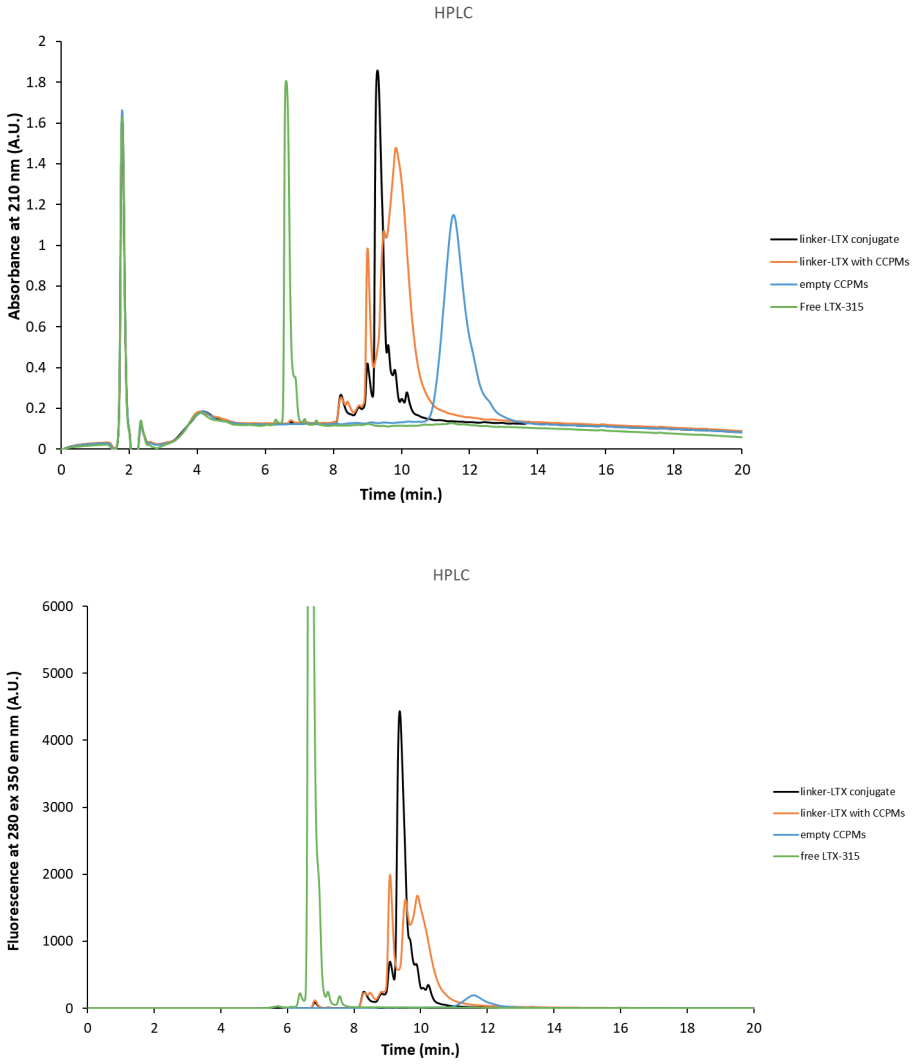

Figure S3.3: HPLC chromatograms of the linker-LTX conjugate (black) incubated with CCPMs for 3 hours without purification (orange), compared to reference empty CCPMs (blue) and free LTX-315 peptide (green), recorded with 210 nm absorbance (top) and $\lambda_{ex}/\lambda_{em}$ 280/350 nm fluorescence (bottom). The peak of linker-LTX (black) disappears upon mixing with CCPMs (orange), and a more hydrophilic CCPM peak as compared to the empty CCPM peak (blue) is observed. No free LTX (green) is detected during the click entrapment. See figure S2.6 for the MALDI spectrum of the newly formed peak at R_t = 9.0 minutes.

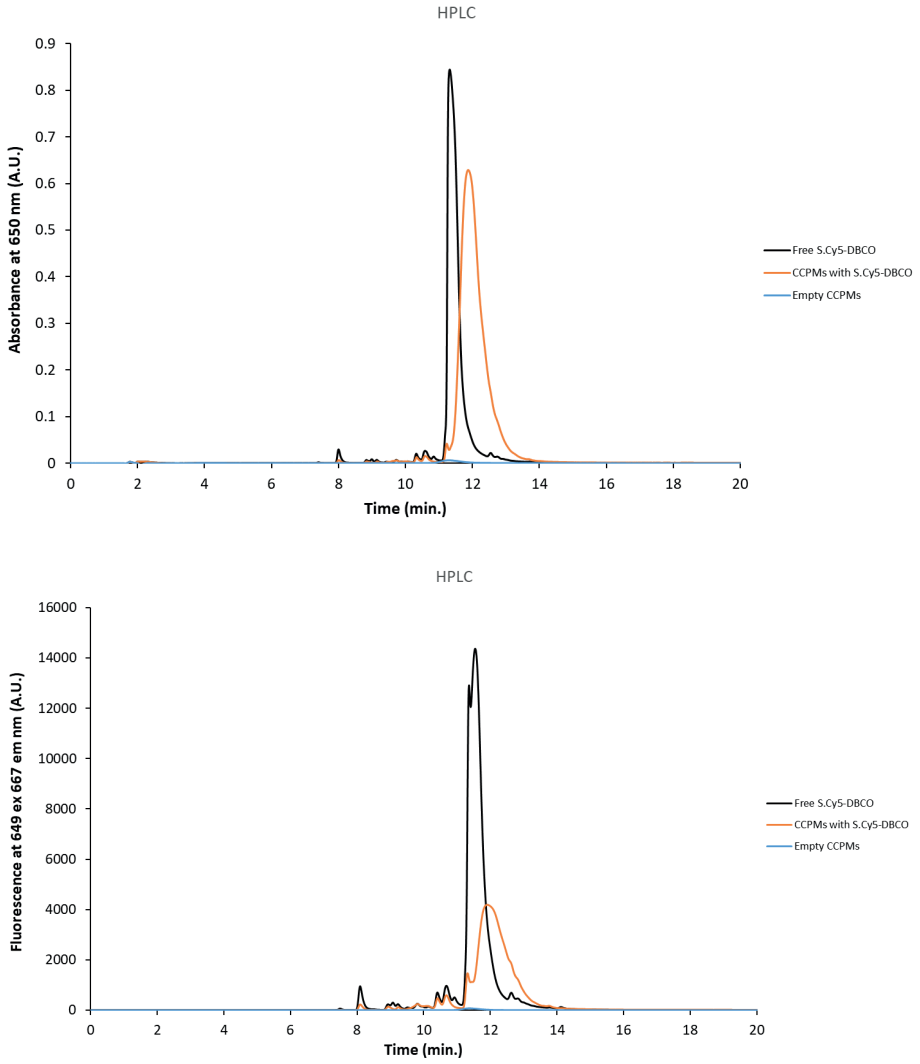

Figure S3.4: HPLC chromatograms of S.Cy5-DBCO (blue) loaded into CCPMs (grey) before TFF purification, compared to reference empty CCPMs (yellow), recorded with 650 nm absorbance (top) and $\lambda_{ex}/\lambda_{em}$ 649/667 nm fluorescence (bottom). See figure S3.5 for the chromatogram after TFF purification.

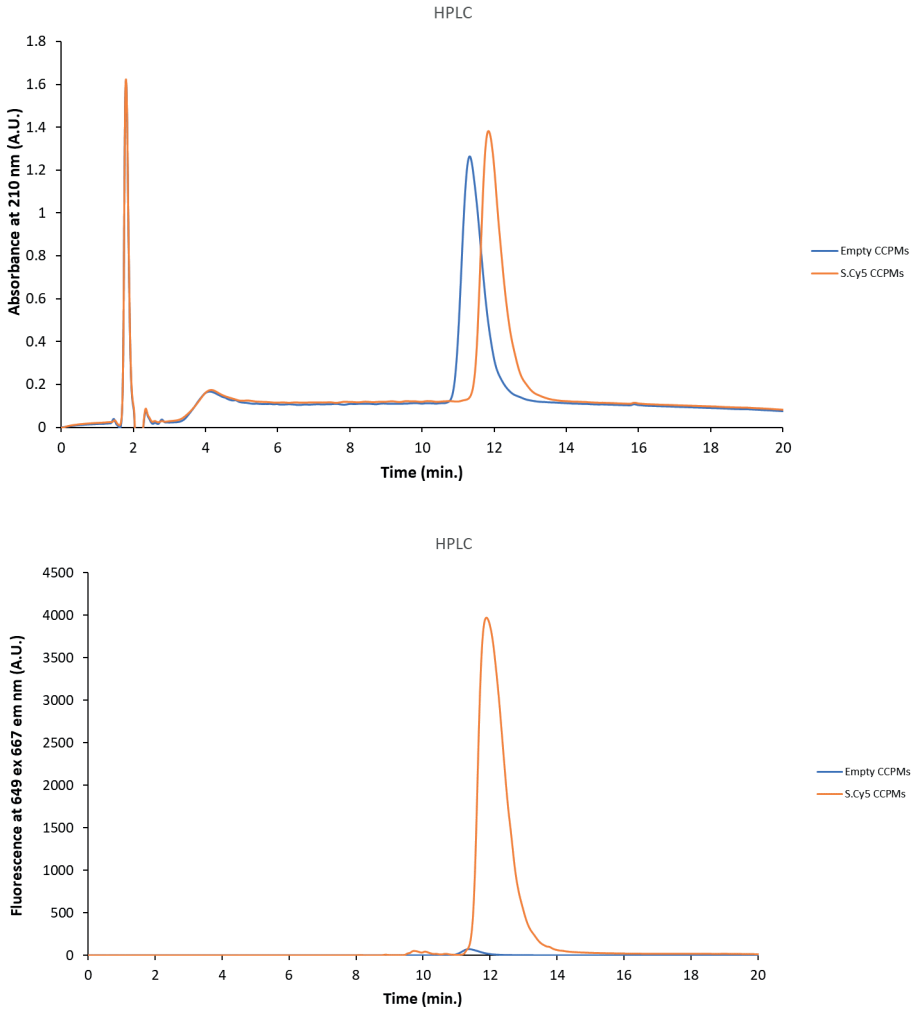

Figure S3.5: HPLC chromatograms of the S.Cy5 loaded CCPMs <u>after</u> TFF purification (orange), compared to reference empty CCPMs (blue), recorded with 210 nm absorbance (top) and $\lambda_{ex}/\lambda_{em}$ 649/667 nm fluorescence (bottom).

UPLC chromatograms

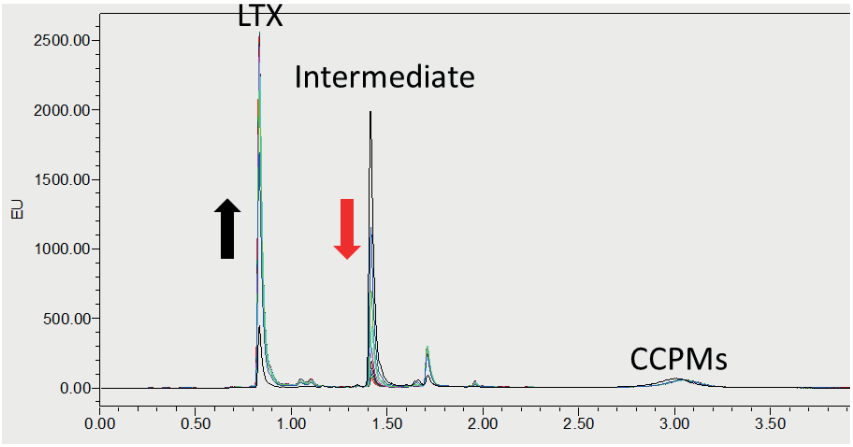

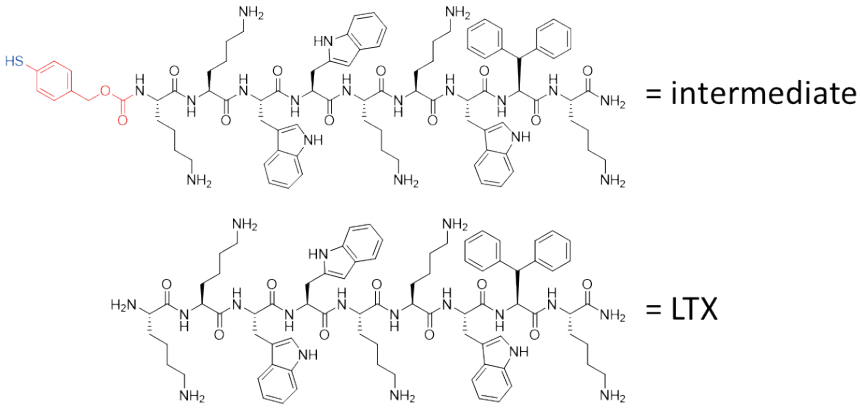

Figure S4.1: Overlayed UPLC chromatograms of the LTX-315 released from the CCPMs under reducing conditions (5 mM GSH), used to quantify the AUC (relative to the highest AUC of native LTX) depicted in figure 1. A clear distinction in retention time is observed between the intermediate state that is almost instantaneously formed and subsequently gradually undergoes 1,6 elimination to form the native LTX peptide. Recorded with $\lambda_{ex}/\lambda_{em}$ 280/350 nm fluorescence.

IR spectra

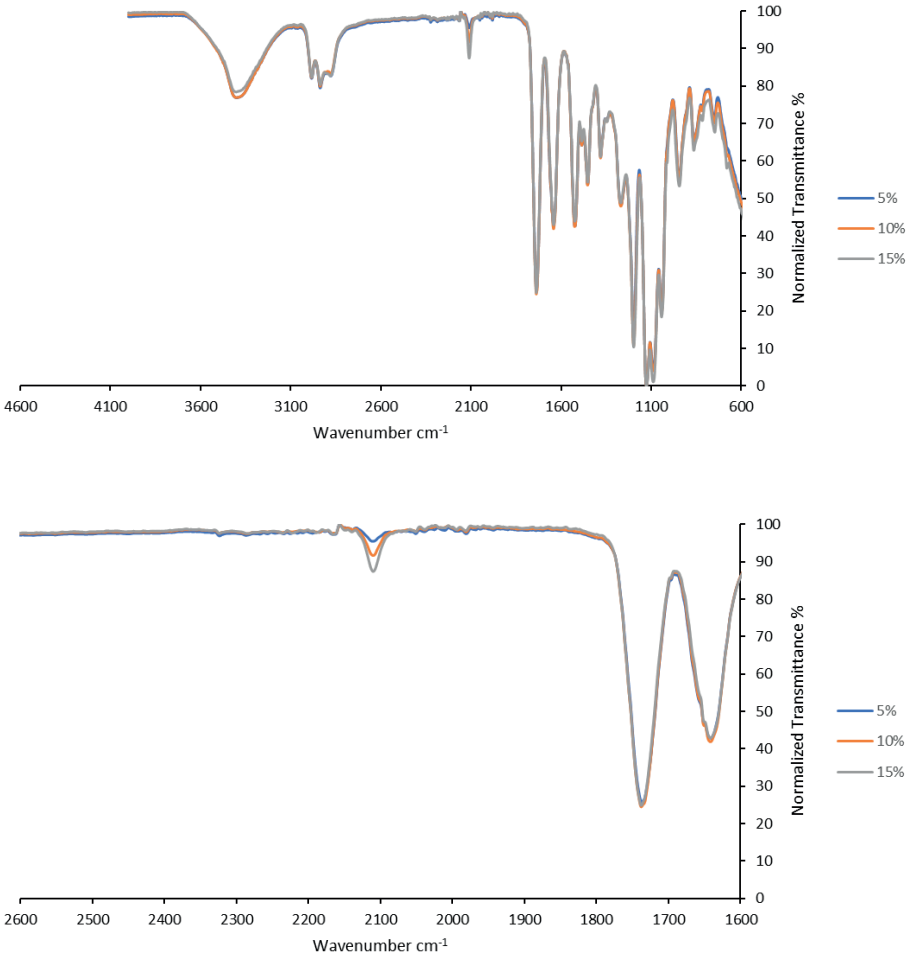

*Figure S5.1: IR spectra of 5, 10 and 15 mol% feed AAA modified polymers (**PA**) showing the characteristic azide peak around 2100 cm^{-1}.*

CHAPTER 8

Click chemistry for the covalent coupling of siRNA to and triggered release from core-crosslinked polymeric micelles

Matt Timmers[1,2], Erik Hebels[1], Marco Kong[2], Jaimie Hak[1], Robert Liskamp[2,3,4], Cristianne J.F. Rijcken[2], Wim E. Hennink[1], Tina Vermonden[1]

[1] Division of Pharmaceutics, Utrecht Institute for Pharmaceutical Sciences (UIPS), Utrecht University, 3508 TB Utrecht, the Netherlands.
[2] Cristal Therapeutics, 6229 EV Maastricht, the Netherlands
[3] Department of Biochemistry, Cardiovascular Research Institute Maastricht (CARIM), Maastricht University, Maastricht 6229 ER, the Netherlands
[4] School of Chemistry, University of Glasgow, Glasgow G12 8QQ, U.K.

Manuscript in preparation

Abstract

Small- interfering RNA's (siRNA) are a promising class of drugs but their clinical use is limited due to their fast degradation and clearance from the circulation and free siRNA is not taken up by cells. Core-crosslinked polymeric micelles (CCPMs) based on mPEG-b-pHPMALac$_n$ demonstrated long circulation and increased tumour uptake upon intravenous administration in both animal models and patients. Here, a strategy is described to load siRNA in these CCPMs. By modifying mPEG-b-pHPMALac$_n$ with azides and functionalizing the siRNA with a recently developed redox-sensitive click linker TMTHSI-disulfide-pentafluorophenyl, the siRNA was covalently coupled to the core of these modified CCPMs in a mild click reaction at room temperature. The entrapment efficiency was 92% with 2 w/w% loading of siRNA in the CCPMs. The loaded siRNA was fully released after incubation with 5 mM GSH overnight at room temperature. These siRNA-loaded particles were taken up by HeLa and HEK293T cells, showing promise of these CCPMs for siRNA delivery.

Introduction

Small interfering RNA (siRNA) is a promising therapeutic modality for the treatment of many diseases by selectively binding and degrading its target mRNA, resulting in silencing of disease-related genes. However, widespread application of siRNA is hampered [1-7] due to its unfavourable pharmacokinetics and susceptibility for enzymatic degradation. [8-10] Besides, this large polyanionic molecule is not able to pass cellular membranes by diffusion and therefore hardly reaches their target mRNAs which are present in the cytosol. [11,12]

Much research has therefore been performed to improve the serum stability, short circulation time and limited cellular uptake of siRNA. To mention, a wide array of chemical modifications of the sugar ring, phosphate backbone or bases has been developed to improve the stability of siRNA against nuclease-mediated degradation. [13-15] However, these modified siRNA's still lack poor pharmacokinetics and cellular uptake. Therefore, nanoparticulate carriers have been extensively investigated to protect the loaded siRNA against enzymatic degradation, to improve circulation kinetics and allow cellular uptake . [16] Nucleic acids loaded in lipid-based systems such as liposomes and lipid based particles[17], nanocapsules[18], lipoplexes[19] and solid lipid nanoparticles (sLNPs) [20,21] have shown efficacy both *in vitro*, in different animal models and also in the clinic. [22] Polymer-based nanoparticles of siRNA and chitosan, [23-25] poly-peptoid based triblock copolymer, [26] or cyclodextrin [27,28] also showed significant benefits regarding circulation kinetics and cellular uptake of siRNA and subsequent gene silencing. However, nearly all these nanoparticles end up in particularly the macrophages in the liver. [29-31] Ideally, a carrier is able to evade liver uptake long enough to exert an organ targeting effect.

Core-crosslinked polymeric micelles (CCPMs) based on methoxy polyethylene glycol-*b*-poly[*N*-(2-hydroxypropyl) methacrylamide-lactate] (m-PEG-*b*-pHPMAmLac$_n$) block-copolymers as carriers for multiple small molecule active pharmaceutical ingredients have shown significant improvement in circulation time of drugs and tumour uptake in both animal models [32,33] and in patients. [34] While retaining the hydrophobic drugs covalently entrapped inside the hydrophobic core, the extended circulation time of these CCPMs compared to free cargo also allows for tumour targeting, utilizing the enhanced permeation and retention (EPR) effect, [35,36] as demonstrated by 4-fold higher tumour uptake in patients compared to the intravenously administered free drug. [37] These promising results strengthen the interest of expanding this platform towards new therapeutic modalities, such as siRNA. CCPMs might be an attractive carrier for siRNA as the enhanced circulation time may improve the tumour uptake of siRNA-loaded

CCPMs. Besides, this approach avoids the use of cationic moieties such as polylysine as previously used by Kataoka et al., [38-40] which are considered toxic. [41] Additionally, such polycationic polymers and liposomes can induce complement activation, [42-45] whereas this was not observed for these CCPMs. [46,47] The high density of PEG on the surface of the CCPM limits interaction with serum proteins, which is the hypothesized explanation for the lack of complement activation. [46]

Although CCPMs are attractive carriers for hydrophobic low molecular weight drugs, they are not suitable for physical loading of siRNA because of the incompatibility of the hydrophobic core with this charged hydrophilic cargo. Therefore, covalent coupling of siRNA to the core of CCPMs is an option to load these therapeutics. However, the fragile nature of siRNA needs to be considered upon coupling of siRNA to CCPMs, since harsh conditions are used to form the links between the polymer chains in the core. For m-PEG-b-pHPMAmLac$_n$ based CCPMs, radical crosslinking is applied using potassium persulfate (KPS) to polymerize methacrylate groups present on the polymer and cargo (e.g. small molecule or peptidic drugs), which results in a grafting of the cargo to the crosslinked core. To introduce methacrylate groups in siRNA for grafting to the core of the CCPM using radical polymerization is very likely not an option since radicals damage siRNA. [48,49]

To covalently link siRNA to the core of CCPMs, a new post-crosslinking approach is therefore investigated in this study. To achieve this, m-PEG-b-pHPMAmLac$_n$, also functionalized with methacrylate groups, was modified with azides in the hydrophobic block as described in **chapter 7**. Importantly, it was shown that the azides remained functional after radical crosslinking. Here, siRNA was used with redox-sensitive click linker **1** (Scheme 1, linker synthesis described in **chapter 7**) to allow its introduction into pre-formed and crosslinked micelles by exploiting click chemistry that occurs fast and under mild conditions ensuring the structural integrity of the coupled siRNA. In the linker a disulfide bond is present which can be cleaved under reducing conditions as present in the cytosol of the target cell. [50,51] The aim of this study was to 1) functionalize siRNA with the redox-sensitive click linker **1**, 2) load this linker-modified siRNA into micelles and 3) show release of siRNA from these micelles. Additionally, the cellular uptake of these siRNA-loaded micelles was explored.

Materials and methods

Materials

The solvents were purchased from Biosolve (Valkenswaard, the Netherland) unless stated otherwise. Reagents were purchased from Sigma-Aldrich (Zwijndrecht, the Netherlands) unless stated otherwise. Click reagent tetramethylthiacycloheptynesulfoximine (TMTHSI) [52] and m-PEG-b-pHPMAmLac$_n$ polymer were kindly provided by Cristal Therapeutics (Maastricht, the Netherlands). siRNA was purchased from Axolabs (Kulmbach, Germany) with the following sequences and modifications:

Fluorescently labelled siRNA (siFL):

Sense: 5'- (NH_2C_6)GfgAfuGfaAfgUfgGfaGfaUfuAfgUf(invdT) -3'

Antisense: 5'- dAsCfuAfaUfcUfcCfaCfuUfcAfuCfcdTsdTs(C6NH)(Rho3B-NHS) -3'

siRNA for silencing firefly luciferase (siLuc):

Sense: 5'-(NH_2C_6)sascCfgaaAfGfGfucUfuaccGfgas(invdT)-3'

Antisense: 5'-UfsCfscgguaagaccuUfucggususu-3'

With:

Af, Gf, Uf, Cf: 2'-Fluoro nucleotide

a, g , u, c: 2'-O-methyl-nucleotide

S: phosphorothioate

(invdT): inverted dT

Rho3B-NHS: Rhodamine 3B fluorescent label (ex 566/em 589) introduced via NHS coupling prior to hybridization.

The used siRNAs were modified with phosphorothioate and methylated or fluorinated at 2' positions for increased stability. At the 5' end of the sense strand, the hexylamine modification was used for covalent linkage with redox-sensitive click linker **1**. siFL was also functionalized with a Rhodamine 3B fluorescent label at the 3' position of the antisense strand for convenient monitoring. The selected siLuc is able to silence firefly luciferase.

m-PEG-b-pHPMAmLac$_n$ was produced on large scale for clinical evaluation [53] and has the following properties: PEG$_{5000}$ hydrophilic block with pHPMA-Lac$_{1-2}$ thermosensitive block, with molar ratio monolactate: dilactate of 48:52. M_n: 18 kDa, PDI: 1.1. 8.9% methacrylation, cloud point: 9°C (see Scheme 2, left, for chemical structure).

Synthesis and characterization

Functionalization of siRNA with redox-sensitive click linker 1

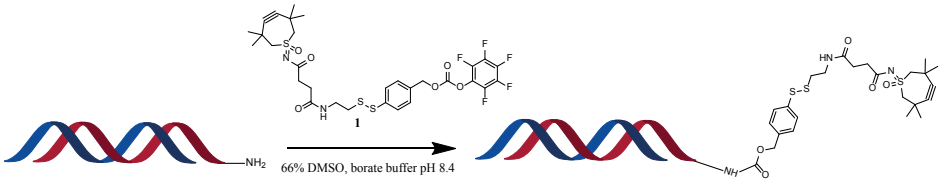

*Scheme 1: functionalization of siLuc with redox-sensitive click linker **1***

In a 2 mL HPLC vial, 10 mg of siRNA (both siFL or siLuc, protocol was identical, 0.68 µmol) with amine handle was dissolved in 500 µL of 100 mM borate buffer with pH adjusted to 8.4, and 800 µL DMSO was added. After the formed heat of mixing was dissipated (after approximately 2 minutes), 200 µL of clickable linker **1** (Scheme 1) in DMSO (10 mg/mL) was added, to have a final mixture of buffer: DMSO with a ratio of 1:2 (v/v) and a molar ratio of 1: 4.2 siRNA to linker equivalents. The reaction mixture was stirred at room temperature for 15 minutes and subsequently diluted with 4 mL of Milli-Q water, washed by Vivaspin centrifugal spinfilter with MWCO of 5 kDa with 30 volumes of Milli-Q water and run through a PD MidiTrap G-25 Sephadex column (5 kDa MWCO) with Milli-Q water as eluent. This eluted solution was subsequently freeze dried and the resulting powder was dissolved in Milli-Q water to obtain a 10 mg/mL stock solution. The reaction was monitored on UPLC using the method described in the Supporting Information S3. In brief, an Acquity BEH C18 Oligo (Waters) column was used with the column temperature set at 89°C to deanneal the two strands of siRNA. A gradient was used consisting of eluent A: 100 mM hexylamine acetic acid and eluent B: 90% ACN 10% 100mM hexylamine acetic acid with a gradual increase of eluent B gradient. Hexylamine pairs with the negatively charged phosphate backbone of siRNA, which results in interaction and thus retention on the C18 column. This interaction is gradually lost with increasing ACN volume fraction in the eluent.

Polymer derivatisation with azide

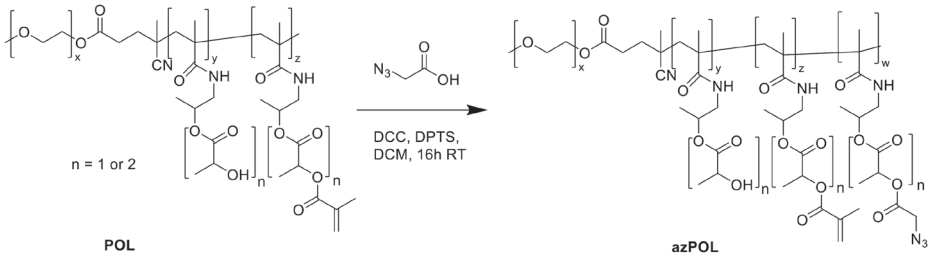

Scheme 2: m-PEG-b-pHPMAmLac$_n$ derivatisation with azidoacetic acid with x= 114 average (PEG$_{5000}$), z= 8.9% (degree of methacrylation), ratio n=1 : n=2 48:52, w= degree of azide functionalisation (10%)

Scheme 2 shows the chemical structures of the used polymer (abbreviated POL) and its functionalization with azide groups, as also described in **chapter 7**. POL (1.0 gram, 55.6 µmol, 2.8 mmol OH groups) was dissolved in 6.4 mL of dichloromethane (DCM) and stock solutions of azido-acetic acid (870 µL of 50 mg/mL stock, 430 µmol), 4-(dimethylamino)pyridinium 4-toluenesulfonate (DPTS) (600 µL of 20 mg/mL stock, 43 µmol) and finally dicyclohexylcarbodiimide (DCC) (1.95 mL of 50 mg/mL stock, 473 µmol) in DCM were added to achieve a final polymer concentration of 100 mg/mL. This reaction mixture was stirred at room temperature overnight and subsequently filtered through a 0.2 µm (polytetrafluorethylene) PTFE syringe filter. Next the polymer was precipitated in cold diethyl ether (DEE) three times. After drying over air, the polymer was dissolved in acetonitrile (ACN): MilliQ 50:50 and freeze dried. For analysis, azide-polymer (azPOL) was hydrolysed by incubation in 33 mM NaOH aqueous solution for at least three hours. The hydrolysed samples were analysed by Ultra Performance Liquid Chromatography (UPLC), measuring azidoacetic acid and lactic acid content to determine the amount of azides per polymer. The used UPLC method is described in Supporting Info S1.

Preparation of azCCPMs

Azide containing micelles were formed and crosslinked as previously described [54] and in **chapter 7**. In brief, 500 mg azPOL was dissolved in 20.8 mL 20 mM sodium phosphate buffer pH 7.4, (24.1 mg/mL), placed on ice and degassed. Tetramethylethylenediamine (TEMED) was added (0.625 mL, 120 mg/mL) and the pH was adjusted to 7.4 using 1M HCl before addition. Ten minutes after addition of TEMED the temperature was increased to 40°C and ethanol (2.5 mL) was added. After another 10 minutes, potassium persulfate

(KPS) (1.125 mL, 30 mg/mL in 20 mM sodium phosphate buffer pH 7.4)) was added and N_2 was flushed for an hour. The final reaction mixture had a volume of 25 mL, with a polymer concentration of 20 mg/mL. Next, the formed core-azide functionalized crosslinked polymeric micelles (further referred to as azCCPMs) were filtered through a 0.2 μm regenerated cellulose filter to remove potentially present aggregates. azCCPMs were further purified using tangential flow filtration with a modified polyethersulfone (mPES) filter module (MWCO 100 kDa) and 20 mM HEPES buffer pH 7.2 as washing buffer.

Characterization of azCCPMs

The particle size of formed azCCPMs was measured by dynamic light scattering (DLS) using a Malvern Zetasizer Nano S at 10 mg/mL polymer concentration, in 20 mM HEPES buffer pH 7.2 at room temperature. DLS results are given as z-average hydrodynamic diameter (Z_{ave}) and polydispersity index (PDI).

The purity of the azCCPMs was determined using size exclusion chromatography (SEC). The details of this SEC method are described in Supporting Info S2.

Additionally, azidoacetic- and lactic acid content was determined of the azCCPMs after hydrolysis by incubation in 333 mM NaOH aqueous solution for at least three hours. The lactic acid content was used to calculate the polymer concentration of the batch, and the azidoacetic acid content was used to calculate the number of azides per polymer chain.

The zeta potential of the azCCPMs was measured using a Malvern Zetasizer Nano Z at 10 μg/mL polymer concentration in 20 mM HEPES buffer pH 7.2.

Loading and characterization of azCCPMS

To 2 mL of azCCPMs in 20 mM HEPES buffer pH 7.2 (7 mg/mL azPOL, 0.77 μmol azPOL; 4.1 μmol azides), 30 μL of siRNA-linker in Milli-Q water (10 mg/mL siRNA, 0.020 μmol) was added and this mixture was stirred for 2 hours at room temperature. No additional purification step was performed as initial analysis indicated no detectable free siRNA present in solution. Purity of micelles was assessed via SEC and additional analysis was performed by DLS and lactic acid content as described for empty azCCPMs. Additionally, the total siRNA content (differentiated between entrapped and free siRNA) and the zeta potential of the siRNA loaded azCPPms were measured. The detailed analytical procedures are described in section 2.5 and in the Supporting Information.

Agarose gel electrophoresis of siFL-loaded azCCPMs was performed using a 3% agarose gel in 40 mM Tris- 20 mM acetate-1 mM EDTA (TAE) buffer at pH 8.6. Samples were

diluted to 20 µg/mL and 20 µL samples were mixed with 4 µL Tricine Sample Buffer (ThermoFisher) containing sodium dodecyl sulfate (SDS) at pH 8.45 and subsequently pipetted into the wells. The gel was run at 170 V for 20 minutes, after which the gel was imaged using fluorescence detection with an excitation wavelength of 566 nm and emission at 589nm.

Release of siRNA from the siRNA-loaded azCCPMs

SiRNA-loaded azCCPMs (7 mg/mL azPOL in 20 mM HEPES buffer pH 7.2, 100 µL) were incubated in 5 mM glutathione (GSH) in HEPES buffer pH 7.2 (50 mM stock of GSH in HEPES buffer, pH adjusted to 7.2 after dissolution, 10 µL added to azCCPMs) at room temperature overnight. Released siRNA was determined using SEC and free siRNA for calibration using a TSKgel G5000PWXL 300 mm column and PBS with 10% methanol as isocratic eluent and fluorescence detection at $566_{ex}/589_{em}$ nm. Additionally, release was determined using the UPLC method with calibrated free siRNA quantification with the method described in section 2.1. For both SEC and UPLC, calibration curves with stock solutions of 1,10,25,50,100 and 1000 µg/mL siFL were used.

Cell culture

HEK293T (CRL-3216) and HeLa (CCL-2) cells were purchased from American Type Culture Collection (ATCC). HeLa, HEK293T and HEK293T-diLuc cells were cultured in Dulbecco's modified Eagle Medium (DMEM) (Gibco) supplemented with 10% fetal bovine serum (FBS) (Gibco, Corning) and incubated at 37°C and 5% CO_2.

Cellular uptake of siFL-loaded azCCPMs

Confocal imaging and flow cytometry studies were performed to investigate possible binding and cellular internalization of siRNA loaded azCCPMs. HeLa and HEK293T cells were plated into a 96-well plate (Agilent # 204626-100) at a density of 10,000 cells/well in DMEM supplemented with 10% FBS and 1% penicillin/streptomycin and incubated at 37°C, 5% CO_2 for 24 hours.

Confocal microscopy

azCCPMs loaded with fluorescently labelled siRNA were added to the cells in a final concentration of 80 µg/mL polymer, 1.6 µg/mL siFL, followed by incubation for 24 hours at 37 °C. Next, the nuclei of living cells were stained using 2 µg/ml Hoechst 33342 for 10 minutes and washed with Hanks' Balanced Salt Solution (HBSS) afterwards. Fluorescence

microscopy images were taken using a Yokogawa CV 7000 Microscope with a 40x objective lens. The fluorescently labelled siRNA (Rhodamine 3B) was measured at an excitation wavelength of 561 nm and an emission filter of 600 ± 37 nm and Hoechst 33342 was measured at an excitation wavelength of 405 nm and an emission filter of 445 ± 45 nm.

Flow cytometry

Fluorescently labelled siRNA-containing azCCPMs were diluted to siFL concentrations of 1 μM, 330 nM and 165 nM in 20 mM HEPES buffer pH 7.2 and added to HeLa and Hek293T cells. After an incubation of 1, 3, 6 and 24 hours at 37°C, the cells were fixated with 1% formaldehyde in PBS for 15 minutes at 37°C and 5% CO_2 and the fluorescent signal was quantified using a Cytoflex flow cytometer, where both the percentage of rhodamine-positive cells and mean rhodamine fluorescence intensity were measured. Rhodamine was measured using an excitation of 561 nm and an emission filter of 582 ± 42 nm. Per timepoint, 10,000 events were counted by the flow cytometer. Free siFL was not taken as control because it has been shown repeatedly that free siRNA is not taken up by living cells[55-58].

Results and discussion

Strategy for functionalization of siRNA

The linker with the structure shown in Scheme 1 has the following characteristics. Firstly, it can undergo an amidation reaction with the amine handle on siRNA with pentafluorphenol as leaving group. Secondly, the TMTHSI group allows it to couple to the azide groups present in the core of the azCCPMs. Thirdly, the disulfide bond is susceptible for reduction in the cytosol of the target cell after internalization of the micelles. [50,51]

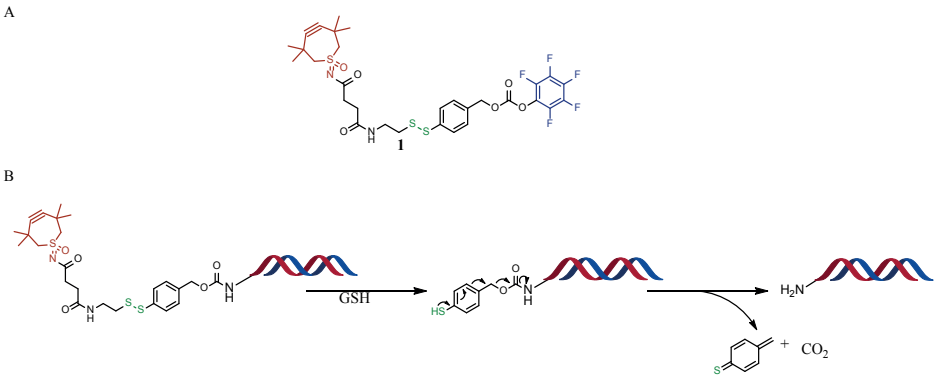

*Figure 1: A: structure of redox-sensitive click linker **1** with amidation activating pentafluorphenyl in blue, TMTHSI click moiety in red and disulfide bond for redox-sensitive release in green. B: mechanism of self-immolative release after GSH reduction*

Functionalization of siLuc siRNA

SiRNA before and after reaction with linker **1** were analyzed using HPLC (Figure 2). Due to the high column temperature of 89°C, the sense and antisense strands dehybridize, which enables their separation. Hexylamine as modifier in the eluent facilitates hydrophobic interaction of the two strands with the C18 column. Analysis of the reaction mixture after reacting siLuc with linker **1**, gave a chromatogram in which the peak of unmodified antisense strand at 5.3 minutes was unaltered, but the peak corresponding to amine-modified sense strand at 5.0 minutes was diminished to less than 95% of its original value, and a new peak with a longer retention time (7.8 minutes) was formed (Figure 2B) which points to a successful and almost quantitative derivatization of the strand with the hydrophobic linker **1**. This high conversion was not unexpected since 4.2 equivalents of linker was added to amine functionalized siRNA. The yield of siRNA-linker conjugate after purification and freeze drying was 85%.

The UPLC analytical method was also used to investigate whether the linker was still functional, by clicking to a model azide and subsequent release of the linker after incubation with gluthathione (GSH). Indeed, upon incubation of functionalized siLuc with an excess of azidoethanol, a new peak in the chromatogram with a shorter retention time (6.6 minutes, figure 2C) was detected indicating that the strained alkyne retained its structural integrity after coupling of the linker to amine functionalized siRNA. Lastly, to study the release of siRNA from the linker, glutathione was added to reduce the disulfide bond present in the linker (Figure 1A). Because of the self-immolative thiobenzyl carbamate moiety present in the linker, reduction of the disulfide bond results

in a subsequent formation of the native amine on the sense strand[59] (Figure 1B). Indeed, incubation of linker-functionalized siLuc with GSH resulted in the formation of the original amine-modified sense strand, with the same retention time as unmodified siRNA at 5.0 minutes (Figure 2D).

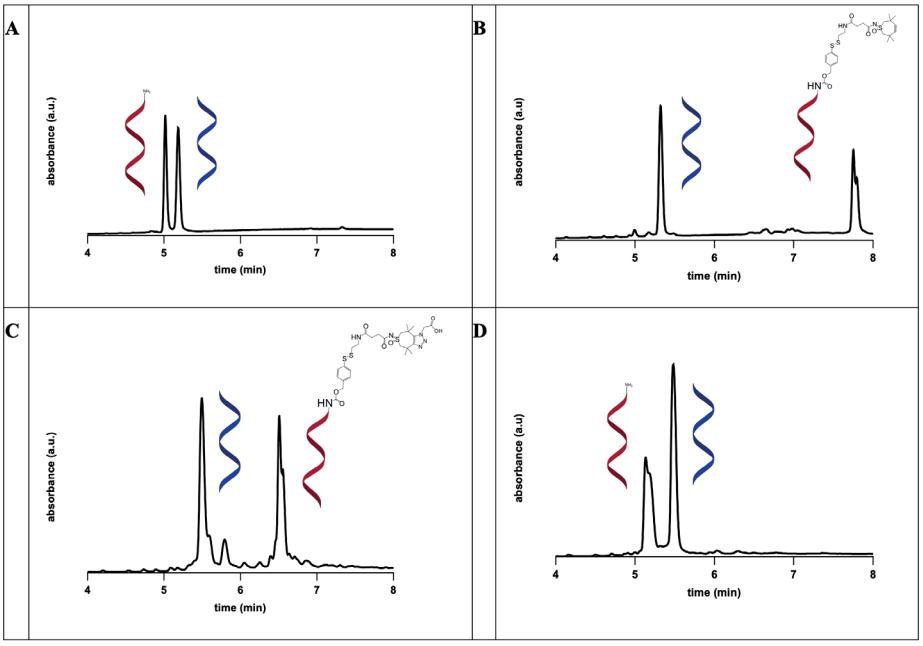

*Figure 2: UPLC chromatograms of siRNA linker before and after functionalization with linker **1** A: siLuc stock solution B: siLuc with linker **1** attached C: siLuc with linker attached upon incubation with an excess of azidoethanol and D: siLuc-linker **1** construct after incubation with GSH.*

Functionalization of siFL

To visualize of siRNA in the micelles, fluorescently labelled siRNA, siFL was coupled to linker **1** and its coupling and triggered release was investigated using UPLC in the same way as for siLuc. The chromatogram of siFL also showed a complete peak shift of the amine-modified strand from 1.5 to 4.9 minutes after reacting with the linker for 15 minutes (Supporting Info figure S4). After purification and incubation of the siFL with GSH, a peak shift of 3.4 minutes to the original retention time of free siFL at 1.5 minutes was observed, demonstrating successful cleavage of the linker and its formation of the native amine-bearing strand (SI figure S4).

Polymer derivatisation with azido acetic acid

Polymer derivatisation of 1 gram of POL with azidoacetic acid (Scheme 2) resulted in the formation of azide-modified polymer (azPOL) with a yield of 0.75 gram (75% yield). UPLC analysis after hydrolysis showed that 5.3 azides were attached per polymer chain (Figure 3). The reaction feed was 7.7 azides per polymer chain, meaning that the coupling efficiency was 68% which is in line with previously reported results (**Chapter 7**).

Micellization and crosslinking

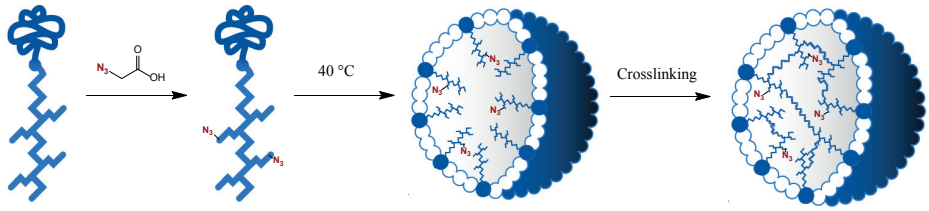

Figure 3: modification of mPEG-b-pHPMA-Lac$_n$ polymers with azidoacetic acid, subsequent micelle formation and crosslinking.

AzCCPMs were prepared by rapidly increasing the temperature of the azPOL aqueous solution from 0 to 40°C and by covalently crosslinking the core by radical polymerization of the methacrylate groups coupled to the thermosensitive blocks (Figure 3). The formed azCCPMs were filtered and purified by TFF, after which they displayed a Z_{ave} of 58 nm and PDI of 0.062 based on DLS analysis. SEC was measured to compare azCCPMs and unmodified CCPMs. The SEC profiles of azCCPMs and unmodified particles are shown in Supporting Info S5. Both size of the azCCPMs (58 nm, as determined with DLS) and SEC profile of the azCCPMs were comparable to non-azide modified CCPMs (64 nm, determined with DLS) as reported before, [33,60] indicating no major impact of introducing azides to the core of the micelles on their size.

Loading and characterization of micelles

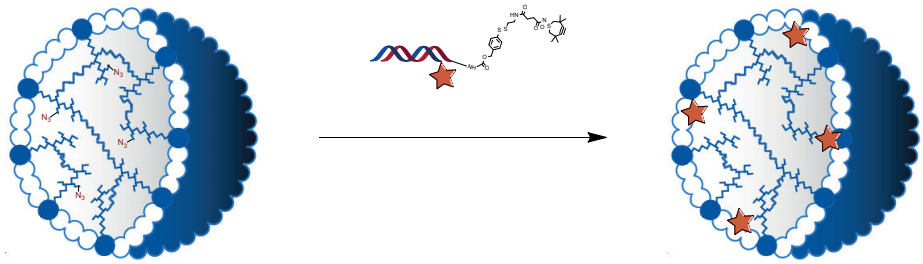

Figure 4: loading of functionalized siRNA into azCCPMs

The freeze dried siFL functionalized with linker **1** was dissolved in water and added to the azCCPMs (Figure 4). After reacting for 2 hours at room temperature, azCCPM with siFL entrapped, as well as empty azCCPPMs and free siFL were analysed by SEC (Figure 5A-C). Figure 5C shows that fluorescent signal was detected at the retention time of the particles, indicating coupling of siRNA to azides present in the core of the crosslinked azCCPMs. As control, siFL without linker was also incubated with azCCPMs and subsequently analyzed with SEC. The chromatogram showed the presence of free siFL (Figure 5D), ruling out noncovalent interaction between siRNA and azCCPM. The results indicate that siRNA was indeed clicked into the azCCPMs at a molar ratio of 50 azides to 1 siRNA molecule.

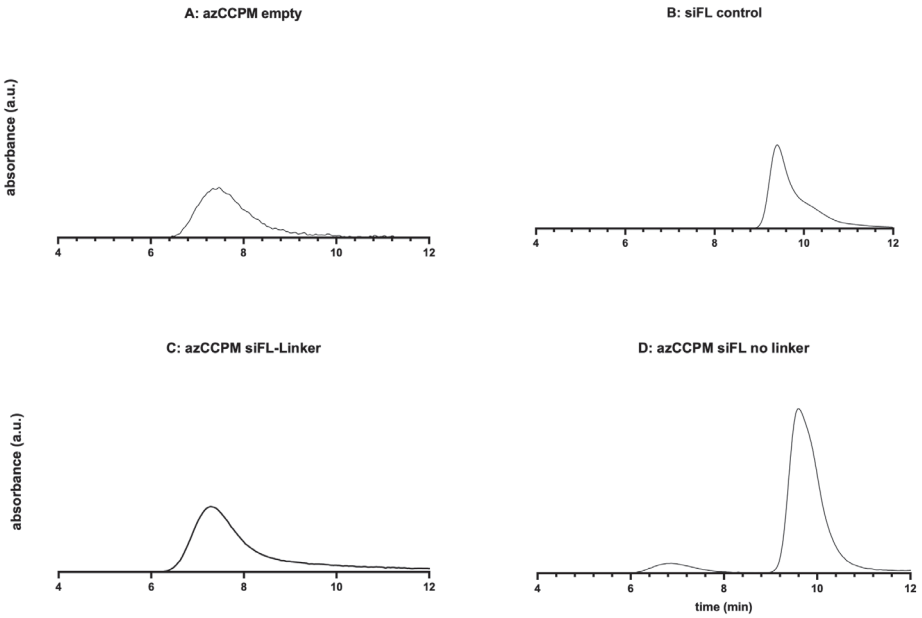

Figure 5: SEC chromatograms of A: empty azCCPMs B: free siFL C: azCCPMs loaded with functionalized siFL and D: azCCPMs with non-functionalized siFL.

Loaded azCCPMs had a size of 64.8 ±3.3 nm, with a PDI of 0.10 ±0.02 (Table 1). DLS indicated a small increase in size (from 58 to 65 nm) upon loading of siLuc. DLS determination of siFL-loaded particles was not possible, as the wavelength of the laser used (633 nm) was absorbed by the fluorescent label, resulting in a non-reliable outcome. [61] Table 1 shows that the zeta potential of empty azCCPMs and siRNA-loaded azCCPMs was -1.6 ± 9.2 and -7.0 ± 7.2, respectively indicating that the PEG shell shields the negative charge of siRNA coupled to the core of the micelles.

In consideration of the molar excess of 50 azides per siRNA and the hydrophilic nature of siRNA, it is likely that siRNA does not permeate into the hydrophobic core but clicks to the azides present at the interface between the core and shell of the particle. To further explain, the azCCPMs with a shell of 5 kDa PEG have a shell thickness of around 8 nm, [62] and siRNA with 21 base pairs has in its stretched conformation a length of 7 nm, but due to flexibility of the backbone its actual average length is shorter. [63] Clicking at the interface would then allows siRNA to fully reside in the PEG shell.

Table 1: Overview of azCCPMs before and after loading with functionalized siFL(n=3 replicates)
*: could not be determined due to absorbance of the light of laser by the fluorescent label.

	Size (nm)	PDI	Z_{pot} (mV)	SEC
Non-modified CCPM	64 ± 1	0.03±0.02	-3.0 ±6.7	
azCCPPM empty	58 ± 1	0.06 ±0.01	-1.6± 9.2	
azCCPM siFL	*	*	-7.0 ± 7.2	
azCCPMs siLuc	65 ± 3	0.10 ±0.02	-9.0 ± 8.3	

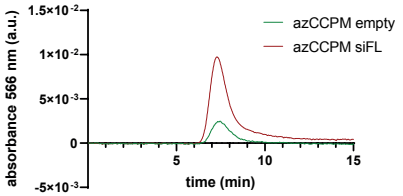

Additionally, entrapment was inspected using gel electrophoresis to separate between siFL and azCCPMs (Figure 6). Free siFL and linker **1**-functionalized siFL migrated through the gel (well 1 and 2, respectively), and empty azCCPMs showed no signal as there was no fluorescent label present (well 3).

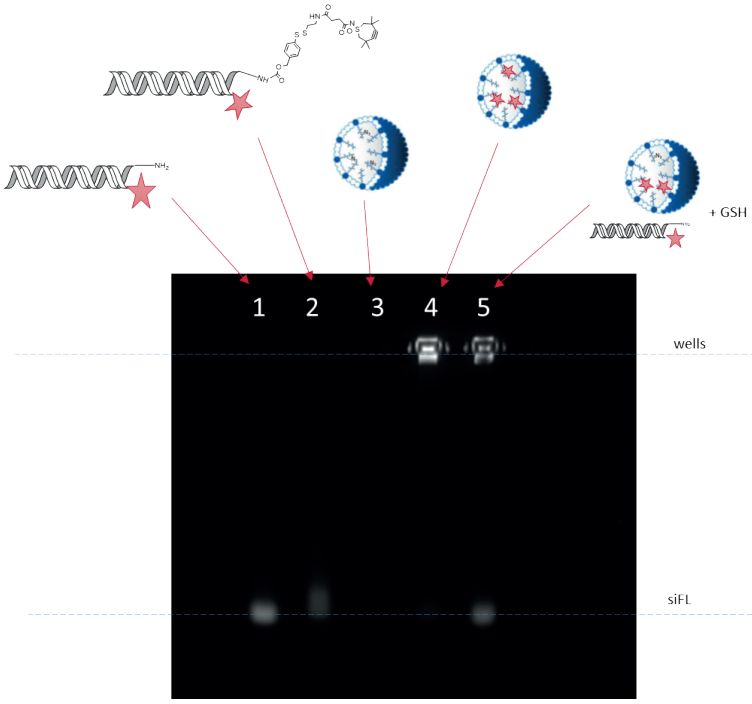

Figure 6: Gel electrophoresis in 3% agarose in TAE buffer, ran for 20 minutes at 170 V. Picture recorded using 566 nm excitation, 589 nm emission. Well 1: siFL. Well 2: siFL functionalized with linker. Well 3: empty azCCPMs. Well 4: azCCPMs with siFL-linker loaded. Well 5: azCCPMs with siFL loaded after 2 hours incubation in 5 mM GSH.

A fluorescent signal was detected in the starting slot of well 4 whereas no signal was seen for free siRNA), indicating that siRNA was entrapped in the azCCPMs. Well 5, containing siRNA-loaded particles which were incubated with GSH, showed fluorescent signal corresponding with free siRNA, demonstrating that free siRNA was released and therefore the entrapment of siRNA in azCCPMs was reversible. Notably, a fluorescent signal can still be seen in the starting slot, indicating that some siRNA was still entrapped in the azCCPMs. In this experiment incubation of siRNA-loaded azCCPMs with GSH was only two hours, which could explain the incomplete release of siRNA from the azCCPMs.

Release of siRNA from micelles

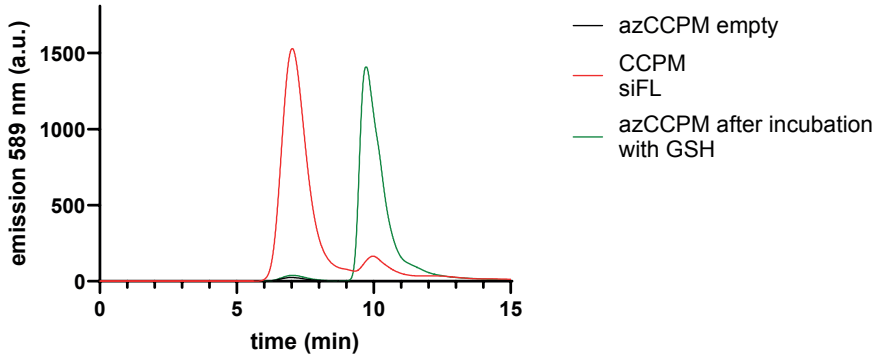

Figure 7: SEC chromatograms of empty azCCPM (blue),siFL loaded azCCPM (red), and released siFL from azCCPMs (green)

Release of siRNA was quantified using SEC equipped with fluorescence detector and fluorescently labelled siRNA for calibration. As seen in Figure 7, azCCPM without fluorescently labelled dye showed a very low signal at the retention time of particles (7.5 minutes, black). AzCCPMs loaded with siFL showed a large signal at the same retention time, indicating that siFL is covalently entrapped in the particles (red). However, the chromatogram shows that there was also some free siRNA present eluting at 10 minutes. This amount of free siRNA corresponds with 10 µg/mL, which was about 8% of the total loaded siFL. Obviously, this low amount of free siRNA was not detected with agarose gel electrophoresis (Figure 6). This free siRNA was also not detected using SEC for entrapment where absorbance was measured at 566 nm (Figure 5), in contrast to more sensitive fluorescence detection.

To azCCPMs loaded with siFL, GSH was added. After 3 hours of incubation, SEC was run (green) and this resulted in a complete decrease of fluorescent signal at the retention

time of the azCCPMs of 7 minutes, and in parallel an increase of fluorescence of free siRNA at retention time of 10 minutes was measured. The free siFL concentration was 120 µg/mL, indicating 110 µg/mL was released from the azCCPMs after correcting for the 10 µg/mL of free siFL which was present before release. Combining the initial free siRNA (10 µg/mL) with the total concentration of siRNA after release (120 µg/mL), an entrapment efficiency of 92% was determined. As 300 µg of siRNA was added to 14 mg of polymer and this was loaded with 92% efficiency, the loading capacity of the micelles is 2.0 % (w/w).

In parallel, released siRNA was measured on UPLC using the previously described strand dehybridization method (Figure 8). This method allowed for parallel quantification and identification of the final found strands to rule out the presence of molecular fingerprints remaining on the strand. Quantification of this released siRNA resulted in a concentration of 120 µg/mL, which corresponds to the value found by the SEC method of Figure 7. Overlap of 100 µg/mL siFL stock injection (black) with released siFL from particles (blue) confirmed the identity of the native strands.

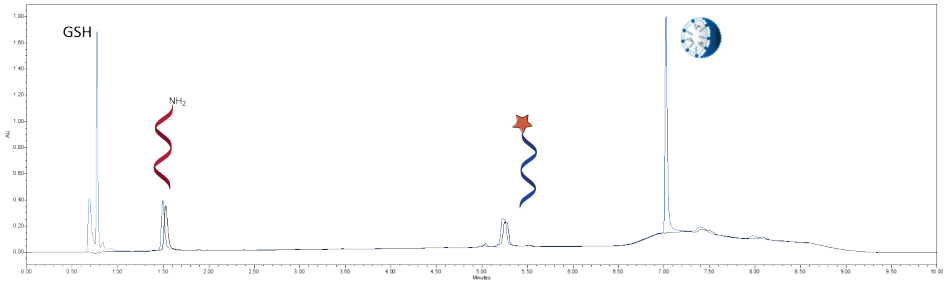

Figure 8: Chromatograms of a stock of siFL solution (black) and the azCCPM sample after incubation with GSH (blue).

Cellular uptake of siFL loaded azCCPMs

Confocal microscopy

Confocal microscopy images of HeLa and HEK293T cells were taken to investigate whether azCCPMs with siFL were taken up by the cell within 24 h. The nuclei of the cells were stained with Hoechst 33342 (blue), while the Rhodamine label on siRNA is shown in orange. The brightfield was used to show the outline of the cells. As shown in Figure 9, the fluorescently labelled siRNA-loaded azCCPMs were taken up by both HeLa and HEK293T cells. The dotted pattern is an indication of endosomal localization, which has been reported previously as route of uptake for these CCPMs. [64]

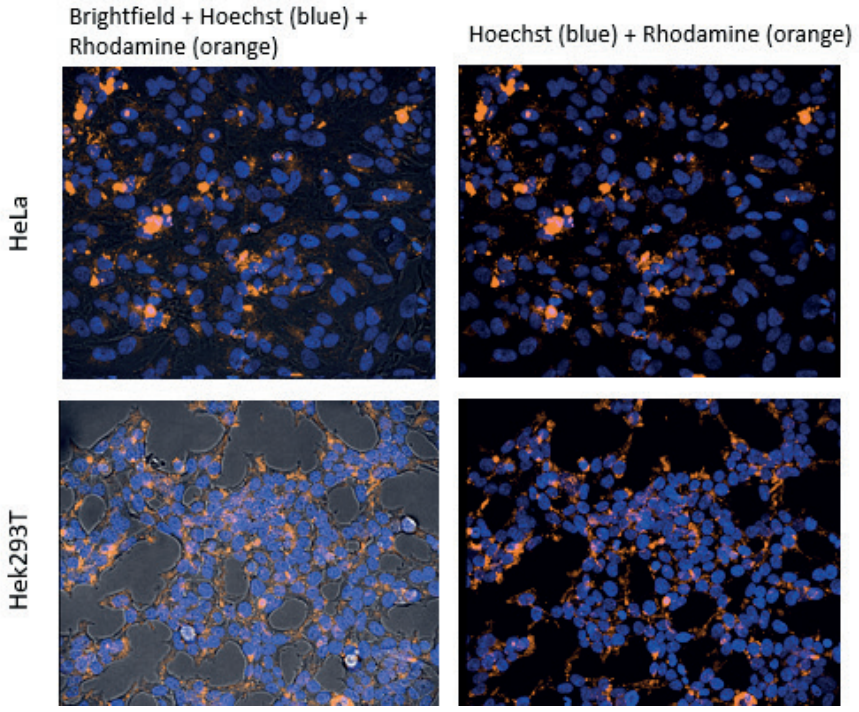

Figure 9: HeLa and HEK293T cells after 24h of incubation at 37 °C with CCPMs loaded with fluorescently labelled siRNA (Rhodamine 3B) and Hoechst 33342 staining. The orange fluorescence represents the labelled siRNA and the blue fluorescence Hoechst 33342. The brightfield overlay is shown on the left to show the outline of the cells.

Flow cytometry

To quantify the amount of fluorescent signal from cells, flow cytometry was performed. Fluorescently labelled siRNA loaded azCCPMs were added and incubated with the cells. Afterwards the percentage rhodamine3B positive cells (%CCPM) of the HeLa and HEK293T cells was measured (Figure 10). For HeLa cells, nearly 100% of the cells were positive for rhodamine after 24 hours. For HEK cells, this plateaued at around 70% independent of the concentrations (histograms of cells shown in Supporting Info S6). These percentages are in line with previous observations of high uptake of small, PEGylated particles[65].

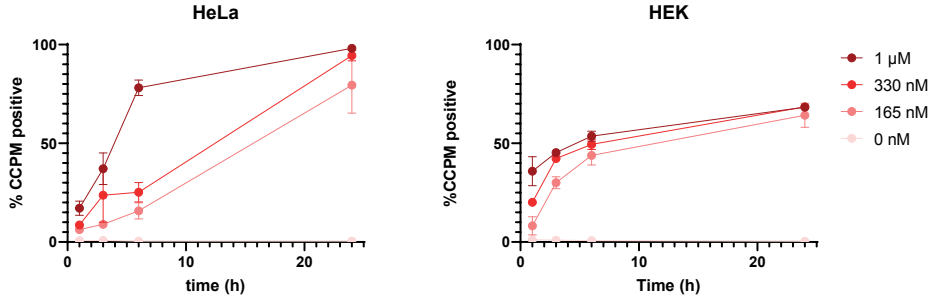

Figure 10: Percentage rho3B positive HeLa and HEK293T cells after incubation with fluorescently labelled siRNA in azCCPMs (Rhodamine 3B). Error bars represent standard deviations of the means obtained from three separate measurements for the HeLa cells and two separate measurements for the HEK293T cells. For each timepoint 10,000 events were counted with the flow cytometer.

While cellular uptake of these azCCPMs is demonstrated, it is likely that they end up in endo/lysosomes. To demonstrate efficacy of these siRNA-loaded azCCPMs, gene silencing assays are required. However, an introductory experiment showed that upon incubation of HEK293T cells producing luciferase with siLuc-loaded azCCPMs, no gene silencing was seen. This might be ascribed to a lack of endosomal escape of the particles. Moreover, a control formulation of siLuc with lipofectamine did not show gene silencing either, which argues the reliability of the performed assay. This is potentially due to a sequence mismatch on two positions between the siLuc and the luciferase expressed in the cell line.

Therefore, more in depth gene silencing studies are required, using different functional siRNAs to demonstrate that the azCCPMs indeed are able to release functional siRNA in the cytosol of target cells.

It is further remarked that the specificity of the particles can be improved by surface decoration with targeting ligands. Moreover, moieties such as cell penetrating peptides can be coupled to the core of the micelles via an acid-sensitive linker, to trigger endosomal escape.

Conclusion

mPEG-b-HPMALac$_n$ was modified with azidoacetic acid and formed azCCPMs with similar properties (size and charge) as CCPMs from nonmodified mPEG-b-pHPMALac$_n$. In parallel, siRNA was functionalized with a clickable linker designed to couple this cargo to the azide functionalities in the CCPMs, while containing a reduction sensitive cleavage site for triggered release. Combining these two resulted in siRNA-loaded azCCPMs, with an entrapment efficiency of 92% and loading capacity of 2.0%. Such a high entrapment efficiency is especially beneficial as siRNA is a costly drug and limited waste is an advantage, especially looking towards larger scale manufacturing. The loaded azCCPMs readily released native siRNA after incubation with GSH, proving the reversibility of this loading. Cellular uptake was demonstrated in both HEK and HeLa cells, making this approach of clicking siRNA into CCPMs a good platform for improving the circulation time and tissue targeting of siRNA as therapeutic modality. Further *in vitro* and *in vivo* experiments are needed to demonstrate that the loaded azCCPMs are able to deliver functional siRNA into target cells.

References

(1) Sajid, M. I.; Moazzam, M.; Tiwari, R. K.; Kato, S.; Cho, K. Y. Overcoming barriers for siRNA therapeutics: From bench to bedside. *Pharmaceuticals* **2020**, *13* (10), 1-25

(2) Friedrich, M.; Aigner, A. Therapeutic siRNA: State-of-the-Art and Future Perspectives. *BioDrugs* **2022**, *36* (5), 549-571

(3) Kulkarni, J. A.; Witzigmann, D.; Thomson, S. B.; Chen, S.; Leavitt, B. R.; Cullis, P. R.; van der Meel, R. The current landscape of nucleic acid therapeutics. *Nature Nanotechnology* **2021**, *16* (6), 630-643

(4) Senapati, D.; Patra, B. C.; Kar, A.; Chini, D. S.; Ghosh, S.; Patra, S.; Bhattacharya, M. Promising approaches of small interfering RNAs (siRNAs) mediated cancer gene therapy. *Gene* **2019**, *719* (June), 144071-144071

(5) Paul, A.; Muralidharan, A.; Biswas, A.; Kamath, B. V.; Joseph, A.; Alex, A. T. siRNA therapeutics and its challenges: Recent advances in effective delivery for cancer therapy. *OpenNano* **2022**, *7* (July), 100063-100063

(6) Alshaer, W.; Zureigat, H.; Al Karaki, A.; Al-Kadash, A.; Gharaibeh, L.; Hatmal, M. m. M.; Aljabali, A. A. A.; Awidi, A. siRNA: Mechanism of action, challenges, and therapeutic approaches. *European Journal of Pharmacology* **2021**, *905* (December 2020), 174178-174178

(7) Hu, B.; Zhong, L.; Weng, Y.; Peng, L.; Huang, Y.; Zhao, Y.; Liang, X.-J. Therapeutic siRNA: state of the art. *Signal Transduction and Targeted Therapy* **2020**, *5* (1), 101-101

(8) Haupenthal, J.; Baehr, C.; Kiermayer, S.; Zeuzem, S.; Piiper, A. Inhibition of RNAse A family enzymes prevents degradation and loss of silencing activity of siRNAs in serum. *Biochemical Pharmacology* **2006**, *71* (5), 702-710

(9) Abdelhady, H. G.; Lin, Y.-L.; Sun, H.; ElSayed, M. E. H. Visualizing the Attack of RNase Enzymes on Dendriplexes and Naked RNA Using Atomic Force Microscopy. *PLOS ONE* **2013**, *8* (4), e61710

(10) Whitehead, K. A.; Langer, R.; Anderson, D. G. Knocking down barriers: advances in siRNA delivery. *Nature Reviews Drug Discovery* **2009**, *8* (2), 129-138

(11) Fusco, D.; Bertrand, E.; Singer, R. H. Imaging of single mRNAs in the cytoplasm of living cells. *Prog Mol Subcell Biol* **2004**, *35*, 135-150

(12) Stephens, S. B.; Dodd, R. D.; Lerner, R. S.; Pyhtila, B. M.; Nicchitta, C. V. Analysis of mRNA partitioning between the cytosol and endoplasmic reticulum compartments of mammalian cells. *Methods Mol Biol* **2008**, *419*, 197-214

(13) Choung, S.; Kim, Y. J.; Kim, S.; Park, H. O.; Choi, Y. C. Chemical modification of siRNAs to improve serum stability without loss of efficacy. *Biochemical and Biophysical Research Communications* **2006**, *342* (3), 919-927

(14) Kenski, D. M.; Butora, G.; Willingham, A. T.; Cooper, A. J.; Fu, W.; Qi, N.; Soriano, F.; Davies, I. W.; Flanagan, W. M. SiRNA-optimized modifications for enhanced in vivo activity. *Molecular Therapy - Nucleic Acids* **2012**, *1* (1), e5-e5

(15) Selvam, C.; Mutisya, D.; Prakash, S.; Ranganna, K.; Thilagavathi, R. Therapeutic potential of chemically modified siRNA: Recent trends. *Chemical biology & drug design* **2017**, *90* (5), 665-665

(16) Abosalha, A. K.; Ahmad, W.; Boyajian, J.; Islam, P.; Ghebretatios, M.; Schaly, S.; Thareja, R.; Arora, K.; Prakash, S. A comprehensive update of siRNA delivery design strategies for targeted and effective gene silencing in gene therapy and other applications. *Expert Opinion on Drug Discovery* **2022**, *18* (2), 149-162

(17) Yonezawa, S.; Koide, H.; Asai, T. Recent advances in siRNA delivery mediated by lipid-based nanoparticles. *Advanced Drug Delivery Reviews* **2020**, *154-155*, 64-78

(18) Jiang, Y.; Tang, R.; Duncan, B.; Jiang, Z.; Yan, B.; Mout, R.; Rotello, V. M. Direct cytosolic delivery of siRNA using nanoparticle-stabilized nanocapsules. *Angewandte Chemie - International Edition* **2015**, *54* (2), 506-510

(19) Kubota, K.; Onishi, K.; Sawaki, K.; Li, T.; Mitsuoka, K.; Sato, T.; Takeoka, S. Effect of the nanoformulation of siRrNAa-lipid assemblies on their cellular uptake and immune stimulation. *International Journal of Nanomedicine* **2017**, *12*, 5121-5133

(20) Mukherjee, S.; Ray, S.; Thakur, R. Solid lipid nanoparticles: a modern formulation approach in drug delivery system. *Indian journal of pharmaceutical sciences* **2009**, *71* (4), 349

(21) Tenchov, R.; Bird, R.; Curtze, A. E.; Zhou, Q. Lipid Nanoparticles from Liposomes to mRNA Vaccine Delivery, a Landscape of Research Diversity and Advancement. *ACS Nano* **2021**, *15* (11), 16982-17015

(22) Akinc, A.; Maier, M. A.; Manoharan, M.; Fitzgerald, K.; Jayaraman, M.; Barros, S.; Ansell, S.; Du, X.; Hope, M. J.; Madden, T. D.; et al. The Onpattro story and the clinical translation of nanomedicines containing nucleic acid-based drugs. *Nature Nanotechnology* **2019**, *14* (12), 1084-1087

(23) Du, H.; Liu, M.; Yang, X.; Zhai, G. The design of pH-sensitive chitosan-based formulations for gastrointestinal delivery. *Drug Discovery Today* **2015**, *20* (8), 1004-1011

(24) Mao, S.; Sun, W.; Kissel, T. Chitosan-based formulations for delivery of DNA and siRNA. *Advanced Drug Delivery Reviews* **2010**, *62* (1), 12-27

(25) Alameh, M.; Lavertu, M.; Tran-Khanh, N.; Chang, C. Y.; Lesage, F.; Bail, M.; Darras, V.; Chevrier, A.; Buschmann, M. D. SiRNA Delivery with Chitosan: Influence of Chitosan Molecular Weight, Degree of Deacetylation, and Amine to Phosphate Ratio on in Vitro Silencing Efficiency, Hemocompatibility, Biodistribution, and in Vivo Efficacy. *Biomacromolecules* **2018**, *19* (1), 112-131

(26) Capelôa, L.; Yazdi, M.; Zhang, H.; Chen, X.; Nie, Y.; Wagner, E.; Lächelt, U.; Barz, M. Cross-Linkable Polyion Complex Micelles from Polypept(o)ide-Based ABC-Triblock Copolymers for siRNA Delivery. *Macromolecular Rapid Communications* **2022**, *43* (12), 2100698-2100698

(27) Mousazadeh, H.; Pilehvar-Soltanahmadi, Y.; Dadashpour, M.; Zarghami, N. Cyclodextrin based natural nanostructured carbohydrate polymers as effective non-viral siRNA delivery systems for cancer gene therapy. *Journal of Controlled Release* **2021**, *330*, 1046-1070

(28) Singh, R. P.; Hidalgo, T.; Cazade, P. A.; Darcy, R.; Cronin, M. F.; Dorin, I.; O'Driscoll, C. M.; Thompson, D. Self-Assembled Cationic β-Cyclodextrin Nanostructures for siRNA Delivery. *Molecular Pharmaceutics* **2019**, *16* (3), 1358-1366

(29) Lorenzer, C.; Dirin, M.; Winkler, A.-M.; Baumann, V.; Winkler, J. Going beyond the liver: Progress and challenges of targeted delivery of siRNA therapeutics. *Journal of Controlled Release* **2015**, *203*, 1-15

(30) Zhang, Y.-N.; Poon, W.; Tavares, A. J.; McGilvray, I. D.; Chan, W. C. Nanoparticle–liver interactions: Cellular uptake and hepatobiliary elimination. *Journal of controlled release* **2016**, *240*, 332-348

(31) Haute, D. V.; Berlin, J. M. Challenges in realizing selectivity for nanoparticle biodistribution and clearance: lessons from gold nanoparticles. *Therapeutic Delivery* **2017**, *8* (9), 763-774

(32) Rijcken, C. J.; Snel, C. J.; Schiffelers, R. M.; van Nostrum, C. F.; Hennink, W. E. Hydrolysable core-crosslinked thermosensitive polymeric micelles: Synthesis, characterisation and in vivo studies. *Biomaterials* **2007**, *28* (36), 5581-5593

(33) Hu, Q.; Rijcken, C. J.; Bansal, R.; Hennink, W. E.; Storm, G.; Prakash, J. Complete regression of breast tumour with a single dose of docetaxel-entrapped core-cross-linked polymeric micelles. *Biomaterials* **2015**, *53*, 370-378

(34) Miedema, I. H. C.; Zwezerijnen, G. J. C.; Huisman, M. C.; Doeleman, E.; Mathijssen, R. H. J.; Lammers, T.; Hu, Q.; van Dongen, G. A. M. S.; Rijcken, C. J. F.; Vugts, D. J.; et al. PET-CT Imaging of Polymeric Nanoparticle Tumor Accumulation in Patients. *Advanced Materials* **2022**, *34* (21),

(35) Maeda, H. The enhanced permeability and retention (EPR) effect in tumor vasculature: the key role of tumor-selective macromolecular drug targeting. *Advances in Enzyme Regulation* **2001**, *41* (1), 189-207

(36) Maeda, H.; Wu, J.; Sawa, T.; Matsumura, Y.; Hori, K. Tumor vascular permeability and the EPR effect in macromolecular therapeutics: a review. *Journal of Controlled Release* **2000**, *65* (1-2), 271-284

(37) Atrafi, F.; Eerden, R. A. G. v.; Vlieg, M. A. M. v. H.; Hoop, E. O.-d.; Bruijn, P. d.; Lolkema, M. P.; Moelker, A.; Rijcken, C. J.; Hanssen, R.; Sparreboom, A.; et al. Intratumoral Comparison of Nanoparticle Entrapped Docetaxel (CPC634) with Conventional Docetaxel in Patients with Solid Tumors. *Clinical Cancer Research* **2020**, *26* (14), 3537-3545

(38) Matsumoto, S.; Christie, R. J.; Nishiyama, N.; Miyata, K.; Ishii, A.; Oba, M.; Koyama, H.; Yamasaki, Y.; Kataoka, K. Environment-Responsive Block Copolymer Micelles with a Disulfide Cross-Linked Core for Enhanced siRNA Delivery. *Biomacromolecules* **2009**, *10* (1), 119-127

(39) Oe, Y.; Christie, R. J.; Naito, M.; Low, S. A.; Fukushima, S.; Toh, K.; Miura, Y.; Matsumoto, Y.; Nishiyama, N.; Miyata, K.; et al. Actively-targeted polyion complex micelles stabilized by cholesterol and disulfide cross-linking for systemic delivery of siRNA to solid tumors. *Biomaterials* **2014**, *35* (27), 7887-7895

(40) Amjad, M. W.; Kesharwani, P.; Mohd Amin, M. C. I.; Iyer, A. K. Recent advances in the design, development, and targeting mechanisms of polymeric micelles for delivery of siRNA in cancer therapy. *Progress in Polymer Science* **2017**, *64*, 154-181

(41) Lv, H.; Zhang, S.; Wang, B.; Cui, S.; Yan, J. Toxicity of cationic lipids and cationic polymers in gene delivery. *Journal of Controlled Release* **2006**, *114* (1), 100-109

(42) Plank, C.; Mechtler, K.; Szoka Jr, F. C.; Wagner, E. Activation of the complement system by synthetic DNA complexes: a potential barrier for intravenous gene delivery. *Human gene therapy* **1996**, *7* (12), 1437-1446

(43) Reddy, S. T.; Van Der Vlies, A. J.; Simeoni, E.; Angeli, V.; Randolph, G. J.; O'Neil, C. P.; Lee, L. K.; Swartz, M. A.; Hubbell, J. A. Exploiting lymphatic transport and complement activation in nanoparticle vaccines. *Nature biotechnology* **2007**, *25* (10), 1159-1164

(44) Szebeni, J. Complement activation-related pseudoallergy: A stress reaction in blood triggered by nanomedicines and biologicals. *Molecular Immunology* **2014**, *61* (2), 163-173

(45) Szebeni, J.; Muggia, F.; Gabizon, A.; Barenholz, Y. Activation of complement by therapeutic liposomes and other lipid excipient-based therapeutic products: Prediction and prevention. *Advanced Drug Delivery Reviews* **2011**, *63* (12), 1020-1030

(46) Atrafi, F.; Dumez, H.; Mathijssen, R. H. J.; Menke van der Houven van Oordt, C. W.; Rijcken, C. J. F.; Hanssen, R.; Eskens, F. A. L. M.; Schöffski, P. A phase I dose-escalation and pharmacokinetic study of a micellar nanoparticle with entrapped docetaxel (CPC634) in patients with advanced solid tumours. *Journal of Controlled Release* **2020**, *325*, 191-197

(47) Alberg, I.; Kramer, S.; Schinnerer, M.; Hu, Q.; Seidl, C.; Leps, C.; Drude, N.; Möckel, D.; Rijcken, C.; Lammers, T.; et al. Polymeric Nanoparticles with Neglectable Protein Corona. *Small* **2020**, *16* (18),

(48) Shafirovich, V.; Dourandin, A.; Huang, W.; Geacintov, N. E. The Carbonate Radical Is a Site-selective Oxidizing Agent of Guanine in Double-stranded Oligonucleotides. *Journal of Biological Chemistry* **2001**, *276* (27), 24621-24626

(49) Tanaka, M.; Chock, P. B. Oxidative modifications of RNA and its potential roles in biosystem. *Frontiers in Molecular Biosciences* **2021**, *8*, 685331

(50) Meng, F.; Hennink, W. E.; Zhong, Z. Reduction-sensitive polymers and bioconjugates for biomedical applications. *Biomaterials* **2009**, *30* (12), 2180-2198

(51) Brülisauer, L.; Gauthier, M. A.; Leroux, J.-C. Disulfide-containing parenteral delivery systems and their redox-biological fate. *Journal of Controlled Release* **2014**, *195*, 147-154

(52) Weterings, J.; Rijcken, C. J. F.; Veldhuis, H.; Meulemans, T.; Hadavi, D.; Timmers, M.; Honing, M.; Ippel, H.; Liskamp, R. M. J. TMTHSI, a superior 7-membered ring alkyne containing reagent for strain-promoted azide–alkyne cycloaddition reactions. *Chemical Science* **2020**, *11* (33), 9011-9016

(53) Van Eerden, R. A. G.; Atrafi, F.; vanHylckama Vlieg, M. A. M.; Oomen-de Hoop, E.; de Bruijn, P.; Moelker, A.; Lolkema, M. P.; Rijcken, C. J. F.; Hanssen, R.; Eskens, F. A.; et al. Comparison of intratumoral docetaxel exposure in cancer patients between nanoparticle entrapped docetaxel (CPC634) and conventional docetaxel (Cd): The CriTax study. *Annals of Oncology* **2019**, *30*, v184-v184

(54) Hu, Q.; Rijcken, C. J. F.; van Gaal, E.; Brundel, P.; Kostkova, H.; Etrych, T.; Weber, B.; Barz, M.; Kiessling, F.; Prakash, J.; et al. Tailoring the physicochemical properties of core-crosslinked polymeric micelles for pharmaceutical applications. *Journal of Controlled Release* **2016**, *244*, 314-325

(55) Movassaghian, S.; Xie, Y.; Hildebrandt, C.; Rosati, R.; Li, Y.; Kim, N. H.; Conti, D. S.; da Rocha, S. R. P.; Yang, Z.-Q.; Merkel, O. M. Post-Transcriptional Regulation of the GASC1 Oncogene with Active Tumor-Targeted siRNA-Nanoparticles. *Molecular Pharmaceutics* **2016**, *13* (8), 2605-2621

(56) Xie, Y.; Kim, N. H.; Nadithe, V.; Schalk, D.; Thakur, A.; Kılıç, A.; Lum, L. G.; Bassett, D. J. P.; Merkel, O. M. Targeted delivery of siRNA to activated T cells via transferrin-polyethylenimine (Tf-PEI) as a potential therapy of asthma. *Journal of Controlled Release* **2016**, *229*, 120-129

(57) Evers, M. J. W.; Van De Wakker, S. I.; De Groot, E. M.; De Jong, O. G.; Gitz-François, J. J. J.; Seinen, C. S.; Sluijter, J. P. G.; Schiffelers, R. M.; Vader, P. Functional siRNA Delivery by Extracellular Vesicle–Liposome Hybrid Nanoparticles. *Advanced Healthcare Materials* **2022**, *11* (5), 2101202

(58) O'Loughlin, A. J.; Mäger, I.; De Jong, O. G.; Varela, M. A.; Schiffelers, R. M.; El Andaloussi, S.; Wood, M. J. A.; Vader, P. Functional Delivery of Lipid-Conjugated siRNA by Extracellular Vesicles. *Molecular Therapy* **2017**, *25* (7), 1580-1587

(59) Senter, P. D.; Pearce, W. E.; Greenfield, R. S. Development of a drug-release strategy based on the reductive fragmentation of benzyl carbamate disulfides. *The Journal of Organic Chemistry* **1990**, *55* (9), 2975-2978

(60) Ojha, T.; Hu, Q.; Colombo, C.; Wit, J.; Geijn, M.; Steenbergen, M. J.; Bagheri, M.; Königs-Werner, H.; Buhl, E. M.; Bansal, R.; et al. Lyophilization stabilizes clinical-stage core-crosslinked polymeric micelles to overcome cold chain supply challenges. *Biotechnology Journal* **2021**, *16* (6), 2000212-2000212

(61) Geißler, D.; Gollwitzer, C.; Sikora, A.; Minelli, C.; Krumrey, M.; Resch-Genger, U. Effect of fluorescent staining on size measurements of polymeric nanoparticles using DLS and SAXS. *Analytical Methods* **2015**, *7* (23), 9785-9790

(62) Ramzi, A.; Rijcken, C. J. F.; Veldhuis, T. F. J.; Schwann, D.; Henninkj, W. E.; Van Nostrum, C. F. Core-Shell Structure of Degradable, Thermosensitive Polymeric Micelles Studied by Small-Angle Neutron Scattering. *Journal of Physical Chemistry B* **2008**, *112* (3), 784-792

(63) Reynolds, A.; Leake, D.; Boese, Q.; Scaringe, S.; Marshall, W. S.; Khvorova, A. Rational siRNA design for RNA interference. *Nature Biotechnology* **2004**, *22* (3), 326-330

(64) Sahay, G.; Alakhova, D. Y.; Kabanov, A. V. Endocytosis of nanomedicines. *Journal of Controlled Release* **2010**, *145* (3), 182-195

(65) Pamujula, S.; Hazari, S.; Bolden, G.; Graves, R. A.; Chinta, D. D.; Dash, S.; Kishore, V.; Mandal, T. K. Cellular delivery of PEGylated PLGA nanoparticles. *J Pharm Pharmacol* **2012**, *64* (1), 61-67

Supporting Info

S1: Analytical method for polymer content

0.3 mg of polymer was weighed and dissolved in 100 µL of 20 mM HEPES buffer. To 20 µL of polymer solution, 10 µL of 0.1 M NaOH was added. After 3 hours, the solution was acidified with 20 µL of 0.1 M HCl and injected on UPLC using a gradient (see below) which could separate the formed lactic acid from azidoacetic acid. Both peaks could be identified and using a calibration curve, the peak area was used to calculate the concentrations of lactic acid (and thus polymer) and azidoacetic acid in the sample. free lactic acid and azidoacetic acid were not detected in the non-hydrolysed polymer.

UPLC method details:

UPLC system:	Waters H-Class
UPLC column:	HSS T3, 1.8 µm, 3.0 x 150 mm
Eluent A:	10 mM KH_2PO_4 pH2.5
Eluent B:	90 % ACN / 10 % H_2O / 0.1 % phosphoric acid (% v/v)
Needle flush solvent:	MilliQ water
Sample tray Temperature:	5° C
Column Temperature:	30° C
Flow:	0.85 mL/min
Injection volume:	7.0 µL
UV Detection:	210 nm
Detection mode	2D
Sampling rate	5 points/sec
Filter time constant	Normal
Resolution	1.2 nm
Exposure time	Auto
Run time:	8 minutes

Gradient:

Time (min)	Flow (mL/min)	% A	% B
0	0.85	100	0
2.5	0.85	100	0
3.5	0.85	0	100
5.0	0.85	0	100
6.0	0.85	100	0
8.0	0.85	100	0

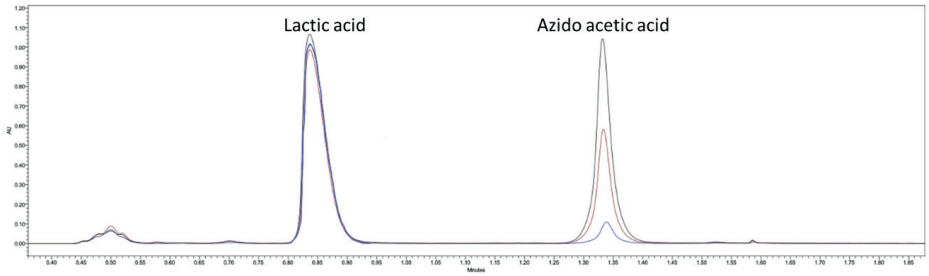

Figure S 1: Chromatogram showing peak separation of lactic acid with different amounts of azidoacetic acid mixed in as control

S2: Analytical method for SEC

HPLC system:	Waters: Binary Solvent manager, Sample manager, UV detector
Column:	TSKgel 5000PWXL; 10 µm, 7.8x 300 mm (Tosoh)
Eluent A (isocratic):	PBS 10%MeOH
Needle flush solvent:	MilliQ water/MeOH 90:10
Sample tray Temperature:	20 °C
Column Temperature:	25 °C
Flow:	1.0 mL/min
Injection volume:	20 µL
UV Detection:	258 nm, 280 nm
Detection mode	UV
Sampling rate	5 points/sec
Filter time constant	Normal
Resolution	1.2 nm
Exposure time	Auto
Run time:	18 minutes

S3: Analytical method for siRNA on UPLC

UPLC system:	Waters H-Class
UPLC column:	Acquity BEH C18 1.7 µm, 100 x 2.1 mm
Eluent A:	100mM Hexylamine acetic acid
Eluent B:	90% ACN 10% 100mM Hexylamine acetic acid
Needle flush solvent:	ACN:MQ 90:10
Sample tray Temperature:	20° C
Column Temperature:	89° C
Flow:	0.3 mL/min
Injection volume:	5.0 µL
UV Detection:	258 nm
Detection mode	2D
Sampling rate	10 points/sec
Filter time constant	Normal
Resolution	1.2 nm
Exposure time	Auto
Run time:	10 minutes

Time (min)	Flow (mL/min)	% A	% B
0	0.3	60	40
0.50	0.3	60	40
5.00	0.3	45	15
5.50	0.3	15	85
7.00	0.3	15	85
7.50	0.3	60	40
10.00	0.3	60	40

S4: functionalization of siFL with linker 1

	chromatogram
A. Stock solution	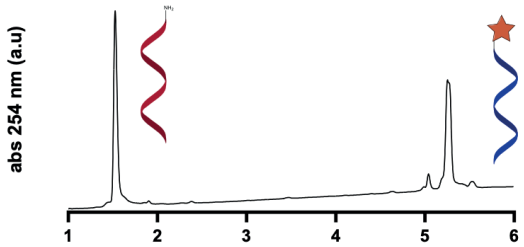
B. Linker attachment to siFL	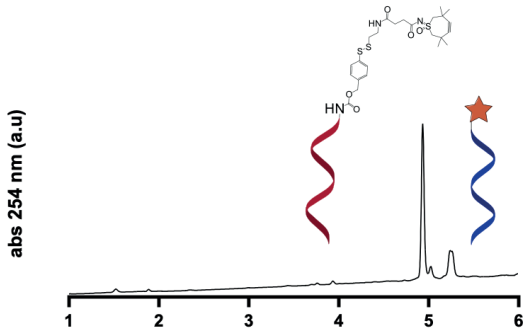
C. Release from linker under GSH	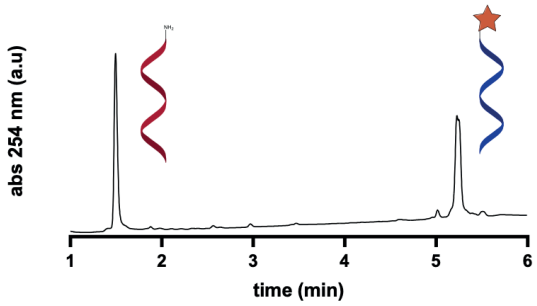

S5: SEC of nonmodified particles and azCCPMs

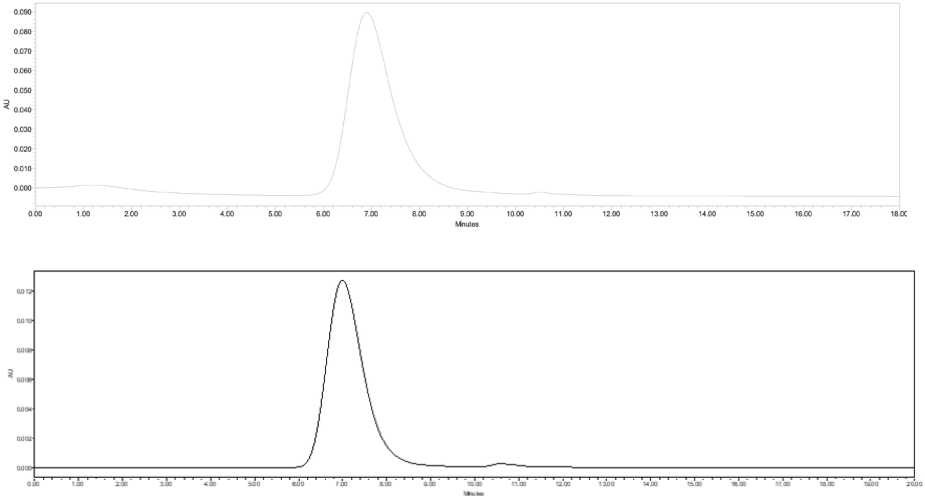

Figure 11: SEC chromatogram of azCCPMs (top) and comparison to unmodified CCPMs (bottom)

S6: Histograms of HeLa and HEK cells

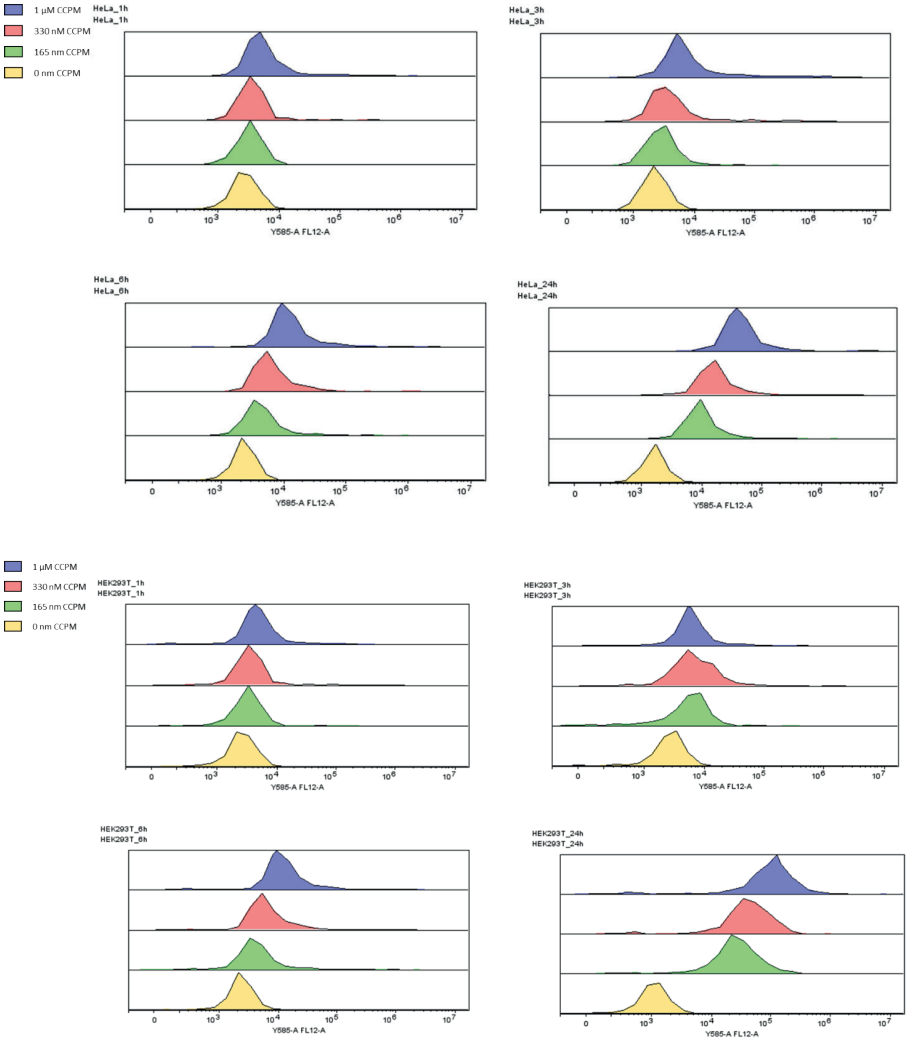

CHAPTER 9

Summary, discussion and perspectives

Summary with discussion

Polymeric micelles (PMs) are formed in aqueous solution by amphiphilic block copolymers that assemble into structures of a hydrophobic core and a hydrophilic shell, and they are an important category of nanoparticles for drug solubilization and targeting within the field of nanomedicine. [1–3] Their synthetic nature allows for high tunability and chemical versatility to vary both their chemical and physical properties. [1–6] Core-crosslinked polymeric micelles (CCPMs) are obtained by crosslinking the PM core, resulting in improved structural stability and circulation time *in vivo* compared to non-crosslinked PMs. [7–9] Owing to their small, tunable size (usually <100 nm) and prolonged circulation kinetics, CCPMs show great potential for enhanced tissue accumulation, particularly in tumors, through a phenomenon known as the enhanced permeability and retention (EPR) effect. [10,11]

The work presented in this thesis is focused on PMs constituting methoxy polyethylene glycol (mPEG, M_n = 5000 Da) as hydrophilic block and either poly(*N*-isopropylacrylamide) (PNIPAM) or poly*(N*-2-hydroxypropyl methacrylamide-lactate) (PHPMAmLac$_n$) as thermosensitive blocks. Owing to the thermosensitive nature of the PNIPAM [12] and PHPMAmLac$_n$ [13–16] blocks in the block copolymer, reversible micellization occurs upon surpassing the so-called critical micellization temperature (CMT) at polymer concentrations above the critical micellization concentration (CMC). Upon crosslinking of the core (for example by free radical crosslinking [13] or by native chemical ligation [17]) to obtain CCPMs, the constituent polymers can no longer return into their unimer state (even when falling below the CMT and/or CMC).

CCPMs can also be covalently conjugated with drugs and/or diagnostic cargos, allowing for local triggered drug release or monitoring distribution. [18–23] The type of crosslinking chemistry employed needs to be compatible with the drug cargo to be loaded, avoiding damage from unintended side reactions. Hereto native chemical ligation (NCL, a biorthogonal reaction resulting in an amide bond under mild conditions) presenting an interesting avenue. [17] Furthermore, compatible linker chemistries that allow for the triggered release of drug cargos are crucial for the development of CCPM-based nanomedicine platforms.

Gold nanoclusters (AuNCs, <2 nm sized, ligand stabilized gold structures) are interesting candidates for light-induced release of cargos and use as diagnostic tools owing to their fluorescence properties. [24] NCL is particularly advantageous to combine with AuNCs as free thiol moieties remain after the crosslinking reaction that can subsequently be employed as ligands for AuNC stabilization within the CCPM core. Alternatively,

triggers that are activated by the biological environment, such as reduction sensitive disulfides, are also interesting candidates for cargo release. [25–27]

In **chapter 1**, the conceptual elements that underlie the aims of this thesis are introduced, from the roles and types of nanocarriers presently being investigated and clinically employed, to the constituents of CCPMs, their crosslinking and linker chemistries to attach and release the coupled cargo. The relevance of therapeutic peptides as a category of active pharmaceutical ingredients (APIs) and the latest advancements in their nanocarrier-assisted delivery are also briefly addressed.

Chapter 2 describes the current state of the art of AuNCs, by stratifying their use into categories of diagnostics, therapy and combination applications. The fluorescent properties of AuNCs allow for diagnostic applications whilst the photo-thermal conversion ability presents opportunities for therapeutic applications. The overall good biocompatibility of AuNCs and success of numerous pre-clinical studies warrants their investigation in nanocarriers.

Previous work highlighted the application of AuNCs in PMs (not crosslinked) based on thermosensitive methoxy polyethylene glycol-*b*-poly(*N*-isopropylacrylamide) (mPEG-*b*-PNIPAM) for fluorescent imaging. [28] However, only one terminal thiol per polymer chain was present limiting the total loading of AuNCs (at the required thiol to gold ratio of 3:1 for AuNC formation) and the polymers were not crosslinkable (and hence limited *in vivo* stability). Additionally, no API was encapsulated with therapeutic applications in mind. Therefore, we aimed to utilize the photo-thermal properties of AuNCs as a drug release trigger in **chapter 3**, by introducing them into CCPMs for laser-guided cell killing employing thiolated doxorubicin. By synthesizing mPEG-*b*-PNIPAM based diblock copolymers with either cysteine or oxo-ester containing groups in the PNIPAM block, temperature induced micellization and NCL crosslinking resulted in CCPMs. The free thiols (resulting from the NCL reaction) present in the core were utilized as capping ligands to stabilize AuNCs formed *in situ*, allowing for a higher AuNC to polymer ratio than previously achieved. [28] Through simultaneous addition of 2-iminothiolane modified doxorubicin (DOX-SH), this chemotherapeutic was entrapped by use of the thiol handle. Despite that this thiol derivate is 12-fold less potent than DOX itself, as a result of the llight induced drug release, highly selective cancer cell killing was achieved using CCPMs with AuNCs and DOX-SH *in vitro*.

As discussed in **chapter 1**, NIPAM based polymers are not hydrolysable, which raises concerns towards their biodegradability and hence applications *in vivo*. In contrast, $HPMAmLac_n$ based polymers can hydrolyze (due to ester bonds present in the side

chains) under physiological conditions to form hydrophilic PHPMA chains and lactic acid, which are expected to be cleared from circulation (if PHPMA sizes are less than 100 kDa [29]) and metabolized, respectively. [14–16] This attractive feature of HPMAmLac$_n$ based polymers and the additional availability of hydroxyl groups on the side chains for functionalization has paved the way for the clinical evaluation of CCPMs based on these polymers, the technology being known as CriPec®. [30] CriPec® CCPMs are obtained by partial methacrylic acid functionalization of the HPMAmLacn block (Mw < 20kDa) and subsequent free-radical crosslinking above the CMT of mPEG-*b*-PHPMAmLac$_n$. [13] If preferred, an API-linker is added during this free radical crosslinking steps, resulting in co-core crosslinking of the API.

In **chapter 4**, NCL was investigated as alternative crosslinking chemistry to the previously employed free radical approach that potentially can damage therapeutic peptides (particularly those containing lysine, tryptophan and methionine residues) as well as cyanine dyes that are of interest for diagnostic purposes. [31,32] To this end, we synthesized a trifunctional crosslinker containing two cysteine residues for the micelle core-crosslinking reaction and an azide residue for ring-strained alkyne entrapment of model fluorescent dyes. Furthermore, we functionalized mPEG-*b*-PHPMAmLac$_n$ with thioester residues (using ethyl thioglycolate-succinic anhydride, ETSA) for NCL crosslinking with the trifunctional crosslinker under physiological conditions. CCPMs were stable to surfactant exposure in contrast to non-crosslinked PMs, whilst being physiologically degradable through ester hydrolysis, forming lactic acid in the process. Additionally, the model fluorescent dyes sulfo.cy5 and BODIPY were successfully entrapped using two different copper-free click chemistry handles; dibenzocyclooctyne (DBCO) and 3,3,6,6-tetramethylthiacycloheptyne (TMTHSI), respectively. The BODIPY labelled CCPMs were not toxic to prostate cancer cells up to a tested concentration of 2 mg/mL and cellular uptake was shown *in vitro*. In summary, this proved the applicability of NCL as crosslinking strategy in mPEG-*b*-PHPMAmLac$_n$ based micelles, allowing core-entrapment of compounds that are incompatible with free radicals. This NCL approach opens up opportunities to entrap fragile APIs such as therapeutic peptides or dyes, assuming available suitable linker chemistry.

Typically, a certain delay in the disintegration process of CCPM is expected as esters involved in multiple crosslinks first need to hydrolyze first (around 6 connection points per polymer) before the CCPMs start to fall apart. However, this delay was not observed for CCPMs crosslinked with the NCL approach of **chapter 4**. A mechanistic investigation on CCPM degradation is described in **chapter 5**. Here, NCL is employed as crosslinking reaction by two different approaches: 1) by using a di-cysteine (bifunctional) crosslinking

agent to connect mPEG-*b*-PHPMAmLac$_n$ chains with ETSA handles and 2) using cross-reactive (referred to here as complementary) mPEG-*b*-PHPMAmLac$_n$ polymer chains with ETSA handles to ones with cysteine handles. Degradation of both CCPM types resulted in a similar rate of lactic acid formation. However, although on a molar base the same number of NCL reactions occurred in both CCPMs, the bifunctional crosslinker CCPMs had a significantly faster degradation rate than the complementary CCPMs. This is explained by the formation of ineffective crosslinks in the crosslinker approach, which is due to intramolecular reactions of the crosslinker with the same polymer. Clearly, such intramolecular reactions are not possible in a complementary approach, highlighted by the longer degradation and lag time before onset of degradation. Therefore, the crosslinking strategy employed impacts the degradation rate and needs to be carefully considered, particularly if slow degradation and prolonged circulation time are desired.

Following a different strategy, we investigated whether a non-releasable model peptide could be clicked into core-azide containing CCPMs after crosslinking in **chapter 6**, as this would remove the need for mild chemistry (e.g. NCL, which is not orthogonal to disulfide linkers) during crosslinking. The trifunctional crosslinker NCL based CCPM (**chapter 4)** was employed as it allows for direct comparison of the click reaction before and after crosslinking. First, a model copper-free clickable peptide TMTHSI-SAAEWFEKL (non-cleavable, model peptide containing tryptophan for detection by fluorescence) was synthesized via standard solid phase peptide synthesis (SPPS), employing TMTHSI. [33] This synthesis initially demonstrated that N-terminal peptide conjugation of TMTHSI (as opposed to currently available click handles such as BCN and DBCO) [34] via standard SPPS is possible as recently published. [35] Then, TMTHSI-SAAEWFEKL was mixed with purified CCPMs and compared to CCPMs obtained by TMTHSI-SAAEWFEKL clicking before crosslinking.

Remarkably, a >95 % entrapment efficiency was recorded both with the click after crosslink approach and the click before crosslink approach, highlighting the viability of these routes for peptide entrapment. In addition, the entrapment after crosslinking concept was technically also utilized in **chapter 3** for the entrapment/introduction of AuNCs as well as DOX-SH into CCPMs. This implies a drastic conceptual shift, as the necessity of mild crosslinking conditions for the entrapment of fragile APIs in CCPMs is proven to be redundant, since free radical based crosslinking and CCPM purification can be conducted before introduction of the labile linker-cargo construct.

Linker and triggered release chemistry play a crucial role in the development of CCPM based nanomedicines. Although AuNCs show great promise as described in **chapter**

2, the platform complexity and limited tissue penetration of near-infrared light limiting the use of the system described in **chapter 3** present major challenges towards further development. Alternatively, disulfide bonds are widely employed linkages for the selective triggered release of APIs, being cleaved by the elevated levels of glutathione (GSH) in the cytosol as well as the tumor environment as compared to extracellular fluids. [25,26,36,37] Only a limited number of disulfide trigger-based nanocarriers has undergone stability testing *in vivo*. Nonetheless, several disulfide containing prodrugs and antibody-drug conjugates (ADCs) are undergoing clinical evaluation and Besponsa® and Mylotarg® (ADCs used for treatment of blood cancers, notably with sterically hindered disulfides and acid labile hydrazones) are currently on the market, providing confidence for the use of disulfide containing prodrugs and polymeric nanomedicines in a clinical setting. [27,38]

These cumulative findings lead to **Chapter 7**, which describes the development of a first-in-class reduction sensitive copper-free clickable linker containing: 1) TMTHSI, 2) a disulfide bond, which is sensitive to reducing environments in tumor and the cytosol of cells and 3) a thiobenzyl carbamate spacer enabling release of the native cargo upon cleavage of the disulfide via 1,6 elimination. The resistance of TMTHSI to deprotection conditions employed by SPPS was confirmed by conjugation to the N-terminal amine of the oncolytic peptide LTX-315. A clear advantage of an on-the-resin linker conjugation is that any peptide intended for entrapment can be synthesized following the same procedure as also shown in a recent publication. [35] Because the crosslinker used in **Chapter 4**'s CCPMs has some issues, such as creating ineffective crosslinks, requiring reducing conditions for formation, and leaving free thiols after formation, we here used free radical crosslinked CCPMs. These CCPMs with azides in the core were used to trap the linker-LTX conjugate. Clicking of the linker-LTX conjugate to these CCPMs dispersed in water and at room temperature resulted in a loading capacity of 8 mass % of peptide to polymer with 56 % loading efficiency, affirming that clicking after crosslinking is an effective entrapment approach. Furthermore, rapid release of native LTX upon exposure to cytosolic/tumor mimicking reducing conditions was observed as evidenced by cytotoxicity testing on HeLa cells *in vitro*. In conclusion, a reduction triggered, therapeutic peptide releasing CCPM platform was developed as a proof of concept, employing broadly applicable chemistry that opens opportunities to various applications.

As a token to the broad applicability of the **chapter 7** platform with regard to the cargo, **chapter 8** demonstrates the successful entrapment of small interfering RNA (siRNA), employing the same linker and core-azide containing CCPMs. The use of siRNA is of interest for the silencing of disease-related genes and, even more so than with therapeutic peptides, the application is hampered by poor pharmacokinetics and instability issues of

these nucleic acids in the circulation and extracellular fluids. An additional challenge is that intracellular delivery of functional siRNA is required, ideally in the cytosol where siRNA can bind to its mRNA target. In **chapter 8**, the TMTHSI containing linker was reacted with stabilized model amine containing siRNA, either with siRNA containing rhodamine 3b as fluorescent label (siFL) for convenient tracking or with siRNA designed to silence firefly luciferase (siLuc) for *in vitro* functional assessment. By using the click after crosslink approach on azide containing CCPMs, 92 % entrapment efficiency at a feed of 2 weight % of siRNA to polymer was achieved. Furthermore, it was shown that siRNA was quantitatively released under reducing conditions within 3 hours and cellular internalization of siRNA containing CCPMs was observed *in vitro*. In conclusion, although no luciferase silencing was observed (likely due to a non-functional assay as positive control siLuc with lipofectamine did not show silencing either), this work further highlights the entrapment and release capabilities of the CCPM click platform for a broad spectrum of therapeutic agents.

Perspectives

Developing nanocarrier platforms for tumor therapy is a challenging field requiring a diverse range of expertise. Several challenges in generating CCPM based nanomedicine platforms described in this thesis are of synthetic nature and chemistry is thus an important developmental tool. In a very simplified form, these chemical design dependencies can be summarized as follows (not in order of importance):

- Cargo chemistry: The physicochemical characteristics of a drug cargo have to be taken into account to design a linking strategy, as well as the anticipated exposure profile at the pathophysiological target.
- Carrier chemistry: Crosslinking strategy has to be efficient, compatible (thus not damaging) with the cargo as well as the linker being employed and provide an attachment point to facilitate loading of the active substance and/or an imaging agent.
- Linker chemistry: Has to connect the cargo to the carrier with good stability during storage and after administration in e.g. the circulation, and allow for selective release that is ideally triggered upon arrival at its pathophysiological target.

Clearly all aspects have to be chemically compatible with one another, resulting in a complex design process. In addition to this list, a successful platform also has to address the biological complexity of the tumor itself with the aim of reaching the target (particle size and charge being important aspects) and delivering the intended cargo whilst retaining stability during circulation.

In consideration of the platforms described in this thesis, likely further chemical design alterations will be needed upon further platform development and preclinical evaluation. Nonetheless, the key insights into the development of CCPMs with triggered cargo release gained from this work can be summarized as follows:

- NCL can be employed as a crosslinking reaction for CCPM formation in thermosensitive polymer systems based on PNIPAM or PHPMAmLac$_n$. However, the reducing conditions necessary for the NCL reaction means no disulfide (API-) linkers can be employed.
- AuNCs can be utilized as light triggered release functionalities in CCPMs. However, design complexity of the platform as well as limited tissue penetration of the employed near-infrared light are challenges for further clinical development.
- The use of bifunctional crosslinkers to form CCPMs results in considerable ineffective intramolecular crosslinks affecting degradation rate and onset of degradation. The use of complementary polymer systems would omit the need for crosslinkers
- APIs can be entrapped within CCPMs after the crosslinking reaction, removing the need for specific mild crosslinking conditions such as NCL. This simplifies the design consideration for carrier chemistry significantly.
- The TMTHSI containing linker described in **chapter 7** of this thesis can be used for selective N-terminal peptide conjugation via SPPS. Further broad applicability for other amine containing compounds can be envisioned for convenient click entrapment of various payloads to various nanocarriers.
- The TMTHSI containing linker and azide containing CCPM platform described in this thesis can be employed for the entrapment of both hydrophilic peptides and even more hydrophilic siRNAs with astoundingly high entrapment efficiencies and subsequent reduction sensitive release. Such straightforward entrapments have the potential to improve the pharmacokinetic and tumor delivery of these two major classes of therapeutic cargos.

As mentioned in **chapter 1**, industrial applicability is a key consideration in this work for which the platforms described in **chapters 7** and **8** are the most suitable candidates for further development (as compared to those in **chapters 3** and **4**). This is largely owing to the simple azide derivatization of a clinically investigated and well-studied polymer system and the discovery of the entrapment after crosslinking route, circumventing the issue of possible free radical damage of fragile APIs. The development of a robust click linker opens opportunities for a plethora of entrapment applications for the CCPM platform, but also the linker as independent entity. Several considerations and implications as a result of this work with regards to further development could be addressed, as described in the following section.

Click entrapment after CCPM formation

Chapters 6, 7 and **8** demonstrate that a click reaction can occur between a model compound, dye or prodrug (compound classes with different hydrophilicity, molecular weights and charge) containing a ring strained alkyne and azides present in the CCPMs to entrap them. Clearly, this approach presents an advantageous synthetic route that has not been employed previously and has broad implications for the chemistry required to generate CCPMs. Mild chemistry such as NCL, which is a central research topic in this thesis, is simply not required to entrap fragile cargos. Additionally, conditions during drug entrapment that typically influence parameters (such as particle size through the use of organic solvents during crosslinking) are likely not as relevant in a system that is already stabilized by crosslinking, reducing the number of parameters for optimization. Clearly, a broad selection of potential cargos was investigated in this thesis using the click entrapment approach and more could be investigated (such as small/larger therapeutic proteins like cytokines or even nucleic acid based drugs of different sizes) to see how widely applicable this non-conventional approach truly is.

Additionally, it would be of interest to investigate the distribution of the azides within the CCPM core since they were chemically introduced in the core forming block (arguably at random) of the polymers used to generate CCPMs. This also opens the question towards the exact location of the entrapped entities, as a hydrophilic molecule such as a charged peptide or even more so siRNA, likely do not penetrate into the CCPM core. As described in **chapter 7**, it is possible that these entrapped entities are clicked by azides at the outer core, thus at the interface where the hydrophilic PEG shell begins. Certainly for the siRNA in **chapter 8**, the large excess of azides employed increases the likelihood of azides at the interface to react with the siRNA. This has yet to be investigated, ideally first by exploring the loading limits of these compounds in a titration manner. Finally, it would be of interest to attempt whether other core forming hydrophobic polymers such as PNIPAM can also be employed for click entrapment after crosslinking, showing broader approach applicability. This will also provide insight into accessibility of the azides in the core to click reactions as varying levels of core hydration could be envisioned with different polymers, particularly when moving to systems that are not thermosensitive (even more hydrophobic core).

Opportunities for NCL

Although NCL may not be necessary to facilitate entrapment of fragile molecules in CCPMs, the use of the free thiols for the capping of AuNCs was highlighted in **chapter**

3, and was could be expanded into the trifunctional crosslinker based PHPMAmLac$_n$ based CCPMs in **chapter 4**. It would be of interest to investigate what the effects on the CCPM degradation rate are when AuNCs are also incorporated which should in principle crosslink multiple free thiols in the system and increase stability. The primary advantage of using the platform in **chapter 4** over the one in **chapter 3** is that it would be hydrolysable and thus degradable under physiological conditions and therefore more suitable for future clinical applications. Additionally, if desired a complementary polymer approach as was highlighted in **chapter 5** could also be employed instead which guarantees increased CCPM stability and thus delayed degradation.

Selective release evaluation in vivo

The selective cargo release from disulfide based nanocarrier-drug conjugates in the tumor environment as well as after internalization by tumor cells in an *in vivo* setting is a crucial parameter to investigate. This holds true as a necessity for the CCPMs as described in **chapter 7**, where rapid release with subsequently slower 1,6 elimination resulting in the native LTX-315 peptide was observed at cytosolic/tumor mimicking glutathione concentrations. Furthermore, since the release at low glutathione concentrations present in the circulation was limited, assessing true circulation stability and kinetics will be paramount towards claiming release at the target tissue after extravasation exploiting the EPR effect. Whilst LTX-315 may be a useful model peptide to assess tumor killing (as it is cytotoxic if released intra- or extracellularly [39]), to assess premature cleavage of the disulfide bond in circulation, plasma levels of either free SAAEWFEKL or a fluorescent dye would serve as a more realistic model as the positive charges of LTX-315 cause cell adherence resulting in a very short circulation time when released. [40] Additionally, LTX-315 has previously been measured in plasma *in vitro*, having a half-life of only 160 minutes, also once again highlighting the need for entrapment in a CCPM system. [41]

The release profile is to be seen in view of the potency of the API one is working with, and hence what adverse events observed are in case it is released in healthy tissue, as well as efficacy upon release and exposure at the target site. This defines the nanocarrier design criteria, and is always a balance act. In the case of the LTX CCPMs, initial *in vivo* studies with the currently described formulation would be helpful in setting a baseline upon which to improve upon. Given the immunogenic cell death component of LTX-315, it would further be of interest to employ a syngeneic model as opposed to immune compromised animals for indications on efficacy. [42] With that said, some linker design alternatives are discussed in the next section.

Linker design alternatives

As mentioned earlier, steric hindrance of the disulfide bond may be necessary to ensure stable circulation. Although **chapter 7** shows a slow release (<10 % over 90 minutes) of LTX-315 under conditions present in the circulation, increased stability may be required *in vivo* where the pool of GSH (although at low concentration) is not limited like in the described *in vitro* setting. Such chemistry to introduce steric hindrance has already been advanced in the field of antibody-drug conjugates which has progressed significantly in recent years to improve upon circulation stability which in turn significantly impacts toxicity and the therapeutic window. [43] Although several possibilities for steric hindrance are available, a straightforward design for the linker described in **chapter 7** could be as shown in structure 1.

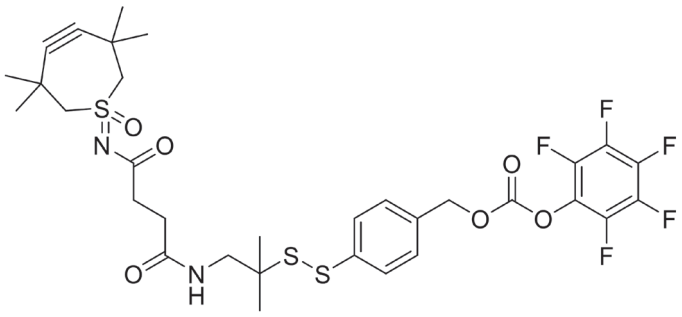

*Structure 1: Sterically hindered disulfide version of the click linker described in **chapter 7**. This compound could likely be attained by employing 1-amino-2-methylpropane-2-thiol as a starting reagent in place of cysteamine, following the same synthetic route as described.*

An additional consideration is the 1,6 elimination rate following cleavage of the disulfide resulting in the release of the native amine containing compound. Although 60 minutes may be sufficient as was found for the original linker, should the need arise, the rate could be increased by replacing the mercaptobenzyl alcohol moiety with 2-mercaptopropan-1-ol as shown in structure 2. Such an aliphatic disulfide has previously been described to result in fast and complete release for the small molecule ciprofloxacin, which was not the case for the mercaptobenzyl alcohol based linker. [44]

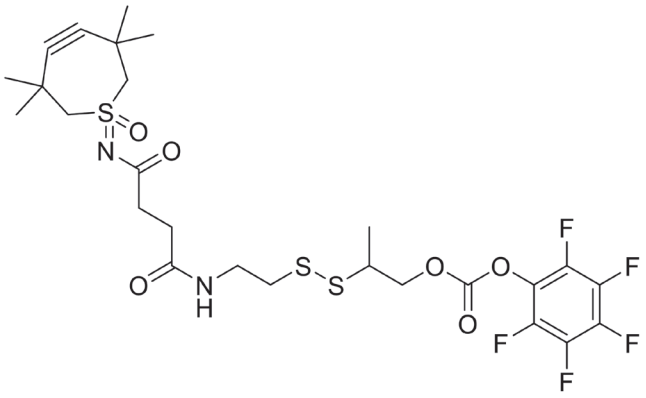

*Structure 2: The 2-mercaptopropan-1-ol version of the click linker described in **chapter 7**.*

Broader applicability of the CCPM and linker chemistry

Given the amine reactivity of the linker described in **chapter 7**, a plethora of compounds can be envisioned for entrapment, as was done with amine containing oligonucleotides such as siRNA in **chapter 8**. [45] Small proteins such as cytokines (IL-2 for example) would be an interesting next step towards immunomodulating nanomedicine. Additionally, several toxins employed in antibody-drug conjugates typically contain amines as conjugation handle, [46] highlighting potential cargos for the CCPM system described in **chapters 7** and **8** or potentially other azide containing agents such as azide modified antibodies. [47]

Upscaling and developability

The lead polymer described in **chapters 7** and **8** involves a single additional reaction to introduce azides onto a polymer that has previously been produced on the kilogram scale for the clinical evaluation of CCPMs. [30] The CCPM formation procedure was followed as described previously and, therefore, upscaling is not expected to be a difficulty for the azide containing CCPMs themselves. As for the linker, currently the largest scale was a 500 mg synthesis which was achieved with good yield. It would yet have to be seen experimentally if flow chemistry (reactions run in stream rather than in batch) could be employed, however currently simple scaling by increasing volumes (and potentially concentration) should at least make a 5-10 gram scale feasible. As for LTX-315, sufficient quantities are currently being produced for its clinical evaluation, which also indicates feasibility. [42] The greatest challenge will likely stem from the linker conjugation to LTX-315 whilst on resin, which does employ substantial amounts of linker with TMTHSI that bears significant costs. Furthermore, larger scale purifications will need to

involve large scale reverse-phase preparative HPLC equipment, which was not presently investigated but is expected to follow similar proceedings as the production of LTX-315. Similar considerations will have to be made in the case of siRNA, though this will not involve wasteful on-the-resin synthesis. Finally, conjugation to the preformed CCPMs is expected to be easily upscaled by volume and ideally through saturation of available azide moieties to allow homogeneous loading even when mixing large volumes. Almost all the chemistry employed here has used standardized methodology and hence confidence for upscaling and manufacturing, if desired, is high.

Acid sensitive linkers

Although not described in this thesis, significant work was conducted in this project on the use of hydrazone based pH sensitive linker designs, [48,49] which will be briefly discussed here. Since it was not considered viable to incorporate a hydrazone on a peptide before acidic deprotection and cleavage from the resin, this site-selective design concept centers around the entrapment of C-terminally modified LTX-315, derived with a hydrazide instead of an amide. This can be achieved by standard SPPS using a 4-(hydroxymethyl)benzoylaminomethyl polystyrene (HMBA) resin and cleaving the peptide using hydrazine. [50] The hydrazide is a minor modification handle and not expected to impact the biological activity of LTX-315, as evident when tested on breast and prostate cancer cells in figure 1, where only a minor difference in IC_{50} value was observed between native LTX-315 and the hydrazide form.

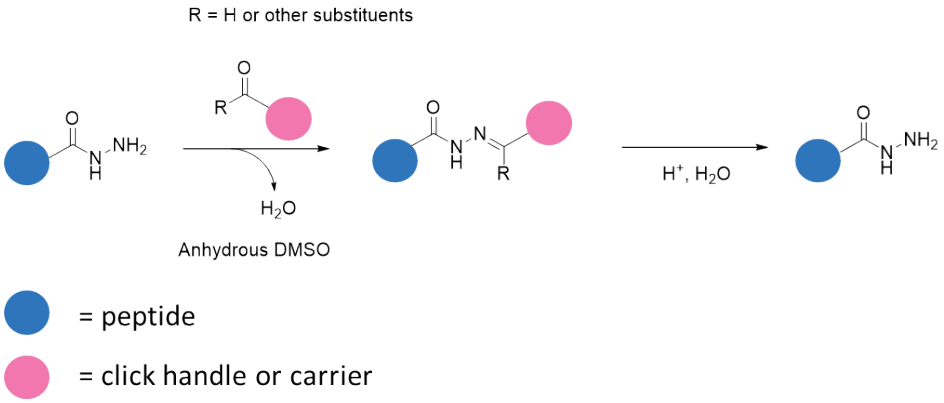

Scheme 1: Intended hydrazone formation between a peptide hydrazide and a linking entity followed by hydrolysis and thereby release under acidic conditions.

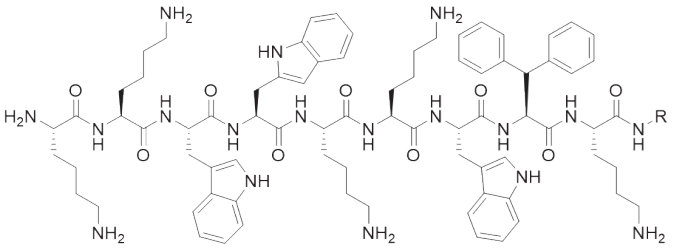

	MDA-MB-231 IC_{50} ± SD (µM)	PC3 IC_{50} ± SD (µM
LTX-315	17.7 ± 0.6	35.9 ± 1.6
LTX-315 hy	23.1 ± 1.7	57.8 ± 1.7

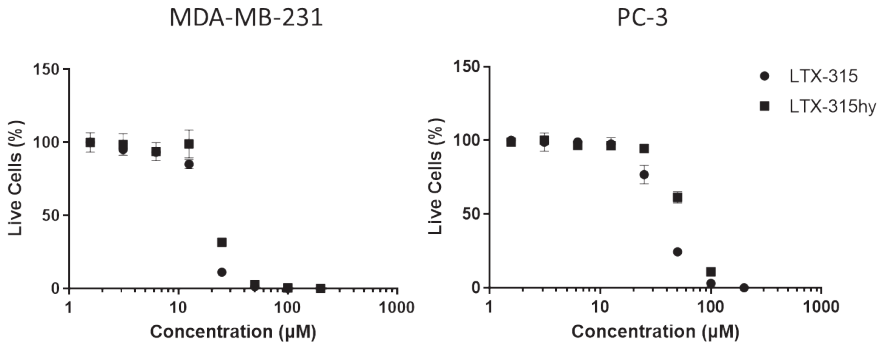

Figure 1: Structure of LTX-315 and its C-terminal hydrazide form as well as cell viability data after 24 hour incubation with MDA-MB-231 and PC-3 cells.

Although this preserved activity may not be the case for all classes of therapeutic peptides, it certainly holds true for this oncolytic peptide who's membrane perturbation action is primarily explained by charge interaction which is not significantly altered by the hydrazide modification. [39,51,52] By using such a C-terminal peptide hydrazide approach, site specific linker conjugation could in principle be achieved for any peptide sequence making this approach relatively universal (thereby also avoiding acidic cleavage conditions from the SPPS resin). However, mixed results were obtained when attempting to conjugate the carbonyl fragments shown in figure 2, to the model peptide SAAEWFEKL-hydrazide and analyzed by HPLC and MALDI-TOF-MS.

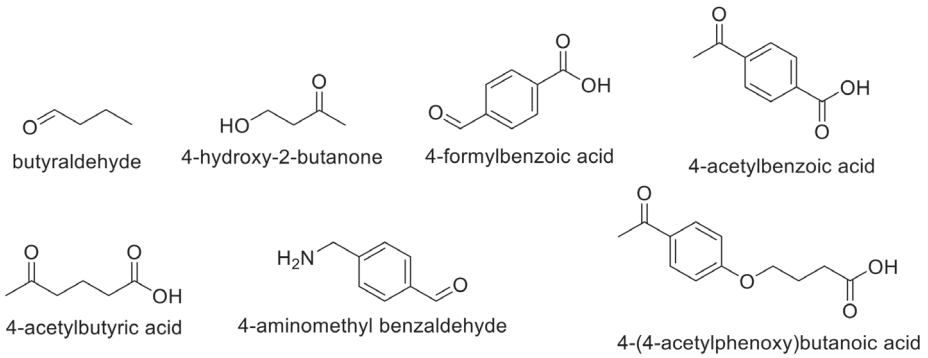

Figure 2: Structures of the carbonyl linker fragments (3 eq.) tested with SAAEWFEKL-hydrazide for hydrazone formation in anhydrous DMSO and release upon addition of 0.1N HCl.

The fastest reacting fragment was 4-formylbenzaldehyde, though this hydrazone was not cleaved by addition of 0.1N HCl. Most other fragments had either questionable formation and/or release with 0.1N HCl as observed during HPLC analysis. The most promising candidate that resulted in hydrazone formation and released under 0.1N HCl was 4-acetylbenzoic acid. Also when tested at pH 4.5, the 4-acetylbenzoic acid conjugate showed releasability (50% of the peptide being in the free form after 2-3 hours at RT, it is important to note that hydrazone bond formation is a reversible reaction and thereby in equilibrium). However, when this compound was used as a clickable peptide-linker conjugate (structure 3), no entrapment into CCPMs (after crosslinking as described in **chapter 6**) was evident from HPLC analysis, after which this route of release development was not further pursued.

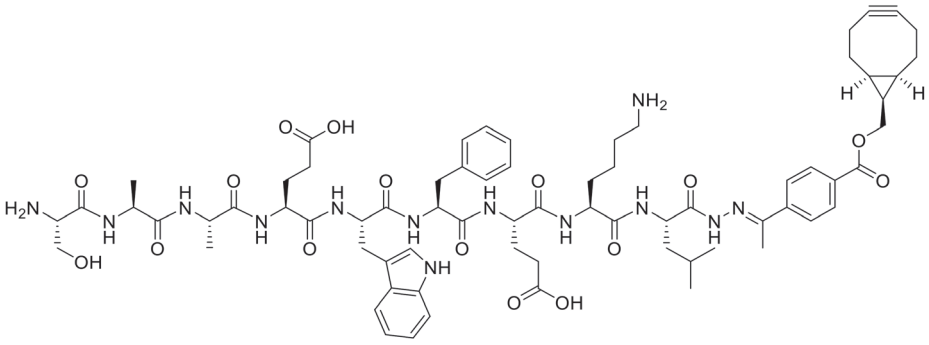

Structure 3: SAAEWFEKL-hydrazide with the 4-acetylbenzoic acid linker functionalized with BCN to enable a click reaction with azide containing CCPMs.

Nonetheless, should a suitable linker fragment with good formation reactivity and releasability around pH 5 be found, the peptide hydrazide approach could yet hold merit.

Conclusion

In conclusion, this thesis has provided key insights into the formation of payload entrapped CCPMs for both diagnostic and therapeutic purposes and described innovative chemical tools for their development. Particularly, the click-based disulfide linker chemistry developed here has broad applicability. Moreover, click-loading after CCPM formation allows entrapment of a much broader spectrum of cargos, opening up opportunities beyond the compounds and platforms described in this thesis. Preclinical evaluation is essential to assess the disulfide linker stability in circulation, the efficacy and safety of API loaded CCPMs in relevant tumor models. Upon significant improvement of the therapeutic index versus free drug, this novel linker and CCPM approach is eligible to develop a new class of anticancer products, all for the benefit of patients

References

(1) Varela-Moreira, A.; Shi, Y.; Fens, M. H. A. M.; Lammers, T.; Hennink, W. E.; Schiffelers, R. M. Clinical Application of Polymeric Micelles for the Treatment of Cancer. *Mater. Chem. Front.* **2017**, *1* (8), 1485–1501.

(2) Cabral, H.; Miyata, K.; Osada, K.; Kataoka, K. Block Copolymer Micelles in Nanomedicine Applications. *Chem. Rev.* **2018**, *118* (14), 6844–6892.

(3) Ghezzi, M.; Pescina, S.; Padula, C.; Santi, P.; Del Favero, E.; Cantù, L.; Nicoli, S. Polymeric Micelles in Drug Delivery: An Insight of the Techniques for Their Characterization and Assessment in Biorelevant Conditions. *J. Control. Release* **2021**, *332* (February), 312–336.

(4) Hwang, D.; Ramsey, J. D.; Kabanov, A. V. Polymeric Micelles for the Delivery of Poorly Soluble Drugs: From Nanoformulation to Clinical Approval. *Adv. Drug Deliv. Rev.* **2020**, *156*, 80–118.

(5) Nishiyama, N.; Kataoka, K. Current State, Achievements, and Future Prospects of Polymeric Micelles as Nanocarriers for Drug and Gene Delivery. *Pharmacol. Ther.* **2006**, *112* (3), 630–648.

(6) Houdaihed, L.; Evans, J. C.; Allen, C. Overcoming the Road Blocks: Advancement of Block Copolymer Micelles for Cancer Therapy in the Clinic. *Mol. Pharm.* **2017**, *14* (8), 2503–2517.

(7) Talelli, M.; Barz, M.; Rijcken, C. J. F.; Kiessling, F.; Hennink, W. E.; Lammers, T. Core-Crosslinked Polymeric Micelles: Principles, Preparation, Biomedical Applications and Clinical Translation. *Nano Today* **2015**, *10* (1), 93–117.

(8) Fan, W.; Zhang, L.; Li, Y.; Wu, H. Recent Progress of Crosslinking Strategies for Polymeric Micelles with Enhanced Drug Delivery in Cancer Therapy. *Curr. Med. Chem.* **2019**, *26* (13), 2356–2376.

(9) van Nostrum, C. F. Covalently Cross-Linked Amphiphilic Block Copolymer Micelles. *Soft Matter* **2011**, *7* (7), 3246.

(10) Fang, J.; Nakamura, H.; Maeda, H. The EPR Effect: Unique Features of Tumor Blood Vessels for Drug Delivery, Factors Involved, and Limitations and Augmentation of the Effect. *Adv. Drug Deliv. Rev.* **2011**, *63* (3), 136–151.

(11) Maeda, H.; Wu, J.; Sawa, T.; Matsumura, Y.; Hori, K. Tumor Vascular Permeability and the EPR Effect in Macromolecular Therapeutics: A Review. *J. Control. Release* **2000**, *65* (1–2), 271–284.

(12) Najafi, M.; Hebels, E.; Hennink, W. E.; Vermonden, T. Poly(N -isopropylacrylamide): Physicochemical Properties and Biomedical Applications. In *Temperature-Responsive Polymers*; Wiley: Chichester, UK, 2018; pp 1–34.

(13) Hu, Q.; Rijcken, C. J. F.; van Gaal, E.; Brundel, P.; Kostkova, H.; Etrych, T.; Weber, B.; Barz, M.; Kiessling, F.; Prakash, J.; Storm, G.; Hennink, W. E.; Lammers, T. Tailoring the Physicochemical Properties of Core-Crosslinked Polymeric Micelles for Pharmaceutical Applications. *J. Control. Release* **2016**, *244*, 314–325.

(14) Soga, O.; van Nostrum, C. F.; Ramzi, A.; Visser, T.; Soulimani, F.; Frederik, P. M.; Bomans, P. H. H.; Hennink, W. E. Physicochemical Characterization of Degradable Thermosensitive Polymeric Micelles. *Langmuir* **2004**, *20* (21), 9388–9395.

(15) Soga, O.; van Nostrum, C. F.; Hennink, W. E. Poly(N -(2-Hydroxypropyl) Methacrylamide Mono/Di Lactate): A New Class of Biodegradable Polymers with Tuneable Thermosensitivity. *Biomacromolecules* **2004**, *5* (3), 818–821.

(16) Soga, O.; van Nostrum, C. F.; Fens, M.; Rijcken, C. J. F.; Schiffelers, R. M.; Storm, G.; Hennink, W. E. Thermosensitive and Biodegradable Polymeric Micelles for Paclitaxel Delivery. *J. Control. Release* **2005**, *103* (2), 341–353.

(17) Najafi, M.; Kordalivand, N.; Moradi, M. A.; Van Den Dikkenberg, J.; Fokkink, R.; Friedrich, H.; Sommerdijk, N. A. J. M.; Hembury, M.; Vermonden, T. Native Chemical Ligation for Cross-Linking of Flower-Like Micelles. *Biomacromolecules* **2018**, *19* (9), 3766–3775.

(18) Talelli, M.; Iman, M.; Varkouhi, A. K.; Rijcken, C. J. F.; Schiffelers, R. M.; Etrych, T.; Ulbrich, K.; van Nostrum, C. F.; Lammers, T.; Storm, G.; Hennink, W. E. Core-Crosslinked Polymeric Micelles with Controlled Release of Covalently Entrapped Doxorubicin. *Biomaterials* **2010**, *31* (30), 7797–7804.

(19) Read, E. S.; Armes, S. P. Recent Advances in Shell Cross-Linked Micelles. *Chem. Commun. (Camb).* **2007**, No. 29, 3021–3035.

(20) Talelli, M.; Barz, M.; Rijcken, C. J. F.; Kiessling, F.; Hennink, W. E.; Lammers, T. Core-Crosslinked Polymeric Micelles: Principles, Preparation, Biomedical Applications and Clinical Translation. *Nano Today* **2015**, *10* (1), 93–117.

(21) Rijcken, C. J.; Snel, C. J.; Schiffelers, R. M.; van Nostrum, C. F.; Hennink, W. E. Hydrolysable Core-Crosslinked Thermosensitive Polymeric Micelles: Synthesis, Characterisation and in Vivo Studies. *Biomaterials* **2007**, *28* (36), 5581–5593.

(22) Deng, C.; Jiang, Y.; Cheng, R.; Meng, F.; Zhong, Z. Biodegradable Polymeric Micelles for Targeted and Controlled Anticancer Drug Delivery: Promises, Progress and Prospects. *Nano Today* **2012**, *7* (5), 467–480.

(23) Biancacci, I.; Sun, Q.; Möckel, D.; Gremse, F.; Rosenhain, S.; Kiessling, F.; Bartneck, M.; Hu, Q.; Thewissen, M.; Storm, G.; Hennink, W. E.; Shi, Y.; Rijcken, C. J. F.; Lammers, T.; Sofias, A. M. Optical Imaging of the Whole-Body to Cellular Biodistribution of Clinical-Stage PEG-b-PHPMA-Based Core-Crosslinked Polymeric Micelles. *J. Control. Release* **2020**, *328* (September), 805–816.

(24) Hembury, M.; Chiappini, C.; Bertazzo, S.; Kalber, T. L.; Drisko, G. L.; Ogunlade, O.; Walker-Samuel, S.; Krishna, K. S.; Jumeaux, C.; Beard, P.; Kumar, C. S. S. R.; Porter, A. E.; Lythgoe, M. F.; Boissière, C.; Sanchez, C.; Stevens, M. M.; Langer, R. Gold-Silica Quantum Rattles for Multimodal Imaging and Therapy. *Proc. Natl. Acad. Sci. U. S. A.* **2015**, *112* (7), 1959–1964.

(25) Brülisauer, L.; Gauthier, M. A.; Leroux, J. C. Disulfide-Containing Parenteral Delivery Systems and Their Redox-Biological Fate. *J. Control. Release* **2014**, *195*, 147–154.

(26) Lei, J.; Zhang, Q.; Jin, X.; Lu, H.; Wang, S.; Li, T.; Sheng, Y.; Zhang, F.; Zheng, Y. Drug Release from Disulfide-Linked Prodrugs: Role of Thiol Agents. *Mol. Pharm.* **2021**, *18* (7), 2777–2785.

(27) Wang, Q.; Guan, J.; Wan, J.; Li, Z. Disulfide Based Prodrugs for Cancer Therapy. *RSC Adv.* **2020**, *10* (41), 24397–24409.

(28) Hembury, M.; Beztsinna, N.; Asadi, H.; Van Den Dikkenberg, J. B.; Meeldijk, J. D.; Hennink, W. E.; Vermonden, T. Luminescent Gold Nanocluster-Decorated Polymeric Hybrid Particles with Assembly-Induced Emission. *Biomacromolecules* **2018**, *19* (7), 2841–2848.

(29) Cartlidge, S. A.; Duncan, R.; Lloyd, J. B.; Kopečkova—Rejmanová, P.; Kopeček, J. Soluble, Crosslinked N-(2-Hydroxypropyl)Methacrylamide Copolymers as Potential Drug Carriers. *J. Control. Release* **1987**, *4* (4), 253–264.

(30) Rijcken, C. J. F.; De Lorenzi, F.; Biancacci, I.; Hanssen, R. G. J. M.; Thewissen, M.; Hu, Q.; Atrafi, F.; Liskamp, R. M. J.; Mathijssen, R. H. J.; Miedema, I. H. C.; Menke - van der Houven van Oordt, C. W.; van Dongen, G. A. M. S.; Vugts, D. J.; Timmers, M.; Hennink, W. E.; Lammers, T. Design, Development and Clinical Translation of CriPec®-Based Core-Crosslinked Polymeric Micelles. *Adv. Drug Deliv. Rev.* **2022**, *191*, 114613.

(31) Shirangi, M.; Sastre Toraño, J.; Sellergren, B.; Hennink, W. E.; Somsen, G. W.; Van Nostrum, C. F. Methyleneation of Peptides by N, N, N, N -Tetramethylethylenediamine (TEMED) under Conditions Used for Free Radical Polymerization: A Mechanistic Study. *Bioconjug. Chem.* **2015**, *26* (1), 90–100.

(32) Cadée, J. A.; Van Steenbergen, M. J.; Versluis, C.; Heck, A. J. R.; Underberg, W. J. M.; Den Otter, W.; Jiskoot, W.; Hennink, W. E. Oxidation of Recombinant Human Interleukin-2 by Potassium Peroxodisulfate. *Pharm. Res.* **2001**, *18* (10), 1461–1467.

(33) Weterings, J.; Rijcken, C. J. F.; Veldhuis, H.; Meulemans, T.; Hadavi, D.; Timmers, M.; Honing, M.; Ippel, H.; Liskamp, R. M. J. TMTHSI, a Superior 7-Membered Ring Alkyne Containing Reagent for Strain-Promoted Azide–Alkyne Cycloaddition Reactions. *Chem. Sci.* **2020**, *11* (33), 9011–9016.

(34) La–Venia, A.; Dzijak, R.; Rampmaier, R.; Vrabel, M. An Optimized Protocol for the Synthesis of Peptides Containing Trans -Cyclooctene and Bicyclononyne Dienophiles as Useful Multifunctional Bioorthogonal Probes. *Chem. – A Eur. J.* **2021**, *27* (54), 13632–13641.

(35) Timmers, M.; Kipper, A.; Frey, R.; Notermans, S.; Voievudskyi, M.; Wilson, C.; Hentzen, N.; Ringle, M.; Bovino, C.; Stump, B.; Rijcken, C. J. F.; Vermonden, T.; Dijkgraaf, I.; Liskamp, R. Exploring the Chemical Properties and Medicinal Applications of Tetramethylthiocycloheptyne Sulfoximine Used in Strain-Promoted Azide–Alkyne Cycloaddition Reactions. *Pharmaceuticals* **2023**, *16* (8), 1155.

(36) Kennedy, L.; Sandhu, J. K.; Harper, M.-E.; Cuperlovic-Culf, M. Role of Glutathione in Cancer: From Mechanisms to Therapies. *Biomolecules* **2020**, *10* (10), 1429.

(37) Deng, Z.; Hu, J.; Liu, S. Disulfide-Based Self-Immolative Linkers and Functional Bioconjugates for Biological Applications. *Macromol. Rapid Commun.* **2020**, *41* (1), 1900531.

(38) Eras, A.; Castillo, D.; Suárez, M.; Vispo, N. S.; Albericio, F.; Rodriguez, H. Chemical Conjugation in Drug Delivery Systems. *Front. Chem.* **2022**, *10* (May), 1–23.

(39) Mirjolet, J.-F.; Haug, B. E.; Mortensen, B.; Berg, K.; Camilio, K. A.; Stensen, W.; Bichat, F.; Serin, G.; Eliassen, L. T.; Svendsen, J. S.; Rekdal, Ø. Discovery of a 9-Mer Cationic Peptide (LTX-315) as a Potential First in Class Oncolytic Peptide. *J. Med. Chem.* **2016**, *59* (7), 2918–2927.

(40) Klaiss-Luna, M. C.; Jemioła-Rzemińska, M.; Strzałka, K.; Manrique-Moreno, M. Understanding the Biophysical Interaction of LTX-315 with Tumoral Model Membranes. *Int. J. Mol. Sci.* **2022**, *24* (1), 581.

(41) Haug, B. E.; Camilio, K. A.; Eliassen, L. T.; Stensen, W.; Svendsen, J. S.; Berg, K.; Mortensen, B.; Serin, G.; Mirjolet, J.-F.; Bichat, F.; Rekdal, Ø. Discovery of a 9-Mer Cationic Peptide (LTX-315) as a Potential First in Class Oncolytic Peptide Supporting Info. *J. Med. Chem.* **2016**, *59* (7), 2918–2927.

(42) Liao, H.-W.; Garris, C.; Pfirschke, C.; Rickelt, S.; Arlauckas, S.; Siwicki, M.; Kohler, R. H.; Weissleder, R.; Sundvold-Gjerstad, V.; Sveinbjørnsson, B.; Rekdal, Ø.; Pittet, M. J. LTX-315 Sequentially Promotes Lymphocyte-Independent and Lymphocyte-Dependent Antitumor Effects. *Cell Stress* **2019**, *3* (11), 348–360.

(43) Gao, W.-C.; Tian, J.; Shang, Y.-Z.; Jiang, X. Steric and Stereoscopic Disulfide Construction for Cross-Linkage via N -Dithiophthalimides. *Chem. Sci.* **2020**, *11* (15), 3903–3908.

(44) He, M.; Li, J.; Han, H.; Borges, C. A.; Neiman, G.; Røise, J. J.; Hadaczek, P.; Mendonsa, R.; Holm, V. R.; Wilson, R. C.; Bankiewicz, K.; Zhang, Y.; Sadlowski, C. M.; Healy, K.; Riley, L. W.; Murthy, N. A Traceless Linker for Aliphatic Amines That Rapidly and Quantitatively Fragments after Reduction. *Chem. Sci.* **2020**, *11* (33), 8973–8980.

(45) Lau, S.; Graham, B.; Boyd, B. J.; Pouton, C. W.; White, P. J. Commercially Supplied Amine-Modified SiRNAs May Require Ultrafiltration Prior to Conjugation with Amine-Reactive Compounds. *J. Nucleic Acids* **2011**, *2011*, 1–5.

(46) Wang, Z.; Li, H.; Gou, L.; Li, W.; Wang, Y. Antibody–Drug Conjugates: Recent Advances in Payloads. *Acta Pharm. Sin. B* **2023**, No. xxx.

(47) Zhang, X.; Ou, C.; Liu, H.; Wang, L.-X. Synthesis and Evaluation of Three Azide-Modified Disaccharide Oxazolines as Enzyme Substrates for Single-Step Fc Glycan-Mediated Antibody-Drug Conjugation. *Bioconjug. Chem.* **2022**, *33* (6), 1179–1191.

(48) Sonawane, S. J.; Kalhapure, R. S.; Govender, T. Hydrazone Linkages in PH Responsive Drug Delivery Systems. *Eur. J. Pharm. Sci.* **2017**, *99*, 45–65.

(49) Kölmel, D. K.; Kool, E. T. Oximes and Hydrazones in Bioconjugation: Mechanism and Catalysis. *Chem. Rev.* **2017**, *117* (15), 10358–10376.

(50) Pedersen, S. L.; Jensen, K. J. Peptide Release, Side-Chain Deprotection, Work-Up, and Isolation. In *Methods in Molecular Biology*; 2013; Vol. 1047, pp 43–63.

(51) Eike, L.-M.; Yang, N.; Rekdal, Ø.; Sveinbjørnsson, B. The Oncolytic Peptide LTX-315 Induces Cell Death and DAMP Release by Mitochondria Distortion in Human Melanoma Cells. *Oncotarget* **2015**, *6* (33), 34910–34923.

(52) Sveinbjørnsson, B.; Camilio, K. A.; Haug, B. E.; Rekdal, Ø. LTX-315: A First-in-Class Oncolytic Peptide That Reprograms the Tumor Microenvironment. *Future Med. Chem.* **2017**, *9* (12), 1339–1344.

9

APPENDICES

Nederlandse samenvatting

Nanomedicijnen betekent het verpakken van geneesmiddelen in dragers die extreem klein zijn, namelijk nanometer dimensies. Dit beoogt minimaal 2 doelen: 1) bescherming van het lichaam voor het actieve geneesmiddel en vice versa, en 2) accumulatie op de beoogde plaats van werking te bevorderen in vergelijking met het vrije medicijn (zonder drager). Met name chemotherapie (behandeling van kanker) is toxisch voor gezond weefsel, met (serieuze) bijwerkingen als gevolg. De ongunstige balans tussen werking en bijwerking verhindert regelmatig continuering van de behandeling en/of hogere doseringen, resulterend in suboptimale behandeling van de patient.

Een nanomedicijn zal niet snel in gezond weefsel terecht komen, aangezien de bloedvaten intact zijn en enkel selectief stoffen opnemen (e.g. suiker, vitamine). In contrast, in tumoren zijn de bloedvaten vaak “lek” door de abnormaal snelle groei van tumoren. Hierdoor zal een nanodrager met de juiste eigenschappen zich in de loop van de tijd selectiever in de tumor kunnen ophopen. Een van de eerste voorbeelden van deze strategie is Doxil®. Het chemotherapeuticum doxorubicine is ingesloten in nanodragers gemaakt van vetten waardoor dit veel beter getolereerd wordt door eierstokkankerpatiënten, dan wanneer het vrije doxorubicine wordt toegepast.

Synthetische nanodragers zijn bijvoorbeeld polymeren micellen, structuren die gevormd worden wanneer polymeren bestaande uit waterminnende koppen en waterafstotende staarten in water gesuspendeerd worden (zoals zeep). De waterminnende koppen schermen de waterafstotende kern af, wat meestal resulteert in een bolvormige structuur. Door de grootte van het polymeer (meestal het waterafstotende deel van het polymeer) te veranderen, kan de grootte van de polymeren micel zelf worden veranderd en dus naar wens worden aangepast. Daarnaast kunnen in zo’n polymeren systeem functionaliteiten worden geïntroduceerd die twee dingen mogelijk maken: 1) stabilisatie van de polymeren micelstructuur door zogenaamde crosslinking en 2) (tijdelijke) chemische koppeling van het geneesmiddel door gebruik van een linker. Crosslinking betekent dat polymeerketens die zijn samengevoegd tot de polymeren micelstructuur niet meer uit elkaar kunnen vallen in afzonderlijke polymeren (het resultaat noemen we core-crosslinked polymeric micelles ofwel CCPMs). Chemische koppeling van het geneesmiddel voorkomt dat het middel voortijdig uit de kern lekt. Daarnaast kan deze linker ervoor zorgen dat het geneesmiddel enkel vrijkomt door een bepaalde trigger, idealiter op de beoogde doellocatie (zoals de tumor). Tot slot, door het inbouwen van afbreekbare stukken in de CCPM’s breken de polymeren na verloop van tijd af, vallen en CCPM uit elkaar, en uit het lichaam worden verwijderd. Deze biodegradeerbaarheid is een essentiele eigenschap voor de beoogde toepassing bij mensen.

Een voorbeeld van deze CCPM technologie werd eerder ontwikkeld door de afdeling farmaceutische technologie van Universiteit Utrecht en verder in (pre) klinische ontwikkeling gebracht (bekend geworden als CriPec®) door het bedrijf Cristal Therapeutics, de partner in dit industriële promotietraject. Het doel van dit promotieproject was om alternatieve chemie te ontwikkelen voor het maken van CCPMs, De oorspronkelijke crosslink methode bleek namelijk niet geschikt te zijn voor labiele stoffen (e.g. nieuwe geneesmiddelen zoals peptides en fluorescerende kleurstoffen voor beeldvorming). Het doel was een milde chemie voor crosslinking van zowel polymeren, evenals een nieuwe linkerchemie voor het beladen en gecontroleerd vrijzetten van geneesmiddelen zoals therapeutische peptiden.

De onderzochte concepten zijn erg divers en zijn hieronder samengevat in een kort hoofdstukoverzicht:

Hoofdstuk 1 is een korte introductie in het concept van nanodragers, polymeren micellen, crosslinking, orthogonale chemie voor linkers met gecontroleerde afgifte.

Hoofdstuk 2 is een systematisch overzicht van gouden nanoclusters (ultrakleine structuren van goud, klein genoeg om bijvoorbeeld in een CCPM te passen) en hun gebruik in biomedische toepassingen. Gouden nanoclusters interageren met onschadelijk bijna-infrarood licht en zetten dit om in andere kleur, licht en warmte. Als zodanig zijn ze interessant als omvormer voor laser-gebaseerde therapieën, om bijvoorbeeld een ingesloten geneesmiddel vrij te geven. In de praktijk omvat dit diagnostiek, therapie en de combinatie van beide; theranostiek. In dit hoofdstuk wordt een overzicht gegeven van de laatste stand van zaken.

Hoofdstuk 3 gebruikt gouden nanoclusters in een CCPM-systeem en integreert doxorubicine (een relevant chemotherapeuticum dat hierboven al is genoemd) voor mogelijke laser-gebaseerde therapie. De effectiviteit van deze gouden nanocluster bevattende CCPMs is aangetoond bij kankercellen. Deze technologie is veelbelovend maar nog niet direct klaar voor klinische toepassingen.

Hoofdstuk 4 introduceert een milde crosslinking-chemie (bekend als native chemical ligation) in het polymeersysteem dat wordt gebruikt in CriPec®. We laten zien dat modelstoffen (fluorescerende kleurstoffen) kunnen worden ingesloten in deze CCPMs. Belangrijke resultaten zijn dat stabiele CCPM gevormd worden, én dat de fluorescente stoffen na blootstelling aan deze alternatieve crosslinking chemie nog volledig intact zijn.

Hoofdstuk 5 beschrijft het degradatiemechanisme van CCPMs die gevormd zijn door twee verschillende methodes, om inzicht te krijgen in de factoren die de stabiliteit

beïnvloeden. CCPMs die gestabiliseerd worden door korte crosslinkers bleken sneller af te breken dan CCPMs met directe verbindingen tussen complementaire polymeerketens. Dit designprincipe is een belangrijke factor waar rekening mee gehouden mag worden, afhankelijk van de stabiliteit vereiste.

In hoofdstuk 6 is een nieuwe manier van medicijninsluiting en in CCPMs onderzocht. De vernieuwing isdat het medicijn via click chemie covalent ingesloten wordt ná vorming van CCPMs. Dit heeft als voordeel dat uiteenlopende crosslink strategieën (dus niet enkel de chemie zoals in hoofdstuk 4 beschreven) gebruikt kunnen worden, aangezien het geneesmiddel pas na de vorming van CCPMs wordt geïntroduceerd.

Hoofdstuk 7 maakt gebruik van de bovenstaande lessen en introduceert een click-linker aan therapeutische peptiden. Het conjugaat kan dan reageren met de ‘standaard’ geproduceerde CCPMs. Deze kliklinker maakt het mogelijk om een breed spectrum aan (stabiele én labiele) therapeutische moleculen te conjugeren en (gecontroleerd) vrij te geven onder omstandigheden die verwacht worden in, bijvoorbeeld, tumorweefsel.

Hoofdstuk 8 toont een ander voorbeeld van het gebruik van de click-linker van hoofdstuk 7 voor zogenaamde nucleotides, met mogelijke toepassing voor de behandeling van diverse ziekten. Dit hoofdstuk demonstreert de grote verscheidenheid aan moleculen die in CCPMs kunnen worden ingesloten.

Tot slot, dit proefschrift beschrijft de criteria voor het ontwerp van CCPMs en linkers die het insluiten en vrijgeven van een breed spectrum aan therapeutica mogelijk maken. Het meest waardevolle aspect is de click-linker die ontwikkeld is, en die in principe de koppeling van verschillende moleculen aan verschillende nanodragers (anders dan CCPMs) en zelfs antilichamen mogelijk maakt. Als volgende stappen zal de stabiliteit van deze linker in de bloedbaan evenals de vrijgifte van gekoppelde geneesmiddelen in tumorweefsel onderzocht worden. Daarnaast zullen de bevindingen in dit proefschrift ook helpen bij toekomstige CCPM-ontwikkelingsprojecten, met als uiteindelijk doel het leven van patiënten te verbeteren.

Layman's summary

The field of nanomedicines is about the entrapment of drug compounds into carrier vehicles that are extremely small (in the nanometer size range). This aim is to shield the body from the active drug and vice versa, and promote accumulation at the intended site of action relative to the free drug (i.e. without vehicle). This is particularly attractive in cancer therapy (chemotherapy more specifically) as the drug cargo is toxic also to healthy tissue, which results in side effects that quickly become an issue, limiting extended treatment and higher dosing possibilities (can the tumor be killed before the patient). By having a tumor killing agent entrapped within a carrier, it is anticipated that the environment in the tumor (specifically blood vessels) is leaky due to abnormal tumor growth, and therefore allows a nanocarrier to accumulate within the tumor over time whilst circulating in the patient's blood stream. An early example of the success of this sort of strategy is Doxil®, which is the chemotherapeutic doxorubicin entrapped within nanocarrier vehicles made of lipid membranes (similar to the membranes of cells) which is far better tolerated by patients for the treatment of ovarian cancer than the free drug doxorubicin would be on its own.

In terms of the nanocarrier, significant efforts have been made towards generating these carriers entirely synthetically. One of these forms are polymeric micelles, which are structures formed when polymers with water loving heads and water repelling tails are suspended in water (much like soap). The water loving heads shield the water repelling core, typically resulting in a spherical structure. By changing the size of the polymer (usually the water repelling part of the polymer), the size of the polymeric micelle itself can be changed and therefore tailored as required. Additionally, by having a synthetic system, custom attachment handles can be introduced that allow for two things; 1) stabilization of the polymeric micelle structure by so called crosslinking and 2) chemical attachment of the drug cargo by use of a linker. Crosslinking means that polymer chains assembled into the polymeric micelle structure can no longer fall apart into individual polymers (we call these core-crosslinked polymeric micelles or CCPMs). Chemical cargo attachment prevents the drug compound from leaking out of the core and the linker used for this attachment also releases this cargo, ideally at the intended target site (like the tumor). Finally, through incorporation of degradable structural elements into these synthetic polymers, the CCPMs can be broken down and cleared from circulation over time, a feature deemed quite critical for the intended in-human use.

One example of this technology was previously developed in the Pharmaceutics department at Utrecht University and further brought into clinical development (becoming known as

CriPec®) by the company Cristal Therapeutics, the partner in this industrial doctorates program. This spin-off was established in 2011. This project aimed to change the chemistry employed in the generation of the CCPMs, as the previous technology would not be compatible with more labile compounds (e.g. new generation therapeutics and fluorescent dyes). Therefore, mild and compatible chemistry for crosslinking of the polymers as well as new linker chemistry for loading and (controlled) release of cargo such as therapeutic peptides was aimed to be developed within the scope of this PhD project.

Without going into too much technical detail, the concepts that are explored are quite diverse and are best summarized with a brief chapter overview:

Chapter 1 is a brief introduction into the concept of nanocarriers, polymeric micelles, crosslinking, mild compatible chemistry and triggered release chemistry. An overview of the chapters is also presented.

Chapter 2 is a systematic review of gold nanoclusters (ultra-small structures of gold, small enough for example to fit numerous into a single CCPM) and their use in biomedical applications. As gold nanoclusters interact with harmless near-infra red light and convert this into other light and heat, they serve as an interesting transducer for laser guided therapies, to release the drug for example. The principle includes diagnostics, therapy and the combination of both; theranostics. An overview of the state-of-the-art is presented here.

Chapter 3 uses gold nanoclusters in a CCPM system and incorporates doxorubicin (a relevant chemotherapeutic agent as mentioned above) for laser guided therapy as shown on cancer cells. Although promising, we conclude that this sort of technology is not yet ripe for clinical applications and further development is required.

In Chapter 4 we introduce a specific type of mild crosslinking chemistry (known as native chemical ligation) to the polymer system previously employed in CriPec®. We show that model compounds (fluorescent dyes) can be entrapped in these CCPMs, though no linker system is employed that can release these compounds.

In Chapter 5, we study the degradation mechanism of 2 types of generated CCPMs which gives insight into their stability. We found that CCPMs formed by the approach in chapter 4 break down faster than formed by the approach similar to chapter 3, which needs to be taken into consideration should higher stability be required.

In chapter 6 we find a new way of entrapping cargo into CCPMs, using so called click chemistry and entrapping after the CCPMs have already been formed (though with a

linker that cannot release the compound). This is new as previously the cargo would typically be present during the crosslinking reaction. This also implies that the mild crosslinking chemistry developed in chapter 4 for crosslinking is not necessary, as the cargo can be introduced after CCPM formation.

Chapter 7 uses the above lessons and also introduces a release capable click linker which is capable of loading therapeutic peptides formed by standard production techniques into 'standard' CCPMs. This linker and nanocarrier system should allow for a range of therapeutic molecules to be loaded and released under conditions expected in the tumor.

Chapter 8 shows another example of the use of the CCPM system of chapter 7 for another class of molecules that allow for controlling of gene expressions, which could be in several diseases. This serves as a token to the large diversity of molecules that can be entrapped in these CCPMs.

In summary, this thesis described the criteria for the design of CCPMs and linkers allowing entrapment and release of a wide spectrum of therapeutic agents. The most valuable aspect is the click linker that was developed, which in principle should allow for linking of diverse molecules to diverse nanocarriers (other than CCPMs) and even antibodies. Of course, the stability of the linker in the bloodstream and the extent of preferential release inside a tumor still needs to be investigated. Additionally, the findings in this thesis will also help guide the work of future CCPM development projects, ultimately aiming to improving the lives of patients.

About the author

Erik Reinhard Hebels was born on the 26th of May, 1995 in Seremban Malaysia. Shortly thereafter, his family relocated to Zimbabwe where he was raised. Having been home-schooled until age 14, he then attended Speciss College for his final 3 years of high school, completing his Cambridge O- and A-levels. Driven by a passion for organic chemistry and desire to have an impact on the world, he searched to apply chemistry for the progression of medicine which led him to the college of pharmaceutical sciences in Utrecht (September 2013), an honors program specialized in drug development. Throughout the program, he was always keeping an eye out for deepening his chemical knowledge. Having graduated cum laude (2016), this was followed up by the masters program drug innovation, which constituted a research internship in the pharmaceutics department in Utrecht and at the ETH in Zurich. The latter was undergone as member of the U-Select life sciences honors program, during which the opportunity to apply for the industrial doctorates program arose. Following the successful application and candidate defense with the Dutch research council, he finalized his masters program (cum laude) and began the PhD track in December 2018. In addition to the research program, Erik was also a member of the future medicine fellows (an honors track for PhDs). Although experiments were inhibited by the Corona pandemic, Erik's official PhD period was concluded after 4 years after which he joined the team of Genmab in April 2023, with the aim of using his chemistry expertise to strive towards bringing new therapies to patients. During this time, he also finalized his thesis writing and publications resultant from the work conducted.

Publications

Najafi, M.; **Hebels, E**.; Hennink, W. E.; Vermonden, T. Poly(N -isopropylacrylamide): Physicochemical Properties and Biomedical Applications. In *Temperature-Responsive Polymers*; Wiley: Chichester, UK, **2018**; pp 1–34.

Schmidt, A. C.; **Hebels, E. R.**; Weitzel, C.; Stoessel, B.; Bao, Y.; Altmann, K.-H.; Leroux, J.-C. Ammonia Uptake by Transmembrane PH Gradient Poly(Isoprene)- Block -Poly(Ethylene Glycol) Polymersomes. *Soft Matter* **2020**, *16* (11), 2725–2735.

Schmidt, A. C.; **Hebels, E. R.**; Weitzel, C.; Kletzmayr, A.; Bao, Y.; Steuer, C.; Leroux, J. Engineered Polymersomes for the Treatment of Fish Odor Syndrome: A First Randomized Double Blind Olfactory Study. *Adv. Sci.* **2020**, *7* (8), 1–8.

Hebels, E. R.; Najafi, M.; van den Dikkenberg, J.; Beztsinna, N.; van de Looij, S.; Wilbie, D.; Meeldijk, J.; Hembury, M.; Vermonden, T. Luminescent Gold Nanocluster-Decorated Polymeric Hybrid Particles for Laser Guided Therapy. *Eur. Polym. J.* **2021**, *152* (October 2020), 110467.

van de Looij, S. M.; **Hebels, E. R.**; Viola, M.; Hembury, M.; Oliveira, S.; Vermonden, T. Gold Nanoclusters: Imaging, Therapy, and Theranostic Roles in Biomedical Applications. *Bioconjug. Chem.* **2022**, *33* (1), 4–23.

Hebels, E. R.; Bindt, F.; Walther, J.; van Geijn, M.; Weterings, J.; Hu, Q.; Colombo, C.; Liskamp, R.; Rijcken, C.; Hennink, W. E.; Vermonden, T. Orthogonal Covalent Entrapment of Cargo into Biodegradable Polymeric Micelles via Native Chemical Ligation. *Biomacromolecules* **2023**, *24* (10), 4385–4396.

Hebels, E. R.; van Steenbergen, M. J.; Haegebaert, R.; Seinen, C. W.; Mesquita, B. S.; van den Dikkenberg, A.; Remaut, K.; Rijcken, C. J. F.; van Ravensteijn, B. G. P.; Hennink, W. E.; Vermonden, T. Mechanistic Study on the Degradation of Hydrolysable Core-Crosslinked Polymeric Micelles. *Langmuir* **2023**, *39* (34), 12132–12143.

Hebels, E. R.; Dietl, S.; Timmers, M.; Hak, J.; van den Dikkenberg, A.; Rijcken, C. J. F.; Hennink, W. E.; Liskamp, R. M. J.; Vermonden, T. Versatile Click Linker Enabling Native Peptide Release from Nanocarriers upon Redox Trigger. *Bioconjug. Chem.* **2023**, *34* (12), 2375–2386.

Posters and presentations

Posters/Pitches:

“The particle with the golden gun.“ - Dutch polymer days (DPD), Lunteren, 25-26MAR, 2019

“The particle with the golden gun.“ - Advanced functional polymers for medicines (AFPM), Helsinki, Finland, 5-7JUN, 2019

“Native chemical ligation as a drug ligation strategy in CriPec® nanoparticles.” – Brightlands polymer days, Veldhoven, 7-9NOV, 2021

“Native chemical ligation as a drug ligation strategy in CriPec® nanoparticles.” – Controlled release society, Aachen, Germany, 9-11MAR, 2022

“The covalent entrapment of fragile compounds into biodegradable polymeric micelles via a native chemical ligation crosslinker.” European symposium on controlled drug delivery (ESCDD), Egmond aan Zee, 12-15APR, 2022

“The covalent entrapment of fragile compounds into biodegradable polymeric micelles via a native chemical ligation crosslinker.” Utrecht institute for pharmaceutical sciences symposium (UIPS), Utrecht, 20MAY, 2022

“The covalent entrapment of fragile compounds into biodegradable polymeric micelles via a native chemical ligation crosslinker.” Advanced functional polymers for medicines (AFPM), Nice, France, 1-3JUN 2022, Best poster/pitch presentation award

“Traceless release of clickable peptides by disulfide cleavage.” – NWO Chains, Veldhoven, 21-22SEP, 2022, NOTE: Presenter ill, poster present

“Traceless release of clickable peptides by disulfide cleavage.” – Science for life, Utrecht, 14NOV, 2022

Oral presentations:

"Native chemical ligation for core-crosslinked micelle synthesis." – NWO Chains, Online parallel session, 7-8DEC, 2021

"The covalent entrapment of fragile compounds into biodegradable polymeric micelles via a native chemical ligation crosslinker." – Early career scientist day CRS BNLF, Egmond aan Zee, 12APR, 2022, Best oral presentation award

"A native chemical ligating crosslinker for the preparation of biodegradable core-crosslinked polymeric micelles and click conjugation of model compounds." – Globalization of pharmaceutics education network (GPEN), Minneapolis, USA, 19-22OCT, 2022

Acknowledgements

There practically is no “I” in science… It should have been called sc-we-ence. As this part of my career comes to an end now, I would like to mention the numerous people who contributed either directly or in support of these efforts as well as being a significant part of my life. I will likely not catch everyone, as I reflect so many of you have played a part, thank you for that.

Dear **Tina**, having met each other during the honors program of my bachelor some 9 years ago, you have been the primary individual to shape my education and navigating the academic world as a mentor as well as supervisor. You have always taken the time to help solve problems, share your knowledge, never lost patience, opened doors not many others would have and believed in me. I knew that I wanted to do a PhD under your supervision, especially after the major internship in my Master, which was a primary reason to return to Utrecht. When personal troubles arose my side, you showed support throughout, and as I reflect, this was quite the ride. Tina, I have learned the most from you and I cannot find words that do you justice, thank you for everything.

Dear **Wim**, your meticulous strive for quality science and thorough investigation has been a valuable lesson time and again. Even when everyone thinks everything has been accounted for, you still find gaps and errors. I take these lessons forward, being tough at times, it has certainly made me a more critical thinker. I would like to thank you for all the effort, care and time you devoted to these projects. The quality would never have reached what it is without you on board.

Dear **Cristianne**, I distinctly remember the first exchange we had when we finally met in person at Cristal Therapeutics at the start of this PhD journey. It was on the lines of: “Better stop smoking now that you are working with an oncology company!”. Although this did not happen during the PhD, I happily report now that this has finally come to fruition. I have seen the data… The betterment of society lies at your core, and what you achieved with Cristal Therapeutics is nothing short of remarkable, which I have the deepest respect for. I am proud and honored to have had the opportunity to work with you and would like to thank you for always giving your fullest commitment, resources and energy to the project. Also on a mentoring level your lessons are duly noted, you have no doubt helped pave my way to industry. I look forward with curiosity to what the future holds.

Dear **Rob**, every single meeting we have had I have walked away from feeling hopeful and inspired. Your chemical expertise have been a boon to this PhD work, and I learned

so much more chemistry from you, I cannot thank you enough. I very much miss working together and hope that also in future we will find new ways to connect. This also extends to **Matt**, for the brief time we were working closely together when you joined pharmaceutics was absolutely fantastic. The ideas we generated and motivation gained was unlike any other. If only we could have tried this sooner, maybe cancer would no longer be a worry. **Bas**, you have been the most helpful in figuring out the mechanisms of the degradation of our particles, this is certainly not forgotten. Thank you for the science, and also the fun. We should play padel again sometime.

Dear **Mies**, it is safe to say that no single person has taught me more technical skills than you have. Running a lab full of stressed PhDs where everything needs to happen yesterday cannot be easy. Finally being out of the pressure bubble myself aids in the recognition of that. That you still sing and smile is no doubt a tribute to your positive character, which is a rarity. Thank you for all your input, effort and understanding over all these years (that started already in my master).

Dear **Barbara**, you are the glue that holds the pharmaceutics department together. Thank you for all your assistance in setting up numerous meetings, providing support and countless karaoke sessions. I truly miss those. Additionally, thank you **Jamie**, **Antionette**, **Roel**, **Joep**, **Louis**, **Imro**, **Kim**, and **Esmeralda** for all the technical assistance provided and readiness to help out where it was needed and being approachable. It is not always a given. This also extends to the entire staff of the pharmaceutics department and beyond that the entire Utrecht institute for pharmaceutical sciences (**Enrico**, **Rene**, **Olivier**, **Robbert-Jan**, **Marcel**, **Massimiliano**, **Dirk**, **Tim**, **John**, **Javier** and many more) thank you for all your help and interest.

Also to the former team of Cristal Therapeutics, your input is duly noted and appreciated. My thanks especially go to **Jimmy**, **Marielle**, **Rachel**, **Michiel**, **Claudio**, **Alex** and **Marco**. You also contributed significantly to my understanding of how a company approaches research projects and, although the planning was frustrating at times, allowed me to become better at managing such projects. I especially cherish memories of the annual company outings, which were nothing short of fun and memorable thanks to such a fantastic team.

Finally I also extent my thanks to the team at Genmab who have been very welcoming, supportive and understanding during the final stretch of finishing this thesis. Particularly **Bart** and **Rita**, thank you for all your support.

Now to my dear paranymphs **Dario** and **Sanne**. **Dario**, more than 10 years ago we started this journey at the college of pharmaceutical sciences. Our friendship truly bloomed over

this period, as we both grew and also developed into critical scientists. Professional and personal, your council always has the highest of value, I would like to take this moment to say I appreciate you immensely and look forward to our future shenanigans (also in extension to you **Verginia**). And **Sanne**, you were truly a star student, I am pleased the chance to join pharmaceutics for a PhD arose and that you can stand by me for my own defense. The review in this thesis is a testament to your incredible writing skills. If anyone could answer questions on gold nanoclusters the best, it would certainly be you.

Speaking of former students (who have all been absolutely brilliant!), this also brings me to acknowledge **Felix**, you were my first and your data is also captured both in this thesis and a research paper. Thank you for all the efforts and providing your can-do attitude. **Stefanie**, I do not think any student at pharmaceutics has made more linkers than you have. In addition to your positive energy and motivation that never wavered even when things just didn't work out, you laid the foundation to the disulfide linker used in two chapters here. That you and **Sanne** were also both part of the U-select honors program was the cherry on top of it all for me. I truly look forward to our exchanges in future! **Barbara**, you certainly did not see the best phase of this PhD and myself as I was in the final sprint, which did not deter you from tackling a project met with great difficulty towards acid triggered drug release. I was impressed with your determination and tenacity. Thank you all truly, you helped make this project great and I have no doubt the future looks bright upon you all.

Now to my partners in crime at the pharmaceutics department. Dear **Johanna**, the times have often not been easy, and I am glad we always had each other to count on. And when it was time to have fun, we sure always did our best to enjoy it all. Thank you for your friendship, I carry forward the time spent with joy and look forward to sharing our future endeavors. The same I would like to extend to **Barbara**. **Sjaak**, you have the biggest heart and are amongst the dearest of friends to me, and so are you as well **Serena**. You both are wonderful together and I truly miss you in Utrecht. I also thank you **Sjaak** for all the chemistry you taught me, the council you have provided and always being there when I needed help. I am lucky to count you all as friends. Needless to say, I find it a real pity I no longer get to enjoy the daily company of so many colleagues/friends, particularly: **Mahsa**, **Stefania**, **Danny**, **Lucas**, **Eleonora**, **Vivian**, **Lies**, **Mathew**, **Carl**, **Blessing**, **Martina**, **Cristina**, **Ada**, **Deja**, **Jerry**, **Levent**, **Myriam**, **Matej**, **Matthijs**. Also a few additional mentions: **Jerry**, thank you for being such a wonderful peptide synthesis teacher, I learned so much form you. **Mahsa**, I truly cherish our friendship and your macroinitiator. **Lucas**, I always enjoy(ed) a good game of tennis with you! It's too bad you prefer lipids to polymers though. **Danny**, I especially enjoyed going

to our conferences together. **Stefania**, I always enjoy a good cocktail night together, I think chemists truly connect when it comes to mixing. **Cristina**, you are one of the most gifted scientists I know, keep it up and keep practicing pool. **Martina**, you are one of the kindest people I ever met. This could go on, but I have to finish this thesis for printing soon so thank you to the entire pharmaceutics team for having been a part of this journey, and in the future.

Dear Die Hards, **Esther**, **Thao**, **Anthon**, (and **Renier** when he is in town) I look forward with great excitement to every time we get to see each other and always have the best time. You are such wonderful people and scientists, I am glad we managed to keep our regular meetups going since the honors program. A good mixture of booze, scientific conundrums and humor is something we always excel at. Thank you for that.

Broski, dear **Max**, as we both set out to make something of our lives I still cannot believe sometimes how fortunate we have been to end up in such close proximity to one another. You truly are my brother from another mother (and father), and I certainly love you as such. With all the challenges we've both faced coming into this western world, for certain anything in future will be overcome, especially knowing that we will always be able to count on each other. I look forward to all the fun that is yet to come.

John, my man, one of the best parts of coming home for a visit is seeing your joyful visage and catching up on all the many things we needed and wanted to. Your company never seizes to entertain, share wisdom and spread joy. Thank you for your friendship of 11 years now (I believe). Looking forward to a time where paths will cross more often.

Dear **Naud**, we had lived together for 7 years in total, I want to thank you for all the wonderful times we had together. I always enjoyed philosophizing about life, having a good drink, talking nonsense and having a good laugh together. It is with great fondness I look back at this time, and with joy I look forward to our exchanges in future.

Dear **Marijke**, this success is one owing also to you. You brought me to the Netherlands and made every effort and investment to smooth my start into an entirely new world, now more than 10 years ago. This will never be forgotten, thank you for everything.

Beste **Annemarie**, ook jij hebt er voor gezorgd dat ik goed met mijn studies had kunnen beginnen. Het was altijd wel rustgevend om te weten dat er familie dichtbij is, ook was het in het verre Winschoten. Dankjewel voor al je moeite.

Lieber **Thomas**, Liebe **Marita**, ihr seid für mich wie eine Zweitfamilie, und es gibt mir jedes Mal aufs neue große Freude euch zu sehen, auf einen besuch in der Mühle wo es

immer gemütlich ist. Ich schätze euch sehr und bedanke mich für allen Rat und Gesellschaft die mit mir geteilt wurde. Bröseln wir bald mal wieder einen. Oder auch zwei…

Dear **Udo** and **Keiko**, thank you for all the wonderful years of friendship. There is not a more favorite place of mine in the world than to visit you on the Vumba and celebrate new year together as has been tradition since as long as my memory serves. Teaching me to play the piano is a gift beyond comprehension in value, especially when keeping up a bridge over troubled water when needed, thank you for that **Keiko**.

Dear **Sara**, I could not have asked for a better sister nor could I be any more proud of you. I often learn new wisdoms from you in so many ways, and really appreciate that we can talk science together as well. Thank you for all your support and belief all these years, it has helped a lot. I hope in future we will be living a bit closer again and see each other more often.

Lieblingsmütterchen und Lieber Gerhard, vielen Dank für all die Unterstützung die ihr mir über all diese Jahre gegeben habt. Ihr bemüht euch immer um uns beiden zur Seite zu stehen, uns eine gute Zukunft zu ermöglichen und Lösungen zu finden wenn es auch mal nicht so sanft abläuft. Habt Dank und seit gewiss, dass ich es sehr schätze. Ich hab euch beide unendlich lieb und freue mich sehr, dass wir diese Leistung alle zusammen feiern können. Bleibt schön gesund und freudig, es kommt sicherlich noch einiges hinzu.

Lieber **Albert**, dein Weg traf sein Ende als der meine nach Holland schickte. Mein Streben steht auch dir zum Dank, und sehr gerne hätte ich noch ein paar Jahre gehabt um es auch mit dir zu Teilen. Und wenn mich der Verlust deiner auch heute noch rüttelt, das wichtigste hast du gelehrt ist der Humor, den ich auch heute noch immer versuchen werde weiter zu führen.

My dearest **Irina**, although we did not exactly meet at the ideal time, I consider it the luckiest thing that we did. Any time I get to spend with you is never enough and exchanging thoughts with you always leaves me wiser afterwards. The time with you has been wholesome and fun and I look forward to what the future brings, together.

Sincerely yours,

Erik

Factum est